

Energy and Time Histograms: Fluxes determination in calorimeters

Khalid Hassoun*^{}

Vincent Boudry†^{}

March 7, 2024

Abstract

In high-granularity calorimetry, as proposed for detectors at future Higgs factories, the requirements on electronics can have a strong impact on the design of the detector, especially via the cooling and acquisition systems. This project aims to establish the typical fluxes in the calorimeters: deposited energy, number of cells above the electronics threshold, additional heat, and associated data, etc. Here, a software package is presented which outputs histograms for different selections of the calorimeter components from fully simulated physics and background events. The ILD calorimeter system is taken as a specific example, upon which different histograms are obtained for representative parts of the calorimeter and for various machine configurations. Examples of histograms are shown, along with all details of the data used and the simulation.

1 Introduction

One of the ways to improve the performance of the detectors for future Higgs, Electroweak or top factories (such as the ILC, CLIC, CEPC and FCC-ee) is to make use of the Particle Flow Algorithms [1]; this is the approach adopted for e.g. the SiD [2], ILD [3], CLICdet [4], CEPC baseline [5] and CLD [6] detector concepts. The PFA performance relies on imaging calorimeters, able to distinguish the individual contributions from neutral and charged particle showers, associated with a precision tracker system. The required granularity is typically below the centimetre scale for the ECAL, and slightly above for the HCAL [7, 5], resulting in 10 to 100 million channels for each of them.

The original designs, SiD and ILD, have been made for the ILC running conditions, with center-of-mass (CM) energy of 250 to 1000 GeV, and bunch rate of 5 Hz. Since then, other colliders have been proposed with widely different running conditions: CLIC can reach a much higher CM energy (3 TeV) and repeating rates. FCC-ee and CEPC would have continuous operation with huge luminosity for the Z-boson peak at a CM energy of 91.2 GeV.

Given the need to potentially adapt the calorimetric system to various conditions, estimating the static and dynamic behaviour of particle energy deposition became necessary. The former can be represented by the energy distribution along with its spatial derivatives (radius, azimuthal angle), and the latter can be represented by the time distribution along with its derivatives. These distributions will serve as a guide to the power needed from the electronics to optimize the electronics and prevent them from overshooting the target, thereby ensuring they do not adversely affect the calorimeter's physics.

This paper presents a software package ¹ that enables obtaining the desired distributions for any chosen part of the calorimeter from a full simulation of the main expected physics processes. We apply it here first on the simulated ILD calorimeter, which is a very suitable choice because the ILD calorimeter is divided into logical coordinates, which facilitates the selection of various parts of the

*University of Hawaii at Manoa

†Laboratoire Leprince-Ringuet (LLR), CNRS, École polytechnique, Institut Polytechnique de Paris, 91120 Palaiseau, France.

¹It can be found here: <https://github.com/LLR-ILD/CalorimeterFluxes>

calorimeter.

The paper is divided into four parts, starting with an introduction that presents the terminology used, in detail. In the next part, the produced sets of histograms are explained, including their description and classification. The used data sample is then detailed, and finally, we present some results along with preliminary conclusions.

2 Terminology

The calorimetric system of ILD is composed of 11 systems; some are redundant as options. Two options are proposed (and simultaneously simulated) for the ECAL, named after their sensor's technology: ScECAL for the scintillators and SiW-ECAL for the Silicon. Also, two options are available for the HCAL. The AHCAL is based on tiles of scintillators, while the SDHCAL's sensors are segmented Resistive Plate Chambers. Both the ECAL and HCAL have two main parts: the Barrel for the central region and the Endcaps for the forward and backward regions. The Barrel has an inner shape of an octagonal prism, closed by 8 "Staves". The Endcaps inner shape is a square, formed by 4 quadrants. They are complemented by "rings" filling the gaps between the Barrel and Endcaps for the HCAL, and between the Endcaps and the beam tube for the ECAL. Each system may be divided into a hierarchy of sub-regions: stave or quadrant, modules, towers, layers, cells, each addressed by a logical coordinate: C:S:M:T:L:I:J². This segmentation follows that foreseen for the electronics, and therefore might be a bit complex in terms of geometry.

A hit is defined as a cell whose energy exceeds the electronics threshold defined for the system. The threshold is set at 1/3rd or 1/4th of a "MIP" energy scale, defined as the most probable value of the energy distribution yielded by a minimum ionizing particle (in practice medium energy muons) crossing the sensor with a normal incidence.

2.1 Direct and Indirect Selections

In our analysis, we distinguish between what we call direct selections and indirect selections. The former is given by directly stating the calorimeter coordinates. For example, the selection {system = ScEcalBarrel, Stave = 1, Module = 2, Tower = 5} is a direct selection of the calorimeter coordinates. An indirect selection will be given through what we call Boolean complex functions. For instance, the selection {all modules and layers satisfying the equation: 2Module + 2Layer = 10} is an indirect selection because the choices of modules and layers depend on each other through an equation (the same as specifying a boolean function that is true if and only if the coordinates satisfy the given equation). If no selection is imposed on a coordinate, all such coordinates will be included. For instance, in the direct selection example above, no condition is requested on the layers; this means that all the layers are included. The same applies to the indirect selections.

The introduction of these indirect selections was necessary in some special cases to restore the symmetry in some distributions as the direct selections were not enough in providing a separation of distributions, as will be shown later.

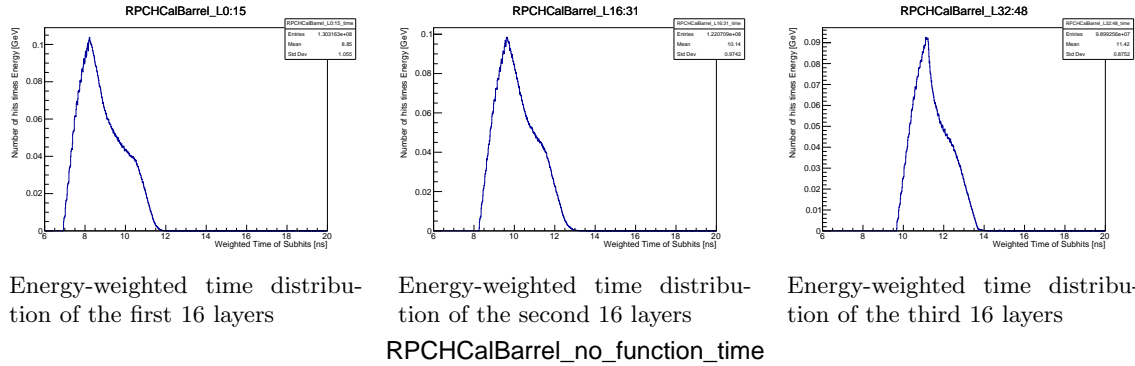
2.2 Primary and Secondary histograms

The histograms in which we store direct information from the hits and events are called primary, while the histograms that are built from other histograms are called secondary. For example, one important histogram is that of energy. The primary histogram would have the unit of the X-axis to be in GeV. On the other hand, one secondary histogram would be exactly the same, but with the unit being a MIP. This secondary histogram is just a scaling of the X-axis of its primary counterpart.

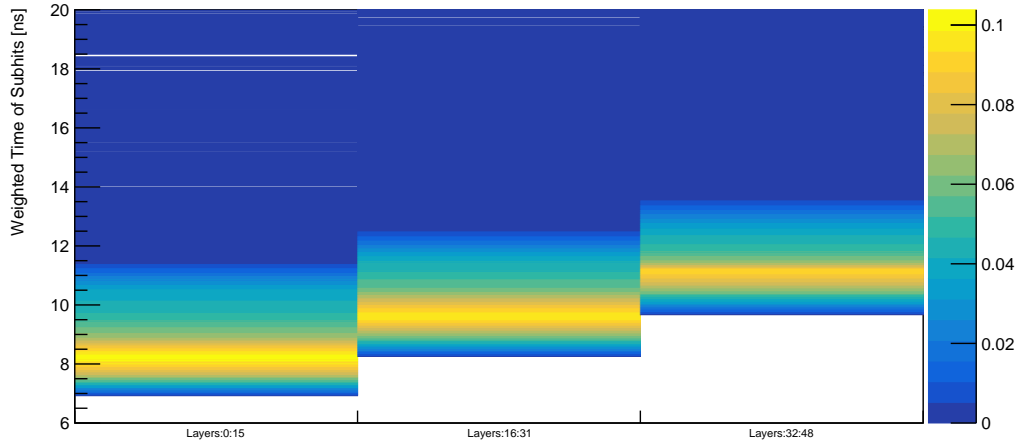
²C stands here for the calorimeter System, S for the Stave, M for the module, T for the tower, L for the layer, I and J for the logical coordinates

2.3 1D and 2D histograms

For practical reasons, the primary histograms are 1D, meaning the Y-axis represents the number of hits, events, or energy-weighted hits, while the X-axis corresponds to a physics quantity such as energy, time, or number of hits. To enhance clarity, multiple 1D histograms are combined into a single 2D histogram, where each bin represents a 1D histogram. For example, consider the energy distribution of the following direct selection: {System = ScEcalBarrel, Module = 1, Layer=(0-9)}. This selection will give the energy distribution for the system ScEcalBarrel in its module 1 and the first 10 layers (and indirectly for all staves and cells). Considering the same distribution, but with the layers being from 10 to 19 and another one with the layers ranging between 20 and 29, will produce 3 different 1D histograms. We can put them together in one 2D histogram with 3 bins, such that each 1D histogram represents a single bin. The 1D Y-axis becomes the 2D Z-axis, while the 1D X-axis transitions to the 2D Y-axis. This will give an aid in visualization and will show the angular distribution. An illustrative example is shown in figure 1.



Energy-weighted time distribution of the first 16 layers Energy-weighted time distribution of the second 16 layers Energy-weighted time distribution of the third 16 layers



Energy-weighted time distribution of all the layers in RPCHCalBarrel system, where each bin represents a 1D histogram. 'no_function' in the title stands for direct selections (no boolean functions involved for indirect selections)

Figure 1: Time distributions of shooting muons in the RPCHCalBarrel system, for verification purposes. The three 1D histograms represent the energy-weighted time distribution for three sequential groups of 16 layers each. The 2D histogram is the collection of the 1D histograms in one plot. The 2D histograms can be very helpful in visualizing the angular distribution. It can be seen clearly that there is a time shift because the muons travel in the layers in order.

3 Histogram Sets

As indicated in the introduction, the software is versatile in that it can be easily adapted to produce any types of desired histograms. For our current analysis, we are concerned with mainly 8 histograms:

5 of primary type and 3 of secondary type.

3.1 Primary Histograms

Some distributions are split into low-scale and high-scale parts; the low-scale part uses fixed, high-density binning, while the high-scale part starts at the end of the low-scale and is automatically re-scaled upwards to capture all the tails. The binning is defined so that a complete spectrum can be rebuilt by regrouping bins from the low-scale part.

The following primary histograms have been defined:

1. **Lower-Scale Energy:** This is the histogram of the energy distribution of simulated calorimeter cells. It can be used to define the MIP of a system, and check the incidence of the thresholds variations on the number of hits. Depending on the type of sensor, it will peak near 0 or at MIP scale.
2. **Upper-Scale Energy:** This histogram capture the high energy tails of the cells. After calibration, it will give access to the dynamic range required for the electronics.
3. **Lower-scale Number of Hits:** This histogram stores the number of hits until a certain value. This aids in identifying which events contribute most to data flux and the power consumption from conversion (ADC and TDC), under various hypotheses of noise, and electronics treatments, emulated by the digitization. The X-axis is the number of hits and the Y-axis is the number of events.
4. **Upper-Scale Number of Hits:** This histogram captures the high number of hits tails. Combined with the lower-scale part, it allows calculating the average number of hits per event, hence the data rates when scaled by the luminosity and cross-section.
5. **Weighted Time:** This histogram presents the time distribution of simulated calorimeter sub-hits, with each weighted by its energy. This will end up with the energy plotted as a function of time. This histogram give the overall timing behaviour, which is useful to design the electronics making use of the timing in the particle showers reconstruction. Currently, this corresponds to the lower-scale part (up to 20 ns). A higher-scale part would be useful to estimate the contribution from neutrons of previous events, and will be implemented.

3.2 Secondary Histograms

1. **Scaled Upper-Scale Energy:** This is just scaling the Upper-Scale-Energy X-axis' histogram by dividing it by the MIP. It is helpful to see the trailing effect as a function of the MIP instead of the normal GeV unit that is not always illuminating. The maximum range of this histogram give the dynamic range of the electronics, when divided by the precision needed on the low-energy scale (i.e. the precision on the MIP).
2. **Lower-Scale Power:** The power histogram is always a function of the primary histogram, but the exact function form depends on the electronics implementation. Usually, it is one of two things: either expressed through the following equation: $Power = a \times Energy + b$ where a and b are real positive numbers with a representing the proportionality constant between the power and energy and b is the power-on offset of the electronics or $Power = a \times \#hits\text{-above-given threshold}$. The latter case is for when ADCs are only triggered at some energy with a constant power consumption.
3. **Upper-Scale Power:** This is just applying the power equation to the upper-scale-energy histogram to cover all the power required from the electronics.

4 Geometric Selections

This section features geometric plots generated by shooting medium-energy muons. These plots display the hits' geometric coordinates on the x-axis and y-axis, while a colour bar on the z-axis represents properties such as staves, modules, etc.

4.1 Direct Geometric Selections

Geometric selections should be made such that different selections would be grouping obvious symmetric regions, while yielding distributions illustrating the evolution of asymmetric ones. Taking the Silicon-ECAL-Barrel system as an illustrative example, the figure 2 shows how the staves are distributed in an azimuthal symmetric manner as the beam originates from the origin. Thus, there is no need to make a selection on a specific staff as they all yield the same distributions. Additionally, because there are 30 layers, it is impractical to select each layer individually; doing so would result in many similar distributions, which is not useful. The categorization here is that the layers are always categorized into three blocks with each block containing 10 layers.

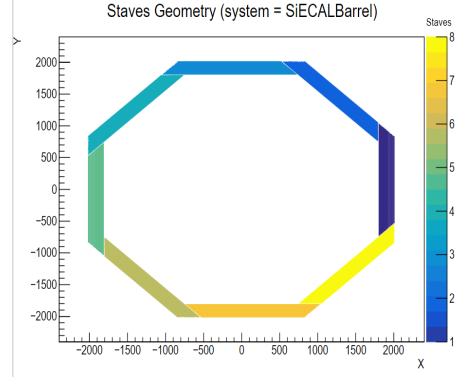


Figure 2: Staves numbering of cells of the SiECALBarrel system in the x - y plane

Referring to figure 3a, it is clear that the layers' number is an indicator of the depth or the radial profile. To get the polar-angle profile, the extension of one of the staves (arbitrarily chosen as all the staves yield the same behaviour) is shown along the Z-axis in figure 3b. The central module (module 3) is the one at $\theta = 90^\circ$ and the other modules present deviations from this right angle. To study the evolution of the distributions along the polar angle, different selections must be made on different modules. It is true that module 2 and 4 are symmetric, and the same applies to modules 1 and 5; however, making a selection on each of them would serve as a cross-check with the prediction that the yielded distributions are to be symmetric. In conclusion, to study the radial profile, three selections are made on the layers, with each selection corresponding to one block of 10 layers. To study the polar-angle profile, five selections are made on the modules, with each selection corresponding to one module. In total, this approach results in $3 \times 5 = 15$ selections.

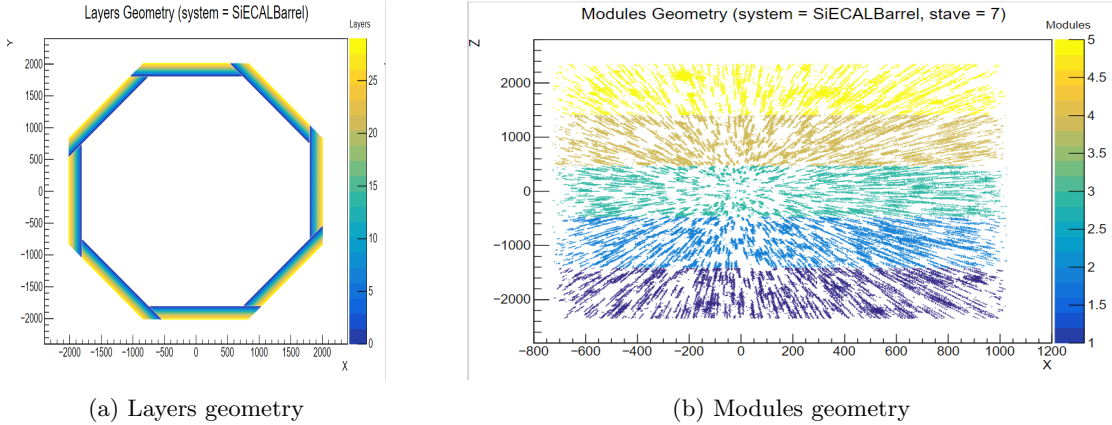


Figure 3: Layers and modules geometry of the Silicon-ECAL-Barrel system

4.2 Indirect Geometric Selections

In certain systems, direct selections alone are insufficient, necessitating the use of indirect methods. Taking the scintillator-HCAL-Barrel system as an illustrative example, as in the previous one, the system has a symmetry of 8 in polar angle and the radial profile can be studied through the layers. The HCAL comprises 48 layers, which, as in the previous example, are categorized into three blocks, each containing 16 layers. This is directly addressed by the direct selection on Layers, and indirectly grouping the Staves. Refer to figure 4.

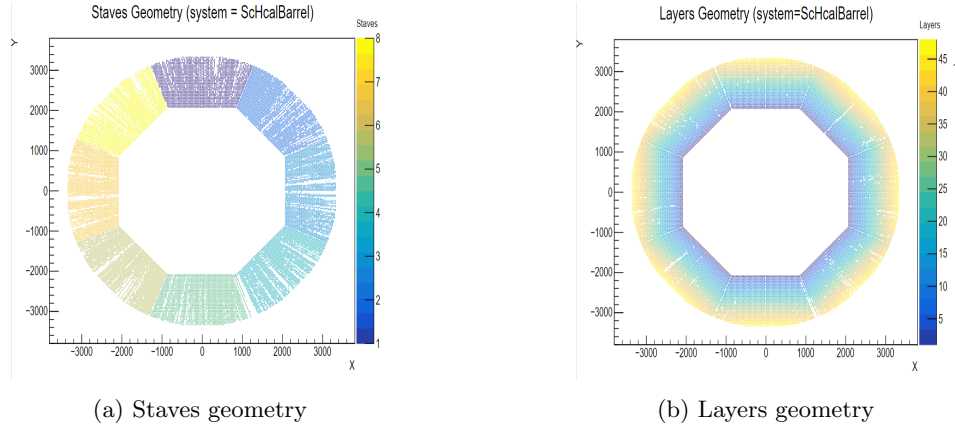


Figure 4: Layers and modules geometry of the scintillator-HCAL-Barrel system

However, for the evolution of the azimuth-angle profile, selections of modules and towers are not appropriate: the modules indices are presented for stave 5 in figure 5a. The HCAL barrel has only 2 modules, symmetric regarding their azimuthal angle. Each stave has 2 towers, displayed for the stave 5 in figure 5b, symmetric in polar angle. Therefore, applying an indirect selection to cell indices becomes necessary.

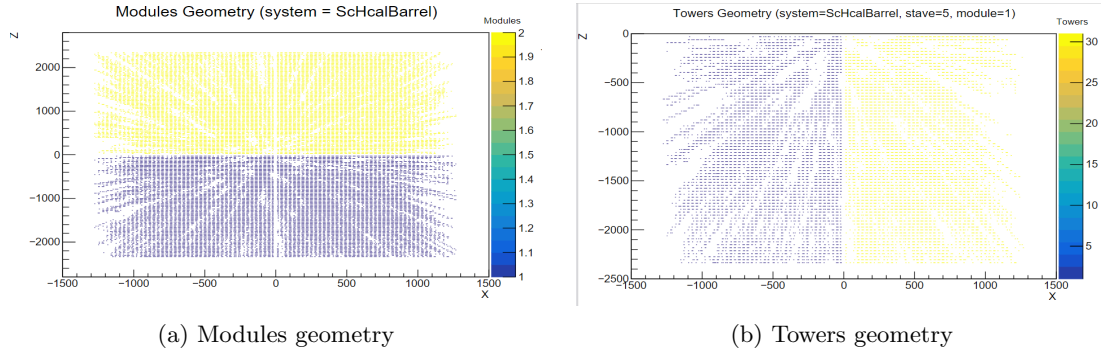


Figure 5: Layers and modules geometry of the scintillator-HCAL-Barrel system

A combination of M and J is defined by the equation $MJ = 2J(M - 1.5) + 38$, where J is the logical position of the cell along z and M is the module index. MJ takes values between 0 and 76, symmetric in z, as shown in figure 6.

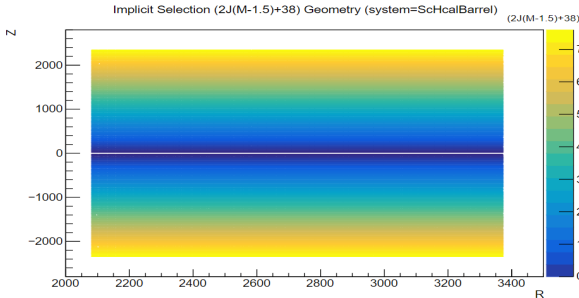


Figure 6: MJ coordinate geometry

MJ values are categorized into three groups: 0-29, 30-59, and 60-76. Thus, the total number of selections is $3+3=6$ selections. From a coding perspective, a Boolean function includes hit information only if the MJ value falls within the selected block, returning 'True' in these cases. For this function, we choose the arbitrary name to be *complex.happy*.

In this example, the radial profile is studied by the direct selection of three groups of layers and the polar-angle profile is looked at by an indirect selection imposed on the coordinate MJ, also by grouping them in three categories.

5 Simulated Data Samples

The generated histograms described above count events and timed energy distributions for a given process simulated sample. To estimate the total event rates, hit rates or power, the histograms must be properly scaled and then summed for all (or at least the main) possible contributing physics processes or machine background.

For physics processes, the histogram scaling is $\sigma \times \mathcal{L}_{\text{int.}}/N_{\text{evt}}$, where σ is the cross-section, $\mathcal{L}_{\text{int.}}$ is the instantaneous luminosity, and N_{evt} is the number of simulated events.

In the case of machine background, simulations are conducted over a specified number of bunch-crossings. The histogram scaling must then be $f_{\text{BX}}/N_{\text{BX}}$, where f_{BX} and N_{BX} are the frequency of colliding and the number of simulated bunch-crossings.

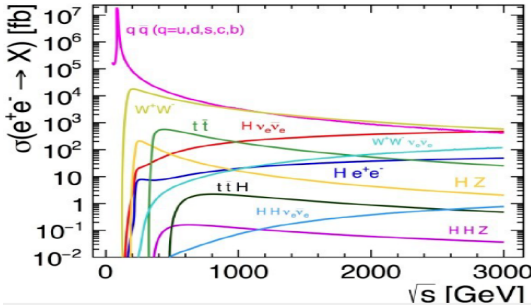
For the FCC studies, the simulated data are run at four collider configurations, defined by a center-of-mass (CM) energy, and an instantaneous luminosity, display in figure 7

1. **91.2 GeV:** The Z pole;
2. **162.5 GeV:** W^+W^- threshold;
3. **240 GeV:** The resonance energy of the $ee \rightarrow ZH$ decay channel;
4. **365 GeV:** Above the $t\bar{t}$ threshold.

(The details of the simulation are shown in appendix A):

5.1 Physics Data

For each CM energy, we simulate the dominant physics processes with the smallest biases. At 91.2 GeV, the simulated Z-decay channels are (a) $ee \rightarrow qq$ and (b) $ee \rightarrow ll$ where $q = u, c, s, b, d$ and $l = \mu, \tau$. At 162.5 GeV, we simulate the channels (a) and (b) as for 91.2 GeV and add the channel (c) $ee \rightarrow WW$ since we are around the resonance energy of the W production. At 240 GeV, we simulate channels (a), (b), and (c) and add channel (d) $ee \rightarrow ZH$. At 365 GeV, (a), (b), (c), and (d) are simulated and added to channel (e) $ee \rightarrow t\bar{t}$.



Cross-section as per decay channels

Since Bhabha scattering can be used in calibration and cross-check, this might be helpful.

The simulated data for each decay channel at each energy scale comprise 10,000 events, for which the cross-section is calculated. The data are summarized in tables (1 - 4).

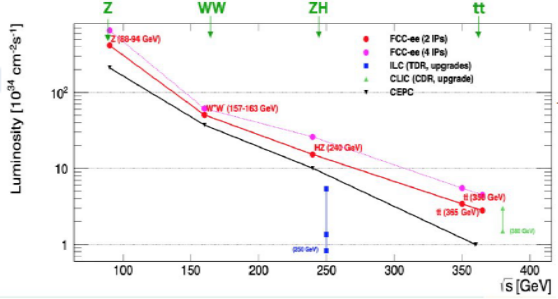


Figure 7: Luminosity of the different energy scales. At 91.2 GeV, the considered run is FCC-ee (4 IPs).

The $ee \rightarrow ee$ is treated separately, due to the interference between the production and scattering processes, and the domination of the Bhabha cross-section at low angle. An angular cut of 10 degrees is applied on the resulting electron and positron to avoid the huge forward and backward scattering at low angle. The simulation phase space domain is partitioned into two parts based on the mass of the outgoing electron-positron system, set at a value of 30 GeV. This partitioning allows simulating fewer events from the channel with a smaller cross-section and to save simulation time if needed. It also aids in the visualization.

5.2 Machine Background

A sizable amount of the contribution in the calorimeters can find an origin in the beam-induced backgrounds, either directly, for the parts close to the beam pipe, or indirectly via back-scattered particles on the elements at low radius. Several beam-induced backgrounds must be modelled [3] (section 6.5), [8] (section 1.3.1), [9]:

- Bremsstrahlung: the strong in-beam electric fields near the interaction region will produce photons and "incoherent" electron-positron pairs, mostly in the direction of the beams, but which might interact with neighbouring materials and scatter back in all the detector. They are highly dependent on the beam bunches geometry. It is simulated using the Guinea-Pig++ package[10].
- Synchrotron Radiation: arise from the beam focusing and steering in the final stages near the detector. It is usually shielded to avoid illuminating any part of the detector, but back-scattering is hard to avoid completely. It is highly dependent on the detailed implementation of elements along the beamline, and can then be estimated by e.g., the BBBrem and GuineaPig++ packages. It was not considered in this study.
- Muons: at linear colliders, non-Gaussian tails of the beam can interact with nearby material, creating muon pairs, which will follow the beam line all the way to the detector. They can be deflected by toroidal magnets. They are not considered here.
- Neutrons: A flux of neutrons will be produced by all the above sources hitting heavy elements. Previous estimations show it must be low and can be neglected [11].

Table 1: 91.2 GeV

($N = 10000$, $\mathcal{L}_{\text{int.}} = 1.4 \times 10^{-3} \text{ fb}^{-1} \text{ s}^{-1}$)

Channels	σ (10^5 fb)	$\sigma \times \mathcal{L}_{\text{int.}}/N$ (s^{-1})
$ee \rightarrow qq$	344	4.82
$ee \rightarrow ll$	34.6	0.484
$ee \rightarrow ee$		
($M_{ee} < 30 \text{ GeV}$)	1.01	0.0141
$ee \rightarrow ee$		
($M_{ee} > 30 \text{ GeV}$)	57.8	0.809

Table 2: 162.5 GeV

($N = 10000$, $\mathcal{L}_{\text{int.}} = 2.14 \times 10^{-4} \text{ fb}^{-1} \text{ s}^{-1}$)

Channels	σ (10^5 fb)	$\sigma \times \mathcal{L}_{\text{int.}}/N$ (s^{-1})
$ee \rightarrow qq$	1.55	3.32×10^{-3}
$ee \rightarrow ll$	0.241	5.16×10^{-4}
$ee \rightarrow WW$	0.0504	1.08×10^{-4}
$ee \rightarrow ee$		
($M_{ee} < 30 \text{ GeV}$)	0.240	5.14×10^{-4}
$ee \rightarrow ee$		
($M_{ee} > 30 \text{ GeV}$)	12.9	2.76×10^{-2}

Table 3: 240 GeV

($N = 10000$, $\mathcal{L}_{\text{int.}} = 6.9 \times 10^{-5} \text{ fb}^{-1} \text{ s}^{-1}$)

Channels	σ (10^5 fb)	$\sigma \times \mathcal{L}_{\text{int.}}/N$ (s^{-1})
$ee \rightarrow qq$	0.550	3.80×10^{-4}
$ee \rightarrow ll$	0.100	6.88×10^{-5}
$ee \rightarrow WW$	0.167	1.15×10^{-4}
$ee \rightarrow ZH$	0.00204	1.41×10^{-6}
$ee \rightarrow ee$		
($M_{ee} < 30 \text{ GeV}$)	0.120	8.29×10^{-5}
$ee \rightarrow ee$		
($M_{ee} > 30 \text{ GeV}$)	5.92	4.09×10^{-3}

Table 4: 365 GeV

($N = 10000$, $\mathcal{L}_{\text{int.}} = 1.2 \times 10^{-5} \text{ fb}^{-1} \text{ s}^{-1}$)

Channels	σ (10^5 fb)	$\sigma \times \mathcal{L}_{\text{int.}}/N$ (s^{-1})
$ee \rightarrow qq$	0.228	2.74×10^{-5}
$ee \rightarrow ll$	0.0430	5.16×10^{-6}
$ee \rightarrow WW$	0.111	1.33×10^{-5}
$ee \rightarrow ZH$	0.00123	1.47×10^{-7}
$ee \rightarrow tt$	0.00372	4.46×10^{-7}
$ee \rightarrow ee$		
($M_{ee} < 30 \text{ GeV}$)	0.0499	5.99×10^{-6}
$ee \rightarrow ee$		
($M_{ee} > 30 \text{ GeV}$)	2.58	4.65×10^{-6}

6 Results

The histograms are obtained for 11 different systems with various direct and indirect selections; just a few of them are displayed here as an illustration³. The plots shown in this section correspond to all the merged physics processes at a specific energy, each scaled by its weight according to tables (1-4) along with the weighted machine background.

6.1 Angular Distribution

The number-of-hits histograms for the ECAL Barrel at angle $\theta = 90^\circ$ (module 3) show that most of the hits are in the first 2 layer blocks (the first 20 layers).

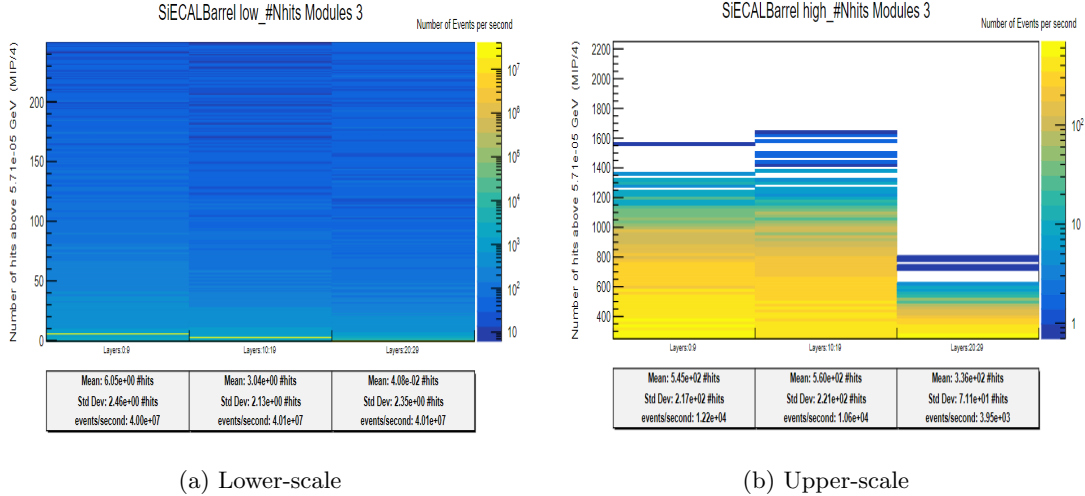


Figure 8: Lower and upper scales of the number-of-hits-above-(MIP/4) histograms for 3 different layers blocks in module 3 of the silicon-ECAL-Barrel system at $\sqrt{s} = 91.2$ GeV

To study the polar-angular behaviour, the same histogram types are shown but for the first layer block (It is one of the blocks with most of the hits) with all the modules as further selections.

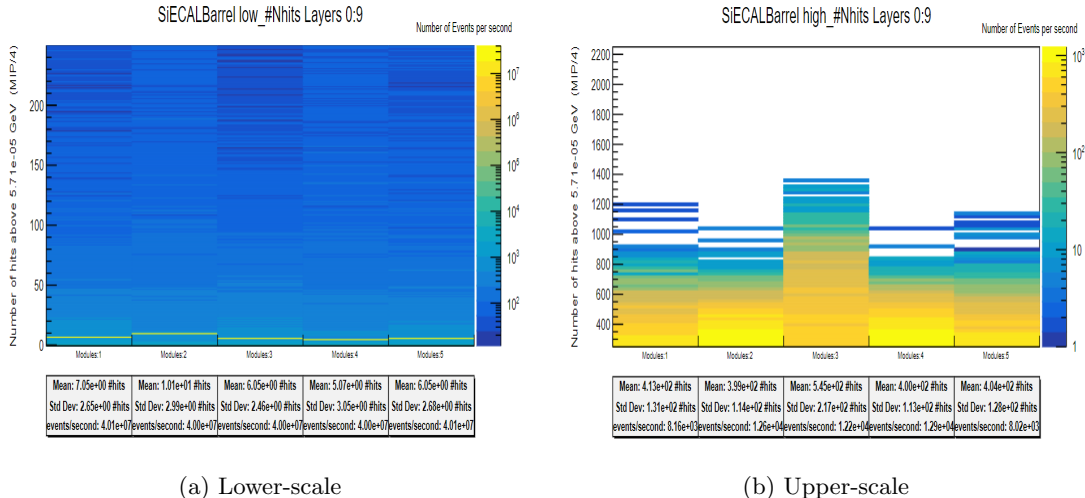


Figure 9: Lower and upper scales of the number-of-hits-above-(MIP/4) histograms for 5 different modules in the first 10-layer block of the silicon-ECAL-Barrel system at $\sqrt{s} = 91.2$ GeV

³The full set of histograms can be found here: <https://github.com/LLR-ILD/CalorimeterFluxes/tree/main/Histograms>

The conclusion is that there is no significant angular dependence as all the modules exhibit similar statistics except for the central module. The uniqueness in the central-module behaviour traces back to the fact that at 91.2 GeV, the output particles are produced back-to-back, giving more hits near $\theta = 90^\circ$.

In contrast, the analysis of the HCAL Endcap leads to different conclusions. First, like the ECAL, most of the hits are not recorded in the third layers block (the last 16 layers). This can be seen from the central towers (towers 4-7 are chosen). Central towers are the closest to the beam pipe, and hence they get most of the hits.

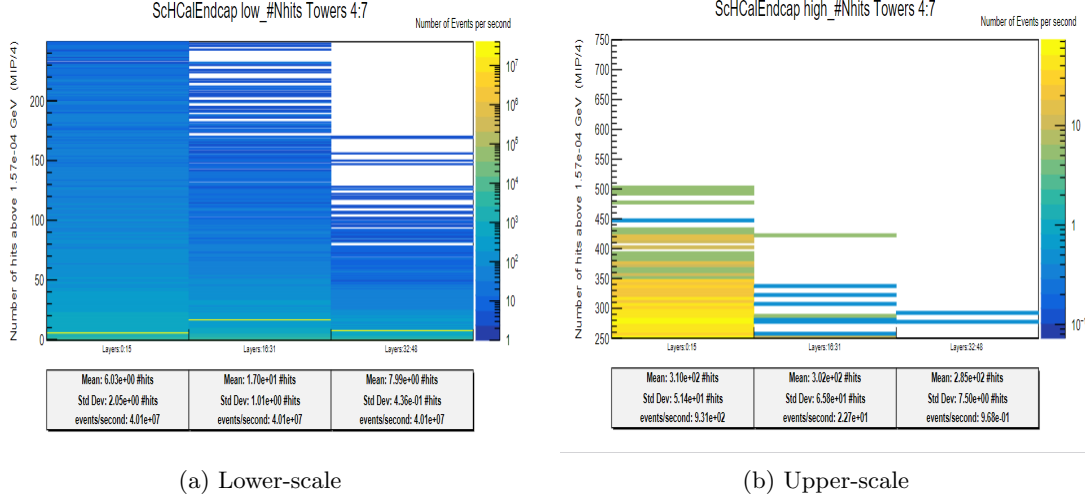


Figure 10: Lower and upper scales of the number-of-hits-above-(MIP/4) histograms for 3 different layers blocks in towers 4-7 of the scintillator-HCAL-Endcap system at $\sqrt{s} = 91.2$ GeV

Referring to Figure 11, the right side is roughly symmetrical to the left side in the lower and upper scale plots, consistent with the prediction that the line of symmetry here originates from the beam pipe. However, if our analysis is limited to one side only (i.e., the first 8 towers or the last 8 towers), it becomes evident that the tower selections are asymmetric, and the angular dependency is significant here, unlike in the case of the ECAL Barrel, where all modules exhibited symmetric distributions except for the central module, as discussed. This difference is attributed to the fact that the central towers (i.e., towers 4-7 or towers 8-11) are closer to the beam pipe than the other towers, and hence, they receive more hits.

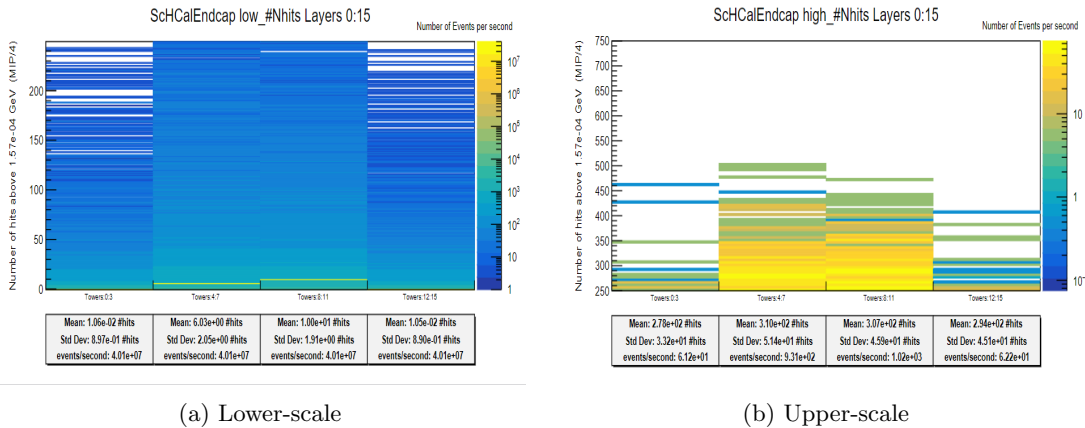


Figure 11: Lower and upper scales of the number-of-hits-above-(MIP/4) histograms for 4 different towers selections in the first 16-layer block of the scintillator-HCAL-Endcap system at $\sqrt{s} = 91.2$ GeV

6.2 Dynamic Range

Another important result that can be extrapolated from these plots is the dynamic range represented by the maximum energy in the unit of MIP. The questions that need to be answered are what is the maximum energy to be covered by the electronics and if it also depends on the beam energy. Thus, the histogram type that is needed here is the scaled upper-scale energy.

It can be seen that the maximum energy falls in the same range for both $\sqrt{s} = 91.2$ GeV and $\sqrt{s} = 240$ GeV. The example chosen is tower 0 ($\theta = 90^\circ$) in the silicon-ECAL-Endcap system; however, different tower selections would yield similar results.

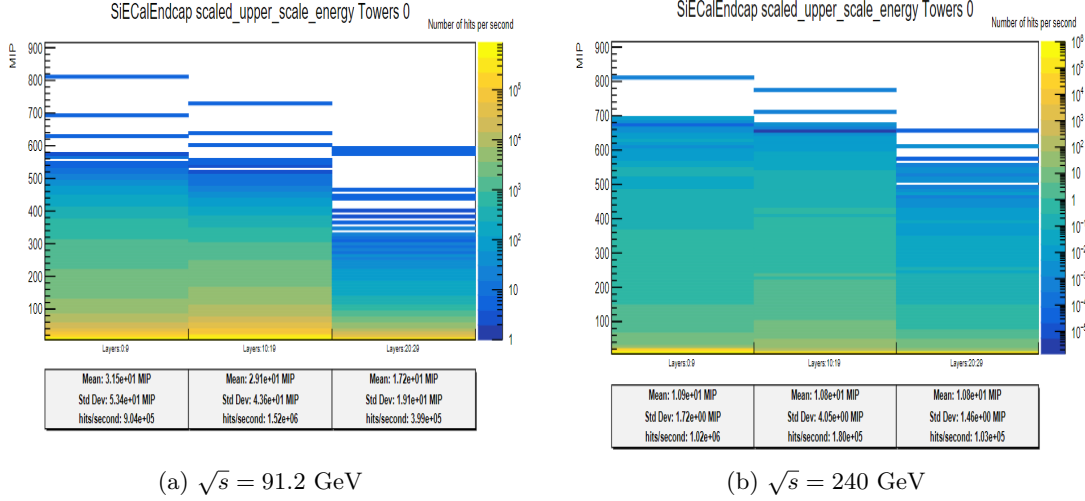


Figure 12: Scaled upper-scale energy distributions in the MIP unit of 3 different layer blocks at tower 0 of the silicon-ECAL-Endcap system at $\sqrt{s} = 91.2$ GeV and $\sqrt{s} = 240$ GeV

This behaviour is not obeyed in the RPC. Figure 13 shows 2 things:

1. The energy range is much bigger for the RPC compared to the silicon. The maximum energy was around 800 MIP for the silicon, whereas for the RPC system, it reached 11000 MIP and 25000 MIP for beam energy of 91.2 GeV and 240 GeV, respectively.
2. The beam energy makes much difference in the dynamic range for the RPC.

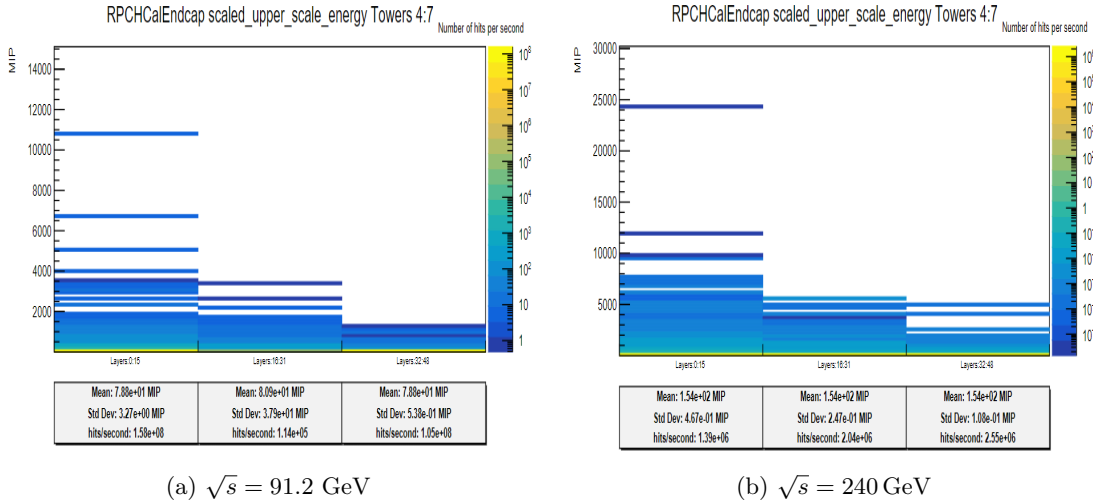


Figure 13: Scaled upper-scale energy distributions in the MIP unit of 3 different layer blocks at towers 4-7 of the RPC-HCAL-Endcap system at $\sqrt{s} = 91.2$ GeV and $\sqrt{s} = 240$ GeV

Conclusion

In this project, a versatile software package was introduced to produce different sets of histograms of different parts of the calorimeter. At four different energy scales and different runs, dominating physics processes and machine background were simulated in ILLD to capture the full output of the calorimeter distributions. Different results were shown of applying the package on the output physics.

The future work will entail an extension of this package to other parts of the ILLD detector, such as the tracker. Additionally, an expansion can be applied on the calorimeters of other detectors rather than the ILLD. Finally, on the technical side, LCIO [12] package is to be replaced with EDM4hep [13] which is the common event-data model of key4HEP stack software [14] aiming for more coherence with other HEP detectors and experiments.

Appendix A: Physics Data Simulation

At the generator level, the data is simulated by Whizard 3.0.3 [15]. The hadronization is simulated by Pythia6 [16]. Whizard and Pythia are integrated together using EventProducer package [17].

At the detector level, iLCSoft software framework [18] is used. The used version is v02-02-02. DD4hep [19] is the common detector geometry description in iLCSoft which is component based. DDG4 [20] is the component affiliated with the full simulation, which relies on Geant4 [21]. Thus, the ILD geometry is described using DD4hep as explained above. Afterward, a python program called ddsim, being a part of DD4hep, is used to run the full simulation. The detector geometry has multiple versions. The one used here is ILD_L5_v02.

The output of the full simulation is given in LCIO format, which is the common event-data model of iLCSoft. Our software package starts operating by decoding the slcio files (LCIO files format) and retrieving the information to be fed into the selected histograms.

References

- [1] J.-C. Brient and H. Videau, “The calorimetry at the future e+ e- linear collider,” in *Proceedings of APS / DPF / DPB Summer Study on the Future of Particle Physics (Snowmass 2001)*, Snowmass, Colorado, 30 Jun - 21 Jul 2001, Pp E3047., 2002.
- [2] M. Breidenbach, J. E. Brau, P. Burrows, T. Markiewicz, M. Stanitzki, J. Strube, and A. P. White, “Updating the SiD Detector concept,” *arXiv:2110.09965 [hep-ex, physics:physics]*, Oct. 2021. [Online]. Available: <http://arxiv.org/abs/2110.09965>
- [3] The ILD Collaboration, “International Large Detector: Interim Design Report,” *ArXiv200301116 Hep-Ex Physicsphysics*, Mar. 2020. [Online]. Available: <https://arxiv.org/abs/2003.01116>
- [4] Lucie Linssen (CERN), Akiya Miyamoto (KEK), Marcel Stanitzki (DESY), Harry Weerts (ANL), Ed., *Physics and detectors at CLIC: CLIC conceptual design report*, ser. CERN. Geneva: CERN, 2012, no. 2012,3. [Online]. Available: <https://clidp.web.cern.ch/content/conceptual-design-report>
- [5] The CEPC Study Group, “CEPC Conceptual Design Report: Volume 2 - Physics & Detector,” *arXiv:1811.10545 [hep-ex, physics:hep-ph]*, Nov. 2018. [Online]. Available: <http://arxiv.org/abs/1811.10545>
- [6] N. Bacchetta, J.-J. Blaising, E. Brondolin, M. Dam, D. Dannheim, K. Elsener, D. Hynds, P. Janot, A. M. Kolano, E. Leogrande, L. Linssen, A. Nürnberg, E. F. Perez, M. Petrič, P. Roloff, A. Sailer, N. Siegrist, O. Viazlo, G. G. Voutsinas, and M. A. Weber, “CLD – A Detector Concept for the FCC-ee,” Dec. 2019. [Online]. Available: <https://arxiv.org/abs/1911.12230>
- [7] M. A. Thomson, “Particle Flow Calorimetry and the PandoraPFA Algorithm,” *Nucl. Instrum. Meth.*, vol. A611, pp. 25–40, 2009.
- [8] T. Behnke, J. E. Brau, B. Foster, J. Fuster, M. Harrison, J. M. Paterson, M. Peskin, M. Stanitzki, N. Walker, and H. Yamamoto, “The International Linear Collider Technical Design Report - Volume 1: Executive Summary,” Tech. Rep. ILC-REPORT-2013-040, ANL-HEP-TR-13-20, 1347945, Jun. 2013, 00272. [Online]. Available: <http://www.osti.gov/servlets/purl/1347945/>
- [9] A. Ciarma and M. Boscolo, “Background calculations in the FCC-ee,” presented at FCC Week 2023 - London 06/06/2023. [Online]. Available: https://indico.cern.ch/event/1202105/contributions/5390909/attachments/2660725/4609253/2023-06-06_FCCWeek_ciarma.pdf
- [10] D. Schulte, “Beam-beam simulations with guinea-pig,” in *Proceedings of the 5th International Computational Accelerator Physics Conference, ICAP '98*, K. Ko and R. D. Ryne, Eds. Monterey, CA, USA: SLAC, Sep. 1999, pp. 127–131, report number: CERN-PS-99-014-LP; CLIC-Note-387, SLAC-R-580.
- [11] R. Kleiss and H. Burkhardt, “BBBREM: Monte Carlo simulation of radiative Bhabha scattering in the very forward direction,” *Comput. Phys. Commun.*, vol. 81, pp. 372–380, 1994, eprint: hep-ph/9401333.
- [12] “LCIO.” [Online]. Available: <https://github.com/iLCSoft/LCIO>
- [13] “EDM4hep.” [Online]. Available: <https://github.com/key4hep/EDM4hep>
- [14] “Key4hep.” [Online]. Available: <https://github.com/key4hep>
- [15] “WHIZARD.” [Online]. Available: <https://whizard.hepforge.org/>
- [16] “PYTHIA.” [Online]. Available: <https://pythia.org/pythia6/>
- [17] HEP-FCC, “EventProducer,” 2023. [Online]. Available: <https://github.com/HEP-FCC/EventProducer#eventproducer>
- [18] “iLCSoft.” [Online]. Available: <https://github.com/iLCSoft>

- [19] “DD4hep.” [Online]. Available: <https://dd4hep.web.cern.ch/dd4hep/>
- [20] “DDG4.” [Online]. Available: <https://github.com/AIDASoft/DD4hep/tree/master/DDG4>
- [21] “Geant4.” [Online]. Available: <https://geant4.web.cern.ch/>

Coherent feedback for quantum expander in gravitational wave observatories

Niels Böttner, Joe Bentley, Roman Schnabel, and Mikhail Korobko*
*Institut für Quantenphysik und Zentrum für Optische Quantentechnologien ,
Universität Hamburg, Luruper Chaussee 149, 22761 Hamburg, Germany*
(Dated: March 7, 2024)

The observation of gravitational waves from binary neutron star mergers offers insights into properties of extreme nuclear matter. However, their high-frequency signals in the kHz range are often masked by quantum noise of the laser light used. Here, we propose the “quantum expander with coherent feedback”, a new detector design that features an additional optical cavity in the detector output and an internal squeeze operation. This approach allows to boost the sensitivity at high frequencies, at the same time providing a compact and tunable design for signal extraction. It allows to tailor the sensitivity of the detector to the specific signal frequency range. We demonstrate that our design allows to improve the sensitivity of the high-frequency detector concept NEMO (neutron star extreme matter observatory), increasing the detection rates by around 15%. Our approach promises new level of flexibility in designing the detectors aiming at high-frequency signals.

I. INTRODUCTION

Since the first detection of gravitational waves (GWs) from a binary black hole merger in 2015 [1], the field of gravitational-wave observation has entered a new phase where events are detected every few days [2–5]. The anticipated new generation of GW detectors, such as Einstein Telescope [6] and Cosmic Explorer [7], will be so sensitive, that they are predicted to sense multiple events per minute. These detectors, like the current generation [8–10], focus on detecting signals at frequencies below 1 kHz. At frequencies above, the detectors are not sensitive enough to observe the post-merger effects that produce signals in the several kHz frequency range. This information, however, is crucial for understanding the fundamental properties of the ultra-dense matter in neutron stars [11–13] or possible deviations from general relativity [14, 15].

The sensitivity of detectors at high frequencies is limited by the optical bandwidth of cavities used to enhance the light and signal powers. Modern detectors feature arm cavities, as well as additional cavities to enhance the light power (power recycling cavity, PRC) and increase the detection bandwidth (signal extraction cavity, SEC). The signal is enhanced by cavities within the detector bandwidth up to ~ 500 Hz, but suppressed at high frequencies above ~ 1 kHz (HF). In order to further increase the sensitivity, current detectors employ frequency-dependent quantum squeezed light [16] suppressing quantum noise in a broad frequency band [17]. This approach however does not increase the detection bandwidth [18]. One way to overcome this limitation is to design a detector specifically targeting HF range by creating an additional optical resonance at kHz frequencies. This can be achieved by three different ways: by detuning the detector from its resonance [19, 20], by increasing the length of the SEC, as planned for the proposed

neutron star extreme matter observatory (NEMO) [21], and by adding a second long SEC in a detuned detector [22–24]. With the HF resonance, the energy exchange between the SEC and arm cavities occurs at the characteristic frequency of a few kHz (called the sloshing frequency [25]), and the signal at these frequencies is resonantly enhanced. Long SEC promises high sensitivity at HF, but also comes at a price of increased complexity and costs of the experiment. At the same time, it restricts the peak operation range to 1-3 kHz signals, limiting the sensitivity towards lower frequency signals.

Several alternative approaches appeared in the recent years, which enhance the detection bandwidth by employing active elements directly inside the detector. This can be achieved in a variety of ways [26–31], and we focus on the internal squeezing approach, where quantum correlated light is produced directly inside the detector, either in a degenerate [32–36] or non-degenerate way [37]. In order to enhance the detection bandwidth, internal squeezing should be combined with the use of HF sloshing resonance, creating a quantum expander (QE) configuration [38]. It can be effectively used both with short and long SEC [39], but in the latter case suffers from the challenges of long SEC.

In this work, we increase the flexibility of the long SEC when used with QE using coherent feedback approach [40–43]. Coherent feedback allows to modify quantum state of the detector without using any additional measurements. In our proposal, is realized via an additional short optical cavity at the output of the detector. The combined Quantum Expander with coherent feedback (QECF), shown in Fig. 1 keeps the expanded detection bandwidth feature of the QE but provides better flexibility in choosing the frequency at which the sensitivity is maximally enhanced. Importantly, it significantly decreases the required SEC length by optimizing the resonance condition in the two cavities. We demonstrate how our approach allows to tailor the sensitivity of the detector to a specific signal frequency range. We compare our approach to the NEMO configuration and show the potential amplitude sensitivity gain of $\sim 15\%$

* mkorobko@physnet.uni-hamburg.de

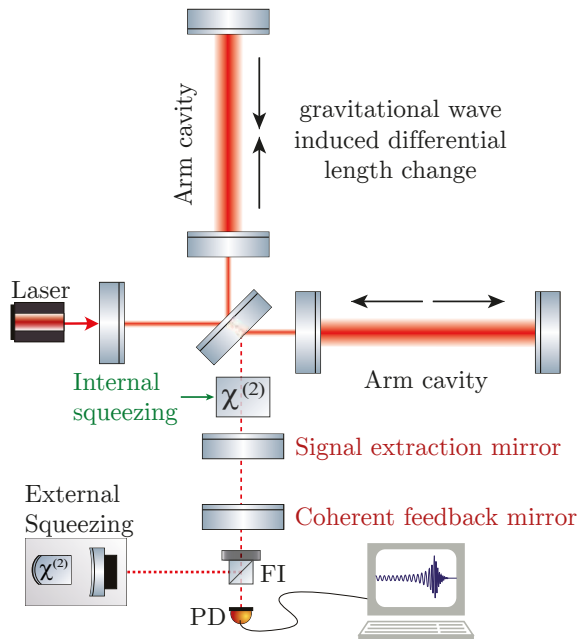


FIG. 1: Conceptual setup of the Quantum Expander with coherent feedback realized by the additional coherent feedback mirror. Internal squeezing is generated by pumping the nonlinear $\chi^{(2)}$ crystal with frequency doubled light. External squeezing is injected into the detector through a Faraday isolator (FI). The differential change in length of the arm cavities due to a gravitational wave, going into the page, is measured on the signal port with a photodiode (PD).

at the optical resonance, and the increase of detection band towards lower frequencies. We perform a statistical analysis of the expected detection rates for neutron star mergers and find that the overall improved sensitivity in the kilohertz-band leads to a median gain in detection rates of $\sim 15\%$ compared to NEMO. Improved low-frequency sensitivity allows QECF to contribute to the detection of pre-merger signals in a global detector network of LIGO [8], Virgo [9], KAGRA [10] and other planned detectors.

II. QUANTUM EXPANDER WITH COHERENT FEEDBACK

In this section we analytically study the response of a GW detector to quantum noise. The detector tuned close to the dark port operation, when no carrier light exits the signal port, reflects all quantum noise entering this port directly back. In this case, the response of the detector to quantum noise is the same as of an equivalent system of coupled cavities, which we study here [44]. Arm cavity is formed by the input and end test masses,

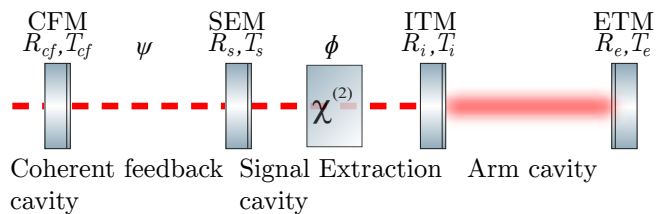


FIG. 2: Simplified theoretical setup for the Quantum Expander with coherent feedback. $R_{cf,s,i,e}$ and $T_{cf,s,i,e}$ are amplitude reflectivities and transmissivities of the coherent feedback (CFM), signal extraction (SEM), input (ITM) and end mirrors (ETM) respectively. $\tau_{\text{arm,SE,cf}} = L_{\text{arm,SE,cf}}/c$ is the single trip time in the arm cavity of length L_{arm} , SEC of length L_{SE} and CFC of length L_{cf} . ψ is the single trip tuning of the coherent feedback cavity and ϕ is the single trip tuning of the signal extraction cavity.

signal extraction cavity (SEC) is formed by the input test mass, and coherent feedback cavity (CFC) is formed by the signal extraction and coherent feedback mirrors, see Fig. 2. All cavities are tuned in a specific way, either on resonance or off resonance. The signal is generated as the phase modulation at the end mirror of the arm cavity, resonates in the cavities (depending on their tuning) and is then detected together with quantum noise at the output of the detector. The sensitivity of the detector is then characterised as the noise spectral density normalized by the signal power transfer function, representing the noise-to-signal ratio at every Fourier frequency. The QECF allows sensitivity enhancement at HF, where the detector is predominantly limited by photon shot noise. Here, we present the main analytical result without considering the effects of quantum radiation pressure noise (QRPN) and optical losses. Full treatment including these effects, which was used to produce the sensitivity curves in this paper, follows the derivation in [45] and can be found in the Supplementary Material.

We start by writing the input-output relations for the fields inside the cavity, and focus on the phase quadrature containing the signal \hat{b} [46], which is split into quantum noise and signal contributions:

$$\hat{b} = \mathcal{R}_a(\Omega)\hat{a} + \mathcal{T}_x(\Omega)x, \quad (1)$$

where $\mathcal{R}_a(\Omega)$ is the quantum noise optical transfer function for each signal frequency $\Omega = 2\pi f$, and $\mathcal{T}_x(\Omega)$ is the signal optical transfer function. In order to gain a physical picture of the effect, we use a single-mode approximation, which assumes that the signal frequency is well contained within one longitudinal resonance of each cavity. The full derivation of the input-output relations and transfer functions is presented in Appendix A 1 and transition to the single mode approximation explained in A 1 a. We achieve the QECF regime by setting $\phi = 0$ and $\psi = \pi/2$ and also assume the transmissivities of SE and CF mirrors to be very close to each other.

In the single-mode approximation, the noise transfer function and signal transfer function with respect to the GW strain $h(\Omega) = x(\Omega)/L_{\text{arm}}$ are given by

$$\mathcal{R}_a(\Omega) = \frac{(\gamma_{cf} - \chi\tilde{\gamma})\Omega + i(\Omega^2 - \omega_{s,-}^2)}{(\gamma_{cf} + \chi\tilde{\gamma})\Omega - i(\Omega^2 - \omega_{s,+}^2)}, \quad (2)$$

$$\mathcal{T}_h(\Omega) = \frac{1}{2} \frac{\sqrt{(\chi+1)(1-\chi)}\xi}{[\gamma_{cf} + \chi\tilde{\gamma}]\Omega - i[\Omega^2 - \omega_{s,+}^2]}. \quad (3)$$

We introduced several effective optical parameters that define the behaviour of the system. In a standard interferometer, the SEC and arm cavities exchange energy at a specific coupling rate, also called the sloshing frequency:

$$\omega_{s,\text{stand.}} = \sqrt{\frac{c^2 T_i^2}{4L_{\text{SE}}L_{\text{arm}}}} = \sqrt{\frac{\gamma_{\text{arm}}}{\tau_{\text{SE}}}}, \quad (4)$$

where $\gamma_n = (T_n^2 c)/(4L_n)$, $n \in \{\text{arm}, s, cf\}$ are the arm cavity, SEC and CFC bandwidths respectively, with corresponding amplitude transmissivity and cavity length. This sloshing frequency is modified by introducing the crystal and the CFC:

$$\omega_{s,\pm} = \omega_{s,\text{stand.}} \sqrt{\tau_{\text{SE}} \left(\gamma_s \frac{\tau_{\text{SE}}}{\tau_{cf}} \pm \chi\gamma_{cf} \right)}, \quad (5)$$

where the bandwidth of the interferometer is also modified:

$$\tilde{\gamma} = \gamma_{\text{arm}} + \gamma_s \frac{\tau_{\text{SE}}}{\tau_{cf}}. \quad (6)$$

Both of them depend on the effective gain parameter,

$$\chi = \frac{e^{2q} - 1}{1 + e^{2q}}, \quad (7)$$

where q is an amplification factor on the single pass through the nonlinear crystal. The acquired signal strength is proportional to the effective optical power in the arms.

$$\xi = \frac{\sqrt{\tau_{\text{SE}}}}{\sqrt{\tau_{\text{arm}}\tau_{cf}}} 4Ek_p \sqrt{\gamma_{\text{arm}}} \sqrt{\gamma_s \gamma_{cf}} L_{\text{arm}}, \quad (8)$$

where E is the large classical amplitude of the carrier light field inside the arm cavity and k_p is the wave vector of the carrier light field.

The double-sided spectral density of the output noise is given by the spectral density of the input field $S_{\text{in}}(\Omega)$ modified by the optical transfer function:

$$S_{\text{out}}(\Omega) = S_{\text{in}}(\Omega) |\mathcal{R}_a(\Omega)|^2, \quad (9)$$

For the purposes of understanding the fundamental behavior of the setup, we assume the incoming light field to be in the vacuum state, $S_{\text{in}}(\Omega) = 1$ [18, 47], which

will be changed to a squeezed state [48] in the next section. The strain sensitivity is calculated by comparing the noise power to the response of the readout field to the strain signal,

$$S_h(\Omega) = \sqrt{\frac{S_{\text{out}}(\Omega)}{|\mathcal{T}_h(\Omega)|^2}} = \sqrt{\frac{|\mathcal{R}_a(\Omega)|^2}{|\mathcal{T}_h(\Omega)|^2}}. \quad (10)$$

From Eqs. 2, 3, we can compute the strain sensitivity

$$S_h(\Omega) = 2 \sqrt{\frac{(\gamma_{cf} - \chi\tilde{\gamma})^2 \Omega^2 + (\Omega^2 - \omega_{s,-}^2)^2}{(\chi+1)(1-\chi)\xi^2}}. \quad (11)$$

The behaviour of the QECF can be understood in terms of coupling between the cavities leading to different resonance conditions for the cavities at different frequencies. At low frequencies, the SEC is off resonance (i.e. the field inside is suppressed), and the CFC is on resonance, creating an effective compound mirror with very low reflectivity since the CFC is almost impedance matched, i.e. $T_s \approx T_{cf}$. The vacuum field entering the signal port of the interferometer is squeezed very mildly inside the SEC by the nonlinear crystal, since the field is suppressed in the anti-resonant condition. The resulting LF sensitivity of QECF resembles the sensitivity of a standard interferometer, with a small suppression of shot noise:

$$S_h(\Omega) \approx 2(\gamma_{cf} - \chi\tilde{\gamma}) \sqrt{\frac{\Omega^2 + \gamma_{\text{det}}^2}{(\chi+1)(1-\chi)\xi^2}} \quad (12)$$

with the new detection bandwidth defined as $\gamma_{\text{det}} = \omega_{s,-}^2 / (\gamma_{cf} - \chi\tilde{\gamma})$.

Without internal squeezing, the LF sensitivity is limited by the detector's bandwidth γ_{baseline} :

$$S_h^{\text{baseline}}(\Omega) = \frac{2}{\xi} \sqrt{\gamma_{cf}^2 \Omega^2 + (\Omega^2 - \omega_{s,\text{baseline}}^2)^2} \approx \frac{2\gamma_{cf}}{\xi} \sqrt{\Omega^2 + \gamma_{\text{baseline}}^2}, \quad (13)$$

$$\omega_{s,\text{baseline}} = \omega_{s,\text{stand.}} \tau_{\text{SE}} \sqrt{\frac{\gamma_s}{\tau_{cf}}}, \quad (14)$$

$$\gamma_{\text{baseline}} = \frac{\omega_{s,\text{baseline}}^2}{\gamma_{cf}}. \quad (15)$$

At HF around $\Omega \approx \omega_{s,-}$, the SEC becomes resonant, and the CFC goes off resonance, thus creating a highly reflective compound mirror (similar to the Khalili etalon effect [49]). In this regime, the field inside the SEC is highly amplified, and the nonlinear crystal creates strong squeezing, thus enhancing the sensitivity:

$$S_h(\Omega) \approx 2 \frac{(\gamma_{cf} - \chi\tilde{\gamma})\omega_{s,-}}{\xi \sqrt{(\chi+1)(1-\chi)}}. \quad (16)$$

At the parametric oscillation threshold, $\chi \rightarrow \gamma_{cf}/\tilde{\gamma}$, the sensitivity becomes maximally improved, $S_h(\omega_{s,-}) \rightarrow 0$.

If another ratio between the CF and SE mirror transmissivities are chosen (i.e. they are not close to each other), the QECF loses the ability to generate squeezing simultaneously at LF and HF.

We note that the resonance condition for the CFC and the SEC depends both on the tuning phases ψ, ϕ and on the relation between the transmissivities of the mirrors, T_{cf}, T_s (i.e. the reflection phase for the field c_s off T_s). Our choice of ψ, ϕ is defined by the requirement of specific conditions to create the desired effect. Other combinations of phases are possible: when both the SEC and the CFC are anti-resonant at LF, the effective reflectivity of the CFC is high, and the optical linewidth of the detector is very low; at HF significant squeezing is created, similarly to the QECF. When the SEC is resonant at LF, squeezing is generated at low frequencies too, which is not the case that is relevant to us. Finally, the cavities could also be detuned, thus shifting the optical resonance. This would also create the optical spring effect from quantum radiation pressure, which enhances LF sensitivity [50, 51]. This effect can be further enhanced by internal squeezing [52, 53]. The study of a detuned QECF falls beyond the scope of this paper, where we focus on expanding the bandwidth towards high frequencies.

III. RESULTS

A. Simultaneous squeezing at low and high frequency

One of the main features of the QECF is its ability to generate simultaneous squeezing at LF and HF despite the presence of detuned cavities. Here, we consider the case without optical losses and QRPN to highlight this feature. Fig. 3 shows the sensitivity of the QECF for a fixed SEM transmissivity of $T_s = \sqrt{0.499}$ and different CFM transmissivities. As discussed before, the closer the transmissivities are to each other the closer is the CFC to being impedance matched. At LF, more vacuum field is transmitted through the CFC and squeezed inside the SEC. Thus, the photon shot noise at LF is more squeezed.

B. QECF compared to the Quantum Expander

Conceptually, the QECF corresponds to the QE with an SE mirror with very high transmissivity, on the order of 95%, which might pose additional challenges for cavity control. The main advantage of the QECF over the QE is the flexibility in choice of the high-frequency resonance where the sensitivity is maximised. Fig. 4 shows the sensitivity of QECF plotted for different lengths of the CFC compared to the QE. We can see that increasing its length

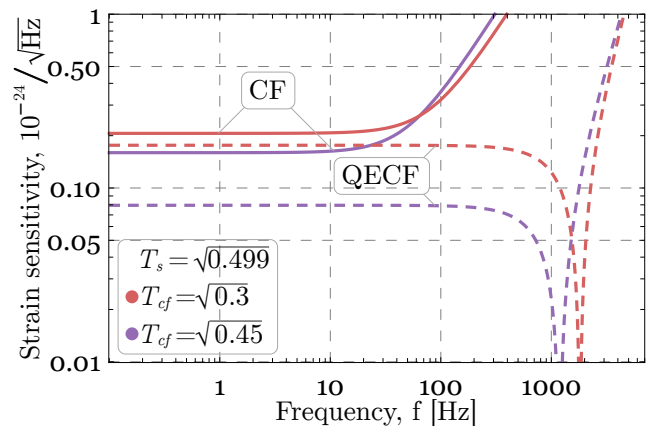


FIG. 3: Strain sensitivity of the Quantum Expander with coherent feedback (QECF), plotted for different transmissivities of the coherent feedback mirror, compared to the coherent feedback detector (CF). The CF shows the sensitivity of the QECF without internally squeezed light. Here, we can see the feature of the QECF to generate simultaneous squeezing at low and high frequency.

TABLE I: Parameters of the Quantum Expander with coherent feedback (QECF) to demonstrate the simultaneous squeezing at low and high frequency.

Parameter	QECF
Laser wavelength	1550 nm
Arm circulating power	4 MW
Test mass weight	200 kg
Input test mass power transmission	7%
Signal extraction mirror power transmission	49.9%
Coherent feedback mirror power transmission	45% or 30%
Arm cavity length	20 km
Signal extraction cavity length	56 m
Coherent feedback cavity length	56 m

decreases the detection bandwidth but improves the sensitivity in a certain frequency range, and vice versa. By shortening the CFC, we can obtain the same sensitivity as the QE. While the high-frequency resonance of the QE could also be tuned by macroscopically changing the SEC length, in the QECF this effect can be achieved by smaller changes in length, as we show in Appendix A 1 b. Moreover, tuning the SEC length is potentially challenging in practice due to the crystal and central beam splitter being present inside.

C. QECF compared to NEMO

The QECF features the high-frequency resonance with a target of observing neutron-star mergers. This relates it to the proposed NEMO detector, which targets the same sensitivity range. We use NEMO design as a benchmark

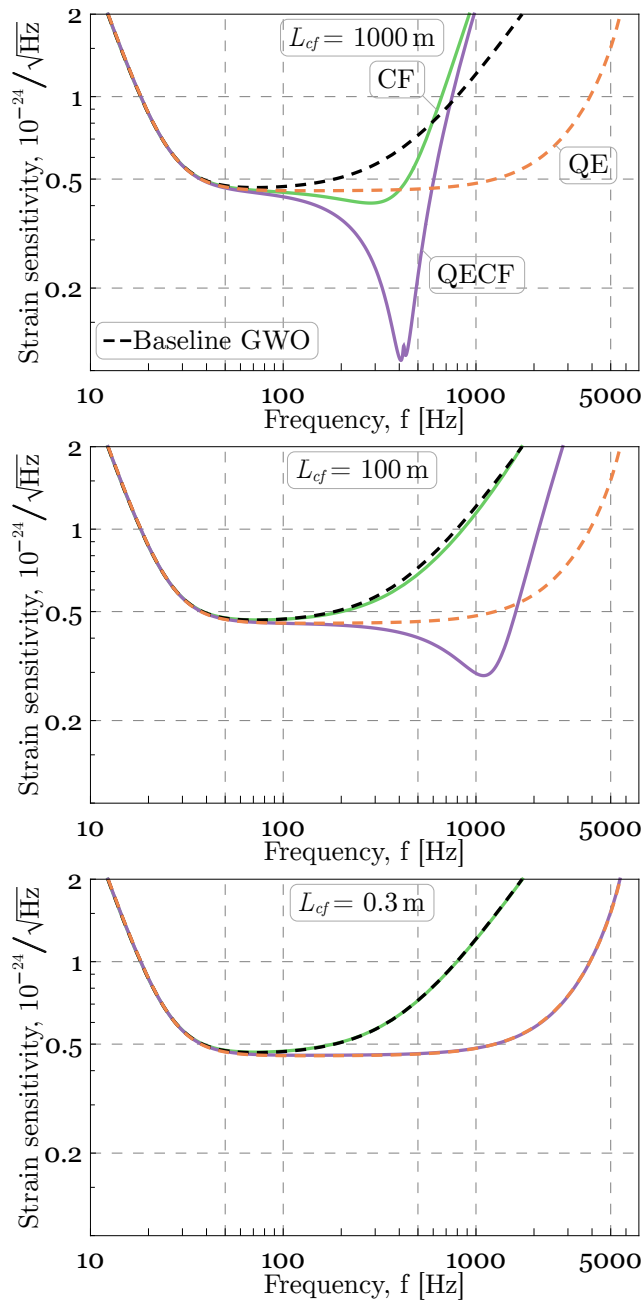


FIG. 4: Demonstration of the flexibility in choice of the high-frequency resonance of the Quantum Expander with coherent feedback (QECF) compared to the Quantum Expander (QE). The sensitivity of the QECF is plotted for different lengths of the coherent feedback cavity. The coherent feedback detector (CF) shows the sensitivity of the QECF without internally squeezed light, while the Baseline GWO is the sensitivity of the QE without internally squeezed light. Both the resonance’s frequency and the sensitivity improvement at that frequency scales inversely with the length, disappearing almost entirely in the last plot.

TABLE II: Parameters of the Quantum Expander (QE) and Quantum Expander with coherent feedback (QECF).

Parameter	QE	QECF
Laser wavelength	1550 nm	1550 nm
Arm circulating power	4 MW	4 MW
Test mass weight	200 kg	200 kg
Input test mass power transm.	7%	7%
End test mass power transm.	5 ppm	5 ppm
Combined power transm. of the coherent feedback cavity compared to QE’s signal extraction mirror	35%	34.8%
Signal extraction mirror power transm.	35%	29.9%
Coherent feedback mirror power transm.	-	3.7%
Arm cavity length	20 km	20 km
Signal extraction cavity length	56 m	56 m
Coherent feedback cavity length	-	100 m
Loss inside the signal extraction cavity	1500 ppm	1500 ppm
Photodiode detection efficiency	99.5%	99.5%

for our sensitivity optimization. First, in Fig. 5 we compare the two designs, matching the parameters of the coherent feedback detector (CF), which corresponds to the QECF without internal squeezing, to NEMO as close as possible to follow the sensitivity of NEMO. We show that we can obtain the same sensitivity as NEMO with the CF. While NEMO plans for 354 m long SEC, the combined length of the SEC and the CFC in the QECF and CF is 82.5 m (56 m and 26.5 m respectively). This potentially reduces costs and simplifies experimental setup and operation of the detector. Furthermore, the multiple cavity structure makes it easier to tune the CF sensitivity. The LF and peak sensitivity can be improved but at the expense of a smaller HF resonance.

The CFC gives freedom in optimizing the cavity lengths and reflectivities of the mirrors while maintaining the same HF resonance frequency. Such optimization allows to enhance the sensitivity compared to NEMO in a broad band, as we show in Fig. 6. For this optimization we also take into account that internal loss inside the SEC is increased compared to NEMO due to addition of the crystal and associated bulk material absorption and reflections at the sides of the crystal. To account for these additional losses, we increase the intra-cavity loss from 1400 ppm assumed by NEMO by 400 and 800 ppm. A loss estimate comes from the known value for the material absorption on the level of 10 ppm/cm [54] and anti-reflective coating with reflectivity of 100 ppm [55]. We assume that the crystal is only a few millimeters in size and thus, that we can neglect the loss due to absorption, which would result in ≈ 400 ppm loss in double pass. We leave room for additional losses and show that in the worst-case scenario the QECF still has the capability to outperform NEMO in a broad band. Of course, the internal squeezing approach can be used in NEMO as well [39], but we don’t discuss this case in detail here

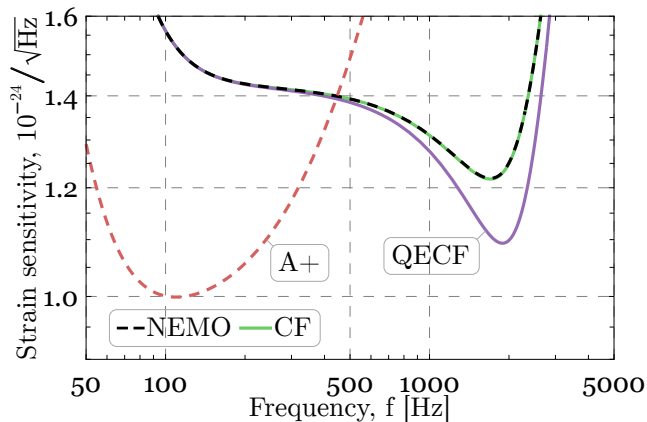


FIG. 5: Strain sensitivity of the Quantum Expander with coherent feedback with internal squeezing (QEFCF) and without it (CF), compared to NEMO. Parameters of CF are chosen to follow the sensitivity of NEMO to demonstrate sensitivity enhancement in the presence of internal squeezing in QEFCF. A+ [56] sensitivity is plotted for the reference.

since we could achieve the resulting sensitivity with the QEFCF as well.

In Fig. 7, we demonstrate the improved detection rates of neutron star mergers. We simulated one year of observation of kHz GWs (1–4 kHz) from neutron star mergers [12, 57] by running Monte-Carlo simulations for different source parameters and a given equation of state (see the details in the Appendix A 2). As we can see in Fig. 7a, both NEMO and the QEFCF significantly improve the detection probability of kHz GWs compared to A+. Here, we assume the detection threshold for a GW event to be a signal-to-noise ratio (SNR) of 5. While no event has an SNR above the threshold for A+, all events have an SNR above the threshold for the QEFCF and NEMO. The increased sensitivity of the QEFCF improves the median of the SNRs from 6.94 (NEMO) to 7.98 (QEFCF). This improvement also depends on the actual amount of loss inside the SEC, which we demonstrated in Fig. 7b.

Since the QEFCF improves the sensitivity at low frequencies as well, it also enhances the cosmological reach for binary black hole mergers by a factor ≈ 1.5 in the volume of the Universe. It is worth mentioning that improved SNRs alone won't make a big difference. A good sky localisation of the source is still needed to boost the multimessenger astronomy [58, 59].

IV. SUMMARY AND CONCLUSION

Coherent feedback is commonly used in the context of quantum networks for modifying the response of the plants generating quantum correlated states. In our work we used this approach for gravitational wave detection, modifying the spectral shape of the quantum noise in the

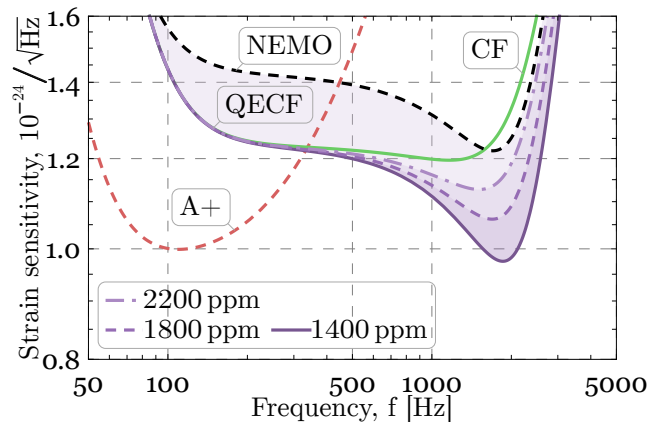


FIG. 6: Strain sensitivity of the Quantum Expander with coherent feedback (QEFCF), plotted for different amounts of loss inside the signal extraction cavity λ_s , compared to NEMO. The coherent feedback detector (CF) shows the sensitivity of the QEFCF without internally squeezed light and for the same loss inside the signal extraction cavity as NEMO. A+ sensitivity is plotted for the reference.

detector. We demonstrated the benefits of QEFCF for detecting high-frequency GW signal in a realistic setting, where the detection and intra-cavity losses limit the impact of quantum enhancement [60]. Our analysis of different cases, including the added loss due to the nonlinear crystal inside the detector, demonstrated the broadband enhancement to the sensitivity of a HF detector, compared to NEMO or QE. The demonstrated gain in sensitivity, which corresponds to an increase in light power inside NEMO's arm cavities by about 32%, significantly expands the volume in which binary black hole mergers are detectable by a factor ≈ 1.5 . We believe that increased complexity due to the additional mirror and nonlinear crystal is within current technological capabilities. The intra-cavity loss, which is one of the main limitations of quantum enhancement, is not greatly increased by the additional nonlinear crystal according to our estimates. However, even in the case of a significant added intra-cavity loss QEFCF still provides the sensitivity gain. The detailed implementation of the crystal inside the detector shall remain the goal of future studies. Other technical challenges, associated with phase noise [17, 61], dephasing [62], mode mismatch [63, 64] and parametric amplification process will need to be addressed.

Our new design demonstrates the promise of using coherent feedback cavities with quantum enhancement for flexible tuning of the detector sensitivity. Such tuning allows to optimize the detector between the observation runs to enhance its sensitivity to particular GW sources, based on the advances in understanding of their properties. Our approach can extend beyond gravitational-wave detection towards other large-scale dark matter or gravity sensors [65, 66].

TABLE III: Parameters NEMO, coherent feedback detector (CF) and Quantum Expander with coherent feedback (QECF).

Parameter	NEMO	CF	QECF matched to NEMO	QECF optimized
Laser wavelength	2000 nm	2000 nm	2000 nm	2000 nm
Arm circulating power	4.5 MW	4.5 MW	4.5 MW	4.5 MW
Test mass weight	74.1 kg	74.1 kg	74.1 kg	74.1 kg
Input test mass power transmission	1.4%	1.4%	1.4%	1.4%
End test mass power transmission	5 ppm	5 ppm	5 ppm	5 ppm
Combined power transmission of the coherent feedback cavity compared to NEMO's signal extraction mirror	4.8%	4.8%	4.8%	6.36%
Signal extraction mirror power transmission	4.8%	29.9%	29.9%	46%
Coherent feedback mirror power transmission	-	0.435%	0.435%	1%
Arm cavity length	4 km	4 km	4 km	4 km
Signal extraction cavity length	354 m	56 m	56 m	56 m
Coherent feedback cavity length	-	26.5 m	26.5 m	45 m
Loss inside the signal extraction cavity without crystal	1400 ppm	1400 ppm	1400 ppm	1400 ppm
Additional loss due to the crystal	-	-	400 ppm	400 ppm
Photodiode detection efficiency	99.7%	99.7%	99.7%	99.7%
Detected external squeezing	7 dB	7 dB	7 dB	7 dB

ACKNOWLEDGMENTS

We thank Y. Ma for fruitful discussions. This work was supported by the Deutsche Forschungsgemeinschaft (DFG) under Germany's Excellence Strategy EXC 2121 "Quantum Universe"-390833306.

Appendix A: Appendices

1. Input-Output relations

The steady-state input-output relations of the phase quadrature of the light field of the QECF are as follows:

$$\hat{c} = \hat{d}e^{2i\Omega\tau_{\text{arm}}} + 2ik_p E x e^{i\Omega\tau_{\text{arm}}}, \quad (\text{A1a})$$

$$\hat{d} = T_i \hat{a}_s + R_i \hat{c}, \quad (\text{A1b})$$

$$\hat{a}_s = \hat{d}_s e^{-q} e^{i\phi} e^{i\Omega\tau_{\text{SE}}}, \quad (\text{A1c})$$

$$\hat{b}_s = -R_i \hat{a}_s + T_i \hat{c}, \quad (\text{A1d})$$

$$\hat{c}_s = \hat{b}_s e^{-q} e^{i\phi} e^{i\Omega\tau_{\text{SE}}}, \quad (\text{A1e})$$

$$\hat{d}_s = T_s \hat{a}_{cf} + R_s \hat{c}_s, \quad (\text{A1f})$$

$$\hat{a}_{cf} = \hat{d}_{cf} e^{i\psi} e^{i\Omega\tau_{cf}}, \quad (\text{A1g})$$

$$\hat{b}_{cf} = -R_s \hat{a}_{cf} + T_s \hat{c}_s, \quad (\text{A1h})$$

$$\hat{c}_{cf} = \hat{b}_{cf} e^{i\psi} e^{i\Omega\tau_{cf}}, \quad (\text{A1i})$$

$$\hat{d}_{cf} = T_{cf} \hat{a} + R_{cf} \hat{c}_{cf}, \quad (\text{A1j})$$

$$\hat{b} = -R_{cf} \hat{a} + T_{cf} \hat{c}_{cf}, \quad (\text{A1k})$$

where $R_{i,s,cf}$, $T_{i,s,cf}$ are the amplitude reflectivity and transmissivity of the input, signal extraction and coherent feedback mirror; q is an amplification factor on the

single pass through the crystal; $\tau_{\text{arm,SE,cf}} = L_{\text{arm,SE,cf}}/c$ is the single trip time in the arm cavity of length L_{arm} , SEC of length L_{SE} and CFC of length L_{cf} , with c being the speed of light; the arm cavity is resonant at zero signal frequency ($\Omega = 0$), ϕ is the single trip tuning of the SEC and ψ is the single trip tuning of the CFC; x is a small displacement of the end mirror due to the GW signal; E is the large classical amplitude of the carrier light field inside the arm cavity and k_p is the wave vector of the carrier light field.

By solving Eqs. A1, we get an expression for the output \hat{b} , which can be split into a noise part and signal part, where $\mathcal{R}_a(\Omega)$ is the noise optical transfer function and $\mathcal{T}_x(\Omega)$ is the signal optical transfer function:

$$\hat{b} = \mathcal{R}_a(\Omega)\hat{a} + \mathcal{T}_x(\Omega)x, \quad (\text{A2})$$

$$\begin{aligned} \mathcal{R}_a(\Omega) = & \frac{e^{2q}(-1 + e^{2i\Omega\tau_{\text{arm}}} R_i)(R_{cf} + e^{2i(\psi + \Omega\tau_{cf})} R_s)}{c_{\text{den}}} \\ & + \frac{e^{2i(\phi + \Omega\tau_{\text{SE}})}(e^{2i\Omega\tau_{\text{arm}}} - R_i)(e^{2i(\psi + \Omega\tau_{cf})} + R_{cf} R_s)}{c_{\text{den}}}, \end{aligned} \quad (\text{A3})$$

$$\mathcal{T}_x(\Omega) = -\frac{2ie^{q+i(\phi+\psi+\Omega(\tau_{\text{arm}}+\tau_{\text{SE}}+\tau_{cf}))} E k_p T_i T_s T_{cf}}{c_{\text{den}}}, \quad (\text{A4})$$

where we defined

$$\begin{aligned} c_{\text{den}} = & e^{2i(\phi + \Omega\tau_{\text{SE}})}(e^{2i\Omega\tau_{\text{arm}}} - R_i)(e^{2i(\psi + \Omega\tau_{cf})} R_{cf} + R_s) \\ & + e^{2q}(-1 + e^{2i\Omega\tau_{\text{arm}}} R_i)(1 + e^{2i(\psi + \Omega\tau_{cf})} R_{cf} R_s). \end{aligned} \quad (\text{A5})$$

Both transfer functions depend, amongst other parameters, on the properties of the cavities.

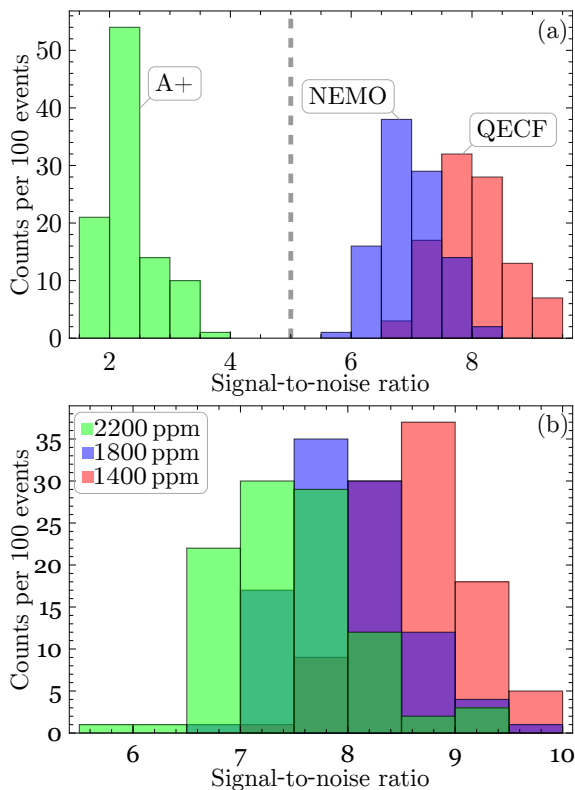


FIG. 7: Histogram for the SNR of the loudest events for 100 Monte-Carlo simulations of neutron star mergers in the kHz GW regime. (a) shows the results of one realization where we compared the Quantum Expander with coherent feedback (QEFCF), NEMO and A+. (b) shows the results of another realization where we compared QEFCF for different amounts of loss inside the signal extraction cavity λ_s .

a. Single mode approximation

The expressions of the noise and signal transfer functions (Eqs. A3, A4) can be simplified by doing a single-mode-approximation, which assumes that the signal frequency of interest is well contained within one free spectral range of the longitudinal resonances of each cavity. Therefore, we assume $\Omega\tau_{\text{arm,SE,cf}} \ll 1$ and $T_{i,s,cf} \ll 1$, so that $e^{i\Omega\tau_{\text{arm,SE,cf}}} \approx 1 + i\Omega\tau_{\text{arm,SE,cf}}$ and $R_{i,s,cf} \approx 1 - T_{i,s,cf}^2/2$. The assumptions made simplify the numerator and denominator of the transfer functions to polynomials of Ω . The coefficients of the polynomials can be further simplified by dropping higher order terms until only the lowest order term or two lowest order terms are left. We monitored the correctness of this method by comparing the roots of the numerator of the noise transfer function with the high-frequency resonance of the actual solution since they should be identical. In this regime, the noise transfer function and signal transfer function with respect to the GW strain $h(\Omega) = x(\Omega)/L_{\text{arm}}$ are

given by Eqs. 2, 3.

b. Scaling of the high-frequency resonance

Fig. 9 compares the efficiency of tuning the high-frequency resonance of the QEFCF and QE. Here, we determined the high-frequency resonance of both systems without optical losses and QRPN. For the QE we changed the length of the signal extraction cavity, while for the QEFCF we kept the length of the signal extraction cavity constant (56 m) and only changed the length of the coherent feedback cavity. The efficiency of the tuning of the QEFCF is significantly better, especially between 56 m and ~ 400 m.

2. Astrophysical analysis

Here we present the details of the astrophysical analysis. The analysis focuses on binary neutron star mergers and follows the method described in [67, 68]. The event rate is estimated to be $1 \text{ Mpc}^{-3} \text{ Myr}^{-1}$ and the searching distance to be 1 Gpc. We ran 100 Monte-Carlo simulations each with 1000 samples. Based on the event rate and search distance, this corresponds to one year of observation. The mass of each neutron star is assumed to follow a Gaussian distribution centered at $1.33 M_{\odot}$ with variance $0.09 M_{\odot}$. Here, we exclude binary neutron stars with a total mass larger than $3.45 M_{\odot}$ because they will quickly collapse into a black hole. The sky position, inclination and polarization angles are taken into account by multiplying the gravitational wave amplitude (Eq. A6) by a sky-averaged reduction factor [67]. The distribution of the source distance follows a uniform distribution between 50 Mpc and 1000 Mpc [68]. We approximate the post-merger waveform as the damped oscillation of a single mode, the parameters of which depend on the neutron-star equation of state. The amplitude in the frequency domain is given by:

$$h(f) = \frac{2}{5} \frac{50}{\pi d} h_p \frac{Q [2f_p Q \cos(\phi_0) - [f_p - 2ifQ] \sin(\phi_0)]}{f_p^2 - 4iff_pQ - 4Q^2(f^2 - f_p^2)}, \quad (\text{A6})$$

where d is the distance to the source in Mpc, h_p is the peak value of the wave amplitude, Q is the quality factor of the post-merger oscillation, ϕ_0 is the initial phase of the source, f_p is the peak frequency of the waveform and $2/5$ is the sky-averaged reduction factor for a L-shaped GW detector. The equation of state of the neutron star is assumed to be relatively stiff [69] and therefore, $Q = 23.3$ and $h_p = 5 \times 10^{-22}$. The peak frequency is given by:

$$f_p = 1 \text{ kHz} \left(\frac{m_1 + m_2}{M_{\odot}} \right) \left[a_2 \left(\frac{R}{1 \text{ km}} \right)^2 + a_1 \frac{R}{1 \text{ km}} + a_0 \right], \quad (\text{A7})$$

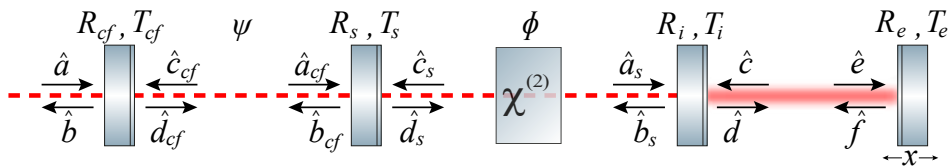


FIG. 8: Simplified theoretical setup for the Quantum Expander with coherent feedback. $R_{cf,s,i,e}$ and $T_{cf,s,i,e}$ are amplitude reflectivities and transmissivities of the coherent feedback, signal extraction, input and end mirrors respectively. ψ is the single trip tuning of the coherent feedback cavity and ϕ is the single trip tuning of the signal extraction cavity. x is a small mirror displacement due to a gravitational wave.

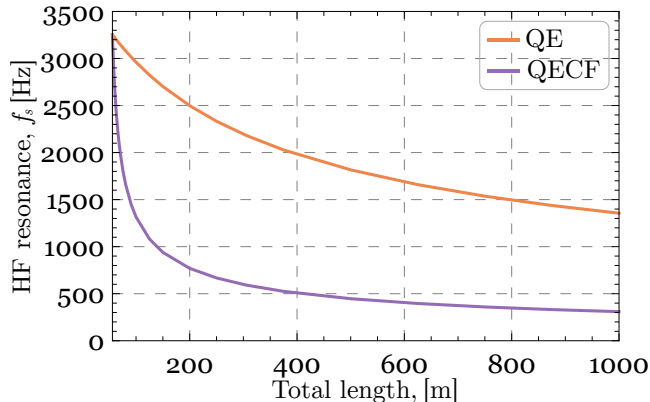


FIG. 9: Scaling of the high-frequency resonance versus total length of the extraction cavities. For the Quantum Expander (QE) we changed the length of the signal extraction cavity, while for the Quantum Expander with coherent feedback (QECF) we kept the length of the signal extraction cavity constant (56 m) and only changed the length of the coherent feedback cavity. The plot highlights the more efficient tuning of the high-frequency resonance in the QECF compared to the QE.

SUPPLEMENTARY: FULL CALCULATION OF THE STRAIN SENSITIVITY

Optical loss is a huge problem for gravitational wave observatories (GWOs). Any source of optical loss reduces the sensitivity of a GWO due to the mixing with vacuum. In this section, we compute the strain sensitivity including optical losses, radiation pressure and injection of external squeezed light by using a transfer matrix approach. The following calculations mirror those in [45].

a. Input-output relation

The setup of the Quantum Expander with coherent feedback (QECF) and quantum fields inside the system with losses are shown in Fig. 10.

We define a vector $\hat{a}(\Omega) = \{\hat{a}_{\text{phase}}(\Omega), \hat{a}_{\text{amplitude}}(\Omega)\}^T$ to describe the phase and amplitude quadrature. We will start by writing down the input-output relations and solving them. The coherent feedback and signal extraction cavity can rotate the quadratures due to its detuning from resonance. The parametric amplification process squeezes and rotates the quadratures. We introduce a rotation matrix:

$$\mathbb{O}(\phi) = \begin{pmatrix} \cos(\phi) & -\sin(\phi) \\ \sin(\phi) & \cos(\phi) \end{pmatrix}, \forall \phi \quad (\text{A9})$$

where $R = 14.42$ km is the radius of each neutron star with masses $m_{1,2}$ and the parameters $a_2 = 0.0157$, $a_1 = -0.5495$, $a_0 = 5.503$ [70]. The signal-to-noise ratio is defined as:

$$\text{SNR} = 2 \sqrt{\int_{f_{\min}}^{f_{\max}} df \frac{|h(f)|^2}{S_{hh}(f)}}, \quad (\text{A8})$$

where $S_{hh}(f)$ is the single-sided noise spectral density of the detectors and $f_{\min} = 1$ kHz and $f_{\max} = 4$ kHz are the integration limits. For each Monte-Carlo simulation, we selected out the loudest event.

and squeezing matrix:

$$\mathbb{S} = \begin{pmatrix} e^q & 0 \\ 0 & e^{-q} \end{pmatrix}, \quad (\text{A10})$$

where q is an amplification factor on the single pass through the crystal. The equations for the coherent feedback cavity are as follows:

$$\hat{a}_{cf} = \mathbb{N}(\psi)\hat{d}_{cf}, \quad (\text{A11a})$$

$$\hat{b}_{cf} = -R_s\hat{a}_{cf} + T_s\hat{c}_s, \quad (\text{A11b})$$

$$\hat{c}_{cf} = \mathbb{N}(\psi)\hat{b}_{cf}, \quad (\text{A11c})$$

$$\hat{d}_{cf} = T_{cf}\hat{a} + R_{cf}\hat{c}_{cf}, \quad (\text{A11d})$$

where we have defined

$$\mathbb{N}(\psi) = \mathbb{O}(\psi)e^{i\Omega\tau_{cf}} \quad (\text{A12})$$

and $R_{cf,s}, T_{cf,s}$ are the amplitude reflectivities and transmissivities of the coherent feedback and signal extraction mirror, $\tau_{cf} = L_{cf}/c$ is the coherent feedback cavity global delay and ψ is the phase delay due to the cavity detuning. The system of equations Eqs. A11 can be solved and we find the following solutions:

$$\hat{a}_{cf} = \mathbb{N}(\psi)\mathbb{A}(T_{cf}\hat{a} + R_{cf}T_s\mathbb{N}(\psi)\hat{c}_s), \quad (\text{A13a})$$

$$\hat{b}_{cf} = \mathbb{A}(-R_sT_{cf}\mathbb{N}(\psi)\hat{a} + T_s\hat{c}_s), \quad (\text{A13b})$$

$$\hat{c}_{cf} = \mathbb{N}(\psi)\mathbb{A}(-R_sT_{cf}\mathbb{N}(\psi)\hat{a} + T_s\hat{c}_s), \quad (\text{A13c})$$

$$\hat{d}_{cf} = \mathbb{A}(T_{cf}\hat{a} + R_{cf}T_s\mathbb{N}(\psi)\hat{c}_s), \quad (\text{A13d})$$

where we have defined

$$\mathbb{A} = (\mathbb{I} + R_{cf}R_s\mathbb{N}^2(\psi))^{-1}. \quad (\text{A14})$$

The solutions can be used to obtain the input-output relations for the coherent feedback cavity:

$$\hat{b} = -R_{cf}\hat{a} + T_{cf}\hat{c}_{cf} = -\tilde{\mathbb{R}}_b\hat{a} + \tilde{\mathbb{T}}_b\hat{c}_s, \quad (\text{A15a})$$

$$\hat{d}_s = T_s\hat{a}_{cf} + R_s\hat{c}_s = \tilde{\mathbb{R}}_d\hat{c}_s + \tilde{\mathbb{T}}_d\hat{a}, \quad (\text{A15b})$$

where

$$\tilde{\mathbb{R}}_b = R_{cf}\mathbb{I} + R_sT_{cf}^2\mathbb{N}(\psi)\mathbb{A}\mathbb{N}(\psi), \quad (\text{A16a})$$

$$\tilde{\mathbb{R}}_d = R_s\mathbb{I} + R_{cf}T_s^2\mathbb{N}(\psi)\mathbb{A}\mathbb{N}(\psi), \quad (\text{A16b})$$

$$\tilde{\mathbb{T}}_b = T_{cf}T_s\mathbb{N}(\psi)\mathbb{A}, \quad (\text{A16c})$$

$$\tilde{\mathbb{T}}_d = T_sT_{cf}\mathbb{N}(\psi)\mathbb{A} \quad (\text{A16d})$$

are the transfer matrices for the fields.

For the signal extraction cavity, we get the following set of equations:

$$\hat{a}_s = \sqrt{1 - \lambda_s}\mathbb{M}[\varphi, \phi]\hat{d}_s + \sqrt{\lambda_s}\mathbb{M}[\varphi, \phi]\hat{n}_1, \quad (\text{A17a})$$

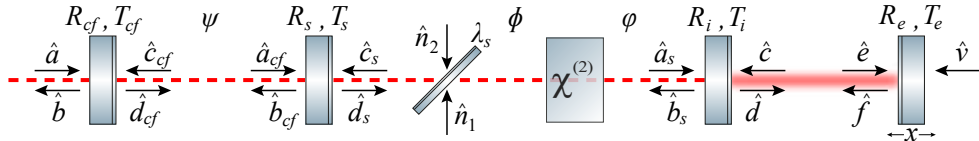


FIG. 10: Quantum fields inside the Quantum Expander with coherent feedback. $R_{cf,s,i,e}$ and $T_{cf,s,i,e}$ are amplitude reflectivities and transmissivities of the coherent feedback, signal extraction, input and end test mirror. ψ is the phase delay due to the detuning of the coherent feedback cavity. ϕ and φ are the phase delays due to the signal extraction cavity detuning before and after the crystal. Intra-cavity loss is represented by a beamsplitter with power reflectivity λ_s .

$$\hat{b}_s = -R_i \hat{a}_s + T_i \hat{c}, \quad (\text{A17b})$$

$$\hat{c}_s = \sqrt{1 - \lambda_s} \mathbb{M}[\phi, \varphi] \hat{b}_s - \sqrt{\lambda_s} \hat{n}_2, \quad (\text{A17c})$$

$$\hat{d}_s = T_s \hat{a}_{cf} + R_s \hat{c}_s, \quad (\text{A17d})$$

where we have defined

$$\mathbb{M}[\varphi, \phi] = \mathbb{O}(\varphi) \mathbb{O}(\theta) \mathbb{S} \mathbb{O}^\dagger(\theta) \mathbb{O}(\phi) e^{i\Omega \tau_{\text{SE}}} \quad (\text{A18})$$

and R_i, T_i are the amplitude reflectivity and transmissivity of the input test mirror, $\tau_{\text{SE}} = L_{\text{SE}}/c$ is the signal extraction cavity global delay, ϕ and φ are the phase delays due to the cavity detuning before and after the crystal, λ_s is the power loss inside the signal extraction cavity and θ is the squeezing angle.

The next step is to insert \hat{d}_s from Eq. A15b into the Eqs. A17. We obtain the input-output relations for the system, which consists of the coherent feedback and signal extraction cavity:

$$\hat{b} = -\hat{\mathbb{R}}_b \hat{a} + \hat{\mathbb{T}}_b \hat{c} + \hat{\mathcal{L}}_{b1} \hat{n}_1 + \hat{\mathcal{L}}_{b2} \hat{n}_2, \quad (\text{A19a})$$

$$\hat{d} = \hat{\mathbb{R}}_d \hat{c} + \hat{\mathbb{T}}_d \hat{a} + \hat{\mathcal{L}}_{d1} \hat{n}_1 + \hat{\mathcal{L}}_{d2} \hat{n}_2, \quad (\text{A19b})$$

where we have defined the following transfer matrices

$$\hat{\mathbb{R}}_b = \tilde{\mathbb{R}}_b + R_i(1 - \lambda_s) \tilde{\mathbb{T}}_b \mathbb{M}[\phi, \varphi] \mathbb{G}_a \mathbb{M}[\varphi, \phi] \tilde{\mathbb{T}}_d, \quad (\text{A20a})$$

$$\hat{\mathbb{R}}_d = R_i \mathbb{I} + T_i^2(1 - \lambda_s) \mathbb{G}_a \mathbb{M}[\varphi, \phi] \tilde{\mathbb{R}}_d \mathbb{M}[\phi, \varphi], \quad (\text{A20b})$$

$$\hat{\mathbb{T}}_b = \sqrt{1 - \lambda_s} \tilde{\mathbb{T}}_b \mathbb{M}[\phi, \varphi] \left(T_i \mathbb{I} - R_i T_i (1 - \lambda_s) \mathbb{G}_a \mathbb{M}[\varphi, \phi] \tilde{\mathbb{R}}_d \mathbb{M}[\phi, \varphi] \right), \quad (\text{A20c})$$

$$\hat{\mathbb{T}}_d = T_i \sqrt{1 - \lambda_s} \mathbb{G}_a \mathbb{M}[\varphi, \phi] \tilde{\mathbb{T}}_d, \quad (\text{A20d})$$

$$\hat{\mathcal{L}}_{b1} = -R_i \sqrt{1 - \lambda_s} \sqrt{\lambda_s} \tilde{\mathbb{T}}_b \mathbb{M}[\phi, \varphi] \mathbb{G}_a \mathbb{M}[\varphi, \phi], \quad (\text{A20e})$$

$$\hat{\mathcal{L}}_{d1} = T_i \sqrt{\lambda_s} \mathbb{G}_a \mathbb{M}[\varphi, \phi], \quad (\text{A20f})$$

$$\hat{\mathcal{L}}_{b2} = R_i(1 - \lambda_s) \sqrt{\lambda_s} \tilde{\mathbb{T}}_b \mathbb{M}[\phi, \varphi] \mathbb{G}_a \mathbb{M}[\varphi, \phi] \tilde{\mathbb{R}}_d - \sqrt{\lambda_s} \tilde{\mathbb{T}}_b, \quad (\text{A20g})$$

$$\hat{\mathcal{L}}_{d2} = -T_i \sqrt{1 - \lambda_s} \sqrt{\lambda_s} \mathbb{G}_a \mathbb{M}[\varphi, \phi] \tilde{\mathbb{R}}_d, \quad (\text{A20h})$$

$$\mathbb{G}_a = \left(\mathbb{I} + R_i(1 - \lambda_s) \mathbb{M}[\varphi, \phi] \tilde{\mathbb{R}}_d \mathbb{M}[\phi, \varphi] \right)^{-1}. \quad (\text{A20i})$$

The equations for the arm cavity are as follows:

$$\hat{e} = \mathbb{P}(\delta) \hat{d}, \quad (\text{A21a})$$

$$\hat{f} = R_e \hat{e} + T_e \hat{v} + 2k_p R_e \mathbb{O}(\pi/2) E \hat{x}(\Omega), \quad (\text{A21b})$$

$$\hat{c} = \mathbb{P}(\delta) \hat{f}, \quad (\text{A21c})$$

$$\hat{d} = R_i \hat{c} + T_i \hat{a}_s, \quad (\text{A21d})$$

where we have defined

$$\mathbb{P}(\delta) = \mathbb{O}(\delta) e^{i\Omega \tau_{\text{arm}}} \quad (\text{A22})$$

and R_e, T_e are the amplitude reflectivity and transmissivity of the end test mirror, $\tau_{\text{arm}} = L_{\text{arm}}/c$ is the arm cavity global delay, k_p is the wave vector of the light field, E is the classical amplitude of the light field and $\hat{x}(\Omega)$ is a small mirror displacement due to the gravitational wave signal. We make the assumption that the gravitational wave signal appears only in the equations for the phase quadrature:

$$E = \sqrt{2} E_{\text{ampl}} \begin{pmatrix} 1 \\ 0 \end{pmatrix}, \quad (\text{A23})$$

where the amplitude E_{ampl} which is connected to the arm cavity light power

$$P_{\text{arm}} = \frac{\hbar k_p c}{2} |E_{\text{ampl}}|^2. \quad (\text{A24})$$

We repeat the last step and insert \hat{d} from Eq. A19b into the Eqs. A21 to obtain the input-output relations for the entire system:

$$\hat{b} = -\mathbb{R}\hat{a} + \mathbb{T}\hat{v} + \mathbb{Z}\hat{x}(\Omega) + \mathcal{L}_1\hat{n}_1 + \mathcal{L}_2\hat{n}_2, \quad (\text{A25})$$

where we have introduced the transfer functions

$$\mathbb{R} = \mathring{\mathbb{R}}_b - R_e \mathring{\mathbb{T}}_b \mathbb{L}_c \mathbb{P}^2(\delta) \mathring{\mathbb{T}}_d, \quad (\text{A26a})$$

$$\mathbb{T} = T_e \mathring{\mathbb{T}}_b \mathbb{L}_c \mathbb{P}(\delta), \quad (\text{A26b})$$

$$\mathbb{Z} = 2k_p R_e \mathring{\mathbb{T}}_b \mathbb{L}_c \mathbb{P}(\delta) \mathbb{O}(\pi/2) E, \quad (\text{A26c})$$

$$\mathcal{L}_1 = \mathring{\mathcal{L}}_{b1} + R_e \mathring{\mathbb{T}}_b \mathbb{L}_c \mathbb{P}^2(\delta) \mathring{\mathcal{L}}_{d1}, \quad (\text{A26d})$$

$$\mathcal{L}_2 = \mathring{\mathcal{L}}_{b2} + R_e \mathring{\mathbb{T}}_b \mathbb{L}_c \mathbb{P}^2(\delta) \mathring{\mathcal{L}}_{d2}, \quad (\text{A26e})$$

$$\mathbb{L}_c = \left(\mathbb{I} - R_e \mathbb{P}^2(\delta) \mathring{\mathbb{R}}_d \right)^{-1}. \quad (\text{A26f})$$

b. Radiation pressure

Radiation pressure is the effect that electromagnetic radiation applies a force to an object from which it is reflected [71]. Radiation pressure causes a constant displacement of a test mirror, which can be compensated with an active feedback control, and a random displacement due to the uncertainty in the amplitude quadrature of the light. This uncertainty leads to the quantum radiation pressure noise.

Light, which is reflected by a perfectly reflective mirror, exerts the radiation pressure force F_{rp} on this mirror [71]:

$$F_{\text{rp}} = \frac{2P}{c}, \quad (\text{A27})$$

where P is the power of the light. From Eq. A27, we can see that the impact of the radiation pressure force only plays a role for the input and end test mirror. This is because we have a high light power inside the arm cavities and therefore a high radiation pressure force acting on the mirrors of the arm cavities. The impact of the radiation pressure force on the signal extraction mirror can be neglected since we have a low light power inside the signal extraction cavity. We assume the radiation pressure force acting on the input and end test mirror to be equal. This allows us to assume the input test mirror to be fixed and instead twice the back action applied on the end test mirror [44]. This approximation holds as long as the amplitudes of the fields acting on the input test mirror and end test mirror are almost equal, which is the case in the single-mode-approximation. With this approximation, we can calculate the radiation pressure force (also called back-action force):

$$F_{ba} = \hbar k_p \left(E^\dagger \hat{e}(\Omega) + R_e E^\dagger \hat{f}(\Omega) \right). \quad (\text{A28})$$

We can split the back-action force into a noise part $F_{fl}(\Omega)$ and an optical spring force, which depends on the mirror displacement $\hat{x}(\Omega)$ and a spring constant $\kappa(\Omega)$. With the solutions from the previous Section A2a, we obtain the following equations:

$$F_{ba} = F_{fl}(\Omega) - \kappa(\Omega) \hat{x}(\Omega), \quad (\text{A29a})$$

$$F_{fl}(\Omega) = \hbar k_p (1 + R_e^2) E^\dagger \mathbb{B} \mathbb{P}(\delta) \left(\mathring{\mathbb{T}}_d \hat{a} + \mathring{\mathcal{L}}_{d1} \hat{n}_1 + \mathring{\mathcal{L}}_{d2} \hat{n}_2 \right) + \hbar k_p T_e E^\dagger \mathcal{L}_v \hat{v}, \quad (\text{A29b})$$

$$\mathbb{B} = \mathbb{I} + R_e \mathbb{P}(\delta) \mathring{\mathbb{R}}_d \mathbb{L}_c \mathbb{P}(\delta), \quad (\text{A29c})$$

$$\mathcal{L}_v = R_e \mathbb{I} + (1 + R_e^2) \mathbb{P}(\delta) \mathring{\mathbb{R}}_d \mathcal{L}_c \mathbb{P}(\delta), \quad (\text{A29d})$$

$$\kappa(\Omega) = -2\hbar k_p^2 R_e E^\dagger \left(R_e \mathbb{O}(\pi/2) E + (1 + R_e^2) \mathbb{P}(\delta) \mathring{\mathbb{R}}_d \mathcal{L}_c \mathbb{P}(\delta) \mathbb{O}(\pi/2) E \right). \quad (\text{A29e})$$

This leads to the following equation of motion for the end test mirror:

$$\hat{x}(\Omega) = \chi_{\text{eff}}(\Omega) F_{fl}(\Omega), \quad (\text{A30})$$

where we have defined an effective susceptibility

$$\chi_{\text{eff}}(\Omega) = \left(\chi^{-1}(\Omega) + \kappa(\Omega) \right)^{-1} \quad (\text{A31})$$

with $\chi(\Omega) = (-m\Omega^2)^{-1}$ being the mechanical susceptibility and m being the mass of the end test mirror.

c. Detection

The sensitivity of a gravitational wave observatory is reduced by detection loss. Similar to the intra-cavity loss, the detection loss is modelled by a beamsplitter with amplitude transmissivity $\sqrt{\eta}$ and reflectivity $\sqrt{1-\eta}$:

$$\hat{b}(\Omega) = \sqrt{\eta}\hat{b}(\Omega) + \sqrt{1-\eta}\hat{n}. \quad (\text{A32})$$

The output \hat{b} is measured by a balanced homodyne detector at homodyne angle ζ . We obtain the following values:

$$\hat{y}(\Omega) = \mathcal{H}^T \hat{b}(\Omega) = \frac{\mathcal{H}^T (-\mathbb{R}\hat{a} + \mathbb{T}\hat{v} + \mathcal{L}_1\hat{n}_1 + \mathcal{L}_2\hat{n}_2)}{\mathcal{H}^T \mathbb{Z}} + \frac{\sqrt{1-\eta}\mathcal{H}^T}{\sqrt{\eta}\mathcal{H}^T \mathbb{Z}} \hat{n} + \hat{x}(\Omega) \quad (\text{A33})$$

which we normalized to the mirror displacement and where \mathcal{H} is the homodyne detection transfer vector

$$\mathcal{H} = \begin{pmatrix} \cos(\zeta) \\ \sin(\zeta) \end{pmatrix}. \quad (\text{A34})$$

The sensitivity can be improved by the injection of squeezed light. In this case, the input field \hat{a} reads as follows:

$$\hat{a} = \mathbb{S}_{ext}(\phi_{ext})\hat{a}_{vac}, \quad (\text{A35})$$

where we have introduced the external squeezing matrix

$$\mathbb{S}_{ext}(\phi_{ext}) = \mathbb{O}(\phi_{ext}) \begin{pmatrix} e^{q_{ext}} & 0 \\ 0 & e^{-q_{ext}} \end{pmatrix} \mathbb{O}(-\phi_{ext}) \quad (\text{A36})$$

and \hat{a}_{vac} is the vacuum field before squeezing, q_{ext} is the external squeezing factor and ϕ_{ext} is the external squeezing angle. The remaining fields \hat{v} , \hat{n} , \hat{n}_1 , and \hat{n}_2 are in the vacuum state.

We get the power spectral density:

$$S_x(\Omega) = S_{xx}(\Omega) + 2 \text{Re} [\chi_{\text{eff}}^*(\Omega)S_{xF}(\Omega)] + |\chi_{\text{eff}}(\Omega)|^2 S_{FF}(\Omega), \quad (\text{A37})$$

where we have defined

$$S_{xx}(\Omega) = \frac{\mathcal{H}^T \left(\mathbb{R}\mathbb{S}_{ext}\mathbb{S}_{ext}^\dagger\mathbb{R}^\dagger + \mathbb{T}\mathbb{T}^\dagger + \mathcal{L}_1\mathcal{L}_1^\dagger + \mathcal{L}_2\mathcal{L}_2^\dagger \right) \mathcal{H}}{|\mathcal{H}^T \mathbb{Z}|^2} + \frac{1-\eta}{\eta|\mathcal{H}^T \mathbb{Z}|^2}, \quad (\text{A38})$$

$$S_{xF}(\Omega) = \frac{\hbar k_p}{\mathcal{H}^T \mathbb{Z}} \left[(1+R_e)^2 \mathcal{H}^T \left(-\mathbb{R}\mathbb{S}_{ext}\mathbb{S}_{ext}^\dagger\mathbb{T}^\dagger + \mathcal{L}_1\dot{\mathcal{L}}_{d1}^\dagger + \mathcal{L}_2\dot{\mathcal{L}}_{d2}^\dagger \right) \mathbb{P}^\dagger(\delta)\mathbb{B}^\dagger E + T_e \mathcal{H}^T \mathbb{T}\mathcal{L}_v^\dagger E \right], \quad (\text{A39})$$

and

$$S_{FF}(\Omega) = \hbar^2 k_p^2 (1+R_e^2)^2 E^\dagger \mathbb{B}\mathbb{P}(\delta) \left(\mathbb{T}_d \mathbb{S}_{ext} \mathbb{S}_{ext}^\dagger \mathbb{T}_d^\dagger + \dot{\mathcal{L}}_{d1} \dot{\mathcal{L}}_{d1}^\dagger + \dot{\mathcal{L}}_{d2} \dot{\mathcal{L}}_{d2}^\dagger \right) \mathbb{P}^\dagger(\delta) \mathbb{B}^\dagger E + \hbar^2 k_p^2 T_e^2 E^\dagger \mathcal{L}_v \mathcal{L}_v^\dagger E. \quad (\text{A40})$$

From Eq. A37, we can compute the power spectral density normalized to the gravitational wave strain yielding, where we take into account the effects of high-frequency corrections [72]:

$$S_h(\Omega) = S_x(\Omega) \frac{4}{m^2 L_{\text{arm}}^2 \Omega^4 |\chi_{\text{eff}}(\Omega)|^2} \frac{\Omega^2 \tau_{\text{arm}}^2}{\sin^2(\Omega \tau_{\text{arm}})}. \quad (\text{A41})$$

-
- [1] B. Abbott *et al.*, Observation of gravitational waves from a binary black hole merger, *Physical Review Letters* **116**, 10.1103/physrevlett.116.061102 (2016).
 [2] B. P. Abbott *et al.*, GW170817: Observation of Gravitational Waves from a Binary Neutron Star Inspiral, *Physical Review Letters* **119**, 161101 (2017).

- [3] B. P. Abbott *et al.*, GWTC-1: A Gravitational-Wave Transient Catalog of Compact Binary Mergers Observed by LIGO and Virgo during the First and Second Observing Runs, *Physical Review X* **9**, 031040 (2019), arXiv: 1811.12907.
- [4] The LIGO Scientific Collaboration and the Virgo Collaboration *et al.*, Gwtc-2.1: Deep extended catalog of compact binary coalescences observed by ligo and virgo during the first half of the third observing run (2022), arXiv:2108.01045 [gr-qc].
- [5] The LIGO Scientific Collaboration and the Virgo Collaboration and the KAGRA Collaboration *et al.*, Gwtc-3: Compact binary coalescences observed by ligo and virgo during the second part of the third observing run, *Physical Review X* **13**, 10.1103/physrevx.13.041039 (2023).
- [6] Marica Branchesi *et al.*, Science with the einstein telescope: a comparison of different designs, *Journal of Cosmology and Astroparticle Physics* **2023** (07), 068.
- [7] Matthew Evans *et al.*, A horizon study for cosmic explorer: Science, observatories, and community (2021), arXiv:2109.09882 [astro-ph.IM].
- [8] LIGO Scientific Collaboration, Advanced LIGO, *Classical and Quantum Gravity* **32**, 74001 (2015).
- [9] F. Acernese *et al.*, Advanced virgo status, *Journal of Physics: Conference Series* **1342**, 012010 (2020).
- [10] Akutsu, T. *et al.*, KAGRA: 2.5 generation interferometric gravitational wave detector, *Nature Astronomy* **3**, 35 (2019), arXiv: 1811.08079.
- [11] J. S. Read, C. Markakis, M. Shibata, K. Uryu, J. D. Creighton, and J. L. Friedman, Measuring the neutron star equation of state with gravitational wave observations, *Physical Review D - Particles, Fields, Gravitation and Cosmology* **79**, 1 (2009), arXiv: 0901.3258.
- [12] A. Bauswein and H. T. Janka, Measuring neutron-star properties via gravitational waves from neutron-star mergers, *Physical Review Letters* **108**, 1 (2012), arXiv: 1106.1616.
- [13] I. Harry and T. Hinderer, Observing and measuring the neutron-star equation-of-state in spinning binary neutron star systems, *Classical and Quantum Gravity* **35**, 145010 (2018).
- [14] L. Baiotti and L. Rezzolla, Binary neutron star mergers: a review of einstein's richest laboratory, *Reports on Progress in Physics* **80**, 096901 (2017).
- [15] R. S. Conklin, B. Holdom, and J. Ren, Gravitational wave echoes through new windows, *Physical Review D* **98**, 10.1103/physrevd.98.044021 (2018).
- [16] D. Ganapathy, W. Jia, M. Nakano, V. Xu, N. Aritomi, T. Cullen, N. Kijbunchoo, S. Dwyer, A. Mullaevy, L. McCuller, *et al.*, Broadband quantum enhancement of the ligo detectors with frequency-dependent squeezing, *Physical Review X* **13**, 041021 (2023).
- [17] R. Schnabel, Squeezed states of light and their applications in laser interferometers, *Physics Reports* **684**, 1 (2017).
- [18] H. J. Kimble, Y. Levin, A. B. Matsko, K. S. Thorne, and S. P. Vyatchanin, Conversion of conventional gravitational-wave interferometers into quantum nondemolition interferometers by modifying their input and/or output optics, *Physical Review D* **65**, 022002 (2001), arXiv: gr-qc/0008026.
- [19] D. Ganapathy, L. McCuller, J. G. Rollins, E. D. Hall, L. Barsotti, and M. Evans, Tuning advanced ligo to kilohertz signals from neutron-star collisions, *Physical Review D* **103**, 10.1103/physrevd.103.022002 (2021).
- [20] J. W. Gardner, T. Gefen, S. A. Haine, J. J. Hope, and Y. Chen, Holevo cramér-rao bound for waveform estimation of gravitational waves (2023), arXiv:2308.06253 [gr-qc].
- [21] K. Ackley *et al.*, Neutron star extreme matter observatory: A kilohertz-band gravitational-wave detector in the global network, *Publications of the Astronomical Society of Australia* **37**, 10.1017/pasa.2020.39 (2020).
- [22] A. Thüring, R. Schnabel, H. Lück, and K. Danzmann, Detuned twin-signal-recycling for ultrahigh-precision interferometers, *Optics Letters* **32**, 985 (2007).
- [23] A. Thüring, C. Gräf, H. Vahlbruch, M. Mehmet, K. Danzmann, and R. Schnabel, Broadband squeezing of quantum noise in a michelson interferometer with twin-signal-recycling, *Opt. Lett.* **34**, 824 (2009).
- [24] C. Gräf, A. Thüring, H. Vahlbruch, K. Danzmann, and R. Schnabel, Length sensing and control of a michelson interferometer with power recycling and twin signal recycling cavities, *Opt. Express* **21**, 5287 (2013).
- [25] Y. Chen, Macroscopic quantum mechanics: Theory and experimental concepts of optomechanics, *Journal of Physics B: Atomic, Molecular and Optical Physics* **46**, 104001 (2013), arXiv: 1302.1924.
- [26] A. Wicht, K. Danzmann, M. Fleischhauer, M. Scully, G. Müller, and R. H. Rinkleff, White-light cavities, atomic phase coherence, and gravitational wave detectors, *Optics Communications* **134**, 431 (1997).
- [27] A. Wicht, M. Müller, R. H. Rinkleff, A. Rocco, and K. Danzmann, Experimental demonstration of negative dispersion without absorption, *Optics Communications* **179**, 107 (2000), publisher: Elsevier Science Publishers B.V.
- [28] S. Wise, G. Mueller, D. Reitze, D. B. Tanner, and B. F. Whiting, Linewidth-broadened Fabry-Perot cavities within future gravitational wave detectors, *Classical and Quantum Gravity* **21**, S1031 (2004).
- [29] H. Miao, Y. Ma, C. Zhao, and Y. Chen, Enhancing the Bandwidth of Gravitational-Wave Detectors with Unstable Optomechanical Filters, *Physical Review Letters* **115**, 211104 (2015), arXiv: 1506.00117v1.
- [30] M. A. Page, M. Goryachev, H. Miao, Y. Chen, Y. Ma, D. Mason, M. Rossi, C. D. Blair, L. Ju, D. G. Blair, *et al.*, Gravitational wave detectors with broadband high frequency sensitivity, *Communications Physics* **4**, 27 (2021).
- [31] C. Wang, C. Zhao, X. Li, E. Zhou, H. Miao, Y. Chen, and Y. Ma, Boosting the sensitivity of high-frequency gravitational wave detectors using p t-symmetry, *Physical Review D* **106**, 082002 (2022).
- [32] H. Rehbein, J. Harms, R. Schnabel, and K. Danzmann, Optical transfer functions of Kerr nonlinear cavities and interferometers, *Physical Review Letters* **95**, 1 (2005).
- [33] V. Peano, H. G. L. Schwefel, C. Marquardt, and F. Marquardt, Intracavity Squeezing Can Enhance Quantum-Limited Optomechanical Position Detection through Deamplification, *Phys. Rev. Lett.* **115**, 243603 (2015).

- [34] M. Korobko, L. Kleybolte, S. Ast, H. Miao, Y. Chen, and R. Schnabel, Beating the Standard Sensitivity-Bandwidth Limit of Cavity-Enhanced Interferometers with Internal Squeezed-Light Generation, *Phys. Rev. Lett.* **118**, 143601 (2017), publisher: American Physical Society.
- [35] M. Korobko, J. Südbeck, S. Steinlechner, and R. Schnabel, Mitigating quantum decoherence in force sensors by internal squeezing, *Phys. Rev. Lett.* **131**, 143603 (2023).
- [36] M. Korobko, J. Südbeck, S. Steinlechner, and R. Schnabel, Fundamental sensitivity limit of lossy cavity-enhanced interferometers with external and internal squeezing (2023), [arXiv:2307.09130 \[quant-ph\]](https://arxiv.org/abs/2307.09130).
- [37] J. W. Gardner, M. J. Yap, V. Adya, S. Chua, B. J. Slagmolen, and D. E. McClelland, Nondegenerate internal squeezing: An all-optical, loss-resistant quantum technique for gravitational-wave detection, *Physical Review D* **106**, 10.1103/physrevd.106.1041101 (2022).
- [38] M. Korobko, Y. Ma, Y. Chen, and R. Schnabel, Quantum expander for gravitational-wave observatories, *Light: Science & Applications* **8**, 118 (2019).
- [39] V. Adya, M. J. Yap, D. Töyrä, T. McRae, P. Altin, L. Sarre, M. Meijerink, N. Kijbunchoo, B. Slagmolen, R. Ward, *et al.*, Quantum enhanced khz gravitational wave detector with internal squeezing, *Classical and Quantum Gravity* **37**, 07LT02 (2020).
- [40] Z. Yan, X. Jia, C. Xie, and K. Peng, Coherent feedback control of multipartite quantum entanglement for optical fields, *Physical Review A* **84**, 062304 (2011).
- [41] Y. Zhou, X. Jia, F. Li, J. Yu, C. Xie, and K. Peng, Quantum coherent feedback control for generation system of optical entangled state, *Scientific Reports* **5**, 11132 (2015).
- [42] X. Pan, H. Chen, T. Wei, J. Zhang, A. M. Marino, N. Treps, R. T. Glasser, and J. Jing, Experimental realization of a feedback optical parametric amplifier with four-wave mixing, *Physical Review B* **97**, 161115 (2018).
- [43] S. Yokoyama, D. Peace, W. Asavanant, T. Tajiri, B. Haylock, M. Ghadimi, M. Lobino, E. H. Huntington, and H. Yonezawa, Feasibility study of a coherent feedback squeezer, *Physical Review A* **101**, 10.1103/physreva.101.033802 (2020).
- [44] A. Buonanno and Y. Chen, Scaling law in signal recycled laser-interferometer gravitational-wave detectors, *Physical Review D* **67**, 10.1103/physrevd.67.062002 (2003).
- [45] M. Korobko, *Taming the quantum noise: How quantum metrology can expand the reach of gravitational-wave observatories*, Ph.D. thesis, University of Hamburg (2020).
- [46] C. M. Caves and B. L. Schumaker, New formalism for two-photon quantum optics. I. Quadrature phases and squeezed states, *Physical Review A* **31**, 3068 (1985).
- [47] V. B. Braginsky and F. Khalilli, *Quantum Measurement* (Cambridge University Press, 1992).
- [48] D. Walls, Squeezed states of light, *Nature* **306** (1983).
- [49] F. Khalili, Reducing the mirrors coating noise in laser gravitational-wave antennae by means of double mirrors, *Physics Letters A* **334**, 67–72 (2005).
- [50] V. B. Braginsky, M. L. Gorodetsky, and F. Y. Khalili, Optical bars in gravitational wave antennas, *Physics Letters A* **232**, 340 (1997).
- [51] A. Buonanno and Y. Chen, Laser-interferometer gravitational-wave optical-spring detectors, *Classical and Quantum Gravity* **19**, 1569–1574 (2002).
- [52] K. Somiya, Y. Kataoka, J. Kato, N. Saito, and K. Yano, Parametric signal amplification to create a stiff optical bar, *Physics Letters A* **380**, 521–524 (2016).
- [53] M. Korobko, F. Khalili, and R. Schnabel, Engineering the optical spring via intra-cavity optical-parametric amplification, *Physics Letters A* **382**, 2238–2244 (2018).
- [54] S. Ast, R. M. Nia, A. Schönbeck, N. Lastzka, J. Steinlechner, T. Eberle, M. Mehmet, S. Steinlechner, and R. Schnabel, High-efficiency frequency doubling of continuous-wave laser light, *Optics Letters* **36**, 3467 (2011).
- [55] C. L. Mueller, M. A. Arain, G. Ciani, R. T. DeRosa, A. Effler, D. Feldbaum, V. V. Frolov, P. Fulda, J. Gleason, M. Heintze, K. Kawabe, E. J. King, K. Kokeyama, W. Z. Korth, R. M. Martin, A. Mullavey, J. Peold, V. Quetschke, D. H. Reitze, D. B. Tanner, C. Vorvick, L. F. Williams, and G. Mueller, The advanced ligo input optics, *Review of Scientific Instruments* **87**, 10.1063/1.4936974 (2016).
- [56] L. Barsotti, L. McCuller, M. Evans, P. Fritschel, *The A+ design curve*, Technical notes T1800042-v5 (<https://dcc.ligo.org/LIGO-T1800042/public>, 2018).
- [57] H. Yang, W. E. East, V. Paschalidis, F. Pretorius, and R. F. Mendes, Evolution of highly eccentric binary neutron stars including tidal effects, *Physical Review D* **98**, 10.1103/physrevd.98.044007 (2018).
- [58] J. W. Gardner, L. Sun, S. Borhanian, P. D. Lasky, E. Thrane, D. E. McClelland, and B. J. Slagmolen, Multimessenger astronomy with a southern-hemisphere gravitational-wave observatory, *Physical Review D* **108**, 10.1103/physrevd.108.123026 (2023).
- [59] I. Gupta, C. Afle, K. G. Arun, A. Bandopadhyay, M. Baryakhtar, S. Biscoveanu, S. Borhanian, F. Broekgaarden, A. Corsi, A. Dhani, M. Evans, E. D. Hall, O. A. Hannuksela, K. Kacanja, R. Kashyap, S. Khadkikar, K. Kuns, T. G. F. Li, A. L. Miller, A. H. Nitz, B. J. Owen, C. Palomba, A. Pearce, H. Phurailatpam, B. Rajbhandari, J. Read, J. D. Romano, B. S. Sathyaprakash, D. H. Shoemaker, D. Singh, S. Vitale, L. Barsotti, E. Berti, C. Cahillane, H.-Y. Chen, P. Fritschel, C.-J. Haster, P. Landry, G. Lovelace, D. McClelland, B. J. J. Slagmolen, J. Smith, M. Soares-Santos, L. Sun, D. Tanner, H. Yamamoto, and M. Zucker, Characterizing gravitational wave detector networks: From a^d to cosmic explorer (2024), [arXiv:2307.10421 \[gr-qc\]](https://arxiv.org/abs/2307.10421).
- [60] H. Miao, N. D. Smith, and M. Evans, Quantum limit for laser interferometric gravitational-wave detectors from optical dissipation, *Physical Review X* **9**, 10.1103/physrevx.9.011053 (2019).

- [61] N. Kijbunchoo, T. McRae, D. Sigg, S. E. Dwyer, H. Yu, L. McCuller, L. Barsotti, C. D. Blair, A. Effler, M. Evans, A. Fernandez-Galiana, V. V. Frolov, F. Matichard, N. Mavalvala, A. Mullavey, B. J. J. Slagmolen, M. Tse, C. Whittle, and D. E. McClelland, Low phase noise squeezed vacuum for future generation gravitational wave detectors, *Classical and Quantum Gravity* **37**, 185014 (2020).
- [62] P. Kwee, J. Miller, T. Isogai, L. Barsotti, and M. Evans, Decoherence and degradation of squeezed states in quantum filter cavities, *Phys. Rev. D* **90**, 062006 (2014).
- [63] L. McCuller *et al.*, Ligo's quantum response to squeezed states, *Phys. Rev. D* **104**, 062006 (2021).
- [64] A. W. Goodwin-Jones, R. Cabrita, M. Korobko, M. van Beuzekom, D. D. Brown, V. Fafone, J. van Heijningen, A. Rocchi, M. G. Schirowski, and M. Tacca, Transverse mode control in quantum enhanced interferometers: A review and recommendations for a new generation, arXiv preprint arXiv:2311.04736 (2023).
- [65] K. M. Backes, D. A. Palken, S. A. Kenany, B. M. Brubaker, S. B. Cahn, A. Droster, G. C. Hilton, S. Ghosh, H. Jackson, S. K. Lamoreaux, A. F. Leder, K. W. Lehnert, S. M. Lewis, M. Malnou, R. H. Maruyama, N. M. Rapidis, M. Simanovskaia, S. Singh, D. H. Speller, I. Urdinaran, L. R. Vale, E. C. van Assendelft, K. van Bibber, and H. Wang, A quantum enhanced search for dark matter axions, *Nature* **590**, 238–242 (2021).
- [66] D. Carney, G. Krnjaic, D. C. Moore, C. A. Regal, G. Afek, S. Bhave, B. Brubaker, T. Corbitt, J. Cripe, N. Crisosto, A. Geraci, S. Ghosh, J. G. E. Harris, A. Hook, E. W. Kolb, J. Kunjummen, R. F. Lang, T. Li, T. Lin, Z. Liu, J. Lykken, L. Magrini, J. Manley, N. Matsumoto, A. Monte, F. Monteiro, T. Purdy, C. J. Riedel, R. Singh, S. Singh, K. Sinha, J. M. Taylor, J. Qin, D. J. Wilson, and Y. Zhao, Mechanical quantum sensing in the search for dark matter, *Quantum Science and Technology* **6**, 024002 (2021).
- [67] H. Yang, V. Paschalidis, K. Yagi, L. Lehner, F. Pretorius, and N. Yunes, Gravitational wave spectroscopy of binary neutron star merger remnants with mode stacking, *Physical Review D* **97**, 10.1103/physrevd.97.024049 (2018).
- [68] H. Miao, H. Yang, and D. Martynov, Towards the design of gravitational-wave detectors for probing neutron-star physics, *Physical Review D* **98**, 10.1103/physrevd.98.044044 (2018).
- [69] H. Shen, H. Toki, K. Oyamatsu, and K. Sumiyoshi, Relativistic equation of state of nuclear matter for supernova and neutron star, *Nuclear Physics A* **637**, 435 (1998).
- [70] A. Bauswein, N. Stergioulas, and H.-T. Janka, Exploring properties of high-density matter through remnants of neutron-star mergers, *The European Physical Journal A* **52**, 10.1140/epja/i2016-16056-7 (2016).
- [71] E. Nichols and G. Hull, The pressure due to radiation, *Astrophysical Journal* **17**, 315 (1903).
- [72] M. Rakhmanov, J. D. Romano, and J. T. Whelan, High-frequency corrections to the detector response and their effect on searches for gravitational waves, *Classical and Quantum Gravity* **25**, 184017 (2008).

Thermally Stable Peltier Controlled Vacuum Chamber for Electrical Transport Measurements

S. F. Poole,¹ O. J. Amin,¹ A. Solomon,¹ L. X. Barton,¹ R. P. Champion,¹ K. W. Edmonds,¹ and P. Wadley¹
School of Physics and Astronomy, University of Nottingham, University Park, Nottingham, NG7 2RD, United Kingdom

(*Electronic mail: Peter.Wadley@nottingham.ac.uk)

(Dated: 7 March 2024)

The design, manufacture and characterisation of an inexpensive, temperature controlled vacuum chamber with millikelvin stability for electrical transport measurements at and near room temperature is reported. A commercially available Peltier device and high-precision temperature controller are used to actively heat and cool the sample space. The system was designed to minimise thermal fluctuations in spintronic and semiconductor transport measurements but the general principle is relevant to a wide range of electrical measurement applications. The main issues overcome are the mounting of a sample with a path of high thermal conductivity through to the Peltier device and the heat-sinking of said Peltier device inside of a vacuum. A copper slug is used as the mount for a sample and a large copper block is used as a thermal feedthrough before a passive heatsink is used to cool this block. The Peltier device provides 20 W of heating and cooling power achieving a maximum range of 30 K below and 40 K above the ambient temperature. The temperature stability is within 5 mK at all set points with even better performance above ambient temperature. A vacuum pressure of 10^{-8} hPa is achievable. As a demonstration, we present experimental results from current-induced electrical switching of a CuMnAs thin film. Transport measurements with and without the Peltier control emphasise the importance of a constant temperature in these applications. The thermal lag between the sample space measurement and the sample itself is observed through magnetoresistance values measured during a temperature sweep.

I. INTRODUCTION

Electrical transport measurements are ubiquitous in materials research, such as in the study of electronic, thermoelectric and spintronic devices¹⁻⁶. In most cases, these devices are used at or near to ambient conditions, with the device encased in a protective case, such as under potting compound. The characterisation measurements performed in the pursuit of such devices, however, are typically performed in atmosphere, lacking effective temperature control, or in cryostats which often do not perform well near to room temperature.

Here, the design, manufacture and characterisation of an inexpensive, stable temperature controlled vacuum chamber for electrical transport measurements at and near room temperature are reported. This system uses a Peltier device (also known as a thermo-electric heat pump, thermo-electric generator, or thermo-electric cooler) to control the sample temperature and has a short thermal path between the sample and a thermal reservoir to aid in the removal of waste heat from the sample.

A Peltier device is a bi-directional heat pump capable of high precision temperature control within a ~ 50 K range relative to room temperature. They are therefore a popular solution for temperature control near ambient temperature in many non-vacuum applications⁷. A Peltier device can rapidly switch between heating and cooling to achieve stable and high precision temperature control. Only a few other systems have been developed which utilise Peltier devices to control temperature inside vacuum chambers, for example for x-ray⁸ and neutron scattering⁹, and material processing applications¹⁰. In Ref. 11, Raihane *et al.* report on a system in which a Peltier device, mounted outside a vacuum chamber, is used to control the temperature for measurements of the glass transition tem-

perature in thin film polymers. Their design is effective for their specific requirements, however for transport measurement applications, several features could be optimised.

In Ref. 11, the vacuum chamber is sealed with copper gaskets making swapping samples expensive and difficult; the sample cell is separately sealed introducing more complexity; and the number of electrical connections to the sample is fewer than required for more general transport measurements. Our aim was to create a system that is more generally applicable to condensed matter research and to also include the following performance criteria: pressure $< 10^{-6}$ hPa, stability within $\pm 10^{-2}$ K and range of $-5-50$ ° C. The sample should have up to 12 electrical connections and there must be a good thermal path between the Peltier device and the sample. Additionally, the Peltier power wires should be electrically shielded from the measurement wires to avoid interference.

The resulting design, photographed in Fig. 1, utilises a large mass of high purity copper as a thermal feedthrough, to which the Peltier device and sample space is attached. This copper is then cooled external to the vacuum using a conventional passive method. The system has since become a staple in our research and so we hope to share our insights with the reader now. In the following, the key design features are explained with some important compromises being highlighted before the performance in terms of vacuum and temperature control are reported. To demonstrate a typical application and highlight the significance of stable temperature control, we present as an example some current-induced switching measurements of an antiferromagnetic CuMnAs thin film. Finally some suggestions and possible improvements are provided for others wishing to produce a similar system who may have slightly different requirements or expectations.

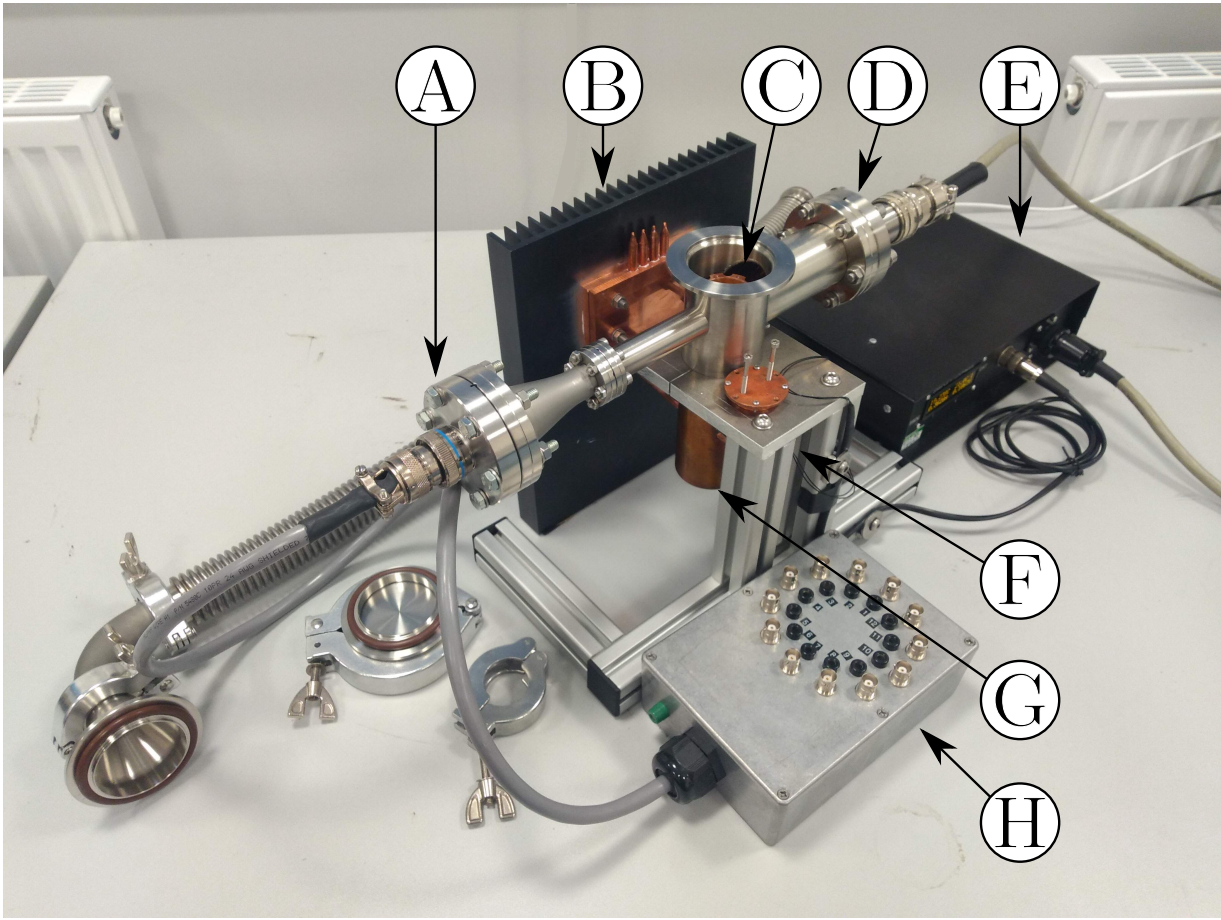


FIG. 1. Photograph of the fully assembled system. The beige cable runs from the power feedthrough (D) to connect the Peltier device and PT100 sensor to the temperature control unit (E) which is in a housing with the mains AC to DC converter, screen and connectors. The black cable connects the external thermocouple (F), which is embedded in the thermal feedthrough (G), to the temperature control unit. The grey cable connects the signal feedthrough (A) to the breakout box (H) which provides convenient access to each of the 12 sample wires using either the central pin of a BNC connector or a 4mm banana plug. The heatsink assembly (B) can be seen and the main chamber (C) which contains the sample space and Peltier device (within the vacuum chamber) is also shown.

II. DESIGN

The system comprises a T-shaped vacuum chamber, as shown in the computer aided design (CAD) drawing of Fig. 2(a), with a pumping port on top and a sealed bottom achieved by vacuum brazing a copper cylinder inside it. This copper cylinder acts both as a mounting point and as a thermal feedthrough. The two arms of the T are used for signal feedthroughs. The Peltier device is sandwiched between a copper sample space and the bottom copper cylinder of the vacuum chamber, with a bracket to tidy the wiring and keep the Peltier device central. Four holes in the copper cylinder below the vacuum chamber allow L-shaped heat pipes to conduct heat between the Peltier device and heatsinks. The heatsink acts as a heat source for the Peltier device when heating the sample space, and as a radiator to expel waste heat when the device is cooled. A two-part copper bracket sandwiches the pipes. A large passive heatsink was chosen over more common, small, fan assisted heatsinks because the vi-

brations of a fan may induce additional noise to sensitive measurements. The signal feedthroughs facilitate a 12-pin header on one side and the two power pins of the Peltier device and four pins of a PT100 platinum resistor on the other. The stand was made from extruded aluminium for the base and aluminium plate for the bracket. Stainless steel threaded rod was used to secure the heatsink to the stand and regular nuts and machine screws were used to apply mounting pressure to the copper bracket and heatsink contact areas. A thermocouple is inserted into the copper cylinder as centrally and as close to the Peltier as possible to provide heatsink temperature monitoring.

The sample space houses the resistor and the 12-pin sample header's matching socket as shown in Fig. 2(b). The sample is attached to a copper slug which runs through the center of the sample header, using thermally conductive varnish or silver conductive paste, before bonding wires are used to connect the sample to the pins of the header. The header can then be put into the socket, The lid and the raised stem of the sample space are designed to apply a small amount of pressure onto

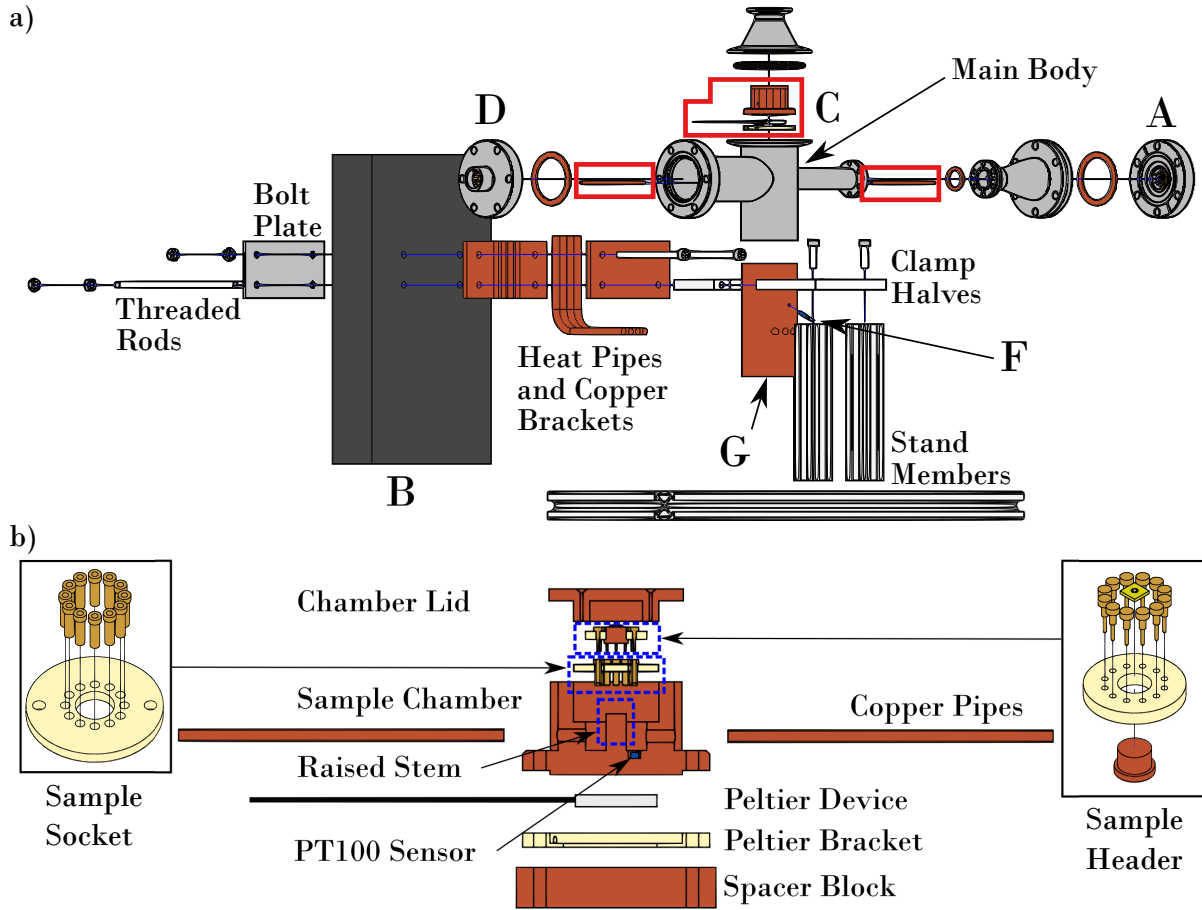


FIG. 2. Exploded views of the 3D CAD drawings for the system excluding wiring and most fasteners. a) shows the assembly of the whole system while b) focuses on the smaller parts of the sample space. The letter labels match those in Figure 1: A is the signal feedthrough, B is the heatsink, C is the sample space sub-assembly, D is the power feedthrough, F is the external thermocouple and G is the thermal feedthrough. The red boxes in (a) correspond to the components drawn in panel (b).

the header to ensure good thermal contact between the sample and the Peltier device through the raised stem. The spacer block is simply the admission of a miscalculation whereby the pipes could not be inserted unless the sample space was raised by a centimetre. The sample socket is mounted to the sample space using two machine screws made from polyether ether ketone (PEEK), a machinable polymer suitable for high vacuum applications. The sample space, Peltier bracket and spacer block are all fastened to the copper cylinder of the vacuum chamber using steel screws.

To control the temperature, an off the shelf 20 W, 20 mm \times 20 mm Peltier device was controlled by a Meerstetter EngineeringTM TEC-1089 precision Peltier temperature controller. This reads both the sample space temperature and the external copper block temperature and has a range of features including protections against over-current when changing from heating to cooling and auto-tuning of the proportional integral derivative (PID) parameters.

III. MANUFACTURE

The main body of the vacuum chamber was manufactured by LewVac by welding the tubes and flanges to make the Tee shape and then vacuum brazing the copper cylinder into the large tube. The body is a 50.8 mm outer diameter (OD) stainless steel tube with one 40 mm OD tube and one 19 mm OD tube. The 50 mm tube has a Klein flange for quick and easy access while the other two flanges are copper flanges for a better and more permanent seal. The 19 mm tube is expanded with an adapter to accommodate a 19-pin signal feedthrough and the 40 mm tube has a 6-pin power feedthrough. Four of these pins are used for the PT100 sensor and the remaining two for the Peltier device itself. Any internal thermal contacting face is joined with, vacuum-safe thermally conductive varnish while all external thermal contacts are joined with thermal paste.

The in-house workshop's computer numerically controlled (CNC) milling machines and manual lathes are the primary tools for the manufacture of the three custom parts and to

drill the four holes in the copper cylinder. These machines are also utilised to manufacture the proprietary headers. All the mounting holes were drilled using the CNC mill and the heatpipe holes in the thermal feedthrough were first drilled and then reamed to enable a press fit.

The sample space and lid were first turned on a lathe before the internal geometries were milled. Through holes were drilled for bolting to the vacuum chamber and holes were drilled and tapped for attaching the lid and sample socket. The Peltier bracket, sample socket body and sample header bodies are made from PEEK. The pins and sockets were press fitted to their respective bodies. The Peltier device is inserted into the bracket with its wires fed through holes in the outer cylindrical face to be fed to the power feedthrough. The copper heatpipe brackets were made by first drilling four holes in a block of copper and then splitting the block in half using a slitting saw on the mill. The meeting face of one bracket and the heatsink were polished, removing the anodising on the heatsink, to maximise thermal conduction. The stand members are made from extruded aluminium and the clamp halves were made by milling a 50.8 mm hole in a piece of 10 mm thick aluminium and then splitting it in twain. One half has a through hole to clear the threaded rods and the other is tapped to a matching thread.

The wiring was done using vacuum safe solder to connect single core enamelled wires to the 12-pin sample socket and the PT100 sensor. The Peltier power wires were multi-core wires protected with ceramic beads. The feedthroughs have been designed such that the feedthrough can be removed from the wires on the inside and outside. The signal feedthrough uses crimp connectors to make a plug that can be inserted to the feedthrough as one piece. The power feedthrough uses double-ended copper screw terminals to make it possible to disconnect the wires so no solder is needed on these connections. On the outside, mil-spec connectors are typical and so these were used. The Peltier controller and necessary power supply and connectors are all housed in one box. The external thermocouple is press fitted into the copper cylinder with thermal paste to improve thermal conductivity and the thermocouple has its own connector on the controller housing (the thin black cable in Fig. 1)

IV. PERFORMANCE CHARACTERISATION

The key performance criteria are vacuum pressure, temperature control range, thermal stability and sample thermal response. Pressures of 10^{-6} hPa are readily achieved just by pumping with a turbo pump. If lower pressures are required, by heating the sample space using nothing but the Peltier device, it is possible to reduce the pressure to 10^{-8} hPa. The turbo pump can be run continuously. If vibrations are found to introduce measurement noise then a valve can be closed to isolate the chamber. The leak rate was estimated to be 10^{-6} hPa s^{-1} and so high vacuum will be lost within an hour.

The maximum temperature range was found to be -8 °C to $+65$ °C with an ambient temperature of 22 °C. The stability was tested and can be seen in Fig. 3 (a-c). The stability was

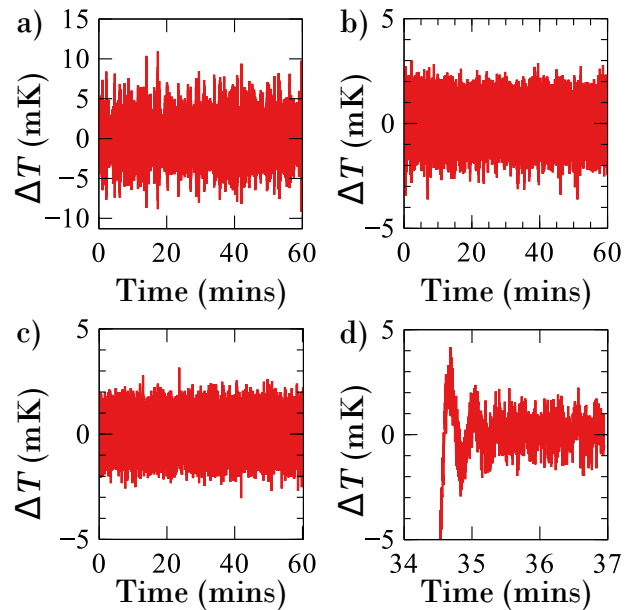


FIG. 3. a-c) Plots of thermal stability over time for a) $T = -5^\circ\text{C}$, b) $T = 21^\circ\text{C}$ and c) $T = 60^\circ\text{C}$ with a room temperature of around 18°C . d) Stabilisation portion of a ramp from $T = 21^\circ\text{C}$ to $T = 60^\circ\text{C}$ with a target ramp rate of 0.01 °C/s.

measured at (a) -5 °C, (b) 21 °C and (c) 60 °C, yielding root-mean-square deviations from the setpoint of 1.6 mK, 0.7 mK and 0.7 mK respectively. Figure 3 (d) shows the amount of overshoot when ramping the temperature from 21 °C to 60 °C using the ramp rate suggested by the autotuning. The maximum overshoot is 4 mK. The system is fully stable within about a minute after reaching the target temperature.

V. APPLICATION EXAMPLE

CuMnAs is an antiferromagnetic material in which the magnetic order parameter can be switched using electrical current pulses^{12,13}. Above a threshold pulse current density, CuMnAs thin films exhibit a resistive switching signal that relaxes to equilibrium over a time-scale of several minutes at room temperature¹⁴⁻¹⁶. The signal amplitude and decay rate display strong temperature dependence, providing an ideal study of the temperature stability in the Peltier controlled transport system.

A room-temperature switching experiment was carried out following the procedures from Refs.^{12,14,16}. An 8-arm device, with 10 μm arm width, was fabricated from a 46 nm layer of CuMnAs epitaxially grown on GaP(001) using established methods¹⁷. Figure 4(a) shows an optical micrograph of the patterned device. The device was secured onto the sample header using GE varnish and wire bonds were made between the device contact pads and the sample header pins. Once the device was loaded into the system sample socket, situated in the sample chamber as shown in Fig. 2(b), the system was evacuated to 10^{-6} hPa pressures.

Current pulses of 51 mA amplitude, 1 ms duration, were

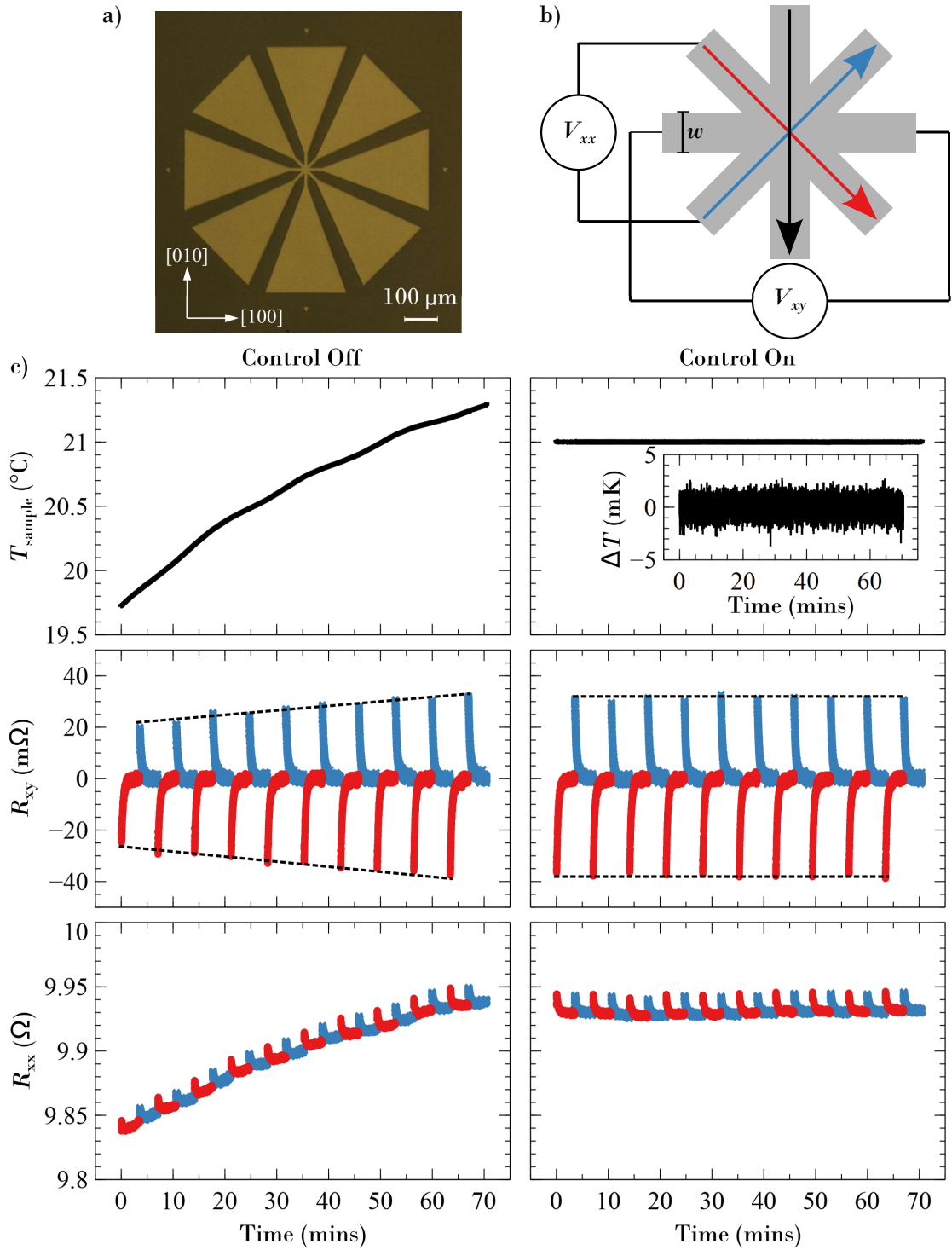


FIG. 4. Current-induced resistive switching experiment conducted in the Peltier-controlled system. a) Optical micrograph of the 8-arm CuMnAs device, with an arm width of $w = 10 \mu\text{m}$. b) Schematic of the pulse and probe geometry with the arm width, w , illustrated. 51 mA electrical pulses were applied along the diagonal arms of the device (red and blue arrows corresponding to red circles and blue crosses in c)). After each pulse a continuous probe current was applied along the vertical arm of the device (black arrow) and the longitudinal voltage, V_{xx} , and transverse voltage, V_{xy} , were measured. c) Switching measurements were carried out with the Peltier controller turned off (left column) and turned on with set temperature 21 $^{\circ}\text{C}$ (right column). The top two plots show the sample space temperature measured by the PT100 sensor. The middle and bottom plots show the respective R_{xy} and R_{xx} measured during a sequence of 10 pairs of pulses. As shown comparing the left and right plots, stable temperature is crucial for achieving reproducible switching data. The size of the R_{xy} signal increases as the system temperature increases and the base R_{xx} value follows the temperature drift.

applied alternately along the diagonal arms of the device, as shown by the red and blue arrows in Fig 4(b). After each pulse, a continuous 1 mA probe current was applied along the vertical arm of the device and the longitudinal voltage, V_{xx} , and transverse voltage, V_{xy} , were measured for the following ~ 200 s. The plots in Fig. 4(c) show the measured sample space temperature (top row), R_{xy} (middle row), and R_{xx} (bottom row) during a pulsing sequence conducted with the Peltier controller turned off (left column) and set to 21 °C (right column). Note that the R_{xy} signals are centred on zero by subtracting the mean of the final 100 points in each trace.

Both the R_{xy} and R_{xx} signals exhibit appreciable temperature dependence. With the Peltier controller turned off, a sample space temperature drift of ~ 1.5 °C caused a change in the R_{xy} signal amplitude of ≈ 30 %, indicated by the dashed lines, and an R_{xx} base value drift of 1 %, following the behaviour of the sample temperature. When the Peltier controller was turned on, a stable sample temperature of 21.000 ± 0.003 °C was achieved. The R_{xy} amplitude was consistent for the complete pulsing set, as shown by the dashed horizontal lines. The R_{xx} base value was stable within an 0.02 % variation.

In order to test the thermal conductivity between the sample and the copper chamber, the transverse and linear resistances were measured during a temperature sweep in the system. The 8-arm device used for this study was fabricated from a 60 nm layer of $\text{CuMnAs}_{0.9}\text{Sb}_{0.1}$ epitaxially grown on GaAs(001). The Sb doping of this sample changes the strain but leaves the conductivity and magnetic properties largely unaffected¹⁸ and so the sample can be considered the same as pure CuMnAs for the sake of this test. A current was applied along the [110] easy axis and the transverse and linear voltages were measured using the geometry shown in Fig. 4(b). Figure 5 shows the resulting R_{xx} and R_{xy} values (red points) and temperature readings (black line) as a function of time during the temperature sweep. The difference between the R_{xx} values and the temperature in panel (a) suggests a thermal lag of ≈ 100 s while the R_{xy} values in panel (b) track the temperature changes almost exactly. The linear resistance value has a direct dependence on the temperature and so this result should be considered to be a more accurate measure of the sample temperature and shows some thermal lag between the sample and the Peltier device readout value. The transverse resistance measurements should not have a large temperature dependence and so this changing value is indicative of mixing between the linear and transverse voltage measurements, as a result of deviations from the perfect device geometry in fabrication, and the delayed response may be hidden by the scatter of the points.

VI. DISCUSSION AND OUTLOOK

A smaller thermal mass, and therefore more rapid thermal response and reduced costs, may appear attractive, however our experiments often include applying high current, short electrical pulses to a sample repeatedly. Because of this, a large thermal mass is preferable to diffuse the generated heat as quickly as possible. It is also helpful simply by increasing

the heat capacity and thus reducing the effect of convection on the external side of the Peltier device. It is also for thermal stability reasons that we chose to place the Peltier device inside the vacuum chamber instead of having it exposed to air. Finally, we chose to cool the heatsink passively to avoid vibrations which may introduce noise in sensitive electrical measurements.

It may seem preferable for the system to be designed such that a heatsink could be directly attached to the thermal feedthrough, eliminating the need for heatpipes. This approach, however, necessitates added complexity in either manufacturing the system or changing the sample, since the system would either need to be designed with a complex shape of thermal feedthrough or be upside down to mount the heatsink to (what is currently) the bottom of the thermal feedthrough. This was deemed worse than the chosen solution for this application.

In its current form, a magnetic field can only be applied along one axis (the in plane axis perpendicular to the arms of the tee) but the system cannot be rotated between the poles of a magnet for full in plane measurements because the arms get in the way. The design could be adapted to enable the use of magnetic fields along more than one axis.

With some adaptation, the sample space could be used for many applications requiring this temperature range, however, if there is no need for a large number of signal wires or a small bore, it may be possible to find a simpler solution such as the one used by Raihane *et al.*¹¹ There are many configurations possible for a Peltier controlled vacuum system, each with different priorities and drawbacks. In our case, thermal stability, ease of sample swapping and mitigation of electrical noise are our three top priorities in the design of the system.

Overall, this system has provided a relatively cheap and convenient way to ensure minimal thermal fluctuations occur in our transport measurements at and near to room temperature, without the need for cryogenics. This was achieved through the combination of a Peltier device placed inside a vacuum chamber, a thermal path almost entirely made of high-purity copper and the used of a high-performance temperature controller. The system allows our samples to be protected from oxidation while under testing and has since become a staple in our research. With some modifications we are confident that most researchers requiring transport measurements would benefit from such a system in their repertoire. The hope is that this design inspires and helps readers looking for a such a solution to discover their ideal system.

ACKNOWLEDGEMENTS

Manufacture and Assembly - Andrew Stuart, Tommy Napier - Engineering Support Team, School of Physics and Astronomy, University of Nottingham, Nottingham UK

¹J. Železný, P. Wadley, K. Olejník, A. Hoffmann, and H. Ohno, *Nat. Phys.* **14**, 220 (2018).

²E. Y. Vedmedenko *et al.*, *J. Phys. D: Appl. Phys.* **53**, 453001 (2020).

³Q. Shao, P. Li, L. Liu, H. Yang, S. Fukami, A. Razavi, H. Wu, K. Wang, F. Freimuth, Y. Mokrousov, M. D. Stiles, S. Emori, A. Hoffmann, J. Åk-

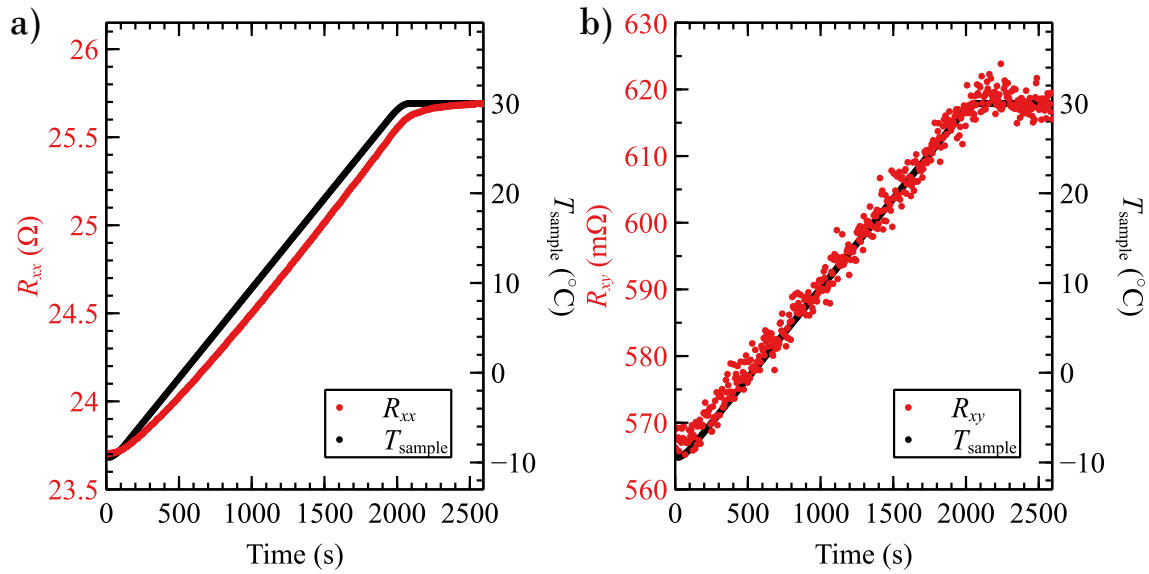


FIG. 5. Plots of (a) R_{xx} and (b) R_{xy} for an 8-arm device with $w = 5 \mu\text{m}$ arms fabricated on a 60 nm layer of $\text{CuMnAs}_{0.9}\text{Sb}_{0.1}$ during a temperature sweep from -8 – $30 \text{ }^\circ\text{C}$ over ≈ 30 minutes, with the measurement continuing for a further 500 s after the sweep. V_{xx} and V_{xy} were measured simultaneously such that the resistances were calculated by dividing these values by the applied current of 0.5 mA.

- erman, K. Roy, J.-P. Wang, S.-H. Yang, K. Garello, and W. Zhang, *IEEE Transactions on Magnetics* **57**, 1 (2021).
- ⁴K. Sun, J. Chen, and X. Yan, *Advanced Functional Materials* **31**, 2006773 (2021).
- ⁵V. K. Sangwan and M. C. Hersam, *Annual review of physical chemistry* **69**, 299 (2018).
- ⁶N. Jia, J. Cao, X. Y. Tan, J. Dong, H. Liu, C. K. I. Tan, J. Xu, Q. Yan, X. J. Loh, and A. Suardi, *Materials Today Physics* **21**, 100519 (2021).
- ⁷M. Shilpa, M. A. Raheman, A. Aabid, M. Baig, R. Veerasha, and N. Kudva, *FDMP-Fluid Dynamics & Materials Processing* **19**, 187 (2023).
- ⁸C. P. Mudd, H. Tipton, A. V. Parsegian, and D. Rau, *Review of scientific instruments* **58**, 2110 (1987).
- ⁹M. Bonetti and P. Calmettes, *Review of scientific instruments* **68**, 4163 (1997).
- ¹⁰C. D. Christiansen, K. K. Nielsen, and R. Bjørk, *Review of Scientific Instruments* **91** (2020).
- ¹¹A. Raihane, R. Tourbot, F. Ladieu, and D. L'Hôte, *Review of Scientific Instruments* **83**, 043903 (2012).
- ¹²P. Wadley, B. Howells, J. Železný, C. Andrews, V. Hills, R. P. Campion, V. Novák, K. Olejník, F. Maccherozzi, S. Dhési, *et al.*, *Science* **351**, 587 (2016).
- ¹³M. Grzybowski, P. Wadley, K. Edmonds, R. Beardsley, V. Hills, R. Campion, B. Gallagher, J. S. Chauhan, V. Novak, T. Jungwirth, *et al.*, *Physical review letters* **118**, 057701 (2017).
- ¹⁴K. Olejník, V. Schuler, X. Martí, V. Novák, Z. Kašpar, P. Wadley, R. P. Campion, K. W. Edmonds, B. L. Gallagher, J. Garcés, *et al.*, *Nature Communications* **8**, 1 (2017).
- ¹⁵T. Matalla-Wagner, M.-F. Rath, D. Graulich, J.-M. Schmalhorst, G. Reiss, and M. Meinert, *Phys. Rev. Appl.* **12**, 064003 (2019).
- ¹⁶Z. Kašpar, M. Surýnek, J. Zubáč, F. Krizek, V. Novák, R. P. Campion, M. S. Wörnle, P. Gambardella, X. Martí, P. Němec, *et al.*, *Nature Electronics* **4**, 30 (2021).
- ¹⁷P. Wadley, V. Novák, R. Campion, C. Rinaldi, X. Martí, H. Reichlová, J. Železný, J. Gazquez, M. Roldan, M. Varela, *et al.*, *Nature communications* **4**, 1 (2013).
- ¹⁸L. Barton, *Sb Doped CuMnAs for Antiferromagnetic Spintronics*, Phd thesis, University of Nottingham (2023).

Characterization of the low electric field and zero-temperature two-level-system loss in hydrogenated amorphous silicon

Fabien Defrance* and Andrew D. Beyer
*Jet Propulsion Laboratory,
California Institute of Technology, Pasadena, CA, USA, 91109*

Shibo Shu, Jack Sayers, and Sunil R. Golwala
California Institute of Technology, Pasadena, CA, USA, 91125
(Dated: December 1, 2023)

Two-level systems (TLS) are an important, if not dominant, source of loss and noise for superconducting resonators such as those used in kinetic inductance detectors and some quantum information science platforms. They are similarly important for loss in photolithographically fabricated superconducting mm-wave/THz transmission lines. For both lumped-element and transmission-line structures, native amorphous surface oxide films are typically the sites of such TLS in non-microstripline geometries, while loss in the (usually amorphous) dielectric film itself usually dominates in microstriplines. We report here on the demonstration of low TLS loss at GHz frequencies in hydrogenated amorphous silicon (a-Si:H) films deposited by plasma-enhanced chemical vapor deposition in superconducting lumped-element resonators using parallel-plate capacitors (PPCs). The values we obtain from two recipes in different deposition machines, 7×10^{-6} and 12×10^{-6} , improve on the best achieved in the literature by a factor of 2–4 for a-Si:H and are comparable to recent measurements of amorphous germanium. Moreover, we have taken care to extract the true zero-temperature, low-field loss tangent of these films, accounting for temperature and field saturation effects that can yield misleading results. Such robustly fabricated and characterized films render the use of PPCs with deposited amorphous films a viable architecture for superconducting resonators, and they also promise extremely low loss and high quality factor for photolithographically fabricated superconducting mm-wave/THz transmission lines used in planar antennas and resonant filters.

©2023. All rights reserved.

I. INTRODUCTION

The standard tunneling model (STM) is the reference model used to describe the properties of amorphous dielectrics at low temperatures (below a few Kelvins) [1, 2]. According to this model, amorphous dielectrics have defect states with two physical configurations (*e.g.*, locations of an atom or groups of atoms) with different energies, forming a quantum two-state (“two-level”) system with inter-state tunneling [1, 3]. When the two-level systems (TLSs) present in amorphous dielectrics have an electric dipole moment, they can couple to an oscillating electric field present in the dielectric (in superconductive resonators used in qubits or kinetic inductance detectors, for example) and convert some of the energy stored in the electric field into phonon emission, resulting in dielectric loss and noise. In superconducting qubits, dielectric loss is a major source of decoherence, as first inferred by Martinis et al. [4]. In kinetic inductance detectors, dielectric loss adds noise and can degrade responsivity and multiplexability [5, 6], especially in parallel-plate capacitor (PPC) geometries that are desirable in some applications. In superconducting transmission line used in photolithographically fabricated planar antennas and resonant bandpass filters at mm-wave/THz frequencies, dielectric loss determines attenuation length [7] and limits spectral resolution [8]. Therefore, low-loss dielectrics are highly desirable for diverse low-temperature applications.

Crystalline dielectrics have very low dielectric loss because of their low density of defects [9], but incorporation of crystalline dielectrics into elements like PPCs or superconducting microstripline transmission lines requires complex fabrication techniques [10, 11]. When simpler techniques are used to fabricate the single-layer equivalents (transmission line resonators using coplanar waveguide (CPW), lumped element resonators using interdigitated capacitors (IDCs), superconducting CPW transmission line), they exhibit TLS loss due to the formation of oxide at the exposed surfaces of the superconducting material and substrate [12–14]. Choosing superconducting materials having a weak reactivity with oxygen, and thus producing a very thin oxide layer, yields interesting results with materials such as rhenium or nitrides (TiN, NbN, etc.) [13–15]. However, this solution limits designs to use of a few superconductive materials.

By contrast, multi-layer structures incorporating an easily deposited, low-loss, amorphous dielectric would have the benefit of confining the electric field inside the dielectric, drastically limiting the participation of surface oxides that enhance the loss of CPW and IDC structures on crystalline dielectric. Such multi-layer structures would enable significant progress in a wide range of low-temperature applications. KID development would benefit from the option of replacing large IDCs limited by poorly controllable surface-oxide loss with order-of-magnitude smaller PPCs limited by well-controlled bulk dielectric film loss. Microstripline KID designs would become less challenging to implement (*cf.* [16]). Low-loss microstripline would also enable more sophisticated planar

* fabien.m.defrance@jpl.nasa.gov

antennas, higher resolution filters in superconductive spectrometers, and microstripline-based traveling-wave parametric amplifiers using kinetic inductance. (The films discussed in this paper have already been successful for the last application [17].)

The main amorphous dielectrics whose GHz–THz *electromagnetic* behavior — believed to be due to electric-dipole-coupled TLS — has been explored to date in the literature are AlO_x , SiO_2 , SiO_x , SiN_x , and hydrogenated amorphous silicon (a-Si:H) (see [18] for an exhaustive review). Very recently, hydrogenated amorphous silicon carbide (a-SiC:H; [19]) and amorphous germanium (a-Ge [20]) have been explored.¹ Prior studies [19, 23–27] show that a-Si:H dielectric loss can, in general, be at least an order of magnitude lower than that of AlO_x , SiO_2 , SiO_x , and SiN_x (though low loss has been achieved for SiN_x [28], albeit with high stress). Loss in a-Ge films are the lowest seen in the literature to date [20]. *In this paper, we demonstrate a-Si:H films with low-power loss tangent 7 and 12×10^{-6} . These films improve on the best, previous, robust measurements for a-Si:H [23] by a factor of 2–4², and are comparable to measurements for a-Ge given their uncertainties [20].*

There is significant, potentially relevant literature on a-Si and a-Si:H in three different contexts: as a photovoltaic, as an example of sub-electronic-bandgap optical absorption, with impact on its use as a mirror coating in laser-interferometric gravitational wave detectors; and, as an exemplar of universal STM behavior. We review this literature in Appendix A, leaving it out of the body of the paper because it is not likely to be relevant for reasons explained there, with the exception of the results of Molina-Ruiz et al. [29]. We do offer a caveat to this conclusion in §VII.

Demonstrations of low loss have not usually addressed robustness: stability of the deposition recipe over time, transferability between deposition machines, and suitability of the recipe for combination with other fabrication steps. For example, films made using the [23, 24] recipe *in the same machine* a decade later yielded much higher loss tangent, and low-loss SiN_x suffers high stress [28], rendering it challenging to incorporate in complex circuits. *We demonstrate here $\approx 10^{-5}$ low-power loss tangent using two different combinations of deposition technique and machine, and our recipes are, by construction, consistent with inclusion in PPCs and microstripline [17].*

Another challenge with measurements of such low loss is systematic uncertainties. As described in Section III, the loss tangent at 0 K and weak electric field, $\tan \delta_{\text{TLS}}^0$, characterizes the intrinsic TLS loss of the film, with none of the two-level systems saturated by temperature or power. Most previ-

ous studies of a-Si:H loss tangent characterized the resonator quality factor Q_i and inferred from it the loss tangent via $\tan \delta = Q_i^{-1}$. The quantity $\tan \delta$ can be smaller than $\tan \delta_{\text{TLS}}^0$ because of the above saturation effects. It can also be larger because it may include additional non-TLS losses ($\tan \delta_{\text{other}}$). Moreover, for a-Si:H loss tangent studies using CPW resonators, separating the TLS loss of a-Si:H from that of surface oxide layers can add systematic uncertainty to the measurements of $\tan \delta_{\text{TLS}}^0$ (e.g., [18, 30]). *We present in this article measurements of $\tan \delta_{\text{TLS}}^0$ that avoid these inaccuracies by design and by measurement technique*³: our LC resonator device design uses PPCs to ensure surface oxide contributions are negligible; and, our measurement technique fits for the dependence of resonant frequency f_{res} on temperature and of inverse quality factor Q_i^{-1} on readout power, two independent techniques that yield broadly consistent results, with the former being more robust.

II. TEST DEVICE DESIGN AND FABRICATION

A. Design

Each test device hosts 6 niobium (Nb) LC resonators inductively coupled to a 50 Ω Nb coplanar waveguide (CPW) feedline that is used for readout. Each resonator is composed of two parallel plate capacitors (PPCs) in series with an inductor, as described in Figure 1. To facilitate their identification, the six resonators are grouped in frequency into two triplets, centered on 0.85 GHz and 1.55 GHz. Within each triplet, the resonators are designed to have resonant frequencies separated by 5%. The physical dimensions of the resonator components and their predicted/simulated electrical values are listed in Table I. Because we initially had a conservative expectation of obtaining TLS loss tangent $\tan \delta \approx 10^{-4}$ and thus internal quality factor $Q_i \approx 10^4$, we designed the coupling quality factor, Q_c , to also be close to 10^4 to maximize the coupling efficiency [5]. Q_c and f_{res} were designed and simulated using Sonnet software and the very useful method developed by Wisbey et al. [33]. The unexpectedly high values of measured Q_i led to $Q_i \gg Q_c$, causing very deep, overcoupled resonances.

³ The utility of PPCs has been known for some time [4] and was emphasized in [23] and, more recently, in [30]. The applicability of the frequency-shift technique was first pointed out in [14, 31, 32], with [31, 32] both: 1) explaining that readout power saturation of TLS does not impact frequency shift vs. temperature because it is sensitive to the full ensemble of TLS while quality factor is only sensitive to TLS within a linewidth of f_{res} (temperature saturation is of course the means by which the frequency shift data yield the low temperature loss tangent); and, 2) recognizing the convenience of the frequency shift technique relative to measuring quality factor at low power. [18] reiterated these points. This technique is, however, only usable when the superconducting film has high enough T_c that the dependence of kinetic inductance on temperature does not dominate over the TLS effect, a caveat that may explain the prevalence of Q_i measurements in the literature. In particular, half of the literature results cited in Section VI use Al superconductor, which can suffer this effect.

¹ We neglect epitaxially grown films (e.g., Al_2O_3 [21, 22], Si [20]) because epitaxy requirements on the substrate or the base film present significant constraints on use in PPCs or microstripline.

² The films presented in [19, 26] could, after corrections and with measurements at lower power, yield comparable low-power loss tangent, but precise numbers at low power are not available. The most robust numbers available for the same deposition process are in [27], 3.6×10^{-5} (see Section VI).

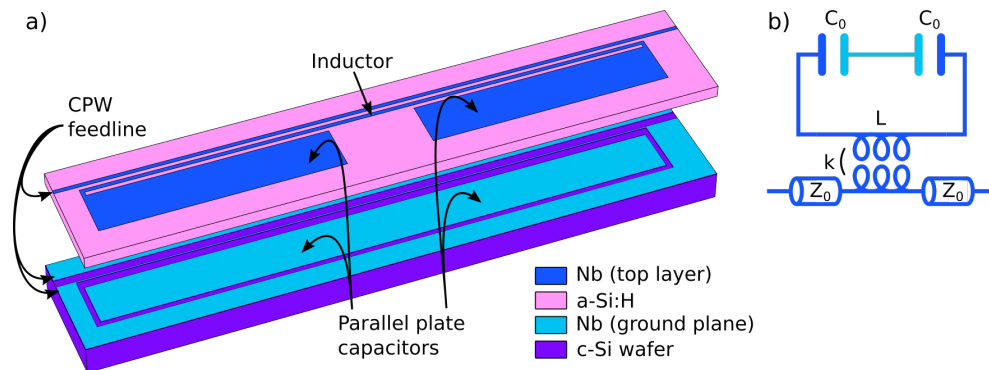


FIG. 1. a) Exploded view, not to scale, showing the geometry of the LC resonators used to measure the loss tangent and internal quality factor of a-Si:H. The CPW feedline is composed of a center conductor on the top Nb layer and ground electrodes on the bottom Nb (“ground plane”) layer separated by the a-Si:H dielectric film to be characterized. The resonator consists of an inductor that runs parallel to the feedline center conductor on the top Nb layer and a series pair of PPCs formed by plates on the Nb top layer and the ground plane. (The a-Si:H layer is only 800 nm thick while the inductor-top plate gap is 22 μm and the CPW center conductor and gap are 20 μm and 12 μm wide, respectively, so the structure is approximately planar in spite of the vertical separation of the center conductor and ground plane.) A 44 μm gap separates the ground plane plate from the surrounding ground plane, though this gap is not strictly necessary because this electrode acts as a virtual ground. The inductor couples the CPW feedline to the LC circuit, and a gap in the ground plane below the inductor mitigates magnetic screening that would reduce the inductance value and feedline coupling. The gap also limits parasitic capacitance with the ground plane. b) Lumped element circuit equivalent. The CPW feedline has an impedance $Z_0 = 50\Omega$, the two capacitances C_0 correspond to the two PPCs, L is the inductance, and k represents the mutual inductance with the CPW.

	PPCs			Inductor			f_{res} [MHz]	Q_c
	w [μm]	ℓ [μm]	C_0 [pF]	w [μm]	ℓ [μm]	L [nH]		
Lower frequency triplet	265	1236	42	20	2920	1.84	810	8×10^3
	245	1223	39	20	2920	1.84	844	8×10^3
	225	1210	35	20	2920	1.84	882	8×10^3
Higher frequency triplet	265	1236	42	20	760	0.54	1489	2×10^4
	245	1223	39	20	760	0.54	1554	2×10^4
	225	1210	35	20	760	0.54	1627	2×10^4

TABLE I. Designed dimensions and electrical parameters of the six resonators present on each device. For the PPCs, w and ℓ correspond respectively to the width and length of the top plates, while, for the inductor, w and ℓ are the width and length of the inductor line. C_0 is the capacitance of each of the two PPCs, so the total capacitance is $C = C_0/2$ (C_0 is calculated using the capacitor dimensions and the permittivity of silicon). The distance between the inductor and the CPW feedline is set to 22 μm to obtain $Q_c \sim 10^4$.

B. Fabrication

We fabricated the devices at the NASA Jet Propulsion Laboratory’s MicroDevices Laboratory (MDL) and at the Caltech Kavli Nanoscience Institute (KNI) clean room facility. For each recipe, we fabricated four devices simultaneously on the same 4-inch high resistivity silicon wafer. In the rest of this article, we will identify each of the four devices (for each recipe) with an index going from 1 to 4. Figure 2 describes the main fabrication steps.

Previous studies demonstrated that TLS impacting resonator behavior reside primarily in oxide layers localized at interfaces (metal-vacuum, metal-dielectric, and dielectric-vacuum) [12–14, 34, 35]. In our PPC geometry, the electric field created by the resonator is confined between the capacitor plates and only the metal-dielectric interfaces are relevant.

Therefore, we took particular care to eliminate any oxide layers at these interfaces: we used buffered oxide etch (BOE) on all silicon surfaces prior to metal-film deposition, we preceded depositions of a-Si:H in the JPL ICP-PECVD machine by Ar^+ ion milling (not possible in the KNI PECVD machine), and we did the same with depositions of Nb on a-Si:H.

We tested many different recipes for a-Si:H, mainly varying the gas composition, gas flow, RF power, temperature, and deposition technique. The two recipes (A & B; Table II) we present here are among those giving the lowest TLS loss values. A more detailed review of all the recipes we have tested, with in-depth analysis of a-Si:H structure and composition in addition to measurements of loss tangent, will be published separately.

Recipe	Gas ratio (SiH ₄ /Ar)	Temperature [°C]	Gas pressure [mTorr]	Gas flow [sccm]	RF Power [W]	ICP Power [W]	Deposition time	Process	Facility
A	5% / 95%	350	800	250	10	N/A	27'11"	PECVD	KNI
B	100% / 0%	350	10	30	50	300	26'06"	ICP-PECVD	JPL

TABLE II. Deposition recipes for a-Si:H. The gas ratio (SiH₄/Ar) corresponds to the relative flow rate of the 2 gases. The two recipes use two different machines and deposition processes. Recipe A uses an Oxford Plasmalab System 100 at Caltech KNI for PECVD while Recipe B uses an Oxford Plasmalab System 100 ICP 380 at JPL MDL for ICP-PECVD. Safety restrictions prevented the use of a pure SiH₄ atmosphere at Caltech KNI.

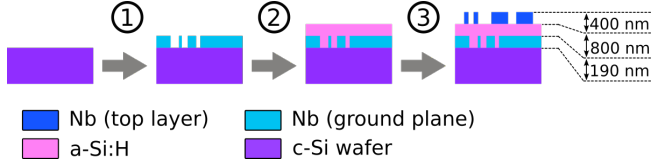


FIG. 2. Schematic showing main device fabrication steps. 1) Deposition and patterning (etch-back) of a 190 nm thick Nb film on a 375 μm thick, 100 mm diameter, high resistivity silicon wafer, forming the ground plane (also including the return conductors of the CPW feedline) and the bottom plate of the PPCs. 2) Deposition of a 800 nm thick layer of a-Si:H using Plasma-Enhanced Chemical Vapor Deposition (PECVD; Caltech KNI) for recipe A and Inductively Coupled Plasma PECVD (ICP-PECVD; JPL MDL) for recipe B. 3) Deposition and patterning (etch-back) of a 400 nm thick Nb film on top of the a-Si:H layer, forming the CPW feedline center conductor, the inductor, and the PPC top plates. We deposit all the metal films using RF magnetron sputtering at JPL MDL with a 6-inch target.

III. THEORETICAL MODEL FOR THE EFFECT OF TWO-LEVEL SYSTEMS ON RESONATOR PARAMETERS

TLS present in dielectrics can couple to a time-varying electric field via their electric dipole moments. They can also emit phonons. The transfer of energy from the electric field to phonon emission is a form of loss for the dielectric. The circuit's total loss can be expressed as [36]:

$$\tan \delta = \tan \delta_{other} + \sum_j F_j \tan \delta_j. \quad (1)$$

with $\tan \delta$ the total loss tangent, $\tan \delta_j$ the loss tangent of each lossy dielectric, F_j the filling factor of each lossy dielectric (indicating the portion of the device's total energy stored in each dielectric material), and $\tan \delta_{other}$ representing additional non-TLS loss mechanisms. The circuit loss tangent, $\tan \delta$, is equivalent to Q_i^{-1} , the inverse of the internal quality factor, which is a quantity easily measurable when the electric circuit is a resonator. In the rest of this article, all loss tangents are small compared to unity, so we use the approximation $\tan \delta \approx \delta$.

The dielectric loss tangent δ_j is not a single number, however, because saturation effects cause it to depend on electric field strength (*i.e.*, stored energy in the resonator, which is determined by readout power) and temperature. Moreover, TLS affect not just the imaginary part of the dielectric constant — *i.e.*, cause loss — but they also affect the real part — *i.e.*,

cause a frequency shift. At microwave frequencies and low temperatures, the standard tunneling model (STM) yields the following expressions for these two effects (*e.g.*, [31]):

$$Q_i^{-1} = \delta_{other} + \sum_j F_j \delta_{j,TLS}^0 \frac{\tanh\left(\frac{hf_{res}}{2k_B T}\right)}{\left[1 + \left(\frac{|\vec{E}_j|}{E_{c,j}}\right)^2\right]^{\beta_j}}, \quad (2)$$

$$\frac{f_{res}(T) - f_{res}(0)}{f_{res}(0)} = \sum_j \frac{F_j \delta_{j,TLS}^0}{\pi} \left[\text{Re} \left[\Psi \left(\frac{1}{2} - \frac{hf_{res}(0)}{2j\pi k_B T} \right) \right] - \ln \left(\frac{hf_{res}(0)}{2\pi k_B T} \right) \right], \quad (3)$$

with $\delta_{j,TLS}^0$ the “intrinsic” or “asymptotic” (zero temperature, low electric field) loss tangent, h and k_B the Planck and Boltzmann constants respectively, T the temperature of the dielectric, \vec{E}_j the electric field inside the j th dielectric film under consideration, $E_{c,j}$ the critical electric field for TLS saturation for the j th dielectric film, Ψ the complex digamma function, and β_j an exponent determined by the TLS density of states in dielectric film j . This exponent is 0.5 for a logarithmically uniform density of states [1], but the experimental literature yields values between 0.15 and 0.35 [29, 37].

Variants on Equation 3 are seen in the literature. The sign of $hf_{res}(0)/(2j\pi k_B T)$ can be either $-$ or $+$ because $\Psi(\bar{z}) = \Psi(z)$, and therefore $\text{Re}[\Psi(\bar{z})] = \text{Re}[\Psi(z)]$. The denominator of the last fraction is sometimes written as $k_B T$ only. The absence of 2π arises from the underlying TLS theory [1], but it results in a frequency offset. A careful demonstration of this formula by J. Gao ([31] Appendix G) shows that the denominator of the last fraction must be $2\pi k_B T$ in order for the right part of the equation to be equal to zero when $T = 0$ K.

Since TLS couple via electric fields, only capacitive elements contribute to TLS loss [30, 38]. Because we use PPCs, the electric field is confined between the capacitor plates. We assume no oxides, and therefore no TLS, remain at the metal-substrate interfaces given the aforementioned oxide-removal steps. Though [30] argued for the importance, in PPC measurements, of accounting for TLS residing in the parasitic capacitance of the inductor, we argue our geometry differs substantially from the one they present, leading to a much smaller

participation of surface oxides. Specifically, considering the half of the resonator that is at positive voltage during a particular half period: 1) the vast majority of field lines emanating from the inductor (present because it is not a virtual ground along its entire length) terminate on the ground plane or the PPC bottom plate, passing through the same a-Si:H being tested with the PPC, because the adjacent PPC top plate sits at a larger voltage; 2) field lines emanating from the PPC top plate strongly prefer to terminate on the PPC bottom plate rather than on the inductor because the former is much closer (800 nm vs. 22 μm); and, 3) any field lines that do travel from the PPC top plate to the inductor primarily pass through the higher ϵ a-Si:H rather than through surface oxides. The same arguments can be made for the half of the resonator that is at negative voltage. Together, these points imply that: the bulk of the inductor's parasitic capacitance is subject to the same TLS as the PPC; and, the fraction of field lines terminating on the inductor and passing through surface oxides is a small fraction of the already fractionally small parasitic capacitance of the inductor.

We thus assume the entirety of the resonator stored energy resides inside the a-Si:H film, which gives a filling factor $F = 1$ and allows us to rewrite Equations 2 and 3 as:

$$Q_i^{-1} = \delta_{other} + \delta_{TLS}^0 \frac{\tanh\left(\frac{hf_{res}}{2k_B T}\right)}{\left[1 + \left(\frac{|\vec{E}|}{E_c}\right)^2\right]^\beta}, \quad (4)$$

$$\frac{f_{res}(T) - f_{res}(0)}{f_{res}(0)} = \frac{\delta_{TLS}^0}{\pi} \left[\text{Re} \left[\Psi \left(\frac{1}{2} - \frac{hf_{res}(0)}{2j\pi k_B T} \right) \right] - \ln \left(\frac{hf_{res}(0)}{2\pi k_B T} \right) \right]. \quad (5)$$

Equation 4 implies that, due to their low energy, TLS saturate at high temperature ($hf_{res} \lesssim 2k_B T$) and under high electric field ($|\vec{E}| \gtrsim E_c$), reducing the dielectric loss [32]. A measurement of Q_i^{-1} as a function of temperature and/or electric field can, in principle, be fit to Equation 4 to determine δ_{other} , E_c , δ_{TLS}^0 , and β . Equation 5 indicates that the frequency shift suffers no field dependence and has a characteristic temperature dependence — behaviors of great practical utility for robustly determining δ_{TLS}^0 , as we will show.

While fitting to Equation 4 may seem the most straightforward approach to finding δ_{TLS}^0 , it can be challenging. Doing so requires determining Q_i , which can be difficult if the complex $S_{21}(f - f_{res})$ trajectory deviates significantly from ideal behavior and/or if $Q_i \gg Q_r$ (the total quality factor Q_r of a resonator is related to its internal quality factor Q_i and its coupling quality factor Q_c by the relation $Q_r^{-1} = Q_i^{-1} + Q_c^{-1}$). More importantly, such a fit requires extensive and sensitive data: $|\vec{E}|$ must be swept from $|\vec{E}| \ll E_c$ to $|\vec{E}| \gg E_c$ to fit the $|\vec{E}|$ -dependence, these data must show clear plateaus at high and low $|\vec{E}|$ to determine δ_{other} and the normalization of the $|\vec{E}|$ -dependence, and either the data must be taken at

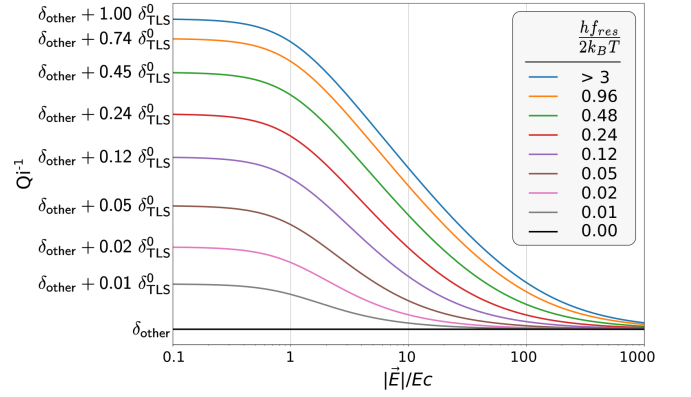


FIG. 3. Log-log plot illustrating Equation 4. Q_i^{-1} converges towards $\delta_{other} + \delta_{TLS}^0 \tanh(hf_{res}/(2k_B T))$ at low $|\vec{E}|/E_c$ and towards δ_{other} at high $|\vec{E}|/E_c$. The exponent β only changes the steepness of the dependence on $|\vec{E}|$; $\beta = 0.5$ was used here, corresponding to a log-uniform TLS density of states. The different curves correspond to different values of $hf_{res}/(2k_B T)$. The plot illustrates that taking data in the fully unsaturated (in T and $|\vec{E}|$) limit yields the best lever arm on determining the true value of δ_{TLS}^0 from Q_i^{-1} data and that taking T -saturated data necessitates applying a correction factor $\tanh(hf_{res}/(2k_B T))$. For reference, $hf_{res}/(2k_B T) \approx 0.96$ (and $\tanh(0.96) = 0.74$) for $f_{res} = 1$ GHz at $T = 25$ mK. Our data probe the range $hf_{res}/(2k_B T) \in [0.08, 0.16]$, requiring a factor of roughly 6–13 correction for T saturation.

$T \ll hf_{res}/k_B$ so the TLS are unsaturated or one must apply a correction for the $\tanh(hf_{res}/(2k_B T))$ dependence. Data over a wide range in T would maximize the robustness of the temperature correction, but taking such data is experimentally time-consuming and not usually done in the literature. It may also be difficult to obtain sufficient signal-to-noise at the low readout power required for $|\vec{E}| \ll E_c$, and it may not be possible to reach the $|\vec{E}| \gg E_c$ regime before the superconductor becomes nonlinear (when the current approaches the critical current) or pair-breaking takes place due to dissipation in the superconductor arising from δ_{other} .

In this article, we take the approach — which have not seen in the literature — of fitting both Equations 4 and 5 and comparing the results in order to better understand the systematics associated with the two methods. We conclude that the frequency-shift approach (Equation 5) is far more robust.

IV. EXPERIMENTAL SETUP

We cooled the devices using a Chase Cryogenics closed-cycle $^3\text{He}/^3\text{He}^4\text{He}$ sorption cooler mounted to the second stage of a Cryomech PT415 cryocooler. Each device resided in its own box sealed to prevent optical radiation from breaking quasiparticles or heating the substrate. A magnetic shield, residing at 4 K and consisting of two layers of Amuneal A4K material, enclosed the devices to limit the impact of Earth's magnetic field. A combination of stainless steel and NbTi semi-rigid coaxial cables carried the readout signal to the devices, with 30 dB and 10 dB in-line attenuators at 4 K and

0.35 K, respectively, to block 300 K thermal noise. Similar NbTi coax carried the signal exiting each device to a cryogenic low-noise amplifier (LNA) at 4 K, with a noise temperature of approximately 5 K, followed by stainless steel coax back to 300 K. Additional LNAs at 300 K ensured the cryogenic LNA dominated the system noise. We monitored the device temperature using a Stanford Research System (SRS) SIM921 reading a Lakeshore Germanium Resistance Thermometer (GRT) located next to the devices. The temperature was varied between 240 mK and 450 mK using a SRS SIM960 analog PID controller supplying a current to a 10 k Ω heater on the mechanical stage holding the devices. A Copper Mountain Technologies SC5065 Vector Network Analyzer (VNA) performed measurements of $S_{21}(f)$ using the above signal chain. We used the Python module SCRAPS [39] to fit the $S_{21}(f)$ data to standard forms (e.g., [5]) to extract the resonance frequency f_{res} and quality factors Q_r , Q_i , and Q_c for each value of T and readout power (electric field).

We varied the readout power applied by the VNA to the feedline, P_{read} , over the approximate range -150 dBm to -70 dBm. Because the SNR decreases with readout power, we had to compensate by reducing the IF bandwidth of the VNA, which results in a proportional increase in measurement time. Each factor of 10 decrease in IF bandwidth yielded a 10 dB reduction of noise floor and a factor of 10 increase in measurement time. We used an IF bandwidth of 1 kHz above -100 dBm, reducing it to 10 Hz at the lowest readout powers.

V. RESULTS

Figure 4 shows fits of the measured $f_{res}(T)$ and $Q_i^{-1}(|\vec{E}|)$ to Equations 5 and 4, respectively. Table III shows the inferred fit parameters δ_{TLS}^0 , δ_{other} , E_c , and β . Figure 5 summarizes and compares the δ_{TLS}^0 values from all the fits for all the devices.

To calculate the electric field $|\vec{E}|$ from the readout power, we use the following equation, which is derived in Appendix B:

$$|\vec{E}| = \sqrt{\frac{1}{\epsilon A_0 d}} \sqrt{\frac{P_{read} Q_r^2}{2\pi f_{res} Q_c}}, \quad (6)$$

where A_0 is the top plate area, ϵ is the permittivity of a-Si:H, $d = 800$ nm is the distance separating the plates of the capacitors, and P_{read} is the readout power at the device. We calculated $A_0 = w \times \ell$ from the dimensions in Table I. We assumed $\epsilon/\epsilon_0 = 11.68$, the experimental value found for crystalline silicon, for the a-Si:H relative permittivity because the systematic uncertainty due to any deviation from this value is negligible given the large logarithmic range in $|\vec{E}|$. Across multiple chips (those presented in this article and others), we measured f_{res} variations smaller than 4%. Since $f_{res} = 1/(2\pi\sqrt{LC})$ and $C = C_0/2 = \epsilon A_0/2d$, the corresponding variation in ϵ/d would be less than 8%. Inductance variations could also affect f_{res} , but simulations indicate that such variations could only occur if the position of the inductor and/or its width varied by more than 2 μ m, ruled out by the photolithography accuracy.

A. δ_{TLS}^0

The best-fit values of δ_{TLS}^0 range from 6.4×10^{-6} to 21.5×10^{-6} for Devices A(1) and A(2) and from 3.5×10^{-6} to 8.9×10^{-6} for Devices B(1) and B(2). The values obtained from frequency shift and quality factor data are within a factor of two of one another.

Among the resonators fabricated using a given recipe (both across resonator frequency and across chips), the frequency-shift values of δ_{TLS}^0 are generally more consistent than the quality-factor values. This difference arises because there are a number of systematic deviations from expected behavior present only in the quality-factor data and fits while the frequency-shift data seem to follow the model well. Figure 4 shows the δ_{TLS}^0 (low power) plateau is generally visible but the δ_{other} (high power) plateau is not always, and in some cases, the data are independent of power. While we can eliminate some of these systematic deviations by excluding the last 5–15 data points, some remain. We consider three different types of deviations in turn.

In the cases of the Device B(1) resonances at 824 MHz and 895 MHz, we see quality factor independent of readout power over the regime where the model fits the data. This behavior makes the data insensitive to δ_{TLS}^0 , so we consider the δ_{TLS}^0 values for these resonators unreliable and we mark them with an asterisk in Table III.

The other resonators on Devices B(1) and B(2) show Q_i^{-1} rising at high power (field), presumably due to readout power generation of quasiparticles [24]. In the cases of the B(1) 855 MHz and B(2) 847 MHz resonances, the inverse quality factor shows a significant decrease at high power before the rise, while the other Device B(1) and B(2) resonances do not (excluding B(1) 824 MHz and B(1) 895 MHz, already discussed above). We find the δ_{TLS}^0 values for the B(1) 855 MHz and B(2) 847 MHz resonance quality factor fits are more consistent with their frequency-shift fits, suggesting this difference in behavior causes these resonators' quality factor fits to be more reliable (smaller systematic uncertainty).

The Device A(1) and A(2) resonators display no high-power plateau and in fact show a downward deviation from the expected saturation behavior. This behavior could be an effect of readout power too, now due to the modification of the quasiparticle distribution function $f(E)$ by readout power [40]. Independent of the explanation, this behavior makes it impossible to fit for δ_{other} .

Overall, it is also not known for certain why Devices A(1) and A(2) show primarily a drop in Q_i^{-1} with field while Devices B(1) and B(2) show a rise, though we may speculate that variations in Nb film properties are the cause.

Our conclusion from the above results and discussion is that the frequency-shift data and fits determine δ_{TLS}^0 far more reliably than do quality factor data and fits. After averaging these values for each recipe, we obtain $\delta_{TLS}^0 \approx 12 \times 10^{-6}$ for recipe A and $\delta_{TLS}^0 \approx 7 \times 10^{-6}$ for recipe B.

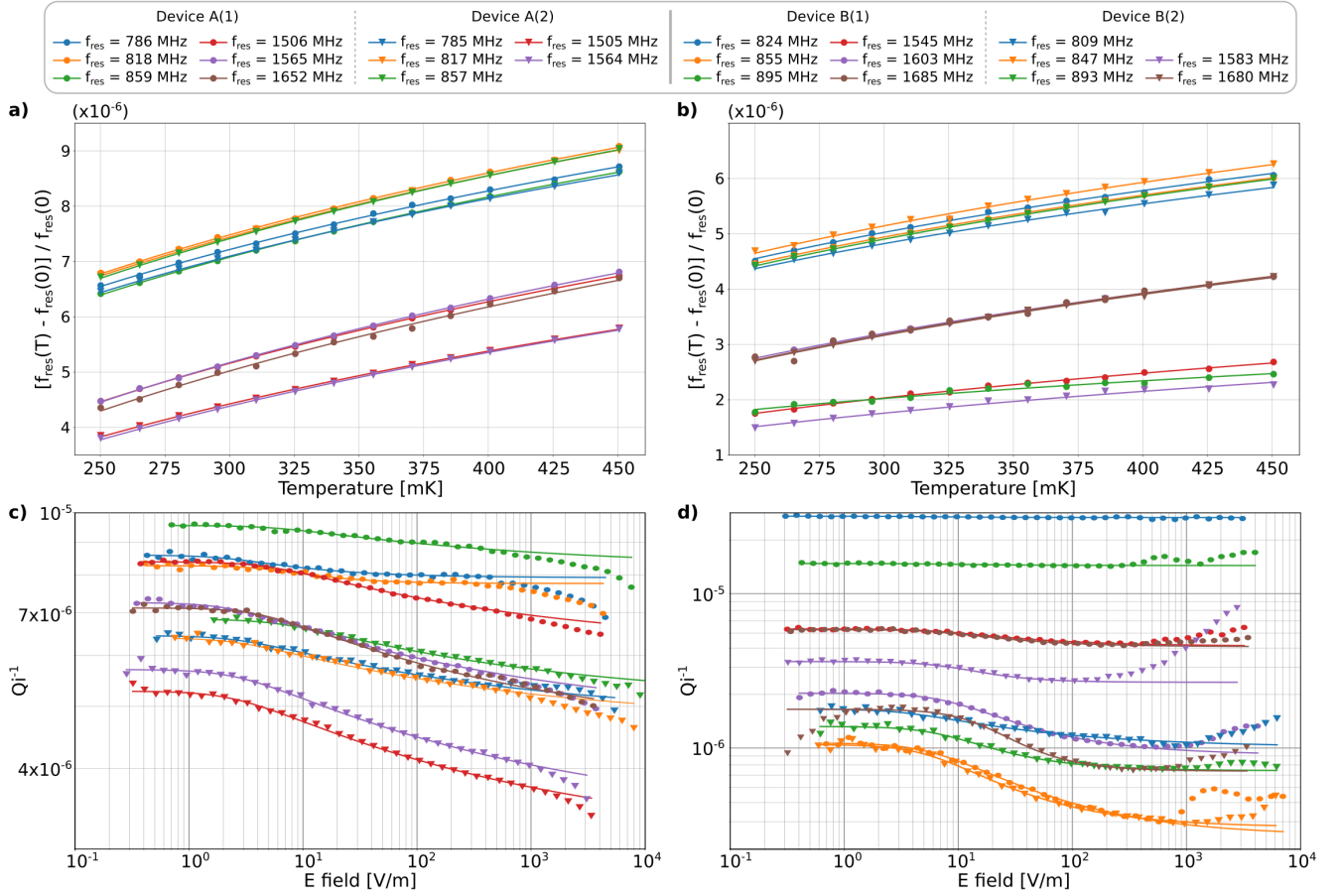


FIG. 4. a), b) Data and best-fit TLS model (Equation 5) for $(f_{\text{res}} - f_{\text{res}}(0))/f_{\text{res}}(0)$ as a function of temperature. c), d) Data and best-fit TLS model (Equation 4) for Q_i^{-1} data as a function of electric field. a), c) Devices A(1) and A(2); b), d) Devices B(1) and B(2). Much of the literature uses photon number instead of $|\vec{E}|$; Figure 6 in Appendix B shows plots c) and d) as a function of photon number to facilitate comparison with published results. Table III lists the best-fit parameters. Disagreements between the model and the data are discussed in the text, in particular how we extract δ_{TLS}^0 and δ_{other} in the presence of such disagreements.

The $f_{\text{res}}(T)$ data were taken at a readout power (at the device) of approximately -100 dBm ($|\vec{E}| \approx 500$ V/m). The $Q_i^{-1}(|\vec{E}|)$ data were taken at 246 mK.

B. δ_{other}

The fitted values of δ_{other} are only valid when a high readout power plateau is visible. For Devices A(1) and A(2), only the A(1) 786 MHz and A(1) 818 MHz resonances show this plateau, yielding, respectively, values of 7.8×10^{-6} and 7.9×10^{-6} . For Devices B(1) and B(2), all resonances show the plateau and yield values of 0.2×10^{-6} to 28×10^{-6} . We see that non-TLS losses vary enormously, even within a single device, and are often non-negligible compared to TLS loss, even at low readout powers. We do not know for certain the cause of this variation, but we again may propose film property variations. Certainly, at the low values of δ_{TLS}^0 obtained here, it is clear that non-TLS sources of loss may become important or dominant and thus they deserve future investigation.

C. Evolution of δ_{TLS}^0 and δ_{other} with time

We fabricated Devices A(1) and A(2) in October, 2017, and Devices B(1) and B(2) in March, 2020. We measured Devices A(1) and B(1) twice: first in June, 2018, and September, 2020, respectively, and second in March, 2022. (We did not remeasure Devices A(2) and B(2).) Between measurements, we stored the devices in the ambient laboratory atmosphere: air rather than N_2 atmosphere; standard air conditioning with generally stable humidity and temperature but no specific additional humidity or temperature control; and, no use of dessicant.

Table IV shows the δ_{TLS}^0 measurement evolution. We see a 19% increase for Device A(1) and a 6% increase for Device B(1) (both averaged over the resonators on the device). We can translate these changes to rates of increase per unit time of $0.36 \times 10^{-6}/\text{month}$ for Device A(1) and $0.33 \times 10^{-6}/\text{month}$ for Device B(1). We thus observe that δ_{TLS}^0 increases with time and that the rate of increase is remarkably consistent

Dataset	$Q_i^{-1}(\vec{E})$					$Q_i^{-1}(\vec{E})$					
f_{res} [MHz]	δ_{TLS}^0 ($\times 10^{-6}$)	δ_{TLS}^0 ($\times 10^{-6}$)	δ_{other} ($\times 10^{-6}$)	E_c [V/m]	β	f_{res} [MHz]	δ_{TLS}^0 ($\times 10^{-6}$)	δ_{TLS}^0 ($\times 10^{-6}$)	δ_{other} ($\times 10^{-6}$)	E_c [V/m]	β
Device A(1)						Device A(2)					
786	12.0	8.7	7.9	2.5	0.30	785	11.0	21.5	*4.8	*2.8	*0.10
818	12.0	6.4	7.8	6.4	0.49	817	12.0	21.0	*4.7	*2.6	*0.10
859	12.0	16.2	*8.2	*5.7	*0.10	857	12.0	21.0	*5.1	*6.1	*0.10
1506	12.0	15.3	*6.2	*4.8	*0.10	1505	11.0	15.1	*3.1	*2.5	*0.10
1565	13.0	16.3	*4.8	*2.4	*0.10	1564	11.0	15.7	*3.3	*2.6	*0.10
1652	13.0	16.1	*4.5	*4.4	*0.11						
Device B(1)						Device B(2)					
824	8.3	*7.1	28.0	*4.2	*0.46	809	7.9	8.9	0.9	3.4	0.20
855	8.3	8.7	0.2	5.8	0.27	847	8.6	8.2	0.3	5.4	0.33
895	3.5	*4.8	13.7	*5.3	*0.35	893	8.4	6.9	0.6	7.3	0.40
1545	5.0	8.1	4.1	7.2	0.27						
1603	8.1	7.9	0.8	8.3	0.32	1583	4.4	5.7	2.4	9.4	0.60
1685	8.3	7.3	4.1	8.2	0.35	1680	8.3	6.0	0.6	15.4	0.60

TABLE III. Best-fit parameters for fits to data shown in Figure 4. Two resonances are missing in Devices A(2) and B(2) due to fabrication yield. The values with an asterisk (*) are considered unreliable. The text explains the fits in more detail and assesses the reliability of the fitted parameters. Of particular interest is the consistency of δ_{TLS}^0 obtained from the frequency-shift and quality-factor data.

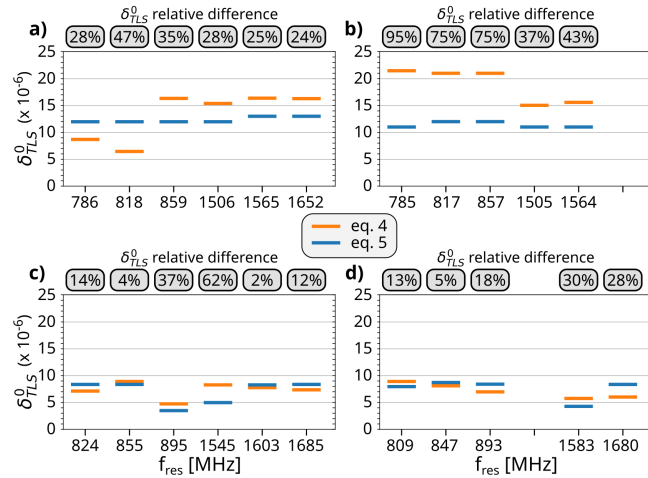


FIG. 5. Values of δ_{TLS}^0 obtained from quality-factor data (orange) and frequency-shift data (blue) for a) Device A(1), b) Device A(2), c) Device B(1), d) Device B(2). The relative difference between the two fitted values of δ_{TLS}^0 is indicated in the grey box above.

between the two devices, with an average value of 0.35×10^{-6} /month. We may speculate that exposure to laboratory air results in uncontrolled uptake of oxygen, hydrogen, or water by the a-Si:H films that gives rise to an increase in TLS density, but it is also possible that an increase in TLS density arises from evolution of the physical structure of the amorphous films simply due to thermal activation. We would need to undertake comparisons to a set of devices stored in more controlled environments (vacuum, dry N_2 atmosphere, dry air atmosphere, finer temperature control) to narrow down the cause. These changes are fairly modest, but it is sensible to

Device A(1)			Device B(1)		
f_{res} [MHz]	new δ_{TLS}^0 ($\times 10^{-6}$)	old δ_{TLS}^0 ($\times 10^{-6}$)	f_{res} [MHz]	new δ_{TLS}^0 ($\times 10^{-6}$)	old δ_{TLS}^0 ($\times 10^{-6}$)
786	12.0	10.0	824	8.3	7.5
818	12.0	9.9	855	8.3	7.7
859	12.0	9.5	895	3.5	4.0
1506	12.0	11.0	1545	5.0	4.5
1565	13.0	N/A	1603	8.1	7.5
1652	13.0	11.0	1685	8.3	7.6

TABLE IV. Degradation of δ_{TLS}^0 with time as evidenced by δ_{TLS}^0 measurements from frequency-shift data taken at different dates. For Device A(1), the old and new measurements are separated by 53 months, while, for Device B(1), they are separated by 18 months.

take simple precautions (*e.g.*, storage with dessicant) to try to prevent such degradation in the future.

Concerning δ_{other} , the evolution with time seems more random. In September, 2020, we measured the high power Q_i^{-1} for Device B(1). Compared to the δ_{other} fits obtained from March, 2022, data and presented in Table III, four resonators show differences smaller than a factor of 2 while two resonators (at 824 MHz and 895 MHz) show increases by factors of 16 and 3, respectively. We observe that the resonators that show the largest degradations are the ones for which the values of δ_{other} are largest, absolutely, and large compared to δ_{TLS}^0 .

The dramatic differences between both the values and the degradation of δ_{other} for resonators on the same device suggest that the cause is not general atmospheric or thermal conditions. Local changes in film properties, such as stress, per-

haps aggravated by thermal cycling during test, seem a more likely culprit. Diagnostic measurements sensitive to local film properties — profilometry or AFM — may be useful in identifying a specific cause. It remains to be seen whether these seemingly occasional large absolute values and degradations of δ_{other} will prove to be a significant practical issue for large arrays of such resonators (*i.e.*, resonator yield).

Jointly, the variations of δ_{TLS}^0 and δ_{other} with time imply that one must take care to fully re-characterize all resonators during each cooldown: values from previous cooldowns may not be sufficiently accurate.

D. Measurements of E_c and β

Recall that β is related to the TLS density of states; $\beta = 0.5$ corresponds to a log-uniform density of states. The values of β seen in the literature, varying from 0.15 to 0.35 [29, 37], motivate us to also fit for β rather than assume the naive value of 0.5. We require $\beta \in [0.10, 0.60]$ to cover both the naive value and the prior literature values.

The position and slope of the $|\vec{E}|$ -dependent region of the $Q_i^{-1}(|\vec{E}|)$ data between the two plateaus (see Figures 3 and 4) determines the values of E_c and β , respectively, via Equation 4. As noted previously, the plateaus are not cleanly visible in all the data, resulting in unreliable values of E_c and β . We note these cases with an asterisk in Table III. Considering only the reliable fits, we find $0.2 < \beta < 0.6$, with the $\beta = 0.6$ values potentially limited by the allowed range for β . The median values of E_c and β for Devices B(1) and B(2) for the reliable fits are 7.3 V/m and 0.33, respectively. The β values are thus consistent with the literature. (E_c values are not available from the literature in general, presumably because, for non-PPC geometries, determining it requires sophisticated modeling of the variation of $|\vec{E}|$ over the resonator at a given P_{read} .) However, we find E_c and β to be fairly degenerate, potentially giving rise to the large variation in β we see. Recall that our data only probe values of $hf_{res}/(2k_B T) \lesssim 0.075$, well away from saturation of the temperature dependence. Data at lower temperature may thus provide a larger sloped region, improving the determination of β and E_c . We thus conclude that our results are consistent with prior data but that we would need lower- T data to constrain β more tightly than prior work.

VI. COMPARISON TO LITERATURE RESULTS; DISCUSSION

To provide context for our results, we review the literature on comparably low-loss, depositable dielectrics.

Comparing these δ_{TLS}^0 results with previously published measurements is not always straightforward, in large part because prior measurements rely almost exclusively on Q_i^{-1} rather than f_{res} data. Considering resonator design, a non-PPC geometry (*e.g.*, CPW, microstripline) results in a design-specific value of F , the TLS fill factor, which is generally calculated and reported to obtain a value of δ_{TLS}^0 . Less frequently,

if ever, reported is the E_c value because, as noted above, determining it requires somewhat sophisticated modeling of the variation of $|\vec{E}|$ over the device and how the variation in field saturation with position determines the overall Q_i^{-1} . Considering measurement technique, determining the true value of δ_{TLS}^0 requires either data taken over a sufficiently broad range of $|\vec{E}|$ (usually done) as well as data taken at sufficiently low T such that the temperature dependence saturates (generally but not always possible) or data taken at a wide enough range of T that the temperature-dependence can be fitted for (possible but rarely done).

We consider in turn other studies of a-Si:H and of other depositable low-loss dielectrics (a-SiC:H and a-Ge).

A. a-Si:H

Among the existing studies of dielectric loss in a-Si:H, the one from O’Connell et al. [23] is most straightforward to compare because they used PPCs also. They found $Q_i^{-1} \in [22 - 25] \times 10^{-6}$ for resonance frequencies close to 6 GHz and at 100 mK. A plot shown in the article also indicates that $\delta_{other} \ll \delta_{TLS}^0$ and that $|\vec{E}| \ll E_c$. We apply a modest correction for incomplete temperature saturation (from Equation 4, $Q_i^{-1}(|\vec{E}| \ll E_c) \approx \delta_{TLS}^0 \tanh(hf_{res}/(2k_B T))$) to their values of Q_i^{-1} to obtain $\delta_{TLS}^0 \in [25 - 28] \times 10^{-6}$.

Mazin et al. [24] used Al microstrip resonators. Because they operated below 100 mK and at about 9 GHz, $\tanh(hf_{res}/(2k_B T)) \approx 1$. Their data show a clear low-power plateau, indicating $\delta_{other} \ll \delta_{TLS}^0$. We thus extract from their data the value $\delta_{TLS}^0 \approx 60 \times 10^{-6}$.

Bruno et al. [25] used Nb lumped-element LC resonators. While measurement details are lacking, it is reasonable to infer that $\delta_{TLS} = 25 \times 10^{-6}$ was obtained at $T = 4.2$ K for $f_{res} = 10.5$ GHz. The correction for $\tanh(hf_{res}/(2k_B T)) \approx 0.06$ is large, yielding $\delta_{TLS}^0 \approx 420 \times 10^{-6}$.

Molina-Ruiz et al. [29] measured Al CPW resonators on a-Si at 10 mK and 4-7 GHz. While this material is not hydrogenated (H is undetectable, with an upper limit of $< 0.1\%$), we include it in discussion of a-Si:H because it can be considered to be on a continuum with a-Si:H. They also used Q_i^{-1} measurements across a wide range of readout powers to extract δ_{TLS}^0 . They tried to correct for the contribution to δ_{TLS}^0 of TLS loss of oxide layers at exposed surfaces or at film interfaces by measuring resonators of the same geometry fabricated directly on a bulk crystalline Si substrate, introducing a systematic uncertainty. The value obtained for their lowest-loss deposition recipe, $\delta_{TLS}^0 = 3.3 \pm 3.5 \times 10^{-4}$, is interestingly low, but it has a large fractional uncertainty for this reason. We note that this film has low acoustic loss tangent, 21×10^{-6} , though Molina-Ruiz et al. [29] also show that acoustic and RF loss have different microscopic sources, with a thinner film showing lower acoustic loss and higher RF loss, so there is no guarantee that the true RF loss is comparable to the low acoustic loss.

Buijtdorp et al. [19, 26] and Hähnle et al. [27] provide the most recent results on a-Si:H loss. While Buijtdorp et al. [19, 26] provide the more extensive study of a-Si:H, their

range of readout power is not large enough to identify the low- and high-power plateaus, so δ_{TLS}^0 cannot be accurately determined. They also make significant corrections for surface oxides that introduce scatter and make it difficult to identify a single number or robust upper limit. Hähnle et al. [27], by contrast, provide Q_i data covering the full range needed, yielding $\delta_{TLS}^0 = 3.6 \pm 0.5 \times 10^{-5}$ (after subtracting δ_{other} ; $\tanh(hf_{res}/(2k_B T)) \approx 1$ for $f_{res} = 6$ GHz and $T = 60$ mK). Hähnle et al. [27] references [26] for deposition parameters, so we assume the former used the lowest loss recipe from the latter.

It is clear from the above summary that many authors have demonstrated a-Si:H films with $\delta_{TLS}^0 < 10^{-4}$. It is of obvious interest to identify under what conditions these results can be obtained and what causes the remaining variability. We summarize in Table V deposition recipes and measured δ_{TLS}^0 for our devices and the above literature results. It is clear that $\delta_{TLS}^0 < 10^{-4}$ seems achievable with a variety of PECVD techniques and recipes and that these various recipes exhibit less than an order of magnitude variation in δ_{TLS}^0 . However, no patterns connecting δ_{TLS}^0 to PECVD deposition technique or parameters readily emerge.

Due to the large uncertainty on δ_{TLS}^0 for e-beam evaporated a-Si films, it is not yet clear whether such films offer comparably low δ_{TLS}^0 . Molina-Ruiz et al. [29] show that a lower substrate temperature during deposition dramatically increases both RF and acoustic loss, while we do not observe a similar dependence for PECVD films, so it does seem that PECVD is a more robust process for achieving $\delta_{TLS}^0 < 10^{-4}$ for a-Si:H. (We note that PECVD films of SiO₂ and SiN_x exhibit significantly higher loss tangents, with the previously noted exception of the high-stress film in [28], so PECVD alone is not sufficient.)

This comparison with the previously published measurements shows that the average value of a-Si:H δ_{TLS}^0 for our recipe B is about 4 times lower than that measured by O’Connell et al. [23], 8 times lower than that measured by Mazin et al. [24], of order a decade lower than that measured by Molina-Ruiz et al. [29], and 5 times lower than that measured by Hähnle et al. [27]. *We thus believe we have obtained the lowest-loss a-Si:H films in the literature. Moreover, the modestly poorer loss obtained from recipe A implies our δ_{TLS}^0 is fairly robust against changes in deposition machine and recipe.*

B. Other Depositable Low-Loss Dielectrics: a-SiC:H and a-Ge

While our focus in this paper has been on a-Si:H because, out of the widely studied depositable dielectrics AlO_x, SiO₂, SiO_x, SiN_x, and a-Si:H, it generally gives the lowest loss tangents, there are other depositable dielectrics with comparably low loss and thus of potentially comparable utility.

Buijtendorp et al. [19] studies hydrogenated amorphous silicon carbide, a-SiC:H, deposited using PECVD. They measure $\delta_{TLS}^0 = 30 \pm 0.4 \times 10^{-6}$ at $f_{res} = 7.4$ GHz and $T = 60$ mK, requiring no $\tanh(hf_{res}/(2k_B T))$ correction. These results are comparable to the same authors’ results for a-Si:H in Hähnle

et al. [27], noted above.

Kopas et al. [20] have demonstrated similar low loss tangents for a-Ge. They use Nb CPW resonators deposited on a 1 μ m thick a-Ge film deposited by thermal evaporation. The temperature (40 mK) and resonance frequency (6.3 GHz and 7.3 GHz) of their measurements ensure that $\tanh(hf_{res}/(2k_B T)) \approx 1$. Their range of readout power reaches the low-power plateau, so their low-power loss tangent measurement $Q_i^{-1} = [11 - 13] \times 10^{-6}$ corresponds to $\delta_{TLS}^0 + \delta_{other}$. Their data do not clearly reach the high-power plateau that would yield δ_{other} , so the measurements are an upper limit on δ_{TLS}^0 . Because the measured loss tangent is so low, they subtract contributions from TLS at various interfaces and in the substrate based on calculated fill factors and literature values [34]: 5.8×10^{-6} , 1.1×10^{-6} , 0.8×10^{-6} , and 2.6×10^{-7} for the metal-substrate, substrate-air, and metal-air interfaces and silicon substrate loss, respectively. They obtain $\delta_{TLS}^0 + \delta_{other} = [4.7 - 4.9] \times 10^{-6}$ for a-Ge alone, which we interpret as an upper limit on δ_{TLS}^0 . However, no uncertainties on these large subtractions are provided, and it is not clear that these subtractions are valid, as [34] employed TiN resonators on crystalline Si while these authors consider Nb resonators on an a-Ge film on crystalline Si. Thus, $\delta_{TLS}^0 < 11 \times 10^{-6}$ is the more robust result.

VII. CONCLUSION

We have reported low-field, low-temperature TLS loss (δ_{TLS}^0) values of 7×10^{-6} and 12×10^{-6} for two similar but far from identical deposition recipes, obtained in two different CVD deposition systems at two different sites. These values are robust and subject to minimal modeling uncertainty thanks to the use of PPCs, multiple resonators spanning a factor of 2 in frequency, and frequency-shift data. We have also determined δ_{TLS}^0 from quality-factor data and found those values to be broadly consistent with the frequency-shift results, but we have explained why quality-factor data is more difficult to model and thus the resulting values subject to greater systematic uncertainty. Our lowest frequency-shift values of TLS loss are a factor of 4 lower than the best previously published, robust results for a-Si:H and are comparable to results for a-Ge [20]. They also depend only modestly (factor of ≈ 1.5) on deposition machine and details of deposition technique. Comparison to the literature reveals no clear reason for the very low observed δ_{TLS}^0 values, though it does suggest that CVD is a robust process for achieving $\delta_{TLS}^0 < 10^{-4}$ with a-Si:H. A variety of fields employing superconducting devices with dielectric film capacitors may benefit from this development.

We have also characterized, with varying levels of robustness, the other parameters δ_{other} , E_c , and β that impact the quality factor of resonators using these films. We observed degradation of both δ_{TLS}^0 and δ_{other} with time when no special storage measures are taken, motivating more precautions in the future.

Lastly, we have demonstrated that the technique of using frequency-shift data with PPC resonators is a highly robust way to study TLS loss and that the use of quality-factor data

Ref / Facility	Process	Gas ratio (SiH ₄ /Ar)	Temperature [°C]	Gas pressure [mTorr]	Gas flow [sccm]	Deposition time	Thickness [nm]	δ_{TLS}^0 ($\times 10^{-6}$)
Caltech KNI	PECVD	5% / 95%	350	800	250	27'11"	800	≈ 12
JPL MDL	ICP-PECVD	100% / 0%	350	10	30	26'06"	800	≈ 7
O'Connell et al. [23]	HD PECVD	66% / 33%	100	2	45	3'15"	unknown	≈ 26
Mazin et al. [24]	HD PECVD	66% / 33%	100	2	45	3'15"	200	≈ 60
Bruno et al. [25]	PECVD	100% / 0%	250	200	unknown	unknown	unknown	420
Molina-Ruiz et al. (no H) [29]	e-beam evap	N/A	50 / 225 / 450	$< 5 \times 10^{-6}$	N/A	19'-106'	59-317	$\geq 330 \pm 350$
Hähnle et al. [27]	PECVD	5% / 95%	350	1000	500	7'0"	250 \pm 15	36 \pm 5

TABLE V. Summary of a-Si:H deposition recipes and measured δ_{TLS}^0 for our devices and previously published results. a-Si:H films measured by Mazin et al. and O'Connell et al. were both fabricated at University of California Santa Barbara (UCSB) using a recipe identical or very close to the one detailed by E. Lucero in his PhD thesis [41], Appendix B.4.6 (private communication from B. Mazin). HD PECVD stands for High-Density Plasma-Enhanced Chemical Vapor Deposition. While most of the above publications use PECVD to deposit a-Si:H, Molina-Ruiz et al. use e-beam evaporation instead to deposit a-Si and thus gas ratio and gas flow are not applicable. O'Connell et al. do not provide precise film thicknesses but indicate their films are hundreds of nm thick, comparable to the other films presented in this table. As noted in the text, Buijtdorp et al. [19, 26] and Hähnle et al. [27] use the same deposition parameters, but the former do not provide precise δ_{TLS}^0 values, while the latter does not provide deposition details. We assume Hähnle et al. [27] used the lowest loss recipe from Buijtdorp et al. [26].

requires careful attention to the temperature and field values at which the data are taken. In the latter case, to infer δ_{other} , E_c , and β — the latter two of which inform us about the microscopic nature of the TLS — a large dynamic range in $|\vec{E}|$ must be probed, covering both the low and higher power plateaus. Other effects (quasiparticle loss and/or heating) may make such analyses challenging.

Future publications in preparation will study: the dependence of the above TLS and non-TLS parameters on deposition parameters in the machines used for this work; and, correlations of TLS loss and TLS noise for these recipes. Future work underway will include: comparisons of these parameters for resonators fabricated using other machines at other sites but with efforts made to mimic deposition recipes; correlation of TLS loss, noise, and room-temperature film-quality diagnostics; and, correlation of RF (~ 1 GHz) and mm-wave (~ 100 –400 GHz) loss.

Future work will study: the dependence of the above TLS and non-TLS parameters on deposition parameters in the machines used for this work; comparisons of these parameters for resonators fabricated using other machines at other sites but with efforts made to mimic deposition recipes; correlation of RF (~ 1 GHz) and mm-wave/THz (~ 100 –400 GHz) loss; correlation of RF loss and RF noise; and, correlation of RF loss and noise with film properties measured at 300 K (O/IR refractive index and absorption, density, H content and elemental composition including binding state, bond types and angles, film strain, short-range and medium-range order, dangling bond density, and perhaps others) and with cryogenic acoustic loss. These efforts will have both practical and fundamental consequences. At a practical level, the study of deposition conditions will test the robustness of our recipes and enable reproduction by other investigators. The correlation with 300 K diagnostics will offer a means to understand the funda-

mental reasons for the low RF loss from underlying material properties as well as a practical way to monitor and tune deposition processes to maintain the low loss (and perhaps further improve it). Noise measurements will test whether, at a practical level, low loss a-Si:H films also will enable low-noise PPC KIDs while also offering another empirical constraint on the fundamental tunneling model explanation of a-Si:H behavior. Mm-wave/THz measurements will test the material's practical utility in that frequency regime as well as probe the electric-dipole-couple TLS density of states at $100\times$ higher energies. Cryogenic acoustic loss measurements will test whether the conclusion of Molina-Ruiz et al. [29], that two types of TLS are present in a-Si, is valid at the 25 – $50\times$ lower RF loss levels observed here; perhaps, there is one species of electric-dipole-coupled TLS that do not interact acoustically while the acoustically active species is also electric-dipole-coupled but more weakly than the former.

ACKNOWLEDGMENTS

This work has been supported by the JPL Research and Technology Development Fund, the National Aeronautics and Space Administration under awards 80NSSC18K0385 and 80NSSC22K1556, and the Department of Energy Office of High-Energy Physics Advanced Detector Research program under award DOE-SC0018126. A. B. and F. D. carried out research/fabrication at the Jet Propulsion Laboratory, operated by the California Institute of Technology under a contract with the National Aeronautics and Space Administration (80NM0018D0004). The authors would like to thank J. Gao for his very helpful comments, B. Mazin for efforts to re-make devices using the O'Connell et al. [23] recipes, and M. Hollister for design and construction of the cryostat used for this work and early resonator measurements.

- [1] W. A. Phillips, Reports on Progress in Physics **50**, 1657 (1987).
- [2] P. Esquinazi, ed., *Tunneling Systems in Amorphous and Crystalline Solids* (Springer Berlin Heidelberg, Berlin, Heidelberg, 1998).
- [3] C. Müller, J. H. Cole, and J. Lisenfeld, Reports on Progress in Physics **82**, 124501 (2019).
- [4] J. M. Martinis, K. B. Cooper, R. McDermott, M. Steffen, M. Ansmann, K. D. Osborn, K. Cicak, S. Oh, D. P. Pappas, R. W. Simmonds, and C. C. Yu, Phys. Rev. Lett. **95**, 210503 (2005).
- [5] J. Zmuidzinas, Annual Review of Condensed Matter Physics **3**, 169 (2012), <https://doi.org/10.1146/annurev-conmatphys-020911-125022>.
- [6] S. R. Siegel, *A Multiwavelength Study of the Intracluster Medium and the Characterization of the Multiwavelength Sub/millimeter Inductance Camera*, Ph.D. thesis, California Institute of Technology (2015).
- [7] C. L. Chang, P. A. R. Ade, Z. Ahmed, S. W. Allen, K. Arnold, J. E. Austermann, A. N. Bender, L. E. Bleem, B. A. Benson, J. E. Carlstrom, H. M. Cho, S. T. Ciocons, J. F. Cliche, T. M. Crawford, A. Cukierman, J. Ding, T. de Haan, M. A. Dobbs, D. Dutcher, W. Everett, A. Gilbert, N. W. Halverson, D. Hanson, N. L. Harrington, K. Hattori, J. W. Henning, G. C. Hilton, G. P. Holder, W. L. Holzzapfel, J. Hubmayr, K. D. Irwin, R. Keisler, L. Knox, D. Kubik, C. L. Kuo, A. T. Lee, E. M. Leitch, D. Li, M. McDonald, S. S. Meyer, J. Montgomery, M. Myers, T. Natoli, H. Nguyen, V. Novosad, S. Padin, Z. Pan, J. Pearson, C. Posada Arbelaez, C. L. Reichardt, J. E. Ruhl, B. R. Saliwanchik, G. Simard, G. Smecher, J. T. Sayre, E. Shirokoff, A. A. Stark, K. Story, A. Suzuki, K. L. Thompson, C. Tucker, K. Vanderlinde, J. D. Vieira, A. Vikhlinin, G. Wang, V. Yefremenko, and K. W. Yoon, IEEE Transactions on Applied Superconductivity **25**, 1 (2015).
- [8] E. Shirokoff, P. S. Barry, C. M. Bradford, G. Chattopadhyay, P. Day, S. Doyle, S. Hailey-Dunsheath, M. I. Hollister, A. Kovács, H. G. Leduc, C. M. McKenney, P. Mauskopf, H. T. Nguyen, R. O'Brien, S. Padin, T. J. Reck, L. J. Swenson, C. E. Tucker, and J. Zmuidzinas, Journal of Low Temperature Physics **176**, 657 (2014).
- [9] S. J. Weber, K. W. Murch, D. H. Slichter, R. Vijay, and I. Siddiqi, Applied Physics Letters **98**, 172510 (2011), <https://doi.org/10.1063/1.3583449>.
- [10] K. L. Denis, N. T. Cao, D. T. Chuss, J. Eimer, J. R. Hinderks, W. Hsieh, S. H. Moseley, T. R. Stevenson, D. J. Talley, K. Uyen, and E. J. Wollack, AIP Conference Proceedings **1185**, 371 (2009), <https://aip.scitation.org/doi/pdf/10.1063/1.3292355>.
- [11] A. D. Beyer, M. I. Hollister, J. Sayers, C. F. Frez, P. K. Day, and S. R. Golwala, Journal of Physics: Conference Series **834**, 012006 (2017).
- [12] J. Gao, M. Daal, A. Vayonakis, S. Kumar, J. Zmuidzinas, B. Sadoulet, B. A. Mazin, P. K. Day, and H. G. Leduc, Applied Physics Letters **92**, 152505 (2008), <https://doi.org/10.1063/1.2906373>.
- [13] H. Wang, M. Hofheinz, J. Wenner, M. Ansmann, R. C. Bialczak, M. Lenander, E. Lucero, M. Neeley, A. D. O'Connell, D. Sank, M. Weides, A. N. Cleland, and J. M. Martinis, Applied Physics Letters **95**, 233508 (2009), <https://doi.org/10.1063/1.3273372>.
- [14] J. M. Sage, V. Bolkhovskoy, W. D. Oliver, B. Turek, and P. B. Welander, Journal of Applied Physics **109**, 063915 (2011), <https://doi.org/10.1063/1.3552890>.
- [15] F. Boussaha, S. Beldi, A. Monfardini, J. Hu, M. Calvo, C. Chaumont, F. Levy-Bertrand, T. Vacelet, A. Traini, J. Firminy, M. Piat, and F. Reix, Journal of Low Temperature Physics **199**, 994 (2020).
- [16] M. Mirzaei, E. M. Barrentine, B. T. Bulcha, G. Cataldo, J. A. Connors, N. Ehsan, T. M. Essinger-Hileman, L. A. Hess, J. W. Mugge-Durum, O. Noroozian, T. M. Oxholm, T. R. Stevenson, E. R. Switzer, C. G. Volpert, and E. J. Wollack, in *Millimeter, Submillimeter, and Far-Infrared Detectors and Instrumentation for Astronomy X*, Vol. 11453, edited by J. Zmuidzinas and J.-R. Gao, International Society for Optics and Photonics (SPIE, 2020) p. 114530M.
- [17] S. Shu, N. Klimovich, B. H. Eom, A. D. Beyer, R. B. Thakur, H. G. Leduc, and P. K. Day, Phys. Rev. Research **3**, 023184 (2021).
- [18] C. R. H. McRae, H. Wang, J. Gao, M. R. Vissers, T. Brecht, A. Dunsworth, D. P. Pappas, and J. Mutus, Review of Scientific Instruments **91**, 091101 (2020).
- [19] B. T. Buijtdorp, S. Vollebregt, K. Karatsu, D. J. Thoen, V. Murugesan, K. Kouwenhoven, S. Hähnle, J. J. A. Baselmans, and A. Endo, Phys. Rev. Appl. **18**, 064003 (2022).
- [20] C. J. Kopas, J. Gonzales, S. Zhang, D. R. Queen, B. Wagner, M. Robinson, J. Huffman, and N. Newman, AIP Advances **11**, 095007 (2021), https://pubs.aip.org/aip/adv/article-pdf/doi/10.1063/5.0041525/12827529/095007_1_online.pdf.
- [21] M. P. Weides, J. S. Kline, M. R. Vissers, M. O. Sandberg, D. S. Wisbey, B. R. Johnson, T. A. Ohki, and D. P. Pappas, Applied Physics Letters **99**, 262502 (2011), arXiv:1111.5083 [cond-mat.supr-con].
- [22] K. H. Cho, U. Patel, J. Podkaminer, Y. Gao, C. M. Folkman, C. W. Bark, S. Lee, Y. Zhang, X. Q. Pan, R. McDermott, and C. B. Eom, APL Materials **1**, 042115 (2013).
- [23] A. D. O'Connell, M. Ansmann, R. C. Bialczak, M. Hofheinz, N. Katz, E. Lucero, C. McKenney, M. Neeley, H. Wang, E. M. Weig, A. N. Cleland, and J. M. Martinis, Applied Physics Letters **92**, 112903 (2008), <https://doi.org/10.1063/1.2898887>.
- [24] B. A. Mazin, D. Sank, S. McHugh, E. A. Lucero, A. Merrill, J. Gao, D. Pappas, D. Moore, and J. Zmuidzinas, Applied Physics Letters **96**, 102504 (2010), <https://doi.org/10.1063/1.3314281>.
- [25] A. Bruno, S. T. Skacel, C. Kaiser, S. Wunsch, M. Siegel, A. V. Ustinov, and M. P. Lisitskiy, Physics Procedia **36**, 245 (2012).
- [26] B. T. Buijtdorp, J. Bueno, D. J. Thoen, V. Murugesan, P. M. Sberna, J. J. A. Baselmans, S. Vollebregt, and A. Endo, in *Millimeter, Submillimeter, and Far-Infrared Detectors and Instrumentation for Astronomy X*, Vol. 11453, edited by J. Zmuidzinas and J.-R. Gao, International Society for Optics and Photonics (SPIE, 2020) pp. 459 – 472.
- [27] S. Hähnle, K. Kouwenhoven, B. T. Buijtdorp, A. Endo, K. Karatsu, D. J. Thoen, V. Murugesan, and J. J. A. Baselmans, Physical Review Applied **16**, 014019 (2021).
- [28] H. Paik and K. D. Osborn, Applied Physics Letters **96**, 072505 (2010), https://pubs.aip.org/aip/apl/article-pdf/doi/10.1063/1.3309703/14426272/072505_1_online.pdf.
- [29] M. Molina-Ruiz, Y. J. Rosen, H. C. Jacks, M. R. Abernathy, T. H. Metcalf, X. Liu, J. L. DuBois, and F. Hellman, Phys. Rev. Materials **5**, 035601 (2021).
- [30] C. R. H. McRae, R. E. Lake, J. L. Long, M. Bal, X. Wu, B. Jugdersuren, T. H. Metcalf, X. Liu, and D. P. Pappas, Applied Physics Letters **116**, 194003 (2020), <https://doi.org/10.1063/5.0004622>.

- [31] J. Gao, *The Physics of Superconducting Microwave Resonators*, Ph.D. thesis, California Institute of Technology (2008).
- [32] D. P. Pappas, M. R. Vissers, D. S. Wisbey, J. S. Kline, and J. Gao, *IEEE Transactions on Applied Superconductivity* **21**, 871 (2011).
- [33] D. S. Wisbey, A. Martin, A. Reinisch, and J. Gao, *Journal of Low Temperature Physics* **176**, 538 (2014).
- [34] W. Woods, G. Calusine, A. Melville, A. Sevi, E. Golden, D. K. Kim, D. Rosenberg, J. L. Yoder, and W. D. Oliver, *Phys. Rev. Applied* **12**, 014012 (2019).
- [35] J. Wenner, R. Barends, R. C. Bialczak, Y. Chen, J. Kelly, E. Lucero, M. Mariantoni, A. Megrant, P. J. J. O'Malley, D. Sank, A. Vainsencher, H. Wang, T. C. White, Y. Yin, J. Zhao, A. N. Cleland, and J. M. Martinis, *Applied Physics Letters* **99**, 113513 (2011), <https://doi.org/10.1063/1.3637047>.
- [36] C. Wang, C. Axline, Y. Y. Gao, T. Brecht, Y. Chu, L. Frunzio, M. H. Devoret, and R. J. Schoelkopf, *Applied Physics Letters* **107**, 162601 (2015), <https://doi.org/10.1063/1.4934486>.
- [37] J. Burnett, L. Faoro, and T. Lindström, *Superconductor Science and Technology* **29**, 044008 (2016).
- [38] M. R. Vissers, M. P. Weides, J. S. Kline, M. Sandberg, and D. P. Pappas, *Applied Physics Letters* **101**, 022601 (2012), <https://doi.org/10.1063/1.4730389>.
- [39] F. W. Carter, T. S. Khaire, V. Novosad, and C. L. Chang, *IEEE Transactions on Applied Superconductivity* **27**, 1 (2017).
- [40] T. Guruswamy, *Nonequilibrium behaviour and quasiparticle heating in thin film superconducting microwave resonators*, Ph.D. thesis, University of Cambridge (2018).
- [41] E. Lucero, *Computing prime factors using a Josephson phase-qubit architecture: $15 = 3 \times 5$* , Ph.D. thesis, University of California Santa Barbara (2012).
- [42] R. Crandall and W. Luft, *Progress in Photovoltaics: Research and Applications* **3**, 315 (1995).
- [43] R. Birney, J. Steinlechner, Z. Tornasi, S. MacFoy, D. Vine, A. S. Bell, D. Gibson, J. Hough, S. Rowan, P. Sortais, S. Sproules, S. Tait, I. W. Martin, and S. Reid, *Phys. Rev. Lett.* **121**, 191101 (2018).
- [44] R. O. Pohl, X. Liu, and E. Thompson, *Rev. Mod. Phys.* **74**, 991 (2002).
- [45] L. J. Swenson, P. K. Day, B. H. Eom, H. G. Leduc, N. Llombart, C. M. McKenney, O. Noroozian, and J. Zmuidzinas, *Journal of Applied Physics* **113**, 104501 (2013), <https://doi.org/10.1063/1.4794808>.

Appendix A: Literature on a-Si and a-Si:H

As noted in §I, there is significant, potentially relevant literature on a-Si and a-Si:H in three different contexts: as a photovoltaic, as an example of sub-electronic-bandgap optical absorption, with impact on its use as a mirror coating in laser-interferometric gravitational wave detectors (GWDs); and, as an exemplar of universal STM behavior. The common thread in the literature of relevance to our work is the impact of dangling bonds in the nominally four-fold coordinated a-Si material, quantifiable via electron paramagnetic resonance measurements. While the photovoltaic studies (see [42] for a review) devote significant attention to the importance of dangling bonds to photovoltaic efficiency and the role of hydrogenation in both improving and degrading that efficiency through its effect on the dangling bond density, the electromagnetic behavior studied is at optical frequencies, where the

processes involved are energetically disparate from those relevant here (eV vs. μeV – meV). The same holds for GWDs: the concern is with optical absorption in the 1–2 μm (150–300 THz; 0.5–1 eV) regime. While there are studies correlating this absorption with dangling bond density at high absorption (extinction coefficient $\gtrsim 10^{-3}$), the absorption at the lower levels of practical interest for GWDs appears to be due to sub-electronic-bandgap states, not dangling bonds [43].

The third context, the study of a-Si and a-Si:H as an example of the STM is, in contrast, quite qualitatively relevant: the modern introduction of a-Si/a-Si:H for GHz superconducting device applications by O'Connell et al. [23] identified a-Si/a-Si:H as the most promising easily deposited material from the extensive database of thermal conductivity and acoustic attenuation data in amorphous materials presented in Pohl et al. [44], whose goal was to assess the universality of the low-energy excitations on which the STM is based. However, even there, it is now clear the connection to that extensive prior literature is tangential: Molina-Ruiz et al. [29] demonstrated that, at least in some regimes of TLS density, there appear to be two types of TLS: some that couple strongly to elastic strain (phonons) and some that couple strongly via electric-dipole interaction to electromagnetic fields. We are of course interested in the latter, while the literature on a-Si/a-Si:H prior to Molina-Ruiz et al. [29] was primarily concerned with the former. At the moment, this two-TLS model suggests the extensive prior literature is not quantitatively relevant for the work here, though we offer a caveat in §VII.

Appendix B: Electric field and photon number calculations

The total energy stored in a resonator at a frequency f can be expressed as [5, 6, 45]:

$$W = \frac{1}{1 + 4Q_r^2 x^2} \frac{P_{\text{read}} Q_r^2}{\pi f_{\text{res}} Q_c}, \quad (\text{B1})$$

with $x = (f - f_{\text{res}})/f_{\text{res}}$, and P_{read} the readout power at the device. At $f = f_{\text{res}}$ ($x = 0$), this equation simplifies to:

$$W = \frac{P_{\text{read}} Q_r^2}{\pi f_{\text{res}} Q_c}. \quad (\text{B2})$$

The total time-averaged stored energy W is composed of time-averaged magnetic and electric energies, respectively, which are identical and half of the total energy: $W_e = W_m = W/2$. Only the electric energy W_e should be considered for calculating the rms electric field magnitude (which we denote, for brevity, by $|\vec{E}|$) between the parallel plates of the capacitor. The generic formula for a single parallel-plate capacitor is:

$$|\vec{E}| = \sqrt{\frac{2W_e}{\epsilon A d}}, \quad (\text{B3})$$

where ϵ is the permittivity of the dielectric between the capacitor plates, A is the area of each capacitor plate, and d is the separation of the plates (the thickness of the dielectric film). However, in our specific case, because we have two identical

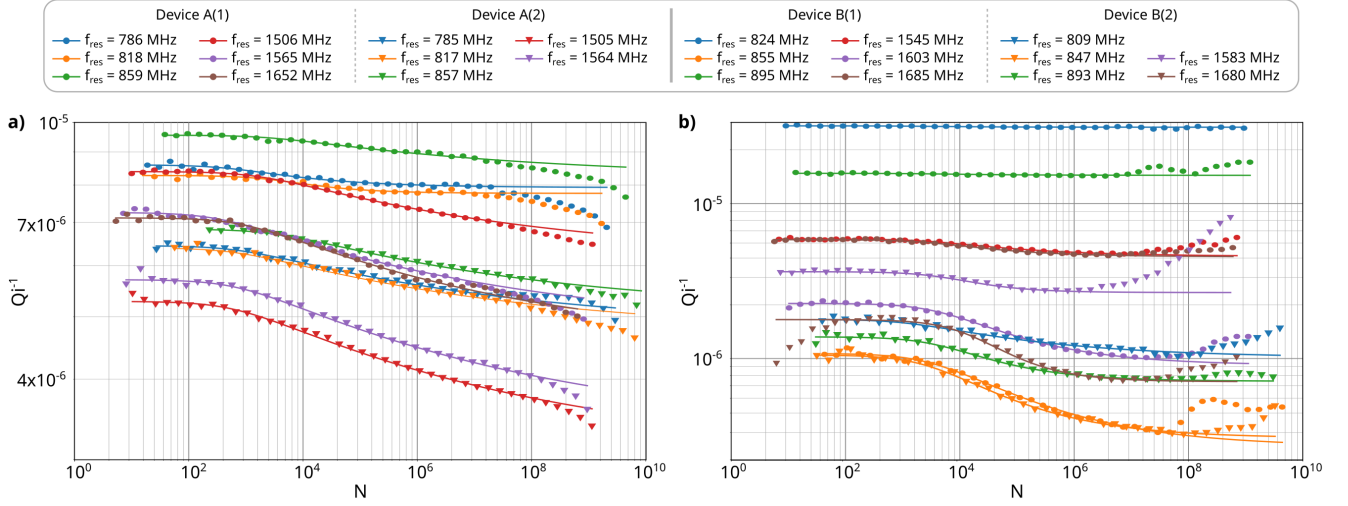


FIG. 6. a), b) Data and best-fit TLS model (Equation 4) for Q_i^{-1} data as a function of photon number. The data shown on this plot are the same as in Figure 4 c) & d) but $|\vec{E}|$ has been converted to photon number N using Equation B5.

capacitors in series, the electric energy stored in each of them is $W_e/2$, so we can rewrite Equation B3 as:

$$|\vec{E}| = \frac{\sqrt{\langle V^2 \rangle}}{d} = \frac{1}{d} \sqrt{\frac{W_e}{C_0}} = \sqrt{\frac{1}{\epsilon A_0 d}} \sqrt{\frac{P_{read}}{2\pi f_{res}}} \frac{Q_r^2}{Q_c}, \quad (\text{B4})$$

where A_0 is the top plate area and C_0 is the capacitance of each of the two capacitors in series. We use the above formula to convert the applied P_{read} to the $|\vec{E}|$ values used for our plots and fits.

The energy stored in a resonator can also be converted into

a number of stored photons. In the literature, photon number is frequently reported in place of readout power. The relation between the two is (also used by Molina-Ruiz et al. [29]):

$$N = \frac{W}{hf_{res}} = \frac{P_{read}}{\pi h f_{res}^2} \frac{Q_r^2}{Q_c}, \quad (\text{B5})$$

where $W = W_e + W_m$ is the total electric and magnetic energy stored in the resonator and h is the Planck constant. We use it to plot Q_i^{-1} data as a function of photon number in Figure 6 to enable comparisons on that basis. Photon number has no special relevance in this work, as we believe E_c is a more fundamental microscopic parameter.

Pulse shape discrimination in an organic scintillation phoswich detector using machine learning techniques

Yujin Lee, Jinyoung Kim, Byoung-cheol Koh, and Chang Hyon Ha

Department of Physics, Chung-Ang University, Seoul 06974, Republic of Korea

Young Soo Yoon

Korea Research Institute of Standards and Science, Daejeon 34113, Republic of Korea

Abstract

We developed machine learning algorithms for distinguishing scintillation signals from a plastic-liquid coupled detector known as a phoswich. The challenge lies in discriminating signals from organic scintillators with similar shapes and short decay times. Using a single-readout phoswich detector, we successfully identified γ radiation signals from two scintillating components. Our Boosted Decision Tree algorithm demonstrated a maximum discrimination power of 3.02 ± 0.85 standard deviation in the 950 keV region, providing an efficient solution for self-shielding and enhancing radiation detection capabilities.

Keywords:

I. INTRODUCTION

Organic scintillators are indispensable tools across diverse technological and scientific realms, from environmental monitoring to the investigation of rare nuclear events [1–3]. Their light-emitting property, activated when constituent molecules undergo deexcitation from ionizing radiations such as alphas, betas, gamma-induced electrons, neutron-induced protons, and cosmic-ray muons makes them vital in radiation detection, medical imaging, and nuclear physics research [4, 5]. Particularly, they are crucial elements in the quest to detect particles like dark matter and neutrinos, demanding highly sensitive detectors for the detection of ultra-low levels of radiation [6, 7]. The appeal of organic scintillators lies in their fast decay time, ease of fabrication, and scalability, distinguishing them as a preferred choice in comparison to other scintillator options [5]

Dark matter particles and neutrinos, ubiquitous yet weakly interacting, pose significant challenges in measurement due to their elusive nature and poorly understood physical properties. Therefore, large-scale experiments are essential to study these particles comprehensively. Organic scintillators play a crucial role in rare decay experiments, enhancing detector capabilities through improved positioning of particle interactions. For instance, in dark matter direct detection experiments, precise positioning aids in background rejection by distinguishing radioactivity in the surrounding environment from that of the main target material [7]. Segmentation concepts, particularly beneficial in short baseline neutrino experiments, exploit variable oscillation baselines within a single experiment [8, 9].

This study introduces a novel single-readout detector called a phoswich (phosphor sandwich) [10] where plastic scintillator (PS) serves as the inner target, and liquid scintillator (LS) acts as the outer guard. Traditional light sensors such as Photomultiplier Tubes (PMTs), containing a significant amount of natural U/Th/K radioactivities, tend to elevate the background level, particularly when placed in close proximity to the target material. The phoswich target-guard approach can improve the target’s background contamination by physically distancing PMTs and identifying interactions detected in the guard material, which also serves as a light guide. In addition to pinpointing interactions, the identification of particles such as gammas, alphas, and neutrons with signal shape analyses could enhance detector sensitivity with a reduced number of PMTs per target volume. Despite the challenge posed by the similar decay times of a few nanoseconds for the two organic

scintillators within the phoswich setup, this study utilizes machine learning techniques to effectively discriminate gamma signals between the two scintillators, marking an important first step towards a large-scale position-sensitive low-background detector concept.

II. MATERIALS AND METHODS

A. Experimental setup

In our setup, a phoswich configuration is implemented, wherein two scintillators with distinct pulse shapes are optically coupled and share a common readout system through PMTs. The implementation of pulse shape discrimination (PSD) serves to segregate signals originating from each scintillator, facilitating the identification of radiation interaction types and, consequently, their source locations.

The primary objective in designing the detector for this analysis is to efficiently collect scintillation photons from the two scintillators. To achieve this, we utilize a plastic scintillator as the inner material and a liquid scintillator as the guard material. The detector configuration comprises a reflective polytetrafluoroethylene (PTFE) cylinder which houses the inner plastic scintillator, encapsulated by a thin polymethylmethacrylate (PMMA) case positioned in the middle of the main cylinder. Importantly, the PMT photocathodes are in direct contact with the liquid scintillator, eliminating the need for any intermediate optical interfaces.

The PS [24] component is precision-machined into a cylindrical shape with dimensions of 45.7 mm in diameter and 49 mm in length. The surfaces of the PS cylinder undergo a polishing process using lapping films to achieve high transparency. To protect PS from chemically reacting with LS, a cylindrical container is fabricated with a diameter of 50.3 mm, a length of 59 mm, and a thickness of 2 mm. Two 1 mm-thick lids made of PMMA are prepared for sealing. The PS cylinder is placed within the PMMA container, and its surfaces are optically coupled by filling small gaps with silicon grease [25]. Subsequently, the container is sealed by attaching the lids using optical cement and adhesives.

For the main container, two cylindrical tubes made of 22 mm-thick PTFE are prepared, each with an inner diameter of 76 mm and a length of 120 mm. One end of these tubes features a 53 mm hole where the PMT rear glass part is fitted and sealed with an O-ring, while

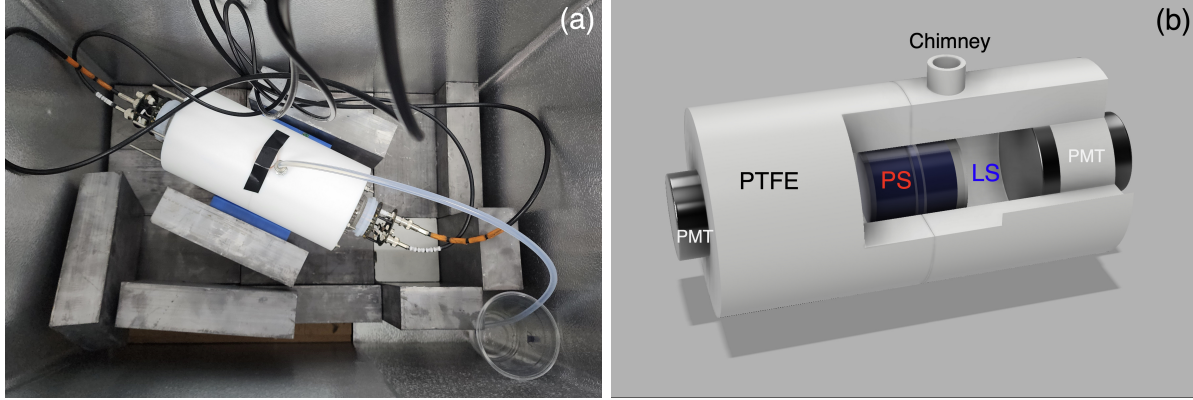


FIG. 1: Phoswich detector. (a) The photo of the setup for the detector and the dark box, (b) The drawing of the detector with internal area exposed. The 3-inch PMTs are attached to both sides of the detector to measure the photons emitted from the guard liquid and inner plastic scintillator. LS is introduced into and removed from the chimney, which also prevents overflow caused by thermal expansion.

the other end is left open to align with the second half of the assembled structure. When the PMMA cylinder is centered within the PTFE container, the outer PTFE components are connected using an O-ring and six long connecting bolts through PTFE flanges. A small PMMA support piece stabilizes the inner PS assembly at the center of the PTFE tube. The inner surface of the PTFE container serves as a diffusive light reflector. The container is filled with LS through the hole under the chimney.

The properties of the LS counter have been extensively examined in experiments requiring detectors with substantial volume or irregular shapes [11]. Linear alkylbenzene (LAB), chosen for its non-toxic and cost-effective attributes, is used as the LS solvent. For initial fluorescence, a concentration of 3 g/L of 2,5-diphenyloxazole is dissolved in the solvent, and for a wavelength shift, 30 mg/L of p-bis(o-methylstyryl) benzene is added [12].

The detector assembly features two three-inch PMTs manufactured by Hamamatsu (R12669SEL). These PMTs show a typical gain of 1.0×10^6 , a spectral response range of 300 to 650 nm, and a peak wavelength of 420 nm. The entire assembly is placed within a dark box with lead shielding averaging 50 mm in thickness. Figure 1 illustrates the completed experimental setup and a schematic drawing of the detector.

B. Readout system and data collection

The data acquisition process involves passing signals through an analog-to-digital converter (FADC), specifically employing a 500 Megasamples/s FADC with a 2.5 V, 12-bit dynamic range. The custom Data Acquisition (DAQ) system, provided by the local company Notice Korea, has a proven track record in various experiments [13].

For event construction, an 8000 ns readout window is established when both PMTs register coincidence pulses within 200 ns, each requiring a discrimination threshold of 10 ADC (where 1 ADC corresponds to approximately 0.6 mV). Utilizing delay settings, the positive pulse starting position is set near 2400 ns, and pedestals are subtracted on an event-by-event basis by averaging the first 500 ns region where no signal is present. High voltages are carefully adjusted such that the PMT signal pulses with less than about 2 MeV energy are not saturated. Synchronization of the two PMT gains is achieved through fine-tuning each high voltage using the Compton edges of the ^{60}Co gamma peaks. The raw data in binary format are subsequently converted into ROOT format for post-processing [14].

Regular gamma calibration data are obtained using ^{60}Co (1173.2 and 1332.5 keV) and ^{137}Cs (661.7 keV) sources. This calibration ensures the accuracy and reliability of the collected data throughout the experimental duration.

C. Pulse Shapes

Typical organic scintillator pulses are fast having a decay time less than 5 ns and rising time of about 2 ns. The decay time for PS is 2.1 ns [15] while that of LAB-based LS is 4.0 ns [16]. With a convolution of PMT transit time of 60 ns (9.5 ns rise time and 13 ns spread), the shape discrimination of output signal waveforms from two scintillators are non-trivial problem, requiring a careful analysis.

Figure 2 shows the average waveform distributions of the PS (red dashed line) and the LS (blue solid line), normalized by the area and for the same energy region. These separate measurements are done by two independent detector assemblies with a ^{60}Co source where the target materials are directly coupled with two PMT photocathodes. The start time (t_0) of the waveform is defined as the time at which a pulse crosses 6-ADC threshold. The distributions show that the leading edge and trailing edge of the PS waveform are relatively

steeper than those of the LS waveform. Therefore, we explored this shape characteristics by developing various discriminating variables.

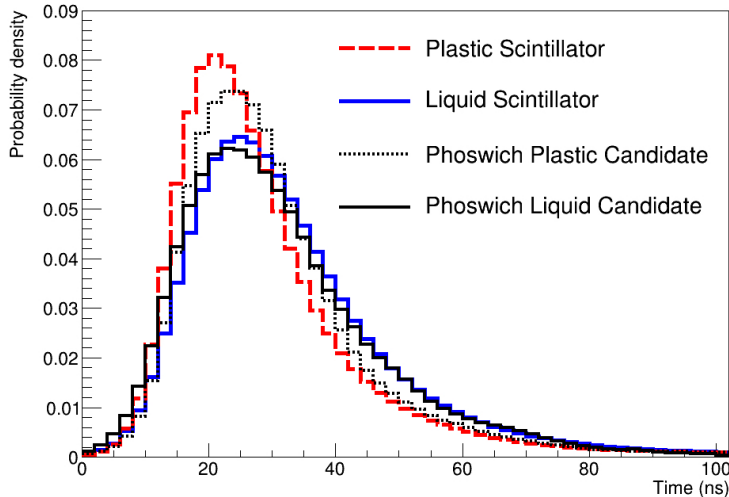


FIG. 2: Pulse shape distributions of each scintillator. The red dashed line indicates the PS average waveform as a probability density distribution while the blue solid line is for LS. The black dotted and solid lines are PS-candidate and LS-candidate events, respectively from the phoswich data. The PS waveforms show a faster rise and decay in time than LS.

Additionally, we examined representative candidate events from the phoswich data. One candidate event (depicted by the black solid line) originates from the liquid segment of the phoswich, while the other (depicted by the black dotted line) is derived from the plastic component, as superimposed in Figure 2. The signal shape of the phoswich-PS part exhibits noticeable degradation, especially at the leading edge, when compared to the PS-only measurement. This degradation suggests a potential scenario where early scintillation photons might have encountered scattering and/or reabsorption by the guard LS before reaching a PMT. Nonetheless, the shape information of the phoswich detector remains intact, and we delved into the subtle yet conceivable shape differences by formulating various parameters.

D. Discrimination Variables

The objective of parameter development is to effectively discern the pulse shape differences between two scintillators utilizing measurements from the ^{60}Co source. Given that

the primary characteristic of the waveforms is the time-amplitude structure, our focus is on fractions of amplitudes in different parts of the waveform, average times, their variances, and the degree of template matches.

We use the balance of the deposited charge from two PMTs, Charge Asymmetry (Eq. 1 also shown in **(a)** of Fig. 4) [12], the ratio R_{head} of the integrated charge in the 10 ns to 30 ns time window (head) to the total collected charge in the first 150 ns time span (Eq. 2 also shown in **(b)** of Fig. 4) [17], the ratio R_{tail} of the integrated charge in the 25 ns to 150 ns time window (tail) to the total collected charge in the first 150 ns time span (Eq. 3 also shown in **(c)** of Fig. 4) [18], the charge-weighted mean time MT of pulses within first 25 ns and 150 ns (Eq. 4 also shown in **(d)** and **(e)** of Fig. 4) [19], the variance of the charge-weighted mean time MV (Eq. 5 also shown in **(f)** and **(g)** of Fig. 4) [20], the likelihood ratio parameter LR using PS and LS waveform templates in first 150 ns (Eq. 6 also shown in **(h)** of Fig. 4) [17], and the total charge QC (Eq. 7 also shown in **(i)** of Fig. 4). The LS waveform with diagrams for understanding these variables is shown in Fig. 3. The definitions of each variable used in the PSD algorithms are following,

$$\text{Charge Asymmetry} = (Q_1 - Q_2)/(Q_1 + Q_2) \quad (1)$$

$$R_{\text{head}} = \frac{\sum_{10 \text{ ns}}^{30 \text{ ns}} q_i}{\sum_{0 \text{ ns}}^{150 \text{ ns}} q_i} \quad (2)$$

$$R_{\text{tail}} = \frac{\sum_{25 \text{ ns}}^{150 \text{ ns}} q_i}{\sum_{0 \text{ ns}}^{150 \text{ ns}} q_i} \quad (3)$$

$$MTL = \frac{\sum_{0 \text{ ns}}^{25 \text{ ns}} q_i t_i}{\sum_{0 \text{ ns}}^{25 \text{ ns}} q_i} \quad \text{and} \quad MT = \frac{\sum_{0 \text{ ns}}^{150 \text{ ns}} q_i t_i}{\sum_{0 \text{ ns}}^{150 \text{ ns}} q_i} \quad (4)$$

$$MVL = \frac{\sum_{0 \text{ ns}}^{25 \text{ ns}} q_i t_i^2}{\sum_{0 \text{ ns}}^{25 \text{ ns}} q_i} - MTL^2 \quad \text{and} \quad MV = \frac{\sum_{0 \text{ ns}}^{150 \text{ ns}} q_i t_i^2}{\sum_{0 \text{ ns}}^{150 \text{ ns}} q_i} - MT^2 \quad (5)$$

$$LR = \ln L_{ps} - \ln L_{ls}, \quad \text{where} \quad L_{ps(ls)} = \sum_{0 \text{ ns}}^{150 \text{ ns}} (T_i - W_i + W_i \ln \frac{W_i}{T_i}) \quad (6)$$

$$QC = \sum_{0 \text{ ns}}^{150 \text{ ns}} q_i, \quad (7)$$

where $Q_{1,2}$ indicates individual PMT integrated charges, and q_i and t_i are waveform amplitudes and times for each 2 ns bin, respectively. T_i and W_i are the heights of the i^{th} time bin in the template and the data waveform, respectively. With the exception of the Charge Asymmetry and QC parameters, an average value is used for the calculations of all other

parameters, considering both PMTs.

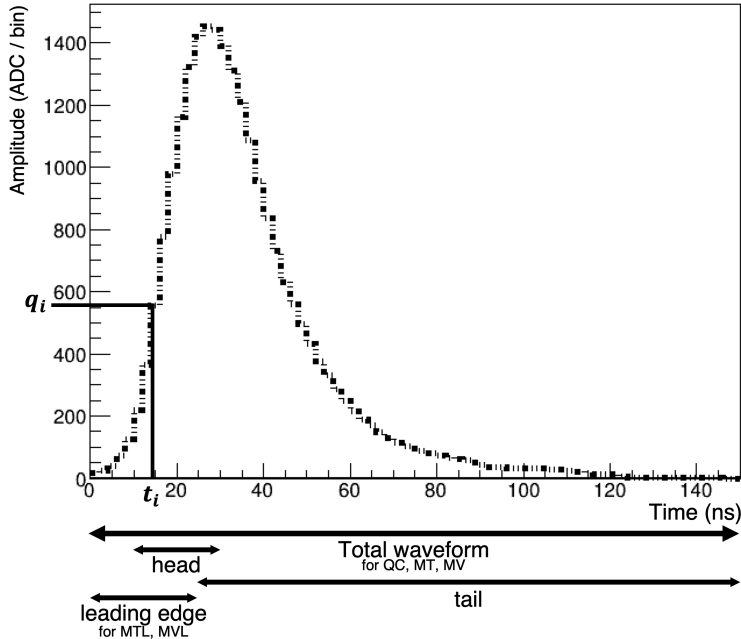


FIG. 3: Variable calculation methods for a waveform. An example LS waveform and the diagram for representing the parameters and the time range of the variables are displayed.

The LR parameter is derived through the use of templates for each scintillator shown in Fig. 2. After obtaining the normalized waveform for a single event, the heights of the normalized waveform and the corresponding template for each time bin are incorporated into the Poisson-based likelihood ($L_{ps(ls)}$ in Eq. 6). The template preferences for each scintillator are established, and the difference between them is employed as the LR variable. For example, in the case of an LS candidate event normalized to have the same area as the templates in Fig. 2, closely resembling the LS template, the LR value is situated within the LS region, notably distant from the plastic scintillator (PS) region (plot **(h)** of Fig. 4).

III. RESULTS WITH THE BOOSTED DECISION TREE ALGORITHM

Boosted Decision Trees (BDTs) were trained using above-mentioned eight variables except QC within TMVA packages [21]. BDT is an ensemble learning method that combines the outputs of multiple weak learners (decision trees) to create a stronger, more accurate model. We use a BDT with 850 trees, each with a maximum depth of 3 levels, and Ad-

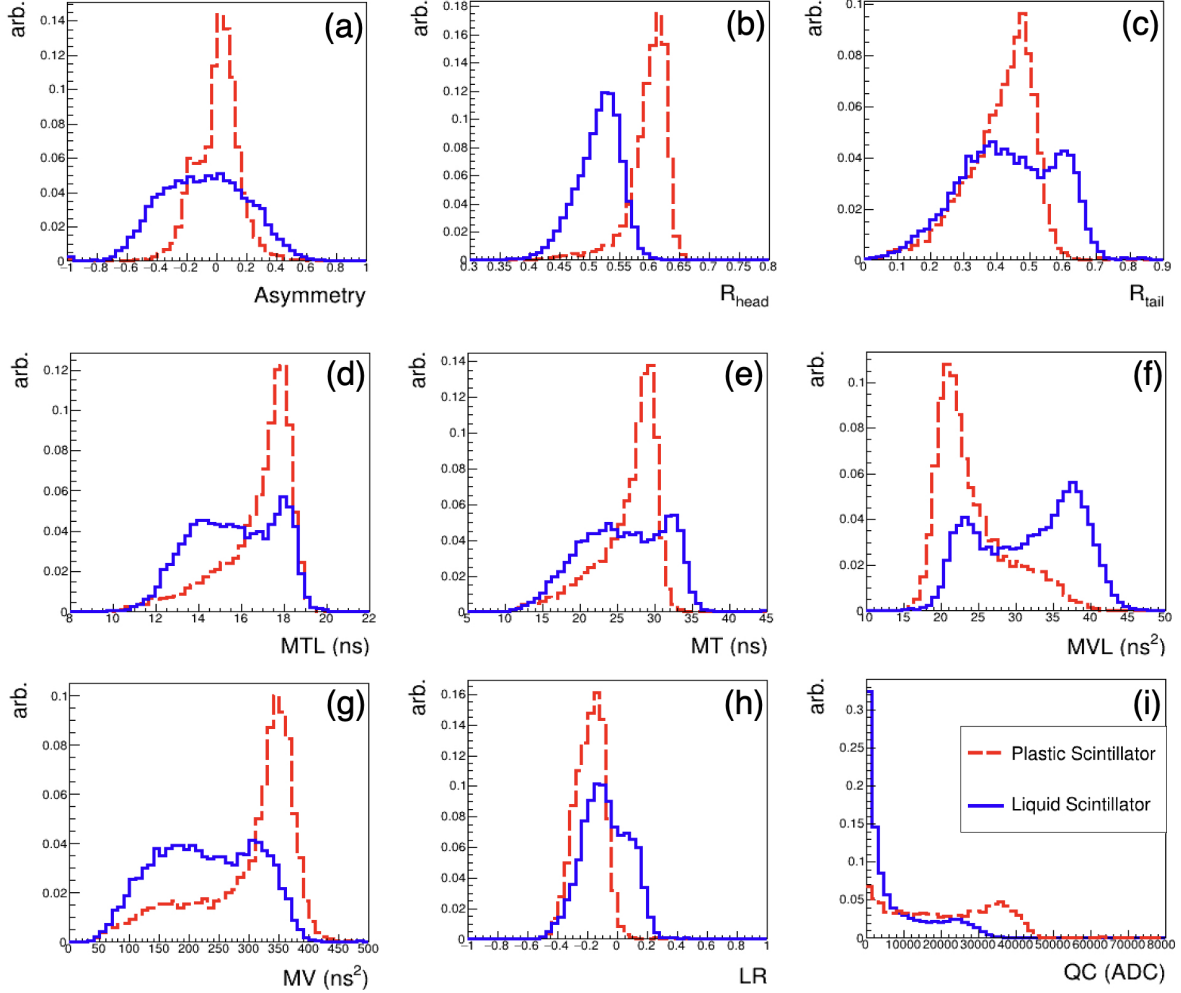


FIG. 4: Discrimination variables. These variables are labeled as **(a)** Asymmetry, **(b)** R_{head} , **(c)** R_{tail} , **(d)** MTL, **(e)** MT, **(f)**, MVL **(g)** MV, **(h)** LR, and **(i)** QC. Please see the text for the variable descriptions.

aBoost [22] with a learning rate of $\beta=0.5$. A constraint on the minimum number of samples for node splitting is set to 2.5% of the total samples. We use a total of 9940 and 9984 events in the BDT input as PS and LS sample, respectively. These samples are further divided in half for training and testing process. The resulting training shows no overtraining when evaluated with the Kolmogorov-Smirnov (KS) test between training and testing sample [23]. The PS sample shows the KS probability value of 9.7% and it is 38.9% for LS. The MVL parameter shows the best performance out of the training. The electron/gammas signal models for each scintillator is obtained from the ^{60}Co calibrations of the separate

measurements. The training shows a clear separation for PS and LS training samples as shown in Fig. 5.

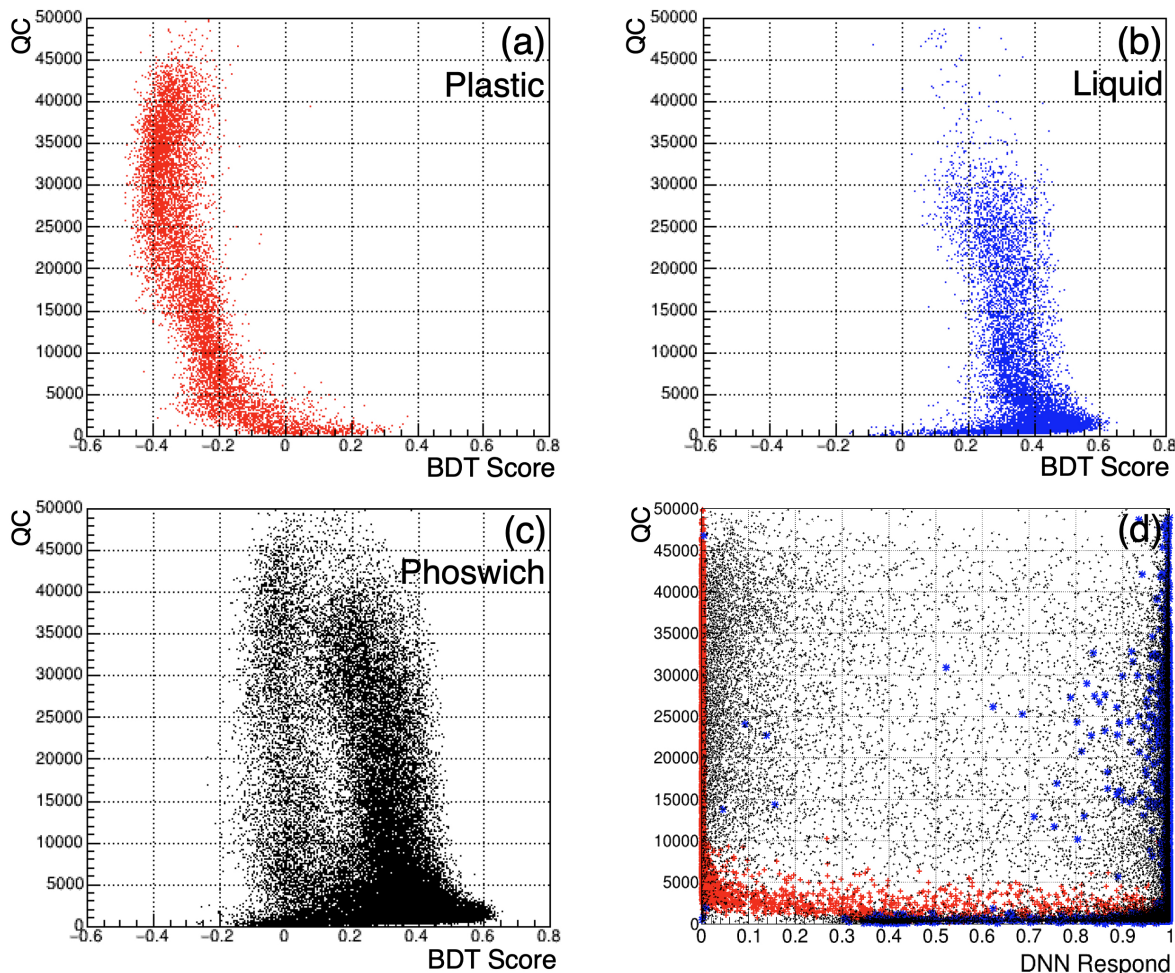


FIG. 5: BDT and DNN result distributions of scintillators. (a) BDT result of the PS training data, (b) BDT result of the LS training data and (c) BDT result of the phoswich detector. (d) represents the DNN results, the red cross for the PS, the blue star for the LS, and the black dot for the phoswich. Please note that the BDT response in the phoswich data is different from the training data especially for the PS part because the light from the phoswich PS part is attenuated more than that of the training setup.

The trained machine is, then, applied to newly acquired ^{60}Co data for the phoswich detector showing the separation between PS and LS originating signals within the phoswich detector. To quantify the discriminating power, we calculated significance of separation

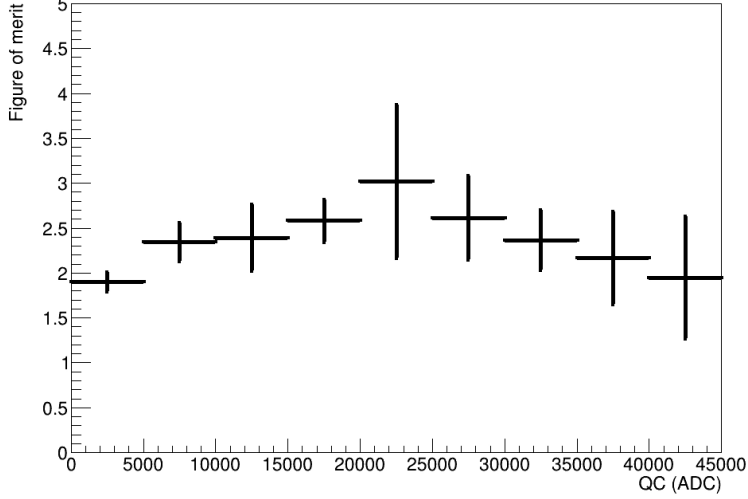


FIG. 6: Figure of merit as a function of QC. The maximum figure of merit is reached at QC between 20,000 ADC and 25,000 ADC. Note that the distribution has a slight charge dependence due to t_0 variations in waveforms.

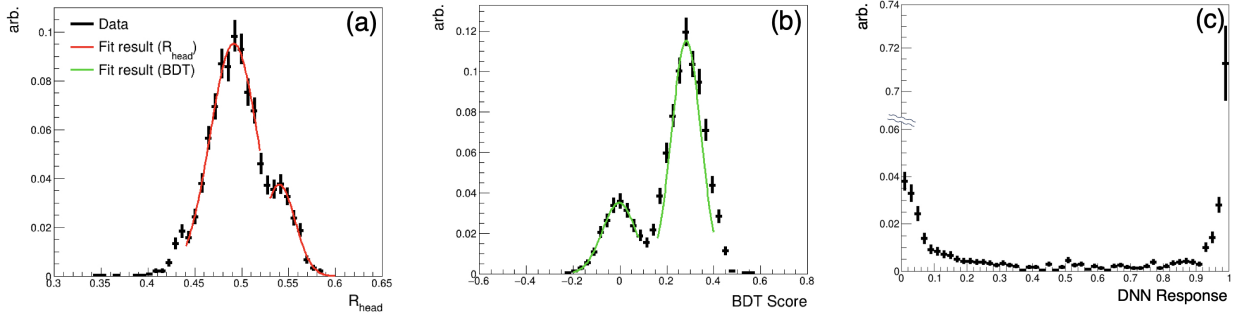


FIG. 7: Distribution of (a) R_{head} , (b) BDT score, and (c) DNN response of the phoswich from 20,000 ADC to 25,000 ADC. For the R_{head} and BDT parameters, Gaussian fit lines are provided on the data points where smaller bumps indicate the PS part of the phoswich data. Note that the middle part of the y-axis of the right plot has been suppressed to increase the readability.

using the figure of merit (FoM) as

$$\text{FoM} = \frac{|\langle m_{\text{LS}} \rangle - \langle m_{\text{PS}} \rangle|}{\sqrt{\sigma_{\text{LS}}^2 + \sigma_{\text{PS}}^2}}, \quad (8)$$

where $\langle m_{\text{LS(PS)}} \rangle$ indicates the means of each distribution and $\sigma_{\text{LS(PS)}}$ for widths obtained from a Gaussian fit respectively for PS and LS after selecting sections of the QC energy proxy. The FoM distribution calculated from Eq. 8 as a function of the total charge (QC)

is shown in Fig. 6.

The best separation power, $\text{FoM}=3.02\pm 0.85$ as a standard deviation is obtained at the QC region between 20,000 ADC and 25,000 ADC which is the LS energy range equivalent between 859 keV and 1036 keV. The power is degraded as the energy is decreased due to small signals having lack of information. By comparing with a single variable FoM using popular PSD parameter R_{head} ($\text{FoM}=1.59$) shown in Fig. 7, BDT based method improves the separation by a factor 1.90. We checked and confirmed that the target volume ratio between PS and LS of 3.38 ± 0.01 matches with the selected event count ratio of 3.41 ± 0.17 . The standard deviation reaches to 1 unit at the threshold of 297 keV below which pulses are not distinguishable with the current method.

We conducted tests using alternative machine learning algorithms on the same PSD data, using identical input parameters to assess algorithmic stability. In Fig. 5 (d), it is evident that the PS-only and LS-only data are well-differentiated towards the extremes (0 or 1) of the Deep Neural Network response. However, the phoswich data displays a distribution where the majority of events are distinctly assigned to either the PS or the LS region, yet some events in between are not effectively separated. Moreover, Fig. 7 (c) indicates that a significant proportion of events are misclassified as LS events, mismatching the target volume ratio. Consequently, the BDT method is more suitable for effectively distinguishing signals from the phoswich.

IV. DISCUSSION

In the phoswich detector, while the pulse shape of the guard LS closely resembles the training dataset, the pulse shape from the inner PS differs from the training data. Consequently, the BDT scores for PS are attenuated in the phoswich setup. This discrepancy arises because the training data for PS is acquired by directly attaching the PMTs to the surface of the PS material before the phoswich assembly, where LS is present between PS and PMT photocathodes. Consequently, scintillation light from PS must traverse through LS, with some photons being either reabsorbed by LS or excessively scattered and reflected within the phoswich, resulting in a loss of the original shape information.

To enhance the separation power, we anticipate that improvements in the light attenuation quality of LS would be beneficial. Therefore, the energy threshold defined at the

moment would be improved. Specifically, refining the light attenuation characteristics of LS could potentially mitigate the impact of signal distortion within the phoswich setup, leading to a more accurate and reliable discrimination of scintillation signals from the inner PS. We have examined the improved LS spectra in resolutions and gains when the nitrogen bubbling is performed to remove oxygen impurities in LS. The method was effective to improve the quality of LS for a short term.

Employing a single-readout phoswich detector, we successfully identify γ radiation signals from two distinct scintillating components. The BDT algorithm demonstrates a discrimination power of 3.02σ between the two scintillators. Our exploration of signal separation using the DNN algorithm indicates that the BDT is better suited for this task. Future efforts will focus on enhancing the detector to have a possible neutron versus γ classification in a phoswich detector.

Conflict of Interest Statement

The authors declare that the research was conducted in the absence of any commercial or financial relationships that could be construed as a potential conflict of interest.

Author Contributions

CHH contributed to the conception and design of the study. YJL, JK, and BCK built the experimental setup with the datataking software tools. YJL organized the data acquisition and performed the statistical analysis. YSY provided the calibration facility. YJL and CHH wrote the first draft of the manuscript. All authors contributed to manuscript revision, read, and approved the submitted version.

Funding

This research was supported by the Chung-Ang University Research Grants in 2022 and by the National Research Foundation of Korea (NRF) grant funded by the Korean government (MSIT) (No. 2021R1A2C1013761).

Data Availability Statement

The datasets analyzed for this study can be provided with a reasonable request to the corresponding authors.

- [1] Beaulieu L, Beddar S. Review of plastic and liquid scintillation dosimetry for photon, electron, and proton therapy. *Physics in Medicine & Biology* **61** (2016) R305.
- [2] Nattress J, Jovanovic I. Response and calibration of organic scintillators for gamma-ray spectroscopy up to 15-mev range. *Nuclear Instruments and Methods in Physics Research Section A: Accelerators, Spectrometers, Detectors and Associated Equipment* **871** (2017) 1.
- [3] Kharzheev YN. Scintillation counters in modern high-energy physics experiments (review). *Physics of Particles and Nuclei* **46** (2015) 678.
- [4] Birks JB. *The Theory and Practice of Scintillation Counting* (Pergamon Press, London) (1964).
- [5] Knoll GF. *Radiation detection and measurement* (John Wiley and Sons, New York) (2010).
- [6] Shirai J, for the KamLAND Zen Collaboration. Results and future plans for the kamland-zen experiment. *Journal of Physics: Conference Series* **888** (2017) 012031.
- [7] Ianni A. Neutrino physics with borexino. *Progress in Particle and Nuclear Physics* **66** (2011) 405. Particle and Nuclear Astrophysics.
- [8] Ashenfelter J, et al. The PROSPECT Reactor Antineutrino Experiment. *Nuclear Instruments and Methods in Physics Research Section A: Accelerators, Spectrometers, Detectors and Associated Equipment* **922** (2019) 287.
- [9] Abreu Y, Amhis Y, Arnold L, Barber G, Beaumont W, Binet S, et al. Solid: a short baseline reactor neutrino experiment. *Journal of Instrumentation* **16** (2021) P02025.
- [10] Wilkinson DH. The phoswich—a multiple phosphor. *Review of Scientific Instruments* **23** (1952) 414.
- [11] Wen L, Cao J, Wang Y. Reactor neutrino experiments: Present and future. *Annual Review of Nuclear and Particle Science* **67** (2017) 183.
- [12] Adhikari G, et al. Initial Performance of the COSINE-100 Experiment. *European Physical Journal C* **78** (2018) 107.

- [13] Adhikari G, et al. The COSINE-100 Data Acquisition System. *Journal of Instrumentation* **13** (2018) P09006.
- [14] Brun R, Rademakers F. ROOT - An Object Oriented Data Analysis Framework. *Nuclear Instruments and Methods in Physics Research Section A: Accelerators, Spectrometers, Detectors and Associated Equipment* **389** (1997) 81.
- [15] Eljen Technology, *GENERAL PURPOSE EJ-200, EJ-204, EJ-208, EJ-212* (2023).
- [16] Zhong WL, Li ZH, Yang CG, Cao J. Measurement of decay time of liquid scintillator. *Nuclear Instruments and Methods in Physics Research Section A: Accelerators, Spectrometers, Detectors and Associated Equipment* **587** (2008) 300.
- [17] Adhikari G, de Souza EB, Carlin N, Choi J, Choi S, Djamel M, et al. Lowering the energy threshold in cosine-100 dark matter searches. *Astroparticle Physics* **130** (2021) 102581.
- [18] Ko YJ, Jang CH, Siyeon K, Kim JY, Kim HS, Seo KM, et al. Comparison of fast neutron rates for the neos experiment. *Journal of the Korean Physical Society* **69** (2016) 1651.
- [19] Gerbier G, Mallet J, Mosca L, Tao C, Chambon B, Chazal V, et al. Pulse shape discrimination with NaI(Tl) and results from a WIMP search at the Laboratoire Souterrain de Modane. *Astroparticle Physics* **11** (1999) 287.
- [20] Adhikari G. *Dark Matter Search with NaI(Tl) crystal and lowering the analysis threshold for COSINE-100 experiment*. Ph.D. thesis, The Graduate School Sejong University (2020).
- [21] Speckmayer P, Hocker A, Stelzer J, Voss H. The toolkit for multivariate data analysis, TMVA 4. *Journal of Physics: Conference Series* **219** (2010) 032057.
- [22] Schapire RE. Explaining adaboost. *Empirical inference* (Springer) (2013), 37.
- [23] Massey FJ. The kolmogorov-smirnov test for goodness of fit. *Journal of the American Statistical Association* **46** (1951) 68.
- [24] Eljen Technology EJ-200
- [25] EJ-550 is used

Complete NLO corrections to top-quark pair production with isolated photons

Daniel Stremmer and Malgorzata Worek

*Institute for Theoretical Particle Physics and Cosmology, RWTH Aachen University,
D-52056 Aachen, Germany*

E-mail: daniel.stremmer@rwth-aachen.de, worek@physik.rwth-aachen.de

ABSTRACT: We compute for the first time the so-called complete NLO corrections to top-quark pair production with one and two isolated photons in the di-lepton top-quark decay channel. The Narrow Width Approximation is used for the modeling of unstable top quarks and W bosons. Higher-order QCD and EW effects as well as photon bremsstrahlung are consistently included at all stages: in production and top-quark decays. We present results at the integrated and differential fiducial cross-section level for both processes for the LHC Run II center-of-mass energy of $\sqrt{s} = 13$ TeV. In addition, we investigate the scale choice in photonic observables. Finally, the individual size of each subleading contribution is discussed in detail and the origin of the main subleading corrections is scrutinised. For the latter case, alternative calculations are performed in which the subleading NLO corrections are included only in the production of $t\bar{t}\gamma$ and $t\bar{t}\gamma\gamma$.

KEYWORDS: Higher-Order Perturbative Calculations, Top Quark, Specific QCD Phenomenology

TTK-24-06, P3H-24-005

Contents

1	Introduction	1
2	Definition of the leading and subleading contributions	4
2.1	LO contributions	4
2.2	NLO contributions	6
3	Computational framework	10
3.1	Real corrections	11
3.2	Virtual corrections	14
4	LHC Setup for numerical predictions	16
5	Top-quark pair production with one isolated photon	18
5.1	Integrated fiducial cross sections	18
5.2	Differential fiducial cross sections	20
6	Top-quark pair production with two isolated photons	24
6.1	Integrated fiducial cross sections	24
6.2	Differential fiducial cross sections	25
7	Summary	28

1 Introduction

Of all the associated production of a top-quark pair with one electroweak gauge boson ($pp \rightarrow t\bar{t}V$, $V = Z, W^\pm, \gamma$) at the LHC, the $pp \rightarrow t\bar{t}\gamma$ process has the largest cross section [1, 2] and is the most interesting to model. First of all, already at the lowest order in the perturbative expansion, the $pp \rightarrow t\bar{t}\gamma$ process requires various cuts to keep the prompt photon well isolated and render the whole process infrared (IR) finite, even in the presence of stable top quarks. Secondly, due to its massless nature, the photon can be emitted from all stages of the process, i.e. in the production of $t\bar{t}$ and top-quark decays. In the latter case, prompt photons can originate not only from top quarks, but also from their decay products, including the bottom quarks, W^\pm gauge bosons and charged leptons. In addition, they can be radiated from incoming partons. It is a well-known fact that a large fraction of isolated photons comes from radiative decays of top quarks [3, 4]. With fairly inclusive cuts applied on the finale states, that are currently used in measurements of inclusive and differential cross sections of $t\bar{t}\gamma$ production, the contribution of photons at the decay stage reaches almost 50%. Consequently, proper modeling of $pp \rightarrow t\bar{t}\gamma$ is very challenging. The $pp \rightarrow t\bar{t}\gamma$ process probes the $t - \gamma$ electroweak coupling and provides a direct way to measure the top quark electric charge [5]. The latter is known to be consistent with the Standard Model (SM), although it was measured only indirectly in the production of $t\bar{t}$ [6, 7]. Precise measurements of the $t - \gamma$ coupling at the LHC serve as an additional test of the SM. However, any deviations from the SM prediction, for example in the p_T spectrum of the photon, could point to new physics through anomalous dipole moments of the top quark [8–12]. In addition,

the $pp \rightarrow t\bar{t}\gamma$ process plays an important role in studies of the top-quark charge asymmetry (A_C^t) [13–16]. Indeed, it provides complementary information to the measured asymmetries in $t\bar{t}$ production, where A_C^t appears for the first time at next-to-leading order (NLO) only. Contrary, for the $pp \rightarrow t\bar{t}\gamma$ process this asymmetry is present already at LO in quark-induced subprocesses due to the interference effects between Feynman diagrams in which the photon is emitted from quarks in the initial state and diagrams in which it is emitted from quarks in the final state. The overall asymmetry in the $pp \rightarrow t\bar{t}\gamma$ process at the LHC with $\sqrt{s} = 13$ TeV has a negative value and is of the order of 1%–2% depending on the fiducial phase-space regions that are scrutinised [15, 16]. However, A_C^t can be modified by beyond the SM (BSM) physics. Indeed, substantial deviations from the SM prediction can be expected in the case of BSM models with a light colour octet [17–20] or an additional Z' [21]. In both BSM cases, the absolute value of A_C^t is predicted to be much smaller [13].

In the case of the $pp \rightarrow t\bar{t}\gamma\gamma$ process, the situation is only somewhat similar to the case of $t\bar{t}\gamma$. Among all the associated production of a top-quark pair with two gauge vector bosons, i.e. $t\bar{t}W^+W^-$, $t\bar{t}ZZ$, $t\bar{t}\gamma\gamma$, $t\bar{t}W^\pm\gamma$, $t\bar{t}W^\pm Z$ and $t\bar{t}Z\gamma$, the $pp \rightarrow t\bar{t}\gamma\gamma$ process is the second largest [1]. The importance of $pp \rightarrow t\bar{t}\gamma\gamma$ stems from the fact that it is the main (irreducible) background process in SM Higgs-boson studies for the $pp \rightarrow t\bar{t}H$ signal process in the $H \rightarrow \gamma\gamma$ decay channel. However, the similarities to the production of $t\bar{t}\gamma$ are due to the distribution of photons in the $pp \rightarrow t\bar{t}\gamma\gamma$ process and the importance of the contribution, which is not entirely related to the production stage of the process. The effect of photon bremsstrahlung in the $pp \rightarrow t\bar{t}\gamma\gamma$ process has recently been studied in detail [22]. It has been shown that the so-called mixed contribution, in which two photons occur simultaneously in the production and decay of the $t\bar{t}$ pair, is the dominant contribution at the integrated and differential fiducial cross-section level.

Evidence for the production of a top-quark pair in association with an isolated photon has already been reported in $p\bar{p}$ collisions at the Tevatron collider at $\sqrt{s} = 1.96$ TeV by the CDF Collaboration [23]. The production of $t\bar{t}\gamma$ final states has been observed for the first time at the LHC at $\sqrt{s} = 7$ TeV by the ATLAS Collaboration [24]. To date, both ATLAS and CMS have observed the production of $t\bar{t}\gamma$ at the LHC at $\sqrt{s} = 8$ TeV and $\sqrt{s} = 13$ TeV [25–30], respectively. So far, no significant deviations from the SM predictions have been found, even though the measured cross sections are larger than theoretical predictions. In addition, within the current and still rather large uncertainties also, the analysed differential cross-section distributions have been fairly well described by the NLO theory predictions. The measurements in the $pp \rightarrow t\bar{t}\gamma$ process have also been interpreted in the framework of the standard model effective field theory, where rather stringent limits on the two relevant Wilson coefficients have been found. Furthermore, the measurement of the top-quark charge asymmetry in $pp \rightarrow t\bar{t}\gamma$ has recently been performed by the ATLAS collaboration [31]. Also in this case the measurement is compatible with the SM predictions within the present uncertainties. However, in all these cases, current precision is still limited, mainly due to statistical and various systematic uncertainties, leaving room for potential future improvements. Finally, the $pp \rightarrow t\bar{t}\gamma\gamma$ process has not yet been experimentally observed at the LHC.

On the theory side, NLO QCD corrections to the $pp \rightarrow t\bar{t}\gamma$ production process with stable top quarks have been calculated over ten years ago [32, 33] and calculated afresh in Ref. [1]. The results with NLO electroweak (EW) corrections have also been delivered later [34]. The results presented there have shown that for differential cross-section distributions the NLO EW corrections are significant in the high energy region due to the EW Sudakov effect. Recently, the so-called complete NLO predictions for $pp \rightarrow t\bar{t}\gamma$ have been calculated [16], again for stable top quarks only. In addition to the NLO QCD and EW corrections at $\mathcal{O}(\alpha_s^3\alpha)$ and $\mathcal{O}(\alpha_s^2\alpha^2)$ respectively, various subleading contributions, along

with their higher-order effects, have been taken into account to form the complete NLO result. In detail, the set of all the possible contributions at $\mathcal{O}(\alpha_s^2\alpha)$, $\mathcal{O}(\alpha_s\alpha^2)$ and $\mathcal{O}(\alpha_s^0\alpha^3)$ at LO, where the middle one results from the interference of the other two results at the amplitude level and from the photon initiated partonic process $g\gamma \rightarrow t\bar{t}\gamma$, as well as at $\mathcal{O}(\alpha_s^3\alpha)$, $\mathcal{O}(\alpha_s^2\alpha^2)$, $\mathcal{O}(\alpha_s\alpha^3)$ and $\mathcal{O}(\alpha_s^0\alpha^4)$ at NLO is what is denoted as the complete NLO result. Finally, the approximate NNLO cross section, with second-order soft-gluon corrections added to the NLO result including QCD and EW corrections, has been calculated in Ref. [35]. On top of the stable top-quark approximation, various predictions that take into account top-quark decays are available in the literature. First, NLO QCD theoretical predictions for $t\bar{t}\gamma$ have been matched with the PYTHIA parton shower program [36]. In this approach top-quark decays have been treated in the parton-shower approximation omitting $t\bar{t}$ spin correlations and photon emission in the parton-shower evolution. More realistic predictions at NLO in QCD have been presented in Ref. [3]. In this case, top-quark decays in the Narrow Width Approximation (NWA) have been included, maintaining $t\bar{t}$ spin correlations in the top-quark decay products. In addition, photon radiation off charged top-quark decay products has been incorporated. A complete description of the $pp \rightarrow t\bar{t}\gamma$ process in the di-lepton top-quark decay channel at NLO in QCD has also been finally provided [37]. This calculation is based on matrix elements for the $e^+\nu_{e\mu}^-\bar{\nu}_\mu b\bar{b}\gamma$ final state including all resonant and non-resonant Feynman diagrams, interferences and off-shell effects of the top quarks and W gauge bosons. Finally, a dedicated comparison between the full off-shell calculation and the results in the NWA has also been carried out [4]. For the $pp \rightarrow t\bar{t}\gamma\gamma$ process the situation is much more simpler. NLO QCD predictions for the process with stable top quarks have already been known for some time and have been further matched to parton shower programs [1, 38–40]. In addition to higher-order QCD effects, NLO EW corrections for $t\bar{t}\gamma\gamma$ have recently been reported [16], but again only for stable top quarks. Finally, very recently NLO QCD corrections in the NWA for the di-lepton and lepton + jet top-quark decay channels have been calculated for the $pp \rightarrow t\bar{t}\gamma\gamma$ process [22].

From the above description, we can quite clearly see a rather diverse picture for $pp \rightarrow t\bar{t}\gamma$ and $pp \rightarrow t\bar{t}\gamma\gamma$. On the one hand, we already have the complete NLO result for $t\bar{t}\gamma$, albeit only for stable top quarks. On the other hand, no such predictions exist for $t\bar{t}\gamma\gamma$. In both cases, the complete NLO result with more realistic final states is still missing. With this article, we want to mitigate the current situation and to calculate for the first time the complete NLO predictions for both $pp \rightarrow t\bar{t}\gamma$ and $pp \rightarrow t\bar{t}\gamma\gamma$ in the di-lepton top-quark decay channel.

The aim of our work is, therefore, manifold. Firstly, we perform a detailed study of the predictions with complete NLO corrections included for $pp \rightarrow t\bar{t}\gamma$ and $pp \rightarrow t\bar{t}\gamma\gamma$ in the di-lepton top-quark decay channel. Secondly, as we calculate these higher order effects within the same framework, while using the same input parameters, we want to examine whether there are common features or significant differences between the theoretical predictions for $pp \rightarrow t\bar{t}\gamma$ and $pp \rightarrow t\bar{t}\gamma\gamma$. Thirdly, we plan to analyse the impact of subleading NLO corrections on integrated and differential fiducial cross sections and systematically study the theoretical uncertainties due to missing higher orders. Finally, we are going to scrutinise the individual size of each subleading contribution and investigate the origin of the main subleading corrections. For this purpose, we perform alternative calculations for both processes in which the subleading NLO corrections are included only in the production of $t\bar{t}\gamma(\gamma)$.

The rest of the paper is organised as follows. All leading and subleading contributions at LO and NLO are carefully defined in Section 2. In Section 3 we describe the framework of the calculations and discuss various changes as well as cross-checks that have been performed. All input parameters and fiducial cuts that have been used to simulate detector response are outlined in Section 4. Numerical results for the integrated and differential cross sections for the $pp \rightarrow t\bar{t}\gamma$ process at the LHC are

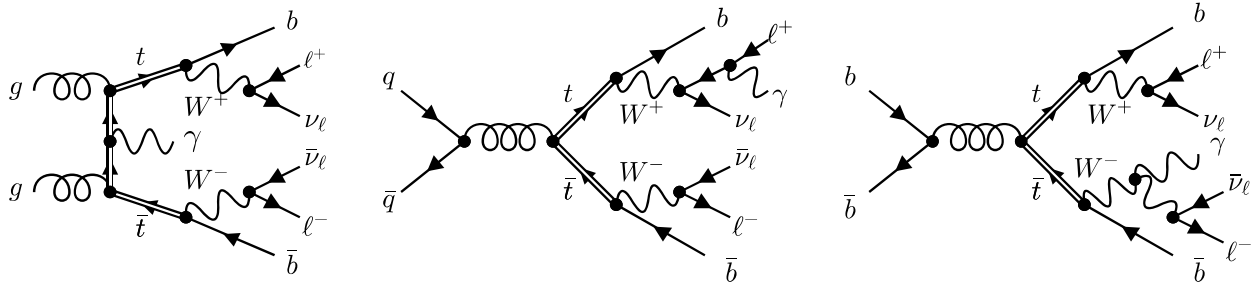


Figure 1. Example Feynman diagrams for $pp \rightarrow t\bar{t}\gamma$ contributing to LO_1 . All Feynman diagrams in this paper were produced with the help of the FEYNGAME program [48].

presented in detail in Section 5. Our results for the $pp \rightarrow t\bar{t}\gamma\gamma$ process, on the other hand, are discussed in Section 6. We summarise our findings in Section 7.

2 Definition of the leading and subleading contributions

We calculate the full set of leading and subleading LO contributions and NLO corrections to top-quark pair production with one and two isolated photons at the LHC. We consistently include photon bremsstrahlung as well as QCD and EW corrections in both the production and decay of the top-quark pair. Decays of unstable top quarks and W gauge bosons are treated in the NWA preserving spin correlations, i.e. in the limit when $\Gamma_t/m_t \rightarrow 0$ ($\Gamma_W/m_W \rightarrow 0$). In this approximation all contributions without two resonant top quarks (and W gauge bosons) are neglected and the Breit-Wigner propagators lead to delta-functions which force the unstable particles to be on-shell, see e.g. Ref. [4, 41–47] for more details. We consider the di-lepton top-quark decay channel leading to the following decay chains

$$\begin{aligned}
 pp &\rightarrow t\bar{t}(\gamma) \rightarrow W^+W^-b\bar{b}(\gamma) \rightarrow \ell^+\nu_\ell\ell^-\bar{\nu}_\ell b\bar{b}\gamma + X, \\
 pp &\rightarrow t\bar{t}(\gamma\gamma) \rightarrow W^+W^-b\bar{b}(\gamma\gamma) \rightarrow \ell^+\nu_\ell\ell^-\bar{\nu}_\ell b\bar{b}\gamma\gamma + X,
 \end{aligned}
 \tag{2.1}$$

with $\ell^\pm = \mu^\pm, e^\pm$ and where the brackets indicate that photon bremsstrahlung is allowed at each stage of the process. For brevity, we refer to these processes as $pp \rightarrow t\bar{t}\gamma$ and $pp \rightarrow t\bar{t}\gamma\gamma$ in the di-lepton top-quark decay channel, respectively. At LO there are in total 5 (15) possibilities or resonance histories from which the photons can be radiated off in the decay chain of $t\bar{t}\gamma(\gamma)$. At NLO, the number of resonance histories increases to 15 (35) for real radiation with an additional photon and to 15 (45) for additional QCD radiation.

2.1 LO contributions

At LO, both processes get contributions from three different orders of α_s and α . The dominant contribution is at the order $\mathcal{O}(\alpha_s^2\alpha^{4+n_\gamma})$, where n_γ is the number of photons appearing in the Born-level process, and we call it LO_1 , following the notation in Ref. [49, 50]. At this order, we encounter the typical QCD production of a top-quark pair, which leads to the following partonic subprocesses

$$\begin{aligned}
 gg &\rightarrow \ell^+\nu_\ell\ell^-\bar{\nu}_\ell b\bar{b}\gamma(\gamma), \\
 q\bar{q}/\bar{q}q &\rightarrow \ell^+\nu_\ell\ell^-\bar{\nu}_\ell b\bar{b}\gamma(\gamma), \quad b\bar{b}/\bar{b}b \rightarrow \ell^+\nu_\ell\ell^-\bar{\nu}_\ell b\bar{b}\gamma(\gamma),
 \end{aligned}
 \tag{2.2}$$

with $q = u, d, c, s$. Example Feynman diagrams for the LO_1 contribution are shown in Figure 1. We work in the five-flavour scheme and consistently include in the initial state all PDF suppressed channels

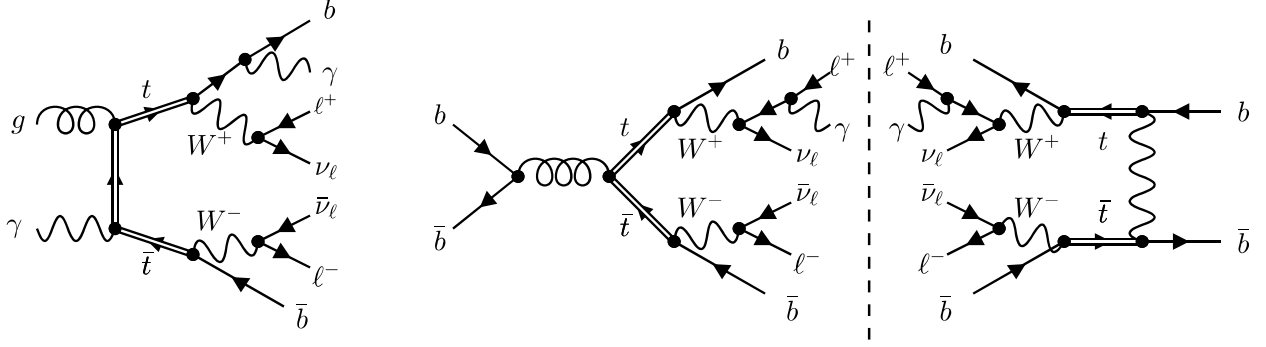


Figure 2. Example Feynman diagrams for $pp \rightarrow t\bar{t}\gamma$ contributing to LO_2 .

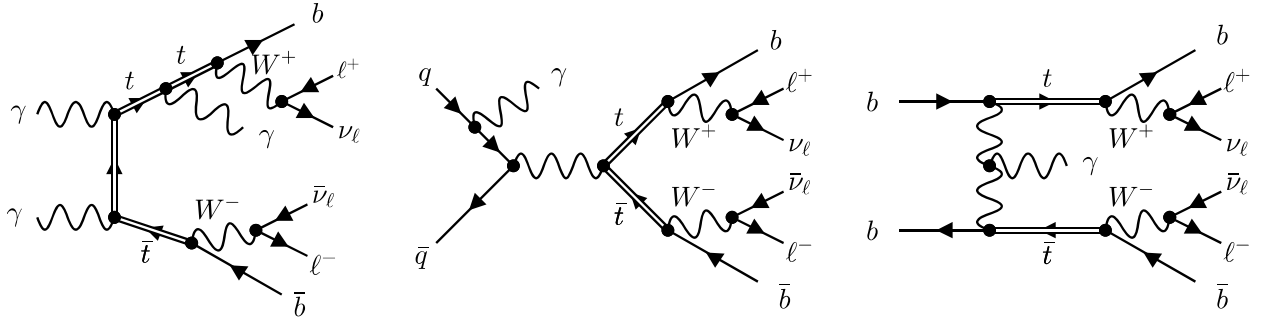


Figure 3. Example Feynman diagrams for $pp \rightarrow t\bar{t}\gamma$ contributing to LO_3 .

from bottom quarks as well as photons in all subleading contributions. The LO_1 contribution can be obtained from the square of matrix elements at the order $\mathcal{O}(g_s^2 g^{4+n_\gamma})$. The $q\bar{q}$ and $b\bar{b}$ subprocesses provide additional contributions to the amplitudes at the order $\mathcal{O}(g^{\delta+n_\gamma})$. The interference of both types of matrix elements gives rise to the first subleading LO contribution at $\mathcal{O}(\alpha_s^1 \alpha^{5+n_\gamma})$ which we refer to as LO_2 . This interference is exactly zero for the $q\bar{q}$ initial state due to color algebra, but does not vanish for the $b\bar{b}$ subprocess due to additional t -channel Feynman diagrams with an intermediate W boson, as shown on the right in Figure 2. Similar Feynman diagrams do not exist for $q\bar{q}$ because we keep the Cabibbo-Kobayashi-Maskawa (CKM) mixing matrix diagonal. In addition, at this order we encounter for the first time photon-induced channels with the $g\gamma$ initial state, as illustrated on the left in Figure 2. Thus, the partonic subprocesses of LO_2 can be summarised as

$$g\gamma/\gamma g \rightarrow \ell^+ \nu_\ell \ell^- \bar{\nu}_\ell b\bar{b} \gamma(\gamma), \quad b\bar{b}/b b \rightarrow \ell^+ \nu_\ell \ell^- \bar{\nu}_\ell b\bar{b} \gamma(\gamma). \quad (2.3)$$

The third and last subleading LO contribution, LO_3 , is the purely EW induced production of a top-quark pair at the order $\mathcal{O}(\alpha^{6+n_\gamma})$. Example diagrams are depicted in Figure 3. Again, only the $q\bar{q}$ and $b\bar{b}$ channels are present, as well as the highly suppressed $\gamma\gamma$ channel. Therefore, the following reactions must be taken into account for LO_3

$$\begin{aligned} \gamma\gamma &\rightarrow \ell^+ \nu_\ell \ell^- \bar{\nu}_\ell b\bar{b} \gamma(\gamma), \\ q\bar{q}/\bar{q}q &\rightarrow \ell^+ \nu_\ell \ell^- \bar{\nu}_\ell b\bar{b} \gamma(\gamma), \quad b\bar{b}/\bar{b}b \rightarrow \ell^+ \nu_\ell \ell^- \bar{\nu}_\ell b\bar{b} \gamma(\gamma). \end{aligned} \quad (2.4)$$

With respect to LO_1 , this contribution is not only suppressed by the power coupling, but also the gluon PDF does not enter this contribution at all. Finally, we denote as LO the the sum of all three LO contributions

$$\text{LO} = \text{LO}_1 + \text{LO}_2 + \text{LO}_3. \quad (2.5)$$

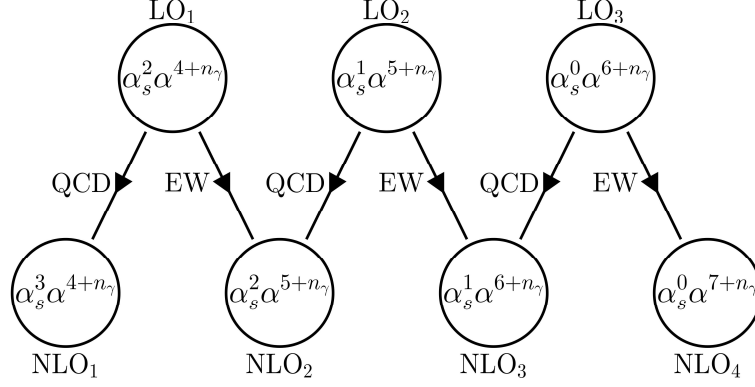


Figure 4. LO and NLO contributions for $pp \rightarrow t\bar{t}\gamma(\gamma)$ with $n_\gamma = 1(2)$.

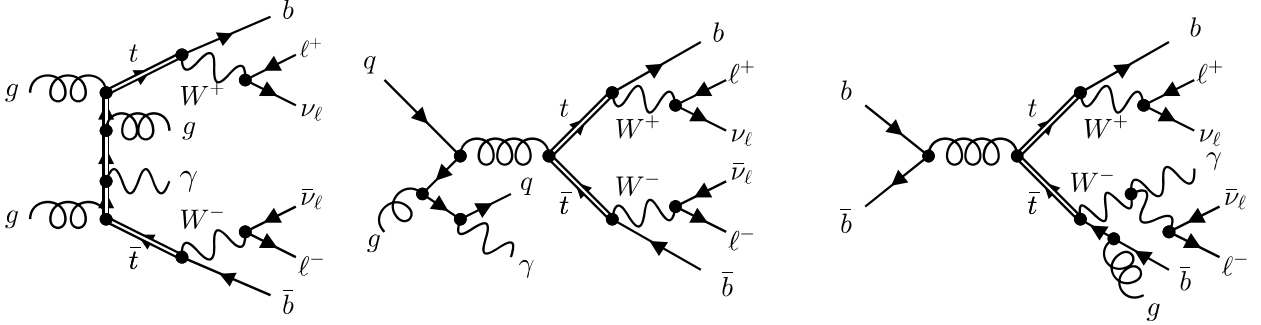


Figure 5. Example Feynman diagrams for $pp \rightarrow t\bar{t}\gamma$ contributing to NLO₁.

2.2 NLO contributions

At NLO, we obtain corrections of QCD and/or EW nature to all LO contributions, as demonstrated in Figure 4. The dominant higher-order corrections at NLO, denoted as NLO₁, arise from the QCD corrections to LO₁ at order $\mathcal{O}(\alpha_s^3 \alpha^{4+n_\gamma})$. We call the sum of the two NLO_{QCD} with

$$\text{NLO}_{\text{QCD}} = \text{LO}_1 + \text{NLO}_1, \quad (2.6)$$

and use it as a starting point to quantify the size of all subleading LO and NLO contributions. While the partonic subprocesses for the virtual corrections in NLO₁ are identical to those of LO₁, for the real emission part additional reactions due to extra QCD radiation have to be taken into account. In particular, all partonic subprocesses can be obtained by adding an additional gluon and all possible crossings of partons, leading to

$$\begin{aligned} gg &\rightarrow \ell^+ \nu_\ell \ell^- \bar{\nu}_\ell b\bar{b} \gamma(\gamma) g, \\ q\bar{q}/\bar{q}q &\rightarrow \ell^+ \nu_\ell \ell^- \bar{\nu}_\ell b\bar{b} \gamma(\gamma) g, & b\bar{b}/\bar{b}b &\rightarrow \ell^+ \nu_\ell \ell^- \bar{\nu}_\ell b\bar{b} \gamma(\gamma) g, \\ gq/qg &\rightarrow \ell^+ \nu_\ell \ell^- \bar{\nu}_\ell b\bar{b} \gamma(\gamma) q, & g\bar{q}/\bar{q}g &\rightarrow \ell^+ \nu_\ell \ell^- \bar{\nu}_\ell b\bar{b} \gamma(\gamma) \bar{q}, \\ gb/bg &\rightarrow \ell^+ \nu_\ell \ell^- \bar{\nu}_\ell b\bar{b} \gamma(\gamma) b, & g\bar{b}/\bar{b}g &\rightarrow \ell^+ \nu_\ell \ell^- \bar{\nu}_\ell b\bar{b} \gamma(\gamma) \bar{b}. \end{aligned} \quad (2.7)$$

Example Feynman diagrams for the real emission part of NLO₁ are shown in Figure 5. The real corrections also consistently include additional photon and gluon radiation in all stages, i.e. in the $t\bar{t}$ production and the decays of top quarks and W gauge bosons.

The next contribution, NLO₂, at the order $\mathcal{O}(\alpha_s^2 \alpha^{5+n_\gamma})$, cannot be completely separated into parts with only QCD or EW corrections. When calculating the corresponding virtual corrections we

have on the one hand, the interference of tree-level diagrams at $\mathcal{O}(g^{6+n_\gamma})$ with one-loop diagrams at $\mathcal{O}(g_s^4 g^{4+n_\gamma})$ and on the other hand, the interference between tree-level diagrams at $\mathcal{O}(g_s^2 g^{4+n_\gamma})$ and one-loop diagrams at $\mathcal{O}(g_s^2 g^{6+n_\gamma})$. The first contribution can be seen as a part of the NLO QCD corrections to LO₂. For the second contribution, no clear distinction is possible, since it can be seen as either the NLO QCD corrections to LO₂ or the NLO EW corrections to LO₁. Finally, for the $g\gamma$ channel, we have the interference of tree-level diagrams at $\mathcal{O}(g_s^1 g^{5+n_\gamma})$ with one-loop diagrams at $\mathcal{O}(g_s^3 g^{5+n_\gamma})$. Compared to NLO₁, the real corrections in NLO₂ include more partonic subprocesses, involving QCD and QED-like singularities. The first set of real corrections is obtained by additional QCD radiation to LO₂, which leads to

$$\begin{aligned}
q\bar{q}/\bar{q}q &\rightarrow \ell^+ \nu_\ell \ell^- \bar{\nu}_\ell b\bar{b} \gamma(\gamma) g, & b\bar{b}/\bar{b}b &\rightarrow \ell^+ \nu_\ell \ell^- \bar{\nu}_\ell b\bar{b} \gamma(\gamma) g, \\
gq/qg &\rightarrow \ell^+ \nu_\ell \ell^- \bar{\nu}_\ell b\bar{b} \gamma(\gamma) q, & g\bar{q}/\bar{q}g &\rightarrow \ell^+ \nu_\ell \ell^- \bar{\nu}_\ell b\bar{b} \gamma(\gamma) \bar{q}, \\
gb/bg &\rightarrow \ell^+ \nu_\ell \ell^- \bar{\nu}_\ell b\bar{b} \gamma(\gamma) b, & g\bar{b}/\bar{b}g &\rightarrow \ell^+ \nu_\ell \ell^- \bar{\nu}_\ell b\bar{b} \gamma(\gamma) \bar{b}.
\end{aligned} \tag{2.8}$$

In this case, we have the interference of tree-level diagrams at order $\mathcal{O}(g_s^3 g^{4+n_\gamma})$ and $\mathcal{O}(g_s^1 g^{6+n_\gamma})$. Although the $q\bar{q}$ channel is exactly zero in LO₂, its NLO QCD corrections no longer vanish, and the corresponding virtual and real corrections must be taken properly into account. In particular, the interference of initial- and final-state gluon radiation gives rise to the non-vanishing contribution, as explained in Refs. [51, 52]. The latter contribution induces singularities that are of soft nature only. Consequently, there are no collinear singularities in the $q\bar{q}$ channel and gluon radiation still vanishes in top-quark decays. It also follows that the gq and $g\bar{q}$ channels contain no collinear singularities and turn out to be IR finite. Therefore, no dipole subtraction is required for these channels and the naive usage of it can even affect the efficiency of the phase-space integration. In the Nagy-Soper [53] subtraction scheme, which is used in our calculation, the corresponding collinear subtraction terms vanish by construction if the underlying Born-level matrix element is exactly zero, since they are directly proportional to it. This is, however, not a general feature of dipole subtraction schemes. For example, in the Catani-Seymour subtraction scheme [54, 55], the corresponding subtraction term is a sum of the dipole terms \mathcal{D}_k^{ai} involving color-correlated matrix elements. These dipole terms and the momentum mapping to the underlying Born-level process depend on the spectator parton k . Therefore, the sum of the dipole terms vanishes only in the exact collinear limit, where the dependence on the spectator parton k vanishes and the sum becomes proportional to the Born-level matrix element. In principle, it is possible for such initial-state singularities to choose exactly one spectator parton and to substitute the color correlator $\mathbf{T}_k \cdot \mathbf{T}_{ai} \rightarrow -\mathbf{T}_{ai}^2$ in \mathcal{D}_k^{ai} . In this way the corresponding subtraction term is always proportional to the Born-level matrix element and would vanish as in the Nagy-Soper case. On the other hand, collinear singularities are present in the bottom-quark induced channels. In this case, gluon radiation in top-quark decays must be consistently included. Furthermore, additional partonic subprocesses, which originate from LO₁ with additional photon radiation, have to be included, leading to

$$\begin{aligned}
gg &\rightarrow \ell^+ \nu_\ell \ell^- \bar{\nu}_\ell b\bar{b} \gamma\gamma(\gamma), \\
q\bar{q}/\bar{q}q &\rightarrow \ell^+ \nu_\ell \ell^- \bar{\nu}_\ell b\bar{b} \gamma\gamma(\gamma), & b\bar{b}/\bar{b}b &\rightarrow \ell^+ \nu_\ell \ell^- \bar{\nu}_\ell b\bar{b} \gamma\gamma(\gamma).
\end{aligned} \tag{2.9}$$

Similar to the calculation of NLO QCD corrections to the $pp \rightarrow t\bar{t}j(j)$ process in the NWA [44, 56], photons can appear simultaneously in the production and decays, as illustrated in Figure 6. Therefore, the relevant dipoles must be consistently included at each stage of the decay chain. Finally, we have new photon-induced partonic subprocesses which are constructed by gluon radiation from the $g\gamma$ channel in LO₂ and by crossing from the processes listed in Eq. (2.9), resulting in

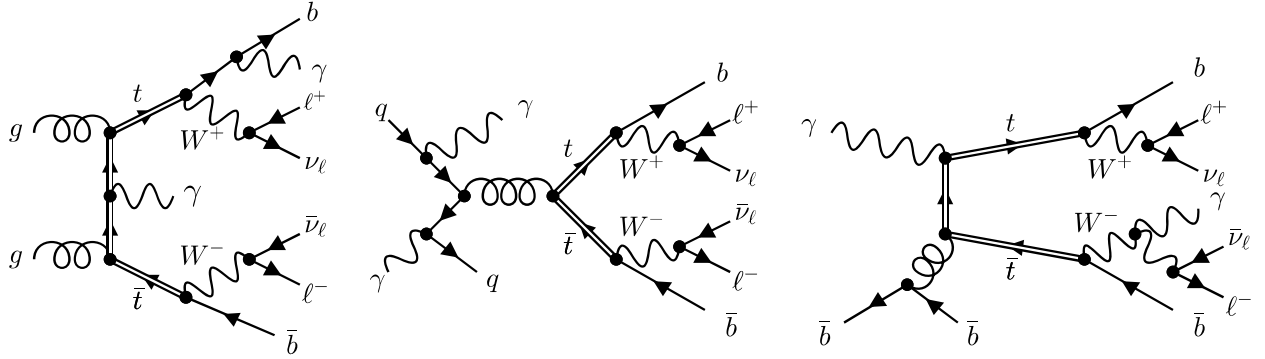


Figure 6. Example Feynman diagrams for $pp \rightarrow t\bar{t}\gamma$ contributing to NLO_2 .

$$\begin{aligned}
& g\gamma/\gamma g \rightarrow \ell^+\nu_\ell\ell^-\bar{\nu}_\ell b\bar{b}\gamma(\gamma)g, \\
& \gamma q/q\gamma \rightarrow \ell^+\nu_\ell\ell^-\bar{\nu}_\ell b\bar{b}\gamma(\gamma)q, \quad \gamma\bar{q}/\bar{q}\gamma \rightarrow \ell^+\nu_\ell\ell^-\bar{\nu}_\ell b\bar{b}\gamma(\gamma)\bar{q}, \\
& \gamma b/b\gamma \rightarrow \ell^+\nu_\ell\ell^-\bar{\nu}_\ell b\bar{b}\gamma(\gamma)b, \quad \gamma\bar{b}/\bar{b}\gamma \rightarrow \ell^+\nu_\ell\ell^-\bar{\nu}_\ell b\bar{b}\gamma(\gamma)\bar{b}.
\end{aligned} \tag{2.10}$$

While the $g\gamma$ channel clearly contains only QCD singularities due to gluon radiation, for the remaining partonic processes we simultaneously encounter QCD and QED initial-state singularities arising from the $\gamma \rightarrow q\bar{q}$ and $q \rightarrow gq$ splittings, as shown in Figure 6. This clearly illustrates that even real corrections cannot be divided into those of QCD or EW origin, as we have already seen in the calculation of virtual corrections.

The next subleading NLO contribution at the order $\mathcal{O}(\alpha_s^1\alpha^{6+n_\gamma})$, NLO_3 , features a similarly wide range of virtual and real corrections with respect to NLO_2 . This contribution is obtained from EW corrections to LO_2 and QCD corrections to LO_3 . Thus, EW corrections to the $q\bar{q}$ channel in LO_2 vanish again, since with respect to the Born level the color structure remains unchanged by these corrections. The virtual corrections consist of the interference of tree-level diagrams at $\mathcal{O}(g_s^2g^{4+n_\gamma})$ with the one-loop amplitude at $\mathcal{O}(g^{8+n_\gamma})$ and the tree-level matrix element at $\mathcal{O}(g^{6+n_\gamma})$ with one-loop diagrams at $\mathcal{O}(g_s^2g^{6+n_\gamma})$. The first contribution can be seen as part of the NLO EW corrections to LO_2 , and thus it vanishes for $q\bar{q}$ as explained before, and only has to be included for the $b\bar{b}$ initial state. In the second term again no distinction between QCD and EW corrections is possible for the $q\bar{q}$ and $b\bar{b}$ channels, while for the $\gamma\gamma$ channel this contribution consists of pure QCD corrections to LO_3 . Finally, for $g\gamma$ we have the interference of tree-level diagrams at $\mathcal{O}(g_s^1g^{5+n_\gamma})$ with one-loop diagrams at $\mathcal{O}(g_s^1g^{7+n_\gamma})$. The real corrections can be summarised as follows. First, we have the NLO QCD corrections to LO_3 , which can be obtained by additional gluon radiation, bringing about the following contributions

$$\begin{aligned}
& \gamma\gamma \rightarrow \ell^+\nu_\ell\ell^-\bar{\nu}_\ell b\bar{b}\gamma(\gamma)g, \\
& q\bar{q}/\bar{q}q \rightarrow \ell^+\nu_\ell\ell^-\bar{\nu}_\ell b\bar{b}\gamma(\gamma)g, \quad b\bar{b}/\bar{b}b \rightarrow \ell^+\nu_\ell\ell^-\bar{\nu}_\ell b\bar{b}\gamma(\gamma)g.
\end{aligned} \tag{2.11}$$

The crossing of initial- and final-state partons leads to the additional set of partonic subprocesses

$$\begin{aligned}
& gq/qg \rightarrow \ell^+\nu_\ell\ell^-\bar{\nu}_\ell b\bar{b}\gamma(\gamma)q, \quad g\bar{q}/\bar{q}g \rightarrow \ell^+\nu_\ell\ell^-\bar{\nu}_\ell b\bar{b}\gamma(\gamma)\bar{q}, \\
& gb/bg \rightarrow \ell^+\nu_\ell\ell^-\bar{\nu}_\ell b\bar{b}\gamma(\gamma)b, \quad g\bar{b}/\bar{b}g \rightarrow \ell^+\nu_\ell\ell^-\bar{\nu}_\ell b\bar{b}\gamma(\gamma)\bar{b},
\end{aligned} \tag{2.12}$$

which again contain simultaneously QCD and QED initial-state singularities, as illustrated in Figure 7. Next, we obtain additional contributions from photon radiation off the partonic subprocesses in LO_2 , as exemplified in Figure 7. Together with all possible crossings of partons and photons we obtain

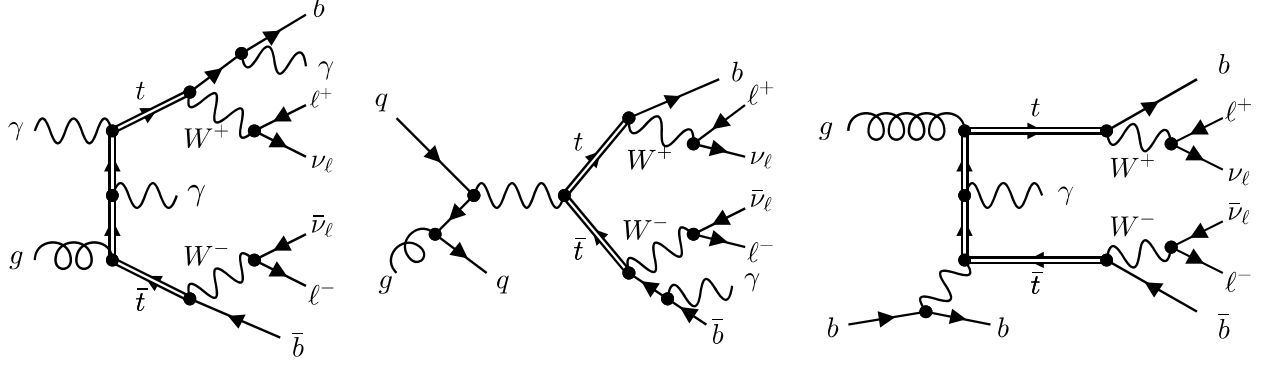


Figure 7. Example Feynman diagrams for $pp \rightarrow t\bar{t}\gamma$ contributing to NLO₃.

$$\begin{aligned}
g\gamma/\gamma g &\rightarrow \ell^+\nu_\ell\ell^-\bar{\nu}_\ell b\bar{b}\gamma\gamma(\gamma) & b\bar{b}/\bar{b}b &\rightarrow \ell^+\nu_\ell\ell^-\bar{\nu}_\ell b\bar{b}\gamma\gamma(\gamma), \\
\gamma b/b\gamma &\rightarrow \ell^+\nu_\ell\ell^-\bar{\nu}_\ell b\bar{b}\gamma(\gamma)b & \gamma\bar{b}/\bar{b}\gamma &\rightarrow \ell^+\nu_\ell\ell^-\bar{\nu}_\ell b\bar{b}\gamma(\gamma)\bar{b}.
\end{aligned}
\tag{2.13}$$

In addition, $q\bar{q}$ and $\gamma q/\gamma\bar{q}$ subprocesses vanish due to color, as additional photon radiation does not change the color structure already present in LO₂.

Since in NLO₃ we find for the first time EW 1-loop corrections in photon-initiated subprocesses, in particular in the $g\gamma$ channel, we briefly mention here the choice of the renormalisation scheme for the electromagnetic coupling α , which will be explained in detail later in the article. As we are interested in the experimental signature with at least one (two) isolated photon(s), we do not consider the $\gamma \rightarrow f\bar{f}$ splitting for final state photons. Therefore, the electromagnetic coupling constant connected with final state photons has to be renormalised in the on-shell scheme to obtain IR finite results, see e.g. Refs. [16, 57]. However, the electromagnetic coupling associated with initial state photons must be renormalised in a $\overline{\text{MS}}$ -like scheme, because $\gamma \rightarrow f\bar{f}$ splittings are included in the evolution of the proton PDF. Thus, we use the G_μ scheme in this case and the remaining IR ϵ poles from the sum of real and virtual corrections are absorbed into a redefinition of PDFs, as for all other QCD and QED collinear initial state singularities. This leads to a collinear factorisation counterterm of the form

$$\frac{\alpha}{2\pi} \frac{1}{\Gamma(1-\epsilon)} \frac{1}{\epsilon} \left(\frac{4\pi\mu_R^2}{\mu_F^2} \right)^\epsilon P_{\gamma\gamma}(x),
\tag{2.14}$$

which has to be convoluted with the corresponding Born-level cross section. The one-loop Altarelli-Parisi QED kernel $P_{\gamma\gamma}(x)$, see e.g. Ref. [50] for more details, is given by

$$P_{\gamma\gamma}(x) = -\frac{2}{3} \delta(1-x) \sum_f N_{c,f} Q_f^2,
\tag{2.15}$$

where the summation runs over all massless, charged fermions, $N_{c,f}$ is a color factor, which is 3 for quarks and 1 for leptons, and Q_f is the charge of the fermion f . Unlike all other QCD and QED splitting functions, $P_{\gamma\gamma}(x)$ contains only a virtual contribution given by the delta distribution.

Finally, we have the NLO EW corrections to LO₃, called NLO₄, and all new partonic subprocesses can simply be obtained from additional photon radiation and crossing, leading to

$$\begin{aligned}
\gamma\gamma &\rightarrow \ell^+\nu_\ell\ell^-\bar{\nu}_\ell b\bar{b}\gamma\gamma(\gamma), \\
q\bar{q}/\bar{q}q &\rightarrow \ell^+\nu_\ell\ell^-\bar{\nu}_\ell b\bar{b}\gamma\gamma(\gamma), & b\bar{b}/\bar{b}b &\rightarrow \ell^+\nu_\ell\ell^-\bar{\nu}_\ell b\bar{b}\gamma\gamma(\gamma), \\
\gamma q/q\gamma &\rightarrow \ell^+\nu_\ell\ell^-\bar{\nu}_\ell b\bar{b}\gamma(\gamma)q, & \gamma\bar{q}/\bar{q}\gamma &\rightarrow \ell^+\nu_\ell\ell^-\bar{\nu}_\ell b\bar{b}\gamma(\gamma)\bar{q}, \\
\gamma b/b\gamma &\rightarrow \ell^+\nu_\ell\ell^-\bar{\nu}_\ell b\bar{b}\gamma(\gamma)b, & \gamma\bar{b}/\bar{b}\gamma &\rightarrow \ell^+\nu_\ell\ell^-\bar{\nu}_\ell b\bar{b}\gamma(\gamma)\bar{b},
\end{aligned}
\tag{2.16}$$

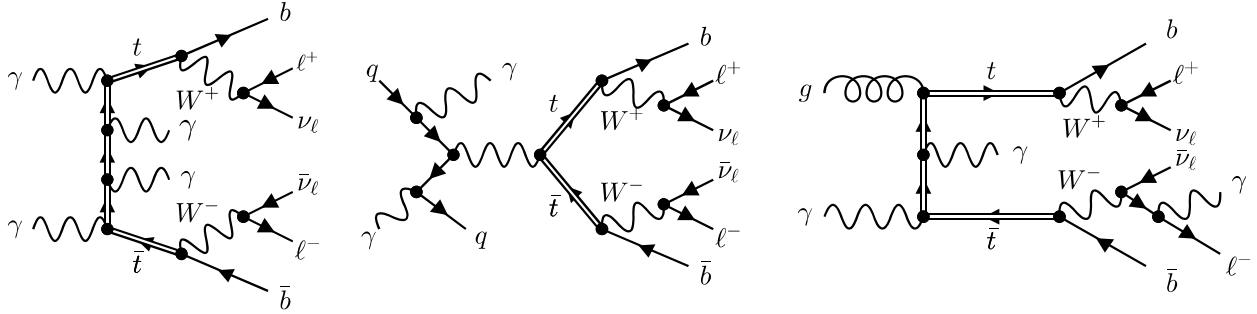


Figure 8. Example Feynman diagrams for $pp \rightarrow t\bar{t}\gamma$ contributing to NLO₄.

where example Feynman diagrams are shown in Figure 8.

We denote the complete result at NLO, including all subleading contributions, as NLO. The latter result is given by the following sum

$$\text{NLO} = \text{LO}_1 + \text{LO}_2 + \text{LO}_3 + \text{NLO}_1 + \text{NLO}_2 + \text{NLO}_3 + \text{NLO}_4. \quad (2.17)$$

We refrain from dividing our complete NLO calculation into different resonant contributions based on the origin of photon emission, as already done at NLO QCD for the $pp \rightarrow t\bar{t}\gamma$ process in Refs. [3, 4] and for $pp \rightarrow t\bar{t}\gamma\gamma$ in Ref. [22]. It is because additional photon radiation introduces further complications due to mixing of Born-level processes with different photon radiation patterns at LO. This issue has already been examined in detail in the case of the calculation of NLO QCD corrections to $pp \rightarrow t\bar{t}jj$ [56]. Instead, we perform an alternative calculation, labelled as NLO_{prd}, which we define according to

$$\text{NLO}_{\text{prd}} = \text{LO}_1 + \text{LO}_2 + \text{LO}_3 + \text{NLO}_1 + \text{NLO}_{2,\text{prd}} + \text{NLO}_{3,\text{prd}} + \text{NLO}_{4,\text{prd}}, \quad (2.18)$$

where the subscript *prd* indicates that photon bremsstrahlung and subleading NLO corrections are only included in the production stage of the $pp \rightarrow t\bar{t}\gamma(\gamma)$ process. In detail, in NLO_{prd}, all LO (LO₁, LO₂, LO₃) contributions as well as NLO₁ are fully included in both the $t\bar{t}\gamma(\gamma)$ production and decays of the top-quark pair. On the other hand, the subleading NLO corrections (NLO₂, NLO₃, NLO₄) are only included in the production stage of the $t\bar{t}\gamma(\gamma)$ process when the photon (the two photons) are also present there. In this way, we investigate the origin of the main subleading corrections. This approximation is motivated by the fact that, on the one hand, it leads to an enormous simplification of the calculations, especially for the real emission part, and ultimately in the matching to parton shower programs. On the other hand, the largest subleading NLO contributions are expected to originate from EW Sudakov logarithms in the tails of dimensionful observables. However, it is known that high p_T phase-space regions are dominated by the case where all photons are produced in the $t\bar{t}$ production [3, 4, 22], which should directly reduce the relevance of including subleading NLO corrections in other radiation patterns. With the calculation of NLO_{prd} we would like to confirm that this is the case for the $pp \rightarrow t\bar{t}\gamma(\gamma)$ process for various differential cross-section distributions. For the sake of completeness, we will also show the NLO_{prd} result for the $t\bar{t}\gamma(\gamma)$ integrated fiducial cross section.

3 Computational framework

As we have already alluded to in Section 2 the calculation of real corrections is performed with the Nagy-Soper subtraction scheme [53], which has recently been extended to NLO QCD calculations in the NWA involving internal on-shell resonances [56]. To check the validity of the results, we also use the Catani-Seymour subtraction scheme [54, 55]. Furthermore, for additional cross-checks in both

cases we utilize the phases-space restriction on the subtraction terms [58–61]. For the purposes of this study, both subtraction schemes, that are implemented in the HELAC-DIPOLES MC program [62], have been extended to deal with soft and collinear singularities of QED origin that plague the real radiation contributions of NLO EW calculations. In the following we describe both extensions in detail and discuss how the calculation of virtual corrections is organised for the purposes of our study.

3.1 Real corrections

At NLO QCD, we have to deal with contributions of different origin, on the one hand with virtual corrections due to the interference of one-loop and tree-level amplitudes, and on the other hand with real corrections arising from the emission of additional QCD partons. However, both contributions themselves are divergent, and only the sum of them is finite for IR safe observables. A standard approach nowadays is the use of a subtraction scheme, where an auxiliary cross section is introduced, which is designed to locally mimic the singular limits of the real-correction cross section. Moreover, this auxiliary cross section has to be simple enough so that the integration over the one-parton subspaces, which cause the soft and collinear divergences, is possible either analytically or numerically, leading to the so-called integrated subtraction terms and/or dipoles. These can then be combined with the virtual corrections to cancel all IR divergences. In general, the subtraction term in QCD can be written as

$$\mathcal{A}^{\text{D}} = \sum_{i,j,k=1}^{n+1} \mathcal{A}^{\text{B}}(\{\tilde{p}\}_n^{ijk}) \otimes \mathcal{D}^{(ijk)}(\{\tilde{p}\}_n^{(ijk)}, \{p\}_{n+1}) (\mathbf{T}_{ij} \cdot \mathbf{T}_k), \quad (3.1)$$

where \mathcal{A}_{B} is the tree-level matrix element of the underlying Born-level process which results from the recombination of the two partons i and j . The terms $\mathcal{D}^{(ijk)}$ are the so-called dipoles and $\{\tilde{p}\}_n^{(ijk)}$ is the new set of momenta for the underlying Born-level process, which is obtained by a momentum mapping from the initial momenta $\{p\}_{n+1}$. Spin correlations between the squared Born-level matrix element and the dipoles are indicated by the symbol \otimes . Finally, \mathbf{T}_k are color operators according to the definitions given in Ref. [54]. The indices i, j, k indicate that in general the dipoles as well as the momentum mapping depend on the two splitting partons i, j and potentially also on the spectator parton k . The QED subtraction scheme can be obtained from the QCD one by simple substitutions. In particular, the color operators have to be replaced by charge operators according to

$$\mathbf{T}_{ij} \cdot \mathbf{T}_k \rightarrow \mathbf{Q}_{ij} \mathbf{Q}_k, \quad (3.2)$$

where \mathbf{Q}_k is the charge of the particle with a relative minus sign between final- and initial-state particles, and possible further simple replacements of color factors. However, this cannot be applied to the case where the splitting pair is recombined into a photon ($Q_{ij} = 0$). Instead, in this case we perform the following substitution

$$\mathbf{T}_{ij} \cdot \mathbf{T}_k \rightarrow -w_k \mathbf{Q}_i^2 \quad \text{with} \quad \sum_k w_k = 1. \quad (3.3)$$

The particular choice of these weights w_k is completely arbitrary and, in our case we simply set it to δ_{k,k_0} , which implies that we choose exactly one spectator particle. In general, this spectator particle must be the same in the actual subtraction and in the calculation of the integrated dipoles, since the momentum mapping and dipoles terms depend on k . We note that in the Nagy-Soper subtraction scheme, both the momentum mapping and the collinear dipole terms are independent of the spectator particle, so that the choice of k_0 plays no role in the calculation. Finally, the structure of HELAC-DIPOLES has been modified to simultaneously keep track of different orders in α_s and α and to allow

the reweighting to different renormalisation and factorisation scale settings on the fly. To verify the new modifications, we have reproduced the results of Ref. [51] at the integrated and differential cross section level. In detail, we have calculated afresh NLO EW corrections to the $pp \rightarrow t\bar{t} + X$ process in the di-lepton top-quark decay channel for the LHC Run II center-of-mass energy of $\sqrt{s} = 13$ TeV. In this calculation all finite-width effects, resonant and non-resonant contributions of the top quark and W^\pm/Z gauge bosons as well as interference effects have been included.

Next, we discuss the changes in the Nagy-Soper subtraction scheme for calculations involving resonant particles. These modifications are to a large extent independent of QCD or QED-like singularities. To this end, we first briefly recall the notation and main aspects of the Nagy-Soper subtraction scheme which were presented in detail in Ref. [53]. We focus on the case of final-state splittings since initial-state splittings remain unaffected. We first introduce the following definitions

$$Q = p_1 + p_2 = \sum_{l=3}^{n+1} p_l, \quad (3.4)$$

$$P_{ij} = p_i + p_j \quad \text{and} \quad K = Q - P_{ij}, \quad (3.5)$$

where Q is the total momentum of the process, P_{ij} is the momentum sum of the splitting partons and K is the so-called collective spectator. The momentum mapping from $\{p\}_{n+1}$ to $\{\tilde{p}\}_n^{(ij)}$ is then defined by the condition that the momentum of the splitting parton \tilde{p}_i should lie in the Q - P_{ij} plane according to

$$P_{ij} = \beta \tilde{p}_i + \gamma Q, \quad (3.6)$$

where β and γ are uniquely fixed by the following two conditions

$$\tilde{Q} = Q, \quad (3.7)$$

$$\tilde{K}^2 = K^2. \quad (3.8)$$

From Eq. (3.7) it is clear that the momentum mapping from K to \tilde{K} is given by a Lorentz transformation ($k_i^\mu = \Lambda(K, \tilde{K})^\mu{}_\nu \tilde{k}_i^\nu$), which is defined as [53, 63]

$$\Lambda(K, \tilde{K})^\mu{}_\nu = g^\mu{}_\nu - \frac{2(K + \tilde{K})^\mu(K + \tilde{K})_\nu}{(K + \tilde{K})^2} + \frac{2K^\mu \tilde{K}_\nu}{K^2}. \quad (3.9)$$

Next, the dipole terms $\mathcal{D}^{(ijk)}$ in Eq. (3.1) are decomposed into diagonal terms $W^{(ii,j)}$ containing soft and collinear singularities and interference terms $W^{(ik,j)}$ including only soft singularities according to

$$\mathcal{D}_{\tilde{s}_1 \tilde{s}_2}^{(ijk)} = W_{\tilde{s}_1 \tilde{s}_2}^{(ii,j)} \delta_{ik} + W_{\tilde{s}_1 \tilde{s}_2}^{(ik,j)} (1 - \delta_{ik}), \quad (3.10)$$

where \tilde{s}_1 and \tilde{s}_2 are the helicity values of the splitting parton. The diagonal and interference terms are further split into a sum of so-called splitting functions $v^{(ij)}$ as specified by

$$W_{\tilde{s}_1 \tilde{s}_2}^{(ii,j)} = \sum_{s_i, s_j} v_{\tilde{s}_1 s_i s_j}^{(ij)} \left(v_{\tilde{s}_2 s_i s_j}^{(ij)} \right)^*, \quad (3.11)$$

$$W_{\tilde{s}_1 \tilde{s}_2}^{(ik,j)} = \sum_{s_i, s_j} v_{\tilde{s}_1 s_i s_j}^{(ij), eik} \left(v_{\tilde{s}_2 s_i s_j}^{(kj), eik} \right)^*, \quad (3.12)$$

where $v^{(ij), eik}$ is the eikonal approximation of these splitting functions. In QCD the $v^{(ij), eik}$ function reduces to a much simpler expression given by

$$v_{\tilde{s}_i s_i s_j}^{(ij), eik} = \sqrt{4\pi\alpha_s} \delta_{\tilde{s}_i s_i} \frac{\epsilon(p_j, s_j)^* \cdot p_i}{p_i \cdot p_j}. \quad (3.13)$$

The splitting functions are obtained by factorising the splitting $\tilde{p}_i \rightarrow p_i + p_j$ from the divergent matrix element in the following way $\mathcal{M}_{n+1}^{\text{div}} = \mathcal{M}_n \otimes v^{(ij)}$. The exact form for the different QCD splittings for final- and initial-state splittings can be found in Ref. [63].

The original Nagy-Soper subtraction scheme can directly be used in the case of unresolved partons in the production process. However, if an unstable particle is part of the emitter pair, then we use the spin-averaged versions of the dipole terms $\mathcal{D}^{(ijk)}$ in Eq. (3.1). In addition, we use the eikonal approximation for the splitting functions in the diagonal term $W^{(ii,j)}$ given in Eq. (3.11) when a W gauge boson is part of the emitter pair. These modifications are also applied to unstable particles in nested decay chains, such as W gauge bosons in radiative top-quark decays. Further modifications are required for the dipole subtraction in decay processes. The first change concerns the momentum mapping which is required to preserve the total momentum of the decay process, i.e. the momentum of the decaying mother particle. This is achieved by replacing the total momentum Q in the original momentum mapping with the momentum of the mother particle, which is called Q_{dec} in analogy. By definition Q_{dec} is then preserved under the momentum mapping according to the condition defined in Eq. (3.7). The dipole terms $\mathcal{D}^{(ijk)}$ also have an explicit and an additional implicit dependence on Q by the axial gauge with Q as reference vector used for the polarisation vectors of gluons and photons. Thus, to reuse all the results of the original subtraction scheme, we have to perform the replacement $Q \rightarrow Q_{\text{dec}}$ also in all the dipole terms $\mathcal{D}^{(ijk)}$ and apply a gauge transformation to the external polarisation vectors entering the splitting functions $v^{(ij)}$. The mother particle is excluded from the list of possible emitters in the dipole subtraction, but it is still included as a possible spectator particle. To properly account for all soft singularities associated with the mother particle, we replace $W^{(ik,j)}$, defined in Eq. (3.11), in the case where the mother particle is the spectator k , by $W_{\text{dec}}^{(ik,j)}$, which we define as

$$W_{\text{dec}}^{(ik,j)} = W^{(ik,j)} + W^{(ki,j)} - W^{(kk,j),eik}. \quad (3.14)$$

For the calculation of the corresponding integrated dipoles we closely follow the semi-numerical approach of Ref. [53]. In this case, the spin-averaged diagonal and interference terms are cast in the following form

$$\overline{W}^{(ii,j)} - \overline{W}_{\text{dec}}^{(ik,j)} = \underbrace{\left(\overline{W}^{(ii,j)} - \overline{W}^{(ii,j),eik} \right)}_{\mathcal{D}_{ii}} + \underbrace{\left(\overline{W}^{(ii,j),eik} - \overline{W}_{\text{dec}}^{(ik,j)} \right)}_{\mathcal{I}_{ik,\text{dec}}}, \quad (3.15)$$

where \mathcal{D}_{ii} can only have collinear singularities by construction and are already known from the original formulation. The second term can have soft and collinear singularities and can be further simplified to

$$\mathcal{I}_{ik,\text{dec}} = 4\pi\alpha_s \frac{-((p_j \cdot p_k)p_i - (p_i \cdot p_j)p_k)^2}{(p_i \cdot p_j)^2(p_j \cdot p_k)^2}. \quad (3.16)$$

We have calculated and implemented this new dipole in the case of massless and massive splitting partons \tilde{p}_i . The latter case is required for the calculation of EW corrections to top-quark decays, i.e. for $W^\pm \rightarrow W^\pm\gamma$ splittings. In addition, it can also be used for e.g. NLO QCD corrections with massive bottom quarks inside top-quark decays. In summary, our implementation of the Nagy-Soper subtraction scheme allows us to calculate QCD and EW radiative corrections for any number of coloured, charged, massive and massless particles in nested decay chains.

We have carried out several tests to confirm the correctness of the modifications we have made. First of all, we have already used this new extension for the calculation of the NLO QCD corrections to the $pp \rightarrow t\bar{t}jj$ process in the di-lepton top-quark decay channel in the NWA [56]. These results, were

cross-checked with an alternative calculation using the Catani-Seymour subtraction scheme and its extension to the NWA case [4, 44, 64]. In addition, we have recalculated the NLO QCD corrections of the top-quark width with massive bottom quarks [65, 66] as well as the corresponding real corrections, which are presented in the appendix of Ref. [45]. Finally, we have reproduced the calculation of the NLO electroweak corrections to the top-quark decay width while treating the internal W boson in the NWA [67].

In our current calculation of the $pp \rightarrow t\bar{t}\gamma(\gamma)$ process in the NWA, we have computed the real correction part of the NLO calculations with the Nagy-Soper subtraction scheme. We have utilised two different values of the phase-space restriction on the subtraction terms and found excellent agreement for the obtained results within the corresponding MC errors. Finally, we have reproduced the results of $\text{NLO}_{i,\text{prd}}$ with $i = 1, 2, 3, 4$ using the Catani-Seymour subtraction scheme. A full comparison with the Catani-Seymour subtraction is not yet possible as our implementation is currently limited to massless emitters in decay processes.

3.2 Virtual corrections

The calculation of the virtual corrections is organized using reweighting techniques [60, 68]. In practice, partially unweighted events [69] that are generated at the Born level, are then used to calculate the one-loop corrections. The phase-space integration is performed using the programs PARNI [70] and KALEU [71]. The combined tree-level and one-loop results are then stored in modified Les Houches Event Files (LHEFs) [72, 73], which have been extended to save, for each event, the necessary information for all contributions at different orders of α_s and α . This allows us, among other things, to reweight our results to different renormalisation and factorisation scale settings. Tree-level and one-loop matrix elements are obtained with the help of the RECOLA matrix element generator [74, 75]. We have modified the calculation of the matrix elements in RECOLA to incorporate the random polarisation method [53, 76, 77] which leads to significant performance improvements in the phase-space integration. Following the notation of Ref. [74], every one-loop amplitude can be written as a linear combination of tensor integrals

$$\mathcal{A}_{1\text{-loop}} = \sum_t c_{\mu_1 \dots \mu_{r_t}}^{(t)} T_{(t)}^{\mu_1 \dots \mu_{r_t}} + \mathcal{A}_{\text{CT}}, \quad (3.17)$$

where \mathcal{A}_{CT} include the counterterms, $c_{\mu_1 \dots \mu_{r_t}}^{(t)}$ are the tensor coefficients that do not depend on the loop momentum q , t classifies the different tensor integrals needed for the process and r_t labels the rank of the tensor integral. Furthermore, the tensor integrals are given by

$$T_{(t)}^{\mu_1 \dots \mu_{r_t}} = \frac{(2\pi\mu)^{4-D}}{i\pi^2} \int d^D q \frac{q^{\mu_1} \dots q^{\mu_{r_t}}}{D_0^{(t)} \dots D_{k_t}^{(t)}}, \quad D_i^{(t)} = (q + p_i^{(t)})^2 - (m_i^{(t)})^2, \quad (3.18)$$

where k_t is the number of propagators. The tensor coefficients are calculated by RECOLA similarly to the tree-level amplitudes by recursive construction of loop off-shell currents [75, 78]. The relevant tensor integrals are computed with the COLLIER library [79] which implements the reduction techniques of [80, 81] and the scalar integrals of [82]. Alternatively, we have implemented the reduction to scalar integrals with CUTTOOLS [83]. The resulting scalar integrals are computed with ONELOOP [84]. The CUTTOOLS program implements the OPP reduction method [85], which is based on double, triple and quadruple cuts. A similar approach has already been employed in the OPENLOOPS program [86]. In our case, the OPP reduction and the evaluation of the scalar integrals are performed with quadruple precision, while the tensor coefficients are calculated with double precision. Not only do we use this second reduction scheme for additional cross-checks of our framework, but also for phase-space points containing tensor integrals that have been flagged by COLLIER as possibly unstable.

As explained in Ref. [74] the RECOLA program offers the possibility to select the resonant parts of the amplitude, and can therefore be employed to calculate matrix elements in the pole approximation. In this approximation, only the resonant parts of the amplitude are kept, thus, the complex squared mass of the resonant particle ($\mu^2 = m^2 - i\Gamma m$) is replaced by its real part ($\Re(\mu^2) = m^2$) everywhere in the amplitude except for the denominators of resonant propagators where the width Γ of the unstable particle is still present. The NWA matrix element is then obtained by performing the usual limit $\Gamma/m \rightarrow 0$ in the Breit-Wigner propagators. Finally, we correct the symmetry factor calculated in RECOLA for processes involving identical particles in the final state but originating from different subprocesses in the decay chain, as explained in Ref. [87].

As an alternative, we have implemented a second fully automatic method for the construction of one-loop matrix elements in the NWA, which is based on the calculation of the on-shell amplitudes for the individual contributions needed in e.g. the $pp \rightarrow t\bar{t}(\gamma\gamma)$ process in the di-lepton top-quark decay channel. To this end, we compute separately the subamplitudes for $pp \rightarrow t\bar{t}(\gamma\gamma)$, $t \rightarrow W^+b(\gamma\gamma)$, $\bar{t} \rightarrow W^- \bar{b}(\gamma\gamma)$, $W^+ \rightarrow \ell^+ \nu_\ell(\gamma\gamma)$ and $W^- \rightarrow \ell^- \bar{\nu}_\ell(\gamma\gamma)$ with RECOLA and then combine them appropriately in color and helicity space to obtain the full one-loop amplitude. This alternative implementation is particularly useful for cross-checking because in this case we can switch on and off one-loop corrections for specific contributions. We note here, that we have already used both approaches in Ref. [56] where NLO QCD calculations for the $pp \rightarrow t\bar{t}jj$ process in the di-lepton top-quark decay channel have been carried out.

We have performed various cross-checks between RECOLA and RECOLA2 [88] for all partonic subprocesses. Specifically, for each subprocess and for several phase-space points we checked the finite remainders as well as the coefficients of the poles in ϵ of the virtual amplitudes. For testing purposes we utilised the Background-Field-Method (BFM) as implemented in RECOLA2 [57, 89, 90]. The BFM, which is an alternative formulation for the quantisation of gauge fields that can be seen as a different gauge, can be used as a complementary method in the calculation of one-loop matrix elements besides the usual formulation.

The proper description of unstable particles like W^\pm gauge bosons and top quarks in perturbation theory requires the introduction of the complex-mass scheme (CMS), which was first proposed for lowest-order calculations in Ref. [41] and then generalised to higher orders in Refs. [42, 91]. In this scheme, complex masses are introduced at the level of the Lagrangian by splitting the bare masses into complex renormalised masses and complex counterterms. This corresponds to a rearrangement of the perturbative expansion without changing the underlying theory and preserving gauge invariance. Unitarity is respected up to higher orders as long as unstable particles are excluded from the final states. Renormalisation must nevertheless be treated carefully as not to spoil these properties of the bare theory. To this end, the standard on-shell scheme has been generalised in Ref. [42] to the complex-mass case by requiring unit residues of propagators at complex poles and by taking into account the imaginary parts of the self-energies in the renormalisation constants. This necessitates, however, the calculation of the self-energies for complex squared momenta. This complication can be avoided by expanding the self-energies present in the renormalisation constants about real arguments such that one-loop accuracy is preserved. In case of the W^\pm gauge boson and top-quark, extra constants must be added to the expanded self-energies in order not to spoil the one-loop accuracy of the results due to the presence of branch cuts introduced by infrared divergences. The simplified version of the complex renormalisation is described in detail in Refs. [42, 57], where all renormalisation constants are provided as well. These renormalisation constants are implemented in RECOLA and employed in our calculation of NLO QCD and EW corrections to the $pp \rightarrow t\bar{t}\gamma(\gamma)$ process in the di-lepton top-quark decay channel

without any modifications.

As already mentioned in Section 2.1, the presence of final-state photons in the Born-level process requires special care in the renormalisation of the electromagnetic coupling constant α . In particular, we split the total power of α^n into $\alpha_{G_\mu}^{n-n_\gamma} \alpha(0)^{n_\gamma}$ where $n_\gamma = 1$ ($n_\gamma = 2$) for the underlying Born-level process $pp \rightarrow t\bar{t}\gamma(\gamma)$. The powers of the electromagnetic coupling constant associated with final-state photons are renormalised in the on-shell scheme (the $\alpha(0)$ scheme) [16, 42, 57]. The remaining powers of α are renormalised in the G_μ scheme, where the renormalized electromagnetic coupling α is derived from the Fermi constant G_F , measured in muon decays, and the masses of the W and Z bosons. The renormalisation in this mixed scheme is realised by first performing the complete renormalisation of all powers of α in the G_μ scheme. The renormalisation scheme is then changed for $\alpha(0)^{n_\gamma}$ by introducing a new counterterm which is given by

$$2n_\gamma \operatorname{Re} \left(\delta Z_e|_{\alpha(0)} - \delta Z_e|_{G_\mu} \right) d\sigma^{\text{LO}} = n_\gamma \operatorname{Re} \left(\Delta r^{(1)} \right) d\sigma^{\text{LO}}, \quad (3.19)$$

where $\Delta r^{(1)}$ are the NLO EW corrections to the muon decay [92–95] and $\delta Z_e|_{\alpha(0)}$ as well as $\delta Z_e|_{G_\mu}$ are the renormalisation constants of the electric charge e in the on-shell and G_μ scheme, respectively. We note that in Eq. (3.19) and in general in the whole calculation, the electromagnetic coupling is always set to $\alpha = \alpha_{G_\mu}$ and the final result is then rescaled by $(\alpha(0)/\alpha_{G_\mu})^{n_\gamma}$. This also implies that the relative EW corrections are always calculated with $\alpha = \alpha_{G_\mu}$. In order to test the consistency of the calculation in this mixed approach we have explicitly checked the cancellation of all IR singularities in the sum of virtual corrections and integrated dipoles for a few phase-space points for all partonic subprocesses.

4 LHC Setup for numerical predictions

The calculations of complete NLO corrections for $pp \rightarrow t\bar{t}\gamma$ and $pp \rightarrow t\bar{t}\gamma\gamma$ in the di-lepton top-quark decay channel are performed for proton-proton collisions at the LHC with a center of mass energy of $\sqrt{s} = 13$ TeV. When both higher-order QCD and EW corrections as well as photon-initiated subprocesses are considered, the PDFs with QED effects and the photon content of the proton are essential. To this end, we use the NLO NNPDF3.1luxQED PDF set [96–99] with $\alpha_s(m_Z) = 0.118$, where photons are properly taken into account in the PDF evolution, at LO and NLO. The PDF set as well as the running of the strong coupling constant with two-loop accuracy is obtained using the LHAPDF interface [100]. As already explained in the last section, for α a mixed scheme is considered. In particular, α is first calculated in the G_μ -scheme according to

$$\alpha_{G_\mu} = \frac{\sqrt{2}}{\pi} G_\mu m_W^2 \left(1 - \frac{m_W^2}{m_Z^2} \right), \quad G_\mu = 1.1663787 \cdot 10^{-5} \text{ GeV}^{-2}, \quad (4.1)$$

with $m_W = 80.379$ GeV and $m_Z = 91.1876$ GeV. However, α associated with Born-level final-state photons is treated in the on-shell scheme, where we use $\alpha^{-1} = \alpha^{-1}(0) = 137.035999084$ [101] as the input parameter. Additional photon radiation from the real emission part of the NLO calculation is evaluated with α_{G_μ} . We use the following input values for the masses and widths of the unstable particles

$$\begin{aligned} m_t &= 172.5 \text{ GeV}, & \Gamma_W &= 2.0972 \text{ GeV}, \\ m_H &= 125 \text{ GeV}, & \Gamma_H &= 4.07 \cdot 10^{-3} \text{ GeV}, \end{aligned}$$

The width of the Z boson is set to zero to avoid artificial higher-order terms that would otherwise appear due to the complex-mass scheme, since the width of the W boson is assumed to be zero

everywhere except in the propagators, as explained in Ref. [51]. All other particles are assumed to be massless. We use the same top-quark width at LO and NLO. Taking into account NLO QCD and EW corrections, the latter width is given by

$$\Gamma_t^{\text{NLO}} = 1.3735727 \text{ GeV}, \quad (4.2)$$

where we adapt the conventions given in Ref. [102], while the NLO QCD corrections are obtained from Ref. [65] for $\mu_R = m_t$. We note here that, contrary to what is usually done when calculating NLO QCD corrections, in this study we use the same PDF set as well as top-quark width for both LO and NLO predictions. This should help us to directly examine the relative magnitude of the subleading contributions, while simultaneously separating out the effects coming from the use of different settings at LO and NLO. The NLO EW corrections are computed numerically with the help of HELAC-DIPOLES and RECOLA. As already indicated in Eq. (2.18), in this scheme, the LO and NLO contributions can simply be added to give the complete result.

The event selection and scale choice are based on our previous work on NLO QCD corrections to the $pp \rightarrow t\bar{t}\gamma\gamma$ process [22]. All final-state partons with pseudo-rapidity $|\eta| < 5$ are clustered into jets with separation $R = 0.4$ in the rapidity azimuthal-angle plane via the IR-safe *anti- k_T* jet algorithm [103]. We require two oppositely charged leptons, at least two b -jets and at least one (two) photon(s) for $t\bar{t}\gamma(\gamma)$, respectively. The IR safety of the $t\bar{t}\gamma(\gamma)$ cross section involving jets and prompt photon(s) is ensured by using the smooth photon isolation prescription as described in Ref. [104]. Therefore, the event is rejected unless the following condition is fulfilled before the jet algorithm is applied

$$\sum_i E_{T_i} \Theta(R - R_{\gamma i}) \leq \epsilon_\gamma E_{T_\gamma} \left(\frac{1 - \cos(R)}{1 - \cos(R_{\gamma j})} \right)^n, \quad (4.3)$$

for all $R \leq R_{\gamma j}$ with $R_{\gamma j} = 0.4$ and $\epsilon_\gamma = n = 1$. The transverse energy of the parton i /photon is denoted by E_{T_i}/E_{T_γ} and $R_{\gamma i}$ is given by

$$R_{\gamma i} = \sqrt{(y_\gamma - y_i)^2 + (\phi_\gamma - \phi_i)^2}. \quad (4.4)$$

In subleading NLO corrections we also encounter partonic processes with an additional photon in the final state with respect to the Born-level subprocesses. In this case, the smooth photon isolation prescription can be extended to additionally require the isolation of photons with charged leptons and photons, as suggested in Ref. [16]. In this approach, after the smooth photon isolation, charged leptons and partons are recombined with only non-isolated photons based on a jet clustering algorithm. In general, the use of the smooth photon isolation prescription is not required in this case. Alternatively, it is sufficient to perform the photon recombination directly with charged leptons and partons, where additionally the following recombination rule $\gamma + \gamma \rightarrow \gamma$ is allowed. Similar schemes have already been applied in associated photon production processes, see e.g. Refs. [105, 106]. We have used both approaches for the calculation of higher-order corrections to the $pp \rightarrow t\bar{t}\gamma$ process, where the photon recombination has also been performed with the *anti- k_T* jet algorithm with the radius parameter $R = 0.4$. We have found no phenomenologically relevant differences even at the differential cross-section level. Therefore, we remain with the second approach, not using the smooth isolation prescription in these contributions. After the jet algorithm/photon recombination, the prompt photons are defined with the following conditions

$$p_{T,\gamma} > 25 \text{ GeV}, \quad |y_\gamma| < 2.5, \quad \Delta R_{\gamma\gamma} > 0.4. \quad (4.5)$$

In order to ensure well-observable isolated b -jets and charged leptons in the central-rapidity region, we require

$$\begin{aligned} p_{T,b} > 25 \text{ GeV}, & & |y_b| < 2.5, & & \Delta R_{bb} > 0.4, \\ p_{T,\ell} > 25 \text{ GeV}, & & |y_\ell| < 2.5, & & \Delta R_{\ell\ell} > 0.4. \end{aligned} \quad (4.6)$$

In addition, charged leptons and photons need to be well separated from any b -jet in the rapidity-azimuthal angle plane as well as from each other

$$\Delta R_{l\gamma} > 0.4, \quad \Delta R_{lb} > 0.4, \quad \Delta R_{b\gamma} > 0.4. \quad (4.7)$$

Finally, there are no restrictions on the kinematics of the extra light jet/photon (if resolved by the jet algorithm) and the missing transverse momentum, $p_T^{\text{miss}} = |\vec{p}_{T,\nu_\ell} + \vec{p}_{T,\bar{\nu}_\ell}|$. Based on the findings in Ref. [22] we set the factorisation and renormalisation scale to a common dynamical scale setting, μ_0 , given by

$$\mu_R = \mu_F = \mu_0 = \frac{E_T}{4}, \quad (4.8)$$

with

$$E_T = \sqrt{m_t^2 + p_{T,t}^2} + \sqrt{m_t^2 + p_{T,\bar{t}}^2} + \sum_{i=1}^{n_\gamma} p_{T,\gamma_i}, \quad (4.9)$$

where $p_{T,t}$ and $p_{T,\bar{t}}$ are the transverse momenta of the on-shell top quarks. In addition, for dimensionful cross-section distributions constructed from the photon kinematics, we present results for the fixed scale setting, $\mu_0 = m_t$. Theoretical uncertainties due to missing higher orders are estimated by a 7-point scale variation, where the factorisation and renormalisation scales are independently varied in the range

$$\frac{1}{2} \mu_0 \leq \mu_R, \mu_F \leq 2 \mu_0, \quad \frac{1}{2} \leq \frac{\mu_R}{\mu_F} \leq 2, \quad (4.10)$$

which leads to the following pairs

$$\left(\frac{\mu_R}{\mu_0}, \frac{\mu_F}{\mu_0} \right) = \left\{ (2, 1), (0.5, 1), (1, 2), (1, 1), (1, 0.5), (2, 2), (0.5, 0.5) \right\}. \quad (4.11)$$

By searching for the minimum and maximum of the resulting cross sections we obtain the displayed uncertainty bands. We use the 7-point scale variation both at the integrated and differential cross-section level.

5 Top-quark pair production with one isolated photon

5.1 Integrated fiducial cross sections

Now we turn to the discussion of the numerical results. We begin with our findings for the $pp \rightarrow t\bar{t}\gamma$ process at the integrated fiducial cross-section level. In particular, in Table 1 we present the results for LO, NLO, NLO_{QCD} and NLO_{prd}, as defined in the last section, with the corresponding theoretical uncertainties obtained by scale variation. In addition, we display the decomposition of the LO and NLO results into the individual LO_{*i*} and NLO_{*i*} contributions calculated at the different orders in α_s and α . Finally, the relative size of all results with respect to the dominant LO contribution, LO₁, is given in the last column. We find that both subleading LO contributions, LO₂ and LO₃, are below 0.5% of LO₁. In addition, LO₃ is slightly larger than LO₂ due to cancellations in LO₂ between the $g\gamma$ and $b\bar{b}$ subprocesses. It turns out that the latter channel gives a negative result that can be attributed to the interference between the different orders in α_s and α . Although, the $b\bar{b}$ initial state is PDF suppressed

		σ_i [fb]	Ratio to LO ₁
LO ₁	$\mathcal{O}(\alpha_s^2\alpha^5)$	55.604(8) ^{+31.4%} _{-22.3%}	1.00
LO ₂	$\mathcal{O}(\alpha_s^1\alpha^6)$	0.18775(5) ^{+20.1%} _{-15.4%}	+0.34%
LO ₃	$\mathcal{O}(\alpha_s^0\alpha^7)$	0.26970(4) ^{+14.3%} _{-16.9%}	+0.49%
NLO ₁	$\mathcal{O}(\alpha_s^3\alpha^5)$	+3.44(5)	+6.19%
NLO ₂	$\mathcal{O}(\alpha_s^2\alpha^6)$	-0.1553(9)	-0.28%
NLO ₃	$\mathcal{O}(\alpha_s^1\alpha^7)$	+0.2339(3)	+0.42%
NLO ₄	$\mathcal{O}(\alpha_s^0\alpha^8)$	+0.001595(8)	+0.003%
LO		56.061(8) ^{+31.2%} _{-22.1%}	1.0082
NLO _{QCD}		59.05(5) ^{+1.6%} _{-5.9%}	1.0620
NLO _{prd}		59.08(5) ^{+1.5%} _{-5.9%}	1.0626
NLO		59.59(5) ^{+1.6%} _{-5.9%}	1.0717

Table 1. Integrated fiducial cross section for the $pp \rightarrow t\bar{t}\gamma + X$ process in the di-lepton top-quark decay channel at the LHC with $\sqrt{s} = 13$ TeV. Results are shown for LO, NLO, NLO_{QCD} and NLO_{prd} with the corresponding scale uncertainties. Additionally, all LO_{*i*} and NLO_{*i*} contributions and the ratio with respect to LO₁ are displayed. MC integration errors are given in parentheses. Results are provided for $\mu_0 = E_T/4$ and the NLO NNPDF3.1luxQED PDF set.

with respect to the $q\bar{q}$ one, it provides the dominant contribution to LO₃, and is more than three times larger than the $q\bar{q}$ channel, due to the presence of additional t -channel Feynman diagrams that do not appear in the $q\bar{q}$ subprocess. The $\gamma\gamma$ initiated contribution is smaller than the MC integration error of the LO result and thus completely negligible. Consequently, at the integrated fiducial cross-section level, the subleading LO contributions are phenomenologically insignificant, especially when compared to the scale uncertainties of the complete LO result (or the dominant LO₁ contribution for that matter). The theoretical errors of both LO and LO₁ are of similar size and amount to 31%.

As expected, the dominant NLO corrections originate from the NLO QCD corrections (NLO₁) to LO₁ and lead to an increase of the integrated fiducial cross section by about 6.2%. All subleading NLO contributions are again found to be less than 0.5% of LO₁. In more detail, NLO₂ and NLO₃ are of the same order of magnitude and NLO₄ is completely negligible compared to the NLO scale uncertainties and even MC integration errors. We note that in all the contributions we used the same top-quark width ($\Gamma_t^{\text{NLO,QCD+EW}} = 1.3735727$ GeV). In particular, if the LO top-quark width ($\Gamma_t^{\text{LO}} = 1.4806842$ GeV) has been used instead for LO₁ and the NLO QCD one ($\Gamma_t^{\text{NLO,QCD}} = 1.3535983$ GeV) for NLO_{QCD}, as it is often done in higher-order QCD calculations, we would obtain NLO QCD corrections of about 27%. Furthermore, we note that the sum of all subleading LO and NLO contributions increases the NLO_{QCD} result by about 1% and therefore plays only a minor role at the integrated fiducial cross-section level compared to the NLO_{QCD} scale uncertainties that are of the order of 6%. The scale uncertainties themselves remain unchanged by the inclusion of the subleading higher-order contributions, and are thus completely driven by the NLO_{QCD} part. Finally, we can observe that NLO_{prd} and NLO_{QCD} agree within the MC errors, which results from the cancellation of subleading LO contributions (0.8%) and the subleading NLO corrections to the production of $pp \rightarrow t\bar{t}\gamma$ (-0.7%). In addition, the difference

between NLO and NLO_{prd} , and thus the subleading NLO corrections involving radiative top-quark decays (including photon radiation and/or QCD/EW corrections), is of similar (absolute) size as the other two effects (0.9%).

5.2 Differential fiducial cross sections

While at the integrated fiducial cross-section level the effects of the subleading LO and NLO contributions are small, it is expected that these effects might be enhanced for particular observables in certain phase-space regions. To this end, in Figure 9 we present the differential cross-section distributions for the transverse momentum of the hardest photon, p_{T,γ_1} , the invariant mass of the two hardest b -jets, $M_{b_1b_2}$, as well as their transverse momenta, denoted as p_{T,b_1} and p_{T,b_2} , respectively. In the upper panels we provide the absolute predictions for LO, NLO, NLO_{QCD} and NLO_{prd} . The middle panels show the ratio of the three NLO results to NLO_{QCD} . In addition, both panels display the NLO_{QCD} theoretical uncertainties obtained from scale variation. Finally, the lower panels present the relative size of all subleading LO_i and NLO_i contributions with respect to LO_1 .

For p_{T,γ_1} we find that the largest NLO corrections arise from NLO_1 and lead in the tail of the distribution to an increase of the LO_1 cross section by about 25%. The inclusion of all subleading LO and NLO contributions reduces the NLO_{QCD} prediction by up to 4% due to EW Sudakov logarithms induced by NLO_2 . All other subleading contributions remain below 1%. The NLO_{prd} contribution, where the subleading NLO corrections are only included in the production stage of $t\bar{t}\gamma$, underestimates the full calculation by about 2%. The overall picture remains the same for the $M_{b_1b_2}$ observable. In particular, we again find that NLO_2 is the dominant subleading contribution, leading to a reduction in the NLO_{QCD} prediction of about 5%. This reduction is about half the size of the corresponding scale uncertainties. On the other hand, NLO_{prd} recovers the full calculation correctly in the tails and only small differences up to 1.5% are found at the beginning of the spectrum. In the case of the transverse momenta of the hardest and second hardest b -jet, p_{T,b_1} and p_{T,b_2} , the relative size of NLO_2 with respect to LO_1 is increased to 10%. On the contrary, the impact of all subleading contributions on the final NLO result seems to be very different. Indeed, we find for p_{T,b_1} that NLO_3 is enhanced in the tail and amounts to 3% – 4%, thus partially cancelling the EW Sudakov logarithms in NLO_2 . Moreover, we find large NLO QCD corrections to LO_1 of up to 95%, which further suppress the importance of the subleading contributions. However, both effects, the enhancement of NLO_3 and the large NLO_1 contribution, have the same origin and arise from large NLO QCD real corrections to LO_1 and LO_3 , induced by hard jet recoil against the $t\bar{t}$ system. This can be seen by inspecting the size of the NLO scale uncertainties, which increase continuously towards the tail of the distribution and become closer in size to those at LO. Thus, the relative size of the subleading corrections is highly dependent on the fiducial phase space and might be enhanced if a more exclusive event selection and/or jet vetos are applied. On the other hand, for p_{T,b_2} the subleading contributions have a more significant impact on its spectrum, reducing the NLO_{QCD} prediction by up to 10%. The scale uncertainties of NLO_{QCD} are about 15% and therefore comparable in size. Moreover, we find that the larger size of the subleading contributions can also affect the scale uncertainties, which in this case increase to about 20% for the complete NLO case. Finally, we can observe that, for both b -jet transverse momentum spectra the NLO_{prd} predictions fully recover the complete NLO result.

Following the findings of our previous work on the calculation of the NLO QCD corrections to the $pp \rightarrow t\bar{t}\gamma\gamma$ process in the di-lepton top-quark decay channel [22], where a traditional fixed scale setting, $\mu_0 = m_t$, led to a reduction of NLO QCD corrections and scale uncertainties for photonic observables, in the following we reexamine the p_{T,γ_1} observable also for this scale choice. To this end, in Figure 10 we present p_{T,γ_1} afresh for $\mu_0 = m_t$. We find that for this fixed scale choice the NLO_1 contribution

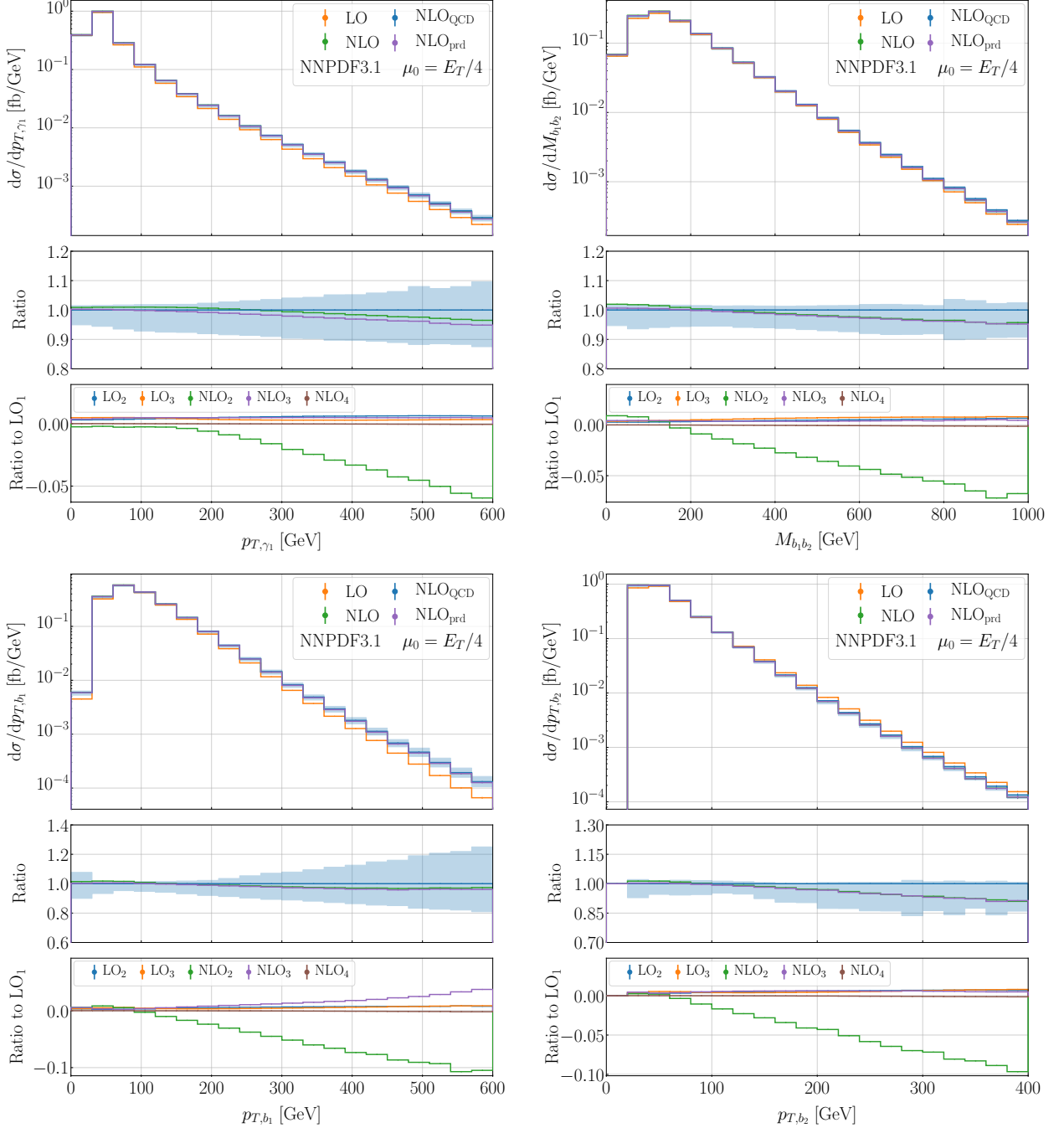


Figure 9. Differential cross-section distributions for the observables p_{T,γ_1} , $M_{b_1 b_2}$, p_{T,b_1} and p_{T,b_2} for the $pp \rightarrow t\bar{t}\gamma + X$ process in the di-lepton top-quark decay channel at the LHC with $\sqrt{s} = 13$ TeV. The upper panels present absolute predictions for LO, NLO, NLO_{QCD} and NLO_{prd} together with the NLO_{prd} uncertainty bands. Middle panels show the ratio of all NLO results with respect to NLO_{QCD} and the lower panels display the relative size of all subleading LO_{*i*} and NLO_{*i*} contributions compared to LO₁. Results are provided for $\mu_0 = E_T/4$ and the NLO NNPDF3.1_{luxQED} PDF set.

is reduced from 25% to 13%. Moreover, while for the default scale setting, $\mu_0 = E_T/4$, the largest NLO QCD corrections are present in the tail, for $\mu_0 = m_t$ the LO and NLO_{QCD} predictions coincide in this phase-space region. Furthermore, the differences of up to 13% are found at the beginning of

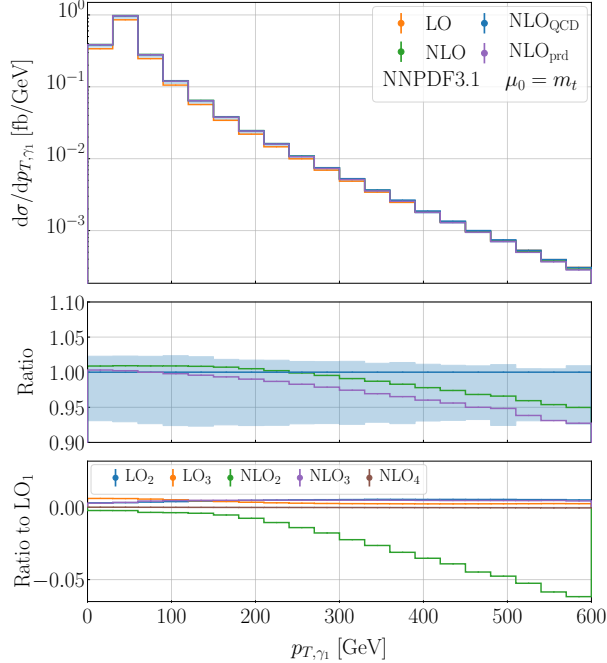


Figure 10. Same as Figure 9 but for the observable p_{T,γ_1} . The result is shown for $\mu_0 = m_t$.

the spectrum. The relative size of the subleading LO and NLO contributions is basically unchanged and leads to a reduction of the complete calculation of about 5% compared to 4% for $\mu_0 = E_T/4$. In addition, the scale uncertainties are slightly reduced to 7% – 9% compared to 10% – 11%. Thus, for the scale setting $\mu_0 = m_t$, the subleading contributions become more important, since the subleading effects and the scale uncertainties are of similar size.

We continue the discussion and present in Figure 11 other differential cross-section distributions. In detail, we display the transverse momentum of the $b_1 b_2$ and $\ell^+ \ell^-$ systems, denoted as $p_{T,b_1 b_2}$ and $p_{T,\ell^+ \ell^-}$, respectively. Furthermore, we show the angular separation between γ_1 and ℓ^+ as well as γ_1 and b_1 , denoted as $\Delta R_{\ell^+ \gamma_1}$ and $\Delta R_{b_1 \gamma_1}$, respectively. The two dimensionful observables, $p_{T,b_1 b_2}$ and $p_{T,\ell^+ \ell^-}$, are affected by huge NLO QCD corrections to LO₁ of about 450% and 200%. These corrections arise from a kinematical suppression at LO [47, 102, 107–109]. Indeed, at the LO level the two top quarks are predominantly produced in the back-to-back configuration, so that the transverse momentum of both b -jets or leptons may separately be large, but they largely cancel each other out in the combined system. At NLO, however, this suppression is weakened due to hard jet recoil against the $t\bar{t}$ system. This leads, on the one hand, to huge NLO QCD corrections to LO₁, and on the other hand, also to an enhancement of the NLO QCD corrections with respect to LO₃ as part of NLO₃. In particular, for $p_{T,b_1 b_2}$ we find that NLO₃ is about 10% of LO₁. The NLO₂ contribution is of similar magnitude but has the opposite sign. Consequently, NLO₃ and NLO₂ cancel each other out, and the NLO_{QCD} and NLO predictions coincide. Since the two NLO subleading contributions are of different origins, this cancellation is too a large extend accidental and highly dependent on the event selection and for example jet vetos. Especially, vetoing undesired additional jets would drastically reduce the size of NLO₁ and NLO₃. Also for $p_{T,\ell^+ \ell^-}$ we find a similar but less pronounced cancellation of NLO₂ (–5%) and NLO₃ (2%). The NLO_{prd} approximation is again able to fully recover the complete NLO calculation.

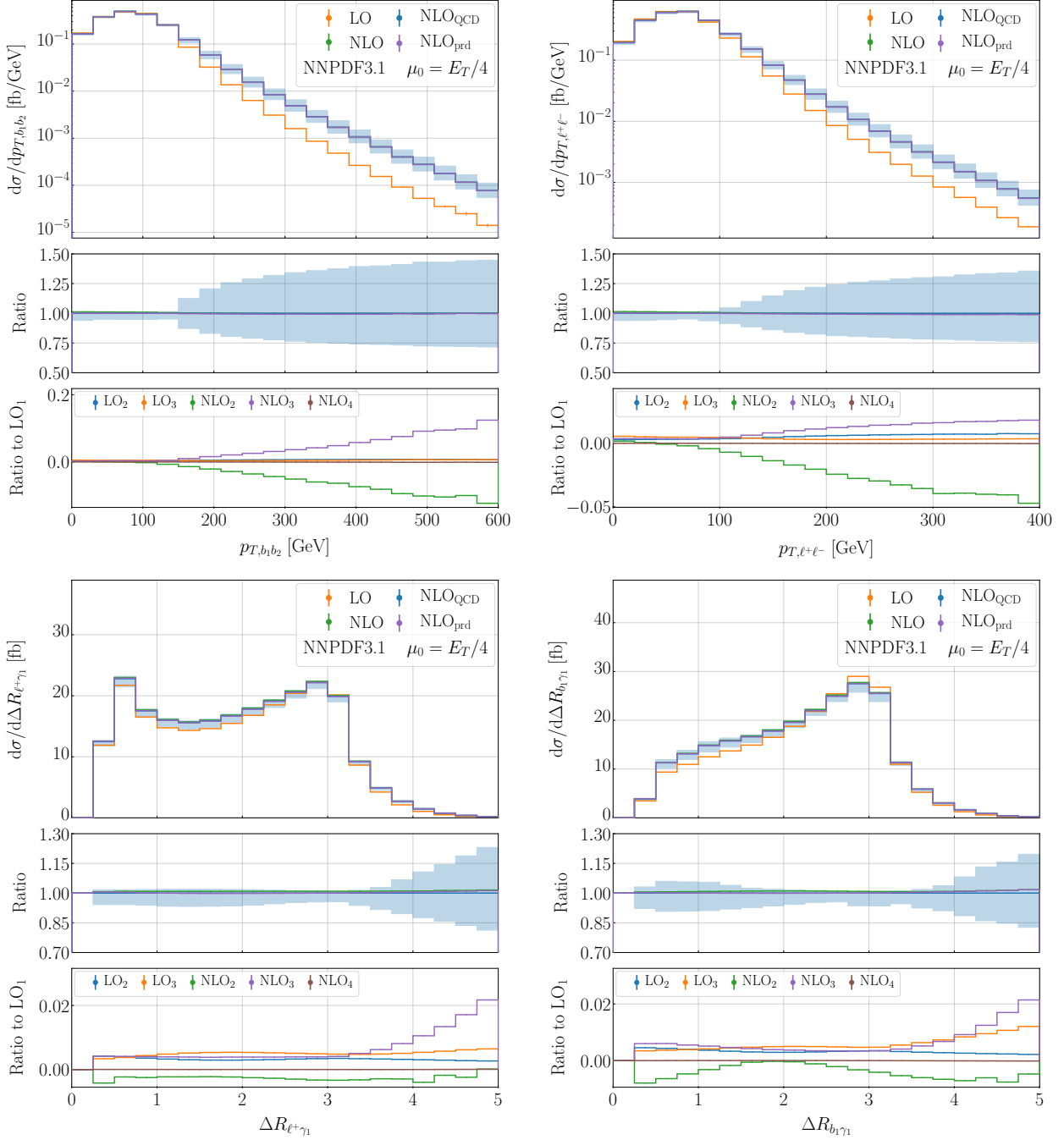


Figure 11. Same as Figure 9 but for the observables $p_{T,b_1 b_2}$, $p_{T,\ell^+ \ell^-}$, $\Delta R_{\ell^+ \gamma_1}$ and $\Delta R_{b_1 \gamma_1}$.

For angular distributions such as regular rapidity distributions, ΔR separations or (azimuthal) opening angles between two final states, we find no significant effects from any of the subleading LO or NLO contributions. Indeed, they are individually in the range of 0.5% – 1.0% when compared to LO₁. Only for the ΔR separation between a photon and a b -jet or charged lepton, such as $\Delta R_{\ell^+ \gamma_1}$ and $\Delta R_{b_1 \gamma_1}$, we find a small enhancement for the NLO₃ contribution when comparing to LO₁. This enhancement, of about 2%, is visible for large values of the ΔR separation. However, these phase-space regions are generally not only less populated but also characterized by substantial NLO scale

		σ_i [fb]	Ratio to LO ₁
LO ₁	$\mathcal{O}(\alpha_s^2\alpha^6)$	0.15928(3) ^{+31.3%} _{-22.1%}	1.00
LO ₂	$\mathcal{O}(\alpha_s^1\alpha^7)$	0.0003798(2) ^{+25.8%} _{-19.2%}	+0.24%
LO ₃	$\mathcal{O}(\alpha_s^0\alpha^8)$	0.0010991(2) ^{+10.6%} _{-13.1%}	+0.69%
NLO ₁	$\mathcal{O}(\alpha_s^3\alpha^6)$	+0.0110(2)	+6.89%
NLO ₂	$\mathcal{O}(\alpha_s^2\alpha^7)$	-0.00233(2)	-1.46%
NLO ₃	$\mathcal{O}(\alpha_s^1\alpha^8)$	+0.000619(1)	+0.39%
NLO ₄	$\mathcal{O}(\alpha_s^0\alpha^9)$	-0.0000166(2)	-0.01%
LO		0.16076(3) ^{+30.9%} _{-21.9%}	1.0093
NLO _{QCD}		0.1703(2) ^{+1.9%} _{-6.2%}	1.0690
NLO _{prd}		0.1694(2) ^{+1.7%} _{-5.9%}	1.0637
NLO		0.1700(2) ^{+1.8%} _{-6.0%}	1.0674

Table 2. Same as Table 1 but for the $pp \rightarrow t\bar{t}\gamma + X$ process in the di-lepton top-quark decay channel.

uncertainties up to 15%. Such theoretical uncertainties are induced by large NLO QCD corrections to LO₁. Thus, this small enhancement of NLO₃ is still negligible.

In summary, subleading LO and NLO contributions are generally only important in the tails of dimensionful observables. In particular, the presence of EW Sudakov logarithms in NLO₂ can reduce differential predictions by up to 10%. In addition, we have found that for observables affected by large NLO QCD corrections due to real radiation, the NLO₃ contribution can be enhanced. This can lead to an accidental cancellation with NLO₂ since the origin of both contributions is vastly different. Furthermore, the cancellation might be heavily influenced by the event selection and a possible jet veto. Finally, the NLO_{prd} prediction is able to mimic the complete NLO calculation for hadronic observables, while it underestimates the complete prediction by up to 1% – 2% for non-hadronic ones. Nevertheless, such small effects are well within the theoretical uncertainties due to scale dependence. Thus, the NLO_{prd} theoretical prediction can be safely used to model various differential cross-section distributions in phenomenological studies at the LHC for the $pp \rightarrow t\bar{t}\gamma + X$ process in the di-lepton top-quark decay channel taking into account the current theoretical precision for this process.

6 Top-quark pair production with two isolated photons

6.1 Integrated fiducial cross sections

Next we continue with the $pp \rightarrow t\bar{t}\gamma\gamma$ process and start with the discussion of the integrated fiducial cross section, again focusing our attention on the di-lepton top-quark decay channel. In particular, we are interested in any differences between this process and $pp \rightarrow t\bar{t}\gamma$. In Table 2 we present the integrated fiducial cross section for LO, NLO, NLO_{QCD} and NLO_{prd} as well as the corresponding scale uncertainties. We also present the numerical results for all individual LO_{*i*} and NLO_{*i*} contributions. We find again that all subleading LO contributions amount to less than 1% of LO₁ and are therefore negligible when comparing to the LO scale uncertainties. The NLO₁ contribution is similar in size with 6.9% compared to 6.2% for $pp \rightarrow t\bar{t}\gamma$. As expected, this contribution yields the largest higher-order

corrections at the NLO level. The biggest difference between the two processes is found for NLO₂. Indeed, the NLO₂ contribution increases from -0.3% to -1.5% , which is consistent with the findings in the literature for the process at hand but with stable top quarks [16]. The NLO₃ contribution remains at the level of 0.4% . Finally, NLO₄ contributes at the level of 0.01% only. This contribution is therefore smaller than the MC integration error and phenomenologically completely irrelevant. Due to the increase in size of NLO₂, there are larger cancellations between the individual contributions, so that the difference between the NLO_{QCD} and NLO predictions decreases and both results agree within their corresponding MC errors. As for the $pp \rightarrow t\bar{t}\gamma$ process, also in this case the scale uncertainties at the integrated fiducial cross-section level are barely affected by the subleading contributions. Including all subleading LO contributions and subleading NLO corrections to the production of $pp \rightarrow t\bar{t}\gamma\gamma$ in NLO_{prd} leads to a decrease of the NLO_{QCD} result by about -0.5% . Similar to the previous process, we again have cancellations between the subleading LO contributions (0.9%) and the subleading NLO corrections (-1.4%). The differences between NLO and NLO_{prd} are reduced to 0.4% compared to 0.9% for the $pp \rightarrow t\bar{t}\gamma$ process, implying that subleading NLO corrections involving radiative top-quark decays are less important, at least at the integrated fiducial cross-section level.

6.2 Differential fiducial cross sections

Similarly to $t\bar{t}\gamma$ production, also for the $pp \rightarrow t\bar{t}\gamma\gamma + X$ process we are investigating the impact of all subleading contributions and subleading higher-order corrections on various differential cross-section distributions. In Figure 12 we show the observables $p_{T,\gamma_1\gamma_2}$, $M_{\gamma_1\gamma_2}$, p_{T,γ_1} and p_{T,b_1} . As in the case of $pp \rightarrow t\bar{t}\gamma + X$, here we again present in the upper panels the absolute predictions for LO, NLO, NLO_{QCD} and NLO_{prd}. The middle panels display the ratio with respect to NLO_{QCD}, including the scale uncertainties of NLO_{QCD}, and the lower panels show the size of the subleading contributions compared to LO₁.

First, we focus on $p_{T,\gamma_1\gamma_2}$ and $M_{\gamma_1\gamma_2}$. Their importance stems from the fact that both differential cross-section distributions can be seen as the direct and irreducible background to the kinematics of the Higgs boson in $pp \rightarrow t\bar{t}H$ production with the $H \rightarrow \gamma\gamma$ decay. For both observables we find that NLO₁ is the dominant source of NLO corrections, leading to an increase of LO₁ of up to 30% in the tails. The subleading LO and NLO contributions are dominated by NLO₂, due to EW Sudakov logarithms, which amounts to -8% for $p_{T,\gamma_1\gamma_2}$ and -5% for $M_{\gamma_1\gamma_2}$ with respect to LO₁. This results in a decrease of the full calculation by about 5% and 3% , respectively. At the same time, in these phase-space regions, the NLO scale uncertainties are larger by a factor of 2 for $p_{T,\gamma_1\gamma_2}$ and 4 for $M_{\gamma_1\gamma_2}$. The NLO_{prd} prediction fully recovers the complete calculation for $p_{T,\gamma_1\gamma_2}$ and differences of only about 1% can be found for $M_{\gamma_1\gamma_2}$. Thus, NLO_{prd} is more than sufficient to properly describe the shape of the two observables in the presence of subleading LO contributions and subleading NLO corrections.

We then turn to the p_{T,γ_1} differential cross-section distribution, where NLO QCD corrections up to $25\% - 30\%$ can be found. The subleading contributions reduce the NLO calculation by about $5\% - 6\%$ and are therefore slightly larger than those found for the $pp \rightarrow t\bar{t}\gamma$ process. Indeed, in the latter case the difference is about 4% . This small rise is due to the increase in the NLO₂ contribution that we have already observed at the integrated cross-section level. In the case of p_{T,b_1} the difference between NLO_{QCD} and NLO is somewhat enlarged in the tails from 4% for $pp \rightarrow t\bar{t}\gamma$ to 6% for the $pp \rightarrow t\bar{t}\gamma\gamma$ process. This can again be attributed to the increase of the NLO₂ corrections from -10% to -13% , while the size of NLO₃ is slight reduced to $2\% - 3\%$ from $3\% - 4\%$ for $pp \rightarrow t\bar{t}\gamma$. In general, the presence of a second photon already at LO affects the kinematics of the $t\bar{t}$ system in such a way that the large NLO QCD corrections in NLO₁ are reduced for several observables such as p_{T,b_1} or p_{T,b_1b_2} compared to the $pp \rightarrow t\bar{t}\gamma$ process. In particular, for p_{T,b_1} we find a reduction from 95% to 55% . It

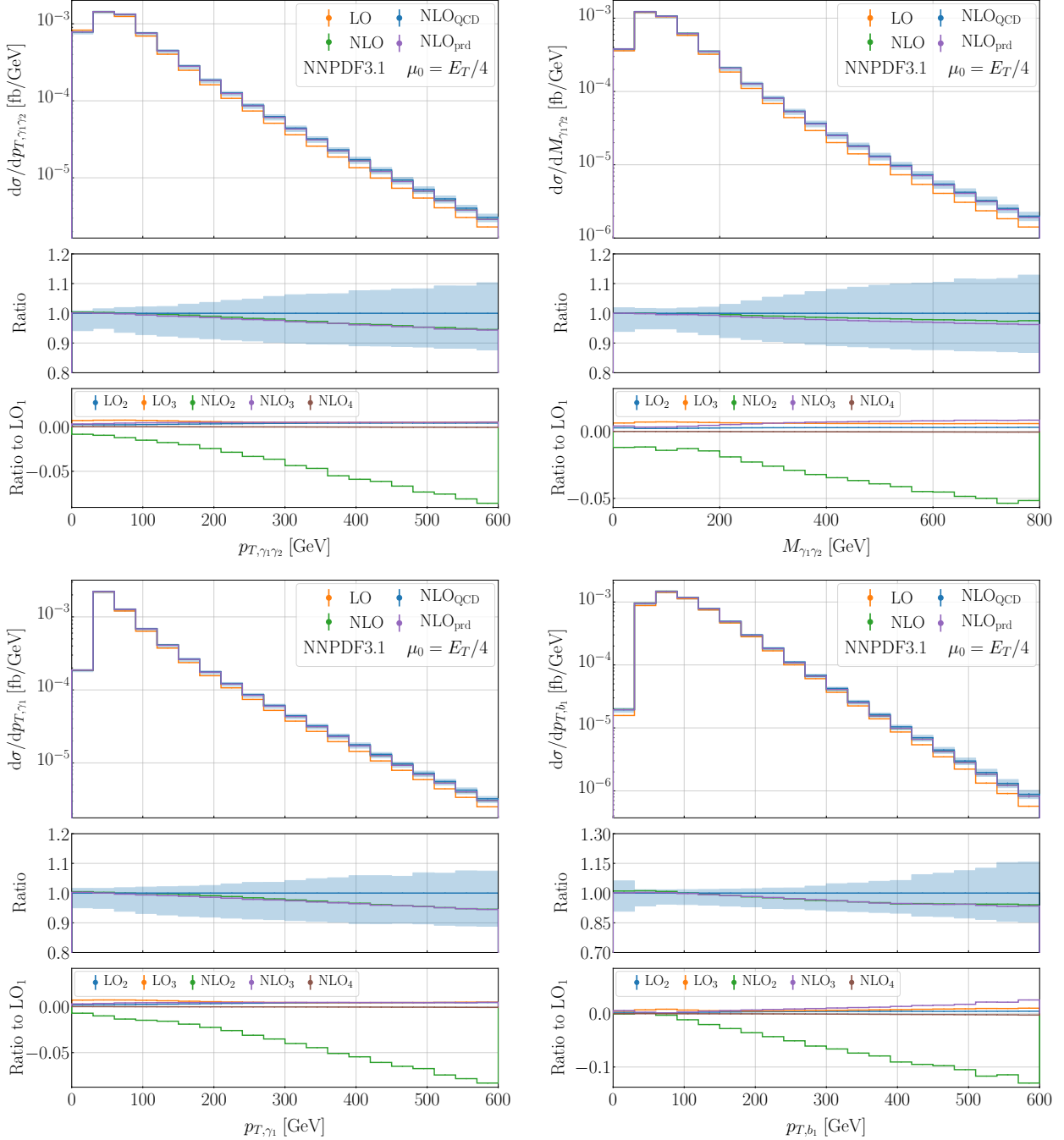


Figure 12. Same as Figure 9 but for the $pp \rightarrow t\bar{t}\gamma\gamma + X$ process in the di-lepton top-quark decay channel and for the observables $p_{T,\gamma_1\gamma_2}$, $M_{\gamma_1\gamma_2}$, p_{T,γ_1} and p_{T,b_1} .

follows directly that the enhancement of NLO₃ in such observables is also reduced. Therefore, the accidental cancellations between NLO₂ and NLO₃, which occurred in the $pp \rightarrow t\bar{t}\gamma$ case, although still present, are substantially reduced.

For comparison purposes and similar to what we have done for photonic observables in case of the $pp \rightarrow t\bar{t}\gamma$ process, also here we show differential cross-section distributions with the alternative scale choice. In detail, in Figure 13 we display $p_{T,\gamma_1\gamma_2}$, $M_{\gamma_1\gamma_2}$ and p_{T,γ_1} for $\mu_R = \mu_F = m_t$. For

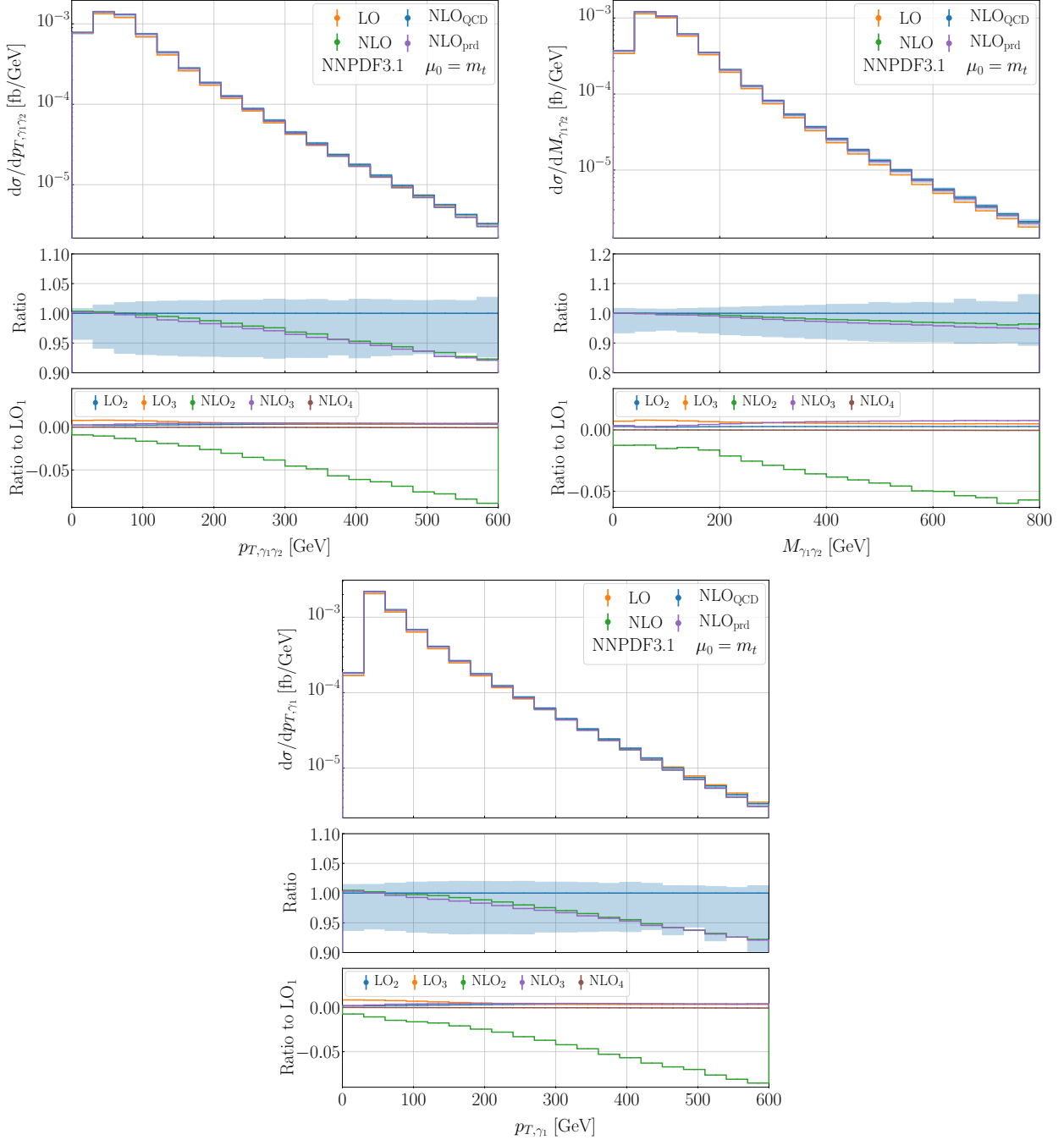


Figure 13. Same as Figure 9 but for the $pp \rightarrow t\bar{t}\gamma\gamma + X$ process in the di-lepton top-quark decay channel and for the observables $p_{T,\gamma_1\gamma_2}$, $M_{\gamma_1\gamma_2}$ and p_{T,γ_1} . Results are shown for $\mu_0 = m_t$.

$p_{T,\gamma_1\gamma_2}$ and $M_{\gamma_1\gamma_2}$, we again find that this scale choice leads to a reduction in the size of the NLO QCD corrections in NLO_1 from about 30% to 10% – 12%. In addition, the scale uncertainties are changed from 12% – 13% to 8% – 10%. Thus, the fixed scale setting not only decreases higher-order corrections in NLO_1 , but also provides improved scale uncertainties. The reduction of higher-order effects in NLO_1 has also a direct impact on the significance of the subleading NLO corrections. In particular, because the relative size of the subleading NLO_2 corrections with respect to LO_1 does not

change for $\mu_0 = m_t$, the overall NLO₂ contribution becomes larger with respect to the complete NLO result. Indeed, we observe the rise of NLO₂ from 5% to 8% as well as from 3% to 4% for $p_{T,\gamma_1\gamma_2}$ and $M_{\gamma_1\gamma_2}$, respectively. Furthermore, for $p_{T,\gamma_1\gamma_2}$ the subleading NLO corrections become as large as the corresponding scale uncertainties of NLO_{QCD}, which are also equal in size to those of the complete NLO result. The same can be observed for the third differential cross-section distribution, namely for p_{T,γ_1} . In this case the NLO₁ contribution is reduced in the tails from 20% for $\mu_0 = E_T/4$ to 5% for $\mu_0 = m_t$. This increases the importance of the NLO₂ contribution again and leads to a reduction of the difference between NLO₂ and NLO by about 8% compared to 5% – 6% for $\mu_0 = E_T/4$. Consequently, the subleading contributions are of similar size as the scale uncertainties of the NLO_{QCD} result, and are at the level of 10%. Lastly, for all three photonic observables, the complete NLO predictions for the two scale settings differ by at most 4% in the tails and are therefore within the respective scale uncertainties.

7 Summary

We have presented the first calculation of the complete set of NLO corrections to $pp \rightarrow t\bar{t}\gamma + X$ and $pp \rightarrow t\bar{t}\gamma\gamma + X$ including top-quark decays at the LHC with $\sqrt{s} = 13$ TeV. In order to study the di-lepton top-quark decay channel we have employed the Narrow Width Approximation that works in the $\Gamma/m \rightarrow 0$ limit and preserves spin correlations. In this approximation all contributions without two resonant top quarks and W gauge bosons are simply neglected. In our calculations we have included the dominant LO contribution at $\mathcal{O}(\alpha_s^2\alpha^5)$ for $pp \rightarrow t\bar{t}\gamma + X$ and $\mathcal{O}(\alpha_s^2\alpha^6)$ for $pp \rightarrow t\bar{t}\gamma\gamma + X$ as well as the corresponding NLO QCD corrections. Furthermore, all subleading LO contributions and all remaining NLO corrections are also taken into account. In addition, NLO corrections, as well as photon radiation are consistently included in the production phase as well as in all decay stages of the process. Even if we have considered the di-lepton decay channel of the top quark, the extension to hadronic decays of the W boson can be straightforwardly incorporated into our framework.

On the technical side, to perform these calculations, we have extended the Nagy-Soper subtraction scheme as implemented in the HELAC-DIPOLES Monte Carlo program for calculations with QED-like singularities and modified the structure of the program to allow the simultaneous calculation of all contributions at different orders in α_s and α .

The main findings of this paper apply to both processes and can be summarised as follows. At the integrated fiducial cross-section level, as well as for all the angular distributions we examined, the subleading LO contributions and subleading NLO corrections are negligibly small with respect to the NLO scale uncertainties of the complete result. On the other hand, the dominant NLO₁ contribution is essential for precise predictions, as it leads to a reduction in scale uncertainties from about 30% to 6%. Furthermore, it also introduces a change in the normalisation as well as in the shape of various differential cross-section distributions. In general, the inclusion of the subleading contributions has been found to be essential only in the tails of dimensionful observables due to one-loop EW Sudakov logarithms. Indeed, the presence of the EW Sudakov logarithms in NLO₂ leads to a reduction in the tails of up to 10% compared to the NLO_{QCD} result. Moreover, the NLO₂ contribution can be as large as the NLO_{QCD} scale uncertainties, potentially affecting the comparison between theoretical predictions and experimental measurements. In addition, for certain observables affected by large higher-order real-emission QCD corrections, e.g. for p_{T,b_1b_2} , the NLO₃ contribution can be enhanced from a few percent up to 10% with respect to LO₁. As the origins of the subleading NLO₂ and NLO₃ contributions are very different and there are random cancellations between them, they should always be considered together. We note here, that both the accidental cancellations between NLO₂ and NLO₃

as well as the size of real-emission QCD corrections depend on the exact event selection and can be substantially affected, for example, by applying a veto on an additional jet. Finally, the subleading LO contributions and the NLO₄ contribution are negligibly small at the integrated and differential fiducial cross-section level with respect to the NLO scale uncertainties.

An important finding of the paper is that the NLO_{prd} approximation models the complete NLO result very well. Indeed, differences of up to 2% only are found for some leptonic and/or photonic observables, but these are negligible compared to the NLO scale uncertainties of the complete result. We remind the readers that in NLO_{prd}, all LO contributions as well as NLO₁ are fully included in both the $t\bar{t}\gamma(\gamma)$ production and decays of the top-quark pair. However, the subleading NLO corrections (NLO₂, NLO₃, NLO₄) are only included in the production stage of the $t\bar{t}\gamma(\gamma)$ process. The same applies to photon radiation for these three NLO contributions. The NLO_{prd} approximation not only provides a great simplification of higher-order calculations, especially when it comes to the real emission corrections, but will ultimately also be of great benefit when matching NLO_{prd} predictions to parton shower programs.

Acknowledgments

We thank Ansgar Denner and Mathieu Pellen for providing us with the results for the NLO EW corrections to the $pp \rightarrow e^+ \nu_e \mu^- \bar{\nu}_\mu b\bar{b} + X$ process that helped to cross check our implementation of the EW corrections in the HELAC-DIPOLES framework.

This work was supported by the Deutsche Forschungsgemeinschaft (DFG) under grant 396021762 – TRR 257: *P3H - Particle Physics Phenomenology after the Higgs Discovery*. Support by a grant of the Bundesministerium für Bildung und Forschung (BMBF) is additionally acknowledged.

The authors gratefully acknowledge the computing time provided to them at the NHR Center NHR4CES at RWTH Aachen University (project number p0020216). This is funded by the Federal Ministry of Education and Research, and the state governments participating on the basis of the resolutions of the GWK for national high performance computing at universities.

References

- [1] F. Maltoni, D. Pagani and I. Tsinikos, *Associated production of a top-quark pair with vector bosons at NLO in QCD: impact on $t\bar{t}H$ searches at the LHC*, *JHEP* **02** (2016) 113 [[1507.05640](#)].
- [2] K. Agashe et al., *Report of the Topical Group on Top quark physics and heavy flavor production for Snowmass 2021*, [2209.11267](#).
- [3] K. Melnikov, M. Schulze and A. Scharf, *QCD corrections to top quark pair production in association with a photon at hadron colliders*, *Phys. Rev. D* **83** (2011) 074013 [[1102.1967](#)].
- [4] G. Bevilacqua, H. B. Hartanto, M. Kraus, T. Weber and M. Worek, *Off-shell vs on-shell modelling of top quarks in photon associated production*, *JHEP* **03** (2020) 154 [[1912.09999](#)].
- [5] U. Baur, M. Buice and L. H. Orr, *Direct measurement of the top quark charge at hadron colliders*, *Phys. Rev. D* **64** (2001) 094019 [[hep-ph/0106341](#)].
- [6] D0 collaboration, *Measurement of the Electric Charge of the Top Quark in $t\bar{t}$ Events*, *Phys. Rev. D* **90** (2014) 051101 [[1407.4837](#)].
- [7] ATLAS collaboration, *Measurement of the top quark charge in pp collisions at $\sqrt{s} = 7$ TeV with the ATLAS detector*, *JHEP* **11** (2013) 031 [[1307.4568](#)].
- [8] U. Baur, A. Juste, L. H. Orr and D. Rainwater, *Probing electroweak top quark couplings at hadron colliders*, *Phys. Rev. D* **71** (2005) 054013 [[hep-ph/0412021](#)].

- [9] A. O. Bouzas and F. Larios, *Electromagnetic dipole moments of the Top quark*, *Phys. Rev. D* **87** (2013) 074015 [[1212.6575](#)].
- [10] R. Röntsch and M. Schulze, *Probing top-Z dipole moments at the LHC and ILC*, *JHEP* **08** (2015) 044 [[1501.05939](#)].
- [11] M. Schulze and Y. Soreq, *Pinning down electroweak dipole operators of the top quark*, *Eur. Phys. J. C* **76** (2016) 466 [[1603.08911](#)].
- [12] O. Bessidskaia Bylund, F. Maltoni, I. Tsinikos, E. Vryonidou and C. Zhang, *Probing top quark neutral couplings in the Standard Model Effective Field Theory at NLO in QCD*, *JHEP* **05** (2016) 052 [[1601.08193](#)].
- [13] J. A. Aguilar-Saavedra, E. Álvarez, A. Juste and F. Rubbo, *Shedding light on the $t\bar{t}$ asymmetry: the photon handle*, *JHEP* **04** (2014) 188 [[1402.3598](#)].
- [14] J. A. Aguilar-Saavedra, *Single lepton charge asymmetries in $t\bar{t}$ and $t\bar{t}\gamma$ production at the LHC*, *Eur. Phys. J. C* **78** (2018) 434 [[1802.05721](#)].
- [15] J. Bergner and M. Schulze, *The top quark charge asymmetry in $t\bar{t}\gamma$ production at the LHC*, *Eur. Phys. J. C* **79** (2019) 189 [[1812.10535](#)].
- [16] D. Pagani, H.-S. Shao, I. Tsinikos and M. Zaro, *Automated EW corrections with isolated photons: $t\bar{t}\gamma$, $t\bar{t}\gamma\gamma$ and $t\gamma j$ as case studies*, *JHEP* **09** (2021) 155 [[2106.02059](#)].
- [17] R. Barcelo, A. Carmona, M. Masip and J. Santiago, *Stealth gluons at hadron colliders*, *Phys. Lett. B* **707** (2012) 88 [[1106.4054](#)].
- [18] G. Marques Tavares and M. Schmaltz, *Explaining the $t\bar{t}$ asymmetry with a light axigluon*, *Phys. Rev. D* **84** (2011) 054008 [[1107.0978](#)].
- [19] E. Alvarez, L. Da Rold, J. I. S. Vietto and A. Szykman, *Phenomenology of a light gluon resonance in top-physics at Tevatron and LHC*, *JHEP* **09** (2011) 007 [[1107.1473](#)].
- [20] J. A. Aguilar-Saavedra and M. Perez-Victoria, *Shaping the top asymmetry*, *Phys. Lett. B* **705** (2011) 228 [[1107.2120](#)].
- [21] E. Alvarez, E. Coluccio Leskow, J. Drobnak and J. F. Kamenik, *Leptonic Monotops at LHC*, *Phys. Rev. D* **89** (2014) 014016 [[1310.7600](#)].
- [22] D. Stremmer and M. Worek, *Associated production of a top-quark pair with two isolated photons at the LHC through NLO in QCD*, *JHEP* **08** (2023) 179 [[2306.16968](#)].
- [23] CDF collaboration, *Evidence for $t\bar{t}\gamma$ Production and Measurement of $\sigma_{t\bar{t}\gamma}/\sigma_{t\bar{t}}$* , *Phys. Rev. D* **84** (2011) 031104 [[1106.3970](#)].
- [24] ATLAS collaboration, *Observation of top-quark pair production in association with a photon and measurement of the $t\bar{t}\gamma$ production cross section in pp collisions at $\sqrt{s} = 7$ TeV using the ATLAS detector*, *Phys. Rev. D* **91** (2015) 072007 [[1502.00586](#)].
- [25] ATLAS collaboration, *Measurement of the $t\bar{t}\gamma$ production cross section in proton-proton collisions at $\sqrt{s} = 8$ TeV with the ATLAS detector*, *JHEP* **11** (2017) 086 [[1706.03046](#)].
- [26] CMS collaboration, *Measurement of the semileptonic $t\bar{t}\gamma$ production cross section in pp collisions at $\sqrt{s} = 8$ TeV*, *JHEP* **10** (2017) 006 [[1706.08128](#)].
- [27] CMS collaboration, *Measurement of the inclusive and differential $t\bar{t}\gamma$ cross sections in the single-lepton channel and EFT interpretation at $\sqrt{s} = 13$ TeV*, *JHEP* **12** (2021) 180 [[2107.01508](#)].
- [28] ATLAS collaboration, *Measurements of inclusive and differential fiducial cross-sections of $t\bar{t}\gamma$ production in leptonic final states at $\sqrt{s} = 13$ TeV in ATLAS*, *Eur. Phys. J. C* **79** (2019) 382 [[1812.01697](#)].

- [29] ATLAS collaboration, *Measurements of inclusive and differential cross-sections of combined $t\bar{t}\gamma$ and $tW\gamma$ production in the $e\mu$ channel at 13 TeV with the ATLAS detector*, *JHEP* **09** (2020) 049 [[2007.06946](#)].
- [30] CMS collaboration, *Measurement of the inclusive and differential $t\bar{t}\gamma$ cross sections in the dilepton channel and effective field theory interpretation in proton-proton collisions at $\sqrt{s} = 13$ TeV*, *JHEP* **05** (2022) 091 [[2201.07301](#)].
- [31] ATLAS collaboration, *Measurement of the charge asymmetry in top-quark pair production in association with a photon with the ATLAS experiment*, *Phys. Lett. B* **843** (2023) 137848 [[2212.10552](#)].
- [32] P.-F. Duan, W.-G. Ma, R.-Y. Zhang, L. Han, L. Guo and S.-M. Wang, *QCD corrections to associated production of $t\bar{t}\gamma$ at hadron colliders*, *Phys. Rev. D* **80** (2009) 014022 [[0907.1324](#)].
- [33] P.-F. Duan, R.-Y. Zhang, W.-G. Ma, L. Han, L. Guo and S.-M. Wang, *Next-to-leading order QCD corrections to $t\bar{t}\gamma$ production at the 7 TeV LHC*, *Chin. Phys. Lett.* **28** (2011) 111401 [[1110.2315](#)].
- [34] P.-F. Duan, Y. Zhang, Y. Wang, M. Song and G. Li, *Electroweak corrections to top quark pair production in association with a hard photon at hadron colliders*, *Phys. Lett. B* **766** (2017) 102 [[1612.00248](#)].
- [35] N. Kidonakis and A. Tonerio, *Higher-order corrections in $t\bar{t}\gamma$ cross sections*, *Phys. Rev. D* **107** (2023) 034013 [[2212.00096](#)].
- [36] A. Kardos and Z. Trócsányi, *Hadroproduction of t anti- t pair in association with an isolated photon at NLO accuracy matched with parton shower*, *JHEP* **05** (2015) 090 [[1406.2324](#)].
- [37] G. Bevilacqua, H. B. Hartanto, M. Kraus, T. Weber and M. Worek, *Hard Photons in Hadroproduction of Top Quarks with Realistic Final States*, *JHEP* **10** (2018) 158 [[1803.09916](#)].
- [38] J. Alwall, R. Frederix, S. Frixione, V. Hirschi, F. Maltoni, O. Mattelaer et al., *The automated computation of tree-level and next-to-leading order differential cross sections, and their matching to parton shower simulations*, *JHEP* **07** (2014) 079 [[1405.0301](#)].
- [39] A. Kardos and Z. Trócsányi, *Hadroproduction of $t\bar{t}$ pair with two isolated photons with PowHel*, *Nucl. Phys. B* **897** (2015) 717 [[1408.0278](#)].
- [40] H. van Deurzen, R. Frederix, V. Hirschi, G. Luisoni, P. Mastrolia and G. Ossola, *Spin Polarisation of $t\bar{t}\gamma\gamma$ production at NLO+PS with GoSam interfaced to MadGraph5_aMC@NLO*, *Eur. Phys. J. C* **76** (2016) 221 [[1509.02077](#)].
- [41] A. Denner, S. Dittmaier, M. Roth and D. Wackerroth, *Predictions for all processes $e^+e^- \rightarrow 4$ fermions + γ* , *Nucl. Phys. B* **560** (1999) 33 [[hep-ph/9904472](#)].
- [42] A. Denner, S. Dittmaier, M. Roth and L. H. Wieders, *Electroweak corrections to charged-current $e^+e^- \rightarrow 4$ fermion processes: Technical details and further results*, *Nucl. Phys. B* **724** (2005) 247 [[hep-ph/0505042](#)].
- [43] K. Melnikov and M. Schulze, *NLO QCD corrections to top quark pair production and decay at hadron colliders*, *JHEP* **08** (2009) 049 [[0907.3090](#)].
- [44] K. Melnikov, A. Scharf and M. Schulze, *Top quark pair production in association with a jet: QCD corrections and jet radiation in top quark decays*, *Phys. Rev. D* **85** (2012) 054002 [[1111.4991](#)].
- [45] J. M. Campbell and R. K. Ellis, *Top-Quark Processes at NLO in Production and Decay*, *J. Phys. G* **42** (2015) 015005 [[1204.1513](#)].
- [46] A. Behring, M. Czakon, A. Mitov, A. S. Papanastasiou and R. Poncelet, *Higher order corrections to spin correlations in top quark pair production at the LHC*, *Phys. Rev. Lett.* **123** (2019) 082001 [[1901.05407](#)].
- [47] M. Czakon, A. Mitov and R. Poncelet, *NNLO QCD corrections to leptonic observables in top-quark pair production and decay*, *JHEP* **05** (2021) 212 [[2008.11133](#)].
- [48] R. V. Harlander, S. Y. Klein and M. Lipp, *FeynGame*, *Comput. Phys. Commun.* **256** (2020) 107465 [[2003.00896](#)].

- [49] R. Frederix, D. Pagani and M. Zaro, *Large NLO corrections in $t\bar{t}W^\pm$ and $t\bar{t}t\bar{t}$ hadroproduction from supposedly subleading EW contributions*, *JHEP* **02** (2018) 031 [[1711.02116](#)].
- [50] R. Frederix, S. Frixione, V. Hirschi, D. Pagani, H. S. Shao and M. Zaro, *The automation of next-to-leading order electroweak calculations*, *JHEP* **07** (2018) 185 [[1804.10017](#)].
- [51] A. Denner and M. Pellen, *NLO electroweak corrections to off-shell top-antitop production with leptonic decays at the LHC*, *JHEP* **08** (2016) 155 [[1607.05571](#)].
- [52] A. Denner, D. Lombardi and G. Pelliccioli, *Complete NLO corrections to off-shell $t\bar{t}Z$ production at the LHC*, *JHEP* **09** (2023) 072 [[2306.13535](#)].
- [53] G. Bevilacqua, M. Czakon, M. Kubocz and M. Worek, *Complete Nagy-Soper subtraction for next-to-leading order calculations in QCD*, *JHEP* **10** (2013) 204 [[1308.5605](#)].
- [54] S. Catani and M. H. Seymour, *A General algorithm for calculating jet cross-sections in NLO QCD*, *Nucl. Phys. B* **485** (1997) 291 [[hep-ph/9605323](#)].
- [55] S. Catani, S. Dittmaier, M. H. Seymour and Z. Trocsanyi, *The Dipole formalism for next-to-leading order QCD calculations with massive partons*, *Nucl. Phys. B* **627** (2002) 189 [[hep-ph/0201036](#)].
- [56] G. Bevilacqua, M. Lupattelli, D. Stremmer and M. Worek, *Study of additional jet activity in top quark pair production and decay at the LHC*, *Phys. Rev. D* **107** (2023) 114027 [[2212.04722](#)].
- [57] A. Denner and S. Dittmaier, *Electroweak Radiative Corrections for Collider Physics*, *Phys. Rept.* **864** (2020) 1 [[1912.06823](#)].
- [58] Z. Nagy and Z. Trocsanyi, *Next-to-leading order calculation of four jet observables in electron positron annihilation*, *Phys. Rev. D* **59** (1999) 014020 [[hep-ph/9806317](#)].
- [59] Z. Nagy, *Next-to-leading order calculation of three jet observables in hadron hadron collision*, *Phys. Rev. D* **68** (2003) 094002 [[hep-ph/0307268](#)].
- [60] G. Bevilacqua, M. Czakon, C. G. Papadopoulos, R. Pittau and M. Worek, *Assault on the NLO Wishlist: $pp \rightarrow t\bar{t}b\bar{b}$* , *JHEP* **09** (2009) 109 [[0907.4723](#)].
- [61] M. Czakon, H. B. Hartanto, M. Kraus and M. Worek, *Matching the Nagy-Soper parton shower at next-to-leading order*, *JHEP* **06** (2015) 033 [[1502.00925](#)].
- [62] M. Czakon, C. G. Papadopoulos and M. Worek, *Polarizing the Dipoles*, *JHEP* **08** (2009) 085 [[0905.0883](#)].
- [63] Z. Nagy and D. E. Soper, *Parton showers with quantum interference*, *JHEP* **09** (2007) 114 [[0706.0017](#)].
- [64] J. M. Campbell, R. K. Ellis and F. Tramontano, *Single top production and decay at next-to-leading order*, *Phys. Rev. D* **70** (2004) 094012 [[hep-ph/0408158](#)].
- [65] M. Jezabek and J. H. Kuhn, *QCD Corrections to Semileptonic Decays of Heavy Quarks*, *Nucl. Phys. B* **314** (1989) 1.
- [66] A. Czarnecki, *QCD corrections to the decay $t \rightarrow Wb$ in dimensional regularization*, *Phys. Lett. B* **252** (1990) 467.
- [67] L. Basso, S. Dittmaier, A. Huss and L. Oggero, *Techniques for the treatment of IR divergences in decay processes at NLO and application to the top-quark decay*, *Eur. Phys. J. C* **76** (2016) 56 [[1507.04676](#)].
- [68] T. Binoth, G. Ossola, C. G. Papadopoulos and R. Pittau, *NLO QCD corrections to tri-boson production*, *JHEP* **06** (2008) 082 [[0804.0350](#)].
- [69] G. Bevilacqua, H. B. Hartanto, M. Kraus and M. Worek, *Off-shell Top Quarks with One Jet at the LHC: A comprehensive analysis at NLO QCD*, *JHEP* **11** (2016) 098 [[1609.01659](#)].
- [70] A. van Hameren, *PARNI for importance sampling and density estimation*, *Acta Phys. Polon. B* **40** (2009) 259 [[0710.2448](#)].

- [71] A. van Hameren, *Kaleu: A General-Purpose Parton-Level Phase Space Generator*, [1003.4953](#).
- [72] J. Alwall et al., *A Standard format for Les Houches event files*, *Comput. Phys. Commun.* **176** (2007) 300 [[hep-ph/0609017](#)].
- [73] Z. Bern, L. J. Dixon, F. Febres Cordero, S. Höche, H. Ita, D. A. Kosower et al., *Ntuples for NLO Events at Hadron Colliders*, *Comput. Phys. Commun.* **185** (2014) 1443 [[1310.7439](#)].
- [74] S. Actis, A. Denner, L. Hofer, J.-N. Lang, A. Scharf and S. Uccirati, *RECOLA: REcursive Computation of One-Loop Amplitudes*, *Comput. Phys. Commun.* **214** (2017) 140 [[1605.01090](#)].
- [75] S. Actis, A. Denner, L. Hofer, A. Scharf and S. Uccirati, *Recursive generation of one-loop amplitudes in the Standard Model*, *JHEP* **04** (2013) 037 [[1211.6316](#)].
- [76] P. Draggiotis, R. H. P. Kleiss and C. G. Papadopoulos, *On the computation of multigluon amplitudes*, *Phys. Lett. B* **439** (1998) 157 [[hep-ph/9807207](#)].
- [77] P. D. Draggiotis, R. H. P. Kleiss and C. G. Papadopoulos, *Multijet production in hadron collisions*, *Eur. Phys. J. C* **24** (2002) 447 [[hep-ph/0202201](#)].
- [78] A. van Hameren, *Multi-gluon one-loop amplitudes using tensor integrals*, *JHEP* **07** (2009) 088 [[0905.1005](#)].
- [79] A. Denner, S. Dittmaier and L. Hofer, *Collier: a fortran-based Complex One-Loop LIBrary in Extended Regularizations*, *Comput. Phys. Commun.* **212** (2017) 220 [[1604.06792](#)].
- [80] A. Denner and S. Dittmaier, *Reduction schemes for one-loop tensor integrals*, *Nucl. Phys. B* **734** (2006) 62 [[hep-ph/0509141](#)].
- [81] A. Denner and S. Dittmaier, *Reduction of one loop tensor five point integrals*, *Nucl. Phys. B* **658** (2003) 175 [[hep-ph/0212259](#)].
- [82] A. Denner and S. Dittmaier, *Scalar one-loop 4-point integrals*, *Nucl. Phys. B* **844** (2011) 199 [[1005.2076](#)].
- [83] G. Ossola, C. G. Papadopoulos and R. Pittau, *CutTools: A Program implementing the OPP reduction method to compute one-loop amplitudes*, *JHEP* **03** (2008) 042 [[0711.3596](#)].
- [84] A. van Hameren, *OneLoop: For the evaluation of one-loop scalar functions*, *Comput. Phys. Commun.* **182** (2011) 2427 [[1007.4716](#)].
- [85] G. Ossola, C. G. Papadopoulos and R. Pittau, *Reducing full one-loop amplitudes to scalar integrals at the integrand level*, *Nucl. Phys. B* **763** (2007) 147 [[hep-ph/0609007](#)].
- [86] F. Buccioni, S. Pozzorini and M. Zoller, *On-the-fly reduction of open loops*, *Eur. Phys. J. C* **78** (2018) 70 [[1710.11452](#)].
- [87] A. Denner, J.-N. Lang and M. Pellen, *Full NLO QCD corrections to off-shell $t\bar{t}b\bar{b}$ production*, *Phys. Rev. D* **104** (2021) 056018 [[2008.00918](#)].
- [88] A. Denner, J.-N. Lang and S. Uccirati, *Recola2: REcursive Computation of One-Loop Amplitudes 2*, *Comput. Phys. Commun.* **224** (2018) 346 [[1711.07388](#)].
- [89] A. Denner, G. Weiglein and S. Dittmaier, *Application of the background field method to the electroweak standard model*, *Nucl. Phys. B* **440** (1995) 95 [[hep-ph/9410338](#)].
- [90] A. Denner, J.-N. Lang and S. Uccirati, *NLO electroweak corrections in extended Higgs Sectors with RECOLA2*, *JHEP* **07** (2017) 087 [[1705.06053](#)].
- [91] A. Denner and S. Dittmaier, *The Complex-mass scheme for perturbative calculations with unstable particles*, *Nucl. Phys. B Proc. Suppl.* **160** (2006) 22 [[hep-ph/0605312](#)].
- [92] A. Sirlin, *Radiative Corrections in the SU(2)-L x U(1) Theory: A Simple Renormalization Framework*, *Phys. Rev. D* **22** (1980) 971.

- [93] A. Denner, *Techniques for calculation of electroweak radiative corrections at the one loop level and results for W physics at LEP-200*, *Fortsch. Phys.* **41** (1993) 307 [[0709.1075](#)].
- [94] W. F. L. Hollik, *Radiative Corrections in the Standard Model and their Role for Precision Tests of the Electroweak Theory*, *Fortsch. Phys.* **38** (1990) 165.
- [95] W. J. Marciano and A. Sirlin, *Radiative Corrections to Neutrino Induced Neutral Current Phenomena in the SU(2)-L x U(1) Theory*, *Phys. Rev. D* **22** (1980) 2695.
- [96] A. Manohar, P. Nason, G. P. Salam and G. Zanderighi, *How bright is the proton? A precise determination of the photon parton distribution function*, *Phys. Rev. Lett.* **117** (2016) 242002 [[1607.04266](#)].
- [97] NNPDF collaboration, *Parton distributions from high-precision collider data*, *Eur. Phys. J. C* **77** (2017) 663 [[1706.00428](#)].
- [98] A. V. Manohar, P. Nason, G. P. Salam and G. Zanderighi, *The Photon Content of the Proton*, *JHEP* **12** (2017) 046 [[1708.01256](#)].
- [99] NNPDF collaboration, *Illuminating the photon content of the proton within a global PDF analysis*, *SciPost Phys.* **5** (2018) 008 [[1712.07053](#)].
- [100] A. Buckley, J. Ferrando, S. Lloyd, K. Nordström, B. Page, M. Rüfenacht et al., *LHAPDF6: parton density access in the LHC precision era*, *Eur. Phys. J. C* **75** (2015) 132 [[1412.7420](#)].
- [101] PARTICLE DATA GROUP collaboration, *Review of Particle Physics*, *PTEP* **2022** (2022) 083C01.
- [102] A. Denner, S. Dittmaier, S. Kallweit and S. Pozzorini, *NLO QCD corrections to off-shell top-antitop production with leptonic decays at hadron colliders*, *JHEP* **10** (2012) 110 [[1207.5018](#)].
- [103] M. Cacciari, G. P. Salam and G. Soyez, *The anti- k_t jet clustering algorithm*, *JHEP* **04** (2008) 063 [[0802.1189](#)].
- [104] S. Frixione, *Isolated photons in perturbative QCD*, *Phys. Lett. B* **429** (1998) 369 [[hep-ph/9801442](#)].
- [105] A. Denner, S. Dittmaier, M. Hecht and C. Pasold, *NLO QCD and electroweak corrections to $W + \gamma$ production with leptonic W -boson decays*, *JHEP* **04** (2015) 018 [[1412.7421](#)].
- [106] A. Denner, S. Dittmaier, M. Hecht and C. Pasold, *NLO QCD and electroweak corrections to $Z + \gamma$ production with leptonic Z -boson decays*, *JHEP* **02** (2016) 057 [[1510.08742](#)].
- [107] A. Denner and R. Feger, *NLO QCD corrections to off-shell top-antitop production with leptonic decays in association with a Higgs boson at the LHC*, *JHEP* **11** (2015) 209 [[1506.07448](#)].
- [108] G. Bevilacqua, H. B. Hartanto, M. Kraus, T. Weber and M. Worek, *Towards constraining Dark Matter at the LHC: Higher order QCD predictions for $t\bar{t} + Z(Z \rightarrow \nu_\ell \bar{\nu}_\ell)$* , *JHEP* **11** (2019) 001 [[1907.09359](#)].
- [109] D. Stremmer and M. Worek, *Production and decay of the Higgs boson in association with top quarks*, *JHEP* **02** (2022) 196 [[2111.01427](#)].

An assessment of Υ -states above $B\bar{B}$ -threshold using a constituent-quark-model based meson-meson coupled-channels framework

P. G. Ortega,^{1,2,*} D. R. Entem,^{1,2,†} F. Fernández,^{2,‡} and J. Segovia^{3,§}

¹*Departamento de Física Fundamental, Universidad de Salamanca, E-37008 Salamanca, Spain*

²*Instituto Universitario de Física Fundamental y Matemáticas (IUFFyM),
Universidad de Salamanca, E-37008 Salamanca, Spain*

³*Departamento de Sistemas Físicos, Químicos y Naturales,
Universidad Pablo de Olavide, E-41013 Sevilla, Spain*

(Dated: March 7, 2024)

The $\Upsilon(10753)$ state has been recently observed by the Belle and Belle II collaborations with enough global significance to motivate an assessment of the high-energy spectrum usually predicted by any reasonable *naïve* quark model. In the framework of a constituent quark model which satisfactorily describes a wide range of properties of conventional hadrons containing heavy quarks, the quark-antiquark and meson-meson degrees of freedom have been incorporated with the goal of elucidating the influence of open-bottom meson-meson thresholds into the Υ states whose masses are within the energy range of the $\Upsilon(10753)$'s mass. It is well known that such effects could be relevant enough as to generate dynamically new states and thus provide a plausible explanation of the nature of the $\Upsilon(10753)$ state. In particular, we have performed a coupled-channels calculation in which the bare states $\Upsilon(4S)$, $\Upsilon(3D)$, $\Upsilon(5S)$ and $\Upsilon(4D)$ are considered together with the threshold channels $B\bar{B}$, $B\bar{B}^*$, $B^*\bar{B}^*$, $B_s\bar{B}_s$, $B_s\bar{B}_s^*$ and $B_s^*\bar{B}_s^*$. Among the results we have described, the following conclusions are of particular interest: (i) a richer complex spectrum is gained when thresholds are present and bare bound states are sufficiently non-relativistic; (ii) those poles obtained in the complex energy plane do not have to appear as simple peaks in the relevant cross sections; and (iii) the $\Upsilon(10750)$ candidate is interpreted as a dressed hadronic resonance whose structure is an equally mixture of a conventional $b\bar{b}$ state and $B^*\bar{B}^*$ molecule.

I. INTRODUCTION

The so-called Υ -family, also known as bottomonia, are bound states made of a b -quark and its antiquark, \bar{b} , with quantum numbers $J^{PC} = 1^{--}$. They were identified for the first time by the E288 Collaboration at Fermilab in 1977 while studying proton scattering on Cu and Pb targets in an energy regime of muon-antimuon invariant mass larger than 5 GeV [1, 2]. The three observed states were called $\Upsilon(1S)$, $\Upsilon(2S)$ and $\Upsilon(3S)$; later, they were better studied at various e^+e^- storage rings and through their radiative decays into the $\chi_{bJ}(2P)$ and $\chi_{bJ}(1P)$ states, with $J = 0, 1, 2$, in a series of experiments in the 1980s [3–6]. Despite such early experimental efforts, during the next two decades there were no significant contributions to the spectrum of the Υ -family, except the presumably radial excitations of S -wave nature $\Upsilon(4S)$, $\Upsilon(10860)$ and $\Upsilon(11020)$ [7, 8]. This has been largely because the B -factories were not considered ideal facilities for the study of the bottomonium system since their beam energy was tuned to peak at the $\Upsilon(4S)$ mass, 10579 MeV, which decays in almost 100% of cases to a $B\bar{B}$ pair.

The situation has changed dramatically in the last twenty years with more than two dozens of unconven-

tional charmonium- and bottomonium-like states, the so-called XYZ mesons, observed at B-factories (BaBar, Belle and CLEO), τ -charm facilities (CLEO-c and BESIII) and also proton-(anti-)proton colliders (CDF, D0, LHCb, ATLAS and CMS). For an extensive presentation of the status of heavy quarkonium physics, the reader is referred to several reviews [9–29].

Within the Υ -family, the Belle collaboration [30] reported in 2019 a cross section measurement of the $e^+e^- \rightarrow \pi^+\pi^-\Upsilon(nS)$, with $n = 1, 2, 3$, at energies from 10.52 to 11.02 GeV, observing a new structure, $\Upsilon(10753)$, with Breit-Wigner parameters:

$$M = (10752.7 \pm 5.9_{-1.1}^{+0.7}) \text{ MeV}, \quad (1)$$

$$\Gamma = (35.5_{-11.3}^{+17.6} {}_{-3.3}^{+3.9}) \text{ MeV}, \quad (2)$$

where the first error is statistical and the second is systematic. The global significance of the new resonance was 5.2 standard deviations, including systematic uncertainty. Later on, the Belle II collaboration [31] reported in 2022 the first observation of $\omega\chi_{bJ}(1P)$ ($J = 0, 1, 2$) signals at $\sqrt{s} = 10.745$ GeV. By combining Belle II data with Belle results at $\sqrt{s} = 10.867$ GeV, they find energy dependencies of the Born cross sections for $e^+e^- \rightarrow \omega\chi_{b1,b2}(1P)$ to be consistent with the shape of the $\Upsilon(10753)$ resonance; this time, the Breit-Wigner parameters were

$$M = (10753 \pm 6) \text{ MeV}, \quad \Gamma = (36_{-12}^{+18}) \text{ MeV}, \quad (3)$$

and the suggested quantum numbers $J^P = 1^-$.

Note also that experimentalists have been able to distinguish the $\Upsilon(1^3D_2)$ state of the triplet $\Upsilon(1^3D_J)$,

* pgortega@usal.es

† entem@usal.es

‡ fdz@usal.es

§ jsegovia@upo.es

with $J = 1, 2, 3$ [32, 33]. In Ref. [33], the $\Upsilon(1^3D_2)$ was observed through the $\Upsilon(3S) \rightarrow \gamma\gamma\Upsilon(1^3D_J) \rightarrow \gamma\gamma\pi^+\pi^-\Upsilon(1S)$ decay chain with a significance of 5.8σ , including systematic uncertainties, and a mass of $(10164.5 \pm 0.8 \pm 0.5)\text{MeV}$. For the other two almost-degenerate members of the $\Upsilon(1^3D_J)$ spin-triplet, $\Upsilon(1^3D_1)$ and $\Upsilon(1^3D_3)$, the significances were much lower, 1.8 and 1.6 respectively, and thus no experimental observation could be claimed.

An enormous theoretical effort has followed the experimental discoveries; in particular, focusing on the bottomonium sector, one can highlight the work done using Lattice-regularized QCD [34, 35], functional methods [36–39], QCD sum rules [40–42], effective field theories [43–46] and quark models [47–51]. Most of the mentioned references focus on the description of conventional bottomonium. This is because the first open-bottom threshold is higher in energy than the corresponding one in the charmonium sector and thus a larger number of conventional states are expected below $B\bar{B}$ -threshold. Moreover, the only experimentally discovered excited states which are above the $B\bar{B}$ -threshold, and so they have the ability to be strongly influenced by meson-meson thresholds, are $\Upsilon(4S)$, $\Upsilon(10860)$ and $\Upsilon(11020)$, besides the unconfirmed state $\Upsilon(10753)$.

Herein, we study the high-energy spectrum of the Υ -family in the framework of a constituent quark model [52] which satisfactorily describes a wide range of properties of conventional hadrons containing heavy quarks [53, 54]. The quark-antiquark and meson-meson degrees of freedom are incorporated with the goal of elucidating the influence of open-bottom meson-meson thresholds in the conventional states but, above all, to shed some light on the nature and structure of the $\Upsilon(10753)$ state. We should briefly mention that *charged* bottomonium-like states $Z_b(10610)^\pm$ and $Z_b(10650)^\pm$ were identified by the Belle Collaboration [55] as peaks in the invariant mass distribution of the $\pi^\pm h_b(mP)$ ($m = 1, 2$) and $\pi^\pm\Upsilon(nS)$ ($n = 1, 2, 3$) subsystems when the $\Upsilon(10860)$ resonance decays into two pions plus an h_b or Υ . The quantum numbers of the Z_b 's were analyzed to be $I^G(J^{PC}) = 1^+(1^{+-})$ [56] and so they belong to the isospin $I = 1$ sector of bottomonium-like particles, disconnected from the conventional bottomonium states of isospin $I = 0$. In fact such exotic mesons were studied by us in Ref. [57].

A variational formalism based on a highly efficient numerical approach named the Gaussian expansion method

(GEM) [58] is used to solve the bottomonium Hamiltonian. Moreover, this Gaussian expansion allows us to compute effective meson-meson interactions from the original quark-(anti-)quark potentials in a simplified way through the so-called Resonating Group Method [59, 60]. Finally, within our approach, the coupling between the quark-antiquark and meson-meson sectors requires the creation of a light quark-antiquark pair. Therefore, the associated operator should be similar to the one describing open-flavor meson strong decays and we adopt the 3P_0 transition operator described in, for instance, Ref. [61]. This theoretical formalism has the advantage of easily introducing the coupling with all meson-meson partial waves and the straightforward computation of the probabilities associated with the different Fock components of the physical state.

The manuscript is organized as follows. After this introduction, the theoretical framework is briefly presented in section II. Section III is mainly devoted to the analysis and discussion of our theoretical results. Finally, we summarize and draw some conclusions in Sec. IV.

II. THEORETICAL FRAMEWORK

A. CONSTITUENT QUARK MODEL

Among the wide range of chiral quark models developed in the last 50 years [62], our theoretical framework is a QCD-inspired constituent quark model (CQM) proposed in Ref. [52] and extensively reviewed in Refs. [53, 54]. Moreover, the CQM has been recently applied with success to conventional mesons containing heavy quarks, describing a wide range of physical observables that concern spectra [63–66], strong decays [67–70], hadronic transitions [71–73] as well as electromagnetic and weak reactions [74–76].

The main pieces of our CQM are spontaneous chiral symmetry breaking of the QCD Lagrangian together with perturbative one-gluon exchange (OGE) and non-perturbative color confining interactions. In the heavy quark sector, chiral symmetry is explicitly broken and Goldstone-boson exchanges do not appear. Thus, OGE and confinement are the only interactions remaining.

The OGE potential contains central, tensor and spin-orbit contributions given by

$$V_{\text{OGE}}^{\text{C}}(\vec{r}_{ij}) = +\frac{1}{4}\alpha_s(\vec{\lambda}_i^c \cdot \vec{\lambda}_j^c) \left[\frac{1}{r_{ij}} - \frac{1}{6m_i m_j} (\vec{\sigma}_i \cdot \vec{\sigma}_j) \frac{e^{-r_{ij}/r_0(\mu)}}{r_{ij} r_0^2(\mu)} \right], \quad (4a)$$

$$V_{\text{OGE}}^{\text{T}}(\vec{r}_{ij}) = -\frac{1}{16} \frac{\alpha_s}{m_i m_j} (\vec{\lambda}_i^c \cdot \vec{\lambda}_j^c) \left[\frac{1}{r_{ij}^3} - \frac{e^{-r_{ij}/r_g(\mu)}}{r_{ij}} \left(\frac{1}{r_{ij}^2} + \frac{1}{3r_g^2(\mu)} + \frac{1}{r_{ij} r_g(\mu)} \right) \right] S_{ij}, \quad (4b)$$

$$V_{\text{OGE}}^{\text{SO}}(\vec{r}_{ij}) = -\frac{1}{16} \frac{\alpha_s}{m_i^2 m_j^2} (\vec{\lambda}_i^c \cdot \vec{\lambda}_j^c) \left[\frac{1}{r_{ij}^3} - \frac{e^{-r_{ij}/r_g(\mu)}}{r_{ij}^3} \left(1 + \frac{r_{ij}}{r_g(\mu)} \right) \right] \\ \times \left[((m_i + m_j)^2 + 2m_i m_j) (\vec{S}_+ \cdot \vec{L}) + (m_j^2 - m_i^2) (\vec{S}_- \cdot \vec{L}) \right], \quad (4c)$$

where $r_0(\mu) = \hat{r}_0 \frac{\mu_{nn}}{\mu_{ij}}$ and $r_g(\mu) = \hat{r}_g \frac{\mu_{nn}}{\mu_{ij}}$ are regulators which depend on μ_{ij} , the reduced mass of the $q\bar{q}$ -pair; for example, $\mu_{nn} = m_n/2$ with m_n the mass of the light quark with $n = u$ - or d -quark. The contact term of the central potential has been regularized as follows

$$\delta(\vec{r}_{ij}) \approx \frac{1}{4\pi r_0^2} \frac{e^{-r_{ij}/r_0}}{r_{ij}}. \quad (5)$$

The wide energy range needed to provide a consistent description of light, strange and heavy mesons requires an effective scale-dependent strong coupling constant. We use the frozen coupling constant of Ref. [52],

$$\alpha_s(\mu_{ij}) = \frac{\alpha_0}{\ln \left(\frac{\mu_{ij}^2 + \mu_0^2}{\Lambda_0^2} \right)}, \quad (6)$$

in which α_0 , μ_0 and Λ_0 are parameters of the model determined by a global fit to the meson spectra.

The different pieces of the color confining potential are

$$V_{\text{CON}}^{\text{C}}(\vec{r}_{ij}) = [-a_c(1 - e^{-\mu_c r_{ij}}) + \Delta] (\vec{\lambda}_i^c \cdot \vec{\lambda}_j^c), \quad (7a)$$

$$V_{\text{CON}}^{\text{SO}}(\vec{r}_{ij}) = -(\vec{\lambda}_i^c \cdot \vec{\lambda}_j^c) \frac{a_c \mu_c e^{-\mu_c r_{ij}}}{4m_i^2 m_j^2 r_{ij}} \\ \times \left[((m_i^2 + m_j^2)(1 - 2a_s) + 4m_i m_j(1 - a_s)) (\vec{S}_+ \cdot \vec{L}) + (m_j^2 - m_i^2)(1 - 2a_s) (\vec{S}_- \cdot \vec{L}) \right], \quad (7b)$$

where the mixture between scalar and vector Lorentz structures of the color confinement is controlled by a_s . Besides, this potential presents at short inter-quark distances a linear behavior with an effective confinement strength given by $\sigma = -a_c \mu_c (\vec{\lambda}_i^c \cdot \vec{\lambda}_j^c)$, while it becomes constant at very large inter-quark distances showing a threshold defined by

$$V_{\text{thr}} = (-a_c + \Delta) \cdot (\vec{\lambda}_i^c \cdot \vec{\lambda}_j^c); \quad (8)$$

viz. there is no $q\bar{q}$ bound states with eigenenergies higher than this threshold; the system suffers a transition from a color string configuration between two static color sources into a pair of static mesons due to the breaking of the color string and the most favored decay into hadrons.

Among the different theoretical formalisms to solve the Schrödinger equation, in order to find the quark-antiquark bound states, we use the Rayleigh-Ritz variational method in which the wave function solution of the Schrödinger equation is expanded as indicated by the Gaussian Expansion Method (GEM) [58]. It has also been proven to be quite efficient on solving the bound-state problem of a few-body system [77–82], providing enough accuracy and simplifying the evaluation of matrix elements.

The radial wave function is then expressed as

$$R_\alpha(r) = \sum_{n=1}^{n_{\text{max}}} c_n^\alpha \phi_{nl}^G(r), \quad (9)$$

where α refers to the channel quantum numbers. The coefficients, c_n^α , and the eigenvalue, E , are determined from the Rayleigh-Ritz variational principle:

$$\sum_{n'=1}^{n_{\text{max}}} \left[(T_{nn'}^\alpha - EN_{nn'}^\alpha) c_{n'}^\alpha + \sum_{\alpha'=1}^{\text{channels}} V_{nn'}^{\alpha\alpha'} c_{n'}^{\alpha'} = 0 \right], \quad (10)$$

where $T_{nn'}^\alpha$, $N_{nn'}^\alpha$ and $V_{nn'}^{\alpha\alpha'}$ are, respectively, the matrix elements of the kinetic energy, the normalization and the potential. $T_{nn'}^\alpha$ and $N_{nn'}^\alpha$ are diagonal, whereas the mixing between different channels is given by $V_{nn'}^{\alpha\alpha'}$.

Following Ref. [58], we employ Gaussian trial functions with ranges in geometric progression. This enables the optimization of ranges employing a small number of free parameters. Moreover, the geometric progression is dense at short distances, so that it enables the description of the dynamics mediated by short range potentials. The fast damping of the Gaussian tail does not represent an issue, since we can choose the maximal range much longer than the hadronic size.

B. COUPLED-CHANNELS CALCULATION

It is well known that conventional mesons must be influenced in a non-perturbative way by meson-meson thresholds when these are close. In order to take into account this effect within the bottomonium sector, we perform a coupled-channels calculation in which the total hadron wavefunction is described by a combination of conventional $b\bar{b}$ states and open-bottom meson-meson channels:

$$|\Psi\rangle = \sum_{\alpha} c_{\alpha} |\psi_{\alpha}\rangle + \sum_{\beta} \chi_{\beta}(P) |\phi_A \phi_B \beta\rangle, \quad (11)$$

where $|\psi_{\alpha}\rangle$ are $b\bar{b}$ eigenstates of the two-body Hamiltonian, ϕ_M is the wavefunction associated with meson $M = A, B$, $|\phi_A \phi_B \beta\rangle$ is the two meson state whose quantum numbers are β and $\chi_{\beta}(P)$ is the relative wave function between the two mesons.

Under the above assumption, two sources of interaction emerge. On one hand, the two- and four-quark sectors can be coupled via the creation of a light-quark-antiquark pair. On the other hand, there is a residual interaction, derived from the microscopic quark-(anti)quark potential described by the CQM, among the two mesons. To derive the latter, we use the Resonating Group Method (RGM) [59, 60] (see also Refs. [26, 83] for further details).

Within RGM, the wave function of a system composed of two mesons with distinguishable quarks is given by

$$\langle \vec{p}_A \vec{p}_B \vec{P} | \vec{P}_{\text{c.m.}} | \phi_A \phi_B \beta \rangle = \phi_A(\vec{p}_A) \phi_B(\vec{p}_B) \chi_{\beta}(\vec{P}), \quad (12)$$

where, *e.g.*, $\phi_A(\vec{p}_A)$ is the wave function of the meson A with \vec{p}_A the relative momentum between its quark and antiquark. The wave function $\chi_{\beta}(\vec{P})$ takes into account the relative motion between the two mesons.

A general process $AB \rightarrow A'B'$ can be described by means of either direct or exchange potentials; the last ones appear due to the possibility of having to consider quark exchanges between clusters. In this study we do not have this case, so we only have direct potentials, which can be written as

$$\begin{aligned} \text{RGM } V_D^{\beta\beta'}(\vec{P}', \vec{P}) &= \sum_{i \in A, j \in B} \int d\vec{p}_{A'} d\vec{p}_{B'} d\vec{p}_A d\vec{p}_B \\ &\times \phi_A^*(\vec{p}_{A'}) \phi_B^*(\vec{p}_{B'}) V_{ij}^{\beta\beta'}(\vec{P}', \vec{P}) \phi_{A'}(\vec{p}_A) \phi_{B'}(\vec{p}_B). \end{aligned} \quad (13)$$

where $\beta^{(\prime)}$ labels the set of quantum numbers needed to uniquely define a certain meson-meson partial wave, $\vec{P}^{(\prime)}$ are the initial (final) relative momentum of the meson-meson pair, and $V_{ij}^{\beta\beta'}(\vec{P}', \vec{P})$ are the microscopic quark-(anti)quark potentials from the CQM and the sum runs over the constituent particles inside each meson cluster.

The coupling between the bottomonia and the open-bottom meson-meson thresholds requires the creation of a light quark-antiquark pair. For that purpose, we use the 3P_0 transition operator which was originally introduced in the 1970s to describe strong decays of mesons

and baryons [61, 84, 85]. The associated non-relativistic operator can be written as [67, 70]:

$$\begin{aligned} T &= -\sqrt{3} \sum_{\mu, \nu} \int d^3 p_{\mu} d^3 p_{\nu} \delta^{(3)}(\vec{p}_{\mu} + \vec{p}_{\nu}) \frac{g_s}{2m_{\mu}} \sqrt{2^5 \pi} \\ &\times \left[\mathcal{Y}_1 \left(\frac{\vec{p}_{\mu} - \vec{p}_{\nu}}{2} \right) \otimes \left(\frac{1}{2} \frac{1}{2} \right) 1 \right]_0 a_{\mu}^{\dagger}(\vec{p}_{\mu}) b_{\nu}^{\dagger}(\vec{p}_{\nu}). \end{aligned} \quad (14)$$

where μ (ν) are the spin, flavor and color quantum numbers of the created quark (antiquark). The orbital angular momentum and spin of the pair are both equal to one. Note that $\mathcal{Y}_{lm}(\vec{p}) = p^l Y_{lm}(\hat{p})$ is the solid harmonic defined in function of the spherical one. The unique parameter of the decay model is the strength of the quark-antiquark pair creation from the vacuum, $\gamma = g_s/2m$, where m is the mass of the created quark (antiquark).

The values of γ can be constrained through meson strong decays. A global fit to charmed, charmed-strange, hidden-charm and hidden-bottom sectors was performed in Ref. [67], finding a running of the strength parameter given by

$$\gamma(\mu) = \frac{\gamma_0}{\log\left(\frac{\mu}{\mu_0}\right)}, \quad (15)$$

where γ_0 and μ_0 are free parameters, whereas μ is the reduced mass of the constituent quark-antiquark pair of the decaying meson. In this work, we use the value of γ corresponding to the bottomonium sector, *i.e.* $\gamma = 0.205$.

From the operator in Eq. (14), we define the meson to meson-meson transition potential $h_{\beta\alpha}(P)$ as

$$\langle \phi_{M_1} \phi_{M_2} \beta | T | \psi_{\alpha} \rangle = \delta^{(3)}(\vec{P}_{\text{cm}}) P h_{\beta\alpha}(P), \quad (16)$$

where P is the relative momentum of the two-meson state. In order to soften the 3P_0 production vertex at high momenta, we follow the suggestion of Ref. [86] and used a Gaussian-like momentum-dependent form factor to truncate the vertex,

$$h_{\beta\alpha}(P) \rightarrow h_{\beta\alpha}(P) e^{-\frac{P^2}{2\Lambda^2}}, \quad (17)$$

with $\Lambda = 0.84$ GeV. This cut-off's value is taken from similar analysis [87, 88], so no fine-tuning of parameters is employed in the present work.

Finally, within the formalism explained above, the coupled-channels equations can be written as

$$\begin{aligned} c_{\alpha} M_{\alpha} + \sum_{\beta} \int h_{\alpha\beta}(P) \chi_{\beta}(P) P^2 dP &= E c_{\alpha}, \quad (18) \\ \sum_{\beta} \int H_{\beta'\beta}(P', P) \chi_{\beta}(P) P^2 dP &+ \\ + \sum_{\alpha} h_{\beta'\alpha}(P') c_{\alpha} &= E \chi_{\beta'}(P'), \quad (19) \end{aligned}$$

where M_{α} are the masses of the bare $b\bar{b}$ mesons and $H_{\beta'\beta}$ is the RGM Hamiltonian for the two-meson states obtained from the naive CQM interaction. In order to explore states above and below meson-meson thresholds,

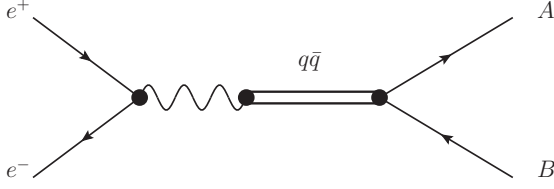


FIG. 1. Production of open-bottom mesons denoted by the AB -pair through a $q\bar{q}$ resonance with $J^{PC} = 1^{--}$. In this case a conventional state of the Υ -family is produced that decays later on in a pair of open-bottom mesons.

the former coupled-channels equations should then be written as a set of coupled Lippmann-Schwinger equations,

$$T_{\beta}^{\beta'}(E; p', p) = V_{\beta}^{\beta'}(p', p) + \sum_{\beta''} \int dp'' p''^2 V_{\beta''}^{\beta'}(p', p'') \times \frac{1}{E - \mathcal{E}_{\beta''}(p'')} T_{\beta}^{\beta''}(E; p'', p), \quad (20)$$

where $V_{\beta}^{\beta'}(p', p)$ is the projected potential that contains the sum of direct potentials, Eq. (13), as well as the effective potential which encodes the coupling with the two-quark sector:

$$V_{\text{eff}}^{\beta'\beta}(P', P; E) = \sum_{\alpha} \frac{h_{\beta'\alpha}(P') h_{\alpha\beta}(P)}{E - M_{\alpha}}. \quad (21)$$

The $\mathcal{E}_{\beta''}(p'')$ is the energy corresponding to a momentum p'' , which in the nonrelativistic case is

$$\mathcal{E}_{\beta}(p) = \frac{p^2}{2\mu_{\beta}} + \Delta M_{\beta}. \quad (22)$$

Herein, μ_{β} is the reduced mass of the meson-meson system corresponding to the channel β , and ΔM_{β} is the difference between the meson-meson threshold and the lightest one, taken as a reference.

Once the T -matrix is calculated, we determine its on-shell part which is directly related to the scattering matrix in the case of non-relativistic kinematics:

$$S_{\beta}^{\beta'} = 1 - 2\pi i \sqrt{\mu_{\beta} \mu_{\beta'}} k_{\beta} k_{\beta'} T_{\beta}^{\beta'}(E + i0^+; k_{\beta'}, k_{\beta}), \quad (23)$$

with k_{β} the on-shell momentum for channel β . All the potentials shall be analytically continued for complex momenta; this allows us to find the poles of the T -matrix in any possible Riemann sheet.

C. Production in annihilation e^+e^- through a resonance

For later convenience, our objective herein is to calculate cross section of the process $e^+e^- \rightarrow AB$ (represented in Fig. 1), with A or B denoting open-bottom

mesons, through an arbitrary set of $b\bar{b}$ resonances with quantum numbers $J^{PC} = 1^{--}$. For that purpose we use the extended Van Royen-Weisskopf formalism for meson leptonic decays, considering non-zero momentum distribution for the quark (antiquark) inside the meson [89]. It should be noticed that the Feynman diagram in Fig. 1 can be used when the quark-antiquark pair acts as free particles and has a certain momentum, in this case weighted with the corresponding Υ meson's wave function, $\phi(\vec{p})$, which gives the probability amplitude of finding a quark with momentum \vec{p} inside the $b\bar{b}$ meson.

The process to be studied is $\langle e^+e^- | AB \rangle_{\beta}$ through one or few $|q\bar{q}\rangle_{\alpha}$ resonances. This process can be factorized as,

$$\langle e^+e^- | AB \rangle_{\beta} = \sum_{\alpha} \langle e^+e^- | q\bar{q} \rangle_{\alpha} \langle q\bar{q} | AB \rangle_{\beta}. \quad (24)$$

In the center-of-mass reference system, the S -matrix of the process $\langle e^+e^- | q\bar{q} \rangle_{\alpha}$ can be written as

$$S = -ie^2 e_q (2\pi)^4 \int d^3p \frac{\delta^{(4)}(P_i - P_f) m_l m_q}{(2\pi)^3 E_p (2\pi)^3 E_q} \times \sum_{M_1 M_2 \mu_L \mu_S} \langle L\mu_L S\mu_S | J\mu_J \rangle \langle \frac{1}{2} M_1 \frac{1}{2} M_2 | S\mu_S \rangle \phi(\vec{p}) \frac{g_{\mu\nu}}{s} \times [\bar{u}_l(q, \xi_1) \gamma^{\mu} v_l(-q, \xi_2)] [\bar{v}_q(-p, M_2) \gamma^{\nu} u_q(p, M_1)], \quad (25)$$

where $\{m_l, e, E_q, \vec{q}, \xi\}$ represents the mass, charge, energy, momentum and spin projection of the incoming electron (positron); $\{m_q, e_q, E_p, \vec{p}, M\}$ the same for the created quark (antiquark), bound in a $J^{PC} = 1^{--}$ state with quantum numbers $\{J, L, S\}$ and $\{\mu_J, \mu_L, \mu_S\}$ projections. We express the Clebsch-Gordan coefficients as $\langle j_1 m_1 j_2 m_2 | j_3 m_3 \rangle$. The virtual photon's four-momentum verifies $k_{\gamma}^2 = s$.

The above S -matrix expression can be simplified and written in terms of the invariant amplitude \mathcal{M} ,

$$S = -2\pi i \delta^{(4)}(\sum p_f - \sum p_i) \mathcal{M}, \quad (26)$$

so we arrive at

$$\mathcal{M} = e^2 e_q \frac{1}{(2\pi)^{3/2}} \frac{m_l}{E_q} \frac{2}{3s} \overline{\Psi(0)} (-1)^{1/2+\xi_2} \frac{E_q + m_l}{2m_l} \left[\left(1 + \frac{q^2}{(E_q + m_l)^2} \right) \langle \frac{1}{2} \xi_1 \frac{1}{2} \xi_2 | 1\mu_J \rangle - \frac{2}{(E_q + m_l)^2} \sum_n (-1)^n \langle \frac{1}{2} \xi_1 \frac{1}{2} \xi_2 | 1n \rangle q_{-n} q_{\mu_J} \right], \quad (27)$$

where we have defined

$$\overline{\Psi(0)} = \left[\Psi(0) \delta_{L,0} - \frac{\sqrt{2}}{6\pi} \sqrt{2L+1} \langle L010 | 10 \rangle I_4 \right]. \quad (28)$$

Here, $\Psi(0)$ is the Υ meson wave function at the origin. The second term encodes the contribution of $L = 2$ states, where

$$I_4 \equiv \int \frac{p^4 dp R_r(p)}{E_p(E_p + m_q)}. \quad (29)$$

It is worth noticing that this definition of $\overline{\Psi}(0)$ allows the contribution of both $\Upsilon \ ^3S_1$ and $\Upsilon \ ^3D_1$ states due to the non-zero quark momentum distribution inside the meson.

Concerning the decay of the Υ meson into two mesons, we can extract the ${}_{\alpha}\langle q\bar{q}|AB\rangle_{\beta}$ amplitude from the coupled channels formalism [83], and it is given by

$${}_{\alpha}\langle q\bar{q}|AB\rangle_{\beta} = \sum_{\alpha'} \bar{h}_{\alpha'\beta}(\sqrt{s}; k) \Delta_{\alpha'\alpha}(\sqrt{s})^{-1}, \quad (30)$$

with k the relative on-shell momentum of the two mesons and $\Delta_{\alpha'\alpha}$ the full resonance propagator, given by

$$\Delta_{\alpha'\alpha}(E) = (E - M_{\alpha})\delta_{\alpha'\alpha} + \mathcal{G}_{\alpha'\alpha}(E) \quad (31)$$

with $\mathcal{G}_{\alpha'\alpha}$ the mass-shift function

$$\mathcal{G}_{\alpha'\alpha}(E) = \sum_{\beta} \int \frac{\bar{h}_{\alpha\beta}(E; q) h_{\beta\alpha'}(q)}{q^2/2\mu + m_A + m_B - E} q^2 dq. \quad (32)$$

The function $\bar{h}^{\beta\alpha}$ can be interpreted as the 3P_0 vertex dressed by the meson-meson interaction

$$\bar{h}_{\beta\alpha}(E; P) = h_{\beta\alpha}(P) - \sum_{\beta'} \int \frac{T_V^{\beta\beta'}(P, q; E) h_{\beta'\alpha}(q)}{q^2/2\mu + m_A + m_B - E} q^2 dq, \quad (33)$$

where $T_V^{\beta\beta'}(P', P; E)$ is the T matrix of the RGM potential excluding the coupling to the $q\bar{q}$ pairs.

The expression for the total cross section $e^+e^- \rightarrow b\bar{b} \rightarrow AB$ in the center-of-mass reference system is given by

$$d\sigma_{\beta} = (2\pi)^4 \frac{E_A E_B}{\sqrt{s} k_0} \delta(k - k_0) \frac{E_q}{2|q|} |\mathcal{M}_{\beta}|^2 d^3k, \quad (34)$$

where the on-shell momentum is

$$k_o = \frac{\sqrt{[s - (m_A + m_B)^2][s - (m_A - m_B)^2]}}{2\sqrt{s}}. \quad (35)$$

Averaging \mathcal{M} over the polarizations of the initial states and sum over final states, we arrive at

$$\sigma_{\beta} = \frac{4\pi^2}{3} e^4 e_q^2 \frac{\sqrt{k_o^2 + m_A^2} \sqrt{k_o^2 + m_B^2} k_o}{s^{5/2}} \times \left| \sum_{\nu, \nu'} \phi_{\nu'\beta}(k_o; \sqrt{s}) \Delta_{\nu'\nu}(\sqrt{s})^{-1} \overline{\Psi}_{\nu}(0) \right|^2, \quad (36)$$

which only depends on the on-shell momentum of the mesons in the final state.

TABLE I. Quark model parameters.

Quark masses	m_n (MeV)	313
	m_s (MeV)	555
	m_b (MeV)	5110
OGE	\hat{r}_0 (fm)	0.181
	\hat{r}_g (fm)	0.259
	α_0	2.118
	Λ_0 (fm $^{-1}$)	0.113
	μ_0 (MeV)	36.976
Confinement	a_c (MeV)	507.4
	μ_c (fm $^{-1}$)	0.576
	Δ (MeV)	184.432
	a_s	0.81

TABLE II. Masses, in MeV, of the bottomonium states with quantum numbers $J^{PC} = 1^{--}$ (the so-called Υ -family) predicted by our constituent quark model. nL identifies the radial excitation, being $n = 1$ the ground state, and the dominant orbital angular momentum component in each wave function.

State	J^{PC}	nL	The. (MeV)	Exp. (MeV) [90]
Υ	1^{--}	1S	9502	9460.40 ± 0.10
		2S	10015	10023.4 ± 0.5
		1D	10117	-
		3S	10349	10355.1 ± 0.5
		2D	10414	-
		4S	10607	10579.4 ± 1.2
		3D	10653	-
		5S	10818	10885.2 ± 3.1
		4D	10853	-
		6S	10995	11000 ± 4
5D	11023	-		

III. RESULTS

The relevant parameters of our *naïve* CQM are shown in Table I, and they are the same used in, *e.g.*, Ref. [54]. Table II shows the predicted bottomonium states with quantum numbers $J^{PC} = 1^{--}$ as well as the world average masses reported in the Review of Particle Physics (RPP) [90] provided by the Particle Data Group. It is inferred from Table II that a global description of the Υ -family is obtained by our CQM.

It is also evident that the model does not provide a conventional state compatible with the experimentally observed $\Upsilon(10753)$ state. One would be tempted to assert that our CQM has some major deficiency; however, it is well known that any reasonable quark model describes well the bottomonium sector, providing a comparable spectrum and having very similar characteristics. This fact may imply that the $\Upsilon(10753)$ cannot be explained

TABLE III. Masses, in MeV, of the isospin-averaged $B\bar{B}$, $B\bar{B}^*$, $B^*\bar{B}^*$, $B_s\bar{B}_s$, $B_s\bar{B}_s^*$ and $B_s^*\bar{B}_s^*$ thresholds, from PDG [90].

Channel	$B\bar{B}$	$B\bar{B}^*$	$B^*\bar{B}^*$	$B_s\bar{B}_s$	$B_s\bar{B}_s^*$	$B_s^*\bar{B}_s^*$
Mass	10558.8	10604.1	10649.4	10733.8	10782.7	10831.6

TABLE IV. Masses and widths, in MeV, of the poles predicted by our constituent-quark-model-based meson-meson coupled-channels calculation. Theoretical uncertainties have been estimated by modifying the most relevant model parameters within a range of 10%.

State	M_{pole}	Γ_{pole}
1	10562 ± 1	29 ± 5
2	10601 ± 5	3 ± 2
3	10645 ± 1	23 ± 1
4	10694 ± 1	8 ± 1
5	10712 ± 5	41 ± 4
6	10835 ± 2	52 ± 7
7	10859 ± 2	13 ± 3
8	10888 ± 1	3 ± 1

as a conventional bottomonium system and thus it has an exotic origin. In other words, there should be another important mechanism in the dynamics of the $\Upsilon(10753)$ that is not implemented in our, even any, *naïve* CQM.

The lowest open-bottom meson-meson threshold is $B\bar{B}$, with a non-interacting mass of about 10.56 GeV. Moreover, the dominant open-bottom meson-meson strong decay channels of the Υ -family are considered to be $B\bar{B}$, $B\bar{B}^*$, $B^*\bar{B}^*$, $B_s\bar{B}_s$, $B_s\bar{B}_s^*$ and $B_s^*\bar{B}_s^*$ ¹. Their non-interacting mass thresholds are shown in Table III and they belong to an energy range between 10.56 to 10.83 GeV. In order to assess agreement between theory and experiment, we should include those coupled-channels effects that may play an important role in our description of the Υ -family, at least, for the $\Upsilon(4S)$ up to the $\Upsilon(4D)$ which fall within the range of energies of the most important open-flavor meson-meson thresholds.

The coupling of bare $b\bar{b}$ states with open-bottom meson-meson channels depends on the relative position of the $b\bar{b}$ mass and the non-interacting meson-meson energy threshold. One may infer from Sec. II that when the value of threshold energy, E , is far from the $b\bar{b}$ mass, M , the coupling effects are small. Moreover, when $M < E$ the effective potential is repulsive and it is unlikely that the coupling can generate relevant non-perturbative emergent phenomena; in fact, one usually obtains the same but dressed state due to the influence of near thresholds, moving to lower masses. However, if $M > E$ the effective potential becomes negative and a variety of emergent

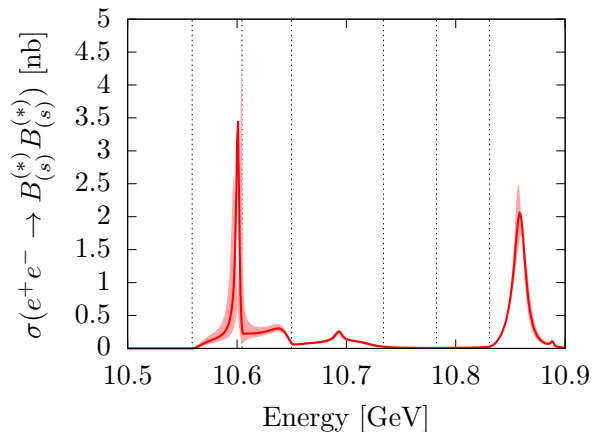


FIG. 2. Production cross section, in nb, of the Υ states when annihilating a pair of electron-positron and measuring in the final state one of the $B_{(s)}^{(*)}\bar{B}_{(s)}^{(*)}$ channels. The vertical black dashed lines indicate the open-bottom meson-meson thresholds which, from left to right, are $B\bar{B}$, $B\bar{B}^*$, $B^*\bar{B}^*$, $B_s\bar{B}_s$, $B_s\bar{B}_s^*$ and $B_s^*\bar{B}_s^*$. Theoretical uncertainties have been estimated by modifying the most relevant model parameters within a range of 10%.

phenomena such as dynamically generated states with a dominant molecular structure may appear.

We perform a coupled-channels calculation in which the bare states $\Upsilon(4S)$, $\Upsilon(3D)$, $\Upsilon(5S)$ and $\Upsilon(4D)$ are considered together with the threshold channels $B\bar{B}$, $B\bar{B}^*$, $B^*\bar{B}^*$, $B_s\bar{B}_s$, $B_s\bar{B}_s^*$ and $B_s^*\bar{B}_s^*$. In order to compensate for the large mass-shifts that higher thresholds add to the bare states, which are already coded in the screened confinement potential, we move up the masses of the bare states 35 MeV. Our results are shown in Tables IV, V and VI. First mentioned table shows the pole position in complex energy plane characterized by mass and width ($E = M - i\Gamma/2$), the second one gives the probability of each channel that compose the wave function of the dressed hadron and the third table provides hadron's decay branching fractions to the different open-bottom meson-meson channels considered herein.

Concerning Table IV, eight poles in the complex energy plane are predicted; all of them are resonances, *i.e.* they are singularities that appear in the physical sheet. It may seem like there are many, at least more than observed experimentally. However, as shown in Fig. 2, only three peaks are present in the most common production process of Υ states: $e^+e^- \rightarrow B_{(s)}^{(*)}\bar{B}_{(s)}^{(*)}$. The two dominant peaks appear at around the masses of well-established $\Upsilon(4S)$ and $\Upsilon(10860)$ states, the small bump at approximately 10.7 GeV is our assignment of the $\Upsilon(10750)$ signal observed in $e^+e^- \rightarrow \pi^+\pi^-\Upsilon(nS)$. If our interpretation is correct, we have learned from Table IV and Fig 2 that (i) a richer complex spectrum is gained when thresholds are present and bare bound states are sufficiently non-relativistic; (ii) those poles obtained in the complex energy plane do not have to appear as simple peaks in the

¹ For now on, we denote $B_{(s)}\bar{B}_{(s)}^* \equiv B_{(s)}\bar{B}_{(s)}^* + \text{h.c.}$

TABLE V. Probability, in %, of each channel that compose the wave function of the poles predicted by our constituent-quark-model-based meson-meson coupled-channels calculation. Theoretical uncertainties have been estimated by modifying the most relevant model parameters within a range of 10%.

State	$\mathcal{P}_{\Upsilon(4S)}$	$\mathcal{P}_{\Upsilon(3D)}$	$\mathcal{P}_{\Upsilon(5S)}$	$\mathcal{P}_{\Upsilon(4D)}$	$\mathcal{P}_{B\bar{B}}$	$\mathcal{P}_{B\bar{B}^*}$	$\mathcal{P}_{B^*\bar{B}^*}$	$\mathcal{P}_{B_s\bar{B}_s}$	$\mathcal{P}_{B_s\bar{B}_s^*}$	$\mathcal{P}_{B_s^*\bar{B}_s^*}$
1	40^{+3}_{-4}	16 ± 5	$1.5^{+0.4}_{-0.3}$	$1.5^{+0.6}_{-0.5}$	33 ± 8	$1.9^{+0.6}_{-0.5}$	$5.2^{+0.4}_{-0.6}$	$0.141^{+0.002}_{-0.006}$	0.05 ± 0.01	$0.24^{+0.01}_{-0.03}$
2	19^{+3}_{-5}	1.1 ± 0.4	$0.13^{+0.02}_{-0.04}$	0.04 ± 0.01	48^{+1}_{-2}	28^{+6}_{-2}	4 ± 1	$0.017^{+0.005}_{-0.007}$	0.11 ± 0.04	0.10 ± 0.04
3	22^{+5}_{-4}	9 ± 1	0.07 ± 0.01	$0.14^{+0.01}_{-0.02}$	6 ± 1	$34.1^{+0.4}_{-0.6}$	28^{+1}_{-2}	0.14 ± 0.02	$0.102^{+0.004}_{-0.006}$	$0.193^{+0.008}_{-0.009}$
4	$1.7^{+0.1}_{-0.2}$	40 ± 2	$0.027^{+0.001}_{-0.004}$	$0.007^{+0.002}_{-0.001}$	$12.0^{+0.8}_{-0.7}$	16 ± 1	29.6 ± 0.1	$0.32^{+0.05}_{-0.04}$	$0.32^{+0.07}_{-0.06}$	$0.029^{+0.005}_{-0.004}$
5	36 ± 5	$8.8^{+0.8}_{-1.0}$	3.3 ± 0.2	0.166 ± 0.003	$4.5^{+1.0}_{-0.9}$	$2.74^{+0.09}_{-0.04}$	43^{+4}_{-5}	0.9 ± 0.2	$0.22^{+0.03}_{-0.02}$	$0.55^{+0.06}_{-0.07}$
6	4 ± 1	$0.71^{+0.06}_{-0.04}$	80^{+2}_{-3}	1.4 ± 0.1	$1.3^{+0.4}_{-0.3}$	$2.1^{+0.5}_{-0.4}$	6 ± 1	0.4 ± 0.1	$1.2^{+0.4}_{-0.3}$	3 ± 1
7	$0.4^{+0.3}_{-0.2}$	0.03 ± 0.01	$53.7^{+0.0}_{-0.9}$	$0.2^{+0.2}_{-0.1}$	1.9 ± 0.1	$4.4^{+0.2}_{-0.1}$	5.7 ± 0.8	$1.33^{+0.06}_{-0.04}$	2.1 ± 0.4	30 ± 1
8	0.004 ± 0.002	0.005 ± 0.002	$0.05^{+0.03}_{-0.02}$	$50.23^{+0.00}_{-0.02}$	16.6 ± 0.1	$16.1^{+0.2}_{-0.3}$	$2.80^{+0.05}_{-0.04}$	4.9 ± 0.1	8.5 ± 0.2	$0.8^{+0.2}_{-0.1}$

TABLE VI. Decay branching fractions, in %, to the different open-bottom meson-meson channels of the poles predicted by our constituent-quark-model-based meson-meson coupled-channels calculation. Theoretical uncertainties have been estimated by modifying the most relevant model parameters within a range of 10%.

State	$\mathcal{BR}_{B\bar{B}}$	$\mathcal{BR}_{B\bar{B}^*}$	$\mathcal{BR}_{B^*\bar{B}^*}$	$\mathcal{BR}_{B_s\bar{B}_s}$	$\mathcal{BR}_{B_s\bar{B}_s^*}$	$\mathcal{BR}_{B_s^*\bar{B}_s^*}$
1	100 ± 0	0 ± 0	0 ± 0	0 ± 0	0 ± 0	0 ± 0
2	100 ± 0	0 ± 0	0 ± 0	0 ± 0	0 ± 0	0 ± 0
3	6 ± 1	94 ± 1	0 ± 0	0 ± 0	0 ± 0	0 ± 0
4	23 ± 1	14^{+1}_{-2}	$63.2^{+0.1}_{-0.2}$	0 ± 0	0 ± 0	0 ± 0
5	8^{+2}_{-1}	$3.0^{+0.4}_{-0.2}$	90 ± 1	0 ± 0	0 ± 0	0 ± 0
6	$7.4^{+0.1}_{-0.3}$	$4.3^{+0.3}_{-0.1}$	$5.5^{+0.6}_{-0.1}$	2 ± 0	4 ± 1	77^{+0}_{-2}
7	$4.1^{+0.3}_{-0.4}$	8 ± 0	$2.2^{+0.1}_{-0.2}$	3.0 ± 0.1	$1.8^{+0.6}_{-0.4}$	$81.4^{+0.1}_{-0.2}$
8	$33.9^{+0.4}_{-0.3}$	$32.9^{+0.3}_{-0.5}$	5 ± 0	$9.8^{+0.3}_{-0.2}$	17.3 ± 0.3	0.8 ± 0.1

relevant cross sections due to many reasons such as their distance from the energy real-axis, coupling with the corresponding final channel, etc; and (iii) when comparing with experiment, the so-called $\Upsilon(4S)$ and $\Upsilon(10860)$ signals are clearly identified but there should be another small one, corresponding to the $\Upsilon(10750)$ case, whose origin cannot be traced back to any bare quark-antiquark bound state.

It is convenient to analyze Tables V and VI together. The first pole has a mass, 10562 MeV, and a total decay width, 29 MeV, compatible with those values collected in the PDG for the $\Upsilon(4S)$ state. Moreover, its wave function has as the dominant channel the $\Upsilon(4S)$, *i.e.* a canonical bottom-antibottom 4S bound state; followed by $B\bar{B}$ and $\Upsilon(3D)$ components; moreover, its decay branching fraction of $B\bar{B}$ is 100%. Therefore, the natural assignment to this dressed state is the experimentally observed $\Upsilon(4S)$ state.

The following two poles seems to be singularities produced dynamically in the complex energy plane due to the coupling between conventional bottomonium states and meson-meson thresholds. In fact this coupling makes them mostly $B\bar{B} - B\bar{B}^*$ and $B\bar{B}^* - B^*\bar{B}^*$ molecules, respectively; having also measurable traces of $\Upsilon(4S)$ and $\Upsilon(3D)$ components in their wave functions. Nevertheless, as one can see in Fig. 2, these structures do not materialize in the production cross section.

We assign the fourth pole to the so-called $\Upsilon(3D)$ state. Our predictions for the mass and total decay width are 10645 MeV and 23 MeV. Its wave function exhibit a dominant $3D\ b\bar{b}$ constituent, followed by important $B\bar{B}$, $B\bar{B}^*$ and $B^*\bar{B}^*$ components. Table VI shows that the decay branching fractions of this state into the $B\bar{B}$, $B\bar{B}^*$ and $B^*\bar{B}^*$ final channels are 23%, 14% and 63%, respectively. As one can see in Fig. 2, this state takes part on the second bump observed in production cross section; however, its contribution is small because it depends on the value of I_4 in Eq. (29), which is small compared to the contribution of S -wave Υ states.

The last observation is connected with our interpretation of the fifth pole as the $\Upsilon(10750)$ candidate because, as one can see in Table V, its corresponding wave function shows a large $\Upsilon(4S)$ component which provides the leverage for its production. Note also that the wavefunction's $B^*\bar{B}^*$ channel is of the same order of magnitude than the former, encouraging us to conclude that this dressed hadronic state is in fact a resonance whose structure is an equally mixture of a conventional $b\bar{b}$ 4S state and $B^*\bar{B}^*$ molecule. Looking at Table IV, its theoretical mass and width are 10712 MeV and 41 MeV, respectively, which are in reasonable agreement with the experimental data, Eq. (3). Finally, Table VI shows that this state decays 90% of the time into $B^*\bar{B}^*$ followed by the $B\bar{B}$ final state with a branching fraction of 8%.

Concerning the bump that can be seen in the production cross section (Fig. 2) at around 10.85 GeV, it is mostly produced by the sixth pole because, as shown in Table V, its wave function exhibits a very dominant $5S\ b\bar{b}$ component, with a probability of 80%; being the rest channels an order of magnitude less probable. Without changing our attention from Table V, the other two poles are constituted by an equally mixture of canonical bottomonium structure and open-bottom meson-meson molecule. Table VI shows the branching fractions of these three dressed states to $B_{(s)}^{(*)}\bar{B}_{(s)}^{(*)}$ channels. For our tentative assignment of the $\Upsilon(5S)$ state as $\Upsilon(10860)$, the theoretical mass and width are in fair agreement with experiment; our mass value is a bit lower than the experimental one, 10885 MeV, whereas our width is higher than the PDG's figure, 37 MeV. This may be explained by the projection in real-axis of the singularities shown in the complex energy plane at the relevant energy, which is the only measurable feature. It is also worth to note that we provide correct orders of magnitude for the branching fractions of the $B^{(*)}\bar{B}^{(*)}$ state whereas unfortunately the one corresponding to the $B_s^*\bar{B}_s^*$ channel is far larger than experiment.

IV. SUMMARY

The $\Upsilon(10753)$ signal seems to be a potential candidate of the Υ -family. It was firstly observed by the Belle collaboration in 2019 and, later on, by the Belle II collaboration in 2022. The joint significance is 5.2 standard deviations; moreover, its mass, total decay width and quantum numbers are also determined: $M = 10753$ MeV, $\Gamma = 36_{-12}^{+18}$ MeV and $J^P = 1^-$. Since this new state does not fit into the spectrum predicted by any reasonable constituent quark model, everything points that it may be an exotic state whose nature is explained by some mechanism that goes beyond the simple quark-antiquark in-

teraction. The most logical extension to the naive quark model is the coupling of bare bottomonia with their closest open-bottom thresholds in order to assess if emergent non-perturbative dynamical states could be produced.

We have analyzed the predicted spectrum of the Υ -family, within an energy range around the $\Upsilon(10753)$'s mass, in the framework of a constituent quark model [52] which satisfactorily describes a wide range of properties of conventional hadrons containing heavy quarks [53, 54]. The quark-antiquark and meson-meson degrees of freedom have been incorporated with the goal of elucidating the influence of open-bottom meson-meson thresholds into the concerning bare states and to shed some light on the nature and structure of the $\Upsilon(10753)$ state. In particular, we have performed a coupled-channels calculation in which the bare states $\Upsilon(4S)$, $\Upsilon(3D)$, $\Upsilon(5S)$ and $\Upsilon(4D)$ are considered together with the threshold channels $B\bar{B}$, $B\bar{B}^*$, $B^*\bar{B}^*$, $B_s\bar{B}_s$, $B_s\bar{B}_s^*$ and $B_s^*\bar{B}_s^*$.

Among the results we have described, the following conclusions are of particular interest: (i) a richer complex spectrum is gained when thresholds are present and bare bound states are sufficiently non-relativistic; (ii) those poles obtained in the complex energy plane do not have to appear as simple peaks in the relevant cross sections; and (iii) the $\Upsilon(10750)$ candidate is interpreted as a dressed hadronic resonance whose structure is an equally mixture of a conventional $b\bar{b}$ state and B^*B^* molecule.

ACKNOWLEDGMENTS

Work partially financed by EU Horizon 2020 research and innovation program, STRONG-2020 project, under grant agreement no. 824093; Ministerio Español de Ciencia e Innovación under grant Nos. PID2019-105439GB-C22, PID2019-107844GB-C22 and PID2022-140440NB-C22; Junta de Andalucía under contract Nos. Operativo FEDER Andalucía 2014-2020 UHU-1264517, P18-FR-5057 and also PAIDI FQM-370.

-
- [1] S. W. Herb *et al.* (E288), *Phys. Rev. Lett.* **39**, 252 (1977).
 - [2] W. R. Innes *et al.* (E288), *Phys. Rev. Lett.* **39**, 1240 (1977), [Erratum: *Phys.Rev.Lett.* 39, 1640 (1977)].
 - [3] K. Han *et al.*, *Phys. Rev. Lett.* **49**, 1612 (1982).
 - [4] G. Eigen *et al.*, *Phys. Rev. Lett.* **49**, 1616 (1982).
 - [5] C. Klopfenstein *et al.*, *Phys. Rev. Lett.* **51**, 160 (1983).
 - [6] F. Pauss *et al.*, *Phys. Lett. B* **130**, 439 (1983).
 - [7] D. Besson *et al.* (CLEO), *Phys. Rev. Lett.* **54**, 381 (1985).
 - [8] D. M. J. Lovelock *et al.*, *Phys. Rev. Lett.* **54**, 377 (1985).
 - [9] R. F. Lebed, R. E. Mitchell, and E. S. Swanson, *Prog. Part. Nucl. Phys.* **93**, 143 (2017), arXiv:1610.04528 [hep-ph].
 - [10] H.-X. Chen, W. Chen, X. Liu, and S.-L. Zhu, *Phys. Rept.* **639**, 1 (2016), arXiv:1601.02092 [hep-ph].
 - [11] H.-X. Chen, W. Chen, X. Liu, Y.-R. Liu, and S.-L. Zhu, *Rept. Prog. Phys.* **80**, 076201 (2017), arXiv:1609.08928 [hep-ph].
 - [12] A. Ali, J. S. Lange, and S. Stone, *Prog. Part. Nucl. Phys.* **97**, 123 (2017), arXiv:1706.00610 [hep-ph].
 - [13] F.-K. Guo, C. Hanhart, U.-G. Meißner, Q. Wang, Q. Zhao, and B.-S. Zou, *Rev. Mod. Phys.* **90**, 015004 (2018), [Erratum: *Rev.Mod.Phys.* 94, 029901 (2022)], arXiv:1705.00141 [hep-ph].
 - [14] S. L. Olsen, T. Skwarnicki, and D. Zieminska, *Rev. Mod. Phys.* **90**, 015003 (2018), arXiv:1708.04012 [hep-ph].
 - [15] Y.-R. Liu, H.-X. Chen, W. Chen, X. Liu, and S.-L. Zhu, *Prog. Part. Nucl. Phys.* **107**, 237 (2019), arXiv:1903.11976 [hep-ph].
 - [16] N. Brambilla, S. Eidelman, C. Hanhart, A. Nefediev, C.-P. Shen, C. E. Thomas, A. Vairo, and C.-Z. Yuan, *Phys. Rept.* **873**, 1 (2020), arXiv:1907.07583 [hep-ex].
 - [17] G. Yang, J. Ping, and J. Segovia, *Symmetry* **12**, 1869 (2020), arXiv:2009.00238 [hep-ph].
 - [18] X.-K. Dong, F.-K. Guo, and B.-S. Zou, *Phys. Rev. Lett.*

- 126**, 152001 (2021), arXiv:2011.14517 [hep-ph].
- [19] X.-K. Dong, F.-K. Guo, and B.-S. Zou, *Commun. Theor. Phys.* **73**, 125201 (2021), arXiv:2108.02673 [hep-ph].
- [20] H.-X. Chen, *Phys. Rev. D* **105**, 094003 (2022), arXiv:2103.08586 [hep-ph].
- [21] X. Cao, *Front. Phys. (Beijing)* **18**, 44600 (2023), arXiv:2301.11253 [hep-ph].
- [22] M. Mai, U.-G. Meißner, and C. Urbach, *Phys. Rept.* **1001**, 1 (2023), arXiv:2206.01477 [hep-ph].
- [23] L. Meng, B. Wang, G.-J. Wang, and S.-L. Zhu, *Phys. Rept.* **1019**, 1 (2023), arXiv:2204.08716 [hep-ph].
- [24] H.-X. Chen, W. Chen, X. Liu, Y.-R. Liu, and S.-L. Zhu, *Rept. Prog. Phys.* **86**, 026201 (2023), arXiv:2204.02649 [hep-ph].
- [25] F.-K. Guo, H. Peng, J.-J. Xie, and X. Zhou, (2022), arXiv:2203.07141 [hep-ph].
- [26] P. G. Ortega and D. R. Entem, *Symmetry* **13**, 279 (2021), arXiv:2012.10105 [hep-ph].
- [27] H. Huang, C. Deng, X. Liu, Y. Tan, and J. Ping, *Symmetry* **15**, 1298 (2023).
- [28] R. F. Lebed, *PoS FPCP2023*, 028 (2023), arXiv:2308.00781 [hep-ph].
- [29] B.-S. Zou, *Sci. Bull.* **66**, 1258 (2021), arXiv:2103.15273 [hep-ph].
- [30] R. Mizuk *et al.* (Belle), *JHEP* **10**, 220 (2019), arXiv:1905.05521 [hep-ex].
- [31] I. Adachi *et al.* (Belle-II), *Phys. Rev. Lett.* **130**, 091902 (2023), arXiv:2208.13189 [hep-ex].
- [32] G. Bonvicini *et al.* (CLEO), *Phys. Rev. D* **70**, 032001 (2004), arXiv:hep-ex/0404021.
- [33] P. del Amo Sanchez *et al.* (BaBar), *Phys. Rev. D* **82**, 111102 (2010), arXiv:1004.0175 [hep-ex].
- [34] S. M. Ryan and D. J. Wilson (Hadron Spectrum), *JHEP* **02**, 214 (2021), arXiv:2008.02656 [hep-lat].
- [35] J. Bulava *et al.*, in *Snowmass 2021* (2022) arXiv:2203.03230 [hep-lat].
- [36] T. Hilger, C. Popovici, M. Gomez-Rocha, and A. Krassnigg, *Phys. Rev. D* **91**, 034013 (2015), arXiv:1409.3205 [hep-ph].
- [37] C. S. Fischer, S. Kubrak, and R. Williams, *Eur. Phys. J. A* **51**, 10 (2015), arXiv:1409.5076 [hep-ph].
- [38] P.-L. Yin, C. Chen, G. a. Krein, C. D. Roberts, J. Segovia, and S.-S. Xu, *Phys. Rev. D* **100**, 034008 (2019), arXiv:1903.00160 [nucl-th].
- [39] P.-L. Yin, Z.-F. Cui, C. D. Roberts, and J. Segovia, *Eur. Phys. J. C* **81**, 327 (2021), arXiv:2102.12568 [hep-ph].
- [40] P. Parui, S. De, A. Kumar, and A. Mishra, (2021), arXiv:2104.05471 [hep-ph].
- [41] W. Chen, R. T. Kleiv, T. G. Steele, B. Bulthuis, D. Harnett, J. Ho, T. Richards, and S.-L. Zhu, in *Meeting of the APS Division of Particles and Fields* (2013) arXiv:1310.0431 [hep-ph].
- [42] R. Kleiv, *QCD sum rule studies of heavy quarkonium-like states*, Ph.D. thesis, Saskatchewan U. (2013), arXiv:1407.2292 [hep-ph].
- [43] N. Brambilla, A. Pineda, J. Soto, and A. Vairo, *Rev. Mod. Phys.* **77**, 1423 (2005), arXiv:hep-ph/0410047.
- [44] N. Brambilla, A. Pineda, J. Soto, and A. Vairo, *Nucl. Phys. B* **566**, 275 (2000), arXiv:hep-ph/9907240.
- [45] J. Segovia, S. Steinbeißer, and A. Vairo, *Phys. Rev. D* **99**, 074011 (2019), arXiv:1811.07590 [hep-ph].
- [46] C. Peset, A. Pineda, and J. Segovia, *Phys. Rev. D* **98**, 094003 (2018), arXiv:1809.09124 [hep-ph].
- [47] T. Barnes, F. E. Close, P. R. Page, and E. S. Swanson, *Phys. Rev. D* **55**, 4157 (1997), arXiv:hep-ph/9609339.
- [48] D. Ebert, R. N. Faustov, and V. O. Galkin, *Phys. Rev. D* **67**, 014027 (2003), arXiv:hep-ph/0210381.
- [49] E. Eichten, S. Godfrey, H. Mahlke, and J. L. Rosner, *Rev. Mod. Phys.* **80**, 1161 (2008), arXiv:hep-ph/0701208.
- [50] J. Ferretti and E. Santopinto, *Phys. Rev. D* **90**, 094022 (2014), arXiv:1306.2874 [hep-ph].
- [51] S. Godfrey and K. Moats, *Phys. Rev. D* **92**, 054034 (2015), arXiv:1507.00024 [hep-ph].
- [52] J. Vijande, F. Fernandez, and A. Valcarce, *J. Phys. G* **31**, 481 (2005), arXiv:hep-ph/0411299.
- [53] J. Segovia, D. R. Entem, F. Fernandez, and E. Hernandez, *Int. J. Mod. Phys. E* **22**, 1330026 (2013), arXiv:1309.6926 [hep-ph].
- [54] J. Segovia, P. G. Ortega, D. R. Entem, and F. Fernández, *Phys. Rev. D* **93**, 074027 (2016), arXiv:1601.05093 [hep-ph].
- [55] A. Bondar *et al.* (Belle), *Phys. Rev. Lett.* **108**, 122001 (2012), arXiv:1110.2251 [hep-ex].
- [56] I. Adachi (Belle), in *9th Conference on Flavor Physics and CP Violation* (2011) arXiv:1105.4583 [hep-ex].
- [57] P. G. Ortega, J. Segovia, and F. Fernandez, *Phys. Rev. D* **104**, 094004 (2021), arXiv:2107.02544 [hep-ph].
- [58] E. Hiyama, Y. Kino, and M. Kamimura, *Prog. Part. Nucl. Phys.* **51**, 223 (2003).
- [59] J. A. Wheeler, *Phys. Rev.* **52**, 1083 (1937).
- [60] Y. C. Tang, M. Lemere, and D. R. Thompson, *Phys. Rept.* **47**, 167 (1978).
- [61] L. Micu, *Nucl. Phys. B* **10**, 521 (1969).
- [62] F. Fernández and J. Segovia, *Symmetry* **13**, 252 (2021).
- [63] J. Segovia, A. M. Yasser, D. R. Entem, and F. Fernandez, *Phys. Rev. D* **78**, 114033 (2008).
- [64] J. Segovia, D. R. Entem, and F. Fernandez, *Phys. Rev. D* **91**, 094020 (2015), arXiv:1502.03827 [hep-ph].
- [65] P. G. Ortega, J. Segovia, D. R. Entem, and F. Fernández, *Phys. Rev. D* **94**, 114018 (2016), arXiv:1608.01325 [hep-ph].
- [66] P. G. Ortega, J. Segovia, D. R. Entem, and F. Fernandez, *Eur. Phys. J. C* **80**, 223 (2020), arXiv:2001.08093 [hep-ph].
- [67] J. Segovia, D. R. Entem, and F. Fernández, *Phys. Lett. B* **715**, 322 (2012), arXiv:1205.2215 [hep-ph].
- [68] J. Segovia, A. M. Yasser, D. R. Entem, and F. Fernandez, *Phys. Rev. D* **80**, 054017 (2009).
- [69] J. Segovia, D. R. Entem, and F. Fernandez, *Phys. Rev. D* **83**, 114018 (2011).
- [70] J. Segovia, D. R. Entem, and F. Fernandez, *Nucl. Phys. A* **915**, 125 (2013), arXiv:1301.2592 [hep-ph].
- [71] J. Segovia, D. R. Entem, and F. Fernández, *Phys. Rev. D* **91**, 014002 (2015), arXiv:1409.7079 [hep-ph].
- [72] J. Segovia, F. Fernandez, and D. R. Entem, *Few Body Syst.* **57**, 275 (2016), arXiv:1507.01607 [hep-ph].
- [73] B. Martín-González, P. G. Ortega, D. R. Entem, F. Fernández, and J. Segovia, *Phys. Rev. D* **106**, 054009 (2022), arXiv:2205.05950 [hep-ph].
- [74] J. Segovia, C. Albertus, D. R. Entem, F. Fernandez, E. Hernandez, and M. A. Perez-Garcia, *Phys. Rev. D* **84**, 094029 (2011), arXiv:1107.4248 [hep-ph].
- [75] J. Segovia, C. Albertus, E. Hernandez, F. Fernandez, and D. R. Entem, *Phys. Rev. D* **86**, 014010 (2012), arXiv:1203.4362 [hep-ph].
- [76] J. Segovia, E. Hernández, F. Fernández, and D. R. Entem, *Phys. Rev. D* **87**, 114009 (2013), arXiv:1304.4970 [hep-ph].

- [77] G. Yang, J. Ping, and J. Segovia, *Few Body Syst.* **59**, 113 (2018), arXiv:1709.09315 [hep-ph].
- [78] G. Yang, J. Ping, P. G. Ortega, and J. Segovia, *Chin. Phys. C* **44**, 023102 (2020), arXiv:1904.10166 [hep-ph].
- [79] G. Yang, J. Ping, and J. Segovia, *Phys. Rev. D* **102**, 054023 (2020), arXiv:2007.05190 [hep-ph].
- [80] G. Yang, J. Ping, and J. Segovia, *Phys. Rev. D* **104**, 094035 (2021), arXiv:2109.04311 [hep-ph].
- [81] G. Yang, J. Ping, and J. Segovia, *Phys. Rev. D* **101**, 074030 (2020), arXiv:2003.05253 [hep-ph].
- [82] G. Yang, J. Ping, and J. Segovia, *Phys. Rev. D* **99**, 014035 (2019), arXiv:1809.06193 [hep-ph].
- [83] P. G. Ortega, D. R. Entem, and F. Fernandez, *J. Phys. G* **40**, 065107 (2013), arXiv:1205.1699 [hep-ph].
- [84] A. Le Yaouanc, L. Oliver, O. Pene, and J. C. Raynal, *Phys. Rev. D* **8**, 2223 (1973).
- [85] A. Le Yaouanc, L. Oliver, O. Pene, and J. C. Raynal, *Phys. Rev. D* **9**, 1415 (1974).
- [86] D. Morel and S. Capstick, (2002), arXiv:nucl-th/0204014.
- [87] P. G. Ortega, J. Segovia, D. R. Entem, and F. Fernandez, *Phys. Rev. D* **94**, 074037 (2016), arXiv:1603.07000 [hep-ph].
- [88] P. G. Ortega, J. Segovia, D. R. Entem, and F. Fernández, *Phys. Rev. D* **95**, 034010 (2017), arXiv:1612.04826 [hep-ph].
- [89] L. A. Blanco, R. Bonnaz, B. Silvestre-Brac, F. Fernandez, and A. Valcarce, *Nucl. Phys. A* **699**, 690 (2002), arXiv:nucl-th/0109080.
- [90] R. L. Workman *et al.* (Particle Data Group), *PTEP* **2022**, 083C01 (2022).

How these characterized higher charmonia shape the puzzling data of the $e^+e^- \rightarrow \eta J/\psi$ cross section

Tian-Cai Peng,^{1,2,3,4,*} Zi-Yue Bai,^{1,2,3,4,†} Jun-Zhang Wang,^{5,1,‡} and Xiang Liu^{1,2,3,4,6,§}

¹*School of Physical Science and Technology, Lanzhou University, Lanzhou 730000, China*

²*Lanzhou Center for Theoretical Physics, Key Laboratory of Theoretical Physics of Gansu Province, Lanzhou University, Lanzhou 730000, China*

³*Key Laboratory of Quantum Theory and Applications of MoE, Lanzhou University, Lanzhou 730000, China*

⁴*Research Center for Hadron and CSR Physics, Lanzhou University and Institute of Modern Physics of CAS, Lanzhou 730000, China*

⁵*School of Physics and Center of High Energy Physics, Peking University, Beijing 100871, China*

⁶*MoE Frontiers Science Center for Rare Isotopes, Lanzhou University, Lanzhou 730000, China*

(Dated: March 7, 2024)

Recently, the BESIII Collaboration performed a precise measurement of the $e^+e^- \rightarrow \eta J/\psi$ cross section. It is puzzling that the resonance parameters of the reported $Y(4230)$ show a substantial divergence from the previously measured results in both the open-charmed and hidden-charmed decay channels, and the line shape asymmetry of the data approaching 4.2 GeV also suggests that it might be difficult to characterize the details of the structure around 4.2 GeV by a single resonance. This has motivated our great curiosity about how the charmonium states are distributed in the measured energy range and how they shape the puzzling data of the $e^+e^- \rightarrow \eta J/\psi$ cross section. In this work, we use five theoretically constructed charmonia in the range of 4.0 ~ 4.5 GeV, i.e. $\psi(4040)$, $\psi(4160)$, $\psi(4220)$, $\psi(4380)$, and $\psi(4415)$, to apply a combined fit to the data, in which their calculated decay ratios into $\eta J/\psi$ via hadronic loop mechanism are taken as input. The fit results can reproduce the measured cross section data well, especially for the subtle line shape around 4.2 GeV, showing that the structure around 4.2 GeV is possible from the contribution of both $\psi(4160)$ and $\psi(4220)$.

I. INTRODUCTION

With the continuous accumulation of data, an increasing number of charmoniumlike XYZ states have been documented in various experimental endeavors, such as Belle, BESIII, LHCb, and CMS. This surge in reported states has invigorated the field of hadron spectroscopy, giving it a remarkable level of activity and importance (see review articles [1–9] for more details). This research landscape has led to significant advances in our construction of hadron spectroscopy. In particular, it has advanced our understanding of the intricate non-perturbative dynamics associated with the strong interactions, which is a central frontier of contemporary physics research.

Recently, the BESIII Collaboration made a remarkable discovery by measuring the $e^+e^- \rightarrow \eta J/\psi$ cross section over a center-of-mass energy range of $\sqrt{s} = 3.808 - 4.951$ GeV [10]. This measurement was made by analyzing a data sample with an integrated luminosity of 22.42 fb^{-1} [10]. To depict this data, BESIII introduced three resonant structures, i.e., the charmonium state $\psi(4040)$ and two charmoniumlike states, namely $Y(4230)$ and $Y(4360)$. The resonance parameters of these introduced states were determined. For the $Y(4230)$ state, the resonance mass was found to be $m_{Y(4230)} = 4219.7 \pm 2.5 \pm 4.5$ MeV, and the corresponding width was measured to be $\Gamma_{Y(4230)} = 80.7 \pm 4.4 \pm 1.4$ MeV. Similarly, the $Y(4360)$ state showed a mass of $m_{Y(4360)} = 4386 \pm 13 \pm 17$ MeV, accompanied by a width of $\Gamma_{Y(4360)} = 177 \pm 32 \pm 13$ MeV [10]. It is worth noting that the observed width of the $Y(4230)$ state,

as reported, exceeds those found in other hidden-charm and open-charm decay channels. These include processes such as $e^+e^- \rightarrow \pi^+\pi^- J/\psi$ [11, 12], $\pi^0\pi^0 J/\psi$ [13], $\psi(2S)\pi^+\pi^-$ [14], $\pi^+\pi^-\psi(3686)$ [15], $h_c\pi^+\pi^-$ [16], $\chi_{c0}\omega$ [17], $K^+K^- J/\psi$ [18], and $D^0D^{*-}\pi^+$ [19]. This difference in width hints at some distinct nature of this reported $Y(4230)$ structure in $e^+e^- \rightarrow \eta J/\psi$ [10].

As collected by the Particle Data Group (PDG) [20], the family of charmonium encompasses two well-established entities, namely $\psi(4160)$ and $\psi(4415)$, in addition to $\psi(4040)$. However, upon meticulous examination of the experimental data reported by BESIII, a conspicuous absence is observed within the cross section distribution of $e^+e^- \rightarrow \eta J/\psi$, pertaining specifically to the aforementioned charmonium states, $\psi(4160)$ and $\psi(4415)$. Remarkably, the established charmonium $\psi(4160)$ possess sizable decay fractions into $\eta J/\psi$ channel according to the theoretical calculation [21]. Moreover, if carefully checking the BESIII's data, we may find an asymmetric line shape, associated with the resonance structure denoted as $Y(4230)$. Confronted by this puzzling phenomenon existing in the cross section data of $e^+e^- \rightarrow \eta J/\psi$ [10], a pressing need arises for the formulation of a cogent resolution to address this perplexing issue. We should mention the distinct characterized energy level structure of higher charmonia within the framework of the unquenched picture, a contribution credited to the diligent efforts of the Lanzhou group [22–24]. In the newly constructed J/ψ family, there are six vector charmonium states in the energy range of 4 ~ 4.5 GeV, i.e., $\psi(4040)$, $\psi(4160)$, $\psi(4220)$, $\psi(4380)$, $\psi(4415)$, and $\psi(4500)$ [22]. In this work, we reveal how these characterized higher charmonia shape the puzzling data of the $e^+e^- \rightarrow \eta J/\psi$ cross section.

This paper is organized as follows. After the introduction, we briefly review the status of these higher charmonia in the range of 4.0 ~ 4.5 GeV, which are used to solve the puzzles

*Electronic address: pengtc20@lzu.edu.cn

†Electronic address: baizy15@lzu.edu.cn

‡Electronic address: wangjzh2022@pku.edu.cn

§Electronic address: xiangliu@lzu.edu.cn

appearing in the cross section data of the $e^+e^- \rightarrow J/\psi\eta$ in Sec. II. We then illustrate the calculation details of these charmonium decays into $\eta J/\psi$ via the hadronic loop mechanism in Sec. II A. Based on these results, we perform a combined fit to show how these characterized higher charmonia shape the puzzling data of the $e^+e^- \rightarrow \eta J/\psi$ cross section in Sec. II B. The paper ends with a short summary in Sec. III.

II. AN ANALYSIS TO THE CROSS SECTION OF

$$e^+e^- \rightarrow \eta J/\psi$$

The continued accumulation of the experimental data in the range of 4.0 ~ 4.5 GeV has deepened our understanding of the spectrum of higher vector charmonium above 4.0 GeV. Recently, the BESIII Collaboration performed a precise measurement of the $e^+e^- \rightarrow \eta J/\psi$ cross section over a center-of-mass energy range of $\sqrt{s} = 3.808 - 4.951$ GeV, and obtained the charmonium state $\psi(4040)$ and the other two charmoniumlike states named $Y(4230)$ and $Y(4360)$ from a Breit-Wigner fit, but the extracted resonance parameters of the observed $Y(4230)$ state against other measurements of the open-charmed and hidden-charmed decay channels [11–19]. And the line shape of the observed $Y(4230)$ looks asymmetric and irregular, and could not be formed by the contribution of just one resonance. It seems that the structure around 4.2 GeV from the measured cross section data of $e^+e^- \rightarrow \eta J/\psi$ may have some substructures.

In order to fully understand these puzzling data, the theoretical inputs of the vector charmonia located in the range of 4.0 ~ 4.5 GeV are crucial. Besides the well constructed charmonia, i.e., $\psi(4040)$, $\psi(4160)$ and $\psi(4415)$ in the range of 4.0 ~ 4.5 GeV, the Lanzhou group indicated that there should exist a narrow charmonium $\psi(4220)$ corresponding to $Y(4220)$ reported in the processes of $e^+e^- \rightarrow J/\psi\pi^+\pi^-$, $e^+e^- \rightarrow h_c\pi^+\pi^-$, $e^+e^- \rightarrow \chi_{c0}\omega$ and $e^+e^- \rightarrow \psi(3686)\pi^+\pi^-$ [25–28]. In Ref. [22], the Lanzhou group used an unquenched potential model with $\psi(4220)$ as the scaling point and predicted another two more charmonium states named $\psi(4380)$ and $\psi(4500)$. The information of these charmonia is summarized in Table I. It is worth mentioning that the BESIII experiment recently indeed found a new structure around 4.5 GeV in the measurement of $e^+e^- \rightarrow K^+K^-J/\psi$ [18], which just can relate to our predicted charmonium $\psi(4500)$. With these six vector charmonia, theoretically established in the range of 4.0 ~ 4.5, they have shown that the experimental cross section measurements of $e^+e^- \rightarrow \psi(2S)\pi^+\pi^-$ [22], $e^+e^- \rightarrow K^+K^-J/\psi$ [23] and $e^+e^- \rightarrow \pi^+D^0D^{*-}$ [24] can be explained in a unified framework. In this work, we aim to show that the newly measured $e^+e^- \rightarrow \eta J/\psi$ cross section data can also be understood by the contributions of the same characterized energy level structures, and how they shape the puzzling $e^+e^- \rightarrow \eta J/\psi$ cross section data.

The contribution of genuine intermediate charmonium to $e^+e^- \rightarrow \eta J/\psi$ can be described by a phase space corrected

Breit-Wigner function, i.e.,

$$\mathcal{M}_\psi(s) = \frac{\sqrt{12\pi}\Gamma_\psi^{e^+e^-} \mathcal{B}(\psi \rightarrow \eta J/\psi)\Gamma_\psi}{s - m_\psi^2 + im_\psi\Gamma_\psi} \times \sqrt{\frac{\Phi_{2 \rightarrow 2}(s)}{\Phi_{2 \rightarrow 2}(m_\psi^2)}}, \quad (1)$$

where m_ψ , Γ_ψ and $\Gamma_\psi^{e^+e^-}$ are the mass, total width and the dielectron width of the intermediate charmonium, respectively. $\Phi_{2 \rightarrow 2}$ is the phase space and s donates the center-of-mass energy. The only remaining unknown term $\mathcal{B}(\psi \rightarrow \eta J/\psi)$ is the branching ratio of the associated charmonium decay into $\eta J/\psi$, we will present the details of the calculation for the $\psi \rightarrow \eta J/\psi$ decay next.

TABLE I: The theoretical mixing angles, assignments, masses, total widths, and dielectron widths of higher charmonia in the range of 4.0 ~ 4.5 GeV, which are obtained from the theoretical predictions [22–24] and some experimental values which are close to the theoretical predictions.

States	θ	Assignment	Mass (MeV)	Γ (MeV)	$\Gamma_\psi^{e^+e^-}$ (keV)
$\psi(4040)$	20°	ψ'_{3S-2D}	4039 ± 1 [20]	80 ± 10 [20]	0.830 [29]
$\psi(4160)$	20°	ψ''_{3S-2D}	4159 ± 20 [30]	78 ± 20 [30]	0.480 [29]
$\psi(4220)$	34°	ψ'_{4S-3D}	4222	44	0.290
$\psi(4380)$	34°	ψ''_{4S-3D}	4389	80	0.257
$\psi(4415)$	30°	ψ'_{5S-4D}	4414	33	0.230
$\psi(4500)$	30°	ψ''_{5S-4D}	4509	50	0.113

A. Calculating the branching ratios of higher charmonium decays into $\eta J/\psi$

In Ref. [22], an S - D mixing scheme was proposed to construct the energy level structure of vector charmonia in the range of 4.0 ~ 4.5 GeV, as shown below,

$$\begin{pmatrix} |\psi'\rangle \\ |\psi''\rangle \end{pmatrix} = \begin{pmatrix} \cos \theta & \sin \theta \\ -\sin \theta & \cos \theta \end{pmatrix} \begin{pmatrix} |\psi(nS)\rangle \\ |\psi((n-1)D)\rangle \end{pmatrix}, \quad (2)$$

where θ denotes the mixing angle.

In this scheme, $\psi(4220)$ was assigned to a $4S$ - $3D$ mixing state while its partner $\psi(4380)$ was predicted. The well-established $\psi(4415)$ was assigned into a $5S$ - $4D$ mixing state while its partner $\psi(4500)$ was predicted and was found to exist in the BESIII measurement of $e^+e^- \rightarrow K^+K^-J/\psi$ [23]. The assignment of $\psi(4040)$ and $\psi(4160)$ with a $3S$ - $2D$ mixing scheme has also been proposed in Ref. [23] to match the experimental dielectron width of $\psi(4160)$ [29]. The mixing angles are listed in Table I. Next, we will utilize the hadronic loop mechanism to calculate the branching ratios of the hidden-charm decays of $\psi \rightarrow \eta J/\psi$ for the above charmonia.

The hadronic loop mechanism has been widely used to study the hidden-flavor decays of heavy quarkonia above the

open-flavor thresholds [31–52] and the calculated branching ratios are usually comparable to the experimental measurements. In the framework of the hadronic loop mechanism, the higher charmonium ψ'/ψ'' within an S - D mixture first decay into a pair of charmed mesons $D^{(*)}\bar{D}^{(*)}$, and reach the $\eta J/\psi$ final states by exchanging a D or D^* meson as shown in Fig. 1. The general expression for the amplitude mediated by the charmed meson loop is

$$\mathcal{M} = \int \frac{d^4q}{(2\pi)^4} \frac{\mathcal{V}_1 \mathcal{V}_2 \mathcal{V}_3}{\mathcal{P}_1 \mathcal{P}_2 \mathcal{P}_E} \mathcal{F}^2(q^2, m_E^2), \quad (3)$$

where \mathcal{V}_i ($i = 1, 2, 3$) are interaction vertices, and \mathcal{P}_i ($i = 1, 2, E$) denote the corresponding propagators of intermediate charmed mesons. The form factor $\mathcal{F}(q^2, m_E^2)$ is introduced to compensate for the off-shell effect of the exchanged $D^{(*)}$ meson and to depict the structure effect of the interaction vertices. In our calculation, the monopole form factor is taken as

$$\mathcal{F}(q^2, m_E^2) = \frac{\Lambda^2 - m_E^2}{\Lambda^2 - q^2}, \quad (4)$$

where m_E and q are the mass and four momentum of the exchanged intermediate meson, respectively. The cutoff Λ can be parameterized as $\Lambda = m_E + \alpha \Lambda_{QCD}$, with $\Lambda_{QCD} = 220$ MeV [31–33], α is usually of order of 1 and depends on the specific processes [52].

The effective Lagrangian approach is used to give the concrete expressions for the decay amplitudes defined in Eq. (3). The Lagrangians of the concrete interactions involved in Fig. 1 are listed below [48],

$$\begin{aligned} \mathcal{L}_{\psi(S)D^{(*)}D^{(*)}} &= ig_{\psi(S)DD}\psi^\mu(\partial_\mu D^\dagger D - D^\dagger \partial_\mu D) \\ &+ g_{\psi(S)DD^*}\varepsilon_{\mu\nu\alpha\beta}\partial^\mu\psi^\nu(D^{*\alpha\dagger}\partial^\nu D - D^\dagger\partial^\beta D^{*\alpha}) \\ &+ ig_{\psi(S)D^*D^*}\psi^\mu(\partial_\nu D_\mu^{*\dagger}D^{*\nu} - D^{*\nu\dagger}\partial_\nu D_\mu^*) \\ &+ D^{*\nu\dagger}\partial_\mu D_\nu^*), \end{aligned} \quad (5)$$

$$\begin{aligned} \mathcal{L}_{\psi(D)D^{(*)}D^{(*)}} &= ig_{\psi(D)DD}\psi^\mu(\partial_\mu D^\dagger D - D^\dagger \partial_\mu D) \\ &+ g_{\psi(D)DD^*}\varepsilon_{\mu\nu\alpha\beta}\partial^\mu\psi^\nu(D^{*\alpha\dagger}\partial^\nu D - D^\dagger\partial^\beta D^{*\alpha}) \\ &+ ig_{\psi(D)D^*D^*}\psi^\mu(\partial_\nu D_\mu^{*\dagger}D^{*\nu} - D^{*\nu\dagger}\partial_\nu D_\mu^*) \\ &+ 4D^{*\nu\dagger}\partial_\mu D_\nu^*), \end{aligned} \quad (6)$$

$$\begin{aligned} \mathcal{L}_{D^{(*)}D^*\eta} &= ig_{DD^*\eta}(D_\mu^{*\dagger}D - D^\dagger D_\mu^*)\partial^\mu\eta \\ &- g_{D^*D^*\eta}\varepsilon_{\mu\nu\alpha\beta}\partial^\mu D^{*\dagger\nu}\partial^\alpha D^{*\beta}\eta \end{aligned} \quad (7)$$

with $D^{(*)\dagger} = (D^{(*)0}, D^{(*)+})$ and $D^{(*)} = (\bar{D}^{(*)0}, \bar{D}^{(*)-})^T$.

With the above preparations, we can write down the amplitudes of $\psi(4040)$ and $\psi(4160)$ decays into $\eta J/\psi$ within the $3S$ - $2D$ mixing scheme defined in Eq. (2), as shown in Fig. 1,

$$\mathcal{M}_{\psi(4040)}^{\text{Total}} = 4 \sum_{i=1}^6 \mathcal{M}_{\psi(4040)}^{(i)}, \quad (8)$$

$$\mathcal{M}_{\psi(4160)}^{\text{Total}} = 4 \sum_{i=1}^6 \mathcal{M}_{\psi(4160)}^{(i)}, \quad (9)$$

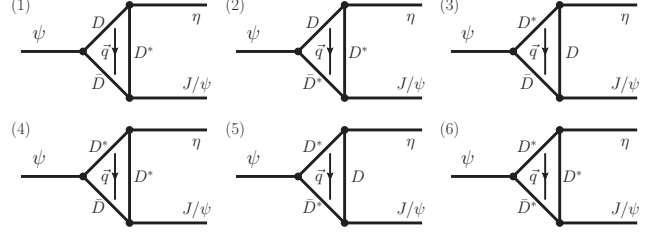


FIG. 1: The schematic diagrams illustrate the decay of higher charmonium into $\eta J/\psi$ via the hadronic loop mechanism.

where the fourfold factor comes from the charge conjugation transformation ($D^{(*)} \leftrightarrow \bar{D}^{(*)}$) and the isospin transformations ($D^{(*)0} \leftrightarrow D^{(*)+}$ and $\bar{D}^{(*)0} \leftrightarrow D^{(*)-}$) of the bridged $D^{(*)}$ mesons. The concrete expressions of $\mathcal{M}_{\psi(4040)}^{(i)}$ and $\mathcal{M}_{\psi(4160)}^{(i)}$ are given in Appendix A, the amplitudes of the others are similar to the group of $\psi(4040)$ and $\psi(4160)$ with different coupling constants and mixing angles.

TABLE II: The coupling constants of the $g_{\psi D^{(*)}D^{(*)}}$ and \mathcal{S} values recommended in Table III of Ref. [23], where $g_{\psi(4040)D^{(*)}D^{(*)}}$ and $g_{\psi(4160)D^{(*)}D^{(*)}}$ are determined by the theoretical partial widths of $\psi(4040)/\psi(4160) \rightarrow D^{(*)}\bar{D}^{(*)}$ listed in Table III.

Charmonia	θ	$g_{\psi DD}$	$g_{\psi DD^*}$ (GeV $^{-1}$)	$g_{\psi D^* D^*}$	\mathcal{S}
$\psi(4040)$	20°	0.378	0.462	8.607	1.140
$\psi(4160)$	20°	-2.730	-0.070	-1.881	-0.762
$\psi(4220)$	34°	0.760	0.054	1.220	1.471
$\psi(4380)$	34°	0.570	-0.150	-0.410	-1.077
$\psi(4415)$	30°	0.680	0.003	0.430	1.705
$\psi(4500)$	30°	0.440	-0.076	-0.015	-33.989

TABLE III: The partial width of $\psi(4040)/\psi(4160) \rightarrow D^{(*)}\bar{D}^{(*)}$ calculated by the quark pair creation (QPC) model, the parameters are in agreement with Ref. [22].

Charmonia	$D\bar{D}$ (MeV)	$D\bar{D}^* + c.c.$ (MeV)	$D^*\bar{D}^*$ (MeV)
$\psi(4040)$	0.433	17.187	40.893
$\psi(4160)$	35.620	0.919	51.223

Finally, the branching ratio of the charmonium decay into $\eta J/\psi$ can be obtained by

$$\mathcal{BR}[\psi \rightarrow J/\psi\eta] = \frac{1}{3} \frac{|\vec{p}_1|}{8\pi m_\psi^2} \sum_{spin} |\mathcal{M}_\psi^{\text{Total}}|^2 / \Gamma_\psi, \quad (10)$$

where m_ψ and Γ_ψ are the mass and total width of the initial charmonium listed in Table I, \vec{p}_1 is the three-momentum of the η meson in the rest frame of the initial state. The coefficient $1/3$ and the sum \sum_{spin} come from the averaging over the polarizations of the initial state and summing up the polarizations of the final state.

TABLE IV: The fitting parameters in Scheme I, and the solutions A, B and C in Scheme II. The g and a are parameters for the background, and \mathcal{BR}_i and ϕ_i (rad) are decay branching ratios into $J/\psi\eta$ and phases for five ψ states (successively $\psi(4040)$, $\psi(4160)$, $\psi(4220)$, $\psi(4380)$ and $\psi(4415)$), respectively.

Parameters	Scheme I	Scheme II		
	Fit I	Solution A	Solution B	Solution C
\mathcal{BR}_1	5.086×10^{-3}	$(2.627 \pm 0.305) \times 10^{-3}$	$(6.708 \pm 0.344) \times 10^{-3}$	$(3.256 \pm 0.232) \times 10^{-3}$
\mathcal{BR}_2	1.516×10^{-3}	$(2.598 \pm 0.626) \times 10^{-3}$	$(6.853 \pm 0.259) \times 10^{-3}$	$(9.461 \pm 0.361) \times 10^{-3}$
\mathcal{BR}_3	1.970×10^{-3}	$(4.332 \pm 0.359) \times 10^{-3}$	$(5.343 \pm 0.226) \times 10^{-3}$	$(2.299 \pm 0.052) \times 10^{-2}$
\mathcal{BR}_4	4.063×10^{-4}	$(1.370 \pm 0.129) \times 10^{-3}$	$(1.663 \pm 0.152) \times 10^{-3}$	$(2.145 \pm 0.182) \times 10^{-3}$
\mathcal{BR}_5	1.746×10^{-3}	$(2.971 \pm 0.570) \times 10^{-4}$	$(3.047 \pm 0.621) \times 10^{-4}$	$(3.147 \pm 0.681) \times 10^{-4}$
ϕ_1 (rad)	2.347 ± 0.294	3.075 ± 0.179	3.841 ± 0.031	3.440 ± 0.045
ϕ_2 (rad)	0.665 ± 0.199	2.698 ± 0.049	1.647 ± 0.029	3.746 ± 0.020
ϕ_3 (rad)	2.413 ± 0.094	4.391 ± 0.086	3.646 ± 0.053	1.311 ± 0.017
ϕ_4 (rad)	5.107 ± 0.128	0.279 ± 0.116	0.070 ± 0.055	6.035 ± 0.051
ϕ_5 (rad)	4.264 ± 0.196	0.217 ± 0.207	0.047 ± 0.237	6.049 ± 0.223
$\chi^2/d.o.f.$	1.653	0.817	0.811	0.806

Below is a brief description of the method for determining the relevant coupling constants, as they appear in the concrete amplitudes outlined in Appendix A.

The coupling constants of $g_{D^{(*)}D^*\eta}$ are given in Ref. [48],

$$\frac{g_{D^*D\eta}}{\sqrt{m_D m_{D^*}}} = g_{D^*D^*\eta} = \frac{2g_H}{f_\pi}\alpha, \quad (11)$$

with $\alpha = \frac{1}{\sqrt{6}} \cos(-19.1^\circ)$ and $f_\pi = 131$ MeV, and $g_H = 0.569$ is determined by the measured decay width of $D^{*+} \rightarrow D^0\pi^+$ [43]. $g_{J/\psi DD} = 7.44$, $g_{J/\psi DD^*} = 3.84$ GeV $^{-1}$ and $g_{J/\psi D^*D^*} = 8.00$ are obtained by the vector meson dominance model [53, 54].

Taking the $3S-2D$ mixing charmonia $\psi(4040)$ and $\psi(4160)$ as examples, the coupling constants of $g_{\psi(4040)D^{(*)}D^{(*)}}$ and $g_{\psi(4160)D^{(*)}D^{(*)}}$ are defined by

$$\begin{cases} g_{\psi(4040)D^{(*)}D^{(*)}} = g_{\psi(3S)D^{(*)}D^{(*)}} \cos \theta + g_{\psi(2D)D^{(*)}D^{(*)}} \sin \theta \\ g_{\psi(4160)D^{(*)}D^{(*)}} = -g_{\psi(3S)D^{(*)}D^{(*)}} \sin \theta + g_{\psi(2D)D^{(*)}D^{(*)}} \cos \theta \end{cases}, \quad (12)$$

The values are determined by the theoretical partial widths of $\psi(4040)/\psi(4160) \rightarrow D^{(*)}D^{(*)}$ calculated by the QPC model [55–57], in which the mixing angle $\theta = 20^\circ$ is considered [23]. The other parameters required by the model are in agreement with Ref. [22], and the calculated partial widths associated with $\psi(4040)$ and $\psi(4160)$ are listed in Table III. Other coupling constants of $g_{\psi(4220)D^{(*)}D^{(*)}}$, $g_{\psi(4380)D^{(*)}D^{(*)}}$, $g_{\psi(4415)D^{(*)}D^{(*)}}$ and $g_{\psi(4500)D^{(*)}D^{(*)}}$ have been calculated in Table III of Ref. [23], which were determined by the corresponding experimental or theoretical partial widths of $\psi \rightarrow D^{(*)}D^{(*)}$. Both of them are listed in Table II. In addition, for convenience, the S factors in the decay amplitudes of Appendix A are defined

as

$$\begin{cases} \mathcal{S}_{\psi(4040)} = \frac{g_{\psi(3S)D^*D^*} \cos \theta + 4g_{\psi(2D)D^*D^*} \sin \theta}{g_{\psi(3S)D^*D^*} \cos \theta + g_{\psi(2D)D^*D^*} \sin \theta} \\ \mathcal{S}_{\psi(4160)} = \frac{-g_{\psi(3S)D^*D^*} \sin \theta + 4g_{\psi(2D)D^*D^*} \cos \theta}{-g_{\psi(3S)D^*D^*} \sin \theta + g_{\psi(2D)D^*D^*} \cos \theta} \end{cases}. \quad (13)$$

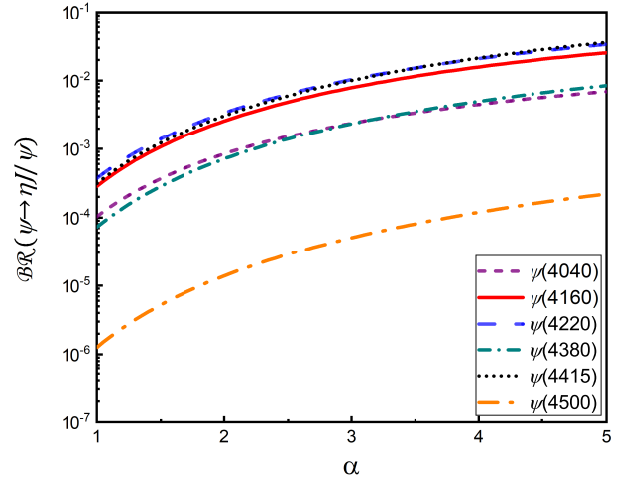


FIG. 2: The α parameter dependence of the predicted branching ratios, including $\mathcal{BR}(\psi(4040) \rightarrow \eta J/\psi)$, $\mathcal{BR}(\psi(4160) \rightarrow \eta J/\psi)$, $\mathcal{BR}(\psi(4220) \rightarrow \eta J/\psi)$, $\mathcal{BR}(\psi(4380) \rightarrow \eta J/\psi)$, $\mathcal{BR}(\psi(4415) \rightarrow \eta J/\psi)$, and $\mathcal{BR}(\psi(4500) \rightarrow \eta J/\psi)$.

With the determined coupling constants discussed above, we calculate the branching ratios of the six theoretically constructed charmonia, i.e., $\psi(4040)$, $\psi(4160)$, $\psi(4220)$, $\psi(4380)$, $\psi(4415)$ and $\psi(4500)$ decays into $\eta J/\psi$, which depend on the cutoff parameter α introduced by the form factor of Eq. (4) in

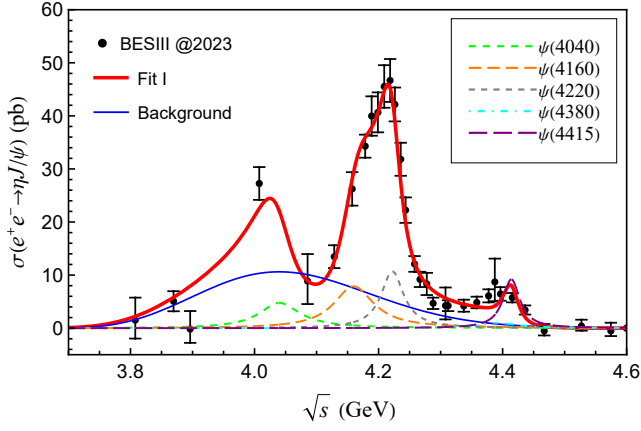


FIG. 3: Our fit to the higher vector charmonium contribution in the cross section distribution of $e^+e^- \rightarrow \eta J/\psi$ within scheme I. Here, the data points are from BESIII measurement [10], the five dashed lines represent the contributions of the higher charmonium states, the blue line represents the background, and the red line represents the total contribution.

the range of [1, 5], as shown in Fig. 2. It can be seen that the branching ratios associated with $\psi(4040)$, $\psi(4160)$, $\psi(4220)$ and $\psi(4380)$, $\psi(4415)$ can reach the order of $10^{-4} \sim 10^{-2}$ and $10^{-4} \sim 10^{-3}$, respectively, while $\mathcal{BR}(\psi(4500) \rightarrow \eta J/\psi)$ is only of order of $10^{-6} \sim 10^{-5}$.

B. A combined fit to the cross section data of $e^+e^- \rightarrow \eta J/\psi$

With the input of the branching ratios $\mathcal{BR}(\psi \rightarrow \eta J/\psi)$ predicted by the hadronic loop mechanism as shown in Fig. 2, we can now obtain the contribution of each vector charmonium to the cross section of $e^+e^- \rightarrow \eta J/\psi$ from Eq. (1), and apply a combined fit to the experimental data.

Since the branching ratio of $\psi(4500) \rightarrow \eta J/\psi$ is at least two orders of magnitude smaller than the others, and there is indeed no signal of structures around 4.5 GeV in the measured data of $e^+e^- \rightarrow \eta J/\psi$, we believe that the contribution of $\psi(4500)$ to the cross section of $e^+e^- \rightarrow \eta J/\psi$ can be safely dropped. In the following, we will use the left five theoretically constructed charmonia, i.e. $\psi(4040)$, $\psi(4160)$, $\psi(4220)$, $\psi(4380)$, $\psi(4415)$, as well as their theoretical branching ratios of decays into $\eta J/\psi$, dependent on the α parameter, to perform a combined fit to the cross section data of $e^+e^- \rightarrow \eta J/\psi$.

The total amplitude of $e^+e^- \rightarrow \eta J/\psi$ can be written as

$$\mathcal{M}_{\text{Total}}(s) = \mathcal{M}_0(s) + \sum_i e^{i\phi_i} \mathcal{M}_{\psi_i}(s), \quad (14)$$

with an exponentially parameterized background formulated as

$$\mathcal{M}_0(s) = g(\sqrt{s} - m_\eta - m_{J/\psi})^2 e^{-a(\sqrt{s} - m_\eta - m_{J/\psi})^2}, \quad (15)$$

where ϕ_i is the phase angle between the resonance amplitude $\mathcal{M}_{\psi_i}(s)$ and the background $\mathcal{M}_0(s)$, g and a are two free parameters.

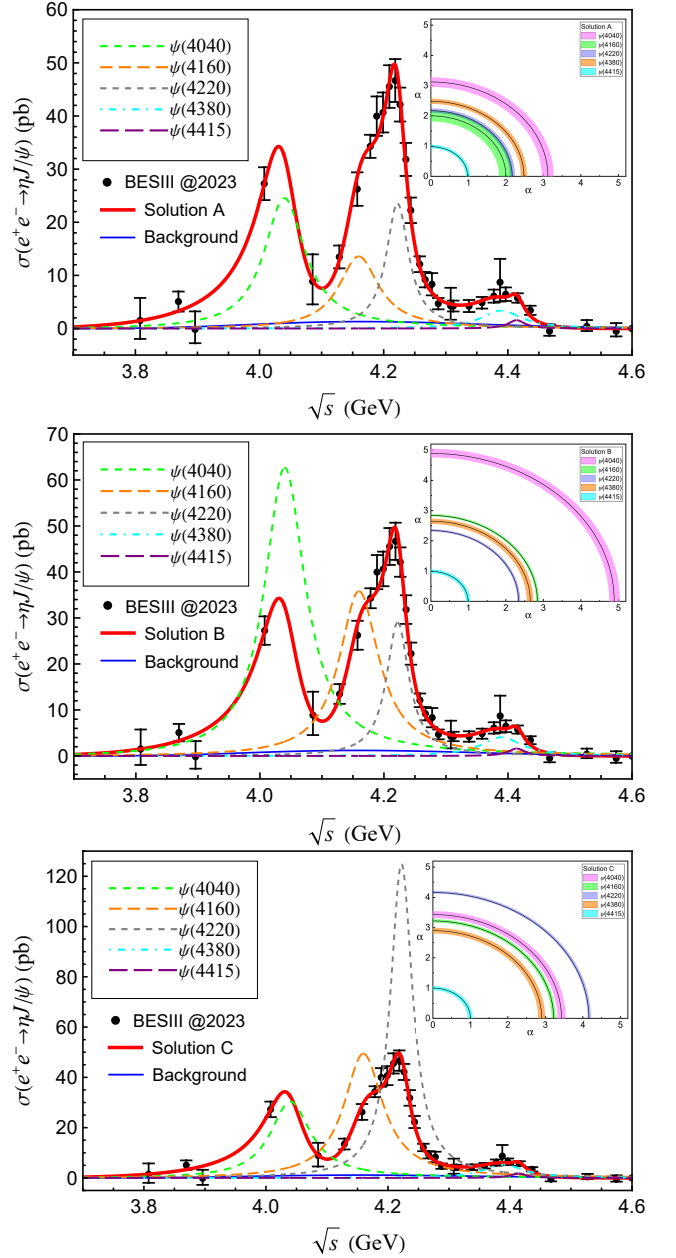


FIG. 4: Our fit to the cross section of the $e^+e^- \rightarrow \eta J/\psi$ process between $E_{cm}=3.808$ to 4.600 GeV by Scheme II. Here, the five dashed lines represent the contributions of the higher charmonium states, the blue line represents the background, and the red line represents the total contribution. The inset plots represent the α values corresponding to the fitted branching ratios in Table IV by the results of the hadronic loop predictions in Fig. 2, where the central values and the errors are represented by the solid black lines and the coloured bands, respectively.

The total cross section can be represented by

$$\sigma(s) = |\mathcal{M}_{\text{Total}}(s)|^2. \quad (16)$$

Here, we employ two fitting schemes. In the first scheme, we assume a same α parameter for all charmonium states. The best fitting result in Scheme I, represented by a red curve, is

shown in Fig. 3, with $\chi^2/d.o.f = 1.65$. The relevant fitting parameters in Scheme I are listed in Table IV.

A direct observation in Fig. 3 shows that the line shape around 4.0 GeV is not well reproduced in Scheme I. This is mainly due to the scarcity of cross section data points around 4.0 GeV, which puzzles us in determining the contribution of the resonance state $\psi(4040)$. Our analysis suggests two resonance contributions from $\psi(4160)$ and $\psi(4220)$ around 4.2 GeV, and also reveals a significant resonance signal from $\psi(4415)$ in $e^+e^- \rightarrow \eta J/\psi$, which should be a focus of future BESIII and Belle II experiments. In particular, we found that the interference effect plays a crucial role in broadening the distribution of the resonance signal associated with $Y(4230)$, explaining its large width of $80.4 \pm 4.4 \pm 1.4$ MeV in the experimental fit and the line shape puzzle around 4.2 GeV in the $e^+e^- \rightarrow \eta J/\psi$ cross section.

In Scheme II, we consider a range of α parameters [1, 5] for the five charmonium states without extra limit. The three solutions A, B and C in scheme II, represented by red curve, are shown in Fig. 4 with $\chi^2/d.o.f$ around 0.81, which is obviously improved compared to that of scheme I. The relevant fitting parameters in Scheme II are listed in Table IV.

Similar to Scheme I, our analysis in Scheme II shows the significant role of the interference effects in broadening the distribution of the resonance signal associated with $\psi(4160)$ and $\psi(4220)$, which naturally explains the asymmetric line shape associated with the resonance structure denoted as $Y(4230)$. Of the three solutions, $\psi(4040)$ gives different contributions to the cross section, and we hope that the experiment will complement the data points around in this part and clarify the contribution of $\psi(4040)$. And around 4.4 GeV, each solution in Scheme II shows an unremarkable resonance signal of $\psi(4415)$ in $e^+e^- \rightarrow \eta J/\psi$. Further investigation in future BESIII and Belle II experiments is indeed necessary to solve the broad width puzzle associated with the resonance structure denoted as $Y(4360)$.

III. SUMMARY

Recently, the BESIII Collaboration measured the Born cross section of $e^+e^- \rightarrow \eta J/\psi$ from 3.808 to 4.951 GeV, and reported three structures, the charmonium $\psi(4040)$ and two other charmoniumlike states, named $Y(4230)$ and $Y(4360)$ [10]. It is curious that the measured width of $Y(4230)$ is so large and has a large difference from the other open-charm and hidden-charm measurements, and the more subtle details of the line shape around 4.2 GeV with asymmetry suggest that the structure of the observed $Y(4230)$ may not be formed by a single resonance.

In order to understand the puzzles arising in the measured data, the energy levels structures of the charmonia from theoretical inputs are crucial. In this work, we focus on the six charmonia constructed by an unquenched potential model in the range of 4.0 ~ 4.5 GeV, i.e., $\psi(4040)$, $\psi(4160)$, $\psi(4220)$, $\psi(4380)$, $\psi(4415)$, $\psi(4500)$. Using the hadronic loop mechanism, we are able to quantitatively calculate the branching ratios of the higher charmonium state decays into $\eta J/\psi$. The results indicate that the contribution of $\psi(4500)$ to the cross section of $e^+e^- \rightarrow \eta J/\psi$ is negligible, which is in agreement with the measured data, while others have sizable contributions. We then perform a combined fit with the left five charmonia to the newly measured cross section data of $e^+e^- \rightarrow \eta J/\psi$, the corresponding branching ratios of these charmonia decaying into $\eta J/\psi$ are constrained within a reasonable range, suggested by the hadronic loop mechanism. We have made two attempts with different cut-off parameter constraint schemes. Both fitting results show that the newly measured cross section of $e^+e^- \rightarrow \eta J/\psi$ can be reproduced by the five charmonia from the theoretical inputs, the puzzling large width and asymmetric line shape of the 4.2 GeV structure can be naturally explained by the contributions of the neighbouring charmonia $\psi(4160)$ and $\psi(4220)$. Moreover, the introduction of $\psi(4380)$ predicted by the theory in the combined fit is compatible with the experimental data, which together with $\psi(4415)$ can reproduce the third broad enhancement structure around 4.4 GeV reported by BESIII. More importantly, the results support the characterized energy level construction of higher vector charmonia in the range of 4.0 ~ 4.5 GeV.

With the increasing accumulation of experimental data on the varieties of final states in this particular charmonium energy range, as well as the continuing attention of experimentalists and theorists, our understanding of the inner nature of higher charmonium states is becoming more mature and profound.

IV. ACKNOWLEDGMENTS

This work is supported by the National Natural Science Foundation of China under Grant Nos. 12335001 and 12247101, the China National Funds for Distinguished Young Scientists under Grant No. 11825503, National Key Research and Development Program of China under Contract No. 2020YFA0406400, the 111 Project under Grant No. B20063, the fundamental Research Funds for the Central Universities, and the project for top-notch innovative talents of Gansu province. J.Z.W. is also supported by the National Postdoctoral Program for Innovative Talent.

Appendix A: The decay amplitudes of hadronic loop mechanism

$$\begin{aligned} \mathcal{M}_{\psi(4040)}^{(1)} &= \int \frac{d^4q}{(2\pi)^4} g_{\psi(4040)DD} \times \epsilon_{\psi}^{\mu}(q_{2\mu} - q_{1\mu})(-g_{DD^*\eta}) p_1^{\alpha} g_{J/\psi DD^*} \epsilon_{\lambda\gamma\beta\rho} p_2^{\lambda} \epsilon_{J/\psi}^{\gamma}(q_2^{\rho} - q^{\rho}) \\ &\quad \times (-g_{\alpha}^{\beta} + q_{\alpha} q^{\beta} / m_{D^*}^2) \frac{\mathcal{F}^2(q^2, m_{B^*}^2)}{q^2 - m_{D^*}^2}, \end{aligned} \quad (\text{A1})$$

$$\begin{aligned} \mathcal{M}_{\psi(4040)}^{(2)} &= \int \frac{d^4q}{(2\pi)^4} g_{\psi(4040)DD^*} \epsilon_{\nu\mu\alpha\beta} \epsilon_{\psi}^{\mu}(q_2^{\beta} - q_1^{\beta})(-g_{D^*D^*\eta}) \epsilon_{\rho\eta\lambda\theta} q^{\rho} q_1^{\lambda} (g_{J/\psi DD^*}) \epsilon_{\delta\theta\tau\gamma} \epsilon_{J/\psi}^{\theta} p_2^{\delta} (q^{\gamma} - q_2^{\gamma}) \\ &\quad \times (-g^{\alpha\eta} + q_1^{\alpha} q_1^{\eta} / m_{D^*}^2)(-g^{\tau\sigma} + q^{\tau} q^{\sigma} / m_{D^*}^2) \frac{\mathcal{F}^2(q^2, m_{B^*}^2)}{q^2 - m_{D^*}^2}, \end{aligned} \quad (\text{A2})$$

$$\begin{aligned} \mathcal{M}_{\psi(4040)}^{(3)} &= \int \frac{d^4q}{(2\pi)^4} g_{\psi(4040)DD^*} \epsilon_{\nu\mu\alpha\beta} \epsilon_{\psi}^{\mu} p^{\nu}(q_2^{\beta} - q_1^{\beta})(g_{D^*D\eta}) p_1^{\gamma} (g_{J/\psi DD}) \epsilon_{J/\psi}^{\rho} (q_{\rho} - q_{2\rho}) \\ &\quad \times (-g_{\gamma}^{\alpha} + q_1^{\alpha} q_1^{\gamma} / m_{D^*}^2) \frac{\mathcal{F}^2(q^2, m_{B^*}^2)}{q^2 - m_{D^*}^2}, \end{aligned} \quad (\text{A3})$$

$$\begin{aligned} \mathcal{M}_{\psi(4040)}^{(4)} &= \int \frac{d^4q}{(2\pi)^4} g_{\psi(4040)DD^*} \epsilon_{\nu\mu\alpha\beta} \epsilon_{\psi}^{\mu}(q_2^{\beta} - q_1^{\beta})(g_{D^*D\eta}) p_1^{\gamma} (g_{J/\psi D^*D}) \epsilon_{J/\psi}^{\rho} [g_{\sigma\rho} q_{2\eta} - g_{\eta\rho} q_{1\sigma} + g_{\theta\eta}(q_{\rho} - q_{2\rho})] \\ &\quad \times (-g^{\alpha\sigma} + q_2^{\alpha} q_2^{\sigma} / m_{D^*}^2)(-g_{\gamma}^{\eta} + q_{\gamma} q^{\eta} / m_{D^*}^2) \frac{\mathcal{F}^2(q^2, m_{B^*}^2)}{q^2 - m_{D^*}^2}, \end{aligned} \quad (\text{A4})$$

$$\begin{aligned} \mathcal{M}_{\psi(4040)}^{(5)} &= \int \frac{d^4q}{(2\pi)^4} g_{\psi(4040)D^*D^*} \epsilon_{\psi}^{\mu} [g_{\beta\mu} q_{2\alpha} - g_{\alpha\mu} q_{1\beta} + \mathcal{S} \cdot g_{\alpha\beta}(q_{1\mu} - q_{2\mu})] (-g_{D^*D^*\eta}) \epsilon_{\rho\sigma\lambda\eta} q_1^{\lambda} q^{\rho} (g_{J/\psi DD^*}) \\ &\quad \times \epsilon_{J/\psi}^{\gamma} [g_{\tau\gamma} q_{2\theta} - g_{\theta\gamma} q_{1\tau} + g_{\tau\theta}(q_{\gamma} - q_{2\gamma})] \\ &\quad \times (-g^{\alpha\eta} + q_1^{\alpha} q_1^{\eta} / m_{D^*}^2)(-g^{\tau\beta} + q_2^{\tau} q_2^{\beta} / m_{D^*}^2)(-g^{\sigma\theta} + q^{\sigma} q^{\theta} / m_{D^*}^2) \frac{\mathcal{F}^2(q^2, m_{B^*}^2)}{q^2 - m_{D^*}^2}, \end{aligned} \quad (\text{A5})$$

$$\begin{aligned} \mathcal{M}_{\psi(4040)}^{(6)} &= \int \frac{d^4q}{(2\pi)^4} g_{\psi(4040)D^*D^*} \epsilon_{\psi}^{\mu} [g_{\beta\mu} q_{2\alpha} - g_{\alpha\mu} q_{1\beta} + \mathcal{S} \cdot g_{\alpha\beta}(q_{1\mu} - q_{2\mu})] (g_{D^*D\eta}) p_1^{\gamma} (g_{J/\psi DD^*}) \epsilon_{\lambda\eta\sigma\rho} \epsilon_{J/\psi}^{\eta} p_2^{\lambda} (q^{\rho} - q_2^{\rho}) \\ &\quad \times (-g_{\gamma}^{\alpha} + q_1^{\alpha} q_{1\gamma} / m_{D^*}^2)(-g^{\beta\sigma} + q^{\beta} q^{\sigma} / m_{D^*}^2) \frac{\mathcal{F}^2(q^2, m_{B^*}^2)}{q^2 - m_{D^*}^2}, \end{aligned} \quad (\text{A6})$$

$$\begin{aligned} \mathcal{M}_{\psi(4160)}^{(1)} &= \int \frac{d^4q}{(2\pi)^4} g_{\psi(4160)DD} \times \epsilon_{\psi}^{\mu}(q_{2\mu} - q_{1\mu})(-g_{DD^*\eta}) p_1^{\alpha} g_{J/\psi DD^*} \epsilon_{\lambda\gamma\beta\rho} p_2^{\lambda} \epsilon_{J/\psi}^{\gamma}(q_2^{\rho} - q^{\rho}) \\ &\quad \times (-g_{\alpha}^{\beta} + q_{\alpha} q^{\beta} / m_{D^*}^2) \frac{\mathcal{F}^2(q^2, m_{B^*}^2)}{q^2 - m_{D^*}^2}, \end{aligned} \quad (\text{A7})$$

$$\begin{aligned} \mathcal{M}_{\psi(4160)}^{(2)} &= \int \frac{d^4q}{(2\pi)^4} g_{\psi(4160)DD^*} \epsilon_{\nu\mu\alpha\beta} \epsilon_{\psi}^{\mu}(q_2^{\beta} - q_1^{\beta})(-g_{D^*D^*\eta}) \epsilon_{\rho\eta\lambda\theta} q^{\rho} q_1^{\lambda} (g_{J/\psi DD^*}) \epsilon_{\delta\theta\tau\gamma} \epsilon_{J/\psi}^{\theta} p_2^{\delta} (q^{\gamma} - q_2^{\gamma}) \\ &\quad \times (-g^{\alpha\eta} + q_1^{\alpha} q_1^{\eta} / m_{D^*}^2)(-g^{\tau\sigma} + q^{\tau} q^{\sigma} / m_{D^*}^2) \frac{\mathcal{F}^2(q^2, m_{B^*}^2)}{q^2 - m_{D^*}^2}, \end{aligned} \quad (\text{A8})$$

$$\begin{aligned} \mathcal{M}_{\psi(4160)}^{(3)} &= \int \frac{d^4q}{(2\pi)^4} g_{\psi(4160)DD^*} \epsilon_{\nu\mu\alpha\beta} \epsilon_{\psi}^{\mu} p^{\nu}(q_2^{\beta} - q_1^{\beta})(g_{D^*D\eta}) p_1^{\gamma} (g_{J/\psi DD}) \epsilon_{J/\psi}^{\rho} (q_{\rho} - q_{2\rho}) \\ &\quad \times (-g_{\gamma}^{\alpha} + q_1^{\alpha} q_1^{\gamma} / m_{D^*}^2) \frac{\mathcal{F}^2(q^2, m_{B^*}^2)}{q^2 - m_{D^*}^2}, \end{aligned} \quad (\text{A9})$$

$$\begin{aligned} \mathcal{M}_{\psi(4160)}^{(4)} &= \int \frac{d^4q}{(2\pi)^4} g_{\psi(4160)DD^*} \epsilon_{\nu\mu\alpha\beta} \epsilon_{\psi}^{\mu}(q_2^{\beta} - q_1^{\beta})(g_{D^*D\eta}) p_1^{\gamma} (g_{J/\psi D^*D^*}) \epsilon_{J/\psi}^{\rho} [g_{\sigma\rho} q_{2\eta} - g_{\eta\rho} q_{1\sigma} + g_{\theta\eta}(q_{\rho} - q_{2\rho})] \\ &\quad \times (-g^{\alpha\sigma} + q_2^{\alpha} q_2^{\sigma} / m_{D^*}^2)(-g_{\gamma}^{\eta} + q_{\gamma} q^{\eta} / m_{D^*}^2) \frac{\mathcal{F}^2(q^2, m_{B^*}^2)}{q^2 - m_{D^*}^2}, \end{aligned} \quad (\text{A10})$$

$$\begin{aligned} \mathcal{M}_{\psi(4160)}^{(5)} = & \int \frac{d^4q}{(2\pi)^4} g_{\psi(4160)D^*D^*} \epsilon_{\psi}^{\mu} [g_{\beta\mu} q_{2\alpha} - g_{\alpha\mu} q_{1\beta} + \mathcal{S} \cdot g_{\alpha\beta} (q_{1\mu} - q_{2\mu})] (-g_{D^*D^*\eta}) \epsilon_{\rho\sigma\lambda\eta} q_1^{\lambda} q^{\rho} (g_{J/\psi D^* D^*}) \\ & \times \epsilon_{J/\psi}^{\gamma} [g_{\tau\gamma} q_{2\theta} - g_{\theta\gamma} q_{1\tau} + g_{\tau\theta} (q_{\gamma} - q_{2\gamma})] \\ & \times (-g^{\alpha\eta} + q_1^{\alpha} q_1^{\eta} / m_{D^*}^2) (-g^{\tau\beta} + q_2^{\tau} q_2^{\beta} / m_{D^*}^2) (-g^{\sigma\theta} + q^{\sigma} q^{\theta} / m_{D^*}^2) \frac{\mathcal{F}^2(q^2, m_{B^*}^2)}{q^2 - m_{D^*}^2}, \end{aligned} \quad (\text{A11})$$

$$\begin{aligned} \mathcal{M}_{\psi(4160)}^{(6)} = & \int \frac{d^4q}{(2\pi)^4} g_{\psi(4160)D^*D^*} \epsilon_{\psi}^{\mu} [g_{\beta\mu} q_{2\alpha} - g_{\alpha\mu} q_{1\beta} + \mathcal{S} \cdot g_{\alpha\beta} (q_{1\mu} - q_{2\mu})] (g_{D^*D^*\eta}) p_1^{\gamma} (g_{J/\psi D^* D^*}) \epsilon_{\lambda\eta\sigma\rho} \epsilon_{J/\psi}^{\eta} p_2^{\lambda} (q^{\rho} - q_2^{\rho}) \\ & \times (-g_{\gamma}^{\alpha} + q_1^{\alpha} q_{1\gamma} / m_{D^*}^2) (-g^{\beta\sigma} + q^{\beta} q^{\sigma} / m_{D^*}^2) \frac{\mathcal{F}^2(q^2, m_{B^*}^2)}{q^2 - m_{D^*}^2}. \end{aligned} \quad (\text{A12})$$

-
- [1] X. Liu, An overview of XYZ new particles, *Chin. Sci. Bull.* **59**, 3815 (2014).
- [2] H. X. Chen, W. Chen, X. Liu, and S. L. Zhu, The hidden-charm pentaquark and tetraquark states, *Phys. Rept.* **639** (2016), 1.
- [3] A. Esposito, A. Pilloni, and A. D. Polosa, Multiquark Resonances, *Phys. Rept.* **668**, 1 (2017).
- [4] H. X. Chen, W. Chen, X. Liu, Y. R. Liu, and S. L. Zhu, A review of the open charm and open bottom systems, *Rept. Prog. Phys.* **80**, 076201 (2017).
- [5] F. K. Guo, C. Hanhart, U. G. Meißner, Q. Wang, Q. Zhao, and B. S. Zou, Hadronic molecules, *Rev. Mod. Phys.* **90**, 015004 (2018); **94**, 029901 (E) (2022).
- [6] S. L. Olsen, T. Skwarnicki, and D. Zieminska, Nonstandard heavy mesons and baryons: Experimental evidence, *Rev. Mod. Phys.* **90**, 015003 (2018).
- [7] Y. R. Liu, H. X. Chen, W. Chen, X. Liu, and S. L. Zhu, Pentaquark and Tetraquark states, *Prog. Part. Nucl. Phys.* **107**, 237 (2019).
- [8] N. Brambilla, S. Eidelman, C. Hanhart, A. Nefediev, C. P. Shen, C. E. Thomas, A. Vairo, and C. Z. Yuan, The XYZ states: experimental and theoretical status and perspectives, *Phys. Rept.* **873**, 1 (2020).
- [9] H. X. Chen, W. Chen, X. Liu, Y. R. Liu, and S. L. Zhu, An updated review of the new hadron states, *Rept. Prog. Phys.* **86**, 026201 (2023).
- [10] M. Ablikim *et al.* [BESIII], Measurement of $e^+e^- \rightarrow \eta J/\psi$ Cross Section from $\sqrt{s} = 3.808$ GeV to 4.951 GeV, [arXiv:2310.03361](https://arxiv.org/abs/2310.03361).
- [11] B. Aubert *et al.* [BaBar], Observation of a broad structure in the $\pi^+\pi^- J/\psi$ mass spectrum around 4.26 GeV/ c^2 , *Phys. Rev. Lett.* **95**, 142001 (2005).
- [12] M. Ablikim *et al.* [BESIII], Precise measurement of the $e^+e^- \rightarrow \pi^+\pi^- J/\psi$ cross section at center-of-mass energies from 3.77 to 4.60 GeV, *Phys. Rev. Lett.* **118**, 092001 (2017).
- [13] M. Ablikim *et al.* [BESIII], Study of the process $e^+e^- \rightarrow \pi^0\pi^0 J/\psi$ and neutral charmonium-like state $Z_c(3900)^0$, *Phys. Rev. D* **102**, 012009 (2020).
- [14] B. Aubert *et al.* [BaBar] Evidence of a broad structure at an invariant mass of 4.32 GeV/ c^2 in the reaction $e^+e^- \rightarrow \pi^+\pi^-\psi(2S)$ measured at BaBar, *Phys. Rev. Lett.* **98**, 212001 (2007).
- [15] M. Ablikim *et al.* [BESIII], Measurement of $e^+e^- \rightarrow \pi^+\pi^-\psi(3686)$ from 4.008 to 4.600 GeV and observation of a charged structure in the $\pi^+\psi(3686)$ mass spectrum, *Phys. Rev. D* **96**, 032004 (2017).
- [16] M. Ablikim *et al.* [BESIII], Evidence of Two Resonant Structures in $e^+e^- \rightarrow \pi^+\pi^- h_c$, *Phys. Rev. Lett.* **118**, 092002 (2017).
- [17] M. Ablikim *et al.* [BESIII], Cross section measurements of $e^+e^- \rightarrow \omega\chi_{c0}$ form $\sqrt{s} = 4.178$ to 4.278 GeV, *Phys. Rev. D* **99**, 091103 (2019).
- [18] M. Ablikim *et al.* [(BESIII), and BESIII], Observation of the Y(4230) and a new structure in $e^+e^- \rightarrow K^+K^- J/\psi$, *Chin. Phys. C* **46**, 111002 (2022).
- [19] M. Ablikim *et al.* [BESIII], Evidence of a resonant structure in the $e^+e^- \rightarrow \pi^+D^0D^{*-}$ cross section between 4.05 and 4.60 GeV, *Phys. Rev. Lett.* **122**, 102002 (2019).
- [20] R. L. Workman *et al.* [Particle Data Group], Review of Particle Physics, *PTEP* **2022**, 083C01 (2022).
- [21] D. Y. Chen, X. Liu and T. Matsuki, η transitions between charmonia with meson loop contributions, *Phys. Rev. D* **87**, 054006 (2013).
- [22] J. Z. Wang, D. Y. Chen, X. Liu and T. Matsuki, Constructing J/ψ family with updated data of charmoniumlike Y states, *Phys. Rev. D* **99**, 114003 (2019).
- [23] J. Z. Wang, and X. Liu, Confirming the existence of a new higher charmonium $\psi(4500)$ by the newly released data of $e^+e^- \rightarrow K^+K^- J/\psi$, *Phys. Rev. D* **107**, 054016 (2023).
- [24] J. Z. Wang, and X. Liu, Identifying a characterized energy level structure of higher charmonium well matched to the peak structures in $e^+e^- \rightarrow \pi^+D^0D^{*-}$, *Phys. Lett. B* **849**, 138456 (2024).
- [25] L. P. He, D. Y. Chen, X. Liu, and T. Matsuki, Prediction of a missing higher charmonium around 4.26 GeV in J/ψ family, *Eur. Phys. J. C* **74**, 3208 (2014).
- [26] D. Y. Chen, X. Liu, and T. Matsuki, Observation of $e^+e^- \rightarrow \chi_{c0}\omega$ and missing higher charmonium $\psi(4S)$, *Phys. Rev. D* **91**, 094023 (2015).
- [27] D. Y. Chen, X. Liu, and T. Matsuki, Search for missing $\psi(4S)$ in the $e^+e^- \rightarrow \pi^+\pi^-\psi(2S)$ process, *Phys. Rev. D* **93**, 034028 (2016).
- [28] D. Y. Chen, X. Liu, and T. Matsuki, Interference effect as resonance killer of newly observed charmoniumlike states Y(4320) and Y(4390), *Eur. Phys. J. C* **78**, 136 (2018).
- [29] M. Ablikim *et al.* [BES], Determination of the $\psi(3770)$, $\psi(4040)$, $\psi(4160)$ and $\psi(4415)$ resonance parameters, *Phys. Lett. B* **660**, 315 (2008).
- [30] R. Brandelik *et al.* [DASP], Total cross section for Hadron Production by e^+e^- Annihilation at Center-of-mass Energies Between 3.6 GeV and 5.2 GeV, *Phys. Lett. B* **76**, 361 (1978).
- [31] X. Liu, X. Q. Zeng, and X. Q. Li, Study on contributions of hadronic loops to decays of $J/\psi \rightarrow$ vector + pseudoscalar mesons, *Phys. Rev. D* **74**, 074003 (2006).

- [32] X. Liu, B. Zhang, and X. Q. Li, The puzzle of excessive non- $D\bar{D}$ component of the inclusive $\psi(3770)$ decay and the long-distant contribution, *Phys. Lett. B* **675**, 441 (2009).
- [33] G. Li, X. h. Liu, Q. Wang, and Q. Zhao, Further understanding of the non- $D\bar{D}$ decays of $\psi(3770)$, *Phys. Rev. D* **88**, 014010 (2013).
- [34] C. Meng, and K. T. Chao, Scalar resonance contributions to the dipion transition rates of $\Upsilon(4S, 5S)$ in the re-scattering model, *Phys. Rev. D* **77**, 074003 (2008).
- [35] C. Mengs, and K. T. Chao, Peak shifts due to $B^{(*)} - \bar{B}^{(*)}$ rescattering in $\Upsilon(5S)$ dipion transitions, *Phys. Rev. D* **78**, 034022 (2008).
- [36] C. Meng, and K. T. Chao, $\Upsilon(4S, 5S) \rightarrow \Upsilon(1S)\eta$ transitions in the rescattering model, and the new *BABAR* measurement, *Phys. Rev. D* **78**, 074001 (2008).
- [37] D. Y. Chen, J. He, X. Q. Li, and X. Liu, Dipion invariant mass distribution of the anomalous $\Upsilon(1S)\pi^+\pi^-$ and $\Upsilon(2S)\pi^+\pi^-$ production near the peak of $\Upsilon(10860)$, *Phys. Rev. D* **84**, 074006 (2011).
- [38] D. Y. Chen, X. Liu, and S. L. Zhu, Charged bottomonium-like states $Z_b(10610)$ and $Z_b(10650)$ and the $\Upsilon(5S) \rightarrow \Upsilon(2S)\pi^+\pi^-$ decay, *Phys. Rev. D* **84**, 074016 (2011).
- [39] D. Y. Chen, and X. Liu, $Z_b(10610)$ and $Z_b(10650)$ structures produced by the initial single pion emission in the $\Upsilon(5S)$ decays, *Phys. Rev. D* **84**, 094003 (2011).
- [40] D. Y. Chen, X. Liu, and X. Q. Li, Anomalous dipion invariant mass distribution of the $\Upsilon(4S)$ decays into $\Upsilon(1S)\pi^+\pi^-$ and $\Upsilon(2S)\pi^+\pi^-$, *Eur. Phys. J. C* **71**, 1808 (2011).
- [41] D. Y. Chen, X. Liu, and T. Matsuki, Explaining the anomalous $\Upsilon(5S) \rightarrow \chi_{bj}\omega$ decays through the hadronic loop effect, *Phys. Rev. D* **90**, 034019 (2014).
- [42] B. Wang, H. Xu, X. Liu, D. Y. Chen, S. Coito, and E. Eichten, Using $X(3823) \rightarrow J/\psi\pi^+\pi^-$ to identify coupled-channel effects, *Front. Phys. (Beijing)* **11**, 111402 (2016).
- [43] B. Wang, X. Liu, and D. Y. Chen, Prediction of anomalous $\Upsilon(5S) \rightarrow \Upsilon(1^3D_J)\eta$ transitions, *Phys. Rev. D* **94**, 094039 (2016).
- [44] Q. Huang, B. Wang, X. Liu, D. Y. Chen, and T. Matsuki, Exploring the $\Upsilon(6S) \rightarrow \chi_{bj}\phi$ and $\Upsilon(6S) \rightarrow \chi_{bj}\omega$ hidden-bottom hadronic transitions, *Eur. Phys. J. C* **77**, 165 (2017).
- [45] Y. Zhang, and G. Li, Exploring the $\Upsilon(4S, 5S, 6S) \rightarrow h_b(1P)\eta$ hidden-bottom hadronic transitions, *Phys. Rev. D* **97**, 014018 (2018).
- [46] Q. Huang, H. Xu, X. Liu, and T. Matsuki, Potential observation of the $\Upsilon(6S) \rightarrow \Upsilon(1^3D_J)\eta$ transitions at Belle II, *Phys. Rev. D* **97**, 094018 (2018).
- [47] Q. Huang, X. Liu, and T. Matsuki, Proposal of searching for the $\Upsilon(6S)$ hadronic decays into $\Upsilon(nS)$ plus $\eta^{(\prime)}$, *Phys. Rev. D* **98**, 054008 (2018).
- [48] Y. S. Li, Z. Y. Bai, Q. Huang, and X. Liu, Hidden-bottom hadronic decays of $\Upsilon(10753)$ with a $\eta^{(\prime)}$ or ω emission, *Phys. Rev. D* **104**, 034036 (2021).
- [49] Z. Y. Bai, Y. S. Li, Q. Huang, X. Liu, and T. Matsuki, $\Upsilon(10753) \rightarrow \Upsilon(nS)\pi^+\pi^-$ decays induced by hadronic loop mechanism, *Phys. Rev. D* **105**, 074007 (2022).
- [50] Y. S. Li, Z. Y. Bai, and X. Liu, Investigating the $\Upsilon(10753) \rightarrow \Upsilon(1^3D_J)\eta$ transitions, *Phys. Rev. D* **105**, 114041 (2022).
- [51] Z. Y. Bai, Q. S. Zhou, and X. Liu, Higher strangeonium decays into light flavor baryon pairs like $\Lambda\bar{\Lambda}$, $\Sigma\bar{\Sigma}$, and $\Xi\bar{\Xi}$, *Phys. Rev. D* **108**, 094036 (2023).
- [52] H. Y. Cheng, C. K. Chua, and A. Soni, Final state interactions in hadronic B decays, *Phys. Rev. D* **71**, 014030 (2005).
- [53] N. N. Achasov, and A. A. Kozhevnikov, Dynamical violation of the OZI rule and G parity in the decays of heavy quarkonia, *Phys. Rev. D* **49**, 275 (1994).
- [54] A. Deandrea, G. Nardulli, and A. D. Polosa, J/ψ couplings to charmed resonances and to π , *Phys. Rev. D* **68** (2003), 034002.
- [55] L. Micu, Decay rates of meson resonances in a quark model, *Nucl. Phys. B* **10**, 521 (1969).
- [56] A. Le Yaouanc, L. Oliver, O. Pene, and J. C. Raynal, Why is $\psi(4.414)$ so narrow?, *Phys. Lett. B* **72**, 57 (1977).
- [57] M. Jacob, and G. C. Wick, On the General Theory of Collisions for Particles with Spin, *Annals Phys.* **7**, 404 (1959); **281**, 774 (2020).

Controlling volume fluctuations for studies of critical phenomena in nuclear collisions

Romain Holzmann,^{1,*} Volker Koch,^{2,3,†} Anar Rustamov,^{1,‡} and Joachim Stroth^{4,1,5,§}

¹*GSI Helmholtzzentrum für Schwerionenforschung, 64291 Darmstadt, Germany*

²*Nuclear Science Division Lawrence Berkeley National Laboratory Berkeley, CA, 94720, USA*

³*ExtreMe Matter Institute EMMI, GSI, 64291 Darmstadt, Germany*

⁴*Institut für Kernphysik, Goethe-Universität, 60438 Frankfurt am Main, Germany*

⁵*Helmholtz Research Academy Hesse for FAIR (HFHF),
Campus Frankfurt , 60438 Frankfurt am Main, Germany*

We generalize and extend the recently proposed method [1] to account for contributions of system size (or volume/participant) fluctuations to the experimentally measured moments of particle multiplicity distributions. We find that in the general case there are additional biases which are not directly accessible to experiment. These biases are, however, parametrically suppressed if the multiplicity of the particles of interest is small compared to the total charged-particle multiplicity, e.g., in the case of proton number fluctuations at top RHIC and LHC energies. They are also small if the multiplicity distribution of charged particles per wounded nucleon is close to the Poissonian limit, which is the case at low energy nuclear collisions, e.g., at GSI/SIS18. We further find that mixed events are not necessarily needed to extract the correction for volume fluctuations, albeit it can help if event statistics is small, which is typically the case for reconstructing the higher-order cumulants. We provide the formulas to correct pure and mixed cumulants of particle multiplicity distributions up to any order together with their associated biases.

arXiv:2403.03598v1 [nucl-th] 6 Mar 2024

* r.holzmann@gsi.de

† vkoch@lbl.gov

‡ a.rustamov@gsi.de

§ j.stroth@gsi.de

I. INTRODUCTION

One of the main goals of studying relativistic heavy-ion collisions is to explore the structure of the QCD phase diagram. Fluctuations of observed particles carrying quantum numbers of conserved charges, baryon number (B), electric charge and strangeness, represent a powerful tool for this endeavor as the cumulants of their distributions measure the derivatives of the grand-canonical partition function, and thus the pressure (P), with respect to the associated chemical potentials. For example, for a thermal system of volume V and temperature T , the cumulants of the net baryon number distribution, within the Grand Canonical Ensemble (GCE), are given by [2]

$$\kappa_n[B] = \frac{\partial^n (\ln Z)}{\partial (\mu_B/T)^n} = \frac{V}{T} \frac{\partial^n P}{\partial (\mu_B/T)^n},$$

where Z is a GCE partition function and μ_B is a baryon chemical potential. Any nontrivial structures in the equation of state such as a possible phase transition [3–6] will result in potentially large derivatives of the pressure and thus in large values of the cumulants of conserved charges. In addition, as cumulants are derivatives of the pressure, they are accessible (at vanishing or small values of chemical potential) to Lattice QCD calculations [7, 8], which in principle enables a direct comparison of results from ab initio QCD calculations with experiment. For example, as pointed out in Ref. [9], the measurement of higher-order cumulants close to vanishing chemical potential may test the remnants of chiral criticality.

Measurements of fluctuations have meanwhile been carried out by many experiments. The STAR collaboration has measured cumulants of the net-proton number up to sixth order over the entire energy range available at RHIC [10, 11]. The HADES experiment has measured cumulants of proton number up to fourth order at the low energy of $\sqrt{s_{NN}} = 2.4$ GeV [12] and ALICE has measured the second- and third-order net-proton number cumulants at $\sqrt{s_{NN}} = 2.76$ and 5.02 TeV [13, 14].

When comparing cumulants measured in experiment with those obtained from lattice QCD or other field theoretical calculations [15] one needs to be aware of several key differences. While theoretical calculations are typically done in the grand canonical ensemble where charges can be exchanged with a heat bath and are only conserved on the average, in experiment charges are explicitly conserved on event by event basis and one has to account for global as well as local charge conservation [16–20]. Also, in experiments one usually is restricted to the measurement of net protons whereas theory can only calculate cumulants of the net baryon number. In the presence of many pions this difference can be corrected for [21]. Finally, and this will be the topic of the present paper, in experiment the size of the particle emitting system is not constant. Even under the tightest centrality selection criteria, this gives rise to so-called volume fluctuations [22] or, equivalently, fluctuations of the number of wounded nucleons [23]. Moreover, centrality is a concept assuming a strict correlation of event activity, i.e., charged particle multiplicity in a broad region around mid rapidity, with the size of the system. This requires a strict separation of the particles used to determine the fluctuation of conserved charges from the ones used for centrality determination. The effects due to volume fluctuations may be sizable, especially at lower energies where the charged particle multiplicity is dominated by the primordial protons, limiting the achievable resolution of the centrality selection. In Ref. [1] a novel and promising method based on event mixing has been proposed to experimentally determine and subtract the contributions to the cumulants caused by volume fluctuations. In the present work we will further elaborate on this topic, generalize the results, and provide the formulas for corrections of any higher-order cumulants.

This paper is organized as follows. In the next section we define the notation. We then present an analytical formulation of event mixing as proposed in Ref. [1]. We find that the cumulants of the mixed events have additional bias terms which were assumed to vanish in the original work of [1], and we discuss the magnitude of these corrections for various scenarios. Next we extend our study to cumulants of higher order before we discuss and summarize our results.

II. NOTATION

In this paper we will mostly work within the wounded-nucleon model [24] to discuss volume or participant fluctuations. We would like to point out that this model has its limitations when applied to low collision energies because of the moderate separation of projectile and target rapidity and a multiplicity of created particles per wounded nucleon much smaller than unity. However, as we shall show later, the formalism can be easily applied also to the situation where one has generic volume fluctuations, as for example discussed in Refs. [22, 23]. Let us start with the expression

of the particle number cumulants $\kappa_j[N]$ in the presence of wounded-nucleon fluctuations (for details see Appendix A):

$$\kappa_1[N] = \langle N_w \rangle \kappa_1[n] = \langle N_w \rangle \langle n \rangle = \langle N \rangle \quad (1)$$

$$\kappa_2[N] = \langle N_w \rangle \kappa_2[n] + \langle n \rangle^2 \kappa_2[N_w] = \bar{\kappa}_2[N] + \langle N \rangle^2 \frac{\kappa_2[N_w]}{\langle N_w \rangle^2} \quad (2)$$

$$\kappa_3[N] = \langle N_w \rangle \kappa_3[n] + 3 \langle n \rangle \kappa_2[n] \kappa_2[N_w] + \langle n \rangle^3 \kappa_3[N_w] = \bar{\kappa}_3[N] + 3 \langle N \rangle \bar{\kappa}_2[N] \frac{\kappa_2[N_w]}{\langle N_w \rangle^2} + \langle N \rangle^3 \frac{\kappa_3[N_w]}{\langle N_w \rangle^3} \quad (3)$$

$$\begin{aligned} \kappa_4[N] &= \langle N_w \rangle \kappa_4[n] + 4 \langle n \rangle \kappa_3[n] \kappa_2[N_w] + 3 \kappa_2^2[n] \kappa_2[N_w] + 6 \langle n \rangle^2 \kappa_2[n] \kappa_3[N_w] + \langle n \rangle^4 \kappa_4[N_w] \\ &= \bar{\kappa}_4[N] + 4 \langle N \rangle \bar{\kappa}_3[N] \frac{\kappa_2[N_w]}{\langle N_w \rangle^2} + 3 \bar{\kappa}_2^2[N] \frac{\kappa_2[N_w]}{\langle N_w \rangle^2} + 6 \langle N \rangle^2 \bar{\kappa}_2[N] \frac{\kappa_3[N_w]}{\langle N_w \rangle^3} + \langle N \rangle^4 \frac{\kappa_4[N_w]}{\langle N_w \rangle^4} \end{aligned} \quad (4)$$

Here N refers to the particles of interest, say protons, and n to the number of these particles arising from one wounded nucleon; thus $\langle n \rangle$ is the average number of particles per wounded nucleon. The cumulants of the wounded-nucleon distribution are denoted by $\kappa_j[N_w]$ while the cumulants for the distribution of particles stemming from one wounded nucleon are $\kappa_j[n]$. The corresponding relations for cumulants of any order can be obtained with the provided software package [25].

The cumulants of interest are those at a fixed number of wounded nucleons. They reflect the true density fluctuations in a system at constant volume. We denote these cumulants for a system with fixed, i.e. non-fluctuating, number of $\langle N_w \rangle$ wounded nucleons as

$$\bar{\kappa}_j[N] = \langle N_w \rangle \kappa_j[n],$$

Below we will also deal with factorial cumulants, which we shall denote by C_j . Factorial cumulants, which measure the deviation from Poisson statistics, tell us about the true correlations in the system. As discussed in the Appendix B, they are linear combinations of the regular cumulants. For the first four orders we have

$$\begin{aligned} C_1[N] &= \kappa_1[N] = \langle N \rangle, \\ C_2[N] &= -\kappa_1[N] + \kappa_2[N], \\ C_3[N] &= 2\kappa_1[N] - 3\kappa_2[N] + \kappa_3[N], \\ C_4[N] &= -6\kappa_1[N] + 11\kappa_2[N] - 6\kappa_3[N] + \kappa_4[N]. \end{aligned}$$

The expressions for the particle number factorial cumulants are similar to Eqs. 1- 4

$$C_1[N] = \langle N_w \rangle C_1[n] = \langle N_w \rangle \langle n \rangle = \langle N \rangle, \quad (5)$$

$$C_2[N] = \bar{C}_2[N] + \langle N \rangle^2 \frac{\kappa_2[N_w]}{\langle N_w \rangle^2}, \quad (6)$$

$$C_3[N] = \bar{C}_3[N] + 3 \langle N \rangle \bar{C}_2[N] \frac{\kappa_2[N_w]}{\langle N_w \rangle^2} + \langle N \rangle^3 \frac{\kappa_3[N_w]}{\langle N_w \rangle^3}, \quad (7)$$

$$C_4[N] = \bar{C}_4[N] + 4 \langle N \rangle \bar{C}_3[N] \frac{\kappa_2[N_w]}{\langle N_w \rangle^2} + 3 \bar{C}_2^2[N] \frac{\kappa_2[N_w]}{\langle N_w \rangle^2} + 6 \langle N \rangle^2 \bar{C}_2[N] \frac{\kappa_3[N_w]}{\langle N_w \rangle^3} + \langle N \rangle^4 \frac{\kappa_4[N_w]}{\langle N_w \rangle^4}. \quad (8)$$

Similar to the cumulants, we denote by

$$\bar{C}_k[N] = \langle N_w \rangle C_k[n]$$

the factorial cumulants for a system at constant volume or number of wounded nucleons, $\langle N_w \rangle$.

III. MIXED EVENTS

In Ref. [1] a mixed event is constructed such that it has the same total multiplicity as a given real event but each particle (track) is drawn from a different event, so that, by construction, the mixed events follow the same total multiplicity distribution as the original events. This is done in order to preserve volume fluctuations as in real events. Since each particle (track) is chosen randomly from a random event, the distribution of particle species will follow a multinomial distribution with the Bernoulli probabilities $p_i = \langle N_i \rangle / \langle M \rangle$ for particles of type i . Here $\langle N_i \rangle$ denotes the mean number of particles of type i and $\langle M \rangle$ the mean total multiplicity. Hence, the probability to find A particles

(successes) of type A and B particles of type B is given by the trinomial probability $B_3(A, B, M; p_A, p_B)$ and so on. Here M denotes the multiplicity of the event under consideration. Thus the distribution, $P_{mix}(A, B)$, of particles of species A and B in the mixed events is obtained by folding the multiplicity distribution $P_M(M)$ with a trinomial (in general multinomial) distribution:

$$P_{mix}(A, B) = \sum_M B_3(A, B, M; p_A, p_B) P_M(M)$$

with

$$p_A = \frac{\langle A \rangle}{\langle M \rangle}, \quad p_B = \frac{\langle B \rangle}{\langle M \rangle}.$$

and

$$B_3(A, B, M; p_A, p_B) = \frac{M!}{A!B!(M-A-B)!} p_A^A p_B^B (1-p_A-p_B)^{M-A-B} \quad (9)$$

The factorial-cumulant generating function for this distribution is

$$\begin{aligned} g_{F,mx}(z_A, z_B) &= \ln \left[\sum_{A,B} P_{mix}(A, B) (z_A)^A (z_B)^B \right] \\ &= \ln \left[\sum_M [h_3(z_A, z_B)]^M P_M(M) \right] \\ &= G_{F,M}(h_3(z_A, z_B)) \end{aligned} \quad (10)$$

where

$$h_3(z_A, z_B) = \sum_{A,B} B_3(A, B; M=1; p_A, p_B) (z_A)^A (z_B)^B = (1-p_A-p_B+p_A z_A + p_B z_B)$$

is the factorial-moment generating function for the trinomial distribution with one trial ($M=1$), and $G_{F,M}(z)$ is the factorial-cumulant generating function for the multiplicity distribution, $P_M(M)$ (see Eq.(B2)). The factorial cumulants are then obtained via

$$C_{i,j}^{mix}[mix] = \frac{\partial^i \partial^j}{\partial (z_A)^i \partial (z_B)^j} G_{F,M}(h_3(z_A, z_B)) \Big|_{z_A=z_B=0} = p_A^i p_B^j C_{i+j}[M]$$

with $C_k[M]$ being the k^{th} -order factorial cumulant. Using the expression for the factorial cumulants of the multiplicity distribution derived in Appendix C, Eq. C5, we get within the wounded-nucleon model

$$\begin{aligned} C_1^{mix}[A] &= \kappa_1^{mix}[A] = p_A \langle N_w \rangle \langle m \rangle \\ C_2^{mix}[A] &= p_A^2 C_2[M] = p_A^2 \left[\kappa_2[N_w] \langle m \rangle^2 + \langle N_w \rangle C_2[m] \right] \\ C_{1,1}^{mix}[A, B] &= p_A p_B C_2[M] = p_A p_B \left[\kappa_2[N_w] \langle m \rangle^2 + \langle N_w \rangle C_2[m] \right]. \end{aligned} \quad (11)$$

For the corresponding cumulants up to second order we get accordingly

$$\begin{aligned} \kappa_1^{mix}[A] &= C_1^{mix}[A] = p_A \langle N_w \rangle \langle m \rangle \\ \kappa_2^{mix}[A] &= C_2^{mix}[A] + C_1^{mix}[A] = p_A^2 \left[\kappa_2[N_w] \langle m \rangle^2 + \langle N_w \rangle (\kappa_2[m] - \kappa_1[m]) \right] + p_A \langle N_w \rangle \langle m \rangle \\ &= p_A^2 \left[\kappa_2[N_w] \langle m \rangle^2 + \langle N_w \rangle (\kappa_2[m] - \langle m \rangle) \right] + p_A \langle N_w \rangle \langle m \rangle \\ cov^{mix}[A, B] &= C_{1,1}^{mix}[A, B] = p_A p_B \left[\kappa_2[N_w] \langle m \rangle^2 + \langle N_w \rangle (\kappa_2[m] - \langle m \rangle) \right]. \end{aligned} \quad (12)$$

With $\langle m \rangle$ denoting the mean number of total particles emitted by a wounded nucleon, we get $\langle a \rangle = p_A \langle m \rangle$ and $\langle b \rangle = p_B \langle m \rangle$ for the mean number of particles per wounded nucleon of type A and B, respectively, and recover the results of Ref.[1]. For that we have to assume that the multiplicity distribution per wounded nucleon is Poissonian,

i.e. that $C_2[m] = \kappa_2[m] - \langle m \rangle = 0$. This has been an implicit assumption in Ref. [1], which however is not valid in general as we shall discuss below.

The main benefit of the event mixing is to be able to relate the factorial cumulants of the various multiplicity distributions, as can be seen from Eq.11. All that enters is the second-order factorial cumulant, $C_2[M]$. The binomial probabilities, p_A and p_B , are in the sense trivial as they can be determined without any mixed events. Thus we may express the fluctuations of the wounded nucleons in terms of the factorial cumulant of the track multiplicity distribution

$$\langle N \rangle^2 \frac{\kappa_2[N_w]}{\langle N_w \rangle^2} = \frac{\langle N \rangle^2}{\langle M \rangle^2} (C_2[M] - \langle N_w \rangle C_2[m]) = \frac{\langle N \rangle^2}{\langle M \rangle^2} (C_2[M] - \bar{C}_2[M]), \quad (13)$$

where $\bar{C}_2[M] = \langle N_w \rangle C_2[m]$ is the second-order factorial cumulant for a system of $\langle N_w \rangle$ wounded nucleons *without* wounded nucleon fluctuations and N stands now for the multiplicity of the particles of interest, i.e., either A or B . While the factorial cumulant of the multiplicity distribution, $C_2[M]$, is accessible to experiment, that of a non-fluctuating system, $\bar{C}_2[M]$, is not. Let us, therefore define a bias term, Δ_2 , as

$$\Delta_2 \equiv \frac{\langle N \rangle^2}{\langle M \rangle^2} \bar{C}_2[M]. \quad (14)$$

In case of a Poissonian multiplicity distribution for one wounded nucleon the bias term vanishes, i.e., $\Delta_2 = 0$, since $\bar{C}_2[M] = \langle N_w \rangle C_2[m] = 0$ in this case, and we recover the results of Ref. [1]. Let us furthermore define the corrected cumulant, $\kappa_2^{corr}[N]$, which is based on measurable quantities only

$$\kappa_2^{corr}[N] = \kappa_2[N] - \frac{\langle N \rangle^2}{\langle M \rangle^2} C_2[M]. \quad (15)$$

Following Eq. 2 and using Eq. 6, the cumulant of the system *without* wounded nucleon fluctuations, $\bar{\kappa}_2[N]$, is given by

$$\bar{\kappa}_2[N] = \kappa_2[N] - \langle N \rangle^2 \frac{\kappa_2[N_w]}{\langle N_w \rangle^2} = \kappa_2^{corr}[N] + \Delta_2. \quad (16)$$

The bias, Δ_2 , while not directly measurable, may be constrained by a fit to the track multiplicity distribution within the wounded-nucleon model [24], as it is commonly done [11, 26, 27]. In addition, we note that for protons at very high collision energies we have $\langle N_p \rangle \ll \langle M \rangle$ so that Δ_2 is suppressed parametrically. This behavior can indeed be illustrated with simulations as presented in Sec. V. Since cumulants scale with the system size, or in our case with the number of wounded nucleons, $\langle N_w \rangle$, it is instructive to scale the (factorial) cumulants with the mean number of particles

$$\frac{\bar{\kappa}_2[N]}{\langle N \rangle} = \frac{\kappa_2[N]}{\langle N \rangle} - \frac{\langle N \rangle}{\langle M \rangle} \left(\frac{C_2[M]}{\langle N \rangle} - \frac{\bar{C}_2[M]}{\langle N \rangle} \right) = \frac{\kappa_2^{corr}[N]}{\langle N \rangle} + \frac{\Delta_2}{\langle N \rangle} \quad (17)$$

The scaled bias is then given by

$$\frac{\Delta_2}{\langle N \rangle} = \frac{\langle N \rangle}{\langle M \rangle} \bar{c}_2[M]. \quad (18)$$

Typically, the scaled cumulants are of order unity, $\kappa_j[N]/\langle N \rangle \sim \mathcal{O}(1)$. In addition, the scaled factorial cumulants, $C_k[N]/\langle N \rangle$, are expected to depend only weakly on the multiplicity. Therefore, the scaled bias should be much smaller than one, $\Delta_2/\langle N \rangle \ll 1$, for the volume correction to be reliable.

Finally, one may express the bias term Δ_2 also in terms of cumulants by using the relation between cumulants and factorial cumulants (see Appendix B), $C_2[M] = \kappa_2[M] - \langle M \rangle$ and and so forth. This gives,

$$\Delta_2 = \frac{\langle N \rangle^2}{\langle M \rangle^2} (\bar{\kappa}_2[M] - \langle M \rangle) \quad (19)$$

A note of caution may be useful in this context. One might be inclined to express the fluctuations of the wounded nucleon directly using the cumulants of the multiplicity distribution, in which case one would get

$$\langle N \rangle^2 \frac{\kappa_2[N_w]}{\langle N_w \rangle^2} = \frac{\langle N \rangle^2}{\langle M \rangle^2} (\kappa_2[M] - \langle N_w \rangle \kappa_2[m]).$$

And since $\langle N_w \rangle \kappa_2[m] = \bar{\kappa}_2[M]$ is not directly accessible to experiment, one may further assign the bias to be $\Delta_2 = \frac{\langle N \rangle^2}{\langle M \rangle^2} \bar{\kappa}_2[M]$. This, however, would considerably overestimate its true value, Eq. 19, as cumulants always contain a ‘‘trivial’’ component proportional to the number of particles, which in principle is measurable.

IV. HIGHER-ORDER RESULTS

Let us now discuss the corrections for volume fluctuations up to fourth order. Given the discussion in the previous section the strategy is straightforward. First we express the fluctuations of the wounded nucleons in terms of factorial cumulants of the multiplicity distribution. Then we identify the parts which are experimentally accessible and those which are not. The latter will be the bias while the former will be subtracted from the expression for the cumulants in order to remove most of the effect of volume fluctuations. The terms involving cumulants of the wounded-nucleon distribution as they appear in the expressions for the cumulants as $\kappa_j[N_w]/\langle N_w \rangle^j$, see Eqs. (6-8) are:

$$\frac{\kappa_2[N_w]}{\langle N_w \rangle^2} = \frac{C_2[M] - \bar{C}_2[M]}{\langle M \rangle^2} \quad (20)$$

$$\frac{\kappa_3[N_w]}{\langle N_w \rangle^3} = -3 \frac{\bar{C}_2[M]}{\langle M \rangle^2} \frac{\kappa_2[N_w]}{\langle N_w \rangle^2} + \frac{C_3[M] - \bar{C}_3[M]}{\langle M \rangle^3} \quad (21)$$

$$\frac{\kappa_4[N_w]}{\langle N_w \rangle^4} = -6 \frac{\bar{C}_2[M]}{\langle M \rangle^2} \frac{\kappa_3[N_w]}{\langle N_w \rangle^3} - \frac{4\bar{C}_3[M]\langle M \rangle + 3\bar{C}_2[M]^2}{\langle M \rangle^4} \frac{\kappa_2[N_w]}{\langle N_w \rangle^2} + \frac{C_4[M] - \bar{C}_4[M]}{\langle M \rangle^4} \quad (22)$$

We note that binomial efficiency corrections do not affect the results as both, numerators and denominators of the right hand side of the above expressions, scale with the same power of the efficiency.

Inserting these expressions into Eqs. (2-4) for the cumulants $\kappa_j[N]$, we can solve for the cumulants of the system with fixed number of wounded nucleons, namely the $\bar{\kappa}_j[N]$. The results are given in the following general form

$$\bar{\kappa}_j[N] = \kappa_j^{corr}[N] + \Delta_j[N] \quad (23)$$

with $\bar{\kappa}_j[N]$ the cumulant of order j for a system with fixed N_w nucleons, $\kappa_j^{corr}[N]$ the cumulant including the measurable corrections for volume fluctuations, and Δ_j the corresponding bias due to quantities that are not measurable. The second-order result we already derived in Sec. A, Eqs. (15) and (14), namely

$$\begin{aligned} \kappa_2^{corr}[N] &= \kappa_2[N] - \frac{\langle N \rangle^2}{\langle M \rangle^2} C_2[M] \\ \Delta_2 &= \frac{\langle N \rangle^2}{\langle M \rangle^2} \bar{C}_2[M]. \end{aligned} \quad (24)$$

For the third order we have

$$\begin{aligned} \kappa_3^{corr}[N] &= \kappa_3[N] - \frac{3C_2[M]\kappa_2[N]\langle N \rangle}{\langle M \rangle^2} + \frac{3C_2[M]^2\langle N \rangle^3}{\langle M \rangle^4} - \frac{C_3[M]\langle N \rangle^3}{\langle M \rangle^3} \\ \Delta_3 &= \bar{C}_2[M] \left(\frac{3\kappa_2[N]\langle N \rangle}{\langle M \rangle^2} - \frac{3C_2[M]\langle N \rangle^3}{\langle M \rangle^4} \right) + \frac{\bar{C}_3[M]\langle N \rangle^3}{\langle M \rangle^3}. \end{aligned} \quad (25)$$

And the fourth order result reads

$$\begin{aligned} \kappa_4^{corr}[N] &= \kappa_4[N] - \left(\frac{6\kappa_2[N]\langle N \rangle^2 (C_3[M]\langle M \rangle - 3C_2[M]^2)}{\langle M \rangle^4} + \frac{4C_2[M]\kappa_3[N]\langle N \rangle}{\langle M \rangle^2} \right. \\ &\quad \left. + \frac{3C_2[M]\kappa_2[N]^2}{\langle M \rangle^2} + \frac{\langle N \rangle^4 (-10C_3[M]C_2[M]\langle M \rangle + 15C_2[M]^3)}{\langle M \rangle^6} + \frac{C_4[M]\langle N \rangle^4}{\langle M \rangle^4} \right) \\ \Delta_4 &= \bar{C}_2[M] \left(-\frac{18C_2[M]\kappa_2[N]\langle N \rangle^2}{\langle M \rangle^4} + \frac{15C_2[M]^2\langle N \rangle^4}{\langle M \rangle^6} - \frac{4C_3[M]\langle N \rangle^4}{\langle M \rangle^5} + \frac{4\kappa_3[N]\langle N \rangle}{\langle M \rangle^2} + \frac{3\kappa_2[N]^2}{\langle M \rangle^2} \right) \\ &\quad + \bar{C}_3[M] \left(\frac{6\kappa_2[N]\langle N \rangle^2}{\langle M \rangle^3} - \frac{6C_2[M]\langle N \rangle^4}{\langle M \rangle^5} \right) + \frac{\bar{C}_4[M]\langle N \rangle^4}{\langle M \rangle^4}. \end{aligned} \quad (26)$$

The corresponding relations for correction and bias terms of any order can be obtained with the provided software package [25].

Equivalent expressions for the factorial cumulants, $C_n[N]$, and their related biases, $\Delta_{n,F}$, may then be obtained by using the relation between factorial cumulants and regular cumulants Eq. B6:

$$C_n^{corr}[N] = \sum_{j=1}^n B_{n,j} (1, -1, 2, \dots, (-1)^{j-1} (n-j+1)!) \kappa_j^{corr}[N]$$

$$\Delta_{n,F} = \sum_{j=1}^n B_{n,j} (1, -1, 2, \dots, (-1)^{j-1} (n-j+1)!) \Delta_j[N]$$

The results for the corrected factorial cumulants, C_k^{corr} and c_k^{corr} , and the associated biases, $\Delta_{k,F}$ and $\delta_{k,F}$, are given in Appendix E.

V. SIMULATIONS

Experimental data are usually analyzed in centrality percentiles, i.e. event classes corresponding to the $n\%$ most central collisions, by introducing selection criteria on e.g. the energy deposited in a forward detector system covering typically the projectile (target) spectator region or the multiplicity of charged particles emitted from the mid-rapidity region, with an acceptance reaching close to the projectile (target) rapidity regions in case of low beam energies [26, 27]. For the latter, care must be taken to ensure that the evaluated particles are not simultaneously used to determine the critical fluctuations [28]. The respective distributions, like e.g., the forward energy deposit or the charged particle

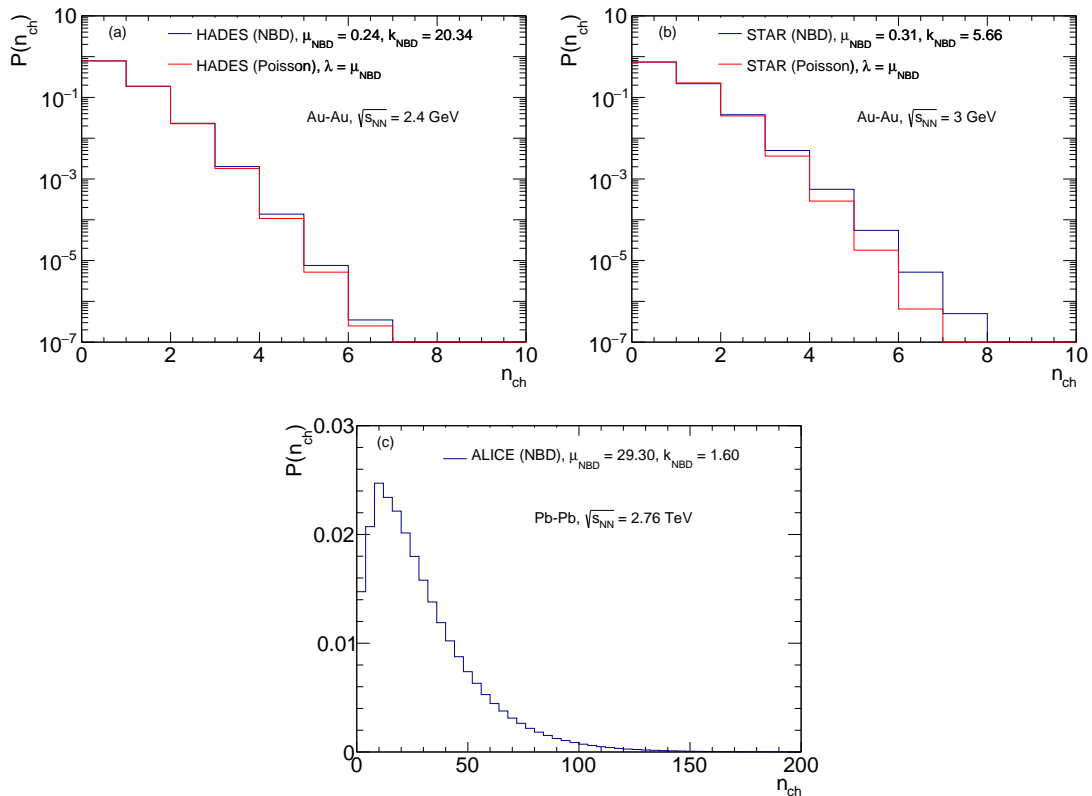


Figure 1. NBD adjusted to HADES (a), STAR (b) and ALICE (c) charged-particle multiplicity distributions (blue line), shown together with a Poisson distribution for the HADES and STAR data (red lines), the parameters used are listed in Table I.

multiplicity, are commonly modelled using the Glauber Monte Carlo Model [29]. The model provides event by event and for a given impact parameter the number of projectile/target nucleons which are “wounded” and responsible for the event activity (multiplicity), and those, which proceed nearly undisturbed into the phase space region covered by the forward detectors. To determine centrality using charged particle multiplicity the respective distribution is generally modelled assuming that particles are “produced” independently from distinct sources following a negative

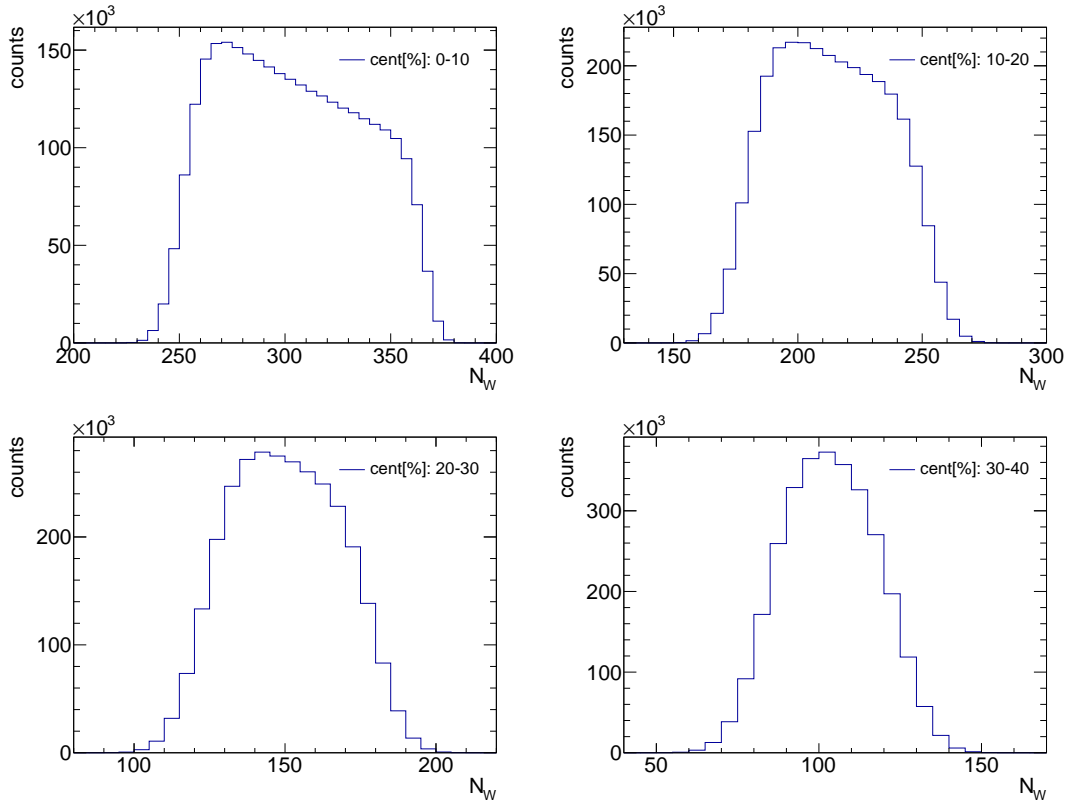


Figure 2. Distribution of wounded nucleons in Au+Au collisions at $\sqrt{s_{NN}} = 2.4$ GeV for four selected centrality classes, as obtained from the Glauber Monte Carlo simulations.

binomial distribution (NBD). Its probability mass function is defined as

$$P(n; \mu, k) = \frac{\Gamma(n+k)}{\Gamma(n+1)\Gamma(k)} \left(\frac{\mu}{k}\right)^n \left(\frac{\mu}{k} + 1\right)^{-(n+k)}, \quad (27)$$

where μ denotes the mean of the NBD, while the combination of μ and k determines its higher-order cumulants

$$\kappa_n^{NBD} = \left. \frac{\partial^n \ln M(t)}{\partial t^n} \right|_{t=0}, \quad (28)$$

with

$$M(t) = \sum_{n=0}^{\infty} e^{tn} P(n; \mu, k) = \left(\frac{k}{k + \mu(1 - e^t)} \right)^k \quad (29)$$

being the moment-generating function of the NBD. The first four cumulants read

$$\kappa_1^{NBD} = \mu, \quad (30)$$

$$\kappa_2^{NBD} = \frac{\mu(k + \mu)}{k}, \quad (31)$$

$$\kappa_3^{NBD} = \frac{\mu(k + \mu)(k + 2\mu)}{k^2}, \quad (32)$$

$$\kappa_4^{NBD} = \frac{\mu(k + \mu)(k^2 + 6k\mu + 6\mu^2)}{k^3}, \quad (33)$$

The parameters of the NBD are fixed in each experiment by the fitting procedure. In a first step the number of particle-emitting sources n_s is determined according to [11, 27]

$$n_s = fN_w + (1 - f)N_{coll}, \quad (34)$$

where N_W and N_{coll} are the numbers of wounded nucleons and binary collisions, respectively. Sampling impact parameters according to $d\sigma = b db$ a list of number of sources, n_s^i , is generated, with $i \in [1, \dots, N_{Event}]$. Then, for each event i , NBD is sampled n_s^i times and the parameters of the NBD, μ , k and f , are adjusted such that the obtained multiplicity distribution agrees with the corresponding experimental one. The mixing parameter f is introduced to improve the description by accounting also particles produced in hard (prompt) processes.

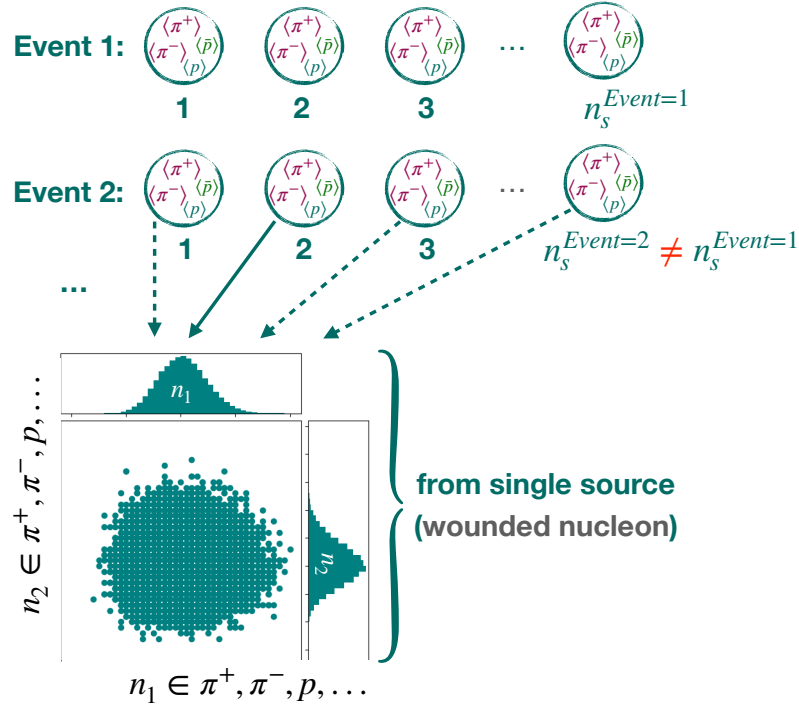


Figure 3. Simulation of particle production within the model of independent sources. The circles indicate the individual sources sampled according to Eq. 34. n_1 and n_2 show particle species used to sample emission from a single source. The distributions per single source can be chosen arbitrarily. See models A and B discussed below.

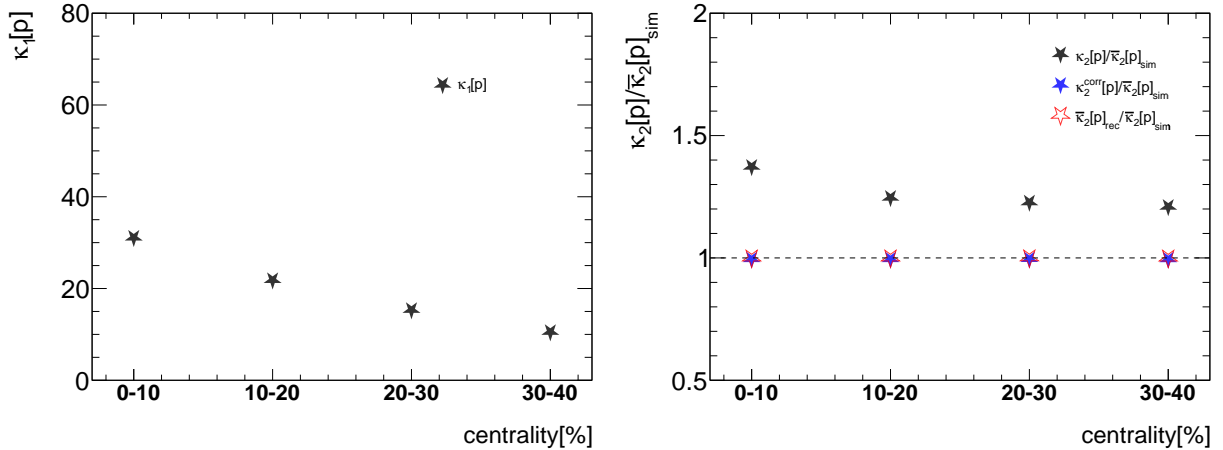


Figure 4. Left panel: Mean number of simulated protons used in Model A as a function of centrality. Right panel: Second-order cumulants of protons in Model A including volume fluctuations (black stars), corrected with Eq. 24 (blue stars) and reconstructed with Eq. 23 (open red stars). The results are normalized to $\bar{\kappa}_2[p]_{sim}$, corresponding to the second-order cumulants of protons in the absence of volume fluctuations.

Panel (a) of Fig. 1 represents the NBD distribution as observed by the HADES experiment for Au+Au collisions at $\sqrt{s_{NN}} = 2.4$ GeV, with parameters $\mu = 0.24$, $k = 20.34$, and $f = 1$ taken from [26]. For comparison, we also present a

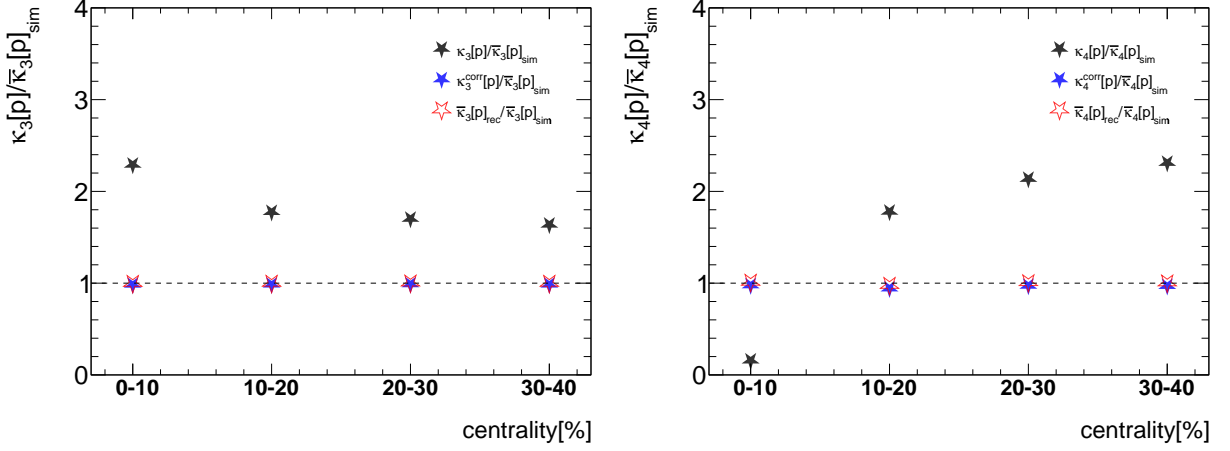


Figure 5. Left panel: Third order cumulants of protons in Model A including volume fluctuations (black stars), corrected with Eq. 25 (blue stars) and reconstructed with Eq. 23 (open red stars). The results are normalized to $\bar{\kappa}_3[p]_{\text{sim}}$, corresponding to the second-order cumulants of protons in the absence of volume fluctuations. Right panel: Fourth order cumulants of protons in Model A including volume fluctuations (black stars), corrected with Eq. 26 (blue stars) and reconstructed with Eq. 23 (open red stars). The results are normalized to $\bar{\kappa}_4[p]_{\text{sim}}$, corresponding to the fourth order cumulants of protons in the absence of volume fluctuations.

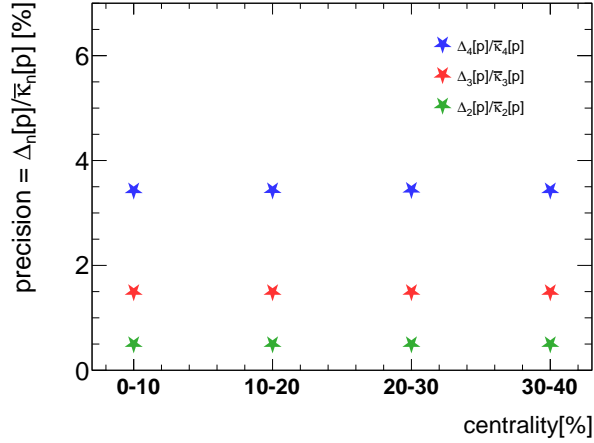


Figure 6. The normalised bias terms in Model A.

Poisson distribution with the same mean, μ . Similar distributions from the STAR [11] and ALICE [27] experiments are presented in panels (b) and (c). Figure 1 shows that at the HADES energy the fitted NBDs are very close to Poisson distributions. Quantitatively this can be seen by evaluating the cumulants of the HADES NBD ($\mu = 0.24$, $k = 20.34$)

$$\kappa_1^{\text{NBD}}(\text{HADES}) = 0.24 \quad (35)$$

$$\kappa_2^{\text{NBD}}(\text{HADES}) = 0.2428, \quad (36)$$

$$\kappa_3^{\text{NBD}}(\text{HADES}) = 0.2486, \quad (37)$$

$$\kappa_4^{\text{NBD}}(\text{HADES}) = 0.2602. \quad (38)$$

For a Poisson distribution all cumulants are equal to its mean and the HADES data are indeed close to fulfilling this condition. The statement, to a lesser extent, is also valid for the STAR Au+Au data at 3 GeV (see Fig. 1). The corresponding ALICE distribution, however, is much wider compared to the Poisson baseline, but the ALICE NBD is obtained for very different acceptance than that used for the cumulant analysis. In Table I we also provide the NBD parameters as obtained by the STAR and ALICE collaborations for Au+Au and Pb+Pb collisions at $\sqrt{s_{\text{NN}}} = 3$ GeV and 2.76 TeV, respectively.

experiments	μ	k	f
HADES	0.24	20.34	1
STAR	0.31	5.66	0.94
ALICE	29.3	1.6	0.8

Table I. NBD parameters as extracted from Glauber fits to particle distributions observed in different experiments. For simulations, the distributions should be folded within the experimental acceptance in which the cumulants are measured.

In the following we test the proposed method using two different simulations referred to as Model A and Model B. While the sampling of wounded nucleons is the same for both models, in Model A we sample different particle species independently while in Model B we introduce correlations between pions and protons via cluster production and decay. We will concentrate on the HADES data. For both methods, we use the Glauber model to extract the distributions of wounded nucleons corresponding to four different centrality classes in Au+Au collisions at $\sqrt{s_{NN}} = 2.4$ GeV. They are presented in Figure 2.

In both models particles are produced from independent sources (cf. Eq. 34). For the HADES data the extracted number of binary collision is zero ($f = 1$, see Table I), the number of sources per event are sampled exclusively from the wounded nucleon distributions presented in Fig. 2. The simulation process is schematically illustrated in Fig. 3.

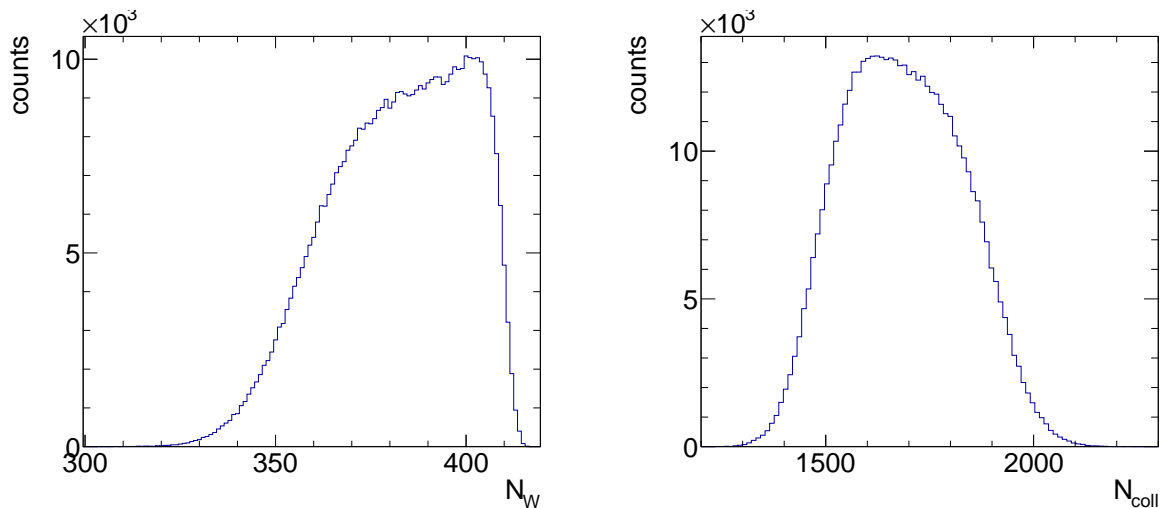


Figure 7. Number of wounded nucleons (left panel) and binary collisions (right panel) as generated with a Glauber Monte Carlo simulation using input from the ALICE experiment [27]. The selection corresponds to the 5% most central Pb-Pb collisions at $\sqrt{s_{NN}} = 2.76$ TeV.

VI. MODEL A

In model A we first generate the charged-particle multiplicity for individual events using the NBD distribution as extracted by experimental measurements. In doing so we sample the NBD distribution n_s times. Different particle species are then taken as fractions of the total number of charged particles. For example, from a randomly sampled NBD distribution a respective fraction is assigned to protons. From the remaining charged particles another fraction is assigned to positively charged pions and the rest is taken as negatively charged pions. These fractions are chosen such that the overall probability of having protons, positively and negatively charged pions correspond to 75%, 9% and 16 % of all charged particles, respectively, based on the actual HADES measurement in Au+Au collisions (see [30] and references therein). In addition, we account for acceptance effects, because the NBD parameters are obtained in different acceptance than that used for the fluctuation analyses. We therefore fold the entire NBD distribution with a binomial distribution such that the experimentally measured mean multiplicities of particles in the acceptance used for fluctuation analysis are reproduced. Volume fluctuations are naturally accounted for as for each event the number of sources n_s are randomly sampled from the corresponding distributions.

The simulated mean numbers of protons are shown in the left panel of Fig. 4 for the four centrality classes. In the right panel of Fig. 4 the reconstructed second-order cumulants of protons are presented, normalized to the expected true cumulant, $\bar{\kappa}_2[p]_{sim}$. The black stars represent the results which include volume fluctuations. The values κ_2^{corr} as calculated using Eq. 15 are shown with blue stars, while the red stars correspond to $\bar{\kappa}_2[p] = \kappa_2^{corr}[p] + \Delta_2[p]$. The results for the third and fourth order cumulants are shown in Fig. 5. The corresponding normalized biases $\Delta_n/\bar{\kappa}_n$ are presented in Fig. 6. We find the normalized biases to be very small, of the order of a few percent, so that the corrected cumulants, κ_n^{corr} are very close to their expected true values, $\bar{\kappa}_n$. As already discussed, this is to be expected since the multiplicity distribution per wounded nucleon in the present Model is close to Poisson.

A. High energy limit

In this section we apply the method to high energy collisions using ALICE data. In doing so we first run Glauber Monte Carlo simulations for Pb-Pb collisions at $\sqrt{s_{NN}} = 2.76$ TeV. The input parameters are taken from Ref. [27]. Following the ALICE experiment [27], different centrality classes are chosen by introducing sharp cuts on the charged-particle distributions. The distributions of wounded nucleons and binary collisions corresponding to the 5% most central collisions are presented in Fig. 7 [23]. The reconstructed mean number of wounded nucleons and binary collisions, corresponding to the 5% most central collisions are $\langle N_W \rangle \approx 382$ and $\langle N_{coll} \rangle \approx 1685$, respectively, consistent with the numbers given in [27]. With these numbers one can estimate a mean number of particle emitting sources, yielding $\langle n_s \rangle \approx 642$ (see Eq. 34). The corresponding mean number of charged particles can be estimated as $\langle N_{ch} \rangle = \langle n_s \rangle \times \mu_{NBD} \approx 18811$. On the other hand, the total number of charged particles measured inside the ALICE acceptance is about 1601 [31]. We thus folded the ALICE NBD distribution with a binomial with the acceptance factor of $\epsilon = 1601/18811 \approx 8.5\%$ to obtain the distribution within the experimental acceptance.¹ The so obtained NBD distribution from ALICE is presented in Fig. 8. We further note that only the acceptance in rapidity is considered. Fluctuation analyses are performed within a finite momentum range. Inclusion of the latter will further reduce the discrepancy between NBD and the corresponding Poisson distribution shown with the red histogram in Fig. 8.

Finally using the NBD distribution presented in Fig. 8, and measured proton number, $\langle N_p \rangle \approx 35$ [31], we estimated $\Delta_2[p] \approx 1.2$. This corresponds to a bias of $\Delta_2[p]/\bar{\kappa}_2[p] \approx 3.3\%$.

VII. MODEL B

In model B we introduce correlations between charged particles, specifically pions and protons by generating clusters (or rather resonances). Especially for HADES energies most of the observed pions are believed to originate from decays of Delta resonances. Therefore, the effect of such decay correlations, while not treated quantitatively here, needs to be taken into account. Specifically, this is done by generating clusters of particles (e.g., resonances) from each source and letting them decay into two different particle species. Moreover, the clusters are generated from a Poisson distribution. In addition we produce independent particles from each source as well, sampled also from a Poisson distribution. Schematic illustration of the model for a single source is given in Fig. 9. Fluctuations of sources are introduced like in the model A. The input parameters for model B are given in Table II.

particles	mean numbers per source
clusters	0.03
independent protons	0.23
other particles	0.21

Table II. Parameters for model B are mean numbers of different particles species per source (see [30] and references therein). In addition, each cluster decays into one proton and one pion. Numbers of clusters, independent protons and other particles are sampled from independent Poisson distributions.

By construction the simulated protons, pions and clusters follow a Poisson distribution. However the distribution of the total number of particles does not, due to the correlation between pions and protons introduced via the cluster decay (see Appendix F).

¹ We note that binomial folding of the NBD distribution, with the acceptance factor ϵ , changes only the parameter μ of the original NBD distribution ($\mu \rightarrow \epsilon\mu$), while the parameter k stays unchanged.

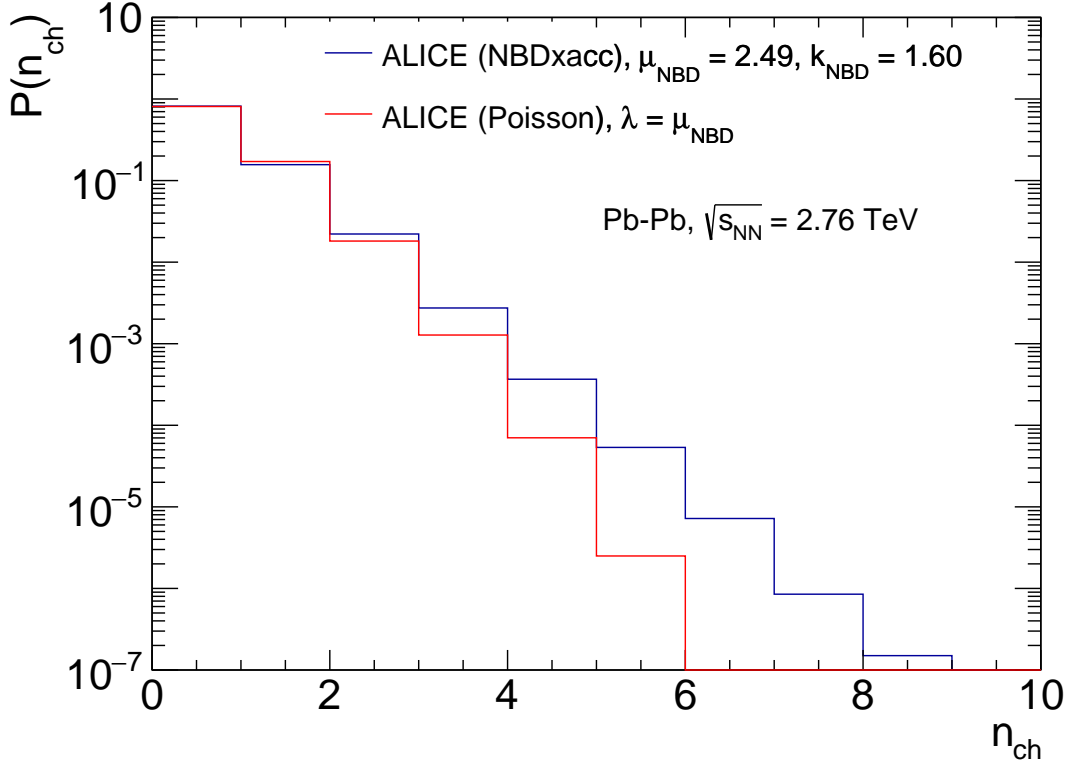


Figure 8. NBD distributions from ALICE as measured by fitting the signal amplitude in VZEROs (left panel) and after folding within the experimental acceptance 8.5% (see the text for details). The red histogram corresponds to a Poisson distribution with the same mean, μ as the folded NBD distribution. The original NBD distribution from ALICE is presented in the panel (c) of Fig. 1.

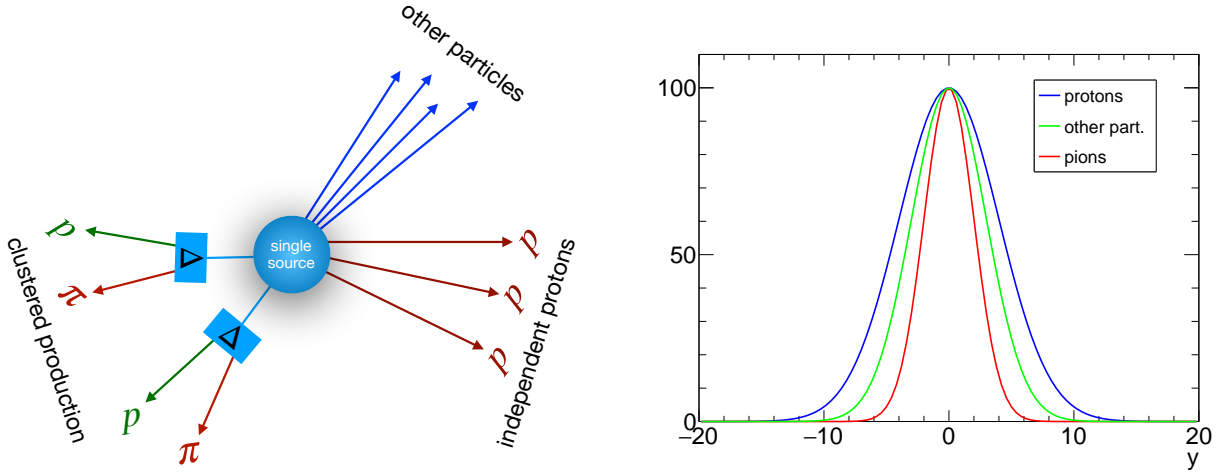


Figure 9. Left panel: Schematic illustration of model B. From a single source two clusters and three protons are produced. The clusters further decay to protons and pions. In simulations both, clusters and independent protons are sampled from Poisson distributions. The corresponding mean values of clusters and independent protons are provided in Table II. Right panel: Schematic rapidity distributions for different particles in order to study acceptance effects.

In experiments measurements are performed inside the finite acceptance by imposing selection criteria in momentum space, e.g., on rapidity and/or transverse momentum of particles. Moreover, such conditions typically lead to different

acceptances for different particle species. In order to study the impact of the finite acceptance on the presented formalism, we introduce arbitrary rapidity distributions for protons, pions and other particles as illustrated in the right panel of Fig. 9. To this end we generate rapidity values for protons, pions and other particles from the corresponding distributions presented in Fig. 9.

In the left panel of Fig. 10 we present mean multiplicities of protons produced via clusters (red circles) and independently (blue circles), while the black circles correspond to the total number of protons. In addition, we produce pions from clusters, and, by construction, their mean values are equal to those of protons from clusters. The right panel of Fig. 10 shows the second-order cumulants of protons divided by the expected value $\bar{\kappa}_2[p]_{sim}$. The black stars represent those including participant (volume) fluctuations, $\kappa_2[p]/\bar{\kappa}_2[p]_{sim}$. The corrected cumulants $\kappa_2^{corr}[p]/\bar{\kappa}_2[p]_{sim}$ (see Eq. 24) are shown with blue symbols, while the open red stars represent the true reconstructed values of fluctuations of protons $\bar{\kappa}_2[p]/\bar{\kappa}_2[p]_{sim}$ as calculated using Eq. 23. Similar results for the third and fourth order cumulants of protons are presented in Fig. 11 (see Eqs. 25, 26, 23). In Fig. 12 the normalized cumulants as a function of cumulant order are presented for the 10% most central collisions. The right panel of Fig. 12 corresponds to the full acceptance, while in the right panel the results in the finite acceptance, delimited as $|y| < 1$, are presented. One clearly observes that in the finite acceptance the precision of the method is significantly better. In Fig. 13 we show the magnitude of the corresponding normalized biases, $\Delta_n/\bar{\kappa}_n$, for the full acceptance (left panel) and for $|y| < 1$ (right panel). While the biases for the full acceptance may at first sight appear rather large ($\sim 40\%$) one should realize that for the most central events the uncorrected fourth order cumulant is more than a factor of 50 larger in magnitude than the true cumulants. In other words the proposed corrections, while not perfect are a huge improvement of the measurement. The situation gets better for the limited acceptance.

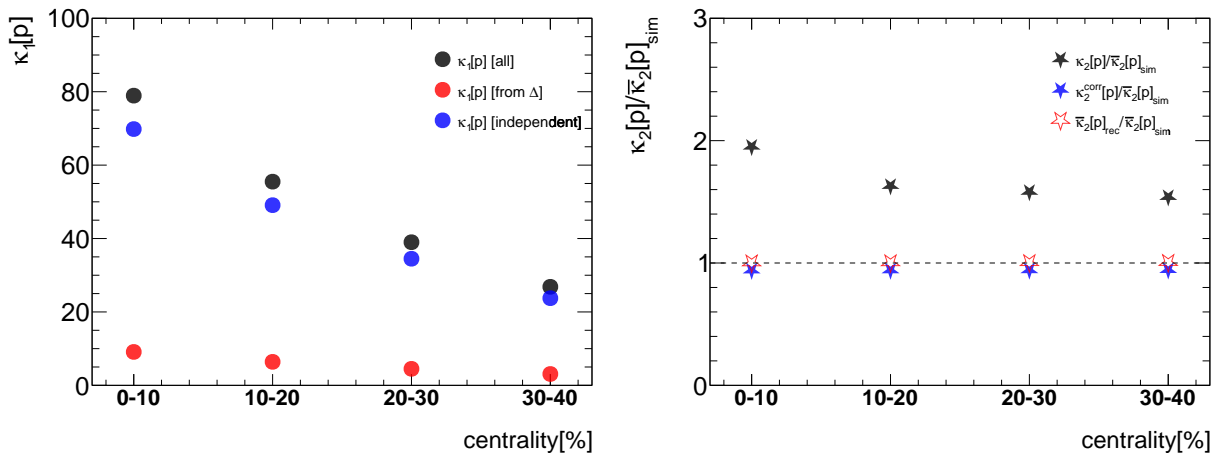


Figure 10. Left panel: Mean number of protons produced via clusters and independently are presented with the red and blue circles respectively. The black circles represent total multiplicity of protons. Pions are produced only via clusters. Right panel: Reconstructed second-order cumulants of protons including participant fluctuations (black stars). Corrected values for cumulants $\kappa_2^{corr}[p]$, i.e., without the bias term $\Delta_2[p]$ are presented with blue stars, while red stars represent fully corrected, against volume fluctuation. The results are normalized to the true second order cumulant, $\bar{\kappa}_2[p]_{sim}$.

VIII. SOFTWARE PACKAGE

A Python package is provided to derive analytical formulas for both mixed and pure cumulants of multiplicity distributions, including participant/volume fluctuations. The correction formulas and their bias terms can be derived as well. The dedicated graphical user interface is presented in Fig. 14 and can be downloaded via Ref. [25].

IX. DISCUSSION AND SUMMARY

- We have shown that using mixed events to determine the contributions of wounded nucleon or volume fluctuations is equivalent to extracting the latter from the track multiplicity distribution. However event mixing may offer an advantage since it allows to generate an almost arbitrarily large event ensemble with the same multiplicity distribution, and thus eliminate possible constraints due to limited event statistics.

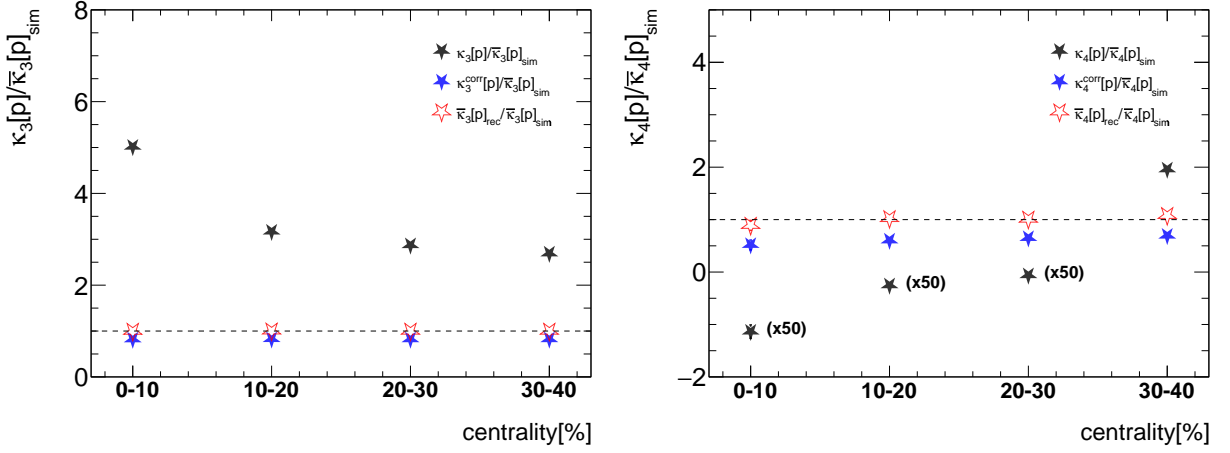


Figure 11. Left panel: Reconstructed third-order cumulants of protons including participant fluctuations (black stars) for model B. Corrected values for cumulants $\kappa_3^{corr}[p]$, i.e. without the bias term $\Delta_3[p]$ are presented with blue stars, while red stars represent fully corrected, against volume fluctuations, values $\bar{\kappa}_3[p] = \kappa_3^{corr}[p] + \Delta_3[p]$. Right panel: Similar to the left panel but for the fourth-order cumulants with volume fluctuations (black stars) need to be multiplied by 50 for the first three centrality classes. The results are normalized to the true third or fourth order cumulant, $\bar{\kappa}_3[p]_{sim}$, $\bar{\kappa}_4[p]_{sim}$, respectively

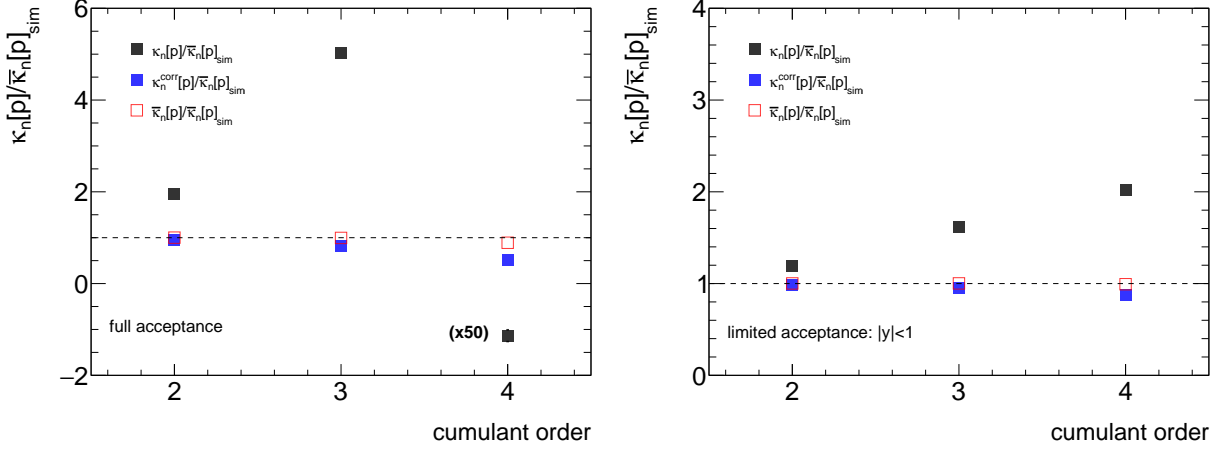


Figure 12. Left panel: Cumulants of protons in the full acceptance, presented for the 10% most central collisions (cf. Figs. 10 and 11). Right panel: Similar plot for the 10% most central collisions, but inside the finite acceptance delimited with the $|y| < 1$ criterion. The results are normalized to the true cumulants, $\bar{\kappa}_n[p]_{sim}$.

In either case, not all contributions can be accessed by a direct measurement. The remaining terms lead to biases, Δ_k , which depend on the multiplicity distribution per wounded nucleon. These biases are, however, parametrically suppressed by powers of $\langle N \rangle / \langle M \rangle$ depending on the order of the cumulants. The biases are also small if the multiplicity distribution per wounded nucleon is close to Poisson. In addition, we suggest to constrain these biases in experiment with fits to the observed multiplicity distribution within the wounded-nucleon model.

- We have worked here within the wounded nucleon model to formulate volume fluctuations. Alternatively, one may introduce generic volume fluctuations as done e.g. in [22]. It is easy to show (see Appendix D) that the resulting expressions for the corrected cumulants, κ_j^{corr} , and the biases, Δ_j , are identical to those derived here, i.e. Eqs. (24-26).
- We note that one gets similar expressions for the fluctuations from the wounded nucleons, Eqs. (20-22), in terms of the factorial cumulants of, for example, pions instead of the total track multiplicity. This has the advantage that the corrections do not involve the particles of interest, protons, in our case. Of course, this approach requires that sufficiently many pions are produced and thus may be limited to collisions at higher energies.

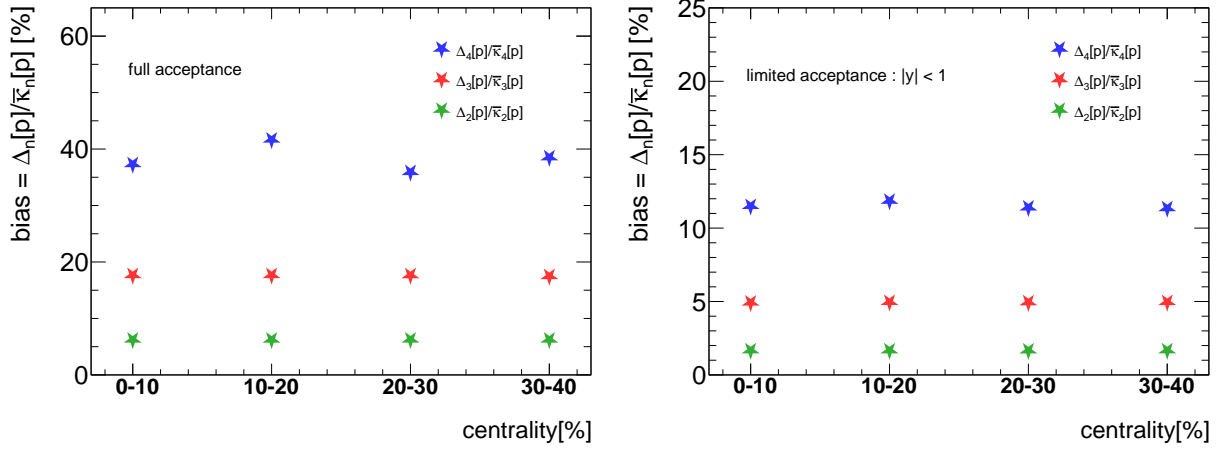


Figure 13. The bias terms for model B, in the full (left panel) and finite (right panel) acceptances. The acceptance, $|y| < 1$ is introduced using rapidity distributions of pions and protons as shown in Fig. 9.

Formulae for participant/volume fluctuations and their corrections

Select cumulant order: 6

Derive formulae for: Volume fluctuations

Derive

Pure cumulants

Deriving formulas for volume fluctuations for order: 6

$$k_1[N] = \langle W \rangle \langle n \rangle$$

$$k_2[N] = \langle W \rangle^2 k_2[n] + \langle n \rangle^2 k_2[W]$$

$$k_3[N] = \langle W \rangle^3 k_3[n] + \langle n \rangle^2 k_3[W] + 3 \langle n \rangle^2 k_2[W] k_2[n]$$

$$k_4[N] = \langle W \rangle^4 k_4[n] + \langle n \rangle^3 k_4[W] + 6 \langle n \rangle^2 k_2[n] k_3[W] + 4 \langle n \rangle^2 k_2[W] k_3[n] + 3 k_2[W] k_2[n]^2$$

$$k_5[N] = \langle W \rangle^5 k_5[n] + \langle n \rangle^4 k_5[W] + 10 \langle n \rangle^3 k_2[n] k_4[W] + 10 \langle n \rangle^2 k_3[W] k_3[n] + 5 \langle n \rangle^2 k_2[W] k_4[n] + 15 \langle n \rangle^2 k_2[n]^2 k_3[W] + 10 k_2[W] k_2[n] k_3[n]$$

$$k_6[N] = \langle W \rangle^6 k_6[n] + \langle n \rangle^5 k_6[W] + 15 \langle n \rangle^4 k_2[n] k_5[W] + 20 \langle n \rangle^3 k_3[n] k_4[W] + 45 \langle n \rangle^2 k_2[n]^2 k_4[W] + 15 \langle n \rangle^2 k_3[W] k_4[n] + 6 \langle n \rangle^2 k_2[W] k_5[n] + 60 \langle n \rangle k_2[n] k_3[W] k_3[n] + 15 k_2[W] k_2[n] k_4[n] + 10 k_2[W] k_3[n]^2 + 10 k_2[W] k_2[n] k_3[n]$$

Mixed cumulants

Deriving formulas for volume fluctuations for order: 6

$$k_{11}[N1N2] = \langle W \rangle k_{11}[n1n2] + \langle n1 \rangle \langle n2 \rangle k_2[W]$$

$$k_{12}[N1N2] = \langle W \rangle k_{12}[n1n2] + \langle n1 \rangle \langle n2 \rangle^2 k_3[W] + \langle n1 \rangle k_2[W] k_2[n2] + 2 \langle n2 \rangle k_{11}[n1n2] k_2[W]$$

$$k_{13}[N1N2] = \langle W \rangle k_{13}[n1n2] + \langle n1 \rangle \langle n2 \rangle^3 k_4[W] + 3 \langle n1 \rangle \langle n2 \rangle k_2[n2] k_3[W] + \langle n1 \rangle k_2[W] k_3[n2] + 3 \langle n2 \rangle^2 k_{11}[n1n2] k_3[W] + 3 \langle n2 \rangle k_{12}[n1n2] k_2[W] + 3 k_{11}[n1n2] k_2[W] k_2[n2]$$

$$k_{14}[N1N2] = \langle W \rangle k_{14}[n1n2] + \langle n1 \rangle \langle n2 \rangle^4 k_5[W] + 6 \langle n1 \rangle \langle n2 \rangle^2 k_2[n2] k_4[W] + 4 \langle n1 \rangle \langle n2 \rangle k_3[n2] k_3[W] + \langle n1 \rangle k_2[W] k_4[n2] + 9 \langle n1 \rangle k_2[n2]^2 k_3[W] + 4 \langle n2 \rangle^3 k_{11}[n1n2] k_4[W] + 6 \langle n2 \rangle^2 k_{12}[n1n2] k_3[W] + 12 \langle n2 \rangle k_{11}[n1n2] k_2[n2] k_3[W] + 4 \langle n2 \rangle k_{13}[n1n2] k_2[W] + 4 k_{11}[n1n2] k_2[W] k_3[n2] + 6 k_{12}[n1n2] k_2[W] k_2[n2]$$

Description: Pure cumulants, including volume fluctuations

$k_n[N]$ -> nth order cumulant of the multiplicity distribution (can be measured)
 $k_n[n]$ -> nth order cumulant of the multiplicity distribution per single source
 $\langle W \rangle$ -> mean number of sources
 $\langle n \rangle$ -> mean number of particles per source

Description: Mixed cumulants, including volume fluctuations

$k_{mn}[N1N2]$ -> covariance of order mn between multiplicity distributions of particles N1 and N2
 $k_{mn}[n1n2]$ -> covariance of order mn between multiplicity distributions of particles n1 and n2 (per source)

A. Rustamov, R. Holzmann, V. Koch, J. Stroh

Figure 14. The GUI for deriving analytic formulas.

- We have checked that the proposed method also works if the multiplicity distribution is determined for a different acceptance than the particle distribution of interest. In this case all quantities in the expression for the corrected cumulants, Eqs.(24-26) involving the multiplicity should be evaluated in the multiplicity acceptance while all quantities involving the particles of interest, such as $\langle N \rangle$ or $\kappa_j[N]$ should be determined in the particle acceptance.
- We have verified that the proposed method is not affected by potentially different rapidity distributions for different particle types.

- We note that the correction term and bias for the second-order cumulant depends on the properties of the multiplicity distribution only while those for higher-order cumulants also involve the (uncorrected) cumulants of interest (at a lower order), $\kappa_n[N]$ (see Eq. (25,26)).
- The proposed method is also applicable for mixed cumulants, such as the covariance between two particle species. The relevant formulas for mixed cumulants between species A and B up to $\kappa_{2,2}[A, B]$ are given in Appendix G. The corresponding relations for correction and bias terms for mixed cumulants of any order can be obtained with the provided software package [25].
- Here we have not explicitly discussed corrections for net proton cumulants. However, those can be easily obtained using the corrections to the mixed cumulants provided in Appendix G. For example, the second-order cumulant of the net proton distribution is given by

$$\kappa_2[N - \bar{N}] = \kappa_2[N] + \kappa_2[\bar{N}] - 2\kappa_{1,1}[N, \bar{N}] \quad (39)$$

The corrected cumulant is the (using Eqs. (24, G8))

$$\kappa_2^{corr}[N - \bar{N}] = \kappa_2[N - \bar{N}] - \frac{(\langle N \rangle - \langle \bar{N} \rangle)^2}{\langle M \rangle^2} C_2[M] \quad (40)$$

with the bias

$$\Delta = \frac{(\langle N \rangle - \langle \bar{N} \rangle)^2}{\langle M \rangle^2} \bar{C}_2[M] \quad (41)$$

For systems at vanishing baryon number chemical potential, such as those created at very high collision energies, $\langle N \rangle = \langle \bar{N} \rangle$ so that the corrected cumulant is identical to the measured one (as discussed in [22]) and the bias vanishes.

In summary, we have presented a method to correct experimentally measured particle number cumulants for the effect of participant or volume fluctuations. The essential idea is to extract the contribution from the volume fluctuations from the distribution of charged particles which, after appropriate re-scaling, may be subtracted from the measured cumulants of interest. Our proposed method is not exact as there remains a bias or remnant which can not be accessed directly from experiment. However, we have shown by model calculations that this bias is very small compared to the contribution from participant fluctuations and we hence consider our method an important step towards measuring the true dynamical fluctuations of the system.

ACKNOWLEDGMENTS

V.K would like to thank GSI and the Institute for Nuclear Theory at the University of Washington for their kind hospitality and stimulating research environment. V.K. has been supported by the U.S. Department of Energy, Office of Science, Office of Nuclear Physics, under contract number DE-AC02-05CH11231, by the INT's U.S. Department of Energy grant No. DE-FG02-00ER41132, and by the ExtreMe Matter Institute EMMI at the GSI Helmholtzzentrum für Schwerionenforschung, Darmstadt, Germany.

Appendix A: Wounded-nucleon model

Here we briefly discuss the wounded-nucleon model following the Appendix of Ref. [32]. The wounded-nucleon model assumes that particles are produced by independent sources, called wounded nucleons or participants. Therefore, the probability to find A particles of type A and B particles of type B can be written as

$$P(A, B) = \sum_w W(w) \sum_{a_1, \dots, a_w} \sum_{b_1, \dots, b_w} p(a_1, b_1) \cdots p(a_w, b_w) \delta_{A, \sum_{k=1}^w a_k} \delta_{B, \sum_{k=1}^w b_k}. \quad (A1)$$

Here $W(w)$ denotes the probability to have w wounded nucleons, and $p(a, b)$ is the probability to have a particles of type A and b particles of type B from one wounded nucleon. The moment-generating function, $h(t_A, t_B)$ is then

$$\begin{aligned}
H(t_A, t_B) &= \sum_{A, B} e^{t_A A} e^{t_B B} P(A, B) \\
&= \sum_w W(w) \sum_{a_1, \dots, a_w} \sum_{b_1, \dots, b_w} p(a_1, b_1) \cdots p(a_w, b_w) e^{t_A \sum_{k=1}^w a_k} e^{t_B \sum_{k=1}^w b_k} \\
&= \sum_w W(w) \sum_{a_1, b_1} p(a_1, b_1) e^{t_A a_1 + t_B b_1} \cdots \sum_{a_w, b_w} p(a_w, b_w) e^{t_A a_w + t_B b_w} \\
&= \sum_w W(w) \left[\sum_{a, b} p(a, b) e^{t_A a + t_B b} \right]^w \\
&= \sum_w W(w) [h_w(t_A, t_B)]^w \\
&= \sum_w W(w) e^{w g_w(t_A, t_B)}
\end{aligned} \tag{A2}$$

where $h_w(t_A, t_B) = \sum_{a, b} p(a, b) e^{t_A a + t_B b}$ is the moment generating function and $g_w(t_A, t_B) = \ln[h_w(t_A, t_B)]$ the cumulant-generating function for one wounded nucleon, respectively. The cumulant-generating function, $G(t_A, t_B) = \ln[H(t_A, t_B)]$, is then given by

$$G(t_A, t_B) = \ln[H(t_A, t_B)] = \ln \left[\sum_w W(w) e^{w g_w(t_A, t_B)} \right] = G_W(g_w(t_A, t_B)) \tag{A3}$$

where $G_W(t) = \ln[\sum_w W(w) e^{w t}]$ in the cumulant-generating function for the wounded-nucleon distribution, $W(w)$. We note, that $g_w(0, 0) = G_W(0) = 0$ by construction. The cumulants are then obtained as

$$\kappa_{j, k}[A, B] = \left. \frac{\partial^j \partial^k}{\partial t_A^j \partial t_B^k} g(t_A, t_B) \right|_{t_A=t_B=0}. \tag{A4}$$

For example:

$$\begin{aligned}
\kappa_1[A] &= \left. \frac{\partial}{\partial t_A} G(t_A, 0) \right|_{t_A=0} = \left. \frac{dG_w}{dg_w} \frac{dg_w(t_A, 0)}{dt_A} \right|_{t_A=0} = \left. \frac{dG_w}{dg_w} \right|_{g_w=0} \left. \frac{dg_w(t_A, 0)}{dt_A} \right|_{t_A=0} \\
&= \kappa_1[N_w] \kappa_1[a] = \langle N_w \rangle \langle a \rangle
\end{aligned} \tag{A5}$$

where $\kappa_1[n] = \langle a \rangle$ denotes the mean number of particles of type A per wounded nucleon and $\kappa_1[w] = \langle N_w \rangle$ the mean number of wounded nucleons. The second-order cumulant is

$$\begin{aligned}
\kappa_2[A] &= \left. \frac{\partial^2}{\partial t_A^2} G(t_A, 0) \right|_{t_A=0} \\
&= \left. \frac{d^2 G_w}{dg_w^2} \left(\frac{dg_w(t_A, 0)}{dt_A} \right)^2 \right|_{t_A=0} + \left. \frac{dG_w}{dg_w} \frac{d^2 g_w(t_A, 0)}{dt_A^2} \right|_{t_A=0} \\
&= \kappa_2[N_w] \kappa_1[a]^2 + \kappa_1[N_w] \kappa_2[a] = \kappa_2[N_w] \langle a \rangle^2 + \langle N_w \rangle \kappa_2[a]
\end{aligned} \tag{A6}$$

The covariance is

$$\begin{aligned}
cov[A, B] &= \left. \frac{\partial}{\partial t_A \partial t_B} G(t_A, t_B) \right|_{t_A, t_B=0} = \left. \frac{\partial}{\partial t_B} \left(\frac{dG_w}{dg_w} \frac{\partial g_w(t_A, t_B)}{\partial t_A} \right) \right|_{t_A, t_B=0} \\
&= \left. \frac{d^2 G_w}{dg_w^2} \frac{\partial g_w(t_A, t_B)}{\partial t_A} \frac{\partial g_w(t_A, t_B)}{\partial t_B} \right|_{t_A, t_B=0} + \left. \left(\frac{dG_w}{dg_w} \frac{\partial^2 g_w(t_A, t_B)}{\partial t_A \partial t_B} \right) \right|_{t_A, t_B=0} \\
&= \kappa_2[N_w] \kappa_1[a] \kappa_1[b] + \kappa_1[N_w] cov[a, b] \\
&= \kappa_2[N_w] \langle a \rangle \langle b \rangle + \langle N_w \rangle cov[a, b]
\end{aligned} \tag{A7}$$

Using the relation between the cumulant and factorial cumulant generating function, Eq. B3, the factorial cumulant generating function is given by

$$G_F(z_A, z_B) = G(\ln(z_A), \ln(z_B)) = G_W(g_w(\ln(z_A), \ln(z_B))) = G_W(g_{F,w}(z_A, z_B)), \quad (\text{A8})$$

with

$$g_{F,w}(z_A, z_B) = \sum_{a,b} p(a, b) z_A^a z_B^b$$

the factorial cumulant generating function for the distribution of one wounded nucleon, $p(a, b)$. The structure is the same as for the cumulant generating function, except that now the argument of the wounded-nucleon cumulant-generating function is the factorial cumulant generating function, $g_{F,w}$. Thus the factorial cumulants are easily obtained by simply replacing all the cumulants of the particle distribution for a given wounded nucleon, $\kappa_{i,j}[a, b]$ with the corresponding factorial cumulants, with $C_1[X] = \kappa_1[X] = \langle X \rangle$

$$\begin{aligned} C_1[A] &= \frac{\partial}{\partial z_A} g_F(z_A, 1)|_{z_A=1} = \kappa_1[N_w] C_1[a] = \langle N_w \rangle \langle a \rangle \\ C_2[A] &= \kappa_2[N_w] \langle a \rangle^2 + \langle N_w \rangle C_2[a] \\ C_{1,1}[A, B] &= \text{cov}[A, B] \end{aligned} \quad (\text{A9})$$

Appendix B: Cumulant and factorial cumulant generating functions

Given a multiplicity distribution for particles of type A and B , $P(A, B)$ the generating functions for cumulants, $g(t_A, t_B)$, and factorial cumulants, $g_F(z_A, z_B)$ are given by

$$g(t_A, t_B) = \ln \left[\sum_{A,B} P(A, B) e^{t_A A} e^{t_B B} \right] \quad (\text{B1})$$

$$g_F(z_A, z_B) = \ln \left[\sum_{A,B} P(A, B) (z_A)^A (z_B)^B \right]. \quad (\text{B2})$$

By construction, $g(t_A = 0, t_B = 0) = 0$ and $g_F(z_A = 1, z_B = 1) = 0$. Cumulants of order (i, j) , $\kappa_{j,k}[A, B]$, are then obtained through

$$\kappa_{j,k}[A, B] = \left. \frac{\partial^j \partial^k}{\partial t_A^j \partial t_B^k} g(t_A, t_B) \right|_{t_A=t_B=0},$$

while the factorial cumulants, $C_{j,k}[A, B]$, are given by

$$C_{j,k}[A, B] = \left. \frac{\partial^j \partial^k}{\partial z_A^j \partial z_B^k} g(z_A, z_B) \right|_{z_A=z_B=1}.$$

The generating functions are related through

$$g_F(z_A, z_B) = g[\ln(z_A), \ln(z_B)] \quad (\text{B3})$$

or vice versa

$$g(t_A, t_B) = g_F(e^{t_A}, e^{t_B}) \quad (\text{B4})$$

These relations may also be used to convert cumulants into factorial cumulants and vice versa. For example, for the diagonal cumulants, $\kappa_n[A]$ we have

$$\kappa_n[A] = \sum_{j=1}^n S(n, j) C_j[A] \quad (\text{B5})$$

where $S(n, j)$ denotes the Sterling numbers of the second kind. The inverse relation is

$$C_n[A] = \sum_{j=1}^n B_{n,j} (1, -1, 2, \dots, (-1)^{j-1} (n-j+1)!) \kappa_j[A] \quad (\text{B6})$$

with $B_{n,j}$ being Bell polynomials. For the first four orders this evaluates to

$$\begin{aligned} \kappa_1 &= C_1 \\ \kappa_2 &= C_1 + C_2 \\ \kappa_3 &= C_1 + 3C_2 + C_3 \\ \kappa_4 &= C_1 + 7C_2 + 6C_3 + C_4 \end{aligned} \quad (\text{B7})$$

and

$$\begin{aligned} C_2 &= \kappa_2 - \kappa_1 \\ C_3 &= 2\kappa_1 - 3\kappa_2 + \kappa_3 \\ C_4 &= -6\kappa_1 + 11\kappa_2 - 6\kappa_3 + \kappa_4 \end{aligned} \quad (\text{B8})$$

Appendix C: Multiplicity Distribution

The multiplicity distribution, $P(M)$, is given by summing over all (charged) particles,

$$P_M(M) = \sum_{A,B,X} P(A, B, X) \delta_{M, A+B+X}, \quad (\text{C1})$$

where

$$P(A, B, X) = \sum_w W(w) \sum_{a_1, \dots, a_w} \sum_{b_1, \dots, b_w} \sum_{x_1, \dots, x_w} p(a_1, b_1, x_1) \cdots p(a_w, b_w, x_w) \delta_{A, \sum_{k=1}^w a_k} \delta_{B, \sum_{k=1}^w b_k} \delta_{X, \sum_{k=1}^w x_k}$$

is the distribution of particles of type A , B and all others, denoted by X . The distribution for particles A and B defined in Appendix A are then given by $P(A, B) = \sum_{X=0}^{\infty} P(A, B, X)$ while that for the particles per wounded nucleons are given by $p(a, b) = \sum_{x=0}^{\infty} p(a, b, x)$

The moment generating function is then given by (proceeding analogously to Eq. A2:

$$\begin{aligned} H_M(t) &= \sum_M P_M(M) e^{tM} = \sum_{M,A,B,X} P(A, B, X) \delta_{M, A+B+X} e^{tM} = \sum_{A,B,X} P(A, B, X) e^{t(A+B+X)} \\ &= \sum_w W(w) \sum_{a_1, \dots, a_w} \sum_{b_1, \dots, b_w} \sum_{x_1, \dots, x_w} p(a_1, b_1, x_1) \cdots p(a_w, b_w, x_w) e^{t \sum_{k=1}^w a_k} e^{t \sum_{k=1}^w b_k} e^{t \sum_{k=1}^w x_k} \\ &= \sum_w W(w) \sum_{a_1} \sum_{b_1} \sum_{x_1} p(a_1, b_1, x_1) e^{t(a_1+b_1+c_1)} \cdots \sum_{a_w} \sum_{b_w} \sum_{x_w} p(a_w, b_w, x_w) e^{t(a_w+b_w+c_w)} \\ &= \sum_w W(w) \left[\sum_a \sum_b \sum_x p(a, b, x) e^{t(a+b+c)} \right]^w \\ &= \sum_w W(w) [h_{m,w}(t)]^w \\ &= \sum_w W(w) e^{w g_{m,w}(t)} \end{aligned}$$

where, $h_{m,w}(t)$ the moment generating function and $g_{m,w}(t) = \ln [h_{m,w}(t)]$ the cumulant generating function of the multiplicity distribution for *one* wounded nucleon, $p(m) = \sum_{a,b,x} p(a, b, x) \delta_{m, a+b+c}$. The cumulant generating function, $G_M(t)$, for the multiplicity distribution, $P(M)$, is then given by

$$G_M(t) = \ln [H_M(t)] = \ln \left[\sum_w W(w) e^{w g_{m,w}(t)} \right] = G_W(g_{m,w}(t)) \quad (\text{C2})$$

The cumulants of the multiplicity distribution are given by (following the analogous Eqs. A5 and A6)

$$\begin{aligned}\kappa_1[M] &= \langle N_w \rangle \langle m \rangle \\ \kappa_2[M] &= \kappa_2[N_w] \langle m \rangle^2 + \langle N_w \rangle \kappa_2[m]\end{aligned}\quad (\text{C3})$$

where $\kappa_i[m]$ denote the cumulants of the multiplicity distribution of *one* wounded nucleon and $\kappa_i[N_w]$ those of the wounded nucleon distribution. Analogous to Eq. A8 the factorial cumulant generating function is readily obtained

$$G_{F,M}(z,) = G_M(\ln(z)) = G_W(g_{m,w}(\ln(z))) = G_W(g_{F,m,w}(z)), \quad (\text{C4})$$

with

$$g_{F,m,w}(z) = \sum_m p(m) z^m$$

the factorial cumulant generating function for the multiplicity distribution of one nucleon, $p(m)$. Again, the factorial cumulants are obtained by replacing the cumulants of the distribution $p(m)$, $\kappa_i[m]$ with the corresponding factorial cumulants, $C_i[m]$, in Eq. C3 by the factorial cumulants

$$\begin{aligned}C_1[M] &= \langle N_w \rangle \langle m \rangle \\ C_2[M] &= \kappa_2[N_w] \langle m \rangle^2 + \langle N_w \rangle C_2[m]\end{aligned}\quad (\text{C5})$$

Appendix D: Wounded Nucleon vs Volume Fluctuations

Here we will discuss the relation between wounded nucleon fluctuations and so-called volume fluctuations as they are discussed e.g. in [22]. Following Ref. [22] the cumulant generating function is given by

$$\Phi(t) = \ln \left[\int dV P(V) e^{V\xi(t)} \right] = \chi^V(\xi(t)) \quad (\text{D1})$$

with $\chi^V(t)$ the cumulant generating function for the distribution of volumes, $P(V)$, and

$$\xi(t) = \frac{1}{V} \ln \left[\sum_N p(N; V) e^{Nt} \right] \quad (\text{D2})$$

the generating function for scaled cumulants, κ/V , given for the distribution of particles at fixed volume, $p(N; V)$. Then, for a fixed volume V , the scaled cumulants are given by

$$\frac{\kappa_j}{V} = \frac{\partial^j}{\partial t^j} \xi(t) \Big|_{t=0}. \quad (\text{D3})$$

For the wounded nucleon model we have (see Appendix A)

$$G(t) = \ln \left[\sum_w W(w) e^{w g_w(t)} \right] = G_W(g_w(t)) \quad (\text{D4})$$

with $G_W(t)$ the cumulant generating function for the wounded nucleon distribution, $W(w)$, and

$$g_w(t) = \ln \left[\sum_n p(n) e^{nt} \right] \quad (\text{D5})$$

the generating function for the distribution of particles for one wounded nucleon. The cumulants per wounded nucleons for a fixed number of wounded nucleons, N_w , are given by

$$\frac{\kappa_j[N]}{N_w} = \kappa_j[n] = \frac{\partial^j}{\partial t^j} g_w(t) \Big|_{t=0}. \quad (\text{D6})$$

Comparing the above expressions, one finds that the cumulants for volume fluctuations can be obtained from those for the wounded-nucleon number by the following replacements

$$\begin{aligned}\kappa_j[N_w] &\rightarrow \kappa_j[V] \\ \bar{\kappa}_j[N] = \langle N_w \rangle \kappa_j[N] &\rightarrow \langle V \rangle \frac{\kappa_j}{V}\end{aligned}$$

Indeed comparing the second-order cumulants for both scenarios we have

$$\begin{aligned}\kappa_2[N] &= \langle N_w \rangle \kappa_2[n] + \langle n \rangle^2 \kappa_2[N_w] = \bar{\kappa}_2[N] + \langle N \rangle^2 \frac{\kappa_2[N_w]}{\langle N_w \rangle^2} \\ \kappa_2[N] &= \langle V \rangle \frac{\kappa_2}{V} + \left(\frac{\kappa_1}{V} \right)^2 \kappa_2[V] = \bar{\kappa}_2[N] + \langle N \rangle^2 \frac{\kappa_2[V]}{\langle V \rangle^2}\end{aligned}$$

where in the second line we used $\kappa_1 = \langle N \rangle$ and $\bar{\kappa}_2 = \langle V \rangle \frac{\kappa_2}{V}$. Obviously, analogous replacements also hold for the factorial cumulants

$$\bar{C}_j[N] = \langle N_w \rangle C_j[n] \rightarrow \langle V \rangle \frac{C_j}{V}$$

with C_j/V the volume scaled factorial cumulants.

Appendix E: Results for factorial cumulants

Here we provide the formulas for the corrected factorial cumulants, C_k^{corr} and c_k^{corr} , and the associated biases, $\Delta_{k,F}$ and $\delta_{k,F}$. Both the factorial cumulants and the biases are related to the corresponding cumulants via the linear relation Eqs. B7 and B8. The corrected factorial cumulants and the associated biases are

$$C_2^{corr} = C_2[N] - \frac{\langle N \rangle^2}{\langle M \rangle^2} C_2[M] \quad (E1)$$

$$C_3^{corr} = C_3[N] - \frac{3C_2[M]C_2[N]\langle N \rangle}{\langle M \rangle^2} + \frac{3C_2[M]^2\langle N \rangle^3}{\langle M \rangle^4} - \frac{C_3[M]\langle N \rangle^3}{\langle M \rangle^3} \quad (E2)$$

$$C_4^{corr} = C_4[N] - \left(\frac{6C_2[N]\langle N \rangle^2 (C_3[M]\langle M \rangle - 3C_2[M]^2)}{\langle M \rangle^4} + \frac{4C_2[M]C_3[N]\langle N \rangle}{\langle M \rangle^2} \right) \quad (E3)$$

$$+ \frac{3C_2[M]C_2[N]^2}{\langle M \rangle^2} + \frac{\langle N \rangle^4 (-10C_3[M]C_2[M]\langle M \rangle + C_4[M]\langle M \rangle^2 + 15C_2[M]^3)}{\langle M \rangle^6} \quad (E4)$$

$$\Delta_{2,F} = \frac{\langle N \rangle^2}{\langle M \rangle^2} \bar{C}_2[M] \quad (E5)$$

$$\Delta_{3,F} = \bar{C}_2[M] \left(\frac{3C_2[N]\langle N \rangle}{\langle M \rangle^2} - \frac{3C_2[M]\langle N \rangle^3}{\langle M \rangle^4} \right) + \frac{\bar{C}_3[M]\langle N \rangle^3}{\langle M \rangle^3} \quad (E6)$$

$$\Delta_{4,F} = \bar{C}_2[M] \left(\frac{4C_3[N]\langle N \rangle}{\langle M \rangle^2} + \frac{3C_2[N]^2}{\langle M \rangle^2} - \frac{18C_2[M]C_2[N]\langle N \rangle^2}{\langle M \rangle^4} - \frac{4C_3[M]\langle N \rangle^4}{\langle M \rangle^5} + \frac{15C_2[M]^2\langle N \rangle^4}{\langle M \rangle^6} \right) \quad (E7)$$

$$+ \bar{C}_3[M] \left(\frac{6C_2[N]\langle N \rangle^2}{\langle M \rangle^3} - \frac{6C_2[M]\langle N \rangle^4}{\langle M \rangle^5} \right) + \frac{\bar{C}_4[M]\langle N \rangle^4}{\langle M \rangle^4} \quad (E8)$$

For the scaled factorial cumulants we have

$$c_2^{corr} = c_2[N] - \frac{\langle N \rangle}{\langle M \rangle} c_2[M] \quad (\text{E9})$$

$$c_3^{corr} = c_3[N] - 3 \frac{\langle N \rangle}{\langle M \rangle} c_2[M] c_2[N] + \left(\frac{\langle N \rangle}{\langle M \rangle} \right)^2 (3c_2[M]^2 - c_3[M]) \quad (\text{E10})$$

$$c_4^{corr} = c_4[N] - \frac{\langle N \rangle}{\langle M \rangle} (3c_2[M] c_2[N]^2 + 4c_2[M] c_3[N]) \quad (\text{E11})$$

$$+ \left(\frac{\langle N \rangle}{\langle M \rangle} \right)^2 (18c_2[M]^2 c_2[N] - 6c_3[M] c_2[N]) \quad (\text{E12})$$

$$+ \left(\frac{\langle N \rangle}{\langle M \rangle} \right)^3 (-15c_2[M]^3 + 10c_2[M] c_3[M] - c_4[M]) \quad (\text{E13})$$

$$\delta_{2,F} = \frac{\langle N \rangle}{\langle M \rangle} \bar{c}_2[M] \quad (\text{E14})$$

$$\delta_{3,F} = 3 \frac{\langle N \rangle}{\langle M \rangle} c_2[N] \bar{c}_2[M] + \left(\frac{\langle N \rangle}{\langle M \rangle} \right)^2 (\bar{c}_3[M] - 3c_2[M] \bar{c}_2[M]) \quad (\text{E15})$$

$$\delta_{4,F} = \frac{\langle N \rangle}{\langle M \rangle} (3c_2[N]^2 \bar{c}_2[M] + 4c_3[N] \bar{c}_2[M]) \quad (\text{E16})$$

$$+ \left(\frac{\langle N \rangle}{\langle M \rangle} \right)^2 (6c_2[N] \bar{c}_3[M] - 18c_2[M] c_2[N] \bar{c}_2[M]) \quad (\text{E17})$$

$$+ \left(\frac{\langle N \rangle}{\langle M \rangle} \right)^3 (15c_2[M]^2 \bar{c}_2[M] - 6c_2[M] \bar{c}_3[M] - 4c_3[M] \bar{c}_2[M] + \bar{c}_4[M]) \quad (\text{E18})$$

Appendix F: Particle production through clusters

Let us assume that particles are produced via clusters and that each cluster further decays into two particles. Moreover, clusters are generated from a Poisson distribution. As each cluster decays into two particles the probability of measuring k particles is equivalent to measuring $k/2$ clusters and can be presented as:

$$p(k; \langle N_{cl} \rangle) = e^{-\langle N_{cl} \rangle} \frac{\langle N_{cl} \rangle^{k/2}}{(k/2)!} \quad (\text{F1})$$

The corresponding moment generating function reads:

$$M(t) = \sum_{k/2=0}^{\infty} e^{tk} e^{-\langle N_{cl} \rangle} \frac{\langle N_{cl} \rangle^{k/2}}{(k/2)!} = e^{\langle N_{cl} \rangle (e^{2t} - 1)}, \quad (\text{F2})$$

where $\langle N_{cl} \rangle$ denotes mean number of clusters produced.

The cumulants of total particle number k can be computed as:

$$\kappa_n[k] = \left. \frac{\partial \ln(M(t))}{\partial t} \right|_{t=0} \quad (\text{F3})$$

For the first two cumulants one gets:

$$\kappa_1[k] = 2\langle N_{cl} \rangle \quad (\text{F4})$$

$$\kappa_2[k] = 4\langle N_{cl} \rangle \quad (\text{F5})$$

One clearly sees from Eqs. F4 and F5 that $\kappa_1(k) \neq \kappa_2(k)$, i.e the total number of particles does not follow a Poisson distribution, although the clusters do. Moreover, one observes that particle production through clusters enhances fluctuations. In general, for clusters following a Poisson distribution and decaying into m particles, the cumulants of total particle number can be written as:

$$\kappa_n[k] = m^n \langle N_{cl} \rangle \quad (\text{F6})$$

Appendix G: Mixed Cumulants

Here we provide the relevant formulas for mixed cumulants. Given the generating function, Eq. A3, the mixed cumulants for particles of type A and B are given by (see Eq. A4)

$$\kappa_{j,k}[A, B] = \left. \frac{\partial^j \partial^k}{\partial t_A^j \partial t_B^k} g(t_A, t_B) \right|_{t_A=t_B=0} \quad (\text{G1})$$

The explicit formulas for the four lowest-order mixed cumulants are:

$$\kappa_{1,1}[A, B] = \bar{\kappa}_{1,1}[A, B] + \langle A \rangle \langle B \rangle \frac{\kappa_2[N_W]}{\langle N_W \rangle^2} \quad (\text{G2})$$

$$\kappa_{2,1}[A, B] = \bar{\kappa}_{2,1}[A, B] + (2\langle A \rangle \bar{\kappa}_{1,1}[A, B] + \langle B \rangle \bar{\kappa}_{2,0}[A, B]) \frac{\kappa_2[N_W]}{\langle N_W \rangle^2} + \langle A \rangle^2 \langle B \rangle \frac{\kappa_3[N_W]}{\langle N_W \rangle^3} \quad (\text{G3})$$

$$\kappa_{1,2}[A, B] = \bar{\kappa}_{1,2}[A, B] + (\langle A \rangle \bar{\kappa}_{0,2}[A, B] + 2\langle B \rangle \bar{\kappa}_{1,1}[A, B]) \frac{\kappa_2[N_W]}{\langle N_W \rangle^2} + \langle A \rangle \langle B \rangle^2 \frac{\kappa_3[N_W]}{\langle N_W \rangle^3} \quad (\text{G4})$$

$$\begin{aligned} \kappa_{2,2}[A, B] = & \bar{\kappa}_{2,2}[A, B] + (\langle A \rangle^2 \bar{\kappa}_{0,2}[A, B] + 4\langle A \rangle \langle B \rangle \bar{\kappa}_{1,1}[A, B] + \langle B \rangle^2 \bar{\kappa}_{2,0}[A, B]) \frac{\kappa_3[N_W]}{\langle N_W \rangle^3} \\ & + (2\langle A \rangle \bar{\kappa}_{1,2}[A, B] + 2\langle B \rangle \bar{\kappa}_{2,1}[A, B] + 2\bar{\kappa}_{1,1}[A, B]^2 + \bar{\kappa}_{0,2}[A, B] \bar{\kappa}_{2,0}[A, B]) \frac{\kappa_2[N_W]}{\langle N_W \rangle^2} \\ & + \langle A \rangle^2 \langle B \rangle^2 \frac{\kappa_4[N_W]}{\langle N_W \rangle^4} \end{aligned} \quad (\text{G5})$$

where, analogous to the notation for the regular cumulants, $\bar{\kappa}_{j,k}[A, B]$ denotes the mixed cumulant for constant number of wounded nucleons $\langle N_W \rangle$. Note, that $\kappa_{j,0}[A, B] = \kappa_j[A]$ and $\kappa_{0,j}[A, B] = \kappa_j[B]$ correspond to the regular cumulant for particles of type A and B respectively. The first order mixed cumulant, $\kappa_{1,1}[A, B] = cov[A, B]$ is also referred to as the co-variance between the distributions of particles A and B . In order to obtain the corrected mixed cumulants we proceed in the same fashion as for the regular cumulant. We express the terms involving cumulants of the wounded nucleons, $\kappa_i[N_W] / \langle N_W \rangle^i$ in terms of the factorial cumulants of the multiplicity distribution (See Eqs. 20-22) and solve for the the mixed cumulants with fixed number of wounded nucleons, $\bar{\kappa}_{j,k}[A, B]$. Again, the results are given in the form

$$\bar{\kappa}_{j,k}[A, B] = \kappa_{j,k}^{corr}[A, B] + \Delta_{j,k} \quad (\text{G6})$$

where $\kappa_{j,k}^{corr}[A, B]$ are the cumulants including the measurable corrections and $\Delta_{j,k}$ are the corresponding biases due to quantities which are not directly measurable.

$$\kappa_{1,1}^{corr}[A, B] = \kappa_{1,1}[A, B] - \frac{\langle A \rangle \langle B \rangle}{\langle M \rangle^2} C_2[M] \quad (G7)$$

$$\Delta_{1,1} = \frac{\langle A \rangle \langle B \rangle}{\langle M \rangle^2} \bar{C}_2[M] \quad (G8)$$

$$\kappa_{2,1}^{corr}[A, B] = \kappa_{2,1}[A, B] - \frac{\langle B \rangle C_2[M] \bar{\kappa}_{2,0}[A, B]}{\langle M \rangle^2} - \frac{2\langle A \rangle C_2[M] \kappa_{1,1}[A, B]}{\langle M \rangle^2} + \frac{\langle A \rangle^2 \langle B \rangle (2C_2[M]^2 - \langle M \rangle C_3[M])}{\langle M \rangle^4} \quad (G9)$$

$$\Delta_{2,1} = \frac{1}{\langle M \rangle^4} [2\langle A \rangle \langle M \rangle^2 \bar{C}_2[M] \kappa_{1,1}[A, B] + \langle B \rangle \langle M \rangle^2 \bar{C}_2[M] \bar{\kappa}_{2,0}[A, B] - \langle A \rangle^2 \langle B \rangle (\bar{C}_2[M] (\bar{C}_2[M] + C_2[M]) - \langle M \rangle \bar{C}_3[M])] \quad (G10)$$

$$\kappa_{1,2}^{corr}[A, B] = \kappa_{1,2}[A, B] - \frac{\langle A \rangle C_2[M] \bar{\kappa}_{0,2}[A, B]}{\langle M \rangle^2} - \frac{2\langle B \rangle C_2[M] \kappa_{1,1}[A, B]}{\langle M \rangle^2} + \frac{\langle B \rangle^2 \langle A \rangle (2C_2[M]^2 - \langle M \rangle C_3[M])}{\langle M \rangle^4} \quad (G11)$$

$$\Delta_{1,2} = \frac{1}{\langle M \rangle^4} [2\langle B \rangle \langle M \rangle^2 \bar{C}_2[M] \kappa_{1,1}[A, B] + \langle A \rangle \langle M \rangle^2 \bar{C}_2[M] \bar{\kappa}_{0,2}[A, B] - \langle A \rangle \langle B \rangle^2 (\bar{C}_2[M] (\bar{C}_2[M] + C_2[M]) - \langle M \rangle \bar{C}_3[M])] \quad (G12)$$

$$\begin{aligned} \kappa_{2,2}^{corr}[A, B] = & \kappa_{2,2}[A, B] + \frac{2\langle A \rangle^2 C_2[M]^2 \bar{\kappa}_{0,2}[A, B]}{\langle M \rangle^4} + \frac{2\langle B \rangle^2 C_2[M]^2 \bar{\kappa}_{2,0}[A, B]}{\langle M \rangle^4} \\ & - \frac{C_2[M] \bar{\kappa}_{0,2}[A, B] \bar{\kappa}_{2,0}[A, B]}{\langle M \rangle^2} - \frac{\langle A \rangle^2 C_3[M] \bar{\kappa}_{0,2}[A, B]}{\langle M \rangle^3} - \frac{\langle B \rangle^2 C_3[M] \bar{\kappa}_{2,0}[A, B]}{\langle M \rangle^3} \\ & + \frac{12\langle A \rangle \langle B \rangle C_2[M]^2 \kappa_{1,1}[A, B]}{\langle M \rangle^4} - \frac{2C_2[M] \kappa_{1,1}[A, B]^2}{\langle M \rangle^2} - \frac{2\langle A \rangle C_2[M] \kappa_{1,2}[A, B]}{\langle M \rangle^2} \\ & - \frac{2\langle B \rangle C_2[M] \kappa_{2,1}[A, B]}{\langle M \rangle^2} - \frac{4\langle A \rangle \langle B \rangle C_3[M] \kappa_{1,1}[A, B]}{\langle M \rangle^3} - \frac{10\langle A \rangle^2 \langle B \rangle^2 C_2[M]^3}{\langle M \rangle^6} \\ & + \frac{8\langle A \rangle^2 \langle B \rangle^2 C_3[M] C_2[M]}{\langle M \rangle^5} - \frac{\langle A \rangle^2 \langle B \rangle^2 C_4[M]}{\langle M \rangle^4} \end{aligned} \quad (G13)$$

$$\begin{aligned} \Delta_{2,2} = & \bar{C}_2[M]^2 \left(-\frac{\langle A \rangle^2 \bar{\kappa}_{0,2}[A, B]}{\langle M \rangle^4} - \frac{\langle B \rangle^2 \bar{\kappa}_{2,0}[A, B]}{\langle M \rangle^4} + \frac{3C_2[M] \langle A \rangle^2 \langle B \rangle^2}{\langle M \rangle^6} \right) \\ & + \bar{C}_2[M] \left(-\frac{C_2[M] \langle A \rangle^2 \bar{\kappa}_{0,2}[A, B]}{\langle M \rangle^4} - \frac{C_2[M] \langle B \rangle^2 \bar{\kappa}_{2,0}[A, B]}{\langle M \rangle^4} + \frac{\bar{\kappa}_{0,2}[A, B] \bar{\kappa}_{2,0}[A, B]}{\langle M \rangle^2} \right. \\ & - \frac{2\bar{C}_3[M] \langle A \rangle^2 \langle B \rangle^2}{\langle M \rangle^5} - \frac{12C_2[M] \langle A \rangle \langle B \rangle \kappa_{1,1}[A, B]}{\langle M \rangle^4} + \frac{2\langle A \rangle \kappa_{1,2}[A, B]}{\langle M \rangle^2} + \frac{2\kappa_{1,1}[A, B]^2}{\langle M \rangle^2} \\ & \left. + \frac{2\langle B \rangle \kappa_{2,1}[A, B]}{\langle M \rangle^2} + \frac{6C_2[M]^2 \langle A \rangle^2 \langle B \rangle^2}{\langle M \rangle^6} - \frac{2C_3[M] \langle A \rangle^2 \langle B \rangle^2}{\langle M \rangle^5} \right) \\ & + \bar{C}_3[M] \left(\frac{\langle A \rangle^2 \bar{\kappa}_{0,2}[A, B]}{\langle M \rangle^3} + \frac{\langle B \rangle^2 \bar{\kappa}_{2,0}[A, B]}{\langle M \rangle^3} + \frac{4\langle A \rangle \langle B \rangle \kappa_{1,1}[A, B]}{\langle M \rangle^3} - \frac{4C_2[M] \langle A \rangle^2 \langle B \rangle^2}{\langle M \rangle^5} \right) \\ & + \frac{\bar{C}_2[M]^3 \langle A \rangle^2 \langle B \rangle^2}{\langle M \rangle^6} + \frac{\bar{C}_4[M] \langle A \rangle^2 \langle B \rangle^2}{\langle M \rangle^4} \end{aligned} \quad (G14)$$

-
- [1] A. Rustamov, J. Stroth, and R. Holzmann, Nucl. Phys. A **1034**, 122641 (2023), arXiv:2211.14849 [nucl-th].
[2] F. Gross *et al.*, Eur. Phys. J. C **83**, 1125 (2023), arXiv:2212.11107 [hep-ph].
[3] M. Stephanov, Phys.Rev.Lett. **102**, 032301 (2009), arXiv:0809.3450 [hep-ph].
[4] M. Stephanov, Phys.Rev.Lett. **107**, 052301 (2011), arXiv:1104.1627 [hep-ph].
[5] A. Bzdak, S. Esumi, V. Koch, J. Liao, M. Stephanov, and N. Xu, Phys. Rept. **853**, 1 (2020), arXiv:1906.00936 [nucl-th].
[6] M. Asakawa, S. Ejiri, and M. Kitazawa, Phys. Rev. Lett. **103**, 262301 (2009), arXiv:0904.2089 [nucl-th].
[7] A. Bazavov *et al.* (HotQCD), Phys. Rev. D **96**, 074510 (2017), arXiv:1708.04897 [hep-lat].
[8] S. Borsanyi, Z. Fodor, J. N. Guenther, S. K. Katz, K. K. Szabo, A. Pasztor, I. Portillo, and C. Ratti, JHEP **10**, 205 (2018), arXiv:1805.04445 [hep-lat].

- [9] B. Friman, F. Karsch, K. Redlich, and V. Skokov, *Eur.Phys.J.* **C71**, 1694 (2011), arXiv:1103.3511 [hep-ph].
- [10] M. Abdallah *et al.* (STAR), *Phys. Rev. C* **104**, 024902 (2021), arXiv:2101.12413 [nucl-ex].
- [11] M. Abdallah *et al.* (STAR), *Phys. Rev. C* **107**, 024908 (2023), arXiv:2209.11940 [nucl-ex].
- [12] J. Adamczewski-Musch *et al.* (HADES), *Phys. Rev.* (2020), arXiv:2002.08701 [nucl-ex].
- [13] S. Acharya *et al.* (ALICE), *Phys. Lett. B* **807**, 135564 (2020), arXiv:1910.14396 [nucl-ex].
- [14] S. Acharya *et al.* (ALICE), *Phys. Lett. B* **844**, 137545 (2023), arXiv:2206.03343 [nucl-ex].
- [15] W.-j. Fu, J. M. Pawłowski, F. Rennecke, and B.-J. Schaefer, *Phys. Rev. D* **94**, 116020 (2016), arXiv:1608.04302 [hep-ph].
- [16] M. Bleicher, S. Jeon, and V. Koch, *Phys. Rev.* **C62**, 061902 (2000), arXiv:hep-ph/0006201 [hep-ph].
- [17] A. Bzdak, V. Koch, and V. Skokov, *Phys. Rev.* **C87**, 014901 (2013), arXiv:1203.4529 [hep-ph].
- [18] P. Braun-Munzinger, A. Rustamov, and J. Stachel, *Nucl. Phys. A* **982**, 307 (2019), arXiv:1807.08927 [nucl-th].
- [19] P. Braun-Munzinger, B. Friman, K. Redlich, A. Rustamov, and J. Stachel, *Nucl. Phys. A* **1008**, 122141 (2021), arXiv:2007.02463 [nucl-th].
- [20] P. Braun-Munzinger, K. Redlich, A. Rustamov, and J. Stachel, (2023), arXiv:2312.15534 [nucl-th].
- [21] M. Kitazawa and M. Asakawa, *Phys. Rev.* **C85**, 021901 (2012), arXiv:1107.2755 [nucl-th].
- [22] V. Skokov, B. Friman, and K. Redlich, *Phys. Rev.* **C88**, 034911 (2013), arXiv:1205.4756 [hep-ph].
- [23] P. Braun-Munzinger, A. Rustamov, and J. Stachel, *Nucl. Phys.* **A960**, 114 (2017), arXiv:1612.00702 [nucl-th].
- [24] A. Bialas, M. Bleszynski, and W. Czyz, *Nucl. Phys. B* **111**, 461 (1976).
- [25] <https://github.com/anarrustamov/VolumeFluctuations>.
- [26] J. Adamczewski-Musch *et al.* (HADES), *Eur. Phys. J. A* **54**, 85 (2018), arXiv:1712.07993 [nucl-ex].
- [27] B. Abelev *et al.* (ALICE), *Phys. Rev. C* **88**, 044909 (2013), arXiv:1301.4361 [nucl-ex].
- [28] J. Adam *et al.* (STAR), *Phys. Rev. Lett.* **126**, 092301 (2021), arXiv:2001.02852 [nucl-ex].
- [29] C. Loizides, J. Nagle, and P. Steinberg, *SoftwareX* **1-2**, 13 (2015), arXiv:1408.2549 [nucl-ex].
- [30] S. Harabasz, J. Kolaś, R. Ryblewski, W. Florkowski, T. Galatyuk, M. Gumberidze, P. Salabura, J. Stroth, and H. P. Zbroszczyk, *Phys. Rev. C* **107**, 034917 (2023), arXiv:2210.07694 [nucl-th].
- [31] B. Abelev *et al.* (ALICE), *Phys. Rev. C* **88**, 044910 (2013), arXiv:1303.0737 [hep-ex].
- [32] A. Bzdak, V. Koch, and V. Skokov, *Eur. Phys. J.* **C77**, 288 (2017), arXiv:1612.05128 [nucl-th].

Optical and spin properties of nitrogen vacancy centers formed along the tracks of high energy heavy ions

Wei Liu*,¹ Aleksi A. M. Leino,² Arun Persaud,¹ Qing Ji,¹ Kaushalya Jhuria,¹ Edward S. Barnard,³ Shaul Aloni,³ Christina Trautmann,^{4,5} Marilena Tomut,^{6,7} Ralf Wunderlich,^{1,8} Hunter Ocker,⁹ Nishanth Anand,⁹ Zhao Hao,⁹ Flyura Djurabekova,² and Thomas Schenkel¹

¹*Accelerator Technology and Applied Physics Division, Lawrence Berkeley National Laboratory, Berkeley, CA 94720, USA*

²*Helsinki Institute of Physics and Department of Physics, University of Helsinki, PO Box 43 (Pietari Kalmin katu 2), 00014, Helsingin yliopisto, Finland*

³*Molecular Foundry, Lawrence Berkeley National Laboratory, Berkeley, CA 94720, USA*

⁴*GSI Helmholtzzentrum für Schwerionenforschung, Planckstraße 1, 64291 Darmstadt, Germany*

⁵*Technische Universität Darmstadt, Institute of Materials Science, Peter-Grünberg-Straße 2, 64287 Darmstadt, Germany*

⁶*GSI Helmholtzzentrum für Schwerionenforschung GmbH, Planckstraße 1, 64291 Darmstadt, Germany*

⁷*Institute of Materials Physics, WWU Münster, Wilhelm-Klemm-Straße 10, 48149 Münster, Germany*

⁸*Faculty of Physics and Earth System Sciences, Felix Bloch Institute for Solid State Physics, Applied Quantum Systems, Leipzig University, Linnéstraße 5, 04103 Leipzig, Germany*

⁹*Earth and Environmental Sciences, Lawrence Berkeley National Laboratory, Berkeley, CA 94720, USA*

(*Electronic mail: weiliu01@lbl.gov)

(Dated: 7 March 2024)

Exposure of nitrogen doped diamond to high energy, heavy ions induces formation of vacancy related color centers aligned along the trajectories of the ions. Quasi 1D chains of coupled NV centers with lengths of a few tens of microns can be building blocks for quantum information processing and they provide insights into harsh radiation-matter interactions. Here, we report on color center formation in diamond (1 ppm nitrogen) with 1 GeV gold and uranium ions. Using depth-resolved photoluminescence, we observe direct formation of single vacancy related color centers (GR1 centers) along the ion tracks. Mobile vacancies can form NV-centers with native nitrogen atoms during thermal annealing. Molecular dynamics simulations indicate that both isolated vacancies and defect clusters form along ion trajectory through electronic stopping processes, leading to broad color center profiles that range from the sample surface to a depth of about 25 microns. We quantify the spin properties of NV-centers formed by swift heavy ions through optical detection of magnetic resonance (ODMR) and validate the feasibility of using swift-heavy-ion-generated NV^- along quasi 1D chains (for isolated tracks from low fluence irradiations) or in thin sheets of coupled 1D spin chains (formed with higher ion fluences) for NV-based magnetometry and for the exploration of quasi 1D and 2D spin textures in diamond.

Negatively charged nitrogen-vacancy (NV^-) color centers in diamond possess an optical accessible spin-1 triplet ground state with up to millisecond longitudinal relaxation time T_1 and coherence time T_2 at room temperature¹. Optical selective optical transitions enable utilizing negatively charged nitrogen vacancy (NV^-) centers for quantum sensing via optical detected magnetic resonance (ODMR), often with superior sensitivity compared to conventional magnetometers². Thanks to the technical simplicity, radiation robustness, chemically inertness, and nanoscale geometry, diamond-NV sensing can be deployed in harsh radiation, biochemical, and geoscience-related environments³⁻⁶. Enabling control of multiple coupled NV^- centers⁷⁻⁹ is essential to realize a variety of functionalities of diamond-NV architectures and unitary fidelity of quantum protocol operations¹⁰⁻¹⁵. Recent studies indicate self-aligned quasi 1D chains of coupled NV^- centers along a length of several tens of microns. This effect is promising for the development of a novel type of quantum register and a building block for NV-based quantum information processing¹⁶⁻¹⁸. Such quasi 1D chain of NV^- centers can be realized by swift heavy ion (SHI, e.g. 1-2 GeV gold/uranium ions) irradiation of single crystal diamonds, which leads to the conversion of native nitrogen atoms to NV centers along the ion trajectories. Adjusting the nitrogen concentration, and the energy and species of the ions allows engineering the average NV^- spacing on the few nanometer scale along ion trajectories and resulting spin chain on the scale of a tens of microns¹⁹⁻²¹. The quasi 1D aligned NV^- centers are promising for the physical implementation of spin chains, which could also be isolated in a later processing step for studies of Ising model spin dynamics and explorations spin textures, spin transport and spin registers²². Formation of GR1 centers and NV centers in diamond by SHI also supports the development of diamond-based single ion track detectors^{21,23} and methods for directional detection of highly energetic dark matter candidates²⁴. Further, the optical readout of NV centers along ion tracks also enables experimental benchmarking for molecular dynamics (MD) simulations of the interaction between SHI and the diamond lattice²⁵.

In this study, we report on GR1 and NV center generation along the tracks of SHI in diamond and quantify the spin properties of NV-centers. Diamond with 1 ppm N density was chosen in order to suppress decoherence induced by the nitrogen spin bath⁹. By using confocal laser scanning fluorescence microscopy¹⁹, we characterized GR1, NV^0 and NV^- centers and the conversion from GR1's to NV-centers. We show that the NV center formation dynamics by SHI can follow the well established two-step process of vacancy formation followed by capture of mobile vacancies by substitutional nitrogen atoms. The SHI induced vacancies can act as optically active

GR1 centers, when presented as individual isolated neutral vacancies. Vacancies form predominantly along the incoming path of SHI where the electronic stopping power is highest. They can further combine with the nearby nitrogen atoms to form NV centers during the latent track cool down. NV⁻ center formation is further enhanced during thermal annealing after SHI irradiations. The micrometer-resolved optical analysis on the NV formation dynamics provides experimental benchmarking data for Monte Carlo simulations of ion track structures and micro-dosimetric models. We probe the spin properties of SHI-induced NV⁻ via ODMR, which shows that SHI-induced NV⁻ centers along quasi 1D chains or in thin sheets (about 30 μm) can be used for applications in high-sensitivity magnetometry and for studies of spin textures in diamonds. Irradiation with SHI is a method for NV-center formation, complementary to more common irradiation with MeV electrons and protons, with the additional feature of alignment of NV centers along the latent tracks of SHI with lengths of tens of microns.

Type IIa diamonds (Element 6) were used in this study with about 1 ppm nitrogen introduced during the chemical vapor deposition growth. $1 \times 10^{13} \text{ cm}^{-2}$ 180 keV Er were implanted into the samples first. One of the purposes of Er implantation²⁶ is to create shallow NV centers at the surface distributed within the top 100 nm as estimated by the stopping and range of ions in matter modeling (SRIM-2008)²⁷. We did not observe optical emission from Er atoms or signatures of NV-Er coupling in optical spectra or in ODMR. Emission from NV-centers near the surface serves as a reference of the sample surface for depth dependent PL measurements. Sample A and sample B were irradiated at the linear accelerator UNILAC at GSI Helmholtzzentrum, Darmstadt, Germany) using 1.1 GeV U ions (a fluence of 1×10^{12} U ions/cm²) and 0.95 GeV Au ions (2.2×10^{12} Au ions/cm²), respectively. Though we used two species of heavy ions in this study, their energy, ranges and the magnitudes of their respective electronic stopping powers were similar (as estimated by SRIM simulations) allowing us to observe common SHI related effects and trends. The samples were covered by a thick honey-comb shaped mask with millimeter sized openings (90% transparency), which allows direct comparison between irradiated and nonirradiated regions during the PL measurements. After irradiation, to enhance the formation of NV⁻ centers, we performed thermal annealing on sample B in two steps and compared the optical properties after the 1st and the 2nd annealing step. The 1st annealing step was for 1 hour at 800 °C in vacuum (10^{-6} mbr), the 2nd annealing step was for 1 hour at 1000 °C in argon atmosphere. We performed secondary ion mass spectrometry (SIMS) measurement on sample B after the thermal annealing steps (See figure S1 in the Supplementary Material). SIMS depth profiles show accumulation of

nitrogen to concentrations of up to $1 \times 10^{19} \text{ cm}^{-3}$ ($\sim 60 \text{ ppm}$) within the top 100 nm depth and then a concentration of $3 \times 10^{16} \text{ cm}^{-3}$ (0.2 ppm), lower than the nominal concentration of 1 ppm indicated by the supplier, Element 6, and also affected by the absolute calibration in SIMS measurements. Er profile is distributed within the 300 nm with an apparent areal density of $4.1 \times 10^{12} \text{ cm}^{-2}$, lower than the nominal implant fluence and potentially affected by the SIMS calibration.

Firstly, we performed depth-dependent PL on sample A (after SHI irradiation with U ions, and without thermal annealing) to characterize the interaction between nitrogen and SHI-formed vacancies along the ion trajectories. Figure 1 (a) shows the PL spectra as a function of the probe depth (refractive index corrected¹⁹) from the surface (marked as red) to the internal depth of $30 \mu\text{m}$ (marked as blue) in the area with SHI irradiation. In the area with Er implantation and without SHI irradiation, we observe a weak GR1 ZPL signal (see figure S2 in the Supplementary Material) that is visible near the sample surface, within the Er ion range. When we probe deeper regions, spectra are dominated by weak emission from native NV^- centers that are present in the as-received sample. The luminescence of GR1 centers is known to originate from individual neutral vacancies²⁸, which evidences that the SHI irradiation generated individual isolated vacancies along the swift ions trajectories by dislodging carbon (or nitrogen) atoms from lattice positions. Meanwhile, weak luminescence from NV^- and NV^0 center can be observed at the ZPLs of 637 nm and 573 nm, respectively. This phenomenon is different from our previous experiment where NV^- centers were preferentially formed in diamond that contained 100 ppm nitrogen following irradiation with SHI ($10^{12} \text{ cm}^{-2} \text{ 1 GeV Au}$)¹⁹. The major difference in the present experiment is the more than 2 orders of magnitude reduced intrinsic nitrogen concentration of 1 ppm, while SHI conditions are similar. Figure 1(b) shows the depth-dependent PL spectrum of sample B in the swift Au irradiated areas after thermal annealing. Here, the spectra are dominated by the typical ZPL of NV^0 at 573 nm and NV^- at 637 nm, with spectral signatures of GR1 centers now absent. The annihilation of GR1 luminescence in sample B after the annealing shows that the SHI-irradiation induced vacancies either combining with nitrogen atoms to form NV centers or annihilated e.g. via recombination with carbon interstitials.

To quantify the PL intensity and analyze conversion between GR1 and NV^- along the swift ion trajectories, Fig. 1 (c) shows an example of deconvolution of the spectra into NV^- and GR1 luminescence component of sample A (at depth = $14 \mu\text{m}$ in the SHI irradiated area)^{29,30}. The deconvolution approach is explained in the Supplementary Material. The GR1 PL intensity is more than one order of magnitude higher than the NV^- intensity after exposure to SHI and be-

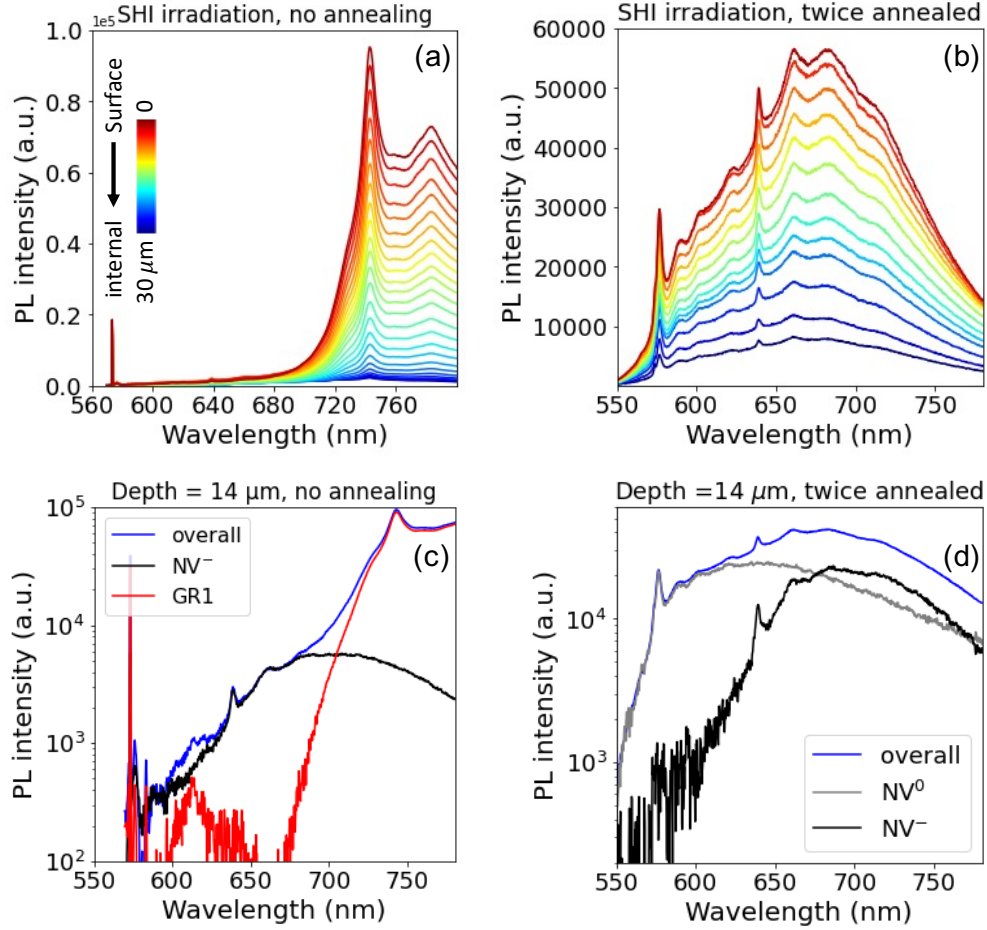


FIG. 1. (a) Color center PL spectrum of sample A (no annealing) as a function of depth from the sample surface to a depth of $30\ \mu\text{m}$ in the area irradiated with 1×10^{12} U ions/ cm^2 fluence of 1.1 GeV energy. (b) Color center PL spectrum of sample B (after two annealing steps) as a function of depth from the sample surface to a depth of $30\ \mu\text{m}$ in the area irradiated with 2.2×10^{12} Au ions/ cm^2 fluence of 0.95 GeV energy. (c) Deconvolution of the PL spectra into NV^- and GR1 luminescence component probed in the SHI irradiated area of sample A at depth = $14\ \mu\text{m}$ (roughly half the SHI range). The red and black spectra show the deconvoluted spectrum resulted from GR1 and NV^- , respectively. The blue spectrum is the full spectrum. (d) Deconvolution of PL spectra of sample B probed in the SHI irradiated area at a depth of $14\ \mu\text{m}$ after annealing. The black and grey spectrum shows the decomposed spectrum resulted from NV^- and NV^0 , respectively.

fore annealing. This indicates that only small portion of SHI-irradiation-created vacancies further combining with nitrogen atom to form NV^- centers at the relatively low nitrogen concentration of nominally 1 ppm. This is in contrast to earlier experiments, where strong NV^- center emission

was observed directly after SHI irradiations and before thermal annealing. At the lower nitrogen concentration, SHI induced vacancies have to move farther to find a nitrogen atom for NV-center formation. At a nitrogen concentration of 100 ppm, the average distance between N atoms is about 5 nm, while it is 20 nm at 1 ppm. Vacancies can diffuse during the cooldown of the (latent) ion track, forming NV's if enough N atoms are present in the track volume and near the track.

As shown in figure 1(d), in the SHI irradiated area, the ratio of the NV^- spectral area to that of NV^0 is enhanced after the 2nd thermal annealing step compared to the 1st annealing step (see figure S3 in the Supplementary Material). NV^0 centers form first during thermal annealing and the charge state balance shifts to NV^- via $NV^0 + e^- \rightleftharpoons NV^-$ during longer annealing times, when vacancy centers dissolve and electrons from the relatively sparse N density can be picked up by thermally activated charge transfer³¹. Performing a 2nd annealing step allows us to thermally drive this process by promoting the ionization of nitrogen donors and to transfer the electron charge to the site of NV^0 centers, consequently converting NV^0 to NV^- .

Figure 2 (a) compares depth profiles of normalized PL intensity of sample A with the GR1 luminescence to that of sample B with dominant NV^- center emissions after annealing. The two PL intensity profiles in figure 2 (a) show a similar plateau up to a depth of 15 μm where the ion energy loss is dominated by electronic stopping process¹⁹. However, at the end of electronic stopping range from 20 to 30 μm depth, the GR1 PL intensity in sample A drops more drastically than the NV^- PL in sample B, presenting two orders of magnitude difference in the GR1 PL intensity between sample surface and the regime of end-of-range ion track. The drastically decrease of GR1 PL intensity at the end of electronic stopping can be related to the clustering of vacancies, which can render them to be optically inactive. The vacancies complexes formation can be further enhanced by nuclear stopping process at end of ion track¹⁹, which causes increase of lattice damage. Differently, in sample B, the reduction of PL intensity of NV^- center emission from sample surface to the end of ion range is less than 1 order of magnitude. We infer that the post annealing convert the extra vacancies into NV^- centers at the end-of-range ion track. These results show that SHI efficiently introduce vacancies along their trajectories in areas of high electronic stopping, in addition to vacancy production at the end of their range where elastic collisions dominate. It also indicates that the NV center formation dynamics by SHI can be governed by a two-step process that depending on the available nitrogen atoms around the track, the SHI-induced vacancies can be in the form of individual neutral vacancies or further combine with the neighboring N to form NV centers. The strong GR1 luminescence introduced directly by SHI irradiation (without thermal

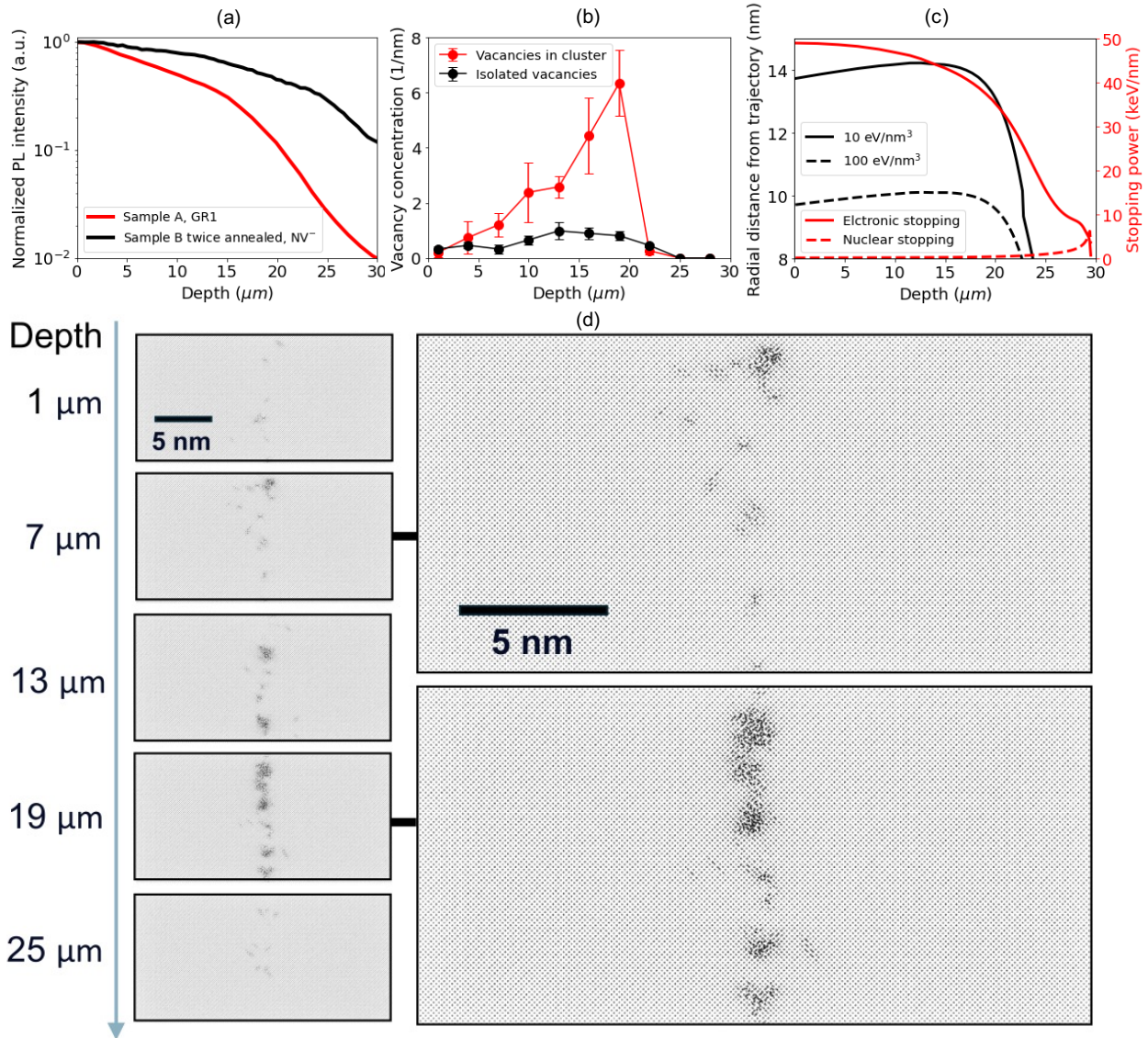


FIG. 2. (a) Comparison of depth-resolved normalized PL intensity (logarithmic scale) of GR1 in sample A (no annealing) and NV^- in the annealed sample B. (b) The simulated concentrations of vacancies in the form of isolated vacancies and vacancy clusters along the ion trajectory from electronic energy loss processes. The contribution from elastic collisions as estimated by SRIM is about 0.5 vacancies/nm in the top 15 microns. (c) Electronic and nuclear stopping powers along the ion trajectory for 1.1 GeV U ions in diamond (right axis). The left axis shows the contour lines of the initial energy density of $10 \text{ eV}/\text{nm}^3$ and $100 \text{ eV}/\text{nm}^3$ after ion impact in the electronic subsystem as estimated as using the delta-ray dose formulas (See supplementary material). (d) Visualization of the MD simulation cells at different depth so that atoms are drawn as gray dots. The arrow on the left shows the ion propagation direction. The left two subfigures show the zoom-in area with defect clusters at 7 μm and 19 μm depth.

annealing) as well as damage repair and re-crystallization via thermal annealing can be unique advantages for applications of diamond as fluorescent nuclear track detector in extreme radiation environments^{20,21}.

To gain insight into vacancy formation resulting from electronic stopping processes for 1.1 GeV U ion, we performed two-temperature MD simulations in pure diamond using the Tersoff potential³². The detailed model is described in Ref.³³ and also in the Supplementary Material. The simulations here exclusively consider the electronic component, omitting nuclear stopping power effects. To circumvent the computation limits, the observed up to 30 μm ion trajectory was segmented into ten small simulations depicting small slabs along the path, each with dimensions of $23 \times 23 \times 11$ nm (XYZ). The trajectory is centered in X and Y directions and penetrates through the cell along the Z axis. Figure 2(b) presents vacancies concentrations along the trajectory determined using the Wigner-Seitz analysis. The plot shows that the concentration of isolated vacancies (Voronoi cells) slightly increase from 0.5 nm^{-1} to 1 nm^{-1} , as the ion track extends from surface to the internal depth of 20 μm . In comparison, the vacancies density in the form of clusters (empty Voronoi cells connected to other cells) increases drastically from 0 to 7 nm^{-1} from the surface to a depth of 20 μm). It is surprising to witness this dramatic increase of vacancy clustering in the range of electronic stopping, while the electronic stopping power decreases monotonically from the surface as shown in 2(c). We tentatively ascribe the enhanced vacancy clustering near 20 μm to the ion velocity effect. Our simulation of the delta-ray radial dose distribution in figure 2(c) reveals that the initial energy density near the trajectory increases due to the decreased velocity of the ion³⁴ until about 20 μm , which leads to strong damage production. Focusing on the role of electronic stopping processes, we exclude contributions to vacancy production from elastic collisions in these summations. From SRIM we estimate the rate of vacancy formation to be ~ 0.5 vacancies/nm from the surface to a depth of 20 microns.

Figure 2(d) shows the visualization atomic disorders along the ion trajectory by the MD simulation at different depth, where atoms are drawn as gray dots. The arrow on the left shows the ion propagation direction. The details of isolated defects and clusters can be seen in the enlarged visualization of the cell at 7 μm and 19 μm depth. The MD simulation results clearly reveal that in the beginning of the ion trajectory (distance to the surface of $< 10 \mu\text{m}$), the damage consists of both isolated interstitial-vacancy (Frenkel) pairs and small defect clusters. The size of the defect clusters tends to gradually increase as the depth of the ion trajectory is greater than 13 μm and less than or equal to 20 μm . In particular, we observe graphitization of the diamond structure showing

amorphous defect clusters near 20 μm depth. In the 20-25 μm range, there is a sharp decrease in the defect concentration, until no defects form at depths greater than 25 μm . Such a velocity effect with graphitization and a sharp decrease of vacancy concentration in the 20-25 μm range can well explain the experimentally observed drastic drop of GR1 emission in this depth range. However, the simulation does not account for nuclear stopping power, due to the calculation complexity. The nuclear stopping power component also becomes significant at the end of the ion ranges, potentially leading to further vacancy defects. Potential synergies of elastic and inelastic energy loss processes on defect kinetics will be explored in future studies³⁵.

We performed ODMR measurements to characterize the electron spin properties of the SHI-induced NV^- after thermal annealing (sample B). The inset in figure 3 shows the example of

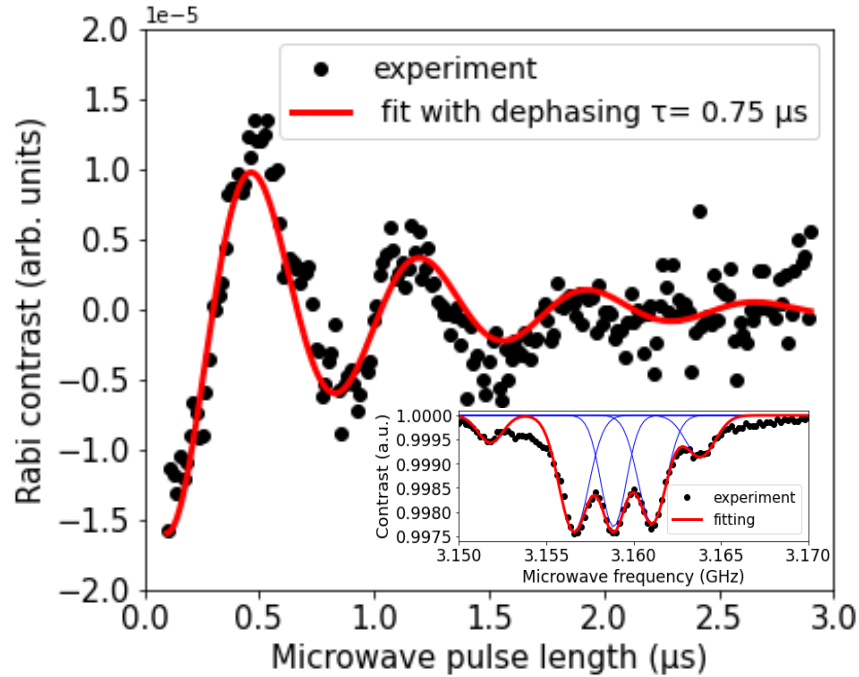


FIG. 3. An example of Rabi oscillations of NV^- spins ($m_s = +1$) probed in the SHI irradiated area of sample B after thermal annealing. The inset shows the ESR signal of the spin state $m_s = +1$ of the NV^- , with an external magnetic field of 100 Gauss was aligned to the $\langle 111 \rangle$ crystallographic orientation. Blue curves correspond to the Gaussian fitted individual resonances, while the red curve corresponds to the accumulative of the fit to multiple resonances.

electron spin resonance (ESR) signal of $m_s = +1$ under 100 Gauss magnetic field, aligned with $\langle 111 \rangle$ crystallographic orientation. It mainly exhibits equal contrast on the three hyperfine reso-

nance lines with a splitting of about 2.2 MHz, which is the typical feature of NV^- electron spins coupled to ^{14}N nuclear spins^{36,37}. The linewidths of the three hyperfine resonance lines is about 1 MHz extracted by Gaussian fitting. The well resolving of ^{14}N hyperfine splitting shows that the SHI approach to NV^- formation preserves a relatively low homogeneous broadening. Additionally, we also observe two well known resonances at both sides of the main peaks with a separation of 12 MHz in Fig. 3(a), and these can be attributed hyperfine interactions with ^{13}C nuclear spins. Fig 3 shows Rabi oscillations of the SHI-induced NV^- ³⁸. We derived an effective dephasing time $\tau = 0.75 \mu\text{s}$ from the decay of amplitude of Rabi oscillation signal, which is comparable to dephasing times reported from NV^- ensembles present in diamonds containing nitrogen concentration in the ppm range^{39,40}. Since the dephasing mechanism of NV^- is mainly governed by the spin bath^{40,41}, the dephasing of NV^- in our sample is affected by a relatively high surface nitrogen concentration as well as other surface charged states. Depth dependent dephasing kinetics can be probed in future studies.

In conclusion, we investigated NV^- center formation dynamics along the trajectories of swift gold and uranium ions in the kinetic energy range of ~ 1 GeV in nitrogen doped diamond. By using confocal laser scanning fluorescence microscopy, we study the interaction between native nitrogen atoms and SHI-induced vacancies during the non-equilibrium process of (latent) ion track formation, and thermal annealing effects on the structural and charge state conversion dynamics between GR1, NV^0 and NV^- centers. We report strong optical emission signals after direct formation GR1 centers along the ion tracks. This direct GR1 formation by SHI through electronic stopping processes can be utilized for the development of diamond-based detectors and methods for dark matter searches with candidates in the extremely high mass range. The NV center formation dynamics by SHI can be a two-step process that is sensitive to the concentration of available nitrogen atoms around the ion trajectory. Molecular dynamics simulations of the diamond lattice subjected to energy deposition through electronic stopping processes from SHI show formation of vacancies. Vacancies can combine with nitrogen atoms in their vicinity forming NV centers during thermal annealing in a well established NV-formation process. MD simulations indicate that that both isolated vacancies and defect clusters form along the ion trajectories. Our simulations further reveal a velocity effect on the rate of vacancy formation that leads to significantly enhanced defect clustering in a depth range where the electronic stopping power is decreasing. We observed that NV^0 is more preferentially formed in diamond with about 1 ppm nitrogen density by SHI excitation, converting to NV^- during consecutive thermal annealing steps. Moreover, we observed an

uplift of NV^- PL profile near the end-of-range of the ions, which indicates additional NV^- centers are activated due to the enhanced nuclear stopping process, providing experimental evidences for future validation of Monte Carlo simulations of ion track structures. We probe the spin properties of the SHI-induced NV^- via ODMR, observing known hyperfine splittings and Rabi oscillations validating that NV^- centers formed by irradiations with SHI are suitable for applications in magnetometry. The presence of NV^- centers in quasi 1D strings along the trajectories of SHI and the formation of 2D sheets of NV^- centers enables studies of spin textures that are complementary to those of NV^- centers formed by more conventional methods, such as irradiation with MeV electrons or protons.

ACKNOWLEDGMENTS

The work is supported by the U.S. Department of Energy Office of Science, Office of Fusion Energy Sciences, under Contract No. DEAC02-05CH11231. Work at the Molecular Foundry was supported by the Office of Science, Office of Basic Energy Sciences, of the U.S. Department of Energy under Contract No. DE-AC02-05CH11231. The ODMR experiments were performed at the geoscience quantum sensing laboratory at Berkeley Lab, supported by the U.S. Department of Energy, Office of Science, Office of Basic Energy Sciences, Chemical Sciences, Geosciences, and Biosciences Division under U.S. Department of Energy Contract No. DE-AC02-05CH11231. The results presented here are based on a UMAT experiment, which was performed at the M-branch of the UNILAC at the GSI Helmholtzzentrum für Schwerionenforschung, Darmstadt (Germany) in the frame of FAIR Phase-0.

DATA AVAILABILITY STATEMENT

The data that support the findings of this study are available from the corresponding author upon reasonable request.

APPENDIXES

Figure S1 shows the layers in sample B after 2ed annealing as measured by SIMS measurement on the depth profile of the native nitrogen and implanted-Er concentration.

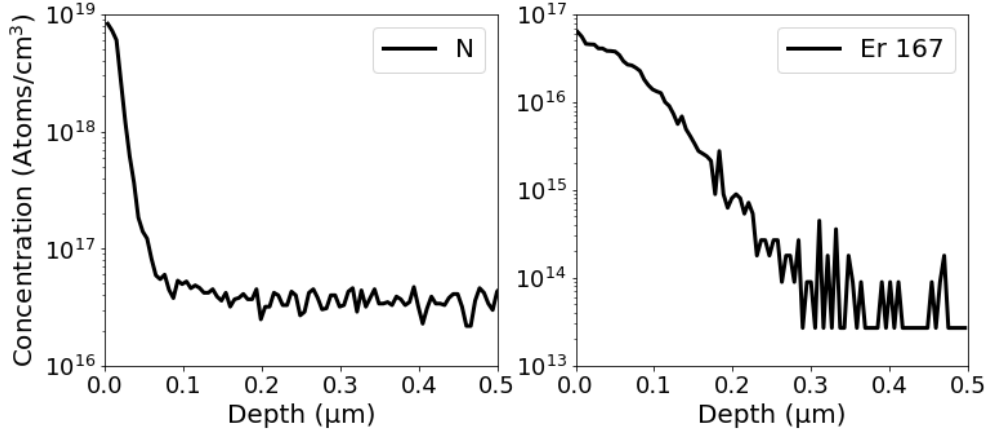


FIG. S1. SIMS measurement of native nitrogen (left) and implanted Er (right) concentration distribution as a function of depth in sample B.

Figure S2 shows the series of PL spectra in the area with only Er implantation and without SHI irradiation of sample A. The spectra probed near the surface (red), where is implanted by Er ions,

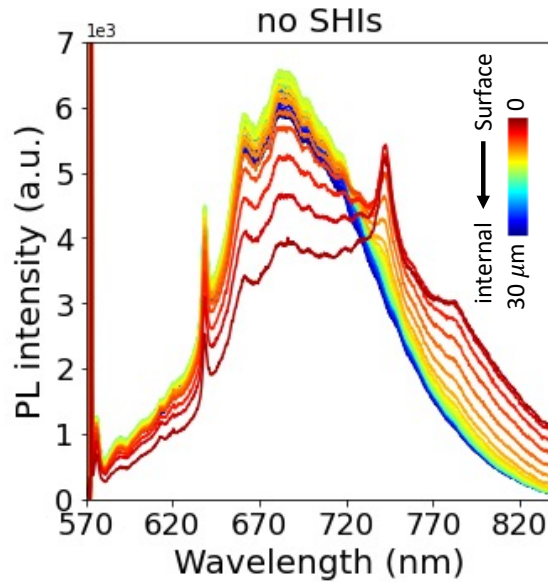


FIG. S2. Depth dependent PL spectrum in the area with only Er implantation and without SHI irradiation of sample A .

reveals stronger GR1 ZPL around 740 nm than the NV^- ZPL at 637 nm. It suggests that GR1 center, as isolated neutral vacancies, tends to be more preferentially formed by Er or other species of heavy ion in the diamond with relative low nitrogen concentration (e.g. 1 ppm). As comparison, as the probing the interior, where beyond the Er ion track range, the spectra (blue) is dominated

by the native NV^- emission.

Deconvolution of spectra: For sample A, the decomposed GR1 spectrum is obtained by subtraction of overall spectrum by an intrinsic NV^- dominated spectrum, which is probed in the internal depth larger than the ion track range. As to sample B, we observed the PL spectra stem from the sample surface are dominated by the NV^0 emission, showing strong 573 nm ZPL and its related phonon side, without appearing any of NV^- ZPL, which can be due to the surface state favorably forming NV^0 . This fortuitous feature allows us to decompose the overall spectrum into NV^0 and NV^- component, separately.

Figure S3 shows the deconvoluted the overall spectrum into NV^- and NV^0 components of the sample B in the SHI irradiated area (after 1st annealing, at depth = 14 μm). We observed that

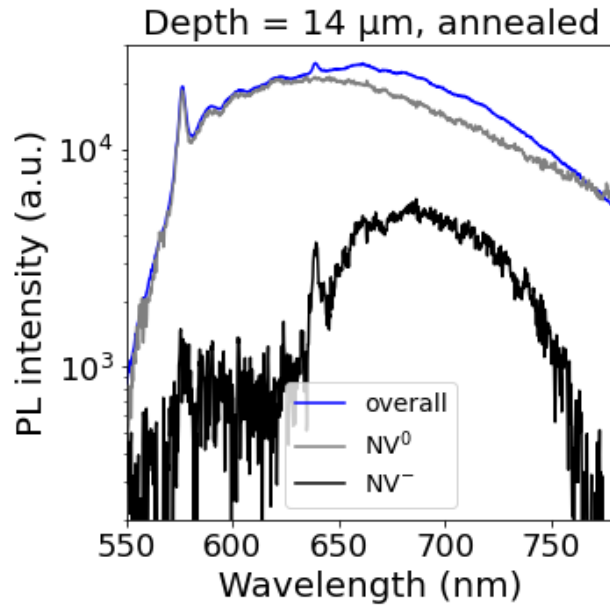


FIG. S3. Deconvolution of PL spectra of sample B probed in the SHI irradiated area at depth = 14 μm by 1st annealing

the NV^0 luminescence is the major component contributed to the overall spectrum, instead of the NV^- , which evidence the higher conversion yield of nitrogen atom to NV^0 by 1st annealing. It is likely due to the limited nitrogen atom (1 ppm) in this sample, which acts as donor to provide electron for NV^- formation. In addition, the parasitic formation of divacancies (V_2) along ion tracks may act as deeper acceptors, which can trap electrons and cause the NV centers mainly as a form of the neutral charge state⁴². Such NV^-/NV^0 ratio variation depending on nitrogen concentration were recently observed in electron-beam irradiated diamond: for the diamond with

a few ppm of nitrogen concentration, electron-beam radiations lead to co-existence of NV^- and NV^0 centers⁴³.

MD-simulations: The two-temperature MD model used for the simulations is the same as in Ref.³³ except for the modification in the electronic heat diffusivity. In Ref.³³, the authors demonstrated the difference between fullerene and gold ions. However, the results revealed a minor deviation in the track formation threshold stopping power for fullerene ions, as a continuous ion track was formed in the simulations at the low velocity regime (0.05 MeV/u), which was, however, not observed experimentally. To improve simulation the accuracy, we adjusted the electronic diffusivity value from 1.3 cm²/s to 2.4 cm²/s, resulting in improved agreement. With the revised value, no continuous ion track is produced at the electronic stopping power 20 keV/nm, whereas a continuous ion track of about 4 nm in diameter forms at 40 keV/nm, which is consistent with the experimental observations. The resulting vacancy and interstitial concentrations in the cell were determined using Wigner-Seitz analysis performed with the Voro++ library⁴⁴ and visualized with the OVITO software⁴⁵. Each simulation is repeated 4 times for statistics. On the other hand, several semi-empirical expressions for the radial dose distribution from delta-rays have developed in the literature^{46,47}. Chunxian et al.⁴⁷ developed a dose formula by combining empirical electron energy-range relation in aluminum with the Rutherford delta-ray production formula. While it was originally developed for microdosimetry, this equation offers a satisfactory level of precision when compared with more complex Monte Carlo simulations also in inorganic materials⁴⁸. The energy density in Fig 2 (d). was estimated using the delta-ray dose formula of Chunxian et al. so that it was normalized with the electronic stopping power at a given depth as predicted by the SRIM 2010 software^{33,48}. The resulting energy density is used in the two-temperature MD model to estimate the initial electronic temperature. Similar approach has been extensively used in prior studies³⁴.

REFERENCES

- ¹L. Rondin, J.-P. Tetienne, T. Hingant, J.-F. Roch, P. Maletinsky, and V. Jacques, "Magnetometry with nitrogen-vacancy defects in diamond," Reports on progress in physics **77**, 056503 (2014).
- ²J. F. Barry, J. M. Schloss, E. Bauch, M. J. Turner, C. A. Hart, L. M. Pham, and R. L. Walsworth, "Sensitivity optimization for nv-diamond magnetometry," Reviews of Modern Physics **92**, 015004 (2020).

- ³T. Zhang, G. Pramanik, K. Zhang, M. Gulka, L. Wang, J. Jing, F. Xu, Z. Li, Q. Wei, P. Cigler, *et al.*, “Toward quantitative bio-sensing with nitrogen–vacancy center in diamond,” *ACS sensors* **6**, 2077–2107 (2021).
- ⁴K.-M. C. Fu, G. Z. Iwata, A. Wickenbrock, and D. Budker, “Sensitive magnetometry in challenging environments,” *AVS Quantum Science* **2**, 044702 (2020).
- ⁵S. Bakhshandeh, “Quantum sensing goes bio,” *Nature Reviews Materials* **7**, 254–254 (2022).
- ⁶G.-Q. Liu, R.-B. Liu, and Q. Li, “Nanothermometry with enhanced sensitivity and enlarged working range using diamond sensors,” *Accounts of Chemical Research* **56**, 95–105 (2023).
- ⁷F. Dolde, I. Jakobi, B. Naydenov, N. Zhao, S. Pezzagna, C. Trautmann, J. Meijer, P. Neumann, F. Jelezko, and J. Wrachtrup, “Room-temperature entanglement between single defect spins in diamond,” *Nature Physics* **9**, 139–143 (2013).
- ⁸A. Jarmola, V. Acosta, K. Jensen, S. Chemerisov, and D. Budker, “Temperature- and magnetic-field-dependent longitudinal spin relaxation in nitrogen-vacancy ensembles in diamond,” *Physical review letters* **108**, 197601 (2012).
- ⁹E. Bauch, C. A. Hart, J. M. Schloss, M. J. Turner, J. F. Barry, P. Kehayias, S. Singh, and R. L. Walsworth, “Ultralong dephasing times in solid-state spin ensembles via quantum control,” *Physical Review X* **8**, 031025 (2018).
- ¹⁰T. H. Taminiou, J. Cramer, T. van der Sar, V. V. Dobrovitski, and R. Hanson, “Universal control and error correction in multi-qubit spin registers in diamond,” *Nature nanotechnology* **9**, 171–176 (2014).
- ¹¹G. Waldherr, Y. Wang, S. Zaiser, M. Jamali, T. Schulte-Herbrüggen, H. Abe, T. Ohshima, J. Isoya, J. Du, P. Neumann, *et al.*, “Quantum error correction in a solid-state hybrid spin register,” *Nature* **506**, 204–207 (2014).
- ¹²X. Rong, J. Geng, F. Shi, Y. Liu, K. Xu, W. Ma, F. Kong, Z. Jiang, Y. Wu, and J. Du, “Experimental fault-tolerant universal quantum gates with solid-state spins under ambient conditions,” *Nature communications* **6**, 8748 (2015).
- ¹³Y. Wang, F. Dolde, J. Biamonte, R. Babbush, V. Bergholm, S. Yang, I. Jakobi, P. Neumann, A. Aspuru-Guzik, J. D. Whitfield, *et al.*, “Quantum simulation of helium hydride cation in a solid-state spin register,” *ACS nano* **9**, 7769–7774 (2015).
- ¹⁴S. Pezzagna and J. Meijer, “Quantum computer based on color centers in diamond,” *Applied Physics Reviews* **8**, 011308 (2021).
- ¹⁵B. Hensen, H. Bernien, A. E. Dréau, A. Reiserer, N. Kalb, M. S. Blok, J. Ruitenberg, R. F.

- Vermeulen, R. N. Schouten, C. Abellán, *et al.*, “Loophole-free bell inequality violation using electron spins separated by 1.3 kilometres,” *Nature* **526**, 682–686 (2015).
- ¹⁶T. Tsuji, H. Ishiwata, T. Sekiguchi, T. Iwasaki, and M. Hatano, “High growth rate synthesis of diamond film containing perfectly aligned nitrogen-vacancy centers by high-power density plasma cvd,” *Diamond and Related Materials* **123**, 108840 (2022).
- ¹⁷S. Greengard, “Qubit devices inch toward reality,” *Communications of the ACM* **64**, 11–13 (2021).
- ¹⁸M. Hamilton and L. Nguyen, “Heterogeneous integration technologies for scaled quantum information processing systems,” *IEEE EPS eNews* (2023).
- ¹⁹R. E. Lake, A. Persaud, C. Christian, E. S. Barnard, E. M. Chan, A. A. Bettioli, M. Tomut, C. Trautmann, and T. Schenkel, “Direct formation of nitrogen-vacancy centers in nitrogen doped diamond along the trajectories of swift heavy ions,” *Applied Physics Letters* **118**, 084002 (2021).
- ²⁰S. Onoda, K. Tatsumi, M. Haruyama, T. Teraji, J. Isoya, W. Kada, T. Ohshima, and O. Hanaizumi, “Diffusion of vacancies created by high-energy heavy ion strike into diamond,” *physica status solidi (a)* **214**, 1700160 (2017).
- ²¹S. Onoda, M. Haruyama, T. Teraji, J. Isoya, W. Kada, O. Hanaizumi, and T. Ohshima, “New application of nv centers in cvd diamonds as a fluorescent nuclear track detector,” *physica status solidi (a)* **212**, 2641–2644 (2015).
- ²²S. Bose, “Quantum communication through an unmodulated spin chain,” *Physical review letters* **91**, 207901 (2003).
- ²³M. Akselrod and J. Kouwenberg, “Fluorescent nuclear track detectors—review of past, present and future of the technology,” *Radiation Measurements* **117**, 35–51 (2018).
- ²⁴M. C. Marshall, M. J. Turner, M. J. Ku, D. F. Phillips, and R. L. Walsworth, “Directional detection of dark matter with diamond,” *Quantum Science and Technology* **6**, 024011 (2021).
- ²⁵J. Liu, H. V. Muinos, K. Nordlund, and F. Djurabekova, “Molecular dynamics simulation of the effects of swift heavy ion irradiation on multilayer graphene and diamond-like carbon,” *Applied Surface Science* **527**, 146495 (2020).
- ²⁶J. Cajzl, P. Nekvindová, A. Macková, P. Malinský, J. Oswald, Z. Remeš, M. Varga, A. Kromka, B. Akhetova, R. Böttger, *et al.*, “Erbium luminescence centres in single- and nano-crystalline diamond—effects of ion implantation fluence and thermal annealing,” *Micromachines* **9**, 316 (2018).
- ²⁷J. B. James Ziegler, M.D. Ziegler, “Software website of the stopping and range of ions in

- matter: <http://www.srim.org/index.htm>,” (2008).
- ²⁸S. Subedi, V. Fedorov, S. Mirov, and M. Markham, “Spectroscopy of gr1 centers in synthetic diamonds,” *Optical Materials Express* **11**, 757–765 (2021).
- ²⁹J. Jeske, D. W. Lau, X. Vidal, L. P. McGuinness, P. Reineck, B. C. Johnson, M. W. Doherty, J. C. McCallum, S. Onoda, F. Jelezko, *et al.*, “Stimulated emission from nitrogen-vacancy centres in diamond,” *Nature communications* **8**, 14000 (2017).
- ³⁰M. Solà-Garcia, S. Meuret, T. Coenen, and A. Polman, “Electron-induced state conversion in diamond nv centers measured with pump–probe cathodoluminescence spectroscopy,” *ACS photonics* **7**, 232–240 (2019).
- ³¹T. Lühmann, J. Meijer, and S. Pezzagna, “Charge-assisted engineering of color centers in diamond,” *physica status solidi (a)* **218**, 2000614 (2021).
- ³²J. Tersoff, “Modeling solid-state chemistry: Interatomic potentials for multicomponent systems,” *Physical review B* **39**, 5566 (1989).
- ³³H. Amekura, A. Chettah, K. Narumi, A. Chiba, Y. Hirano, K. Yamada, S. Yamamoto, A. Leino, F. Djurabekova, K. Nordlund, *et al.*, “Latent ion tracks were finally observed in diamond,” *Nature Communications* **15**, 1786 (2024).
- ³⁴Z. Wang, C. Dufour, E. Paumier, and M. Toulemonde, “The sensitivity of metals under swift-heavy-ion irradiation: a transient thermal process,” *Journal of Physics: Condensed Matter* **6**, 6733 (1994).
- ³⁵T. Schenkel, A. Barnes, A. Hamza, D. Schneider, J. Banks, and B. Doyle, “Synergy of electronic excitations and elastic collision spikes in sputtering of heavy metal oxides,” *Physical review letters* **80**, 4325 (1998).
- ³⁶R. Fischer, A. Jarmola, P. Kehayias, and D. Budker, “Optical polarization of nuclear ensembles in diamond,” *Physical Review B* **87**, 125207 (2013).
- ³⁷B. Smeltzer, L. Childress, and A. Gali, “¹³C hyperfine interactions in the nitrogen-vacancy centre in diamond,” *New Journal of Physics* **13**, 025021 (2011).
- ³⁸D. B. Bucher, D. P. Aude Craik, M. P. Backlund, M. J. Turner, O. Ben Dor, D. R. Glenn, and R. L. Walsworth, “Quantum diamond spectrometer for nanoscale nmr and esr spectroscopy,” *Nature Protocols* **14**, 2707–2747 (2019).
- ³⁹O. R. Rubinas, V. Vorobyov, V. Soshenko, S. Bolshedvorskii, V. Sorokin, A. Smolyaninov, V. Vins, A. Yelissev, and A. Akimov, “Spin properties of nv centers in high-pressure, high-temperature grown diamond,” *Journal of Physics Communications* **2**, 115003 (2018).

- ⁴⁰Y. Mindarava, R. Blinder, C. Laube, W. Knolle, B. Abel, C. Jentgens, J. Isoya, J. Scheuer, J. Lang, I. Schwartz, *et al.*, “Efficient conversion of nitrogen to nitrogen-vacancy centers in diamond particles with high-temperature electron irradiation,” *Carbon* **170**, 182–190 (2020).
- ⁴¹F. Feng, W. Zhang, J. Zhang, L. Lou, W. Zhu, and G. Wang, “Optimizing the density of nitrogen implantation for generating high-density nv center ensembles for quantum sensing,” *The European Physical Journal D* **73**, 1–6 (2019).
- ⁴²P. Deák, B. Aradi, M. Kaviani, T. Frauenheim, and A. Gali, “Formation of nv centers in diamond: A theoretical study based on calculated transitions and migration of nitrogen and vacancy related defects,” *Physical review B* **89**, 075203 (2014).
- ⁴³C. Li, Q. Zhang, N. Zhou, C. Zhang, and Z. Yi, “Impacts of nitrogen concentration and electron irradiation fluence on the formation of nitrogen-vacancy defects in diamond,” *Diamond and Related Materials* **132**, 109623 (2023).
- ⁴⁴C. Rycroft, “Voro++: A three-dimensional voronoi cell library in c++,” Tech. Rep. (Lawrence Berkeley National Lab.(LBNL), Berkeley, CA (United States), 2009).
- ⁴⁵A. Stukowski, “Visualization and analysis of atomistic simulation data with ovito—the open visualization tool,” *Modelling and simulation in materials science and engineering* **18**, 015012 (2009).
- ⁴⁶E. Kobetich and R. Katz, “Energy deposition by electron beams and δ rays,” *Physical review* **170**, 391 (1968).
- ⁴⁷Z. Chunxiang, D. Dunn, and R. Katz, “Radial distribution of dose and cross-sections for the inactivation of dry enzymes and viruses,” *Radiation Protection Dosimetry* **13**, 215–218 (1985).
- ⁴⁸A. Leino, S. Daraszewicz, O. H. Pakarinen, K. Nordlund, and F. Djurabekova, “Atomistic two-temperature modelling of ion track formation in silicon dioxide,” *Europhysics Letters* **110**, 16004 (2015).

Scalable ATLAS pMSSM computational workflows using containerised REANA reusable analysis platform

Marco Donadoni¹, Matthew Feickert², Lukas Heinrich³, Yang Liu⁴, Audrius Mečionis¹, Vladyslav Moisieienkov¹, Tibor Šimko^{1,*}, Giordon Stark⁵, and Marco Vidal García¹

¹CERN, Geneva, Switzerland

²University of Wisconsin–Madison, Madison, United States

³Max-Planck-Institut für Physik, München, Germany

⁴Sun Yat-Sen University, China

⁵SCIPP, UC Santa Cruz, United States

Abstract. In this paper we describe the development of a streamlined framework for large-scale ATLAS pMSSM reinterpretations of LHC Run-2 analyses using containerised computational workflows. The project is looking to assess the global coverage of BSM physics and requires running $O(5k)$ computational workflows representing pMSSM model points. Following ATLAS Analysis Preservation policies, many analyses have been preserved as containerised Yadage workflows, and after validation were added to a curated selection for the pMSSM study. To run the workflows at scale, we utilised the REANA reusable analysis platform. We describe how the REANA platform was enhanced to ensure the best concurrent throughput by internal service scheduling changes. We discuss the scalability of the approach on Kubernetes clusters from 500 to 5000 cores. Finally, we demonstrate a possibility of using additional ad-hoc public cloud infrastructure resources by running the same workflows on the Google Cloud Platform.

1 Introduction

We have developed a streamlined framework for large-scale pMSSM reinterpretations of ATLAS analyses of LHC Run-2 using containerised computational workflows. The project is looking to assess the global coverage of BSM physics and requires running numerous computational workflows representing pMSSM model points. The framework builds upon the idea of RECAST-ing analyses [1] and takes into account the experiences with the previous ATLAS pMSSM reinterpretations from LHC Run-1 period [2].

Following the ATLAS analysis preservation policies, many ATLAS analyses have been preserved as containerised Yadage workflows. After validation they are added to a curated selection of analyses suitable for the pMSSM study. Figure 1 shows one such repository for the supersymmetry searches.

One typical pMSSM computational workflow is presented in Figure 2. The workflow consists of three time-consuming ntupling steps that process data files and run in parallel. The workflow ends with a latter fitting steps that run afterwards. The dependency of steps in

*Corresponding author e-mail: tibor.simko@cern.ch

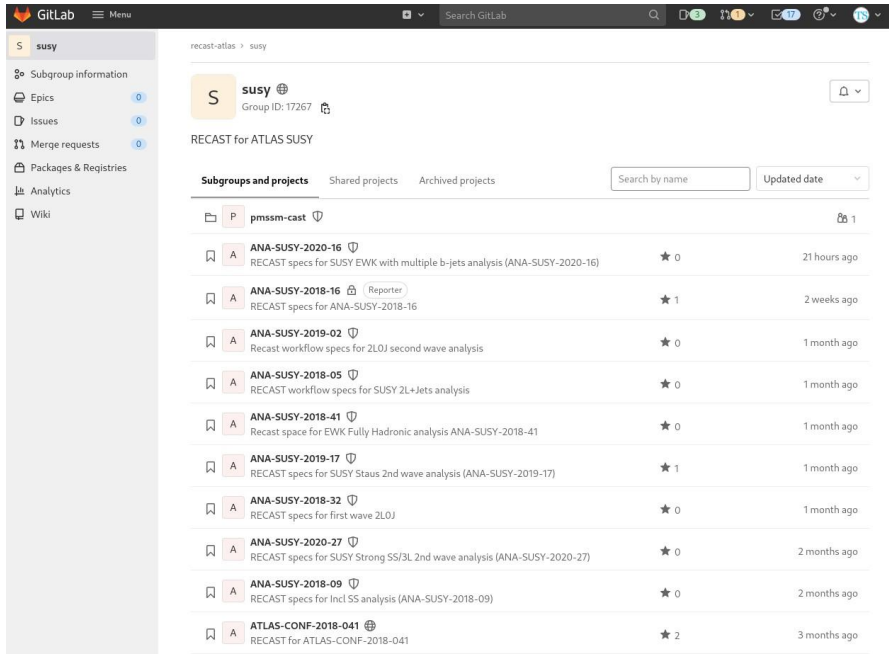


Figure 1. A screenshot of the ATLAS SUSY group analyses preserved on GitLab. Each repository is labeled with the internal ATLAS analysis identifier and contains both workflow files and additional data files needed for the computational processing.

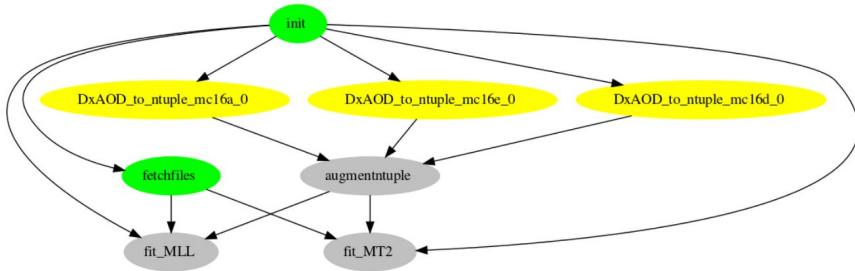


Figure 2. A typical pMSSM workflow. The computational runtime is about 10 minutes without systematics (test payload) and about 10 hours with all systematics (real payload).

the computational graph is rather simple. The complexity of the problem lies in having to run several thousands of these workflows in order to cover a sufficient number of pMSSM model points.

It was the goal of the present work to study the feasibility of running several thousands of these containerised workflows in parallel in an automated way in order to facilitate typical pMSSM studies.

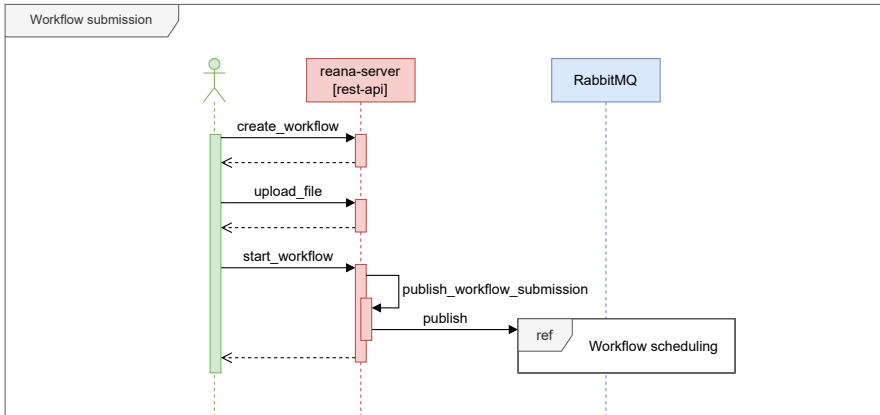


Figure 3. The sequence diagram showing how REANA schedules incoming workflows after submission. The submitted workflows are announced via message queue that is later processed by the workflow scheduler in Figure 4.

2 Method

The computational workflows were run at scale using the REANA reusable analysis platform [3]. The computational backend was the Kubernetes cluster of various sizes (from 500 cores up to 5000 cores). We have been varying several parameters of the cluster such as the number of nodes and the required memory and studied the maximum number of pMSSM workflows that the platform can handle concurrently. After performing several such computational experiments, we have improved the scheduling efficiency of REANA to increase the running bandwidth for the pMSSM style of workflows.

Figure 3 shows the sequence diagram of the workflow submission stage. The incoming workflows are stored in a queue that is later processed by the scheduler. The first task was to improve the performance of the REANA platform’s server submission end points to allow many concurrent workflow starting requests.

Figure 4 shows the next stage of the process, namely how the submitted workflows are being consumed from the incoming queue. The scheduler first checks whether the incoming workflow does not exceed the limits on the total number of workflow the system could handle as well as currently available free memory on the Kubernetes cluster. If the checks succeed, the workflow is accepted for execution. In the opposite case the incoming workflow is being rescheduled and attempted to be accepted for execution several times whilst waiting for the Kubernetes cluster resources to liberate. If the workflow cannot be scheduled for a substantial amount of time, a failure is declared.

Figure 5 shows the stage of the running of the workflow after it has been accepted for execution. Note the interplay of the REANA platform with the underlying Kubernetes cluster: the job is scheduled using the Kubernetes native job scheduler mechanism which include additional scheduling delays that needed to be taken into account for optimisation. The progress of the workflow is monitored until the workflow execution terminates. The workflow steps are launched when the worker nodes are free to run the workload. The status of jobs is published in the message queue.

Figure 6 shows the termination stage of the workflow. When all the steps are finished and the results are produced, the system has to delete the Kubernetes pod and update the status of the workflow in both the message queue and the database. This constituted another layer

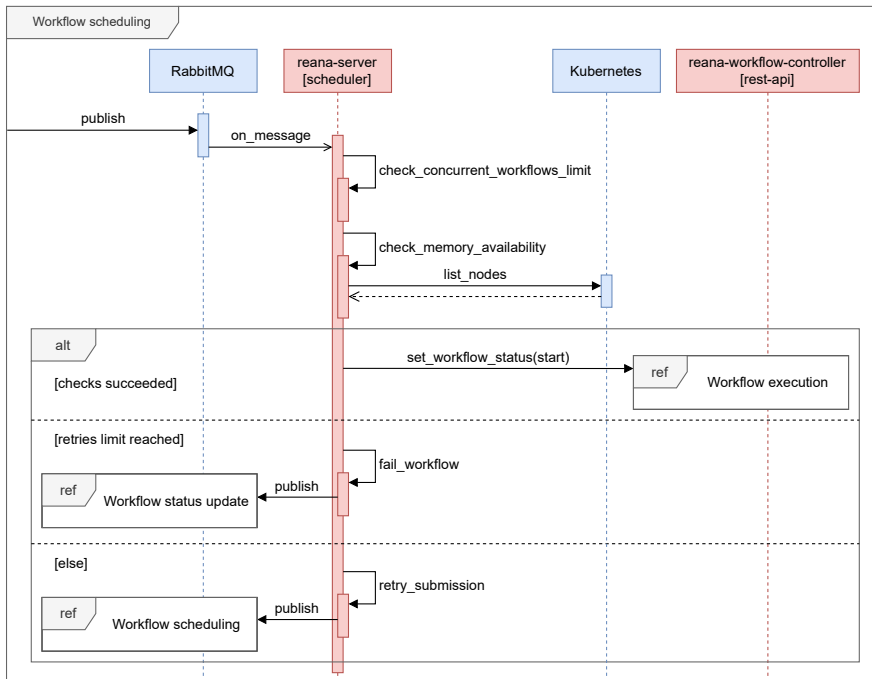


Figure 4. The sequence diagram showing how REANA schedules queued workflows. The system checks for available resources before allowing workflow runs for execution. The checking and rescheduling workflow offers several possibilities for optimisations. The workflows accepted for execution are further processed in Figure 5.

of optimisations in order to handle any status handling processes in an asynchronous manner whilst the platform is starting the new incoming workflows.

3 Results

We have improved the REANA platform scheduling performance in order to maximise the scheduling throughput of incoming workflows at the various stages of the workflow life cycle as described in Section 2. A special attention was paid to measure the CPU and Memory usage of the cluster nodes.

Figure 7 shows a typical snapshot of the status of cluster nodes running the pMSSM workloads. We have used nodes of the `m2.xlarge` flavour which consist of 16 GiB of available memory and 8 virtual cores. One can see the efficient use of cores of the cluster resulting from tuning REANA parameters such as the number of nodes running workflow orchestration tasks, the number of nodes running the pMSSM workflow step jobs themselves, as well as the memory request limits for each ntupling job of the first pMSSM workflow stages.

Figure 8 shows the results of one of our scalability experiment that consisted of submitting 200 new pMSSM workflows every 10 minutes. A cluster with 448 cores presented on the left cannot keep up with such a workload: note the increasing scheduling waiting times (plotted in the orange colour) as well as increasing workflow run times (plotted in blue). The overflow happens because the cluster is allowing more workflows than it can hold. However, note how

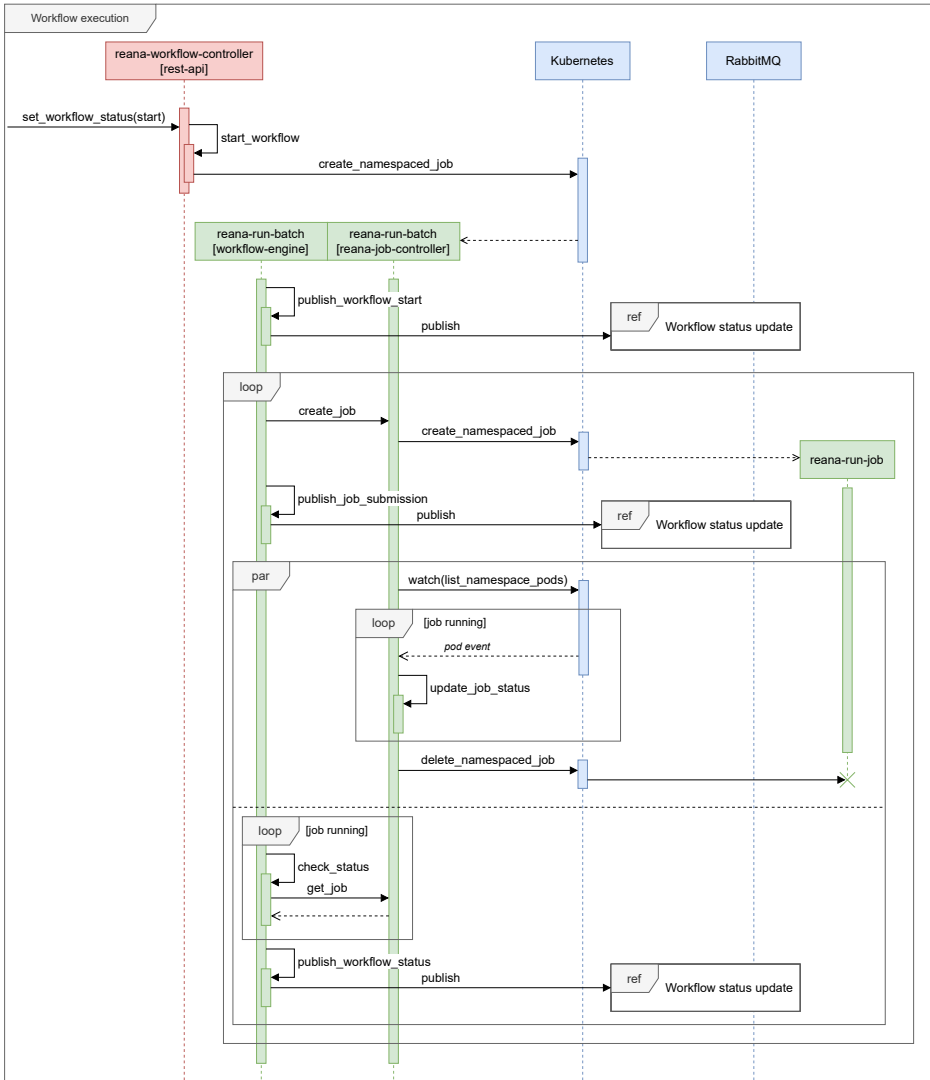


Figure 5. The sequence diagram showing how the REANA executes scheduled workflows. Note the interplay between the scheduler and the Kubernetes cluster. The pod creation offers another space for optimisations. The workflow execution status monitoring is carried out by a watching loop. The workflow jobs are started for each workflow step. The termination procedures are further illustrated in Figure 6.

the same cluster with 1072 cores presented on the right of the Figure holds the same workload very comfortably.

Figure 9 shows the same kind of experiment executed over a longer period of time. This helped to ensure that the platform can sustain the constantly increasing stream of incoming workloads.

We have run several benchmarking experiments in the CERN Computer Centre and, to test the portability, performed a few runs also on the Google Cloud Platform. This allowed

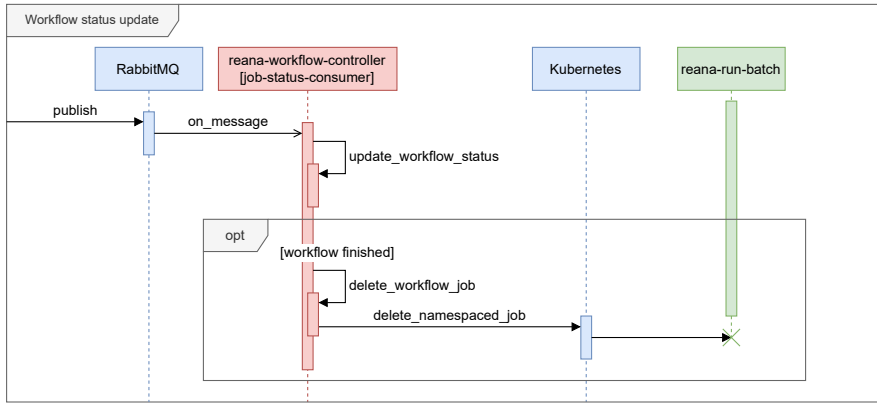


Figure 6. The sequence diagram showing how REANA updates workflow statuses and terminates finished workflows. The procedure involves consuming the message queue, closing the Kubernetes pods, and updating the database about the status of the workflow run. In case of launching several thousands of concurrent workflows, these processes also have to be optimised.

```

$ kubectl top nodes
NAME                                CPU(cores)   CPU%   MEMORY(bytes)   MEMORY%
reanaatlas1-3slyowp42qex-node-15   7858m        98%    12033Mi         82%
reanaatlas1-3slyowp42qex-node-16   7848m        98%    12083Mi         83%
reanaatlas1-3slyowp42qex-node-17   7846m        98%    12210Mi         83%
reanaatlas1-3slyowp42qex-node-18   7773m        97%    8995Mi          61%
reanaatlas1-3slyowp42qex-node-19   7864m        98%    11516Mi         79%
reanaatlas1-3slyowp42qex-node-20   7843m        98%    12177Mi         83%
reanaatlas1-3slyowp42qex-node-21   7376m        92%    8698Mi          59%
reanaatlas1-3slyowp42qex-node-22   7817m        97%    11201Mi         77%
reanaatlas1-3slyowp42qex-node-23   7748m        96%    9978Mi          68%
reanaatlas1-3slyowp42qex-node-24   7854m        98%    12161Mi         83%
reanaatlas1-3slyowp42qex-node-25   7868m        98%    12293Mi         84%
reanaatlas1-3slyowp42qex-node-26   7787m        97%    10991Mi         75%
  
```

Figure 7. An example of the benchmark tests running in the CERN Computer Centre. The REANA scheduling parameters were optimised to maximise the CPU utilisation and the Memory consumption on the cluster for the typical pMSSM ntupling job parallelism (see Figure 2). Note the very good efficiency of CPU cores in the above screenshot.

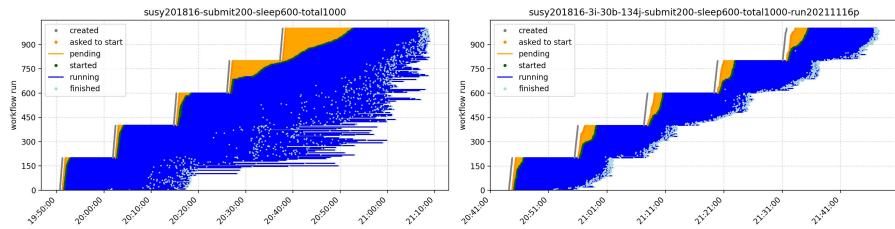


Figure 8. A scalability test submitting 200 workflows every 10 minutes. A cluster with 448 cores (left) cannot keep up with the load. A cluster with 1072 cores (right) can comfortably hold the incoming workload.

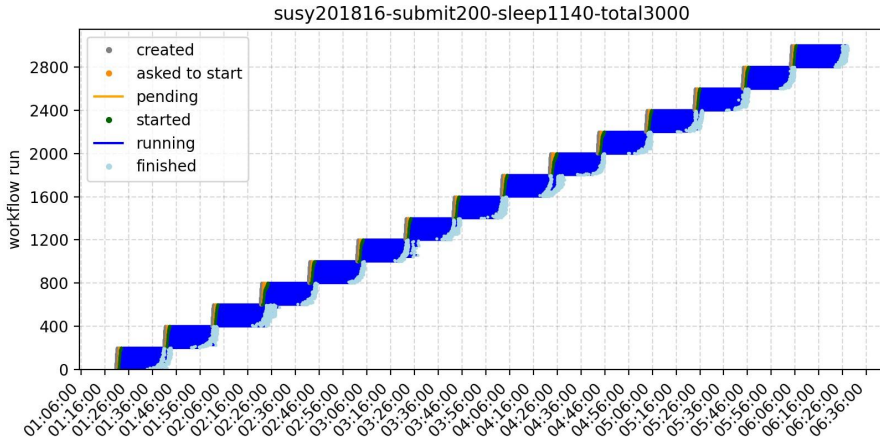


Figure 9. The workload burndown throughput rate is sustainable over a long period of time.

to prove the applicability of the approach on various compute backends, facilitating future reproducibility of containerised workflows irrespective of their original computing environments.

4 Conclusions

ATLAS searches for new physics are being effectively preserved together with containerised computational workflow recipes as part of the ATLAS RECAST project. This enables their future reuse and reinterpretation and greatly facilitates the running of efficient pMSSM studies over a large collection of individual analyses.

We have launched several ATLAS pMSSM workflows on the REANA reproducible analysis platform and studied the performance from workflow scheduling up to workflow execution and termination procedures with the aim of allowing running several thousands of these workflows to cover a sufficient number of pMSSM model points.

The REANA platform has been internally optimised to allow faster workflow scheduling, processing and terminating procedures on an individual workflow level as well as under the stressing conditions of processing many incoming concurrent workloads. A set of benchmarking experiments allowed to optimise and tune the REANA system for the pMSSM workloads on the Kubernetes clusters ranging from medium to large sizes (from 500 to 5000 cores). It was essential to adjust REANA scheduling parameters to the type of the pMSSM workload in order to ensure the best throughput and the efficient cluster CPU and memory resource utilisation.

The developed system was tested on the CERN Computer Centre as well as on the Google Cloud Platform in order to ensure the reproducibility of the approach and is fully ready to run large-scale ATLAS pMSSM reinterpretations of LHC Run-2 analyses. The first results by the ATLAS collaborations are being published [4].

Acknowledgements

L.H. is supported by the Excellence Cluster ORIGINS, which is funded by the Deutsche Forschungsgemeinschaft (DFG, German Research Foundation) under Germany’s Excellence Strategy - EXC-2094-390783311.

M.F. is supported by the U.S. National Science Foundation (NSF) under Cooperative Agreement OAC-1836650 (IRIS-HEP).

References

- [1] K. Cranmer, I. Yavin, “RECAST: Extending the Impact of Existing Analyses”, JHEP 1104:028 (2011), <https://doi.org/10.48550/arXiv.1010.2506>.
- [2] ATLAS Collaboration, “Summary of the ATLAS experiment’s sensitivity to supersymmetry after LHC Run 1 - interpreted in the phenomenological MSSM”, JHEP **10** (2015), 134. <https://doi.org/10.48550/arXiv.1508.06608>.
- [3] T. Šimko, L. Heinrich, H. Hirvonsalo, D. Kousidis, D. Rodríguez, “REANA: A system for reusable research data analyses”, EPJ Web of Conferences 214, 06034 (2019), <https://doi.org/10.1051/epjconf/201921406034>.
- [4] ATLAS Collaboration, “ATLAS Run 2 searches for electroweak production of supersymmetric particles interpreted within the pMSSM”, ATLAS-CONF-2023-055 (13 Sep 2023). <https://cds.cern.ch/record/2870222>.

Know your footprint - Evaluation of the professional carbon footprint for individual researchers in high energy physics and related fields

Valerie Lang^{a,1,*}, Naman Kumar Bhalla^a, Simran Gurdasani^a, Pardis Niknejadi^b

^aAlbert-Ludwigs-Universität, Freiburg, Germany

^bDeutsches Elektronensynchrotron (DESY), Hamburg, Germany

Abstract

Understanding the environmental impact of professional activities is becoming paramount in current times, especially within sectors that historically have had significant resource utilisation, such as High Energy Physics (HEP) and related fields. The *young High Energy Physicists* (yHEP) association launched the *Know your footprint* (Kyf) campaign to evaluate the CO₂-equivalent emissions generated by HEP-related research. This study delves into the carbon footprints associated with four distinct categories: *Experiments*, tied to extensive collaborations with substantial infrastructure; *Institutional*, representing the resource consumption of research institutes and universities; *Computing*, focusing on simulations and data analysis; and *Travel*, covering professional trips such as to conferences, meetings, and workshops. The findings in this assessment are integrated into a tool for self-evaluation, the *Know-your-footprint* (Kyf) calculator, which allows colleagues to assess their personal and professional footprint, and optionally share their data with the yHEP association. The aim of the Kyf campaign is to heighten awareness, foster sustainability, and inspire the community to adopt more environmentally-responsible research methodologies.

Keywords: High Energy Physics, CO₂ emissions, Know your footprint, yHEP

1. Introduction

The impact of the atmospheric presence of CO₂ on the ground temperature of the Earth was first predicted in 1896 [1], indicating temperature variations as a function of the amount of CO₂ (at the time denoted as carbonic acid), the time of the year and the latitude. For Europe, the prediction for doubling the atmospheric CO₂ content amounted to an average temperature increase of around 6 °C.

In 2023, the measured CO₂ content in the atmosphere has reached nearly 425 ppm [2], compared to a maximum of about 300 ppm over the last 800 000 years before industrial age. The CO₂ content in the atmosphere has thus increased by a factor of about 1.4 compared to the maximum, and around 1.9 compared to the mean over the last 800 000 years [3]. The average temperature in Europe in 2023 has climbed up by 1.90 °C compared to pre-industrial levels (reference years: 1850-1900) [4], which is also used as reference for temperature differences in the following. The year 2023 is in direct competition with the year 2020 which was the warmest year on record in Europe with a 2.07 °C increase. Globally, 2023 surpassed the previously warmest year 2016 (1.32 °C increase), reaching an increase of 1.48 °C.

Scientific research has thus been drawing a consistent picture for more than 100 years, with continuously refined measurements and scenario predictions. Decisive actions counteracting the changes to the atmosphere and the planetary ecosystem, however, have been and are still lacking.

According to the Sixth Assessment Report (AR6) by the Intergovernmental Panel on Climate Change (IPCC), Summary for Policymakers (SPM) [5], “[i]t is unequivocal that human influence has warmed the atmosphere, ocean and land”, leading to changes across the climate system that are “unprecedented over many centuries to many thousands of years”.

Relevant for changes of the climate are the cumulative CO₂ emissions. Part of the CO₂ emissions are re-absorbed by carbon sinks on land and ocean, but the higher the cumulative CO₂ emissions are, the lower is the fraction of absorption by land and ocean carbon sinks. This results in higher contributions for both the fraction and the absolute amount that remain in the atmosphere.

The IPCC AR6 SPM estimates historical cumulative anthropogenic CO₂ emissions from 1850 to 2019 to (2390±240) Giga-tonnes of CO₂ (GtCO₂). In order to achieve a likelihood of 67 % to limit human-induced global warming to a maximum increase of 1.5 °C (2.0 °C), which are the two thresholds explicitly mentioned in the Paris Agreement 2015 [6] to reduce risks and impacts of climate change, only 400 GtCO₂ (1150 GtCO₂) remain to be emitted. This remaining carbon budget is defined, starting from the beginning of 2020 until global net zero CO₂ emissions are reached.

Using the most naive assumption of equal yearly emissions until 2050, i.e. for 30 years, and a static population of 8 billion people, which was reached on 15 November 2022 [7], the remaining carbon budget per person per year accumulates to 1.7 tCO₂ (4.8 tCO₂) for a maximum temperature increase of 1.5 °C (2.0 °C).

In Germany, the average CO₂ emissions accumulate to

*Corresponding author

¹Email: valerie.lang@physik.uni-freiburg.de

around 10–11 tCO₂ per person per year [8, 9], i.e. more than a factor of two above what is required for the scenario limiting global warming to an increase of 2.0 °C. This, however, only summarises emissions from private life. For researchers in the area of high energy physics (HEP), emissions resulting from research activities need to be added on top.

The first step for reducing emissions is to quantify current emissions and raise awareness. The *Know your footprint* (Kyf) campaign by the *young High Energy Physicists* (yHEP) association [10] targets these aspects for the professional footprint of researchers in the area of HEP and related fields. While scientific research and development activities contribute only a fraction of the carbon footprint compared to industrial activities, it is crucial for the scientific community to understand and mitigate the environmental impact of their research. Knowledge of the own carbon footprint will allow to identify areas requiring most urgent action and indicate possible starting points for action to reduce the footprint. This paper discusses the data sources and calculations conducted to evaluate the CO₂-equivalent emissions for researchers in HEP for yHEP’s Kyf campaign and Kyf calculator.

2. General setup

The Kyf campaign by the yHEP association evaluates the carbon footprint of researchers in HEP, mostly in, or associated to, Germany. For emissions of private life in Germany, we refer to the *Carbon Calculator* by the German Federal Environment Agency (*Umweltbundesamt* - UBA) [8, 9, 11].

For the professional footprint, we target four distinct categories: *Experiments*, *Institutions*, *Computing* and *Travel*.

The *experimental* footprint comprises the emissions from (large) research infrastructures, collaborations or research projects, i.e. especially in experimental physics, the experimental setup. The *institutional* footprint summarises the emissions from the home university or research centre of the individual researcher, which should be understood as the institution where the researcher spends the larger part of her/his working time. *Computing* focuses on the individual researcher’s footprint of running simulations and data analysis, optionally considering data storage impacts as well. *Travel* covers the individual’s professional trips such as to conferences, meetings, or workshops.

The footprints in each category are broken down to the level of the individual researcher so that they can be placed in relation to each other as well as to the individual’s emissions for private life. Several options in each category allow adjusting to the researcher’s individual situation, although some simplifications are needed to allow for sufficient user-friendliness and manageable scope of the first version of the Kyf calculator by the yHEP association. Refinements are considered possible in the future. The Kyf calculator is published on the webpage of the yHEP association [10].

The calculations that form the basis of the Kyf calculator are discussed in detail in Sections 3 to 6. An example footprint is given in Section 7. The Kyf calculator provides feedback to individual researchers regarding their own professional car-

bon footprint, and optionally allows to share the data anonymously with the yHEP association. This data will be used by the yHEP association to obtain and later publish an overview of the professional footprint of researchers in HEP and related fields in, and associated to, Germany. The focus on Germany implies that numbers for the German electricity grid, German institutions, etc. will be used in the calculations, where applicable. Other institutions or interest groups are encouraged to transfer the considerations by yHEP’s Kyf campaign to different countries, citing this publication as basis for their considerations. In case of questions, contact can be established with us as authors directly, or with the yHEP association through the webpage [10].

3. Experiment, collaboration or project footprint

The experiment, collaboration or project footprint strongly depends on the corresponding experiment, collaboration or project. In order to provide a rough estimate, we use the experiments at the Large Hadron Collider (LHC) as benchmark for large HEP experiments, DESY electricity consumption (excluding the European XFEL) as benchmark for smaller HEP experiments and the European Southern Observatory (ESO) as benchmark for experimental research in astronomy.

To evaluate the per-researcher environmental footprint, two numbers are needed: an estimate of the total amount of emissions by the experiment, collaboration or project in tonne-CO₂-equivalent (tCO₂e), and the number of people that the footprint should be distributed over. The ratio of these two numbers provides the per-person benchmark footprint.

The design of experimental setups in HEP has traditionally been driven, mainly, by the scientific question that is to be answered, without systematic consideration for minimising its carbon footprint. The scientific output is credited to the authors of the scientific publications. In the area of HEP, authorship on the publications typically requires membership in the experimental collaboration. We therefore assign the carbon footprint of the experiment to the members of the experimental collaboration, or the users (and operators) of the experimental facility, where corresponding numbers are available.

More indirect beneficiaries of the knowledge gained in the experiment, collaboration, or project, such as *the industry* or *the public*, are not considered here. These categories are too vague to provide a good reference for the carbon footprint of an experimental collaboration, and do not allow for well-defined boundaries of the organisation, i.e. the experiment, collaboration or project. In contrast to a company, where the footprint could alternatively be assigned to the “product” of the company and could thus be attributed to the “consumer”, *knowledge* as a “product” of scientific experiments is not easily quantifiable and thus not distributable to “consumers”. In order to maintain the responsibility for the emissions with those who can impact their reduction, we estimate the per-researcher footprint without consideration of such indirect benefits. This approach is not intended to scrutinise scientists for the environmental impact of their research, but rather aims to highlight key areas where the

scientific community can focus its sustainability efforts, ensuring a more environmentally responsible approach to advancing knowledge.

3.1. LHC experiments

The LHC [12] is the largest particle accelerator housed at CERN [13] colliding proton beams at the location of four major particle detectors: ATLAS [14], CMS [15], ALICE [16] and LHCb [17]. While ATLAS and CMS are large general-purpose detectors, ALICE and LHCb are specialised for specific investigations. Due to different sizes of the detectors, it is expected that the larger experiments also have higher annual CO₂ emissions compared to the two smaller experiments. Hence, the Kyf calculator aims at estimating separate values for annual emissions per person for the larger (ATLAS and CMS) and smaller (ALICE and LHCb) LHC experiments.

Since 2017, CERN publishes a biennial environmental report listing its CO₂ emissions. In order to estimate the annual footprints for this benchmark scenario, the environmental reports for 2017–18 [18], 2019–20 [19] and 2021–22 [20] were used to get an estimate of years with, as well as without, the LHC in operation. In addition, the latest technical design report from the LHCb collaboration, which includes a section on environment protection and safety, was used to estimate the difference in CO₂ emissions between the larger and smaller LHC experiments [21]. In this section, the annual emissions are distributed into two phases: Run phase (2017, 2018 and 2022) and Shutdown phase (2019–21).

CERN categorises its CO₂ emissions into three scopes: scope 1 for direct emissions from sources such as detector operations and heating, scope 2 for indirect emissions primarily arising from electricity consumption, and scope 3 for emissions from other indirect sources such as travel, commute, waste, catering and procurement. For the estimation of the footprint for affiliation to the LHC experiments, only scopes 1 and 2 are relevant with the following corrections applied:

- Scope 1: CERN includes the emissions from heating, non-LHC experiments and others into scope 1. Since this estimate is only for LHC experiments, the corrected scope 1 value, corresponding to LHC experiments (particle detection and cooling) are extracted using `PlotDigitizer` [22] (see Appendix A) from the figure: *CERN scope 1 emissions for 2017–2022 by category*, on page 18 in CERN’s environmental report 2021–2022 [20]. These total and corrected scope 1 values for all years are listed in Table 1.
- Scope 2: The scope 2 contribution of CERN’s CO₂ emissions include the electricity consumption of the Meyrin and Preveysin sites, which do not correspond to the consumption for powering the LHC and should be corrected for. CERN’s environmental report 2021–2022 mentions that powering the CERN campus corresponds to 5% of the total energy consumption which was used as the correction factor for the scope 2 values [20]. Since, the scope 2 emissions for 2017–20 were recalculated for the 2021–22 environment report, but given only in a figure without the final values, they were extracted using

`PlotDigitizer` [22] from the figure: *CERN scope 2 emissions for 2017–2022*, on page 19 in CERN’s environmental report 2021–2022 [20]. The values for 2021 and 2022 were directly listed in the same report. The total and corrected scope 2 values are listed in Table 2.

	Year	Total	Corrected
Run	2017	193 600	168 293
	2018	192 100	162 718
	2022	184 173	152 444
	Mean	-	161 151
Shutdown	2019	78 169	56 446
	2020	98 997	75 958
	2021	123 174	89 547
	Mean	-	73 984

Table 1: Total and corrected scope 1 contribution to CERN’s total emissions for the various years in Run and Shutdown phases [18, 19, 20]. The corrected values were extracted using `PlotDigitizer` [22] from the figure: *CERN scope 1 emissions for 2017–2022 by category*, on page 18 in CERN’s environmental report 2021–2022 [20]. All emission values are provided in tCO₂e.

	Year	Total	Corrected
Run	2017	66 667	63 333
	2018	74 884	71 140
	2022	63 161	60 003
	Mean	-	64 825
Shutdown	2019	28 527	27 101
	2020	26 202	24 891
	2021	56 382	53 563
	Mean	-	35 185

Table 2: Total and corrected scope 2 contribution to CERN’s total emissions for the various years in Run and Shutdown phases [20]. Values for 2017–20 were not given and were extracted using `PlotDigitizer` [22] from the figure: *CERN scope 2 emissions for 2017–2022*, on page 19 in CERN’s environmental report 2021–2022 [20]. The corrected value is 95% of the total value. All emission values are provided in tCO₂e.

The technical design report of the LHCb experiment lists their total emission for 2022 to be 4400 tCO₂e of which 51% is assigned to scope 1 [21], i.e.

$$S1_{\text{Small}}^{\text{Run}} = 0.51 \times 4400 \text{ tCO}_2\text{e} \\ = 2244 \text{ tCO}_2\text{e} .$$

Since the LHC was operating in 2022, $S1_{\text{Small}}^{\text{Run}}$ is defined as the scope 1 contribution for the smaller experiments in the Run phase. In order to estimate the scope 1 contribution for the smaller experiments in the Shutdown phase ($S1_{\text{Small}}^{\text{SD}}$), it is assumed that the emissions for larger and smaller experiments scale by the same factor between the two phases. This factor ($S1^{\text{Run/SD}}$) can be calculated from the mean corrected scope 1

contribution for the two phases from Table 1 as

$$\begin{aligned} S1^{\text{Run/SD}} &= \frac{161\,151}{73\,984} \\ &= 2.18. \end{aligned}$$

This results in $S1_{\text{Small}}^{\text{SD}}$ being estimated as

$$\begin{aligned} S1_{\text{Small}}^{\text{SD}} &= \frac{S1_{\text{Small}}^{\text{Run}}}{S1^{\text{Run/SD}}} \\ &= \frac{2244\text{ tCO}_2\text{e}}{2.18} \\ &= 1030\text{ tCO}_2\text{e}. \end{aligned}$$

The scope 1 contribution for the larger experiments ($S1_{\text{Large}}$) for each phase can be estimated using the mean corrected scope 1 contribution for all LHC experiments ($S1_{\text{All}}$) from Table 1 and $S1_{\text{Small}}$. This is done by assuming an equal contribution from both the smaller experiments and an equal contribution also from the two larger experiments and calculated as

$$S1_{\text{All}} = 2 \times S1_{\text{Small}} + 2 \times S1_{\text{Large}} \quad (1)$$

$$S1_{\text{Large}} = \frac{S1_{\text{All}} - 2 \times S1_{\text{Small}}}{2}. \quad (2)$$

The resulting values for the larger experiments are

$$\begin{aligned} S1_{\text{Large}}^{\text{Run}} &= 78\,332\text{ tCO}_2\text{e} \text{ and} \\ S1_{\text{Large}}^{\text{SD}} &= 35\,962\text{ tCO}_2\text{e}. \end{aligned}$$

To estimate the scope 2 contribution of individual experiments, it is assumed that all four experiments share an equal contribution to the mean corrected scope 2 emissions of all experiments ($S2_{\text{All}}$) given in Table 2. This assumption is based on the premise that the dominant scope 2 emissions come from the electricity consumption for running the entire accelerator complex, up to and including the LHC, which is equally necessary for all four experiments. In reality, the electricity consumed by the four experiments might vary and could be refined in the future if more data becomes available. The scope 2 contributions for the smaller ($S2_{\text{Small}}$) and larger ($S2_{\text{Large}}$) experiments, calculated individually for the Run and Shutdown phases, are given as

$$S2_{\text{Small}} = S2_{\text{Large}} = \frac{S2_{\text{All}}}{4}. \quad (3)$$

Using this relation, the scope 2 contributions for the Run and Shutdown phases can be calculated as

$$\begin{aligned} S2_{\text{Small}}^{\text{Run}} = S2_{\text{Large}}^{\text{Run}} &= \frac{64\,825\text{ tCO}_2\text{e}}{4} \\ &= 16\,206\text{ tCO}_2\text{e}, \end{aligned}$$

and

$$\begin{aligned} S2_{\text{Small}}^{\text{SD}} = S2_{\text{Large}}^{\text{SD}} &= \frac{35\,185\text{ tCO}_2\text{e}}{4} \\ &= 8\,796\text{ tCO}_2\text{e}. \end{aligned}$$

After summing the contributions from scopes 1 and 2 to obtain the total footprint of smaller and larger experiments in the Run and Shutdown phases, a weighted mean of the two phases is taken assuming a Run phase of 4 years and Shutdown phase of 3 years,

$$\text{Overall annual emission} = \frac{4 \times \text{Total}^{\text{Run}} + 3 \times \text{Total}^{\text{SD}}}{7}. \quad (4)$$

The values for the individual scopes in the Run and Shutdown phases for smaller and larger experiments are summarised in Table 3 along with the total values for each phase and the overall values calculated using Equation 4.

	Phase	Scope 1	Scope 2	Total
Small	Run	2244	16 206	18 450
	SD	1030	8796	9826
	Overall	-	-	14 754
Large	Run	78 332	16 206	94 538
	SD	35 962	8796	44 758
	Overall	-	-	73 204

Table 3: Contribution from individual scopes in the Run and Shutdown phases for smaller and larger experiments along with the total values for each phase, calculated as Total = Scope 1 + Scope 2, and the overall values calculated using Equation 4.

Finally, to calculate the per person annual footprint for someone affiliated with one of the smaller (larger) LHC experiments, the overall contribution from Table 3 is divided by the mean of total members listed on the public webpages of ALICE [23] and LHCb [24] (CMS [25] and ATLAS [26]) experiments. These values are listed in Table 4. The overlap of members between the four experiments is assumed to be negligible. The annual emission per person for smaller (larger) LHC experiments are estimated to be 8.76 tCO₂e (11.91 tCO₂e).

	Experiment	Members	Mean	Emissions
Small	ALICE	1968 [23]	1684	8.76 tCO ₂ e
	LHCb	1400 [24]		
Large	CMS	6288 [25]	6144	11.91 tCO ₂ e
	ATLAS	6000 [26]		

Table 4: Total members affiliated to the four LHC experiments. The values in the *Mean* column is calculated independently for the two smaller and two larger LHC experiments. The *Emissions* column lists the per person annual emission for the smaller and larger LHC experiments. This is calculated by dividing the Overall emissions from Table 3 by the respective values in the *Mean* column.

3.2. DESY

The research centre *Deutsches Elektronensynchrotron* (DESY) in Hamburg, Germany, is the German national laboratory for accelerator development and operation, photon science, particle physics and astroparticle physics. Due to the presence of a significant accelerator and experimental complex,

emissions from DESY are used as proxy for emissions from smaller HEP experiments.

The first DESY sustainability report for 2019–2021 [27] has been published in 2022, but does not include detailed numbers on the emissions from scope 1, 2 or 3 sources as provided in the CERN environmental reports [18, 19, 20]. The DESY webpage, however, provides a figure on the energy consumption at DESY in 2021 [28] which is reproduced in Figure 1.

Electricity consumption in the year 2021 at DESY, excluding the electricity needed for the European XFEL, amount to 152.5 GWh. This includes: the accelerator complex with the accelerators: PETRA, FLASH, LINAC, HERA and DESY (55%), cryogenics (25%), as well as offices, workshops and laboratories, computing centre, cooling centre, canteen and others (20%). Subtracting the contribution from offices, workshops and laboratories, canteen and others as institute footprint, and the computing centre as computing footprint, which are treated separately in the Kyf calculator, the remaining experimental electricity consumption is 128.3 GWh for 2021, which is considered as representative for the annual consumption.

Two conversion factors for electricity consumption to CO₂ emissions are employed, based on data of Ref. [29]: The specific CO₂ emissions averaged over the German grid in 2023 correspond to 416 gCO₂e/kWh; emissions from green energy production assume 100 % photovoltaic (PV)-based electricity production with a footprint of 35 gCO₂e/kWh. Emissions from wind- (13 gCO₂e/kWh) and water- (11 gCO₂e/kWh) based production are lower, so 100 % PV-based production is considered to be a conservative estimate for green electricity production.

The number of guest scientists using the DESY facilities is listed as 3000 in the DESY environmental report [27], which is complemented by an additional 200 accelerator operators. The latter is based on an internal estimate by one accelerator operator, and is considered reasonable given the size of the DESY facilities. Refinements of these numbers are possible in a future version of the Kyf calculator.

Based on the above conversion factors and the number of scientists and operators, the total emissions from DESY are 53 372.8 tCO₂e (4490.5 tCO₂e) for conventional (green) electricity production, corresponding to 16.68 tCO₂e (1.40 tCO₂e) emissions per person per year, given a conventional (green) electricity supply. DESY itself switched to a green electricity contract at the start of 2023, significantly reducing its environmental footprint.

3.3. European Southern Observatory

Since 2020, the annual reports for ESO include a section on the environmental impact of the observatory [30, 31, 32]. In order to estimate the annual CO₂ emissions per person, only the emissions for 2021 were used to stay with the most up-to-date values. This, however, involves contributions from business travels, commute and waste, which do not fit well under this category and need to be subtracted. The breakdown for the various categories was extracted using PlotDigitizer [22] from the figure: *ESO CO₂ emissions 2018–2021*, on page 111 in ESO’s

annual report 2022 [32] and is shown in Table 5. The overall emission after correcting for the contributions from business travels, commute and waste is estimated to be 19 363 tCO₂e.

Category	Emission
Energy (E)	8599
Purchase (P)	5924
Freight (F)	2675
Travel (T)	191
Commuting (C)	1083
Capital Goods (CG)	2166
Waste (W)	127
Total	20 764
Corrected	19 363

Table 5: Breakdown of the total CO₂ emissions of ESO for 2021. The contribution of the various categories are extracted using PlotDigitizer [22] from the figure: *ESO CO₂ emissions 2018–2021*, on page 111 in ESO’s annual report 2022 [32]. The corrected value is calculated as Corrected = Total – T – C – W. All emission values are provided in tCO₂e.

The public webpage of ESO lists more than 22 000 users of the observatory who share this overall emission [33]. The average annual emission per person is hence estimated as 19 363 tCO₂e/22 000 = 0.88 tCO₂e.

More refined evaluation of individual ESO facilities and experiments would be very interesting for future versions of the Kyf calculator, if additional information becomes available.

4. Institute or research centre footprint

Institutes within universities or research centres, as key academic institutions, are an integral part of a researcher’s environmental footprint. As benchmarks, the University of Freiburg, Leibniz University Hannover, and CERN are considered. The choice is based on the location of the universities in Germany, or CERN as central European HEP laboratory, and the publication of environmental reports by the institutions with sufficient information for a calculation.

In the Kyf calculator, the estimate from the University of Freiburg is used as proxy for a German university, the estimate for CERN is used as proxy for a research centre. Our analysis is based on the respective environmental reports, covering the years 2017–2019 for the Leibniz University Hannover, the years 2019–2020 for the University of Freiburg, and the years 2021–2022 for CERN. We base our estimate of the institutional footprint on one example year each (outside of the COVID-19 pandemic), and consider this to be representative for the annual footprint. Future assessments will test this assumption.

The carbon footprint of the institutions is assessed across several categories including electricity, heating/cooling, water, waste, and procurement. The section offers a detailed comparison between these entities, highlighting the diversity and scale of their emissions. Special attention is given to the significant role of procurement in contributing to the overall carbon footprint of universities and research centres.

Energy consumption DESY 2021

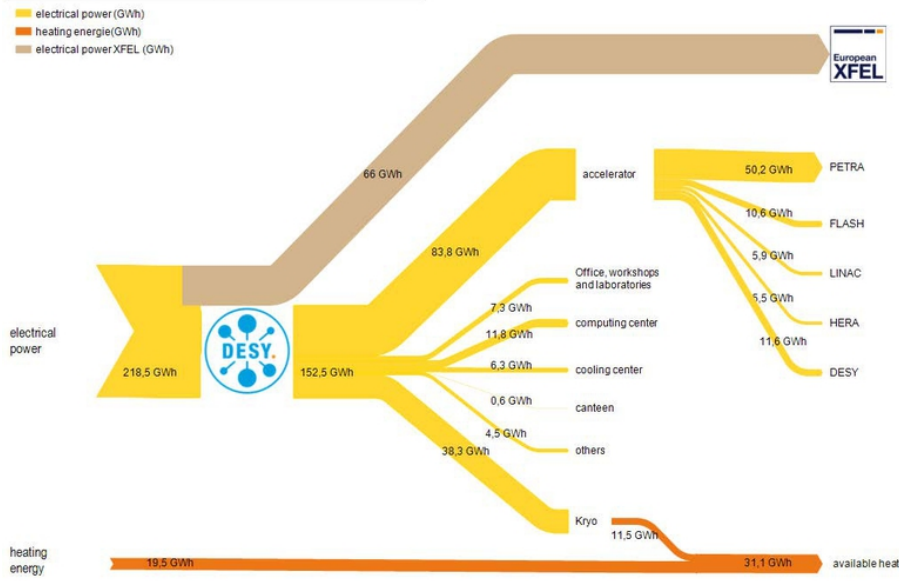


Figure 1: DESY energy consumption in 2021 [28]. Electrical power consumption (yellow) is split into consumption by the European XFEL (brown) and DESY (yellow). Heat consumption (orange) contains a contribution from heat recovery from cryogenics plants which is provided for heating and hot water supply to buildings on the DESY campus.

4.1. University of Freiburg

The environmental footprint for the University of Freiburg is based on the environmental report for 2019/2020 [34], published in 2021. The numbers for 2019 are used as the most recent, pre-pandemic numbers considered to be representative for the annual consumption of the university.

Emissions of the University of Freiburg are included for the categories: Electricity, heating/cooling, water, waste, and procurement. Numbers for vehicle fleet and business travel are provided as well, but are considered separately in the Kyf calculator and are therefore not listed here. The numbers provided for each of the used categories are reproduced in Table 6. Additional detail on the numbers for procurement can be found in Appendix B.

Category	Emissions [tCO ₂ e]
Electricity	2431 (19 224)
Heating/Cooling	13 584
Water	14
Waste	577
Procurement	14 486
Total	31 092 (47 885)

Table 6: Breakdown of the total CO₂ emissions of the University of Freiburg for 2019 [34], summing all categories except *Vehicle fleet + business travel* which is considered separately in the Kyf calculator. Electricity values are provided nominally using green electricity supply. The values in brackets provide the numbers using electricity produced with the German electricity mix. The conversions to tCO₂e are conducted by the University of Freiburg.

The total annual footprint of the University of Freiburg, excluding vehicle fleet and business travel which are considered

separately in the Kyf calculator, is estimated as 31 092 tCO₂e (47 885 tCO₂e) using green electricity (the German electricity grid mix). The University of Freiburg obtains green electricity from certified water-power plants [34]. The largest individual contributor for the University of Freiburg, when considering green electricity supply, is procurement which corresponds to 87 % of the emissions from other categories (excl. vehicle fleet + business travel).

The environmental footprint of the University of Freiburg is distributed over the members of the university (students and employees) which are determined as 31 147 from the environmental report [34]. The institutional footprint per person per year therefore amounts to 1.00 tCO₂e (1.54 tCO₂e) using green electricity (the German electricity grid mix).

4.2. Leibniz University Hannover

The environmental footprint of the Leibniz University Hannover is estimated based on the environmental report for 2017–2019 [35], using numbers from 2019 for direct comparison to the numbers from the University of Freiburg in Section 4.1. Numbers for the Leibniz University Hannover, provided in the environmental report, largely specify the original consumption, hence the conversion to tCO₂e is performed in this study.

Emissions for the Leibniz University Hannover are provided for the categories: Electricity, Heating/Cooling, Water, and Waste. Numbers for procurement are not provided. While the total footprint is therefore not comparable to the one from the University of Freiburg, for the categories except procurement, the numbers from the Leibniz University Hannover provide an interesting cross-check.

Consumption numbers, as provided by the Leibniz University Hannover, conversion factors and CO₂ emissions

are listed in Table 7. The conversion factors for green (conventional) electricity are used as 35 gCO₂e/kWh (416 gCO₂e/kWh) [29] as in Section 3.2. The conversion factor of 98.7 kgCO₂e/MWh [36] (including green house gas emissions other than CO₂) for heating is obtained from the energy provider *enercity* of the Leibniz University Hannover, which is specified to use district heating. The climate impact for water consumption assumes that the used water is drinking water, and the conversion factor of 0.35 gCO₂e/l is obtained from a study comparing the climate impact of bottled vs. tap water [37]. The total amount of waste in 2019, as well as the amount of toxic waste (*Sonderabfall*) in 2019, are read off from two figures contained in the environmental report 2017–2019 by the Leibniz University Hannover [35]. The conversion factors for the CO₂ emissions for waste are not provided in that report, however, in the environmental report by the University of Freiburg [34] sufficient information is provided to calculate conversion factors².

The total emissions for the Leibniz University Hannover are estimated to be 8001 tCO₂e (30 351 tCO₂e), with green (conventional) electricity production. Comparing only the equivalent categories, the emissions of 8001 tCO₂e in case of green electricity are in contrast with 16 606 tCO₂e for the University of Freiburg. The main difference results from the emissions for heating/cooling, where district heating for the Leibniz University Hannover generates significantly fewer emissions than the heating/cooling used at the University of Freiburg. In the latter case, the usage of ground water for cooling is specified, but no information on the type of heating by the University of Freiburg is provided.

The number of students at the Leibniz University Hannover is given in the environmental report 2017–2019 [35] as 29 781, and the number of employees as 4948, summing to 34 729 members of the Leibniz University Hannover. This results in emissions per person per year of 0.23 tCO₂e (0.87 tCO₂e) with green (conventional) electricity supply, with the caveat of not accounting for procurement.

Given the lack of information on procurement for the Leibniz University Hannover, the larger emissions for heating/cooling by the University of Freiburg and approximate similarity in the required other numbers, the values obtained for the University of Freiburg are used as conservative estimate for the institutional footprint of a university.

4.3. Research centre CERN

The environmental footprint for CERN as research centre is based on the values for 2022 (post-pandemic), listed in the newest environmental report for 2021–2022, published in 2023 [20].

²For the University of Freiburg, 88 t of toxic waste are specified to correspond to 24 % of the total amount of emissions from waste, which are given as 577 tCO₂e. This results in a conversion factor of 1.57 tCO₂e/t for toxic waste. The remaining 1019 t of waste for the University of Freiburg are specified to generate 76 % of the emissions, resulting in a conversion factor of 0.43 tCO₂e/t for other waste. These conversion factors are transferred to the waste of the Leibniz University Hannover, assuming implicitly a similar waste composition within the two categories and a similar treatment by the two universities.

The categories considered are similar to the ones for University of Freiburg and Leibniz University Hannover: *Electricity*, *Heating (gas+fuel)* and *Other (scope 1)*, *Water purification*, *Waste*, *Procurement*. A value for business travel is provided as well, but will be considered separately in the professional footprint of the Kyf calculator and is therefore dropped here. Values for catering and personal commutes are provided by the CERN environmental report, in addition; however, in the Kyf calculator, food, diet choices and commute are considered as part of the personal footprint, and are therefore removed from the institutional footprint to avoid double counting. The numbers for each of the employed categories are provided in Table 8.

Emissions for electricity correspond to 5 % of the total electricity-related emissions for 2022, which is specified in the CERN environmental report 2021–2022 [20] as electricity component required for powering the campus. Though not explicitly specified in the report, the effective conversion factor for electricity consumption to CO₂ emissions can be derived as 52 tCO₂e/GWh (= gCO₂e/kWh) from the total electricity consumption in 2022 of 1215 GWh, corresponding to emissions of 63 161 tCO₂e, specified for scope 2 in 2022. Electricity at CERN largely comes from low-carbon nuclear-power plants from France, resulting in a conversion factor significantly lower than the one from the conventional German grid mixture, but still slightly larger than electricity based on renewables, discussed in Section 3.2. The numbers for *Heating (gas+fuel)* and *Other (scope 1)* are obtained from the total scope-1 emissions minus emissions for *LHC experiments: Particle detection* and *LHC experiments: Detector cooling* as well as *Other experiments*, where the LHC-related emissions are considered as part of the experimental contribution, discussed in Section 3.1. The value for the sum of the LHC and non-LHC experimental contributions has been obtained using PlotDigitizer [22] (also see Appendix A). Additional detail on the composition of the procurement category are given in Appendix B.

The total emissions for CERN as a research centre in 2022 sum to 121 433 tCO₂e (16 459 tCO₂e) including (excluding) procurement. They are dominated by the footprint of procurement, followed by heating (gas+fuel), where heating reaches a similar level as for the University of Freiburg. A split up of the emissions from procurement is provided by the CERN environmental report 2021–2022 [20], and discussed further in Appendix B. It is important to note that the emissions from procurement at CERN do not only cover those related to CERN as an institute, but also those related to the experiments, accelerator facilities, as well as future accelerator developments. Some procurement categories such as *Civil engineering, building and technical services* appear more related to the infrastructure of the accelerator and experimental complex; different categories such as *Other* that includes office supplies, furniture, etc. seem more related to CERN as an institute. A clear separation of the procurement categories belonging to CERN as an institute is however not possible. In the future, improved assignment can be done if more granular information becomes available. For the moment, procurement is fully assigned to the CERN institute footprint.

Emissions from electricity and waste play a smaller role in

Category	Consumption	Conversion factor	Emissions [tCO ₂ e]
Electricity	58.66 GWh	35 gCO ₂ e/kWh (416 gCO ₂ e/kWh) [29]	2053 (24 403)
Heating/Cooling	50.01 GWh	98.7 kgCO ₂ e/MWh [36]	4936
Water	696 000 m ³	0.35 g/l [37]	244
Waste	1620 t		
... Toxic waste	63 t	1.57 tCO ₂ e/t [34]	99
... Other waste	1557 t	0.43 tCO ₂ e/t [34]	670
Total			8001 (30 351)

Table 7: Breakdown of the total CO₂ emissions of the Leibniz University Hannover. Consumption values are taken from the environmental report 2017–2019 [35]. Electricity values are provided nominally using green electricity supply. The values in brackets provide the numbers using electricity produced with the German electricity mix. Sources for the conversion factors are indicated, and further explained in the text. Note that the sums are calculated with more decimal places than indicated, resulting in small differences to the sums of the listed values.

Category	Emissions [tCO ₂ e]
Electricity	3158
Heating (gas+fuel) + Other	11 250
Water purification	176
Waste	1875
Procurement	104 974
Total	121 433
Total without Procurement	16 459

Table 8: Breakdown of the total CO₂ emissions of CERN as research institute for 2022 [20]. The categories Business travel and Personnel commutes are considered separately in the Kyf calculator, and thus not listed here. The conversions to tCO₂e are conducted by CERN.

the carbon footprint of CERN as an institute. Differences in the electricity consumption to the university footprints can be primarily attributed to different conversion factors for the type of used electricity. The electricity consumption of the CERN campus in GWh is comparable to that of the University of Freiburg and the Leibniz University Hannover³.

The evaluation of an *effective CERN population* needs to consider that at any time during the year, a certain fraction of CERN users is present at CERN, using electricity, water, heating, etc. and thus contributing to the institutional footprint. The total number of CERN personnel employed by CERN (Employed Members of Personnel - MPE) in 2022 amounts to $N_{\text{MPE}} = 3558$ [38], including staff and CERN fellows. The total number of Associated Members of Personnel (MPA), including CERN users as largest subcategory, corresponds to $N_{\text{MPA}} = 13\,376$ in 2022 [38]. The average presence for MPAs at CERN is evaluated as a weighted average of the *Yearly Presence* of CERN users at CERN, using the midpoint of the percentage bins in Table 11 of Ref. [38] for weighting. This results in an average presence $\bar{p} = 27.9\%$ for MPAs at CERN. The effective CERN population, N_{eff} , is thus calculated as:

$$N_{\text{eff}} = N_{\text{MPE}} + \bar{p} \cdot N_{\text{MPA}},$$

³The electricity consumption for the CERN campus is 5% of 1215 GWh in 2022, corresponding to 60.75 GWh vs. about 50 GWh for the University of Freiburg and 58.66 GWh for the Leibniz University Hannover

and, numerically, determined to be $N_{\text{eff}} = 7295$.

The institutional footprint per person per year for CERN as research institute is estimated to be 16.65 tCO₂e (2.26 tCO₂e) including (excluding) procurement. This is, also excluding procurement, larger than the institute footprint of the University of Freiburg, discussed in Section 4.1. Given the larger experimental facilities at the research centre, higher per-researcher emissions at a research centre compared to a university are expected. The impact of procurement at CERN as an institute is artificially increased, since it also includes contributions relevant to the experiments, accelerators and future developments, which cannot be separated at the moment. The estimate of emissions from procurement at CERN are based on the Greenhouse Gas Protocol spend-based method, which – though already rather advanced – is acknowledged in the CERN environmental report 2021-2022 [20] to have limitations and variable degrees of uncertainty. CERN started the *Environmentally Responsible Procurement Policy Project (CERP3)* in September 2021, to improve the environmental impact of procurement in the future.

5. Computing footprint

Most of research in physical sciences today relies on having High Performance Computing (HPC) Clusters to enable breakthroughs and make advancements within the various sub-fields of physics. Hence, it is essential to consider the environmental impact of such computing clusters. Sustainable research and accelerating scientific progress is very much dependent on rise of awareness of our resource usage [39].

Typical HPC usage involves researchers submitting jobs to computational clusters via a scheduler or interactively. For each job, specific requirements are defined, including the number of CPU-cores or GPUs⁴ needed and a defined time window for execution. For a carbon footprint, average idle times as well as

⁴We do not detail GPU power consumption by individual CUDA cores [40] for two main reasons: the standard power specification of 250W for a PCIe A100 GPU offers a reliable estimate, and the real-world application of GPUs does not involve partitioning by CUDA cores, rendering such a breakdown impractical here.

surplus-power, e.g. due to HPC cooling, need to be considered as well.

The carbon footprint averaged over a year is thus estimated as:

$$\text{Total Footprint [tCO}_2\text{e]} = f_{\text{PUE}} \cdot f_{\text{overh}} \cdot n_{\text{WPC}} \cdot f_{\text{conv}}, \quad (5)$$

where f_{PUE} denotes the HPC's *Power Usage Effectiveness* (PUE) [41], f_{overh} is an overhead factor to account for power consumption of the HPC when its computing cores are idle⁵, n_{WPC} accounts for the *Workload Power Consumption* (WPC), and f_{conv} is the conversion factor from kWh to gCO₂e.

The yearly WPC is estimated taking into account the usage of CPUs and GPUs separately as:

$$n_{\text{WPC}} = p_{\text{CPU-core}} \cdot l_{\text{core-h, CPU}} + p_{\text{GPU}} \cdot l_{\text{h, GPU}}, \quad (6)$$

where $p_{\text{CPU-core}}$ is the power consumption in kW for each CPU core and $l_{\text{core-h, CPU}}$ is the CPU workload measured in core hours. GPU usage is calculated with p_{GPU} representing the power consumption in kW per GPU and $l_{\text{h, GPU}}$ is the total number of hours the GPU is used for.

For the Kyf calculator, the following values are used as default values for an individual researcher's computing footprint. For f_{PUE} , a value of 1.5 has been chosen, which is listed in the CERN environmental report 2021–2022 [20] as global average PUE for large data centres, and which has been declared as the target to be reached by 1 July 2027 for computing centres starting operations before 1 July 2026 in the German law for the improvement of energy efficiency (*Energieeffizienzgesetz - EnEfG*, §11(1)) [42]. The idle-time overhead factor f_{overh} has been estimated by comparing the system power consumption of the *Hawk* supercomputer at the HPC Stuttgart [43] at full load (LinPack operation) (4.1 MW) to normal operation (3.5 MW). The resulting factor of 1.17 is used as default idle-time overhead factor. As conversion factor f_{conv} , the same values as discussed in Section 3.2 are employed, based on Ref. [29]: 416 gCO₂e/kWh (35 gCO₂e/kWh) for a conventional (green) electricity provision at the HPC. Finally, 7.25 W is the default value set for the CPU power consumption per core along with a default power consumption of 250 W per GPU. The CPU value is obtained from the DESY Maxwell cluster with AMD EPYC 75F3 CPU cores [44]. The GPU value is the median of a range, 150–350 W, reported on a forum of NVIDIA GPU users [45]. Both these systems are fairly recent, so the power usages should be representative of newer HPC processing units. The usage load in core-hours for CPU and GPU usage, $l_{\text{core-h, CPU}}$ and $l_{\text{h, GPU}}$, needs to be provided by the researcher when using the Kyf calculator.

The computing footprint estimate can be further personalised by adjusting f_{PUE} , if calculations have been done, for example, at the very new CERN computing centre which targets a PUE

value of 1.1 [20], or by changing f_{overh} to a different value, if better or worse HPC load factors have been obtained. It can also be switched to green electricity, with conventional electricity being used as default.

In recent years, HPC centres have been implementing system-generated reports that inform their users about their usage with high transparency. Resources like the *Production and Distributed Analysis* (PanDA) client [46] or API [47] can also be used by users or software developers to monitor group or individual workload on a system. If the annual carbon footprint is thus known precisely, this can also be entered directly in tCO₂e.

For convenience, four scenarios discussed in the following are provided, based on the estimated usage level: low, medium, high and extremely high. Several factors come into play when deciding whether to utilise a CPU or a GPU for a particular computational task. These factors include the availability of suitable software and libraries, memory requirements, considerations related to parallelisation, as well as potential bottlenecks in data transfer rates. As a result, simulations and analyses are tailored to the specific needs and research objectives of individual researchers. The provided examples thus serve as rough approximations only, and CPU vs. GPU usage cannot necessarily be interchanged easily.

- Case for low usage

Example: A graduate student submits several jobs per week each needing between one to four CPU cores. The consumption corresponds to an average of 4000 CPU core-h used per month resulting in an annual footprint as follows:

$$\begin{aligned} \text{Footprint} &= 1.5 \times 1.17 \times 0.00725 \text{ kW} \\ &\quad \times 12 \times 4000 \text{ CPU core-h/month} \\ &\quad \times 416 \text{ gCO}_2\text{e/kWh} \\ &= 0.25 \text{ tCO}_2\text{e} \end{aligned}$$

- Case for medium usage

Example: A doctoral student or post-doctoral researcher, involved in data analysis 70-100% of their time, submits jobs over the year. For this case, the top five ranked users at the Uni-Freiburg HPC called the Black-Forest Grid (BFG) are used as a blueprint, giving 30 000 CPUcore-h per month. The resulting annual footprint is as follows:

$$\begin{aligned} \text{Footprint} &= 1.5 \times 1.17 \times 0.00725 \text{ kW} \\ &\quad \times 12 \times 30\,000 \text{ CPU core-h/month} \\ &\quad \times 416 \text{ gCO}_2\text{e/kWh} \\ &= 1.91 \text{ tCO}_2\text{e} \end{aligned}$$

- Case for high usage

Example: An accelerator scientist studies accelerator performance with particle tracking codes and semi particle-in-cell (PIC) codes. The studies are both memory and computationally demanding. We assume 2500 GPU h

⁵Generally, an HPC has to estimate the number of cores it operates by predicting the requirements by its users. If too few cores are operated, it leads to long waiting times for jobs to start, but no idle operation time. If too many cores are available, idle times become too large. HPCs will thus aim for a small fraction of idle time, which needs to be considered in the carbon footprint.

used per month with code optimised for GPUs (equivalent to 80 000 CPU core-h per month).

$$\begin{aligned} \text{Footprint} &= 1.5 \times 1.17 \times 0.25 \text{ kW} \\ &\quad \times 12 \times 2500 \text{ GPU h/month} \\ &\quad \times 416 \text{ gCO}_2\text{e/kWh} \\ &= 5.48 \text{ tCO}_2\text{e} \end{aligned}$$

- Case for extremely high usage

Example: A researcher runs PIC simulations or high-resolution imaging analysis. This corresponds to a usage of 8000 GPU h per month (equivalent to 300 000 core-h per month on CPUs).

$$\begin{aligned} \text{Footprint} &= 1.5 \times 1.17 \times 0.25 \text{ kW} \\ &\quad \times 12 \times 8000 \text{ GPU h/month} \\ &\quad \times 416 \text{ gCO}_2\text{e/kWh} \\ &= 17.52 \text{ tCO}_2\text{e} \end{aligned}$$

It is important to acknowledge that the calculations presented here are based on the assumption of optimal core utilisation in HPCs. In practice, however, it is often the case that not all cores are used efficiently, leading to unnecessary energy consumption.

The environmental costs associated with data centres for long-term storage require significant amounts of electricity and water to operate servers and cooling systems. The large scale resources used by experimental collaborations or at institutes are assumed to be accounted for within their respective categories. Within the individual computing footprint, the environmental contribution of data storage is assumed to be small compared to that of actively running jobs and is therefore neglected. If we obtain data that such costs for an individual are high, we will include this contribution in future iterations. If significant amounts of data are stored at a location other than the institute, such as on a commercial cloud, e.g. Microsoft OneDrive [48] or Google Drive [49], an additional CO₂ emission contribution can however be added, based e.g. on the Microsoft emissions impact dashboard [50], or the Google’s Carbon Footprint app [51].

6. Business travel footprint

Travel constitutes another crucial component of High Energy Physics (HEP). The importance of in-person events became notably evident during the COVID-19 pandemic, where their absence made discussions and collaborations more challenging, prompting a reconsideration of our methodologies. In light of this realisation, a meticulous assessment of travel-associated CO₂ emissions is imperative. Business travel, including transportation and accommodations, significantly contributes to CO₂ footprints. Efforts to comprehend and mitigate these emissions involve scrutinising various transportation modes, such as long-distance buses, trains, personal cars, and air travel, each exerting diverse impacts on our environmental footprint [11, 52].

Comparison of CO₂ emissions from various modes of transport are briefly discussed in Appendix C. Additionally, the emissions from factors such as accommodation and event venues play a role, emphasising the need to evaluate the average CO₂ emissions of hotel rooms per night and event venues per day for an individual [53]. Benchmark values used for the Kyf calculator are documented in Table 9. These values are estimated using travel, hotel stay and meeting room usage scenarios in Germany. The footprint corresponding to the event venue assumes an area of 4 m² per person.

Source of Emission	Emission Factor
Long-distance Buses	0.031 kgCO ₂ e/km
Long-distance Trains	0.031 kgCO ₂ e/km
Personal Car	0.17 kgCO ₂ e/km
Flights within Europe	130 kgCO ₂ e/h
Transcontinental Flights	170 kgCO ₂ e/h
Hotel room	12 kgCO ₂ e/night
Event venue	0.19 kgCO ₂ e/day

Table 9: List of dominant contributors to the CO₂ footprint of a business trip with the respective CO₂-equivalent emission value for an average individual in the German scenario.

It is important to note that some institutes, such as the University of Freiburg, compensate for all flights taken by its employees for business trips. The Kyf calculator provides an option for showing the amount of carbon footprint, which was compensated. This might be extended to other sections of the Kyf calculator in future iterations.

Using the values from Table 9, it is possible to obtain a rudimentary estimate for a business trip. Three benchmark scenarios are presented here.

6.1. Train travel within Europe

For someone in Freiburg attending a conference in Hamburg lasting 5 days and travelling by long-distance trains, the total CO₂ emissions are a sum of the following three contributions:

- Travel: Given a one-way distance of 800 km, the footprint for the travel with long-distance trains (both ways) is:

$$\begin{aligned} \text{Footprint (travel)} &= 2 \times 800 \text{ km} \times 0.031 \text{ kgCO}_2\text{e/km} \\ &= 49.6 \text{ kgCO}_2\text{e} . \end{aligned}$$

- Hotel: For a conference from Monday to Friday, a hotel reservation of 5 nights with check-in on Sunday and check-out on Friday is assumed. The footprint for the hotel room is:

$$\begin{aligned} \text{Footprint (hotel)} &= 5 \text{ nights} \\ &\quad \times 12 \text{ kgCO}_2\text{e/night} \\ &= 60 \text{ kgCO}_2\text{e} . \end{aligned}$$

- Venue: Assuming that the conference venue is occupied for 8 hours on all 5 days of the conference, the footprint

for the event venue is:

$$\begin{aligned}\text{Footprint (venue)} &= 5 \text{ days} \times 0.19 \text{ kgCO}_2\text{e/day} \\ &= 0.95 \text{ kgCO}_2\text{e}.\end{aligned}$$

The total CO₂ emission for this benchmark scenario is given by the sum of the three contributions:

$$\begin{aligned}\text{Total Footprint} &= \text{Footprint}(\text{travel} + \text{hotel} + \text{venue}) \\ &= 49.6 \text{ kgCO}_2\text{e} + 60 \text{ kgCO}_2\text{e} + 0.95 \text{ kgCO}_2\text{e} \\ &\approx 111 \text{ kgCO}_2\text{e}.\end{aligned}$$

6.2. Flight travel within Europe

Considering the same scenario as in the previous benchmark, but changing the mode of transport from train to flight, which requires 1.5 hours for the same distance of 800 km one way, the travel contribution increases to:

$$\begin{aligned}\text{Footprint (travel)} &= 2 \times 1.5 \text{ h} \times 130 \text{ kgCO}_2\text{e/h} \\ &= 390 \text{ kgCO}_2\text{e}.\end{aligned}$$

The change to flight as transport mode therefore yields a travel footprint that is 5.4 times larger compared to travel by train. The total footprint for the entire business trip in this case is estimated as:

$$\begin{aligned}\text{Total Footprint} &= 390 \text{ kgCO}_2\text{e} + 60 \text{ kgCO}_2\text{e} \\ &\quad + 0.95 \text{ kgCO}_2\text{e} \\ &\approx 451 \text{ kgCO}_2\text{e}.\end{aligned}$$

To consider an example where travelling by train would not be considered practical, another scenario for a person based in Freiburg attending a conference lasting 5 days in Thessaloniki, Greece is considered. A direct flight from Basel to Thessaloniki takes about 2.5 hours for one way. This results in a travel contribution of:

$$\begin{aligned}\text{Footprint (travel)} &= 2 \times 2.5 \text{ h} \times 130 \text{ kgCO}_2\text{e/h} \\ &= 650 \text{ kgCO}_2\text{e}.\end{aligned}$$

Taking the same contributions for hotel and venue calculated in Section 6.1, the total footprint for the entire business trip in this case is estimated as:

$$\begin{aligned}\text{Total Footprint} &= 650 \text{ kgCO}_2\text{e} + 60 \text{ kgCO}_2\text{e} \\ &\quad + 0.95 \text{ kgCO}_2\text{e} \\ &\approx 711 \text{ kgCO}_2\text{e}.\end{aligned}$$

6.3. Flight travel across continents

This benchmark scenario considers a person travelling to Seoul (South Korea) from Freiburg for a summer school lasting 2 weeks. As in the previous benchmark scenarios, the three contributions are estimated as follows:

- **Travel:** A one-way travel requires a long-distance train from Freiburg to Frankfurt (275 km) followed by an transcontinental flight from Frankfurt to Seoul (12 hours). The footprint of the return trip is estimated as:

$$\begin{aligned}\text{Footprint (travel)} &= 2 \times (275 \text{ km} \times 0.031 \text{ kgCO}_2\text{e/km} \\ &\quad + 12 \text{ h} \times 170 \text{ kgCO}_2\text{e/h}) \\ &= 4097 \text{ kgCO}_2\text{e}.\end{aligned}$$

- **Hotel:** For a summer school lasting 2 weeks, a Hotel reservation of 14 nights is assumed. The footprint for the hotel room is:

$$\begin{aligned}\text{Footprint (hotel)} &= 14 \text{ nights} \\ &\quad \times 12 \text{ kgCO}_2\text{e/night} \\ &= 168 \text{ kgCO}_2\text{e}.\end{aligned}$$

- **Venue:** Assuming that the conference venue is occupied for 8 hours on all 10 business days of the summer school, the footprint for the event venue is:

$$\begin{aligned}\text{Footprint (venue)} &= 10 \text{ days} \times 0.19 \text{ kgCO}_2\text{e/day} \\ &= 1.9 \text{ kgCO}_2\text{e}.\end{aligned}$$

The total footprint for the entire trip is estimated as:

$$\begin{aligned}\text{Total Footprint} &= 4097 \text{ kgCO}_2\text{e} + 168 \text{ kgCO}_2\text{e} \\ &\quad + 1.9 \text{ kgCO}_2\text{e} \\ &\approx 4267 \text{ kgCO}_2\text{e}.\end{aligned}$$

The duration of this trip is extended from the typical 5 day duration observed in other scenarios to recognise that longer-distance trips often require more justification to be funded, e.g. longer educational programs. It must be noted however, that the footprint of hotel stay and event venue remains small compared to that of the travel itself. This implies that the carbon footprint of a shorter trip would be similar as long as the footprint of the flight travel is not compensated. Note that hotel and venue footprints are based on German numbers and are assumed to be valid in the international context as well. This assumption might be refined in a future version of the Kyf calculator.

7. Professional footprint example

An example professional footprint of an early-career researcher in Germany is calculated for a benchmark doctoral student working on one of the large LHC experiments at CERN, being employed by a university in Germany, which is supplied with conventional electricity, medium computing level, where the HPC also uses conventional electricity, and who does two 1-week trips in Germany by train (for example, a DPG spring meeting and a national collaboration meeting), one flight travel within Europe for a week (for example, a conference in Thessaloniki, Greece), and one two-week flight travel across continents (for example, a summer school in Seoul, South Korea) during one particular year. The combined professional footprint

is listed in Table 10, and shown in Figure 2, in comparison with the personal footprint and the remaining carbon budget per person per year, given the climate warming limitation goals discussed in Section 1.

Category	Emissions [tCO ₂ e]
Large LHC experiment	11.91
University (German electricity mix)	1.54
Computing (medium)	1.91
Travel (2xT, 1xF(E), 1xF(C))	5.20
Total	20.56

Table 10: Professional CO₂ footprint of a benchmark doctoral researcher, working on one of the large LHC experiments, employed by a German university, with medium computing usage level and two intra-Germany travels by train (T), one intra-Europe flight travel (F(E)) and one cross-continental flight travel (F(C)) per year.

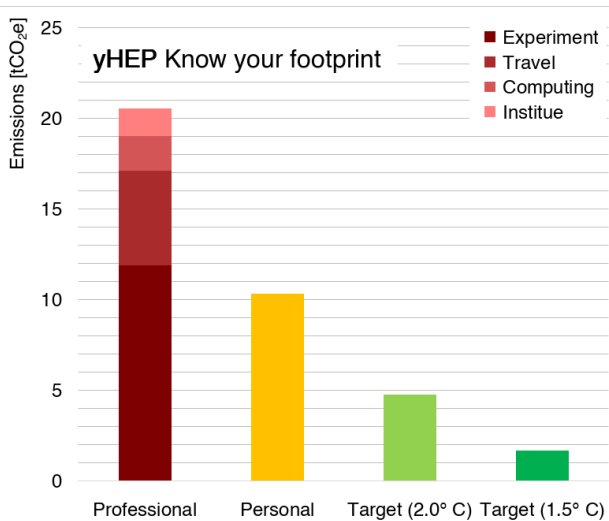


Figure 2: Professional CO₂ footprint of a benchmark doctoral researcher, working on one of the large LHC experiments, employed by a German university, with medium computing usage level and travel as discussed in the text, in comparison with the average personal footprint in Germany, as well as the remaining carbon budget per person per year of 1.7 tCO₂e (4.8 tCO₂e) for a maximum temperature increase of 1.5 °C (2.0 °C).

The annual professional footprint of the benchmark doctoral researcher amounts to 20.56 tCO₂e, which can be compared to the average private footprint of 10–11 tCO₂e per person per year in Germany [8, 9, 11]. The professional footprint is clearly dominated by work in a large LHC experiment, followed by travel. Work on a smaller HEP experiment using a green electricity supply or an astronomy experiment would have resulted in a smaller experimental footprint, leaving the travel footprint dominant. Several cross-continental business travels per year also would result in a significantly larger travel footprint, turning it into the leading contribution. A high or extremely high usage computing level would significantly increase the computing footprint, making it instead the leading contribution. Similarly, employment at a research centre with larger laboratory facilities

could result in the institutional footprint becoming dominant.

For the benchmark doctoral researcher and several other scenarios, the professional footprint thus exceeds the personal footprint, both of which by far exceed the remaining carbon budget per person per year of 1.7 tCO₂e (4.8 tCO₂e) for a maximum temperature increase of 1.5 °C (2.0 °C), as discussed in Section 1 and displayed in Figure 2. It is therefore crucial, that not only personal consumption patterns, including the societal boundaries and incentives, are adjusted, but that also the way research is performed is transformed towards a more sustainable and environmentally friendly practice. The Kyf calculator provides a first idea for an individual researcher where these transformations have to happen first and most urgently, such that the biggest and easiest contributions are addressed first, immediately followed by tackling the more challenging ones. Environmental reports by universities, research centres, experiments, computing centres, etc. provide key information for this purpose, and should become mandatory as soon as possible, followed by action (plans) for the reduction of the carbon footprint. It is clear that changes towards a more sustainable research practice require resources, both financially and personnel-wise. This fact needs to be considered by funding agencies in their future decision-making. The costs for inaction will eventually be higher than those for coordinated and targeted action now.

8. Conclusions

Know your footprint is an essential early step in tackling climate change and for motivating sustainable behaviour. This holds both in the personal as well as in professional life.

In an energy-hungry sector, such as High Energy Physics (HEP) and related fields, awareness is key to start moving towards a more sustainable research practice. The *young High Energy Physicists* (yHEP) association launched the *Know your footprint* (Kyf) campaign to evaluate the CO₂-equivalent emissions generated by HEP-related research.

In the four categories: *Experiments*, *Institutes*, *Computing* and *Travel*, we have evaluated the carbon footprint of research activities. A user-oriented tool is provided [10] to allow for the simple evaluation of the professional footprint of an individual researcher in, or associated to, Germany. The results show that for various combinations, the professional footprint significantly exceeds the personal footprint of an average citizen in Germany, which already exceeds the maximal remaining carbon budget per person per year, allowed for a maximum temperature increase of 1.5 °C (2.0 °C), by factors of around 6 (around 2). Targeted and prompt action is therefore essential. Every gram of CO₂ saved makes a difference.

While it is encouraging to see a growing awareness among individuals and institutions of their carbon footprint, our study shows that significant work in the HEP-related research lies before us. Given that the next 10–20 years will be crucial to mitigate global warming, this work needs to start now. Carbon-footprint accounting provides us with the data to shape strategies and target measures in order to effectively reduce our carbon footprint. Scientific research, starting now, needs

to ensure that our pursuit of scientific and technological progress aligns harmoniously with a strong commitment to environmental sustainability.

Acknowledgements

Our warm thanks go to Ruth Jacobs, Srijan Sehgal, and Dima El Khechen from the yHEP management board for their constructive input on this paper and to Michael Lupberger from the yHEP management board on his feedback to the Kyf calculator. Many thanks also go to further current and former yHEP management board members for their support and constructive input to the Kyf campaign efforts: Farah Afzal, Leonel Morejon, Meike Käßner, Felipe Peña, Philipp Krönert, Alina Nasr-Esfahani, Annika Thiel. Additionally, we would like to express our gratitude for feedback on the paper and the calculator to the following colleagues: Lutz Feld (for the committee for particle physics (KET) in Germany), Uli Katz (for the committee for astro-particle physics (KAT) in Germany), Michael Block (for the committee for physics of nucleons and hadrons (KHuK) in Germany), Eric Bründermann (for the committee for accelerator physics (KfB) in Germany), Denise Völker (as head of the DESY Sustainability group), Sonja Kleiner and Luisa Ulrici (as leaders of the CERN Environment group), Frank Schlünzen (for computing inputs), and Maria Zeitz (from KlimAktiv). We thank KlimAktiv especially for the permission to reference and forward to the UBA carbon calculator for the private footprint. The authors of this paper take responsibility for any errors in this paper.

Appendix A. Digitisation of CERN scope 1 emissions

Numbers from the digitisation of the figure: *CERN scope 1 emissions for 2017–2022 by category*, from page 18 of the CERN environmental report 2021–2022 [20], reproduced in Figure A.3, can be found in Table A.11. The total scope 1 emissions from 2022 determined with PlotDigitizer [22] agree within 0.05 % with the numerical value for the total 2022 scope 1 emissions stated in the environmental report. Given resolution precision, this is considered sufficiently close.

Appendix B. Emissions from procurement

Procurement is a major source of emissions, in particular for organisations such as a university, whose core functionalities: research, teaching and knowledge transfer, can be assigned to the services sector.

The procurement-related emissions by the University of Freiburg, discussed in Section 4.1 and obtained from the environmental report 2019/2020 [34], are based on procurement data from 2017, analysed in a master thesis [54], which is unfortunately not available online. A subsequent report is accessible in Ref. [55], for which the relevant figure has been reproduced. Figure B.4 displays the scope 3 procurement distribution of the categories *Goods and services* and *Capital goods*, contained in Ref. [55]. The combined emissions listed as 15 100 tCO₂e do

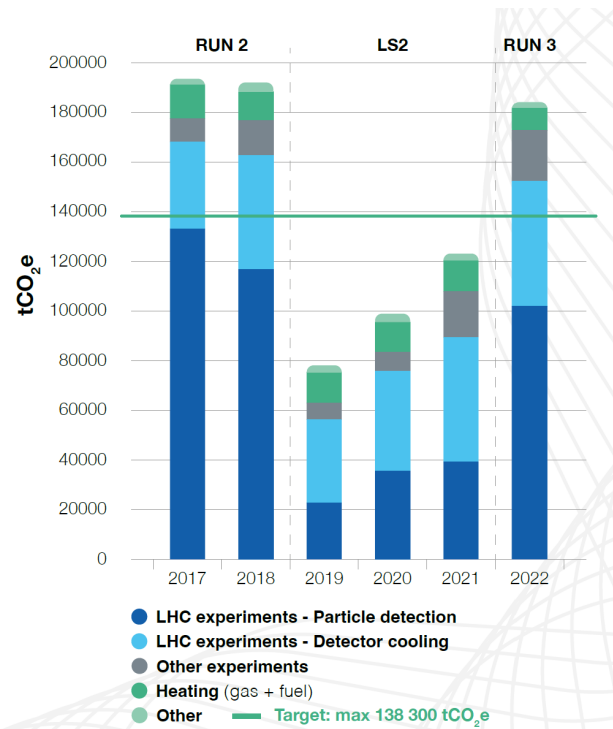


Figure A.3: CERN scope 1 emissions for 2017–2022 by category [20]. The category *Other* includes air conditioning, electrical insulation, emergency generators and the fuel consumption of the CERN vehicle fleet.

not exactly equal the value of 14 486 tCO₂e, quoted in the environmental report 2019/2020 by the University of Freiburg [34], but are very close. The displayed split-up can therefore be seen as representative of the value, quoted in the environmental report 2019/2020.

Largest contributors to the emissions from procurement are the categories: *Chemicals* (3700 tCO₂e), *Medical & Precision Instruments* (3000 tCO₂e), *Furniture & Goods n.e.c.* (1700 tCO₂e), and *Machinery n.e.c.* (1200 tCO₂e), which amount to about 64 % of the procurement-related emissions.

The large number of categories gives an idea of how difficult it is to address the reduction of procurement-related emissions; due to its large overall contribution, it remains critical though. Two approaches are possible for this purpose: demand management by the university, and *green* procurement. The choice of the best approach might differ depending on the category.

Details on procurement-related emissions by CERN are provided in the environmental report 2021–2022 [20]. The figure *Emissions by procurement family 2021–2022* from page 23 of the CERN environmental report 2021–2022 [20] is reproduced in Figure B.5.

The largest contributors to procurement-related emissions in 2022 are the following categories: *Civil engineering, building and technical services*, *Permanent services on the CERN site*, and *Mechanical engineering and raw materials*. These could be related to construction regarding buildings or machinery, which can be seen either as part of the infrastructure of the accelerator complex, usual construction and maintenance of buildings of an organisation, or engineering work, which could also be

Category	Cumulative emissions [tCO ₂ e]
LHC experiments: Particle detection	101 981
LHC experiments: Detector cooling	152 444
Other experiments	172 923
Heating (gas+fuel)	181 857
Other	184 090
Total (specified in the report)	184 173

Table A.11: Digitised values for 2022 of the CERN scope 1 emissions, extracted with PlotDigitizer [22] from Figure A.3. The values correspond to the upper edge of the bar including the specified category. The value for *Other* should therefore correspond to the total scope 1 emissions value specified in the CERN environmental report 2021–2022 [20], listed under *Total (specified in the report)*, which - given resolution precision - is sufficiently close.

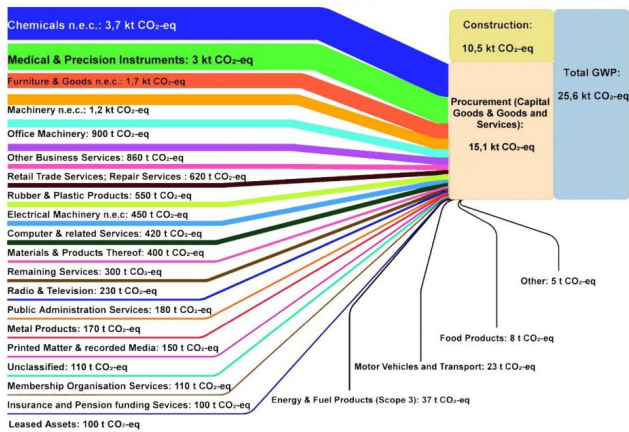


Figure B.4: Distribution of scope 3 greenhouse gas emissions of the two categories *Goods and services* and *Capital goods* for the University of Freiburg in 2017 [55]. *Construction* is listed as separate scope 3 category for comparison, but it is unclear which category in the environmental report 2019/2020 [34] this has been added to.

performed at a university. It is not possible to explicitly assign the procurement categories to the footprints of accelerators, experiments, upgrade activities, or CERN as an institute.

A direct comparison of the procurement categories to those of the University of Freiburg is not possible.

Appendix C. Emissions for various transportation modes

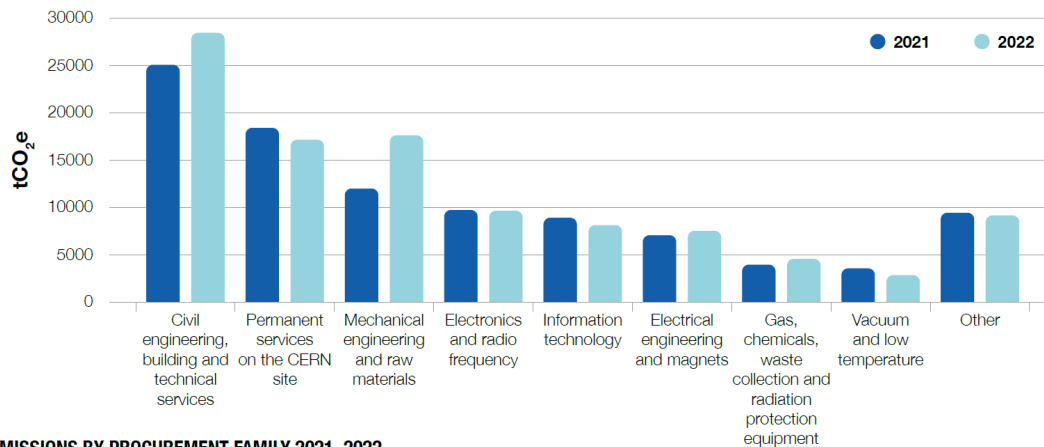
The German Federal Environment Agency (*Umweltbundesamt* - UBA) provides a comparison of CO₂ emissions for various modes of transport per person per kilometre in a table on their webpage [52]. This table represents the data collected for 2022 and is reproduced in Table C.12. For the calculation of the average emission values, an average occupancy is also estimated to obtain a comparable value for an individual across all modes of transport.

For the first version of the Kyf calculator, only long-distance trains (*Eisenbahn, Fernverkehr*), long-distance buses (*Linienbus, Fernverkehr*) and personal car (*Pkw*) were considered. The CO₂ emissions for intra-Europe and transcontinental flights were obtained from Ref. [11] in order to have the emission values corresponding to the duration of the flight rather than the

distance covered by it. This was considered to be more user-friendly for the Kyf calculator. Other modes of transportation listed in Table C.12 are primarily relevant for short-distance commute and were therefore not incorporated in the first version of the Kyf calculator. These could potentially be included in future iterations.

References

- [1] S. Arrhenius, *XXXI. On the influence of carbonic acid in the air upon the temperature of the ground*, The London, Edinburgh, and Dublin Philosophical Magazine and Journal of Science 41 (251) (1896) 237–276. doi:10.1080/14786449608620846. URL <https://doi.org/10.1080/14786449608620846>
- [2] UC San Diego and SCRIPPS Institution of Oceanography, *The Keeling Curve - Full Record*, accessed: 2023-10-22 (2023). URL <https://keelingcurve.ucsd.edu>
- [3] D. Lüthi, M. Le Floch, B. Bereiter, et al., *High-resolution carbon dioxide concentration record 650,000–800,000 years before present*, Nature 453 (2008) 379–382. doi:https://doi.org/10.1038/nature06949.
- [4] Copernicus Climate Change Service/ECMWF, *Surface air temperature for December 2023*, accessed: 2024-02-09 (2023). URL <https://climate.copernicus.eu/surface-air-temperature-december-2023>
- [5] Intergovernmental Panel on Climate Change (IPCC), *Climate Change 2021 – The Physical Science Basis: Working Group I Contribution to the Sixth Assessment Report of the Intergovernmental Panel on Climate Change*, Cambridge University Press, 2023, Ch. *Summary for Policymakers*, pp. 3–32. doi:10.1017/9781009157896.001.
- [6] United Nations, *Paris Agreement*, United Nations Treaty Series 3156 (2015) 79. URL https://treaties.un.org/doc/Treaties/2016/02/20160215%2006-03%20PM/Ch_XXVII-7-d.pdf
- [7] United Nations, *Global issues: Population*, accessed: 2023-10-22 (2023). URL <https://www.un.org/en/global-issues/population>
- [8] K. Schächtele, H. Hertle, *Die CO₂ Bilanz des Bürgers - Recherche für ein internetbasiertes Tool zur Erstellung persönlicher CO₂ Bilanzen*, Umweltbundesamt Förderkennzeichen: 206 42 110 (2007). URL <https://www.umweltbundesamt.de/sites/default/files/medien/publikation/long/3327.pdf>
- [9] S. Schunkert, J. Siewert, P. Pitz, et al., *Der UBA-CO₂-Rechner für Privatpersonen - Hintergrundinformationen*, Umweltbundesamt Forschungskennzahl: 3718 16 313 0 (2022). URL https://www.umweltbundesamt.de/sites/default/files/medien/479/publikationen/texte_97-2022_der_uba-co2-rechner_fuer_privatpersonen.pdf
- [10] young High Energy Physicists Association (yHEP), *Know your footprint*, accessed: December 2023. URL <https://yhep.desy.de/sustainability/>
- [11] Umweltbundesamt, *Carbon Calculator*, accessed: 2023-11-01 (2023). URL https://uba.co2-rechner.de/en_GB/
- [12] *LHC Machine*, JINST 3 (2008) S08001. doi:10.1088/1748-0221/3/08/S08001.



EMISSIONS BY PROCUREMENT FAMILY 2021–2022

"Other" includes: office supplies, furniture, transport, handling and vehicles; centralised expenses and codes for internal use; particle and photon detectors; health, safety and environment; optics and photonics.

Figure B.5: Emissions by procurement family 2021–2022 [20]. The category *Other* includes office supplies, furniture, transport, handling and vehicles; centralised expenses and codes for internal use; particle and photon detectors; health, safety and environment; optics and photonics.

Vergleich der durchschnittlichen Emissionen einzelner Verkehrsmittel des Linien- und Individualverkehrs im Personenverkehr in Deutschland 2022

Quelle: Umweltbundesamt, TREMOD 6.51

Verkehrsmittel	Treibhausgase ¹	Stickoxide	Partikel ⁴	Auslastung
Pkw²	166	0,32	0,013	1,4 Pers./Pkw
^L davon Elektro-Pkw	79	0,08	0,004	
^L davon Hybrid-Pkw	121	0,10	0,008	
^L davon Diesel-Pkw	173	0,52	0,015	
^L davon Benzin-Pkw	165	0,17	0,012	
Flugzeug, Inland	238³	1,03	0,011	57 %
Eisenbahn, Fernverkehr	31	0,04	0,002	46 %
Linienbus, Fernverkehr	31	0,03	0,002	52 %
Eisenbahn, Nahverkehr	58	0,18	0,005	24 %
^L davon Dieseltraktion	90	0,68	0,015	
^L davon Elektrotraktion	49	0,05	0,002	
Linienbus, Nahverkehr⁵	93	0,25	0,008	16 %
^L davon Elektrobusse	72	0,07	0,003	
^L davon Dieselbusse	96	0,27	0,008	
Straßen-, Stadt- und U-Bahn	63	0,06	0,003	15 %
E-Bike	3	0,00	0,000	1 Pers./E-Bike

g/Pkm = Gramm pro Personenkilometer, inkl. der Emissionen aus der Bereitstellung und Umwandlung der Energieträger in Strom, Benzin, Diesel, Flüssig- und Erdgas sowie Kerosin; sämtliche für Elektroantrieb ausgewiesenen Emissionsfaktoren basieren auf Werten zum durchschnittlichen Strom-Mix in Deutschland - Emissionsfaktoren, die auf unternehmens- oder sektorbezogenen Strombezügen basieren (siehe z. B. "CO2Kompass" der Deutschen Bahn AG), können daher von den in der Tabelle dargestellten Werten abweichen

¹ CO₂, CH₄ und N₂O angegeben in CO₂-Äquivalenten gemäß AR5 (5. Sachstandsbericht des IPCC)

² alle Antriebe (Benzin, Diesel, Elektro, Flüssig- und Erdgas, Hybride)

³ inkl. Nicht-CO₂-Effekte, EWF 1,1 (Hauptverkehrsflughäfen)

⁴ ohne Abrieb von Reifen, Straßenbelag, Bremsen, Oberleitungen

⁵ alle Antriebe (Diesel, Elektro, Hybride, Erdgas)

[Für Informationen zu den Emissionen aus Infrastruktur- und Fahrzeugbereitstellung siehe UBA-Broschüre "Umweltfreundlich mobil!"](#)

Table C.12: Comparison of average CO₂-equivalent emissions for various modes of transport in Germany for 2022 listed in gCO₂e [52]. For the first version of the Kyf calculator, only long-distance trains (*Eisenbahn, Fernverkehr*), long-distance buses (*Linienbus, Fernverkehr*) and personal car (*Pkw*) were used.

- [13] Home — cern, accessed: 2024-02-09.
URL <https://home.cern/>
- [14] ATLAS Collaboration, *The ATLAS Experiment at the CERN Large Hadron Collider*, JINST 3 (2008) S08003. doi:10.1088/1748-0221/3/08/S08003.
- [15] CMS Collaboration, *The CMS Experiment at the CERN LHC*, JINST 3 (2008) S08004. doi:10.1088/1748-0221/3/08/S08004.
- [16] ALICE Collaboration, *The ALICE experiment at the CERN LHC*, JINST 3 (2008) S08002. doi:10.1088/1748-0221/3/08/S08002.
- [17] LHCb Collaboration, *The LHCb Detector at the LHC*, JINST 3 (2008) S08005. doi:10.1088/1748-0221/3/08/S08005.
- [18] CERN, *CERN Environment Report – Rapport sur l’environnement 2017–2018* (2020). doi:10.25325/CERN-Environment-2020-001. URL <https://doi.org/10.25325/CERN-Environment-2020-001>
- [19] CERN, *CERN Environment Report – Rapport sur l’environnement 2019–2020* (2021). doi:10.25325/CERN-Environment-2021-002. URL <https://doi.org/10.25325/CERN-Environment-2021-002>
- [20] CERN, *CERN Environment Report – Rapport sur l’environnement 2021–2022* (2023). doi:10.25325/CERN-Environment-2023-003. URL <https://doi.org/10.25325/CERN-Environment-2023-003>
- [21] LHCb Collaboration, Framework TDR for the LHCb Upgrade II: Opportunities in flavour physics, and beyond, in the HL-LHC era (2021).
- [22] Plotdigitizer: Version 3.1.5 (2024).
URL <https://plotdigitizer.com>
- [23] ALICE Collaboration, *Collaboration Map*, accessed: 2024-01-05 (2024). URL <https://alice-collaboration.web.cern.ch/collaboration/map>
- [24] LHCb Collaboration, *The LHCb Collaboration*, accessed: 2024-01-05 (2021). URL <https://lhcb-outreach.web.cern.ch/collaboration/>
- [25] CMS Collaboration, *People Statistics*, accessed: 2024-01-05 (2022). URL <https://cms.cern/index.php/collaboration/people-statistics>
- [26] ATLAS Collaboration, *The Collaboration*, accessed: 2024-01-05 (2024). URL <https://atlas.cern/Discover/Collaboration>
- [27] DESY, *First Sustainability report* (2022). URL https://nachhaltigkeit.desy.de/sustainability_report/index_eng.html
- [28] DESY, *Energy monitoring*, accessed: 2024-01-07 (2023). URL https://nachhaltigkeit.desy.de/energy_management/energy_monitoring/index_eng.html
- [29] Electricity maps, *Germany*, accessed: 2024-01-07 (2023). URL <https://app.electricitymaps.com/zone/DE>
- [30] European Organisation for Astronomical Research in the Southern Hemisphere, *ESO Annual Report 2020*, accessed: 2023-10-16 (2021). URL https://www.eso.org/public/products/annualreports/ar_2020/
- [31] European Organisation for Astronomical Research in the Southern Hemisphere, *ESO Annual Report 2021*, accessed: 2023-10-16 (2022). URL https://www.eso.org/public/products/annualreports/ar_2021/
- [32] European Organisation for Astronomical Research in the Southern Hemisphere, *ESO Annual Report 2022*, accessed: 2023-10-23 (2023). URL https://www.eso.org/public/products/annualreports/ar_2022/
- [33] European Southern Observatory, *About ESO*, accessed: 2024-01-03 (2023). URL <https://www.eso.org/public/about-eso/>
- [34] University of Freiburg, *Umweltbericht 2019/2020* (2021). URL <https://www.nachhaltige.uni-freiburg.de/de/umweltberichte/umweltbericht-2019-2020-2>
- [35] Leibniz University Hannover, *Umweltbericht 2017-2019* (2021). URL https://www.uni-hannover.de/fileadmin/luh/content/webredaktion/universitaet/publikationen/umweltbericht/umweltbericht_17_19.pdf
- [36] Technische Universität Dresden, *Certification for the district heating system from enercity AG Hannover* (2022). URL <https://www.enercity.de/assets/cms/enercity-de/Privatkunden/Produkte/Waerme/Fernwaerme/Downloads/FW309-6.pdf>
- [37] GUTcert, *Vergleich des CO₂-Fußabdrucks von Mineral- und Trinkwasser* (2020). URL https://atiptap.org/files/studie_gutcert_pcf_wasser.pdf
- [38] CERN Annual Personnel Statistics 2022 CERN Annual Personnel Statistics 2022 (2022). URL <https://cds.cern.ch/record/2858688>
- [39] B. Bruers, M. Cruces, M. Demleitner, et al., Resource-aware research on universe and matter: Call-to-action in digital transformation (2023). arXiv:2311.01169.
- [40] Nvidia cuda cores explained, accessed: 2024-03-04. URL <https://www.techcenturion.com/nvidia-cuda-cores/>
- [41] Pue: A comprehensive examination of the metric, accessed: 2024-01-16 (2014). URL <https://www.thegreengrid.org/en/resources/library-and-tools/20-PUE:-A-Comprehensive-Examination-of-the-Metric>
- [42] Gesetz zur steigerung der energieeffizienz in deutschland, effective date: 18 November 2023. URL <https://www.gesetze-im-internet.de/enefg/BJNR1350B0023.html>
- [43] Hpe apollo (hawk), accessed: 2024-01-24. URL <https://www.hlrs.de/solutions/systems/hpe-apollo-hawk>
- [44] F. Schluenzen, Computing cluster power consumption data, private communication (2023).
- [45] How much electricity does the a100 gpu use?, accessed: 2024-01-16. URL <https://wifocuseenergy.com/optimizing-power-consumption-understanding-the-nvidia-a100s-energy-usage>
- [46] Panda dashboard, accessed: 2024-01-16. URL <https://bigpanda.cern.ch/dash/region/>
- [47] Panda system python api reference, accessed: 2024-01-16 (2020). URL <https://panda-wms.readthedocs.io/en/latest/client/rest.html>
- [48] Microsoft onedrive, <https://www.microsoft.com/en-us/microsoft-365/onedrive/online-cloud-storage>.
- [49] Google drive, <https://www.google.com/drive/>.
- [50] Microsoft onedrive emissions impact dashboard, <https://www.microsoft.com/en-us/sustainability/emissions-impact-dashboard>.
- [51] Google drive footprint calculator, <https://cloud.google.com/carbon-footprint>.
- [52] Umweltbundesamt, Emissionsdaten, accessed: 2024-02-12 (2023). URL <https://www.umweltbundesamt.de/themen/verkehr/emissionsdaten>
- [53] UBA CO₂-Rechner für Veranstaltungen (2024), accessed: 2024-03-02 (2024). URL https://uba-event-free.co2-rechner.pro/de_DE/
- [54] M. Eichler, *Evaluating Environmental Impacts of University Procurements – An Environmentally Extended Multiregional Input Output Analysis of Albert-Ludwigs-Universität Freiburg* (2020).
- [55] S. Pauliuk, M. Eichler, B. E. Durán, et al., *Treibhausgasbilanz der Universität Freiburg im Breisgau 2017*, Industrial Ecology Freiburg (IEF) Working Paper 1 (2021). doi:10.6094/UNIFR/176419. URL https://www.blog.industrialecology.uni-freiburg.de/wp-content/uploads/2021/03/Klimabilanz_Uni_Freiburg-IEF_Working_Paper_1_2021.pdf

Probing Recoil Signatures of Inelastic Dark Matter

HONG-JIAN HE,^{a,b*} YU-CHEN WANG,^{a†} JIAMING ZHENG,^{a‡}

^a T. D. Lee Institute & School of Physics and Astronomy,
Key Laboratory for Particle Astrophysics and Cosmology,
Shanghai Key Laboratory for Particle Physics and Cosmology,
Shanghai Jiao Tong University, Shanghai, China.

^b Physics Department and Institute of Modern Physics, Tsinghua University, Beijing, China;
Center for High Energy Physics, Peking University, Beijing, China.

Abstract

Different dark matter (DM) candidates could have different types of DM-lepton and/or DM-quark interactions. For direct detection experiments, this leads to diversity in the recoil spectra, where both DM-electron and DM-nucleus scatterings may contribute. Furthermore, kinematic effects such as those of the inelastic scattering can also play an important role in shaping the recoil spectra. In this work, we systematically study signatures of the light exothermic inelastic DM from the recoil spectra including both the DM-electron scattering and Migdal effect. Such inelastic DM has mass around (sub-)GeV scale and the DM mass-splitting ranges from 1keV to 30keV. We analyze the direct detection sensitivities to such light inelastic DM. For different inelastic DM masses and mass-splittings, we find that the DM-electron recoil and Migdal effect can contribute significantly and differently to the direct detection signatures. Hence, it is important to perform combined analysis to include both the DM-electron recoil and Migdal effect. We further demonstrate that this analysis has strong impacts on the cosmological and laboratory bounds for the inelastic DM.

*Email: hjhe@sjtu.edu.cn

†Email: wangyc21@sjtu.edu.cn

‡Email: zhengjm3@sjtu.edu.cn

Contents

1. Introduction	2
2. Inelastic Dark Matter Interactions for Exothermic Scattering	4
3. Electron Recoil Signals from Exothermic Inelastic Dark Matter	6
3.1. Inelastic DM-Electron Scattering	6
3.2. Inelastic DM-Nucleus Scattering.....	7
4. Limits from Direct Detection Experiments	9
4.1. Constraints by XENONnT Electron Recoil Data.....	9
4.2. Constraints by S2-Only Data of XENON1T.....	13
5. Probing Inelastic DM with Dark Photon Mediator	16
5.1. Model Realization: Inelastic DM with Dark Photon Mediator	17
5.2. Cosmological and Laboratory Constraints on Inelastic DM.....	20
6. Conclusions	24
References	25

1. Introduction

The origin and nature of dark matter (DM) have remained largely unknown so far after decades of dedicated efforts through the direct, indirect and collider searches. Such detection methods depend on how the DM interacts with the standard model (SM) particles. The DM models have provided various DM-SM interactions and are under close inspection via distinct direct search strategies. The searches for nuclear recoil (NR) have set stringent limits on the DM-nucleon scattering cross sections [1–5] on the GeV-TeV scale DM. For lighter dark matter, the nuclear recoil energy falls below the detection threshold. In contrast, an electron acquires much more recoil energy from its direct scattering with light DM particles [6–9]. The electron recoil (ER) signal is thus an important target for searching the (sub-)GeV DM candidates [10]. The electron recoil signal can also probe DM-nucleon interaction through Migdal effect [11][12]. When the DM scatters with an atomic nucleus, the nucleus gains a velocity relative to the electron cloud and may induce atomic ionization and excitation. For sub-GeV DM, this process can generate keV-scale electron recoil signals that are detectable in the direct detection experiments [13–18].

Conventionally, the DM-nucleon and DM-electron interactions are constrained independently. For DM-nucleon spin-independent (SI) interactions, constraints are usually derived by assuming identical

contributions from neutron and proton. This enhances the DM-nucleus scattering cross section by a coherence factor of A^2 , where A is the number of nucleons. However, these assumptions may be violated in various DM models. First, the DM particle in general may interact with both nucleons and electrons. Second, the DM-neutron and DM-proton interactions may not be identical or coherent within the nucleus, so they may induce a coherence factor other than A^2 , which will change not only the overall DM-nucleon event rates, but also the relative strength between DM-electron and DM-nucleon interactions. These may significantly change the constraints on different DM models.

Potential kinematic effects, such as those induced by exothermic inelastic dark matter [19–23], may further complicate the direct detection signals. In such a scenario, the DM particles consist of more than one mass eigenstates. The heavier eigenstate could be cosmologically stable when the mass-splitting between it and the lightest state is $O(\text{keV})$ for GeV-scale DM. When a heavier DM state scatters with a target atom, it converts to the lighter state and deposits energy from the mass-splitting into the kinetic energy of final states. For GeV-scale DM much heavier than the electron, such inelastic DM-electron scattering results in a peak-like ER spectrum. If the DM couples to both the electron and nucleons, this signal can be comparable to the electron recoil signal from the Migdal effect by DM-nucleus scatterings. Hence a joint analysis including both effects is important. The recent direct detection experiments already published the electron recoil data with low threshold and high sensitivity [6–8]. It is ideal to use these datasets and analyze such kinematic effects in DM interactions.

In this work, we study direct detection signatures of the light exothermic inelastic DM with keV-scale mass-splitting. Since electrons, neutrons, and protons may couple differently to the dark sector, we consider various combinations of typical couplings in the present analysis. For each case, we compute the inelastic DM-electron and DM-nucleus scattering rates, including the induced Migdal effect. We demonstrate that the DM-electron scattering spectrum is highly dependent on the mass-splitting, whereas the Migdal effect induced by DM-nucleus scattering is enhanced by the energy injection from the de-excitation of the heavier DM state. We further derive the bounds for each case by confronting the XENONnT ER data [7] and XENON1T S2-only data [9] with the joint effects of DM-electron and DM-nucleon interactions. These results are then applied to concrete DM models.

This paper is organized as follows. In Section 2, we present a generic effective theory formulation of the light exothermic inelastic DM interactions. We consider both the DM-electron scattering and DM-nucleus scattering with Migdal effect. For this we will present the benchmark scenarios of the dark charge assignments. In Section 3, we study the electron recoil signatures from both the direct DM-electron scattering and the Migdal effect (induced by DM-nucleus scattering). In Section 4, we demonstrate how direct detection experiments (such as XENON1T and XENONnT) can constrain the parameter space of the light inelastic DM. We present an explicit minimal model realization of the light inelastic DM in Section 5, and analyze constraints from both the cosmological and laboratory measurements. Finally, we conclude in Section 6.

2. Inelastic Dark Matter Interactions for Exothermic Scattering

In this section, we present a generic effective theory formulation of the light inelastic DM interactions. With this, we will study the interplay between the DM-nucleon and DM-electron interactions.

We consider a two-component dark matter with a mass-splitting Δm . We denote the lighter (heavier) component X (X') for scalar dark matter and χ (χ') for fermionic dark matter. Here X and X' are real scalar fields and form a complex scalar $\hat{X} \equiv (X + iX')/\sqrt{2}$ in the limit $\Delta m \rightarrow 0$. Similarly, χ and χ' are Weyl spinors and can form a pseudo-Dirac spinor $\hat{\chi} \equiv (\chi_1, \chi_2^\dagger)^T$, where $\chi_{1,2} \equiv (\chi \mp \chi')/\sqrt{2}$. When the situation is not sensitive to the spin-statistics of the DM, we will only use the notation (X, X') for both the scalar and fermionic DM. Consider that the DM particles interact with the visible sector through a vector mediator whose effect can be described by the generic dimension-6 effective operators at low energy,

$$\mathcal{O} = \frac{c}{M^2} J_{X\mu} J_{\text{vis}}^\mu, \quad (2.1)$$

where the mediator mass M serves as the cutoff scale and the operator \mathcal{O} is invariant under the SM gauge group. In the above, we denote the dark current $J_{X\mu}$ for scalar DM (X, X'), and this notation is replaced by $J_{\chi\mu}$ for the fermionic DM (χ, χ'). The two dark currents J_X^μ and J_χ^μ take the following forms:

$$J_X^\mu = i(\hat{X}^* \partial^\mu \hat{X} - \hat{X} \partial^\mu \hat{X}^*) = (X' \partial^\mu X - X \partial^\mu X'), \quad (2.2a)$$

$$J_\chi^\mu = \bar{\chi} \gamma_\mu \hat{\chi} = i(\chi'^\dagger \bar{\sigma}_\mu \chi - \chi^\dagger \bar{\sigma}_\mu \chi'). \quad (2.2b)$$

The mass-splitting between the dark components can be induced by the spontaneous symmetry-breaking mechanism that generates the mass of the vector mediator. This will be shown by a concrete UV completion model in Sec. 5. The current for the visible sector can be separated into leptonic and hadronic parts, $J_{\text{vis}}^\mu = J_\ell^\mu + J_q^\mu$, and takes the general form:

$$J_\ell^\mu = c_L \bar{L} \gamma^\mu L + c_e \bar{e}_R \gamma^\mu e_R, \quad (2.3a)$$

$$J_q^\mu = c_Q \bar{Q} \gamma^\mu Q + c_u \bar{u}_R \gamma^\mu u_R + c_d \bar{d}_R \gamma^\mu d_R, \quad (2.3b)$$

where (c_L, c_e) and (c_Q, c_u, c_d) denote respectively the lepton and quark couplings to the vector mediator. For the direct detection analysis, we express the general currents (2.3) for electron and (u, d)-quarks as follows:

$$J_e^\mu = c_e^V \bar{e} \gamma^\mu e + c_e^A \bar{e} \gamma^\mu \gamma^5 e, \quad (2.4a)$$

$$J_q^\mu = c_q^V \bar{q} \gamma^\mu q + c_q^A \bar{q} \gamma^\mu \gamma^5 q, \quad (2.4b)$$

where the quark field $q = u, d$. Hereafter, we will only consider the vector current of quarks in the DM-nucleon scattering for the following reasons. The nuclear expectation value of the quark axial current is proportional to the spin fractions in the target nucleus [24] and is much smaller than the nuclear expectation value of the quark vector current in general cases because the latter is enhanced by the number of nucleons. Besides, the DM current in the effective operator is chosen to be a vector

current, and its couplings with quark (electron) axial currents only contribute to the DM-nucleus (electron) scattering amplitudes with terms suppressed by the small DM-velocity. Hence, we will work at the leading order of the small momentum transfer and neglect the quark or electron axial current in the direct detection analysis. The DM-quark interaction matches to the spin-independent DM-nucleon interactions [25]:

$$\frac{c}{M^2} J_{X\mu} (q_p \bar{p} \gamma^\mu p + q_n \bar{n} \gamma^\mu n), \quad (2.5)$$

where the coupling coefficients (dark charges) for protons and neutrons are $q_p = 2c_u^V + c_d^V$ and $q_n = c_u^V + 2c_d^V$. In the limit of $\Delta m \rightarrow 0$, the DM-nucleon scattering cross section for $X' + (n, p) \rightarrow X + (n, p)$ can be expressed as

$$\sigma_{n,p} \simeq \frac{|c|^2 q_{n,p}^2 \mu_{n,p}^2}{\pi M^4} = \frac{4\alpha q_{n,p}^2 \mu_{n,p}^2}{\Lambda^4}, \quad (2.6)$$

where $\mu_{n,p} = m_{n,p} m_X / (m_{n,p} + m_X)$ is the reduced mass. In the second step of Eq.(2.6), we have defined an effective cutoff scale $\Lambda \equiv M (e/|c|)^{\frac{1}{2}}$, where $\alpha = e^2/4\pi$ denotes the fine structure constant and e is the unit of electric charge. Then, the DM-nucleus (N) spin-independent scattering cross section takes the form:

$$\sigma_N \simeq \frac{4\alpha q_N^2 \mu_N^2}{\Lambda^4}, \quad (2.7)$$

where the DM-nucleus effective coupling $q_N(A, Z) = Z q_p + (A - Z) q_n$ [25][26][27], and the reduced mass $\mu_N = m_N m_X / (m_N + m_X)$. The quantities A and Z denote the nucleon number and the electric charge of the nucleus, whereas m_N denotes the nucleus mass. We can ignore the nuclear form factor because for the parameter space considered in the present study, the momentum transfer in a DM-nucleus scattering is always small as compared to the inverse of the nuclear radius. We can also ignore the nuclear excitations as the energy transfer is relatively small. In parallel, the DM-electron scattering cross section is given by

$$\sigma_e \simeq \frac{4\alpha q_e^2 \mu_e^2}{\Lambda^4}, \quad (2.8)$$

where the dark charge of electron is $q_e = c_e^V$. For the case $m_X \gg m_e$, the reduced mass is $\mu_e \simeq m_e$. Taking the ratio of cross sections of Eqs.(2.7)-(2.8), we have

$$\frac{\sigma_e}{\sigma_N} \simeq \left(\frac{q_e \mu_e}{q_N \mu_N} \right)^2. \quad (2.9)$$

Eq.(2.9) shows that the interplay between DM-electron scattering and (spin-independent) DM-nucleus scattering can be encoded into the charge ratio between q_e and $q_{n,p}$. Although this work is motivated by studying a dark sector with a vector mediator, the parameterization of the signal cross sections ($\sigma_e, \sigma_n, \sigma_p$) applies to general spin-independent interactions. Hence, the analysis of the electron recoil spectrum in the following sections can be applied to other models with modified matching conditions between quark-level and nucleon-level interactions. In the following, we will consider several benchmark combinations of $q_{e,n,p} = 0, \pm 1$ as shown in Table 1. Note that the sign of q_e does not affect the signals. In the same table, we also indicate the corresponding colored curve for each scenario as to be shown in the figures presenting the electron recoil spectra of Section 4. The

Benchmark Scenarios	(e). $(q_e, q_n, q_p) = (1, 0, 0)$, (black solid)
(a). $(q_e, q_n, q_p) = (0, 0, 1)$, (green dashed)	(f). $(q_e, q_n, q_p) = (1, 0, 1)$, (green solid)
(b). $(q_e, q_n, q_p) = (0, 1, 0)$, (blue dashed)	(g). $(q_e, q_n, q_p) = (1, 1, 0)$, (blue solid)
(c). $(q_e, q_n, q_p) = (0, 1, 1)$, (red dashed)	(h). $(q_e, q_n, q_p) = (1, 1, 1)$, (red solid)
(d). $(q_e, q_n, q_p) = (0, 1, -1)$, (purple dashed)	(i). $(q_e, q_n, q_p) = (1, 1, -1)$, (purple solid)

Table 1: Benchmark scenarios with different dark charge assignments of (q_e, q_n, q_p) as discussed in text, which correspond to the colored curves (indicated in this Table) as shown the relevant figures. The charges are expressed as $(q_e, q_n, q_p) = (c_e^V, 2c_u^V + c_d^V, c_u^V + 2c_d^V)$.

benchmark scenarios (a)-(d) have $q_e = 0$, so the electron recoil signal arises only from the Migdal effect of DM-nucleus scattering. The benchmark (e) has $q_{n,p} = 0$ and its signal comes exclusively from the DM-electron scattering. For benchmarks (f)-(j), the signals arise from both DM-nucleus and DM-electron scattering.

3. Electron Recoil Signals from Exothermic Inelastic Dark Matter

In this section, we proceed to discuss the electron recoil signals of exothermic inelastic DM scattering, in which a heavier DM component X' de-excites to a lighter component X , and deposits the energy from the mass-splitting into the kinetic energy of the final states. The electron recoil signatures may arise from direct DM-electron scattering or from the Migdal effect following the DM-nucleon scattering.

3.1. Inelastic DM-Electron Scattering

For the present study of the inelastic DM-electron scattering, we have $m_X \gg m_e$ and $p_X \gg p_e$. Thus, the range of momentum transfer lies in the range, $q_- \leq q \leq q_+$, with

$$\frac{q_{\pm}}{m_X} = \left| v_{\text{DM}} \pm \sqrt{v_{\text{DM}}^2 - 2 \left(\frac{E_R - \Delta m}{m_X} \right)} \right|, \quad (3.1)$$

where v_{DM} stands for the DM velocity [20]. As shown in [22][28][29], the atomic form factors are peaked at $q \sim O(10\text{keV})$. Thus, most of the observed events satisfy $q_- < O(10\text{keV})$, which constrain the width of the electron recoil signal:

$$|E_R - \Delta m| < v_{\text{DM}} \times O(10\text{keV}) \sim 0.01\text{keV}. \quad (3.2)$$

This means that the electron recoil spectrum is sharply peaked at $E_R = \Delta m$.

The differential event rate of the DM-electron scattering with respect to the recoil energy E_R is given by [10][22]:

$$\frac{dR_{\text{ER}}}{dE_R} = \frac{\rho_{\text{DM}}}{m_X} \frac{\sigma_e}{8m_e^2} \int d^3v \frac{f(\vec{v} + \vec{v}_e)}{v} \sum_{n,\ell} \frac{1}{E_R - E_{n\ell}} \int dq q |f_{n\ell}(E_R, q)|^2, \quad (3.3)$$

where $\rho_{\text{DM}} \simeq 0.3 \text{ GeV}/\text{cm}^3$ is the local DM density, $f(\vec{v})$ the local DM velocity distribution function in the galactic frame, \vec{v}_e the velocity of Earth, $E_{n\ell}$ the energy level of atomic electron, and $|f_{n\ell}(E_R, q)|^2$ the atomic form factor. Here for simplicity we assume that the local DM consists of only the heavier DM component.

With the approximation that the out-going electron behaves like free plane wave [10][22], the atomic form factor can be estimated as

$$|f_{n\ell}|^2 = \frac{2\ell+1}{2\pi^3} \frac{m_e(E_R - E_{n\ell})}{q} \int_{k_-}^{k_+} dk k |\chi_{n\ell}(k)|^2, \quad (3.4)$$

where the momenta $k_{\pm} = |\sqrt{2m_e(E_R - E_{n\ell})} \pm q|$ and $\chi_{n\ell}$ denotes the radial wave function. In this work, we adopt the numerical results for the radial wave functions given in [30]. Beyond the plane wave approximation, the wave function of the ionized electron is affected by the attractive potential near the nucleus. This induces an additional enhancement to the above plane wave approximation, similar to the Sommerfeld enhancement. Following [10], we multiply $|f_{n\ell}|^2$ by a Fermi factor which takes the following form in the non-relativistic limit,

$$F_{\text{Fermi}} = \frac{2\pi\eta}{1 - e^{-2\pi\eta}}, \quad (3.5)$$

where $\eta = Z_{\text{eff}}\alpha m_e / \sqrt{2m_e(E_R - E_{n\ell})}$ with $Z_{\text{eff}} = 1$.

The DM velocity is assumed to follow a Maxwell-Boltzmann distribution in the galactic frame and truncated at the galactic escape velocity, $v_{\text{esc}} \simeq 0.00181$ [31],

$$f(v) \propto \begin{cases} \exp(-v^2/v_0^2) - \exp(-v_{\text{esc}}^2/v_0^2), & v \leq v_{\text{esc}}, \\ 0, & v > v_{\text{esc}}, \end{cases} \quad (3.6)$$

where $v_0 \simeq v_e \simeq 0.00073$ is the circular speed of the solar system around the galactic center. The minimum DM velocity for a scattering event to occur with electron recoil energy E_R and momentum transfer q is given by $v_{\text{min}} = |q^2 + 2m_X(E_R - \Delta m)| / (2qm_X)$. Since the integral

$$\xi(E_R, q) \equiv \int_{v_{\text{min}}}^{\infty} d^3v \frac{f(\vec{v} + \vec{v}_e)}{v} \quad (3.7)$$

has an analytic form [31, 32] as a function of the recoil energy E_R and momentum transfer q , it is practically more convenient to evaluate the following integral for the recoil spectrum,

$$\frac{dR_{\text{ER}}}{dE_R} = \frac{\rho_{\text{DM}}}{m_X} \frac{\sigma_e}{8m_e^2} \sum_{n,\ell} \frac{1}{E_R - E_{n\ell}} \int dq q \xi(E_R, q) |f_{n\ell}(E_R, q)|^2. \quad (3.8)$$

3.2. Inelastic DM-Nucleus Scattering

For the inelastic DM-nucleus scattering with $m_X \ll m_N$, we can approximate $q \sim m_X v_{\text{DM}}$ and

$$E_{\text{NR}} \sim \frac{q^2}{m_N} + \frac{m_X}{m_N} \Delta m. \quad (3.9)$$

Its contribution to the electron recoil is further suppressed by a quenching factor \mathcal{L} ,

$$E_{\text{NR} \rightarrow \text{ER}} = \mathcal{L} E_{\text{NR}}. \quad (3.10)$$

As will be discussed in Section 4, for the present study we focus on the case with DM mass range (0.1–10) GeV, thus the $E_{\text{NR} \rightarrow \text{ER}}$ contributions are always below the detection threshold, whereas the direct nuclear recoil signals are significant only when m_X is large.

In a DM-nucleus scattering event, the recoiled nucleus acquires a small velocity relative to its surrounding electron cloud; this may lead to ionization of electrons in the outer orbits, as described by the Migdal effect [11][12]. Exothermic scattering may enhance the Migdal effect [21][33][34] by releasing the extra energy Δm into the ionized atomic electrons,

$$\frac{1}{2}\mu_N v_{\text{DM}}^2 + \Delta m = \frac{1}{2}\mu_N v'^2 + E_{\text{ER}}, \quad (3.11)$$

where v_{DM} is the DM velocity in the laboratory frame, v' the relative velocity after scattering, and $E_{\text{ER}} = E_{n\ell} + E_e$ the total electronic energy release, including the atomic ionization energy $E_{n\ell}$ and the kinetic energy of the ionized electron E_e . The kinematics determines the nuclear recoil energy,

$$E_{\text{NR}} = \frac{\mu_N^2 v_{\text{DM}}^2}{m_N} \left[1 + \frac{\Delta m - E_{\text{ER}}}{\mu_N v_{\text{DM}}^2} - \sqrt{1 + \frac{2(\Delta m - E_{\text{ER}})}{\mu_N v_{\text{DM}}^2}} \cos\theta \right], \quad (3.12)$$

where θ is the scattering angle in the center-of-mass frame. For a given $E_{\text{ER}} > \Delta m$, there is a minimal DM velocity imposed by kinematics,

$$v_{\text{DM}}^{\text{min}} = \sqrt{\frac{2(E_{\text{ER}} - \Delta m)}{\mu_N}}. \quad (3.13)$$

We see that the minimal DM velocity is reduced due to the energy release Δm . The inelastic scattering is always kinematically allowed so long as $E_{\text{ER}} \leq \Delta m$ since this condition removes the lower bound (3.13) on v_{DM} .

The differential electron recoil rate of the Migdal effect per unit target mass with respect to E_{ER} is related to the nuclear recoil rate,

$$\frac{dR_{\text{MIGD}}}{dE_{\text{ER}}} \simeq \int dE_{\text{NR}} dv \left[\frac{dR_{\text{NR}}}{dE_{\text{NR}} dv} \sum_{n,\ell} \frac{1}{2\pi} \frac{dP_{q_e}^c(n, \ell \rightarrow E_e)}{dE_{\text{ER}}} \right], \quad (3.14)$$

where $P_{q_e}^c(n, \ell \rightarrow E_e)$ is the probability of exciting an electron of level- (n, ℓ) to a free electron with kinetic energy E_e [12]. The momentum transfer to the excited Migdal electron is $q_e = 2m_e^2 E_{\text{NR}}/m_N$. Note that here $1/q_e$ is much larger than the typical orbital radius of the atomic electron, and thus $P_{q_e}^c \propto q_e^2$ [12]. Hence, the enhanced q_e due to the exothermic scattering with DM enhances the excitation probability. The differential nuclear recoil rate per unit target mass is given by

$$\frac{dR_{\text{NR}}}{dE_{\text{NR}} dv} \simeq \frac{\rho_{\text{DM}}}{m_X} \frac{\sigma_{\text{Xe}}}{2\mu_N^2} \frac{f(v+v_e)}{v}. \quad (3.15)$$

The nuclear recoil also contributes to the detected electronic energy $E_{\text{det}} = \mathcal{L}E_{\text{NR}} + E_{\text{ER}}$, where $\mathcal{L} \approx 0.15$ is the quenching factor parametrizing the transfer of nuclear recoil energy to the measurable electronic excitations. For the sub-GeV DM and an electron recoil detection threshold around 0.1 keV, the contribution from the quenching of nuclear recoil would be negligible. Nevertheless, we include this effect in our numerical analysis.

4. Limits from Direct Detection Experiments

In this section, using published data from the DM direct detection experiments, we analyze the electron recoil spectrum described in Section 3 and derive constraints on the inelastic DM. We consider the light inelastic DM in the mass range (0.1–10) GeV with a mass-splitting around (1–30) keV in the following analysis.

4.1. Constraints by XENONnT Electron Recoil Data

The XENONnT experiment recently published the low-energy electron recoil data from its first science run [7]. The data can be used to set bounds on the scale Λ for the inelastic interaction introduced in Section 2. We extract the electron recoil data, background model B_0 , and detection efficiency $f_{\text{eff}}(E)$ from Ref. [7]. The detector smearing of the electron recoil spectrum is approximated by a skew-Gaussian distribution [35],

$$f(E_d, E) = \frac{1}{\sqrt{2\pi}w} e^{-\frac{(E_d - \xi)^2}{2w^2}} \left[1 + \text{erf} \left(\alpha \frac{E_d - \xi}{\sqrt{2}w} \right) \right], \quad (4.1)$$

where E is the physical energy, E_d the detected energy, and

$$\alpha(E) = 2.41E^{-0.30}, \quad (4.2a)$$

$$w(E) = 0.374\sqrt{E} + 0.005E, \quad (4.2b)$$

$$\xi(E) = E - \sqrt{\frac{2}{\pi}} \frac{\alpha w}{\sqrt{1 + \alpha^2}}. \quad (4.2c)$$

The function $\alpha(E)$ should not be confused with the fine structure constant $\alpha = e^2/4\pi$ used in this paper. Thus, the event number detected per keV per ton-year is given by

$$\frac{dN}{dE_d} = N_T \int \frac{dR}{dE_R} f(E_d, E_R) f_{\text{eff}}(E_R) dE_R, \quad (4.3)$$

where N_T is the number of target xenon atoms per ton, E_R the (physical) recoil energy and E the detected energy. The physical rate dR/dE_R for DM-electron scattering and the Migdal effect are given in Eqs.(3.8) and (3.14), respectively. Given that the DM mass $m_X \leq 10$ GeV, the mass-splitting $\Delta m \leq 30$ keV, and the quenching factor $\mathcal{L} = 0.15$ [cf. Eq.(3.10)], the nuclear recoil contribution to the electron recoil data [as shown in Eq.(3.10)] is below the detection threshold and thus can be neglected.

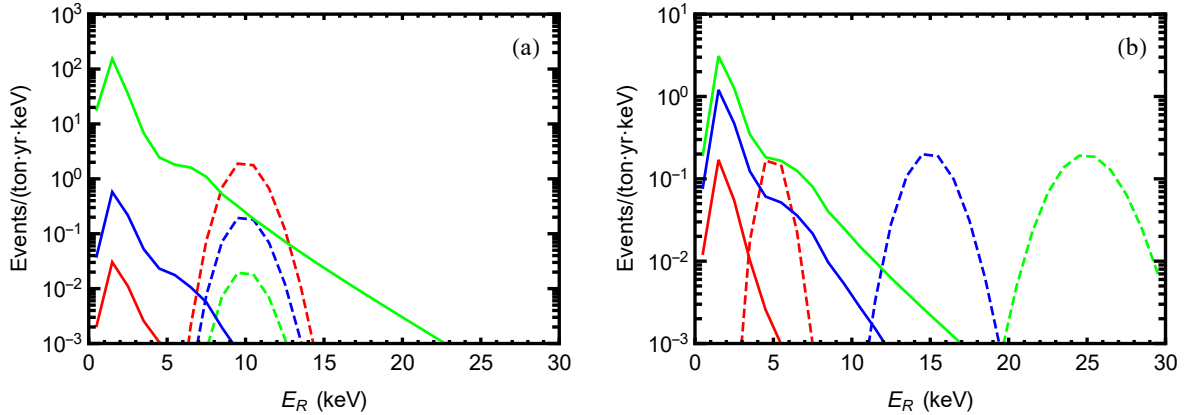


Figure 1: Electron recoil signals for XENONnT detection as induced by the inelastic DM scattering. The solid curves arise from the Migdal effect, and the dashed curves are contributed by the DM-electron scattering. We set the cutoff scale $\Lambda = 500\text{GeV}$, and choose the dark charges $(q_e, q_n, q_p) = (1, 1, -1)$. Plot-(a): The input mass-splitting is set as $\Delta m = 10\text{keV}$. The (red, blue, green) curves present results for the DM mass $m_\chi = (0.1, 1, 10)\text{GeV}$, respectively. Plot-(b): The input DM mass is set as $m_\chi = 1\text{GeV}$. The (red, blue, green) curves present results for $\Delta m = (5, 15, 25)\text{keV}$, respectively.

In Fig. 1, we present the predicted electron recoil spectra for XENONnT detector. (The color of each curve in this figure is not related to those for the benchmark scenarios defined in Table 1 of Section 2.) We see that the shape and position of the spectrum generated by the Migdal effect are almost fixed, whereas the overall normalization depends on the DM mass m_χ and mass-splitting Δm . As for the signals from the DM-electron scattering, their heights are proportional to $1/m_\chi$ due to the local DM number density, and their shapes are always a sharp peak around Δm . This shows that for larger DM mass, the Migdal effect gives the leading contribution to the electron recoil events, while for smaller DM mass, the DM-electron scattering becomes dominant.

Throughout this analysis, we do not fluctuate the background, because its normalization is fixed by the electron recoil data at $E_R = (0-140)\text{keV}$, far beyond the range affected by DM scattering. We calculate the χ^2 value for the background model B_0 [7] with $E_R \leq 30\text{keV}$ and obtain $\chi_{\text{bkg}}^2 = 19.84$. Thus, at the 95% C.L., we set $\chi^2 \leq 19.84 + 3.84$, which corresponds to one degree of freedom (the free parameter Λ). We plot the resulting limits in Fig. 2. The (top, middle, bottom) rows correspond to the DM mass $m_\chi = (10, 1, 0.1)\text{GeV}$, respectively. For each selected m_χ , we present the limits on the cross sections of the DM-electron (DM-nucleon) scattering in the left (right) panels, and the corresponding limits on the cutoff scale Λ . The color of each curve matches the corresponding benchmark scenario as defined in Table 1 of Section 2.

The different impacts from the DM-electron scattering and from the Migdal effect can be seen by comparing the black curve (with $q_n = q_p = 0$) to the colored curves (with $q_n \neq 0$ and/or $q_p \neq 0$) in the left panels of Fig. 2. We note that some exclusion contours are smooth curves whereas others are twisty curves. The smoother ones correspond to the scenarios with the Migdal effect dominating the signal, i.e., when the DM mass is large (in the top panels except the black curve) and/or $q_e = 0$ (the dashed curves). This is because in such cases the shape of the total electron recoil spectrum is almost

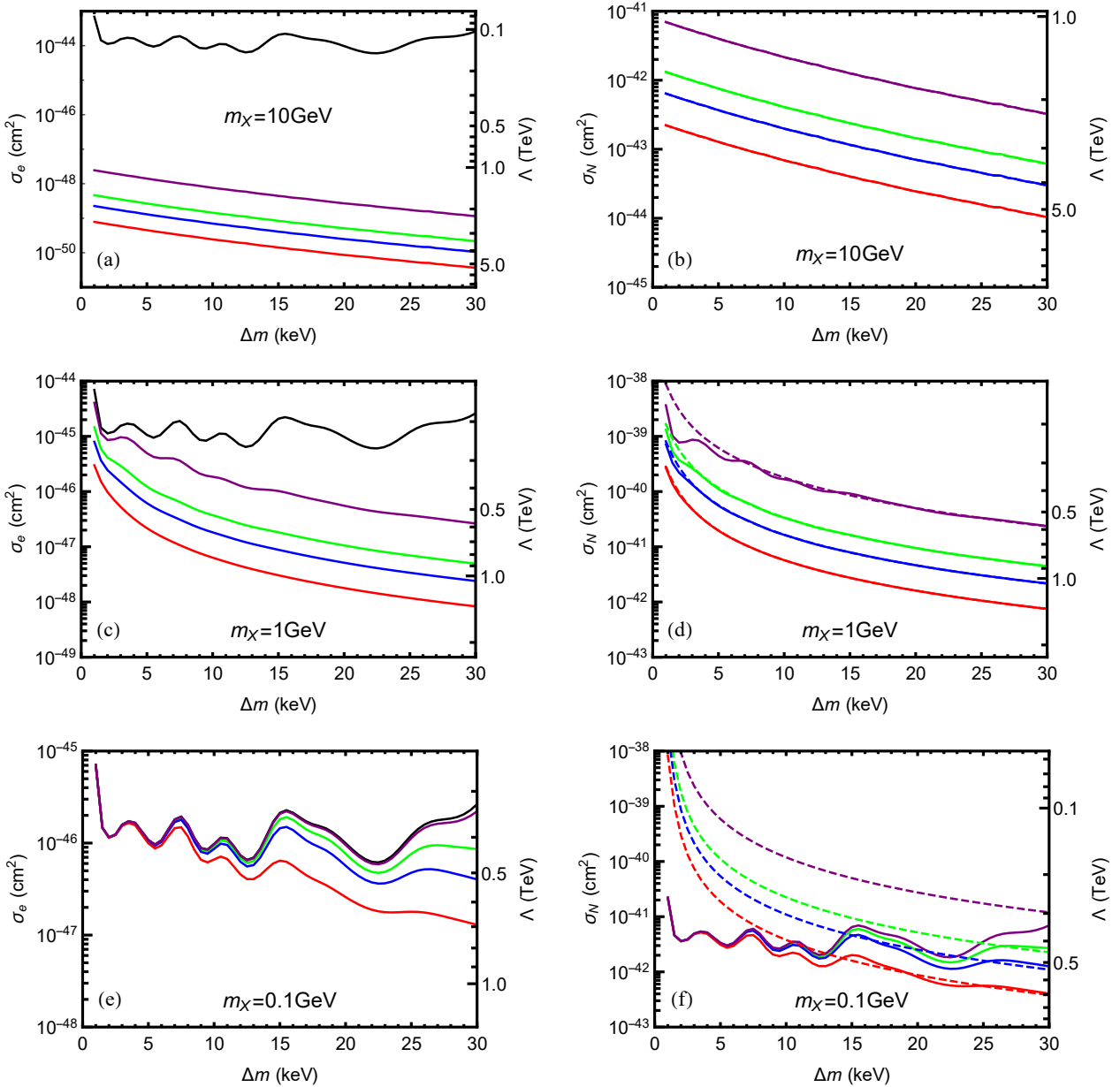


Figure 2: Limits on the DM-electron and DM-nucleon scattering cross sections from the XENONnT ER data, presented in the left and right panels respectively. The panels from top to bottom correspond to the DM masses $m_\chi = (10, 1, 0.1)$ GeV. The color of each curve matches the corresponding benchmark scenario (as indicated) in Table 1 (Section 2), i.e., dashed curves for $q_e = 0$ and solid curves for $q_e = 1$, whereas green curves for $(q_n, q_p) = (0, 1)$, blue curves for $(q_n, q_p) = (1, 0)$, red curves for $(q_n, q_p) = (1, 1)$, purple curves for $(q_n, q_p) = (1, -1)$, and black curves for $(q_n, q_p) = (0, 0)$. The region above each curve is excluded.

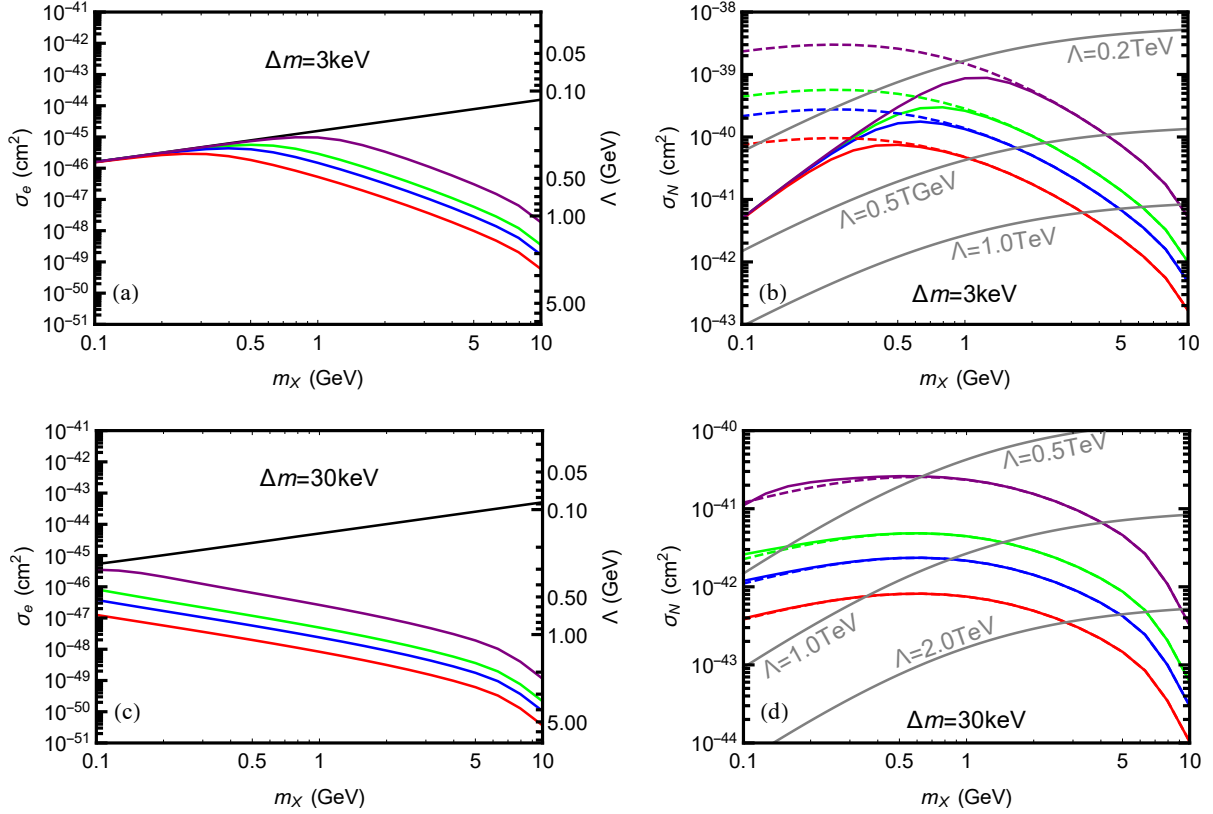


Figure 3: Limits on the DM-electron and DM-nucleon scattering cross sections from the XENONnT ER data, presented in the left and right panels respectively. The upper (lower) panels correspond to $\Delta m = 3\text{keV}$ (30keV). The color of each curve matches the corresponding benchmark scenario (as indicated) in Table 1 (Section 2), i.e., dashed curves for $q_e = 0$ and solid curves for $q_e = 1$, whereas green curves for $(q_n, q_p) = (0, 1)$, blue curves for $(q_n, q_p) = (1, 0)$, red curves for $(q_n, q_p) = (1, 1)$, purple curves for $(q_n, q_p) = (1, -1)$, and black curves for $(q_n, q_p) = (0, 0)$. In plots (b) and (d), the gray curves from top to bottom correspond to $\Lambda = (0.2, 0.5, 1.0)\text{TeV}$, respectively. In all plots the region above each curve is excluded.

fixed, and the height of the peak is a smooth function of Δm . Since most Migdal events are in the region of $E_R < 3\text{keV}$, a low detection threshold for electron recoil is crucial to its detection. On the other hand, when DM-electron scattering is dominant (the solid curves in the bottom panels or the black curves), the total electron recoil spectrum has peak-like structure whose peak positions depend on Δm . Thus, the fluctuations among the data bins make each contour curve exhibit a distinctive twisty shape. A sufficiently high resolution in the electron recoil detection is required to determine the mass-splitting Δm .

We see that the Migdal effect generally dominates the recoil signals for $m_X \gtrsim 1\text{GeV}$ (top and middle panels of Fig. 2) if the DM couples to nucleons. Even for smaller m_X , the Migdal effect can still be significant if the mass-splitting Δm is large and increases the electron ionization probability through the enhanced energy release to electrons. This feature is evident in Fig. 3. For large mass-splitting such as $\Delta m = 30\text{keV}$ in Fig. 3(c)-(d), the DM-electron scattering contribution is always subleading, so that the colored curves ($q_n \neq 0$ and/or $q_p \neq 0$) always give much stronger constraints than the black curve ($q_n = q_p = 0$) in Fig. 3(c), and the differences between dashed curves ($q_e = 0$) and solid curves ($q_e = 1$) in Fig. 3(d) is negligible. In Fig. 3(a)-(b) with $\Delta m = 3\text{keV}$, the DM-electron scattering becomes dominant for $m_X \lesssim 1\text{GeV}$. This makes the colored curves coincide with the black one in the region $m_X \lesssim 1\text{GeV}$ of Fig. 3(a), whereas large differences between the dashed and solid curves appear in the region $m_X \lesssim 1\text{GeV}$ of Fig. 3(b). Such observation signifies the necessity of analyzing the contributions of both DM-electron and DM-nucleus scattering simultaneously because it is nontrivial to determine the relative impacts of the two contributions.

4.2. Constraints by S2-Only Data of XENON1T

The S2-only data of XENON1T [9] can also set non-trivial constraints on the DM models. In this study, we use the datasets, response matrices, and background models provided by XENON1T collaboration [9]. According to [9], we will use the ER data and CEvNS background models for the present analysis, whereas the cathode backgrounds is ignored.

The physical spectra of the electron recoil events include the DM-electron scattering and the Migdal effect, which are given by Eqs. (3.8) and (3.14) respectively. To extract the S2 signals, we first apply the energy cutoff at 0.186keV , and then convert the physical event rate to the binned S2 rate using the response matrix. In Fig. 4, we present a sample of the predicted S2 rates for the XENON1T detector with DM mass values, $m_X = (0.1, 1, 10)\text{GeV}$, respectively. Here the color of each curve does not correspond to the benchmark models (a)-(i) defined in Table 1. Note that the maximum S2 area is 3000 PE which translates to about 4keV , thus for the current analysis of this subsection the DM mass-splitting Δm varies in the range $(0.1 - 5)\text{keV}$.

The nuclear recoil contribution is always negligible for $m_X = 0.1\text{GeV}$ and $m_X = 1\text{GeV}$, with a detection threshold of $O(\text{keV})$. As for $m_X = 10\text{GeV}$, the nuclear recoil signal is significant and the XENON1T collaboration has derived a bound, $\sigma_N < 4 \times 10^{-45}\text{cm}^2$ for the elastic DM case [9]. For the

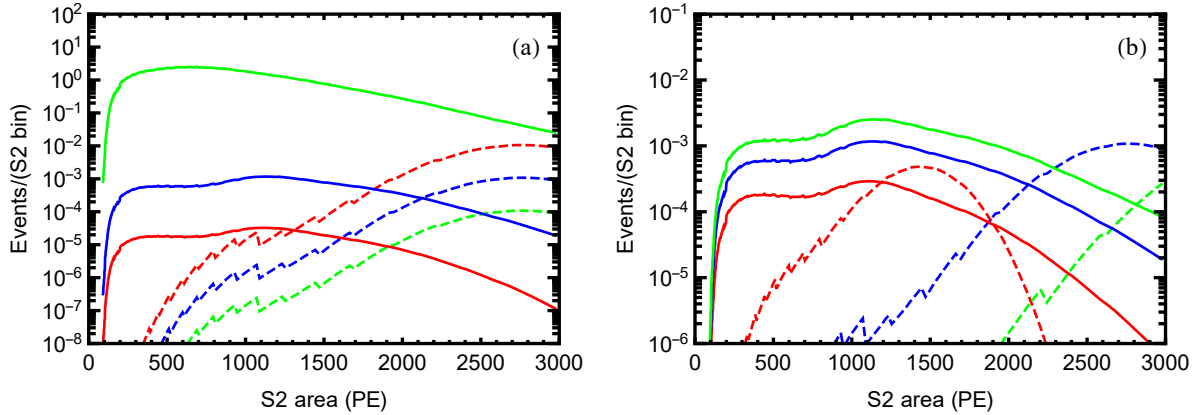


Figure 4: Recoil signals from inelastic DM scattering by using the XENON1T S2-only data. The solid curves present contributions by the Migdal effect, and the dashed curves are given by contributions from the DM-electron scattering. We set the cutoff scale $\Lambda = 500\text{ GeV}$, and choose the dark charges $(q_e, q_n, q_p) = (1, 1, -1)$. Plot-(a): The mass-splitting is set as $\Delta m = 3\text{ keV}$. The (red, blue, green) curves correspond to $m_X = (0.1, 1, 10)\text{ GeV}$, respectively. Plot-(b): The DM mass is set as $m_X = 1\text{ GeV}$. The (red, blue, green) curves correspond to $\Delta m = (1, 3, 5)\text{ keV}$, respectively.

inelastic DM case with $\Delta m < 5\text{ keV}$, we always have

$$\frac{m_X}{m_N} \Delta m < \text{keV}, \quad \text{and} \quad \frac{\Delta m}{m_X v_{\text{DM}}^2} < 1. \quad (4.4)$$

This implies that the contribution from Δm to nuclear recoil is always below the threshold and subdominant as compared to the contribution from the kinetic energy of the incoming DM particle. Thus, the bound set by the XENON1T experiment [9] should remain unchanged for the case of $\Delta m < 5\text{ keV}$.

To derive the constraint for each model and each parameter set of $(m_X, \Delta m)$, we choose a custom S2 region of interest (ROI) before analyzing the search data of XENON1T. As required in Ref. [9], the lower (upper) end of an ROI must lie between the 5th and 60th (40th and 95th) percentile of the S2 spectrum to contain sufficient signals, and should never be below 150 PE. We first scan over all such ROIs on the training dataset and determine the optimized ROI that gives the lowest bound. Then, we apply this ROI on the search dataset (which is independent of the training dataset). The exclusion region (at 95% C.L.) for the parameter θ of a general probabilistic model is determined by the formula:

$$p(\theta) \equiv \sum_{n=0}^{n_{\text{obs}}} \frac{\mu(\theta)^n}{n!} e^{-\mu(\theta)} \leq 0.05, \quad (4.5)$$

where μ is the expected event number in the chosen ROI including the background and signal events, and n_{obs} denotes the observed event number in the chosen ROI. In the excluded region, the probability that more events would have been produced than what are actually observed (i.e., $n > n_{\text{obs}}$) is above 95%. For our scenario under consideration, there is only one free parameter $\theta = \Lambda$.

In Fig. 5, we present the results from analyzing the XENON1T S2-only data with inputs of $m_X = (0.1, 1, 10)\text{ GeV}$, respectively. The plots are arranged in the same way as in Fig. 2. In addition, we derive the constraints for $\Delta m = 3\text{ keV}$ over the DM mass range of $0.1\text{ GeV} \leq m_X \leq 10\text{ GeV}$, as

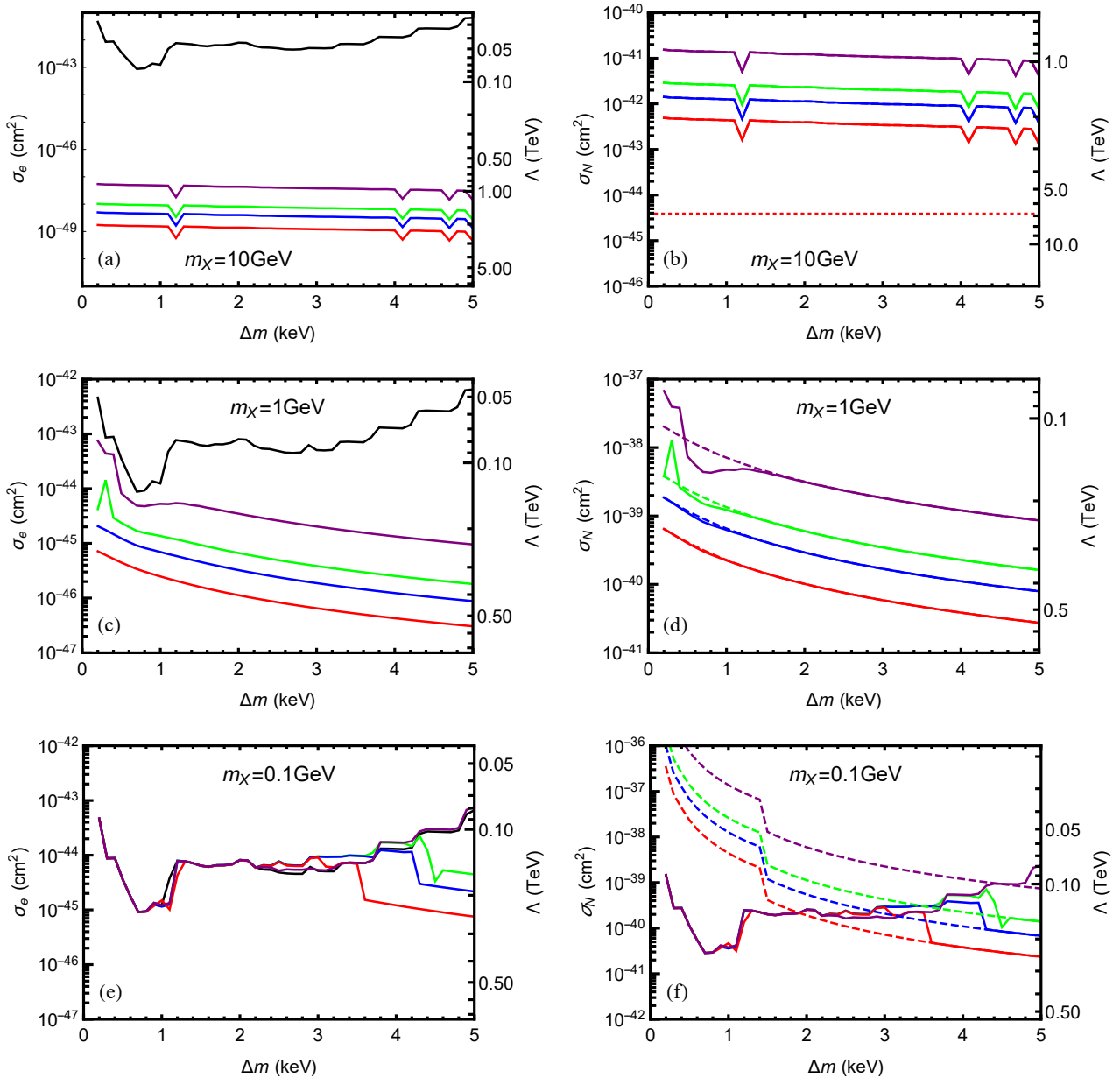


Figure 5: Limits on the DM-electron cross section (left panels) and on the DM-nucleon scattering cross sections (right panels) by using XENON1T S2-only data. The plots from top to bottom choose the DM mass $m_X = \{10, 1, 0.1\}$ GeV, respectively. The color of each curve matches the corresponding benchmark scenario (as indicated) in Table 1 (Section 2), i.e., dashed curves for $q_e = 0$ and solid curves for $q_e = 1$, whereas green curves for $(q_n, q_p) = (0, 1)$, blue curves for $(q_n, q_p) = (1, 0)$, red curves for $(q_n, q_p) = (1, 1)$, purple curves for $(q_n, q_p) = (1, -1)$, and black curves for $(q_n, q_p) = (0, 0)$. The region above each curve is excluded. The red dotted curve in plot-(b) is taken from Ref. [9]. It shows the 90% C.L. upper limit on spin-independent DM-nucleon cross section by NR signals at $m_X = 10$ GeV.

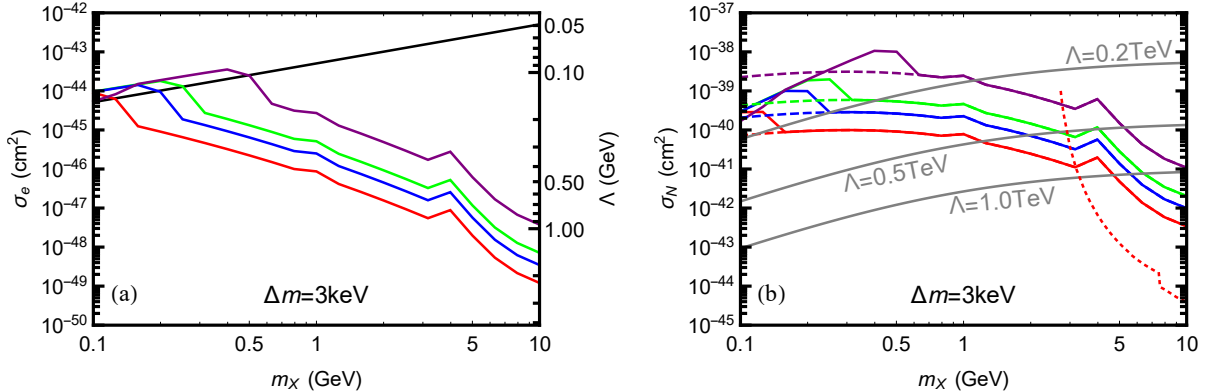


Figure 6: Limits on the DM-electron cross section (left panel) and on the DM-nucleon scattering cross sections (right panel) by using XENON1T S2-only data. The color of each curve matches the corresponding benchmark scenario (as indicated) in Table 1 (Section 2), i.e., dashed curves for $q_e = 0$ and solid curves for $q_e = 1$, whereas green curves for $(q_n, q_p) = (0, 1)$, blue curves for $(q_n, q_p) = (1, 0)$, red curves for $(q_n, q_p) = (1, 1)$, purple curves for $(q_n, q_p) = (1, -1)$, and black curves for $(q_n, q_p) = (0, 0)$. In plot-(b), the gray curves from top to bottom correspond to $\Lambda = (0.2, 0.5, 1.0)$ TeV, respectively. The red dotted curve is taken from Ref. [9]. It stands for the 90% C.L. upper limit on spin-independent DM-nucleon cross section given by NR signals. In both plots the region above each curve is excluded.

shown in Fig. 6. We see that the same pattern appears as in the results from the XENONnT ER data, namely, the dashed curves are smooth, whereas for small DM mass m_X the solid curves are twisty. Because the S2-only event numbers of XENON1T are much smaller than that in the ER data of XENONnT, the statistic fluctuations are more significant. This also leads to the non-smoothness of the ROI choices, which further enlarges the fluctuations in these curves.¹ As we have confirmed, the Migdal effect is more important than DM-electron scattering for larger m_X and/or larger Δm . The red dotted curves in Fig. 5(b) and Fig. 6(b) are the 90% C.L. upper limit on spin-independent DM-nucleon cross section taken from Ref. [9]. We use red color for the dotted curves because this limit corresponds to the $q_n = q_p = 1$ case. This limit is determined solely by elastic nuclear recoil signals, which is neglected in this study. As discussed in Eq. (4.4), the limits are unchanged for inelastic DM with $\Delta m < 5$ keV. In Fig. 6(b) we see that this limit gets weakened rapidly as m_X decreases. In consequence, for larger DM mass ($m_X \gtrsim 5$ GeV), the nuclear recoil signals dominates over that of the electron recoils, whereas for $m_X \lesssim 5$ GeV, the nuclear recoil effects are negligible.

5. Probing Inelastic DM with Dark Photon Mediator

Based upon the above model-independent study, we further construct an inelastic DM model with dark photon mediator via kinetic mixing, which can exhibit the features as we studied in the previous sections. Then, we systematically derive the cosmological bounds and laboratory bounds on

¹Most notably in Fig. 5(f), for $2\text{keV} \lesssim \Delta m \lesssim 4\text{keV}$, the ROIs for the solid curves (chosen by the training dataset) are in regions with higher S2 area. The search dataset in this region contains slightly more observed events above the backgrounds and imposes weaker limits than the dashed curves, whose ROIs are in the regions with lower S2 area which contains zero events in the search dataset [9].

this minimal inelastic DM model.

5.1. Model Realization: Inelastic DM with Dark Photon Mediator

In this model the SM is extended with a dark $U(1)_X$ gauge group, which connects to the SM through kinetic mixing between the dark $U(1)_X$ gauge field \bar{A}'_μ and the SM $U(1)_Y$ gauge field B_μ . Thus, the kinematic terms of the dark $U(1)_X$ and the SM $U(1)_Y$ are given by

$$\mathcal{L} \supset -\frac{1}{4}\bar{A}'_{\mu\nu}\bar{A}'^{\mu\nu} - \frac{1}{4}B_{\mu\nu}B^{\mu\nu} - \frac{\kappa}{2}\bar{A}'_{\mu\nu}B^{\mu\nu}, \quad (5.1)$$

where the dark gauge field strength $\bar{A}'_{\mu\nu} = \partial_\mu\bar{A}'_\nu - \partial_\nu\bar{A}'_\mu$. The dark $U(1)_X$ gauge group is spontaneously broken by the vacuum expectation values (VEVs) of two singlet scalar fields S and ϕ ,

$$\Delta\mathcal{L} \supset |D^\mu S|^2 + M_S^2|S|^2 - \lambda_S|S|^4 + |D^\mu\phi|^2 - M_\phi^2|\phi|^2 + (\lambda_{S\phi}S^3\phi + \text{h.c.}), \quad (5.2)$$

where the dark charges of S and ϕ are $1/3$ and -1 , respectively. This generates a mass term for \bar{A}'_μ through the Higgs mechanism,

$$m_{\bar{A}'}^2 = 2g_X^2(v_\phi^2 + \frac{1}{9}v_S^2), \quad (5.3)$$

where g_X is the $U(1)_X$ coupling, and the VEVs are $v_S = M_S/\sqrt{2\lambda_S}$ and $v_\phi = \lambda_{S\phi}v_S^3/M_\phi^2$. Taking $M_\phi \gg v_S$, we have $v_\phi \ll v_S$. This further gives, $m_{\bar{A}'} \simeq \sqrt{2}g_X v_S/3$ and $v_\phi = 27\lambda_{S\phi}m_{\bar{A}'}^3/(2\sqrt{2}g_X^3M_\phi^2)$.

After the spontaneous breaking of the electroweak gauge group $SU(2)_L \otimes U(1)_Y$, the neutral gauge boson component W_μ^3 of $SU(2)_L$ and the $U(1)_Y$ gauge boson B_μ form their mass eigenstates, $\bar{A}_\mu = B_\mu \cos\theta_W + W_\mu^3 \sin\theta_W$ and $\bar{Z}_\mu = W_\mu^3 \cos\theta_W - B_\mu \sin\theta_W$, where θ_W is the weak mixing angle. Thus, including the W_μ^3 part and all mass terms, we can rewrite the kinetic terms (5.1) as follows:

$$\begin{aligned} \mathcal{L} \supset & -\frac{1}{4}\bar{A}'_{\mu\nu}\bar{A}'^{\mu\nu} - \frac{1}{4}\bar{A}_{\mu\nu}\bar{A}^{\mu\nu} - \frac{1}{4}\bar{Z}_{\mu\nu}\bar{Z}^{\mu\nu} - \frac{\kappa}{2}\bar{A}'_{\mu\nu}(\bar{A}^{\mu\nu}\cos\theta_W - \bar{Z}^{\mu\nu}\sin\theta_W) \\ & + \frac{1}{2}m_{\bar{A}'}^2\bar{A}'_\mu\bar{A}'^\mu + \frac{1}{2}M_{\bar{Z}}^2\bar{Z}_\mu\bar{Z}^\mu, \end{aligned} \quad (5.4)$$

where the gauge field strengths $\bar{A}_{\mu\nu} = \partial_\mu\bar{A}_\nu - \partial_\nu\bar{A}_\mu$ and $\bar{Z}_{\mu\nu} = \partial_\mu\bar{Z}_\nu - \partial_\nu\bar{Z}_\mu$. Then, we can write the interaction terms of the gauge fields ($\bar{A}'_\mu, \bar{A}_\mu, \bar{Z}_\mu$) with matter currents:

$$\mathcal{L}_{\text{Int}} \supset g_X\bar{A}'_\mu J_X^\mu + e\bar{A}_\mu J_{\text{em}}^\mu + \frac{g}{\cos\theta_W}\bar{Z}_\mu J_Z^\mu, \quad (5.5)$$

where J_X^μ is the dark current as in Eq.(2.1), J_{em}^μ the electromagnetic current, and J_Z^μ the weak neutral current.

To diagonalize these kinetic mixing terms and mass terms in Eq.(5.4), we transform the gauge fields from the basis $(\bar{A}'_\mu, \bar{A}_\mu, \bar{Z}_\mu)$ to the non-mixing mass-eigenbasis (A'_μ, A_μ, Z_μ) . For the present study, we consider kinetic mixing parameter $\kappa \lesssim O(10^{-3})$ and dark photon mass $m_{\bar{A}'} \lesssim O(\text{GeV})$. Thus, to the leading order of the mixing parameter κ and the mass ratio $m_{\bar{A}'}^2/M_{\bar{Z}}^2$, we derive

$$\begin{pmatrix} \bar{A}'_\mu \\ \bar{A}_\mu \\ \bar{Z}_\mu \end{pmatrix} \simeq \begin{pmatrix} 1 & 0 & \kappa s_W \\ -\kappa c_W & 1 & 0 \\ -\frac{m_{\bar{A}'}^2}{M_{\bar{Z}}^2}\kappa s_W & 0 & 1 \end{pmatrix} \begin{pmatrix} A'_\mu \\ A_\mu \\ Z_\mu \end{pmatrix}, \quad (5.6)$$

where we denote $(s_W, c_W) = (\sin \theta_W, \cos \theta_W)$. Accordingly, we derive the mass spectrum of the neutral gauge bosons (A'_μ, A_μ, Z_μ) as follows:

$$m_{A'} \simeq m_{\bar{A}'}(1 + \kappa^2 c_W^2)^{\frac{1}{2}}, \quad m_A = 0, \quad M_Z^2 \simeq M_{\bar{Z}}^2(1 + \kappa^2 s_W^2)^{\frac{1}{2}}. \quad (5.7)$$

After the diagonalization of the gauge bosons, the interaction Lagrangian (5.5) becomes:

$$\begin{aligned} \mathcal{L}_{\text{Int}} \supset & g_X(A'_\mu + \kappa s_W Z_\mu)J_X^\mu + e(A_\mu - \kappa c_W A'_\mu)J_{\text{em}}^\mu \\ & + \frac{g}{c_W} \left(Z_\mu - \frac{m_{\bar{A}'}}{M_{\bar{Z}}} \kappa s_W A'_\mu \right) J_Z^\mu + O(\kappa^2), \end{aligned} \quad (5.8)$$

In the following, we define $\epsilon = \kappa \cos \theta_W$ as the mixing parameter.

The inelastic DM consists of two nearly degenerate long-lived states. These states can be formulated by either a pseudo-complex scalar $\hat{X} = (X + iX')/\sqrt{2}$ or a pseudo-Dirac spinor $\hat{\chi} = (\chi_1, \chi_2^\dagger)^T$, which are charged under the dark gauge group $U(1)_X$ with dark charge $+1$ for \hat{X} or dark charge $+\frac{1}{2}$ for $\hat{\chi}$. (This means that the Weyl spinors χ_1 and χ_2 have dark charges $+\frac{1}{2}$ and $-\frac{1}{2}$ respectively.) The mass-splitting Δm between the two DM components can be generated naturally by a seesaw mechanism. For the scalar dark matter \hat{X} , the DM Lagrangian takes the following form:

$$\begin{aligned} \Delta \mathcal{L}_{\text{DM}} \supset & |D^\mu \hat{X}|^2 - m_{\hat{X}}^2 |\hat{X}|^2 - \lambda_X |\hat{X}|^4 + (\lambda_\delta \hat{X}^2 \phi^2 + \text{h.c.}) \\ & - \lambda_{X\phi} |\hat{X}|^2 |\phi|^2 - \lambda_{XS} |\hat{X}|^2 |S|^2. \end{aligned} \quad (5.9)$$

The DM mass is mainly determined by the DM quadratic mass term and the DM couplings to $|S|^2$ and $|\phi|^2$, so the DM mass term is given by

$$\begin{aligned} \Delta \mathcal{L}_{\text{DM}} \supset & -\frac{1}{2}(m_{\hat{X}}^2 + \lambda_{XS} v_S^2 + \lambda_{X\phi} v_\phi^2)(X^2 + X'^2) + \lambda_\delta v_\phi^2 (X^2 - X'^2) \\ = & -\frac{1}{2} \bar{m}_X^2 (X^2 + X'^2) + \frac{1}{2} \delta m^2 (X^2 - X'^2), \end{aligned} \quad (5.10)$$

where the mass parameters $\bar{m}_X = (m_{\hat{X}}^2 + \lambda_{XS} v_S^2 + \lambda_{X\phi} v_\phi^2)^{1/2}$ and $\delta m^2 = 2\lambda_\delta v_\phi^2 \ll \bar{m}_X^2$. The mass-splitting Δm_X between the two DM components is determined by the unique quartic interaction $\hat{X}^2 \phi^2$ which gives rise to the mass-squared difference δm^2 , as shown above. Since $v_\phi \ll v_S, \bar{m}_X$ and thus $\delta m^2 \ll \bar{m}_X^2$, we have

$$m_{X, X'} \simeq \bar{m}_X \mp \frac{\delta m^2}{2\bar{m}_X}. \quad (5.11)$$

With these, we derive the scalar DM mass-splitting as follows:

$$\Delta m_X \simeq \frac{\delta m^2}{\bar{m}_X} \simeq \frac{729 \lambda_\delta \lambda_{S\phi}^2 m_{A'}^6}{4 g_X^6 M_\phi^4 m_X}. \quad (5.12)$$

By setting the sample inputs $(\lambda_\delta, \lambda_{S\phi}) = O(1)$, $g_X = O(10^{-2})$, $(m_X, m_{A'}) = O(\text{GeV})$, and $M_\phi = O(10^2 \text{ TeV})$, we can readily achieve a naturally small mass-splitting $\Delta m_X = O(\text{keV})$.

For the fermionic DM $\hat{\chi}$, the scalar potential (5.2) remains the same and the fermionic DM has the following gauge-invariant Lagrangian terms:

$$\Delta \mathcal{L} \supset \chi_1^\dagger i \bar{\sigma}^\mu D_\mu \chi_1 + \chi_2^\dagger i \bar{\sigma}^\mu D_\mu \chi_2 - (m_{\hat{\chi}} \chi_1 \chi_2 + \text{h.c.})$$

$$+ (y_{\phi\chi_1}\chi_1\chi_1\phi + y_{\phi\chi_2}\chi_2\chi_2\phi^* + \text{h.c.}), \quad (5.13)$$

where the Majorana mass $m_{\widehat{\chi}}$ and Yukawa couplings $(y_{\phi\chi_1}, y_{\phi\chi_2})$ are positive after proper phase rotations of ϕ and (χ_1, χ_2) . The small VEV v_ϕ induces additional Majorana masses for (χ_1, χ_2) through the Yukawa interactions in Eq.(5.13). Thus, we have the following DM mass terms:

$$\mathcal{L}_{\chi_1\chi_2} \supset -m_{\widehat{\chi}}\chi_1\chi_2 + \delta m_1\chi_1\chi_1 + \delta m_2\chi_2\chi_2 + \text{h.c.}, \quad (5.14)$$

where $(\delta m_1, \delta m_2) = (y_{\phi\chi_1}v_\phi, y_{\phi\chi_2}v_\phi)$. To transform (χ_1, χ_2) into the mass-eigenstates (χ, χ') , we make the following decompositions:

$$\chi_1 = \frac{1}{\sqrt{2}}(\chi - \mathbf{i}\chi'), \quad \chi_2 = \frac{1}{\sqrt{2}}(\chi + \mathbf{i}\chi'). \quad (5.15)$$

Since $v_\phi \ll m_{\widehat{\chi}}$, we derive the following Majorana masses for the DM mass-eigenstates (χ, χ') :

$$m_\chi \simeq m_{\widehat{\chi}} - (\delta m_1 + \delta m_2), \quad (5.16a)$$

$$m_{\chi'} \simeq m_{\widehat{\chi}} + (\delta m_1 + \delta m_2), \quad (5.16b)$$

which have a mass-splitting,

$$\Delta m_\chi \simeq 2(\delta m_1 + \delta m_2). \quad (5.17)$$

We choose the sample input parameters, $\lambda_{S\phi}, y_{\phi\chi_1}, y_{\phi\chi_2} = O(0.01)$, $v_S = O(20)$ GeV, and $M_\phi = O(\text{TeV})$. With these, we can readily derive a small VEV $v_\phi = O(0.1)$ MeV, and thus realize the desired mass-splitting $\Delta m_\chi = O(\text{keV})$.

From Eq.(5.9), we deduce the $U(1)_X$ gauge interactions for the scalar DM fields (X, X') :

$$\mathcal{L}_{\text{int}} \supset g_X(X^\dagger\partial_\mu X' - X'^\dagger\partial_\mu X)\bar{A}'^\mu, \quad (5.18)$$

which is consistent with the effective theory formulation in Section 2. We note that the diagonal vertices X - X - A'^μ and X' - X' - A'^μ vanish, whereas the above non-diagonal vertices can induce the desired inelastic scattering. Similar behavior holds for the case of fermionic inelastic DM.

At leading order, the cross sections of DM-electron and DM-nucleon scattering are mediated by the dark photon A'_μ . The contribution from Z -boson exchange is suppressed by $m_{A'}^4/m_Z^4$. Thus, we derive the following cross section formulas:

$$\sigma_{XN} = Z^2 \frac{4\alpha g_X^2 \epsilon^2 \mu^2}{m_{A'}^4}, \quad (5.19a)$$

$$\sigma_{Xe} = \frac{4\alpha g_X^2 \epsilon^2 m_e^2}{m_{A'}^4}. \quad (5.19b)$$

This should correspond to the scenario-(f) in Table 1 of Section 2, where $q_n = 0$ and $|q_p| = |q_e| = 1$, and the effective cutoff scale is given by

$$\Lambda = m_{A'}/\sqrt{g_X\epsilon}. \quad (5.20)$$

In the above formula, we have considered that the momentum transfer $q^2 \ll m_{A'}^2$. This is always true in the DM-electron scattering for $m_{A'} > O(\text{MeV})$, because the atomic form factors are peaked at $q \sim O(10\text{keV})$ as we discussed earlier. But, for the DM-nucleon scattering, we have $|q| \sim m_X v_{\text{DM}} \sim 10^{-3} m_X$. Thus, we will focus on $m_{A'} > 10^{-2} m_X$ in the following analysis.

5.2. Cosmological and Laboratory Constraints on Inelastic DM

Such exothermic inelastic scattering of DM particles with target atoms in the detector requires a significant local abundance of the heavier DM component X' . The conversion between X' and X is mainly due to X' decay, of which the only kinematically allowed channels are $X' \rightarrow X\gamma\gamma$ and $X' \rightarrow X\nu\bar{\nu}$. Since the 3γ decay channel is one-loop suppressed, the dominant decay channel is $X' \rightarrow X\nu\bar{\nu}$, which occurs through the A'/Z exchange due to the neutral gauge boson mixings in Eq.(5.6). We can estimate the X' decay width as follows:

$$\begin{aligned} \Gamma_{X' \rightarrow X\nu\bar{\nu}} &= \frac{e^2}{1260\pi^3 M_Z^4 \cos^4\theta_W} \frac{g_X^2 \epsilon^2}{m_{A'}^4} \Delta m^9 \\ &\approx (4 \times 10^{34} \text{yrs})^{-1} \left(\frac{\Lambda}{100 \text{GeV}} \right)^{-4} \left(\frac{\Delta m}{10 \text{keV}} \right)^9, \end{aligned} \quad (5.21)$$

where we have included the contributions of the final state neutrinos from all three families of the SM. Note that this width is much narrower than that in our previous model [21], because in this model the coupling between A' and $\nu\bar{\nu}$ is suppressed by $m_{A'}^2/M_Z^2$ and cancels the contribution from Z exchange at leading order, resulting in a tiny factor $\Delta m^4/M_Z^4 \simeq 10^{-28}$ in the decay width for $\Delta m = 10 \text{keV}$. This makes the lifetime of X' much longer than the age of the universe. Hence, assuming equal initial abundance of X and X' , we have $\rho_X = \rho_{X'} = \rho_{\text{DM}}/2$ at the present. Consequently, the limits on the cutoff Λ in Figs. 2-3 and Figs. 5-6 should be rescaled by a factor of $2^{-1/4} \simeq 0.84$.

This minimal inelastic DM model is also constrained by cosmological observations. The Planck Collaboration measured the present DM relic abundance [36], $\Omega_X h^2 = 0.120 \pm 0.001$, which can be achieved through the freeze-out mechanism. Since $\Delta m \ll m_X$, the inelastic DM components X and X' are equally abundant in the thermal bath before exiting the equilibrium. For $m_X > m_{A'}$, the dominant annihilation channel is $\hat{X}^\dagger \hat{X} \rightarrow A' A'$. The annihilation cross section scales as g_X^4 and is independent of mixing parameter ϵ , hence the bounds on $\Lambda \propto (g_X \epsilon)^{-1/2}$ from direct detection experiments are irrelevant to the annihilation process. In fact, we can in turn derive the bounds on ϵ by combining the g_X values required by the DM relic density and the bounds on Λ from direct detection experiments. But for $m_X < m_{A'}$, the leading annihilation channel is $\hat{X}^\dagger \hat{X} \rightarrow A'^* \rightarrow f \bar{f}$, where f and \bar{f} are charged SM fermions. The relic abundance of the DM can be estimated as follows [37–39]:

$$\Omega_X h^2 \simeq 0.1 \left(\frac{x_f}{20} \right) \left(\frac{10^{-8} \text{GeV}^{-2}}{\sigma_X} \right), \quad (5.22)$$

where $x_f \equiv T_f/m_X$ with T_f the freeze-out temperature. The DM annihilation cross section $\sigma_X \sim \alpha m_X^2/\Lambda^4$ is highly constrained by direct detection experiments, since the green solid curves in Figs. 2-

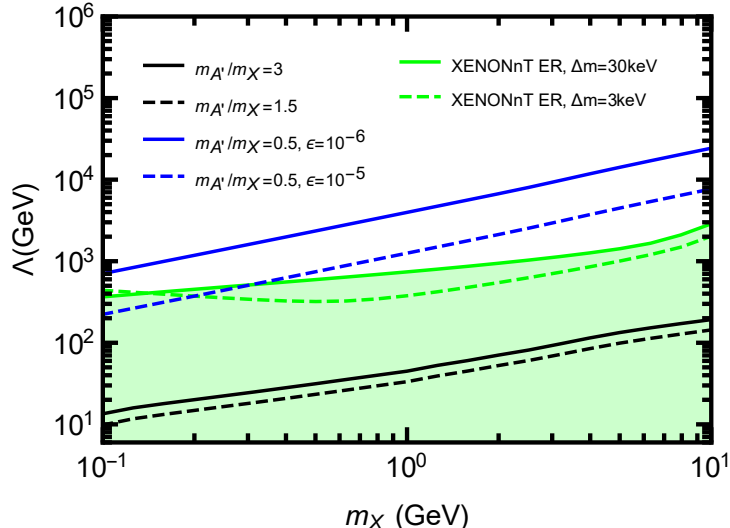


Figure 7: Allowed parameter space of (m_X, Λ) as given by imposing the DM relic density bound together with XENONnT electron recoil bounds of Fig. 3. The parameter space of the black and blue curves can provide the observed DM relic density today, whereas the green region displays the excluded parameter space at 95% C.L. The blue dashed (solid) curve corresponds to the sample inputs of $m_{A'}/m_X = 0.5$ and $\epsilon = 10^{-5}$ ($\epsilon = 10^{-6}$). The black dashed (solid) curve corresponds to the sample input of $m_{A'}/m_X = 1.5$ ($m_{A'}/m_X = 3$); and the green dashed (solid) curve corresponds to the sample input of $\Delta m = 3\text{keV}$ ($\Delta m = 30\text{keV}$) for XENONnT ER bounds with the green shaded area being excluded.

3 and Figs. 5-6 have set $\Lambda \gtrsim O(10^2 \text{ GeV})$. This always results in an overproduction of DM, so that the case of $m_X < m_{A'}$ is disfavored.

To demonstrate this, we present in Fig. 7 the Λ values required by the inelastic DM relic density and compare them to the constraints from direct detection experiments. The green dashed (solid) curve corresponds to the sample inputs of $\Delta m = 3\text{keV}$ ($\Delta m = 30\text{keV}$) for XENONnT ER bounds with the green shaded area being excluded. We compute the DM relic density numerically by using the package `MicrOMEGAs` [40]. We see that for the case of $m_X < m_{A'}$, the sample input of $m_{A'}/m_X = 1.5$ ($m_{A'}/m_X = 3$) is excluded by XENONnT bounds, as shown by the black dashed (solid) curve. As mentioned earlier, the bounds on $\Lambda \propto (g_X \epsilon)^{-1/2}$ are irrelevant to the case of $m_X > m_{A'}$. In order to translate the values of g_X given by imposing DM relic density to Λ , we choose sample inputs of $\epsilon = 10^{-5}$ and 10^{-6} which correspond to the blue dashed and solid curves in Fig. 7, respectively. Since ϵ does not receive any lower bound, we can always choose small enough values of ϵ such that the blue curve is fully above the green shaded region of Fig. 7 and thus escape the constraints.

Another cosmological constraint comes from the CMB anisotropy [41][42]. After the DM freezes out, the annihilation is largely diluted but not completely shut down. The electron/positron injection from A' decay contributes to the CMB anisotropy, which is already constrained by the CMB measurements including Planck [36]. The leading annihilation channel $\hat{X}^\dagger \hat{X} \rightarrow A' A' \rightarrow \ell \bar{\ell} \ell \bar{\ell}$ is s -wave dominant. Its thermally averaged cross section receives an upper bound from the Planck data [36]:

$$f_{\text{eff}} \frac{\langle \sigma v \rangle}{m_X} < 3.2 \times 10^{-28} \text{ cm}^3 \text{ s}^{-1} \text{ GeV}^{-1}, \quad (5.23)$$

where the efficiency factor f_{eff} is the fraction of the DM rest mass energy deposited into the gas [42]. In general, $f_{\text{eff}} \gtrsim 0.1$ and it depends on the lepton energy injected into the gas. This excludes the full parameter space determined by the freeze-out analysis, and would exclude the minimal model for the inelastic DM scenario with dark photon mediator (via kinetic mixing). The same conclusion applies to the case of fermionic DM.

But we note that the dark sector may contain several species of particles and mediators like the visible sector. Thus in this case the CMB anisotropy constraint can be readily relaxed if A' predominantly decays into light particles in the dark sector (rather than leptons) [23]. For instance, the dark sector may contain a light Dirac fermion f' charged under a new gauge group $U(1)_{X'}$ with gauge field A''_μ . The gauge boson A''_μ obtains a mass $m_{A''}$ through either the Higgs mechanism or the Stueckelberg mechanism, of which the detail is irrelevant to the discussion below. The kinetic mixing between $U(1)_{X'}$ and $U(1)_Y$ induces a small coupling between the electromagnetic current and A''_μ as parameterized by $\epsilon' e \ll 1$. The dark fermion f' is charged under both $U(1)_X$ and $U(1)_{X'}$, with a mass that satisfies $m_{A'} > 2m_{f'}$. The interactions of various currents takes the form,

$$\mathcal{L} \supset -g_X \bar{f}' \gamma^\mu f' A'_\mu - g_{X'} \bar{f}' \gamma^\mu f' A''_\mu - \epsilon' e \mathcal{A}''_\mu J_{\text{em}}^\mu, \quad (5.24)$$

where $g_{X'}$ denotes the gauge coupling of $U(1)_{X'}$. There is possible mixing between $U(1)_X$ and $U(1)_{X'}$, which is set to be small (or vanishing), so the coupling between \hat{X} and A'' is always suppressed and thus has negligible effect. In this setup, the ratio between the branching fractions $\text{Br}[A' \rightarrow \ell \bar{\ell}]$ and $\text{Br}[A' \rightarrow f' \bar{f}']$ is suppressed by the tiny factor of ϵ^2 , thus this setup can readily evade the stringent bound from the CMB measurements.² Regarding the density of the stable particles f' , it is depleted by the efficient freeze-out process $f' \bar{f}' \rightarrow A'' \rightarrow \ell \bar{\ell}$.³ This leads to $n_{f'} \ll n_X$, so f' contributes to neither the DM abundance nor the CMB anisotropy. Also, this setup brings a new annihilation channel $\hat{X}^\dagger \hat{X} \rightarrow A'^* \rightarrow f' \bar{f}'$. For $m_X > m_{A'}$, since it is p -wave dominant, i.e., suppressed by $x_f \sim 1/20$ as compared to $\hat{X}^\dagger \hat{X} \rightarrow A' A'$, it barely affects the DM relic density. But for $m_X < m_{A'}$, it becomes the dominant channel because it receives no suppression by ϵ^2 , as compared to $\hat{X}^\dagger \hat{X} \rightarrow A'^* \rightarrow f \bar{f}$. Hence, unlike the minimal model, this setup allows the $m_X < m_{A'}$ case to produce the correct DM relic density, as well as avoiding the CMB anisotropy constraint. Hence, in this simple setup of the dark sector, the interesting interplay between the constraints of the DM relic density and the direct detection still holds as in the minimal model, whereas the cosmological bounds from CMB and BBN are satisfied.

We use the the package `MicrOMEGAs` [40] to compute the inelastic DM relic density for this setup. To be concrete, we choose the inputs $m_X > m_{A'} > 50 \text{ MeV}$, $m_{f'} = 15 \text{ MeV}$, and $m_{A''} = 45 \text{ MeV}$. Hence the freeze-out ends before the BBN at which $T \sim 1 \text{ MeV}$. We set the coupling input $g_{X'} = \sqrt{2\pi}$ (and thus $\alpha_{X'} = g_{X'}^2/4\pi = 0.5$) and the mixing parameter $\epsilon' = 10^{-4}$ (which is allowed by the NA64 bound [43]).

²The annihilation cross section of $XX' \rightarrow \ell \ell \bar{\ell} \bar{\ell}$ through two virtual A' is suppressed by ϵ^4 and satisfies the constraint (5.23) easily.

³The annihilation $f' \bar{f}' \rightarrow \ell \bar{\ell}$ through a virtual A' is insufficient to deplete the f' density based on a similar relation to Eq.(5.22).

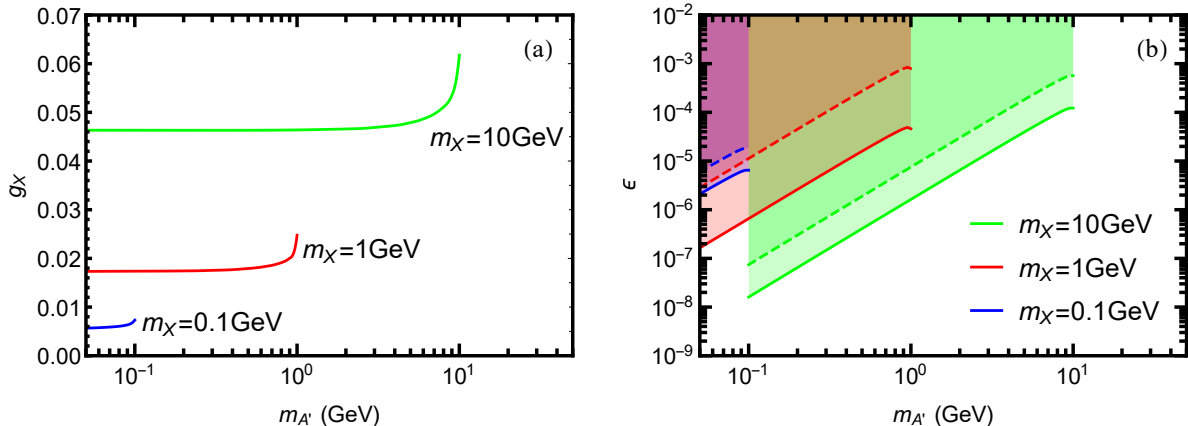


Figure 8: Plot-(a): Predicted $U(1)_X$ coupling g_X versus the dark photon mass $m_{A'}$ as derived by imposing today's DM relic abundance $\Omega h^2 = 0.120$. Plot-(b): Bounds in the $(\epsilon, m_{A'})$ plane. The (green, red, blue) colors denote the DM masses $m_X = (10, 1, 0.1)$ GeV, respectively. The solid (dashed) curves are derived from combining the DM direct detection and the DM relic density, with input $\Delta m = 30$ keV (1 keV).

In Fig. 8(a), we present the g_X values that can give the correct DM relic density. Fig. 8(b) shows the constraints on the dark photon from the direct detection experiments and cosmological observations. In this figure, the (green, red, blue) curves correspond to the DM mass $m_X = (10, 1, 0.1)$ GeV, respectively. They are derived from $\epsilon = g_X^{-1} m_{A'}^2 \Lambda^{-2}$, where the coupling g_X is constrained in Fig. 8(a) as a function of $m_{A'}$, and the cutoff scale Λ is constrained by the direct detection constraints as in Fig. 2. The solid (dashed) curves corresponds to $\Delta m = 30$ keV (1 keV). Note that the green curves only cover the mass region $10^{-2} m_X < m_{A'} < m_X$ as is required in Section 5.1. Throughout the parameter space, we affirm that the relic abundance of f' is always small, $\Omega_{f'} h^2 < 10^{-3}$.

We see that for a given DM mass, the dark coupling g_X is a nonzero constant as $m_{A'} \rightarrow 0$. Thus, we derive the bound on ϵ [shown as solid and dashed curves in Fig. 8(b)] which scales as $m_{A'}^2$ for small dark photon mass. This ensures a high sensitivity to the mixing parameter ϵ , and allows a probe towards the parameter space $10^{-7} < \epsilon < 10^{-3}$ and $0.01 \text{ GeV} < m_{A'} < 10 \text{ GeV}$, where a large portion is previously viable as it is not constrained by other experiments such as the fixed-target experiments [44, 45] and the collider searches [46].

Before concluding this subsection, we also comment on an inelastic DM model with dark photon mediator as introduced in Ref. [21]. In this model, the inelastic DM and the right-handed first generation SM fermions are charged under a $U(1)_R$ gauge group. The electroweak symmetry is spontaneously broken by two Higgs doublets, whose VEVs (v_1, v_2) satisfy $v_h = \sqrt{v_1^2 + v_2^2} \simeq 174 \text{ GeV}$ and $v_1^2 \ll v_2^2$. The dark photon mass is generated by the $U(1)_R$ symmetry breaking.

The DM relic abundance can be provided by the freeze-out mechanism. To obtain the observed DM relic density, a proper DM annihilation rate is needed. Since $\Delta m \ll m_X$, X and X' are equally abundant in the thermal bath before exiting the equilibrium. Thus, the dominant annihilation channel is $XX' \rightarrow A'A'$ when $m_{A'} < m_X$ and $XX' \rightarrow A' \rightarrow f\bar{f}$ when $m_{A'} > m_X$. Since the interactions are suppressed by Λ , the annihilation rate is sufficient only when the channel $XX' \rightarrow A'A'$ is near the

resonance during freeze-out. This requires $m_{A'} \gtrsim 2m_X$.

After the freeze-out, the total DM abundance is already fixed, but the ratio between X and X' can still evolve. As discussed in [21], the leading channel for the conversion $X' \rightarrow X$ is the decay $X' \rightarrow X\nu\bar{\nu}$ decay, which has the decay width,

$$\Gamma \simeq \frac{q_{\text{DM}}^2 g_X^4}{160\pi^3} \frac{v_1^4 \Delta m_X^5}{v_h^4 m_{A'}^4}. \quad (5.25)$$

Ref. [21] sets the mass-splitting around 2.8 keV, whereas in the present study we allow the mass-splitting to vary up to 30 keV, which reduces the value of v_1 to $O(1)$ GeV scale and requires a high VEV ratio $\tan\beta \sim 10^2$.

Although the bounds in this work as imposed by current direct detection experiments are stronger than that of [21], the collider constraints remain unchanged. As is discussed in [21], the case of $m_{A'} > 2m_X$ is disfavored by collider searches. Since it is the only allowed case by the DM relic density constraint, so most parameter space in this model is excluded.

6. Conclusions

The origin and nature of dark matter (DM) remain largely unknown so far except its participation in the gravitational interaction. It is therefore important to probe the DM particles in both large and small mass ranges, and through all possible means including the direct detection, indirect detection, and collider searches.

In this work, we focus on studying the light inelastic DM with mass around (sub-)GeV scale. In Section 2, we gave a generic parameterization of the light inelastic DM interactions. For studying both the DM-electron scattering and DM-nucleus scattering (with Migdal effect) as well as their interplay, we presented the benchmark scenarios of the dark charge assignments as shown in Table 1. Then, in Section 3, we studied the electron recoil signatures from both the direct DM-electron scattering and the Migdal effect (induced by DM-nucleus scattering).

In Section 4, we analyzed the nature of the exothermic inelastic DM scattering process and demonstrated how direct detection experiments (such as XENON1T and XENONnT) can distinguish the signals from the light inelastic DM, as shown in Fig. 1 and Fig. 4. For the different benchmark scenarios of the dark charge assignments, we derived the experimental bounds on the light inelastic DM from the XENONnT ER data and the XENON1T S2-only data as shown in Figs. 2-3 and Figs. 5-6. These bounds depend sensitively on the dark charges (q_e, q_n, q_p) and the mass parameters ($m_X, \Delta m$). We found that for larger DM mass m_X and/or vanishing dark charge q_e , in which case the DM-nucleon scattering dominates, the bounds are set mainly by the amplitudes of Migdal effect with the electron recoil energy around (1–2) keV range, whereas in the case with direct DM-electron scattering being dominant, the signals are concentrated around the $E_R = \Delta m$ region. These facts suggest that a lower energy threshold in the detector can benefit the sensitivity for the DM-nucleon scattering with Migdal effect, and a higher energy resolution can increase the sensitivity to the DM-electron scattering. The

Migdal effect dominates over the direct electron scattering for larger m_X or larger Δm . But, for a general input of $(m_X, \Delta m)$, we demonstrated that it is highly nontrivial to determine which of the two effects is dominant. Hence, it is important to perform a combined analysis of both effects.

Finally, in Section 5, we studied a model realization of such light inelastic DM with the dark photon mediator, and applied the bounds of our benchmark scenarios to constrain this model as shown in Figs. 7 and 8. We further studied the cosmological and laboratory constraints on the inelastic DM.

Acknowledgements

We thank Jingqiang Ye for discussing the XENON1T and XENONnT data analysis. This research was supported in part by the National NSF of China under grants 12175136 and 11835005.

References

- [1] A. H. Abdelhameed *et al.* [CRESST Collaboration], “First results from the CRESST-III low-mass dark matter program,” *Phys. Rev. D* 100 (2019) no.10, 102002 [arXiv:1904.00498 [astro-ph.CO]].
- [2] Z. Z. Liu *et al.* [CDEX Collaboration], “Constraints on Spin-Independent Nucleus Scattering with sub-GeV Weakly Interacting Massive Particle Dark Matter from the CDEX-1B Experiment at the China Jinping Underground Laboratory,” *Phys. Rev. Lett.* 123 (2019) no.16, 161301 [arXiv:1905.00354 [hep-ex]].
- [3] Y. Meng *et al.* [PandaX-4T Collaboration], “Dark Matter Search Results from the PandaX-4T Commissioning Run,” *Phys. Rev. Lett.* 127 (2021) no.26, 261802 [arXiv:2107.13438 [hep-ex]].
- [4] E. Aprile *et al.* [XENON Collaboration], “First Dark Matter Search with Nuclear Recoils from the XENONnT Experiment,” *Phys. Rev. Lett.* 131 (2023) no.4, 041003 [arXiv:2303.14729 [hep-ex]].
- [5] J. Aalbers *et al.* [LZ Collaboration], “First Dark Matter Search Results from the LUX-ZEPLIN (LZ) Experiment,” *Phys. Rev. Lett.* 131 (2023) no.4, 041002 [arXiv:2207.03764 [hep-ex]].
- [6] C. Cheng *et al.* [PandaX-II Collaboration], “Search for Light Dark Matter-Electron Scatterings in the PandaX-II Experiment,” *Phys. Rev. Lett.* 126 (2021) no.21, 211803 [arXiv:2101.07479 [hep-ex]].
- [7] E. Aprile *et al.* [XENON Collaboration], “Search for New Physics in Electronic Recoil Data from XENONnT,” *Phys. Rev. Lett.* 129 (2022) no.16, 161805 [arXiv:2207.11330 [hep-ex]].
- [8] Z. Y. Zhang *et al.* [CDEX Collaboration], “Constraints on Sub-GeV Dark Matter-Electron Scattering from the CDEX-10 Experiment,” *Phys. Rev. Lett.* 129 (2022) no.22, 221301 [arXiv:2206.04128 [hep-ex]].

- [9] E. Aprile *et al.* [XENON Collaboration], “Light Dark Matter Search with Ionization Signals in XENON1T,” *Phys. Rev. Lett.* 123 (2019) no.25, 251801 [arXiv:1907.11485 [hep-ex]].
- [10] R. Essig, J. Mardon and T. Volansky, “Direct Detection of Sub-GeV Dark Matter,” *Phys. Rev. D* 85 (2012), 076007 [arXiv:1108.5383 [hep-ph]].
- [11] A. B. Migdal, *J. Phys. (USSR)* 4 (1941) 449;
- [12] M. Ibe, W. Nakano, Y. Shoji, and K. Suzuki, “Migdal Effect in Dark Matter Direct Detection Experiments,” *JHEP* 03 (2018) 194 [arXiv:1707.07258 [hep-ph]].
- [13] M. J. Dolan, F. Kahlhoefer, C. McCabe, “Directly detecting sub-GeV dark matter with electrons from nuclear scattering,” *Phys. Rev. Lett.* 121 (2018) 101801, [arXiv: 1711.09906 [hep-ph]].
- [14] N. F. Bell, J. B. Dent, J. L. Newstead, S. Sabharwal and T. J. Weiler, “Migdal effect and photon bremsstrahlung in effective field theories of dark matter direct detection and coherent elastic neutrino-nucleus scattering,” *Phys. Rev. D* 101 (2020) no.1, 015012 [arXiv:1905.00046 [hep-ph]].
- [15] R. Essig, J. Pradler, M. Sholapurkar and T. T. Yu, “Relation between the Migdal Effect and Dark Matter-Electron Scattering in Isolated Atoms and Semiconductors,” *Phys. Rev. Lett.* 124 (2020) no.2, 021801 [arXiv:1908.10881 [hep-ph]].
- [16] K. D. Nakamura, K. Miuchi, S. Kazama, Y. Shoji, M. Ibe and W. Nakano, “Detection capability of the Migdal effect for argon and xenon nuclei with position-sensitive gaseous detectors,” *PTEP* 2021 (2021) no.1, 013C01 [arXiv:2009.05939 [physics.ins-det]].
- [17] S. Knapen, J. Kozaczuk and T. Lin, “Migdal Effect in Semiconductors,” *Phys. Rev. Lett.* 127 (2021) no.8, 081805 [arXiv:2011.09496 [hep-ph]].
- [18] W. Wang, K. Y. Wu, L. Wu, and B. Zhu, “Direct detection of spin-dependent sub-GeV dark matter via Migdal effect,” *Nucl. Phys. B* 983 (2022) 115907 [arXiv:2112.06492 [hep-ph]].
- [19] P. W. Graham, R. Harnik, S. Rajendran and P. Saraswat, “Exothermic Dark Matter,” *Phys. Rev. D* 82 (2010) 063512 [arXiv:1004.0937 [hep-ph]]; G. Barello, S. Chang and C. A. Newby, “A Model Independent Approach to Inelastic Dark Matter Scattering,” *Phys. Rev. D* 90 (2014) 094027 [arXiv:1409.0536 [hep-ph]]; E. Del Nobile, G. B. Gelmini, A. Georgescu and J. H. Huh, “Reevaluation of spin-dependent WIMP-proton interactions as an explanation of the DAMA data,” *JCAP* 1508 (2015) 046 [arXiv:1502.07682 [hep-ph]]; M. Baryakhtar, A. Berlin, H. Liu and N. Weiner, “Electromagnetic signals of inelastic dark matter scattering,” *JHEP* 06 (2022) 047 [arXiv:2006.13918 [hep-ph]]; M. Carrillo González and N. Toro, “Cosmology and signals of light pseudo-Dirac dark matter,” *JHEP* 04 (2022) 060 [arXiv:2108.13422 [hep-ph]].
- [20] H. J. He, Y. C. Wang and J. Zheng, “EFT Approach of Inelastic Dark Matter for Xenon Electron Recoil Detection”, *JCAP* 01 (2021) 042 [arXiv:2007.04963 [hep-ph]].

- [21] H. J. He, Y. C. Wang and J. Zheng, “GeV-scale inelastic dark matter with dark photon mediator via direct detection and cosmological and laboratory constraints”, *Phys. Rev. D* 104 (2021) no.11, 115033 [arXiv:2012.05891 [hep-ph]].
- [22] I. M. Bloch, A. Caputo, R. Essig, D. Redigolo, M. Sholapurkar and T. Volansky, “Exploring new physics with O(keV) electron recoils in direct detection experiments,” *JHEP* 01 (2021) 178 [arXiv:2006.14521 [hep-ph]].
- [23] J. Bramante and N. Song, “Electric But Not Eclectic: Thermal Relic Dark Matter for the XENON1T Excess,” *Phys. Rev. Lett.* 125 (2020) no.16, 161805 [arXiv:2006.14089 [hep-ph]].
- [24] J. Engel and P. Vogel, “Spin dependent cross-sections of weakly interacting massive particles on nuclei,” *Phys. Rev. D* 40 (1989) 3132-3135; J. Engel, “Nuclear form-factors for the scattering of weakly interacting massive particles,” *Phys. Lett. B* 264 (1991) 114-119; F. Iachello, L. M. Krauss and G. Maino, “Spin Dependent Scattering of Weakly Interacting Massive Particles in Heavy Nuclei,” *Phys. Lett. B* 254 (1991) 220-224.
- [25] G. Jungman, M. Kamionkowski and K. Griest, “Supersymmetric dark matter,” *Phys. Rept.* 267 (1996) 195-373 [arXiv:hep-ph/9506380].
- [26] K. Griest, “Cross-Sections, Relic Abundance and Detection Rates for Neutralino Dark Matter,” *Phys. Rev. D* 38 (1988) 2357 [erratum: *D* 39 (1989) 3802].
- [27] J. D. Lewin and P. F. Smith, “Review of mathematics, numerical factors, and corrections for dark matter experiments based on elastic nuclear recoil,” *Astropart. Phys.* 6 (1996) 87-112.
- [28] B. M. Roberts, V. A. Dzuba, V. V. Flambaum, M. Pospelov and Y. V. Stadnik, “Dark matter scattering on electrons: Accurate calculations of atomic excitations and implications for the DAMA signal”, *Phys. Rev. D* 93 (2016) 115037, no.11 [arXiv:1604.04559 [hep-ph]].
- [29] B. M. Roberts and V. V. Flambaum, “Electron-interacting dark matter: Implications from DAMA/LIBRA-phase2 and prospects for liquid xenon detectors and NaI detectors”, *Phys. Rev. D* 100 (2019) 063017, no.6 [arXiv:1904.07127 [hep-ph]].
- [30] C. F. Bunge, J. A. Barrientos, and A. V. Bunge, *Atomic Data and Nuclear Data Tables* 53 (1993) 113.
- [31] C. McCabe, “The Astrophysical Uncertainties Of Dark Matter Direct Detection Experiments,” *Phys. Rev. D* 82 (2010) 023530 [arXiv:1005.0579 [hep-ph]].
- [32] C. Savage, K. Freese and P. Gondolo, “Annual Modulation of Dark Matter in the Presence of Streams,” *Phys. Rev. D* 74 (2006) 043531 [arXiv:astro-ph/0607121].
- [33] N. F. Bell, J. B. Dent, B. Dutta, S. Ghosh, J. Kumar and J. L. Newstead, “Low-mass inelastic dark matter direct detection via the Migdal effect,” *Phys. Rev. D* 104 (2021) no.7, 7 [arXiv:2103.05890 [hep-ph]].

- [34] J. Li, L. Su, L. Wu, and B. Zhu, “Spin-dependent sub-GeV inelastic dark matter-electron scattering and Migdal effect. Part I. Velocity independent operator,” JCAP 04 (2023) 020 [arXiv:2210.15474 [hep-ph]].
- [35] E. Aprile *et al.* [XENON Collaboration], “Low-energy Calibration of XENON1T with an Internal ^{37}Ar Source”, Eur. Phys. J. C 83 (2023) no.6, 542 [arXiv:2211.14191 [physics.ins-det]].
- [36] N. Aghanim *et al.* [Planck Collaboration], “Planck 2018 results. VI. Cosmological parameters,” Astron. Astrophys. 641 (2020) A6 [erratum: Astron. Astrophys. 652 (2021) C4] [arXiv:1807.06209 [astro-ph.CO]].
- [37] M. Srednicki, R. Watkins and K. A. Olive, “Calculations of Relic Densities in the Early Universe,” Nucl. Phys. B 310 (1988) 693.
- [38] P. Gondolo and G. Gelmini, “Cosmic abundances of stable particles: Improved analysis,” Nucl. Phys. B 360 (1991) 145.
- [39] R.L. Workman *et al.* [Particle Data Group], “Review of Particle Physics,” Prog. Theor. Exp. Phys. 2022 (2022) 083C01.
- [40] G. Belanger, A. Mjallal and A. Pukhov, “Recasting direct detection limits within micrOMEGAs and implication for non-standard Dark Matter scenarios,” Eur. Phys. J. C 81 (2021) no.3, 239 [arXiv:2003.08621 [hep-ph]].
- [41] T. R. Slatyer, N. Padmanabhan and D. P. Finkbeiner, “CMB Constraints on WIMP Annihilation: Energy Absorption During the Recombination Epoch,” Phys. Rev. D 80 (2009) no.4, 043526 [arXiv:0906.1197 [astro-ph.CO]].
- [42] T. R. Slatyer, “Indirect dark matter signatures in the cosmic dark ages. I. Generalizing the bound on s-wave dark matter annihilation from Planck results,” Phys. Rev. D 93 (2016) no.2, 023527 [arXiv:1506.03811 [hep-ph]].
- [43] Y. M. Andreev *et al.* [NA64 Collaboration], “Search for Light Dark Matter with NA64 at CERN,” Phys. Rev. Lett. 131 (2023) no.16, 161801 [arXiv:2307.02404 [hep-ex]].
- [44] J. P. Lees *et al.* [BaBar Collaboration], “Search for a Dark Photon in e^+e^- Collisions at BaBar,” Phys. Rev. Lett. 113 (2014) no.20, 201801 [arXiv:1406.2980 [hep-ex]].
- [45] A. Anastasi *et al.* [KLOE-2 Collaboration], “Limit on the production of a new vector boson in $e^+e^- \rightarrow U\gamma$, $U \rightarrow \pi^+\pi^-$ with the KLOE experiment,” Phys. Lett. B 757 (2016) 356-361 [arXiv:1603.06086 [hep-ex]].
- [46] R. Aaij *et al.* [LHCb Collaboration], “Search for $A' \rightarrow \mu^+\mu^-$ Decays,” Phys. Rev. Lett. 124 (2020) no.4, 041801 [arXiv:1910.06926 [hep-ex]].



Amplitude analysis of the $\Lambda_b^0 \rightarrow pK^- \gamma$ decay

LHCb collaboration[†]

Abstract

The resonant structure of the radiative decay $\Lambda_b^0 \rightarrow pK^- \gamma$ in the region of proton-kaon invariant-mass up to $2.5 \text{ GeV}/c^2$ is studied using proton-proton collision data recorded at centre-of-mass energies of 7, 8, and 13 TeV collected with the LHCb detector, corresponding to a total integrated luminosity of 9 fb^{-1} . Results are given in terms of fit and interference fractions between the different components contributing to this final state. Only Λ resonances decaying to pK^- are found to be relevant, where the largest contributions stem from the $\Lambda(1520)$, $\Lambda(1600)$, $\Lambda(1800)$, and $\Lambda(1890)$ states.

Submitted to JHEP

© 2024 CERN for the benefit of the LHCb collaboration. CC BY 4.0 licence.

[†]Authors are listed at the end of this paper.

1 Introduction

Rare decays of b hadrons involving flavour-changing neutral currents, such as $b \rightarrow s\ell^+\ell^-$ and $b \rightarrow s\gamma$ transitions, are forbidden at tree level in the Standard Model and further suppressed at loop-level through the GIM mechanism. As a consequence, these decays are very sensitive to potential new particles that can enter virtually through loop-level processes or allow tree-level diagrams, affecting properties of these decays such as branching fractions and angular distributions. The measurements of these processes can probe higher energy scales than those accessible via direct searches.

Thanks to the abundant production of b baryons at the LHC, precision measurements of rare b -baryon decays have become possible for the first time. For example, the LHCb collaboration has performed tests of lepton universality using $\Lambda_b^0 \rightarrow pK^-\ell^+\ell^-$ decays¹ in the dilepton invariant-mass squared range $0.1 < q^2 < 6.0 \text{ GeV}^2/c^4$ and the pK^- invariant-mass range $m_{pK^-} < 2.6 \text{ GeV}/c^2$ [1]. Moreover, the LHCb collaboration has searched for CP violation in $\Lambda_b^0 \rightarrow pK^-\mu^+\mu^-$ decays [2] and measured the branching fraction of the $\Lambda_b^0 \rightarrow \Lambda(1520)\mu^+\mu^-$ decay [3]. Direct interpretations of these results regarding models for physics beyond the Standard Model are difficult given the lack of detailed knowledge of the resonant structure of the pK^- spectrum in different regions of the dilepton invariant-mass spectrum.

An observation of the $\Lambda_b^0 \rightarrow pK^-\gamma$ decay was first reported unofficially in a thesis using Run 1 data (taken during 2011 and 2012) without giving a significance [4]. This paper presents an amplitude analysis of the $\Lambda_b^0 \rightarrow pK^-\gamma$ decay which constitutes the first official observation of this mode. This analysis measures $\Lambda_b^0 \rightarrow pK^-\gamma$ decay properties for the first time and characterises the pK^- spectrum at the photon pole of the recoiling system. Theoretical knowledge of the pK^- spectrum from Λ_b^0 decays, in particular the modelling of form factors, is limited to quark-model calculations [5, 6]. Predictions obtained from lattice QCD [7, 8], HQET [9] and dispersive bounds analyses [10] are only available for the decay via the $\Lambda(1520)$ state. The different Λ resonances in the pK^- spectrum have been studied using fixed target experiments with incident kaons [11, 12]. An amplitude analysis of $\Lambda_b^0 \rightarrow J/\psi pK^-$ decays, which led to the discovery of states compatible with pentaquarks [13], studied the pK^- spectrum from Λ_b^0 decays at the J/ψ resonance in the dimuon invariant-mass spectrum. Additionally, if the amplitudes of the $\Lambda_b^0 \rightarrow pK^-\gamma$ decay are known precisely, this measurement could constitute useful input to a future measurement of the photon polarisation, involving polarised Λ_b^0 baryons, for example from Z boson decays [14].

The $\Lambda_b^0 \rightarrow pK^-\gamma$ decay provides an opportunity to complement the knowledge of the pK^- spectrum, including unique access to heavier states with masses larger than about $2 \text{ GeV}/c^2$ that cannot be accessed with $\Lambda_b^0 \rightarrow J/\psi pK^-$ decays due to the restricted phase space. Measurements of resonance properties are vital inputs to the theoretical description of low-energy QCD as discussed in Ref. [15]. Employing data collected by the LHCb detector in pp collisions during the years 2011–2012 (Run 1) and 2015–2018 (Run 2), corresponding to an integrated luminosity of about 9 fb^{-1} , this paper presents the first amplitude analysis of $\Lambda_b^0 \rightarrow pK^-\gamma$ decays.

¹The inclusion of charge-conjugate processes is implied throughout the text.

2 Detector and selection

The LHCb detector is a single-arm forward spectrometer covering the pseudorapidity range $2 < \eta < 5$, designed for the study of particles containing b or c quarks. The detector includes a high-precision tracking system consisting of a silicon-strip vertex detector surrounding the proton-proton interaction region, a large-area silicon-strip detector located upstream of a dipole magnet with a bending power of about 4 Tm, and three stations of silicon-strip detectors and straw drift tubes placed downstream of the magnet. The tracking system provides a measurement of the momentum of charged particles with a relative uncertainty that varies from 0.5% at low momentum to 1.0% at 200 GeV/ c . The minimum distance of a track to a primary proton-proton collision vertex (PV), the impact parameter (IP), is measured with a resolution of $(15 + 29/p_T) \mu\text{m}$, where p_T is the component of the momentum transverse to the beam, in GeV/ c . Different types of charged hadrons are distinguished using information from two ring-imaging Cherenkov detectors. Photons, electrons and hadrons are identified by a calorimeter system consisting of scintillating-pad (SPD) and preshower detectors, an electromagnetic (ECAL) and a hadronic calorimeter. In addition, a muon system allows the identification of muons.

Samples of simulated events are used to optimise selection requirements and estimate the efficiencies of the signal and backgrounds. The simulated proton-proton collisions are generated using PYTHIA [16] with a specific LHCb configuration [17]. Decays of hadronic particles are described by EvtGen [18], in which final-state radiation is generated using PHOTOS [19]. The interaction of the generated particles with the detector, and its response, are implemented in the Geant4 toolkit [20] as described in Ref. [21]. The $\Lambda_b^0 \rightarrow pK^-\gamma$ decay is generated uniformly in phase space without assumptions on the decay dynamics.

The online event selection is performed by a trigger [22, 23], which consists of a hardware stage, based on information from the calorimeter and muon systems, followed by a software stage, which applies a full event reconstruction. The trigger exploits the presence of a high energy photon reconstructed from clusters in the ECAL. In order to reduce background and improve the mass resolution for the Λ_b^0 and two-body invariant masses, clusters are required to have a transverse energy of $E_T > 2.5\text{--}2.96$ GeV in Run 1 and $E_T > 2.11\text{--}2.7$ GeV in Run 2, respectively, at the hardware trigger level. Moreover, the hardware trigger selects only events with fewer than 600 (450) hits in the SPD for Run 1 (2) to facilitate the reconstruction in the software trigger. In the software trigger, the candidate must contain two high- p_T hadrons that are significantly displaced from the interaction point, as well as a high- E_T photon. During Run 2, a multivariate classifier based on topological criteria complements the cut-based software trigger selection [24]. The Run 1 software trigger requires the di-hadron invariant mass, assuming both hadrons are kaons, to be below 2 GeV/ c^2 . This severely affects the shape of the efficiency as a function of the proton-kaon invariant mass, resulting in the need for separate treatment of Run 1 and Run 2. In addition to this cut in the Run 1 trigger, the large threshold for the photon energy results in low efficiency at high proton-kaon invariant mass. As a consequence, the considered phase space is reduced to a proton-kaon invariant mass of up to 2.5 GeV/ c^2 .

The reconstructed Λ_b^0 candidate is required to have good-quality track and vertex fits. Two tracks, compatible with the kaon and proton hypotheses, are required to have an impact parameter larger than 0.1 mm, a transverse momentum larger than 1 GeV/ c as

well as momentum larger than 5 GeV/ c . The photon must have $E_T > 3$ GeV. The Λ_b^0 decay vertex isolation is used to reject partially reconstructed backgrounds. Specifically, an upper limit is applied on the χ^2 increase in the Λ_b^0 decay vertex fit when adding the most compatible additional track, referred to in the following as $\Delta\chi_{vtx}^2(\Lambda_b^0)$. The Λ_b^0 momentum is further required to point back to the associated primary vertex.

Background candidates resulting from combinations of unrelated protons, kaons, and photons can be suppressed using kinematic variables. A Boosted Decision Tree classifier (BDT) [25] is trained on simulated events as signal proxy and on data candidates with $m(pK\gamma) > m_{\Lambda_b^0} + 300$ MeV/ c^2 as background proxy, to suppress combinatorial background by exploiting mainly kinematic variables. The input variables to the classifier are the momentum, pseudorapidity η , flight distance (FD), $\Delta\chi_{vtx}^2$ of the Λ_b^0 baryon, IP and p_T of the hadrons, and IP, momentum, and p_T of the proton-kaon combination. Additionally, the difference in the vertex-fit χ^2 of the PV associated with the Λ_b^0 baryon reconstructed with and without the Λ_b^0 candidate is used. A further input to the BDT in Run 2 is the isolation variable

$$I_{p_T} = \frac{p_T(\Lambda_b^0) - \sum p_T}{p_T(\Lambda_b^0) + \sum p_T} \quad (1)$$

for which the sum is taken over tracks that are not part of the signal candidate but are associated to the same PV and fall within a cone of half-angle $\Delta R < 1.7$ rad. The half-angle of a track is defined as $(\Delta R)^2 = (\Delta\theta)^2 + (\Delta\phi)^2$, where $\Delta\theta$ and $\Delta\phi$ are the differences in the polar and azimuthal angles of each track with respect to the Λ_b^0 candidate direction. The optimal BDT working point is determined by maximising the ratio $S/\sqrt{S+B}$, where S is the number of expected signal candidates estimated from simulation samples and B is the number of background candidates in the signal region estimated based on the background-dominated regions on either side of the Λ_b^0 peak.

Requirements on the particle identification variables decrease backgrounds stemming from misidentification. Nevertheless, a large amount of misidentified $B_s^0 \rightarrow \phi(\rightarrow K^+K^-)\gamma$ decays passes all particle identification selections and pollutes the sample. These are suppressed by vetoing candidates with a K^+K^- invariant mass, calculated by interpreting the proton candidate as a kaon, between 1.01 and 1.04 GeV/ c^2 . Remaining contributions from misidentified $B_s^0 \rightarrow K^-K^+\gamma$ and $B^0 \rightarrow K^-\pi^+\gamma$ decays are estimated to contribute less than 0.5% of the signal yield and are therefore not included in the baseline model. Background stemming from photon misidentification, such as $\Lambda_b^0 \rightarrow pK^-\pi^0$ or $\Lambda_b^0 \rightarrow pK^-\eta$, is difficult to quantify due to their unknown resonant structures. Estimates using simulation samples assuming a uniform distribution in the respective phase space indicate a contamination of 1–2% relative to the signal decay. Limiting the analysis to a proton-kaon invariant mass of 2.5 GeV/ c^2 removes at least the contributions from potential proton-photon and kaon-photon resonances of these backgrounds which would be the most distorting. Potential contamination from $\Xi_b^0 \rightarrow pK^-\gamma$ decays are investigated and found to be negligible. The data are checked for remaining misidentified backgrounds by applying higher thresholds to the proton and kaon particle identification selection requirements, and by comparing different two-body invariant mass distributions under various alternative mass hypotheses. This reveals misidentified $D^0 \rightarrow K^+K^-$ and $D^0 \rightarrow K^+\pi^-$ decays combined with an unrelated photon, which populate the low mass side band of the signal Λ_b^0 mass peak. A veto on these decays has a strong impact on the shape of the signal acceptance in the Dalitz plane. For this reason, the candidates are retained and treated as part of the combinatorial background. The effect of this treatment is considered as

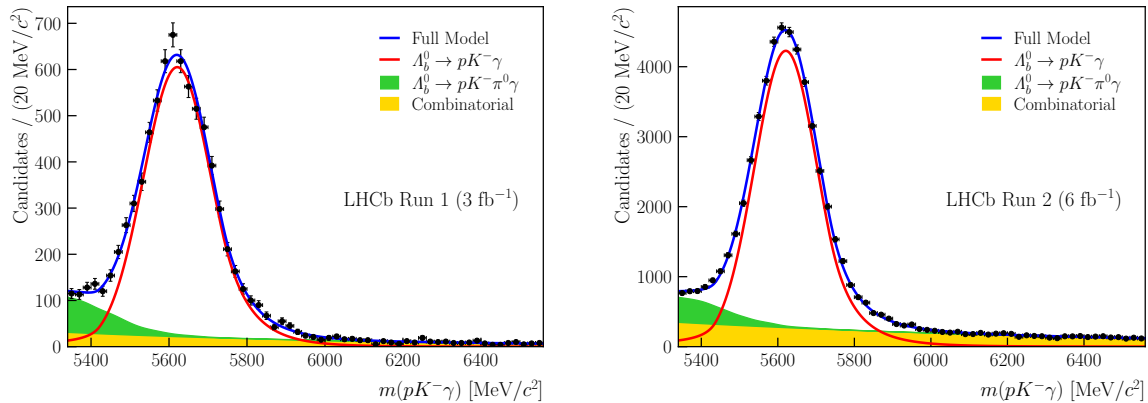


Figure 1: Distribution of the three-body invariant mass of the candidates in the (left) Run 1 and (right) Run 2 data sets. The results of the fits are overlaid.

a systematic uncertainty. Partially reconstructed decays, such as $\Lambda_b^0 \rightarrow pK^{*-}(\rightarrow K^-\pi^0)\gamma$, where the pion is not reconstructed, are also a source of background, which is included in the fit to the three-body invariant-mass distribution described in the following.

3 Invariant mass fit

The three-body invariant mass distribution of the candidates fulfilling all selection criteria is shown in Fig. 1. An unbinned maximum-likelihood fit to these candidates is performed. Following the *sPlot* technique [26], a signal weight (*sWeight*) is assigned to each candidate to statistically disentangle the signal and background components in the subsequent amplitude analysis. The invariant mass fit is performed separately for Run 1 and Run 2, due to differences in the trigger configurations that affect the Dalitz plane distributions and hence require a separate treatment in the amplitude fit.

The signal is modelled by a double-sided Crystal-Ball [27] function comprising a Gaussian core with asymmetric tails. The tail parameters are determined using $\Lambda_b^0 \rightarrow pK^-\gamma$ simulation samples. The remaining background due to random combinations of particles is modelled using a decreasing exponential function where the slope and yield are allowed to vary freely in the fit to data. The shape of the background from partially reconstructed decays is taken from simulation samples of $\Lambda_b^0 \rightarrow pK^{*-}(\rightarrow K^-\pi^0)\gamma$ decays generated uniformly in phase space, reconstructed as signal candidates, and modelled using a kernel density estimator [28] with Gaussian kernels.

Figure 1 also shows the result of the invariant-mass fits to the Run 1 and Run 2 data sets. The signal yields are determined to be 6855 ± 93 and 45558 ± 247 , in Run 1 and Run 2, respectively.

The observed width of the Λ_b^0 mass peak is large compared to the width reconstructed using, for example, $\Lambda_b^0 \rightarrow J/\psi pK^-$ decays [13]. This is a consequence of the large uncertainty in the photon momentum reconstruction, which is based on the ECAL cluster providing only limited directional information. Repeating the vertex fit while fixing the invariant mass of the Λ_b^0 candidate to the known Λ_b^0 mass value [29] reduces the uncertainty in the photon momentum for correctly identified $\Lambda_b^0 \rightarrow pK^-\gamma$ candidates given the excellent precision of the reconstructed proton and kaon momenta [30]. The background-subtracted

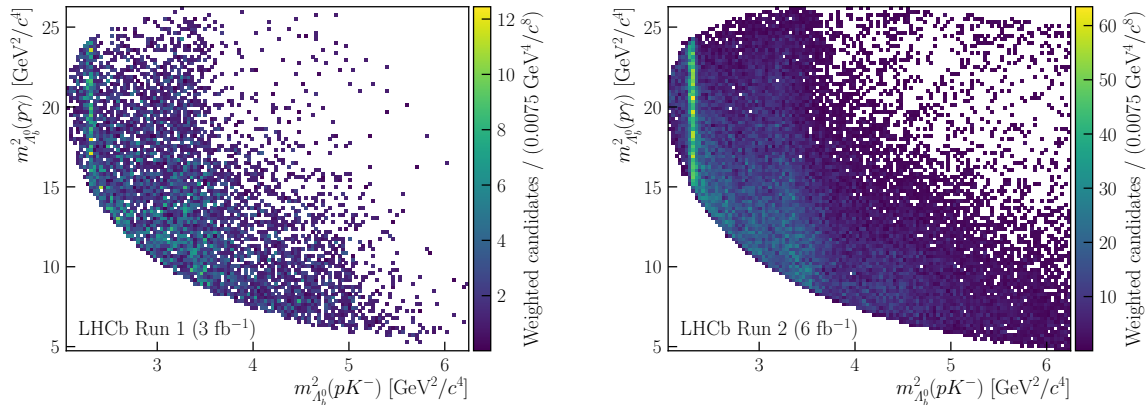


Figure 2: Distribution of the $\Lambda_b^0 \rightarrow pK^- \gamma$ candidates in the Dalitz plane, defined by $m_{\Lambda_b^0}^2(pK^-)$ and $m_{\Lambda_b^0}^2(p\gamma)$, after background-subtraction using the *sPlot* method for (left) Run 1 and (right) Run 2.

data in the Dalitz plane are shown in Fig. 2. The two-body invariant masses displayed here, and used in the amplitude fit later, are calculated using the Λ_b^0 mass constraint as indicated by the Λ_b^0 subscript.

As a cross-check for the combination of data within a single run period, the fit to the three-body invariant mass is performed on the full data set and the data set of each year individually. No significant discrepancies between the fit results are observed. In order to validate the *sPlot* technique, fits to the three-body invariant mass are also performed in bins of the proton-kaon and the proton-photon invariant masses; these fits yield compatible results.

4 Amplitude model

The structures in the data shown in Fig. 2 are described using an amplitude model following the prescription of Ref. [31]. The intermediate Λ resonances decaying to pK^- are modelled assuming Breit–Wigner lineshapes, while their spin-dependent angular distributions are described by the helicity formalism.

The three-body decay of a particle with non-zero spin results in five independent phase-space dimensions. Given that the Λ_b^0 baryons observed by LHCb are produced unpolarised [32], the dimensionality of the phase space relevant to this analysis is reduced from five to two [31]. In the following, the phase-space position is denoted \mathcal{D} . This position can be expressed in terms of the Dalitz variables [33] as shown in Fig. 2 for the background-subtracted data. Equivalently, the phase-space position can be given by the proton-kaon invariant mass, $m(pK^-)$ and the cosine of the proton helicity angle, $\cos \theta_p$, as is used in Ref. [34]. The helicity angle of the proton, θ_p , is the polar angle of the proton momentum in the proton-kaon rest frame where the z axis coincides with the Λ resonance polarisation axis. This angle can be calculated using two steps. First, the proton and resonance momentum are boosted into the Λ_b^0 rest frame where the coordinate system is defined such that the resonance momentum direction coincides with the z axis. Second, the proton momentum is boosted into the proton-kaon rest frame. The magnitude of the z component of the obtained proton momentum, \vec{p} , defines the cosine of the proton

helicity angle

$$\cos \theta_p = \frac{p_z}{|\vec{p}|} . \quad (2)$$

The amplitude of the decay chain $\Lambda_b^0 \rightarrow \Lambda(\rightarrow pK^-)\gamma$ with resonance spin J_Λ and particle helicities denoted by λ_i is

$$\mathcal{A}_{\lambda_\gamma, \lambda_\Lambda, \lambda_p}^A = d_{\lambda_\Lambda \lambda_p}^{J_\Lambda}(\theta_p) H_{\lambda_\Lambda, \lambda_\gamma}^A h_{\lambda_p}^A X_{J_\Lambda}(m(pK^-)) . \quad (3)$$

The function $X_{J_\Lambda}(m(pK^-))$ represents the resonance dynamics. The Wigner d -matrix elements, $d_{\lambda_\Lambda \lambda_p}^{J_\Lambda}(\theta_p)$ [35], describe the rotation of spin states from the Λ helicity frame into the proton helicity frame. The helicity-coupling amplitudes H and h contain the information about the dynamics of the decays $\Lambda_b^0 \rightarrow \Lambda\gamma$ and $\Lambda \rightarrow pK^-$, respectively. Given that the kaon has spin-0, its helicity is also zero and is omitted in the index of the $\Lambda \rightarrow pK^-$ helicity amplitude, h .

Helicity conservation, defined as $\lambda_b = \lambda_\Lambda - \lambda_\gamma$, must be fulfilled. As a result, the resonance helicities can only take the values $\lambda_\Lambda = \pm\frac{1}{2}$ for $J_\Lambda = \pm\frac{1}{2}$ and $\lambda_\Lambda = \pm\frac{1}{2}, \pm\frac{3}{2}$ for $J_\Lambda \geq \frac{3}{2}$. Moreover, the resonance and photon helicities must have the same sign. Subsequently, there are two (four) helicity couplings for each resonance with spin- $\frac{1}{2}$ ($\geq \frac{3}{2}$). Standard parametrisations of resonance dynamics depend on the orbital angular momentum between the children in a decay requiring a transformation of Eq. (3) from the helicity to the canonical basis

$$\begin{aligned} \mathcal{A}_{\lambda_\gamma, \lambda_\Lambda, \lambda_p}^A &= d_{\lambda_\Lambda \lambda_p}^{J_\Lambda}(\theta_p) \sum_{l=|J_\Lambda-s|}^{|J_\Lambda+s|} \sum_{s=|J_p-J_K|}^{|J_p+J_K|} C_{ls}^A h_{ls}^A \\ &\times \sum_{L=|J_b-S|}^{|J_b+S|} \sum_{S=|J_\Lambda-J_\gamma|}^{|J_\Lambda+J_\gamma|} C_{LS}^A H_{LS}^A X_{Ll}^A(m(pK^-)) , \end{aligned} \quad (4)$$

where the angular dependence remains unchanged. This transformation couples the spins of the child particles in a decay to a total spin which is then coupled with their orbital angular momentum. The factors C_{LS}^A and C_{ls}^A are the products of the Clebsch-Gordan coefficients required in the spin-spin and spin-orbital-angular-momentum coupling for the resonance-photon and proton-kaon systems, respectively. In the resonance-photon system, the total spin, S , and orbital angular momentum, L , can take different values such that the product of the Clebsch-Gordan coefficients is

$$C_{LS}^A = \sqrt{\frac{2L+1}{2J_b+1}} \langle J_\Lambda, \lambda_\Lambda; J_\gamma, -\lambda_\gamma | S, (\lambda_\Lambda - \lambda_\gamma) \rangle \cdot \langle L, 0; S, (\lambda_\Lambda - \lambda_\gamma) | J_b, \lambda_b \rangle . \quad (5)$$

The total spin of the pK^- system is $s = \frac{1}{2}$, as the kaon carries no spin. The orbital angular momentum between the proton and the kaon, l , is fixed for a given spin-parity combination due to angular momentum and parity conservation in the strong decay $\Lambda \rightarrow pK^-$. The corresponding Clebsch-Gordan coefficients in the proton-kaon system are

$$C_{ls}^A = 1 \cdot \langle l, 0; J_p, \lambda_p | J_\Lambda, \lambda_p \rangle . \quad (6)$$

Hence, the summation over the spin and orbital angular momentum of the pK^- system can be dropped and only one coupling h_{ls}^A remains and is absorbed into the H_{LS}^A couplings:

$$A_{LS}^A = H_{LS}^A h_{ls}^A . \quad (7)$$

A standard parametrisation of resonance dynamics as employed in previous amplitude analyses (for example in Refs. [13, 36]) is used:

$$X_{Ll}^A(m) = \underbrace{\left(\frac{|\vec{q}|}{q_0}\right)^L B_L(|\vec{q}|, q_0)}_{\Lambda_b^0 \rightarrow \Lambda \gamma} \underbrace{\left(\frac{|\vec{p}|}{p_0}\right)^l B_l(|\vec{p}|, p_0)}_{\Lambda \rightarrow p K^-} \text{BW}(m), \quad (8)$$

where \vec{q} (\vec{p}) is the momentum of the resonance (proton) in the Λ_b^0 (Λ) rest frame and B_l and B_L are Blatt–Weisskopf form factors [37]. Accordingly, the magnitudes of the momenta at the nominal resonance mass are q_0 and p_0 . The resonance is modelled using a Breit–Wigner (BW) distribution [38]

$$\text{BW}(m) = \frac{1}{m_0^2 - m^2 - im_0\Gamma(m)}, \quad \Gamma(m) = \Gamma_0 \left(\frac{p}{p_0}\right)^{2l+1} \frac{m_0}{m} [B_l(p, p_0)]^2, \quad (9)$$

with resonance mass m_0 and width Γ_0 . For the $\Lambda(1405)$ resonance, with a pole-mass below the pK^- threshold, a similar approach as the amplitude analyses of $\Lambda_b^0 \rightarrow J/\psi p K^-$ [13] and $\Lambda_c^+ \rightarrow p K^- \pi^+$ [39] is employed, *i.e.* using a two-component width equivalent to the Flatté parametrisation [40]. The barrier factors, $(|\vec{q}|/m_{\Lambda_b^0})^L$ and $(|\vec{p}|/m_0)^l$, suppress high orbital angular momenta compared to low ones, which will be exploited to simplify the model later on. The Blatt–Weisskopf form factors are equal to one at the resonance pole and shape the resonance peak depending on the orbital angular momentum. This analysis uses the same parametrisation of the Blatt–Weisskopf functions as Ref. [13]. Following the choice made in Ref. [36], the radius of the Λ_b^0 baryon is taken to be $5 \text{ (GeV}/(c\hbar))^{-1}$ and the radius of the Λ resonances is taken to be $1.5 \text{ (GeV}/(c\hbar))^{-1}$.

The final decay rate is the sum over all appearing Λ resonances and their possible helicities, λ_Λ , as well as the initial and final state helicities, $\lambda_b, \lambda_\gamma, \lambda_p$

$$\frac{d\Gamma}{d\mathcal{D}} = \frac{1}{2} \sum_{\lambda_b, \lambda_\gamma, \lambda_p} \left| \sum_{\Lambda} \sum_{\lambda_\Lambda} d_{\lambda_\Lambda \lambda_p}^{J_\Lambda}(\theta_p) C_{l_s}^{\Lambda} \sum_{L=|J_b-S|}^{|J_b+S|} \sum_{S=|J_\Lambda-J_\gamma|}^{|J_\Lambda+J_\gamma|} C_{L_S}^{\Lambda} A_{L_S}^{\Lambda} X_{Ll}^{\Lambda}(m(pK^-)) \right|^2. \quad (10)$$

The decay is assumed to be CP -conserving such that the amplitudes of the decay $\Lambda_b^0 \rightarrow p K^- \gamma$ and $\bar{\Lambda}_b^0 \rightarrow \bar{p} K^+ \gamma$ have the same helicity couplings. As a consequence of isospin suppression, investigated experimentally in Ref. [41] and theoretically in Ref. [42], the $\Lambda_b^0 \rightarrow p K^- \gamma$ decay is dominated by the Λ states and therefore Σ resonances, which have the same quark content but different isospin, are not considered in this analysis. Additionally, resonances in the proton-photon and kaon-photon invariant masses are not included as they almost exclusively populate the phase space at $m(pK) > 2.5 \text{ GeV}/c^2$.

Besides resonances, additional nonresonant components may be necessary to achieve a satisfactory description of the data. Such nonresonant contributions are modelled similarly to the resonances, where the Breit–Wigner peak is replaced by an exponential function or a constant

$$X_{Ll}^{\text{NR,exp}}(m) = \underbrace{\left(\frac{|\vec{q}|}{q_0}\right)^L \left(\frac{|\vec{p}|}{p_0}\right)^l}_{\text{barrier factors}} \exp(-\alpha(m^2 - m_{\text{NR}}^2)), \quad (11)$$

$$X_{Ll}^{\text{NR,const}}(m) = \underbrace{\left(\frac{|\vec{q}|}{q_0}\right)^L \left(\frac{|\vec{p}|}{p_0}\right)^l}_{\text{barrier factors}}.$$

The mass parameter used in the computation of p_0 and q_0 of the nonresonant component is set to the centre of the possible proton-kaon invariant-mass range: $m_{\text{NR}} = 3.5 \text{ GeV}/c^2$. The parameter α is determined by the fit. To incorporate this into the decay rate, the sum over all resonances in Eq. (10) needs to include the nonresonant component. The corresponding coherent sum over the helicity states resembles the sum of a resonant contribution where only the lineshape in Eq. (8) is replaced by the one in Eq. (11).

Finally, the transformation into the LS basis must conserve the number of degrees of freedom (two (four) helicity couplings for each Λ with spin $\frac{1}{2}$ ($\geq \frac{3}{2}$)). However, given that the angular momentum coupling is a purely mathematical transformation and lacks physics knowledge such as $\lambda_\gamma \neq 0$, there are four (six) LS combinations for spin $\frac{1}{2}$ ($\geq \frac{3}{2}$) resonances. Translating $H_{\pm 1/2,0} = 0$ into a combination of LS couplings is non trivial. An approximation omitting all dynamical terms in Eq. (4) is obtained by expressing the two couplings with highest S in terms of the other two or four:

$$\begin{pmatrix} A_{L_{\text{max}}, S_{\text{max}}}^A \\ A_{L_{\text{max}}-1, S_{\text{max}}}^A \end{pmatrix} = - \begin{pmatrix} C_{L_{\text{max}}, S_{\text{max}}}^+ & C_{L_{\text{max}}-1, S_{\text{max}}}^+ \\ C_{L_{\text{max}}, S_{\text{max}}}^- & C_{L_{\text{max}}-1, S_{\text{max}}}^- \end{pmatrix}^{-1} \sum_{L, S < S_{\text{max}}} A_{L, S}^A \begin{pmatrix} C_{LS}^+ \\ C_{LS}^- \end{pmatrix}. \quad (12)$$

The constants C_{LS}^\pm are the Clebsch-Gordan coefficients C_{LS}^A with resonance helicity $\lambda_\Lambda = \pm \frac{1}{2}$ and photon helicity $\lambda_\gamma = 0$. In the case of a spin- $\frac{3}{2}$ resonance for example, there are six LS combinations: $(0, \frac{1}{2}), (1, \frac{1}{2}), (1, \frac{3}{2}), (2, \frac{3}{2}), (2, \frac{5}{2}), (3, \frac{5}{2})$. The transformation in Eq. (12) replaces the latter two and ensures that the amplitude vanishes exactly at the nominal mass of the resonance.

Two interesting quantities that can be extracted from the model are the fit fraction, the relative contribution of a single resonance to the determined full amplitude computed by

$$\text{FF}(n) = \frac{\int_{\mathcal{D}} \left(\frac{d\Gamma(n)}{d\mathcal{D}} \right) d\mathcal{D}}{\int_{\mathcal{D}} \left(\frac{d\Gamma}{d\mathcal{D}} \right) d\mathcal{D}}, \quad (13)$$

and the interference fit fraction

$$\text{IFF}(n, m) = \frac{\int_{\mathcal{D}} \left(\frac{d\Gamma(n, m)}{d\mathcal{D}} \right) d\mathcal{D}}{\int_{\mathcal{D}} \left(\frac{d\Gamma}{d\mathcal{D}} \right) d\mathcal{D}} - \text{FF}(n) - \text{FF}(m). \quad (14)$$

Here, $d\Gamma(n)/d\mathcal{D}$ is the decay rate for a single state n , *i.e.* where the sum in Eq. (10) only contains the state n . Similarly, $d\Gamma(n, m)/d\mathcal{D}$ is the decay rate of two states n, m , *i.e.* where the sum in Eq. (10) only contains the states n and m . In contrast, $d\Gamma/d\mathcal{D}$ is the decay rate containing all states of a given model.

5 Amplitude fit

A simultaneous, unbinned, maximum-likelihood fit of the amplitude model to the Run 1 and Run 2 data sets determines the LS couplings A_{LS} . The negative logarithm of the likelihood function (NLL) is defined as [43]

$$\text{NLL} \equiv -\log(\mathcal{L}) = - \sum_{\text{Run 1}} \log(f_1(\mathcal{D})) w_s - \sum_{\text{Run 2}} \log(f_2(\mathcal{D})) w_s. \quad (15)$$

Table 1: List of well-established Λ resonances and their properties as given in Ref. [29]. J and P are spin and parity of the resonance. The mass m_0 and width Γ_0 correspond to the Breit–Wigner parameters and are given in MeV/c^2 and MeV respectively. The possible mass and width ranges, Δm_0 and $\Delta \Gamma_0$, are also given. If a measurement of mass and width is available, the uncertainties are given instead of a range. The columns σ_{m_0} and σ_{Γ_0} contain the σ values used to estimate the systematic uncertainty related to the resonance parameters. The rightmost columns contain the allowed values of l and L .

Resonance	J^P	m_0	Γ_0	Δm_0	$\Delta \Gamma_0$	σ_{m_0}	σ_{Γ_0}	l	L
$\Lambda(1405)$	$1/2^-$	1405	50.5	± 1.3	± 2	1.3	2	0	0, 1
$\Lambda(1520)$	$3/2^-$	1519	16	1518 – 1520	15 – 17	1	1	2	0, 1, 2
$\Lambda(1600)$	$1/2^+$	1600	200	1570 – 1630	150 – 250	30	50	1	0, 1
$\Lambda(1670)$	$1/2^-$	1674	30	1670 – 1678	25 – 35	4	5	0	0, 1
$\Lambda(1690)$	$3/2^-$	1690	70	1685 – 1695	50 – 70	5	10	2	0, 1, 2
$\Lambda(1800)$	$1/2^-$	1800	200	1750 – 1850	150 – 250	50	50	0	0, 1
$\Lambda(1810)$	$1/2^+$	1790	110	1740 – 1840	50 – 170	50	60	1	0, 1
$\Lambda(1820)$	$5/2^+$	1820	80	1815 – 1825	70 – 90	5	10	3	1, 2, 3
$\Lambda(1830)$	$5/2^-$	1825	90	1820 – 1830	60 – 120	5	30	2	1, 2, 3
$\Lambda(1890)$	$3/2^+$	1890	120	1870 – 1910	80 – 160	20	40	1	0, 1, 2
$\Lambda(2100)$	$7/2^-$	2100	200	2090 – 2110	100 – 250	10	100	4	2, 3, 4
$\Lambda(2110)$	$5/2^+$	2090	250	2050 – 2130	200 – 300	40	50	3	1, 2, 3
$\Lambda(2350)$	$9/2^+$	2350	150	2340 – 2370	100 – 250	20	100	5	3, 4, 5

The weights w_s are the *sPlot* weights presented in Sec. 3 normalised to the effective sample size [44]. The probability distribution functions f_i correspond to the normalised rate in Eq. (10), multiplied by the efficiency map $\varepsilon_i(\mathcal{D})$ of Run 1 or Run 2:

$$f_i(\mathcal{D}) = \frac{\varepsilon_i(\mathcal{D})}{I_i} \frac{d\Gamma}{d\mathcal{D}}, \quad (16)$$

where the normalisation factor is calculated as

$$I_i = \int_{\mathcal{D}} \varepsilon_i(\mathcal{D}) \frac{d\Gamma}{d\mathcal{D}} d\mathcal{D}. \quad (17)$$

The efficiency maps, obtained from simulation samples, are implemented as interpolated histograms. The fit is performed using the `TENSORFLOWANALYSIS` package [45].

Table 1 lists all Λ resonances whose existence ranges from very likely to certain according to Ref. [29]. Such states are rated three or four stars and are derived from analyses of data sets that include precision differential cross sections and polarisation observables, and are confirmed by independent analyses. The allowed values of the orbital angular momenta between the proton and the kaon, l , and the resonance and the photon, L , are given explicitly in the rightmost columns.

The fit parameters are the couplings A_{LS}^A , resulting in 45 independent complex variables when including all listed Λ resonances. A baseline fit comprising these contributions determines $\Lambda(1800)$ as the largest component. To fix the overall phase and magnitude of the full amplitude, its coupling with lowest L is therefore set to $|A_{0,1/2}^{1800}| = 1$ and $\arg(A_{0,1/2}^{1800}) = 0$.

Due to the complexity of the amplitude model, the NLL function has many local minima. Depending on the exact combination of initial values, the fit may converge to different minima. When determining the *best model*, the fit is repeated ten times starting from randomised initial values. Only the result with the lowest NLL out of these ten is compared to the other models. This procedure reduces the risk of choosing the wrong best model based on convergence to a local minimum. While the different minima correspond to different values of the couplings, the values for the fit fractions and interference fit fractions are similar for different minima. As a result of this instability with respect to the couplings, this analysis treats them as nuisance parameters while the derived fit fractions and interference fit fractions are the observables.

The quality of the fit is determined using a binned χ^2 test comparing the two-dimensional weighted data histogram in $(m_{\Lambda_b^0}(pK^-), \cos\theta_p)$ with the fit result. The latter is obtained by generating a large sample of 6×10^6 data points — more than 100 times the combined signal yield — from the fitted pdf. Because some regions of the phase space are only sparsely populated, the histogram is defined using a non-uniform binning with at least 100 observed signal events in each bin. Due to the differences in the Run 1 and Run 2 acceptance shapes, this binning is calculated separately for the two subsets.

The initial model contains all well-known Λ resonances (see Table 1) and no other components. This gives an good description of the major structures in the data. This model is referred to as the *reduced model*. The distribution of the proton-kaon invariant-mass in Run 1 and Run 2 is shown in Fig. 3. The projection of the *reduced model* including all its components is overlaid. While the *reduced model* overall describes the data spectrum well, the model is not satisfactory in the region $m_{\Lambda_b^0}(pK^-) > 2 \text{ GeV}/c^2$. As the heavy Λ states are poorly known, the mass and width of different combinations of heavy states are floated with Gaussian constraints of $100 \text{ MeV}/c^2$ around the values obtained from Ref. [29] in order to improve the fit quality. Allowing the mass and width of the $\Lambda(2100)$ and $\Lambda(2110)$ states to vary, while keeping those of the $\Lambda(2350)$ state fixed, yields the biggest improvement.

Another option to improve the fit quality is the addition of nonresonant contributions. The nonresonant components can affect the entire region of the phase space, and are especially important in regions where resonances with the matching spin-parity may interfere. Nonresonant components with spins up to $\frac{5}{2}$ and both parities, using an exponential or constant lineshape (see Eq. 11), are tested. Both lineshape functions tested yield very similar results for a given set of quantum numbers and the constant one is taken as the default lineshape. The model including a nonresonant component with quantum numbers $J^P = \frac{3}{2}^-$ results in the best fit quality for either lineshape. The fit quality of this model is better than the fit quality of the *reduced model* with floating resonance masses and widths.

As a result, the *best model* used to determine the default result consists of the *reduced model* containing all Λ states with mass and width fixed to the values given in Table 1 and a nonresonant component with quantum numbers $J^P = \frac{3}{2}^-$. Figures 4 and 5 contain projections of the data and the model with its components onto all two-body invariant masses as well as the proton helicity angle for Run 1 and Run 2. Appendix A shows the projections onto the proton-kaon invariant mass using a logarithmic vertical axis. The same set of plots is provided in Appendix B for the fit with floating resonances representing the second best model.

The statistical uncertainties on the fit fractions and interference fit fractions are

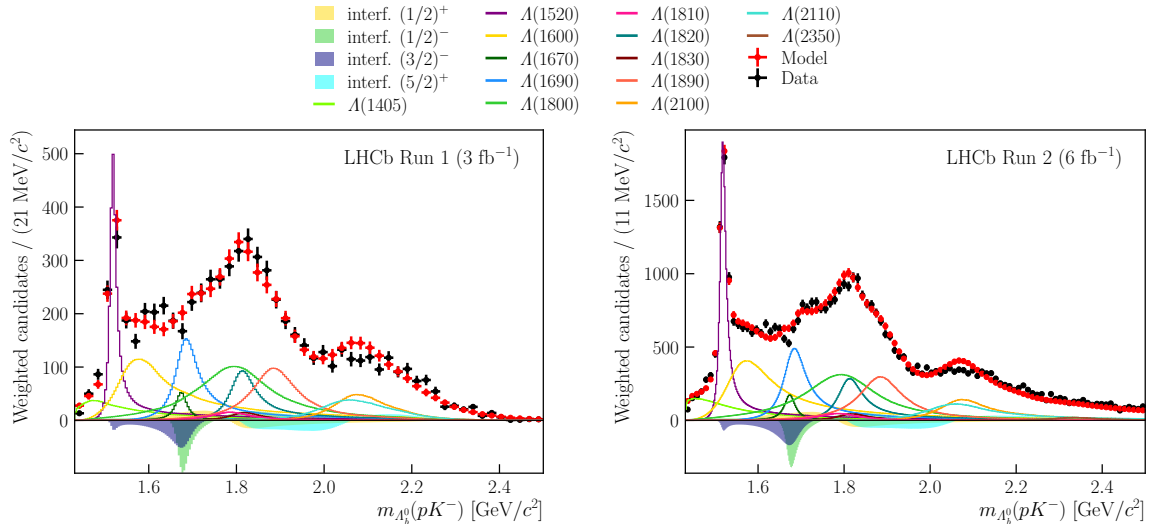


Figure 3: Background-subtracted distribution of the proton-kaon invariant-mass (black dots) for the (left) Run 1 and (right) Run 2 data samples. Also shown is a sample generated according to the result of a simultaneous fit of the *reduced model* to the data (red dots) and its components (lines) as well as the contributions due to interference between states with the same quantum numbers J^P (shaded areas).

determined by bootstrapping the data 250 times. This means that the data set is resampled and a new set of $sWeights$ is calculated from a fit to the three-body invariant mass of each bootstrap sample. Running the amplitude fit on each sample with its respective $sWeights$ results in a distribution for each observable. The value for the statistical confidence interval given later is obtained by finding the shortest 68% interval around the maximum of this distribution.

6 Systematic uncertainties

Systematic uncertainties arise from four major categories: the choice of amplitude model, the acceptance model, the invariant-mass fit model, and potential remaining backgrounds. The individual uncertainties are listed in Table 2 and outlined in the following.

6.1 Amplitude model

In the default fit, the masses and widths of the resonances are set to their world averages and fixed in the fit. To assess the impact of this choice, alternative masses and widths are sampled from Gaussian distributions. The widths of the Gaussians are given in Table 1 as σ_{m_0} and σ_{Γ_0} and are chosen based on the ranges Δm_0 and $\Delta \Gamma_0$. Pseudoexperiments, generated using these alternative mass and width values, are fitted with the default model. The shortest 68% interval around the maximum of the distribution of the difference between the generated and fitted values is taken as a systematic uncertainty.

Similar to the treatment of the masses and widths, also the A_b^0 and A radii used in the Blatt–Weisskopf functions are fixed to $d_{A_b^0} = 5 \text{ (GeV}/(c\hbar))^{-1}$ and $d_A = 1.5 \text{ (GeV}/(c\hbar))^{-1}$ in the default fit. The impact of this choice is assessed by generating samples with

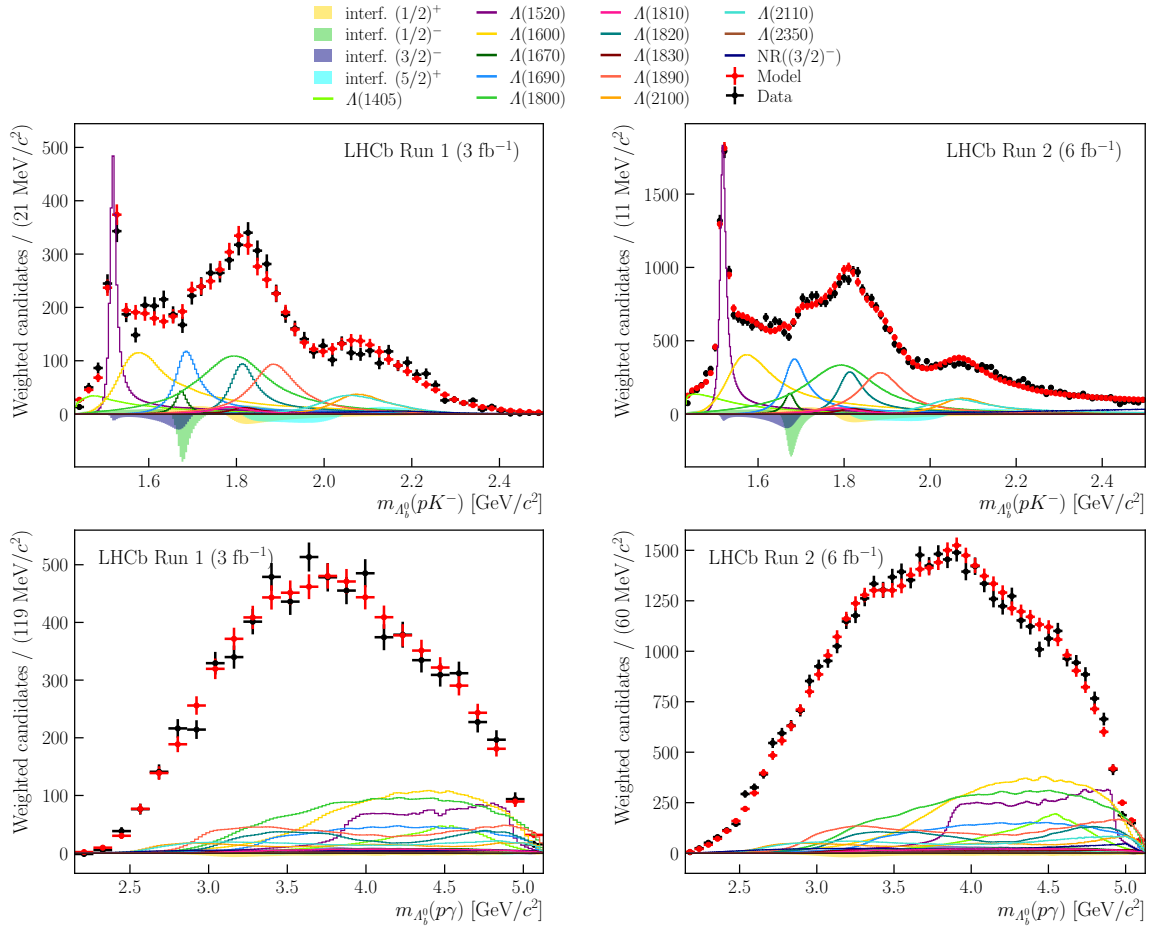


Figure 4: Background-subtracted distribution of the (top) proton-kaon and (bottom) proton-photon invariant-mass (black dots) for the (left) Run 1 and (right) Run 2 data samples. Also shown is a sample generated according to the result of a simultaneous fit of the default model to the data (red dots) and its components (lines) as well as the contributions due to interference between states with the same quantum numbers J^P (shaded areas).

$d_{A_b^0} = 3, 5, 7$ $(\text{GeV}/(c\hbar))^{-1}$ and $d_A = 0.5, 1.5, 2.5, 3.5$ and 4.5 $(\text{GeV}/(c\hbar))^{-1}$. These samples are fitted with the default model. The bias and standard deviation of the differences between the generated and fitted values for each combination of $d_{A_b^0}$ and d_A is taken as systematic uncertainty.

Besides the default model, several other models result in a good description of the data. The systematic effects due to choosing certain components and shapes over others are quantified by generating samples using an alternative model and fitting the default model to the generated pseudosample. The five alternative models are:

- removing the nonresonant component and instead floating mass and width of the $A(2100)$ and $A(2110)$ states using Gaussian constraints (this is the second best model);
- using an exponential function instead of a constant for the lineshape of the nonresonant component;
- employing a sub-threshold Breit–Wigner for the lineshape of the $A(1405)$ state

Table 2: Systematic uncertainties on the fit fractions (top part of the table) and interference fit fractions (bottom part of the table). The values are given in %. The subscripts “BW”, “radius”, “amp.”, and “res.” refer to the systematic uncertainty due to fixing the resonance mass and width, fixing the radius of the hadrons, the choice of amplitude model, and the neglected resolution in the amplitude fit, respectively. The subscripts “finite”, “acc.”, and “kin.” refer to the systematic uncertainties due to the finite simulation sample used to determine the acceptance model, the choice of acceptance model, and the kinematic reweighting respectively. The subscripts “ pK ”, “ $p\gamma$ ”, and “comb.” refer to the systematic uncertainty due to calculating the $sWeights$ in bins of the proton-kaon invariant mass, the proton-gamma invariant mass, and the choice of model for the combinatorial background in the three-body invariant mass fit respectively.

Observable	Amplitude model				Acceptance model			Mass fit model		
	$\sigma_{\text{BW}}^{\Lambda}$	$\sigma_{\text{radius}}^{\Lambda}$	$\sigma_{\text{amp.}}$	$\sigma_{\text{res.}}$	σ_{finite}	$\sigma_{\text{acc.}}$	$\sigma_{\text{kin.}}$	σ_{pK}	$\sigma_{p\gamma}$	$\sigma_{\text{comb.}}$
$\Lambda(1405)$	+1.2 -0.7	+0.0 -0.0	+0.9 +0.2	+0.0 -0.4	+0.2 -0.2	+0.2 -0.2	+0.0 -0.0	+0.0 -0.1	+0.1 -0.0	+0.0 -0.0
$\Lambda(1520)$	+1.0 -1.3	+1.1 -1.1	+0.3 +0.0	+0.0 -0.1	+0.2 -0.2	+0.2 -0.2	+0.1 -0.1	+0.3 -0.0	+0.1 -0.0	+0.0 -0.1
$\Lambda(1600)$	+3.6 -4.5	+1.8 -1.8	+0.5 +0.0	+0.3 -0.2	+0.3 -0.3	+0.2 -0.2	+0.1 -0.1	+0.0 -0.1	+0.1 -0.0	+0.0 -0.0
$\Lambda(1670)$	+1.1 -0.3	+0.2 -0.2	+0.2 -0.2	+0.2 -0.2	+0.1 -0.1	+0.0 -0.0	+0.0 -0.0	+0.0 -0.0	+0.0 -0.0	+0.0 -0.0
$\Lambda(1690)$	+4.1 -0.3	+2.0 -2.0	+1.5 +0.2	+0.6 -0.5	+0.2 -0.2	+0.1 -0.1	+0.0 -0.0	+0.1 -0.0	+0.0 -0.1	+0.0 -0.0
$\Lambda(1800)$	+3.0 -5.9	+1.1 -1.1	+0.1 -0.8	+0.8 -1.5	+0.3 -0.3	+0.1 -0.1	+0.1 -0.1	+0.0 -0.0	+0.6 -0.0	+0.4 -0.0
$\Lambda(1810)$	+3.7 -0.7	+1.1 -1.1	+1.5 +0.1	+0.5 -1.4	+0.2 -0.2	+0.1 -0.1	+0.0 -0.0	+0.1 -0.0	+0.2 -0.0	+0.0 -0.0
$\Lambda(1820)$	+1.8 -4.9	+0.2 -0.2	-0.0 -0.9	+0.3 -0.4	+0.3 -0.3	+0.1 -0.1	+0.0 -0.0	+0.0 -0.3	+0.1 -0.0	+0.0 -0.1
$\Lambda(1830)$	+1.3 -0.9	+0.6 -0.6	+0.3 -0.4	+0.3 -0.5	+0.1 -0.1	+0.1 -0.1	+0.0 -0.0	+0.2 -0.0	+0.1 -0.0	+0.0 -0.0
$\Lambda(1890)$	+4.2 -5.1	+0.8 -0.8	+0.4 -0.4	+0.1 -0.4	+0.2 -0.2	+0.1 -0.1	+0.0 -0.0	+0.1 -0.0	+0.1 -0.0	+0.0 -0.0
$\Lambda(2100)$	+1.0 -2.6	+0.8 -0.8	+0.9 -0.7	+0.2 -0.2	+0.1 -0.1	+0.0 -0.0	+0.0 -0.0	+0.0 -0.0	+0.1 -0.0	+0.1 -0.0
$\Lambda(2110)$	+5.0 -0.6	+1.5 -1.5	+1.5 -0.1	+0.3 -0.2	+0.1 -0.1	+0.1 -0.1	+0.0 -0.0	+0.0 -0.2	+0.0 -0.0	+0.2 -0.0
$\Lambda(2350)$	+0.0 -0.1	+0.0 -0.0	+0.6 -0.2	+0.0 -0.0	+0.0 -0.0	+0.0 -0.0	+0.0 -0.0	+0.1 -0.0	+0.1 -0.0	+0.1 -0.0
$\text{NR}(\frac{3}{2}^-)$	+2.9 +0.3	+0.4 -0.4	+1.0 -2.4	+0.0 -0.6	+0.1 -0.1	+0.1 -0.1	+0.0 -0.0	+0.0 -0.1	+0.0 -0.3	+0.0 -0.0
$\Lambda(1405), \Lambda(1670)$	+0.4 -0.7	+0.3 -0.3	+0.2 -0.0	+0.1 -0.1	+0.1 -0.1	+0.0 -0.0	+0.0 -0.0	+0.0 -0.0	+0.0 -0.0	+0.0 -0.1
$\Lambda(1405), \Lambda(1800)$	+0.5 -3.6	+0.3 -0.3	+0.1 -1.9	+1.7 -0.4	+0.2 -0.2	+0.2 -0.2	+0.0 -0.0	+0.0 -0.0	+0.0 -0.3	+0.1 -0.0
$\Lambda(1520), \Lambda(1690)$	+0.3 -2.3	+0.9 -0.9	-0.1 -0.7	+0.5 -0.4	+0.1 -0.1	+0.0 -0.0	+0.0 -0.0	+0.0 -0.1	+0.0 -0.0	+0.0 -0.0
$\Lambda(1520), \text{NR}(\frac{3}{2}^-)$	+1.2 -2.4	+1.5 -1.5	+0.5 -0.5	+0.8 -0.4	+0.1 -0.1	+0.1 -0.1	+0.0 -0.0	+0.0 -0.0	+0.0 -0.1	+0.0 -0.0
$\Lambda(1600), \Lambda(1810)$	+4.1 -2.8	+0.6 -0.6	+1.5 -0.7	+0.9 -0.4	+0.3 -0.3	+0.2 -0.2	+0.0 -0.0	+0.0 -0.0	+0.0 -0.4	+0.0 -0.4
$\Lambda(1670), \Lambda(1800)$	+1.5 -1.9	+0.4 -0.4	+0.3 -0.2	+0.4 -0.4	+0.1 -0.1	+0.1 -0.1	+0.0 -0.0	+0.0 -0.0	+0.0 -0.0	+0.0 -0.1
$\Lambda(1690), \text{NR}(\frac{3}{2}^-)$	+0.9 -2.2	+1.1 -1.1	+0.2 -2.7	+0.2 -0.5	+0.1 -0.1	+0.1 -0.1	+0.0 -0.0	+0.0 -0.0	+0.0 -0.1	+0.0 -0.0
$\Lambda(1820), \Lambda(2110)$	+2.4 -3.1	+1.6 -1.6	+0.5 -1.6	+0.3 -0.5	+0.2 -0.2	+0.1 -0.1	+0.0 -0.0	+0.2 -0.0	+0.0 -0.3	+0.0 -0.2

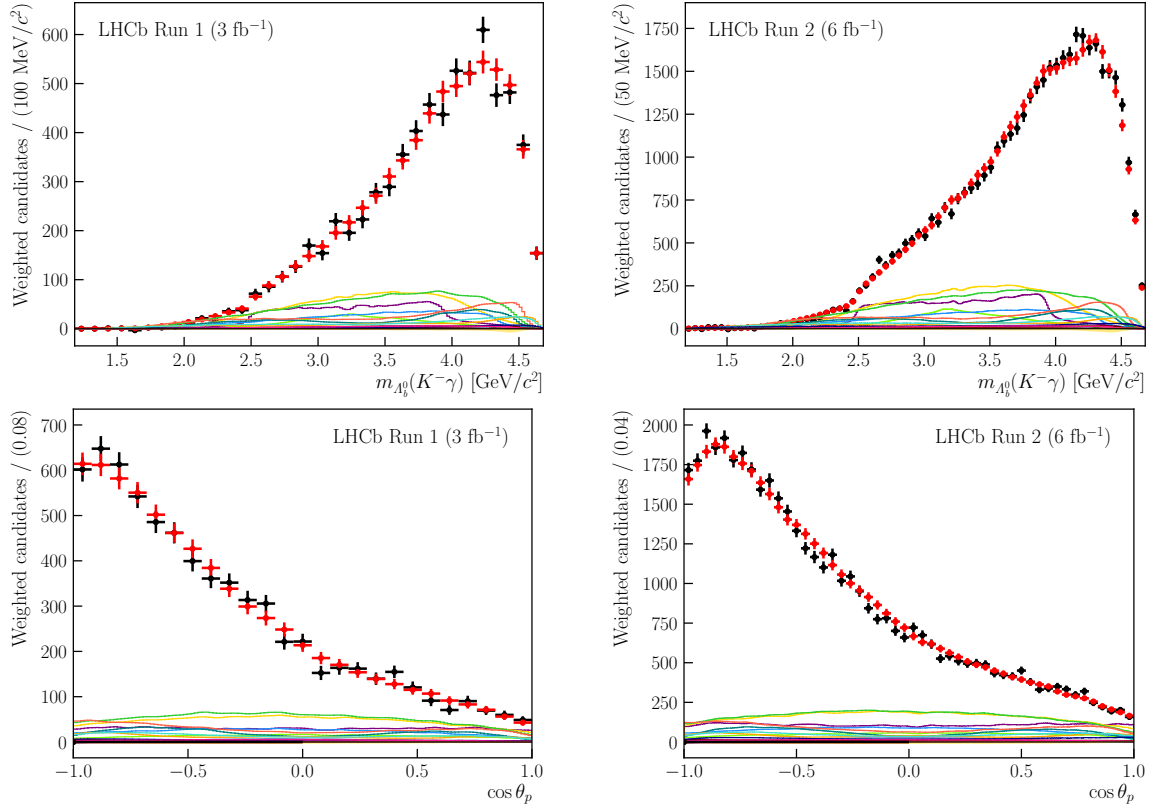


Figure 5: Background-subtracted distribution of (top) the kaon-photon invariant-mass and (bottom) the proton helicity angle (black dots) for the (left) Run 1 and (right) Run 2 data samples. Also shown is a sample generated according to the result of a simultaneous fit of the default model to the data (red dots) and its components (lines) as well as the contributions due to interference between states with the same quantum numbers J^P (shaded areas). See Fig. 4 for the legend.

instead of the Flatté shape;

- adding a second nonresonant component with constant lineshape and $J^P = \frac{5}{2}^+$;
- adding a second nonresonant component with constant lineshape and $J^P = \frac{1}{2}^+$.

The systematic uncertainty due to the model choices is calculated based on the mean and spread of the results obtained using the five alternative models.

Because the resolution is much smaller than the width of the resonances in all regions of the Dalitz plane, the amplitude model does not include resolution effects in the two-body invariant masses, $m_{A_b^0}(pK)$ and $m_{A_b^0}(p\gamma)$. The systematic impact of this choice is tested by generating samples with the default model and smearing the masses according to the resolution determined on simulation samples. Both the unsmeared and smeared samples are fit with the default model which does not account for the resolution. The shortest 68% interval around the maximum of the distribution of the difference between the two results is taken as a systematic uncertainty.

6.2 Acceptance model

The acceptance map is created using a simulation sample generated uniformly in phase space. The finite size of the sample, the choices regarding particle identification and kinematic modelling, as well as the number of bins in the acceptance histogram are varied individually to assess their impact on the observables. The fit to data is repeated with each alternative acceptance map and the difference between the default and alternative result calculated. The spread of the differences for the acceptance-related systematic effects, namely the finite sample size, the acceptance model, and the kinematic weights are taken as individual systematic uncertainties. The uncertainty associated with the particle identification weights is found to be negligible.

6.3 Mass fit model

In order to quantify systematic effects due to choices in the fit to the A_b^0 invariant mass, the analysis is performed for each of these alternatives:

- modelling the combinatorial background using a polynomial instead of an exponential function;
- modelling the partially reconstructed background using an Argus function [46] instead of a kernel density estimator obtained from simulation samples;
- letting the signal tail parameters vary in the fit to data using a Gaussian constraint instead of fixing them;
- calculating the $sWeights$ in bins of $m_{A_b^0}(pK^-)$ and $m_{A_b^0}(p\gamma)$ to account for possible correlations between the Dalitz variables and the three-body invariant mass.

Only changing the shape of the combinatorial background and calculating the $sWeights$ in bins of the two-body invariant masses results in a difference with respect to the default result; this difference is added as a systematic uncertainty.

6.4 Additional background contamination

After the selection, a small number of candidates from misidentified $D^0 \rightarrow K^+K^-$ and $D^0 \rightarrow K^+\pi^-$ decays combined with a random photon remain in the data sample. In the three-body invariant mass, they are predominantly located below the A_b^0 mass peak. The full analysis chain is repeated vetoing both D^0 decays in order to determine the systematic effect of this choice and no difference is observed.

The contamination due to misidentified $B_s^0 \rightarrow K^+K^-\gamma$ and $B^0 \rightarrow K^+\pi^-\gamma$ decays is estimated to not exceed 0.5% of the signal yield. The resulting structures are wide and spread across large parts of the phase space. Nevertheless, the two backgrounds are included in the mass fit constraining their yield to 0.5% of the signal yield. The amplitude fit is repeated using the obtained alternative set of $sWeights$. No difference to the default result is observed.

6.5 Systematic uncertainty combinations

Table 2 contains all individual systematic uncertainties considered for the final result. Sources of systematic uncertainty found to have no impact on the default values are neglected: the limited simulation sample size and the particle identification weights used to determine the acceptance model, the shape of the signal and combinatorial background in the fit to the three-body invariant mass, and the consideration of additional misidentified B_s^0 and B^0 backgrounds in the mass fit as well as vetoing misidentified backgrounds from D^0 decays. All acceptance-related systematic uncertainties are assumed to be Gaussian and centred around the default value. All mass fit systematic uncertainties are also assumed to be Gaussian and centred around the default value, however only allowing values on either the positive or negative side as the nature of these systematic effects is a one-sided bias instead of a double-sided uncertainty. The systematic uncertainty related to the amplitude model is considered to be Gaussian but biased with respect to the default value. Similarly to the statistical uncertainty, the systematic uncertainty due to fixing the resonance parameters and neglecting the resolution are neither centred around the default value nor symmetric.

As a consequence of asymmetric non-Gaussian behaviour of these distributions, the uncertainties can not be combined by taking the square root of the sum of the individual uncertainties squared. Instead, they are combined by numerically convolving the distributions and taking the shortest 68% interval around the maximum of the resulting distribution as the combined uncertainty interval. The uncertainty due to the poorly known Λ resonance parameters dominates the combination. In order to differentiate between the uncertainty due to this external input and the systematic uncertainty related to the analysis choices, the combination is performed once for all sources of systematic uncertainty and once for all but $\sigma_{\text{BW}}^\Lambda$ and σ_{radius} . The two external uncertainties $\sigma_{\text{BW}}^\Lambda$ and $\sigma_{\text{radius}}^\Lambda$ are combined to give $\sigma_{\text{syst}}^{\text{external}}$.

7 Results and conclusion

The results of this analysis, including statistical and systematic uncertainties, are presented in Fig. 6 and Table 3. The statistical correlations between the observables are given in Appendix D. The data and model projections on the invariant masses and proton helicity angle are shown in Figs. 4 and 5. The largest resonant contributions to the $\Lambda_b^0 \rightarrow pK^- \gamma$ decay are found to arise from the $\Lambda(1800)$, $\Lambda(1600)$, $\Lambda(1890)$ and $\Lambda(1520)$ states, in decreasing order. The largest interference term involves the $\Lambda(1405)$ and $\Lambda(1800)$ baryons.

The uncertainties for most observables are dominated by external inputs, specifically the masses and widths of the Λ states. A future measurement including improved knowledge of the different Λ baryons and more data will result in a significant reduction of the uncertainties.

The analysis of $\Lambda_b^0 \rightarrow pK^- \gamma$ decays provides information about the composition of the pK^- spectrum with unique access to the heavier Λ states. A comparison between the composition of the spectrum in $\Lambda_b^0 \rightarrow pK^- \gamma$ and $\Lambda_b^0 \rightarrow J/\psi pK^-$ decays, see Ref. [13], is complicated due to the different phase space and the prominent pentaquark contributions in the latter. Three notable differences are explained in the following. First, the contribution of the sub-threshold resonance $\Lambda(1405)$ is much smaller in the radiative mode. Second, the $\Lambda(1810)$ state appears small in decays to a photon but large in the J/ψ case; the

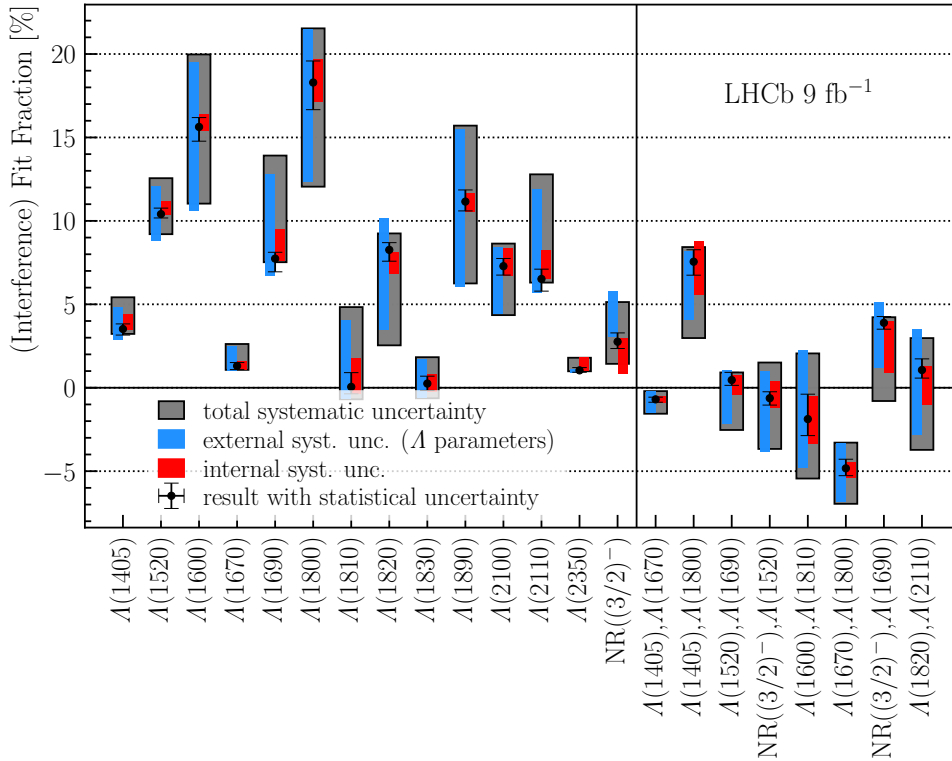


Figure 6: Final results for the fit fractions and interference fit fractions. The vertical line separates the fit from the interference fit fractions. The error bars represent the different sources of uncertainty.

neighbouring $\Lambda(1820)$ state behaves in the opposite way. This observation reveals a potential ambiguity between the two resonances also echoed in the systematic uncertainties on their fit fractions presented in this paper. Third, the heavy resonances $\Lambda(1890)$, $\Lambda(2100)$, $\Lambda(2110)$, and $\Lambda(2350)$ are much larger in the radiative case which is in part due to the phase space enhancement.

In conclusion, an amplitude analysis of the decay $\Lambda_b^0 \rightarrow pK^- \gamma$ is presented for the first time, based on the helicity formalism. A sample of around 50 000 signal candidates is selected from proton-proton collisions recorded by the LHCb experiment at centre-of-mass energies of 7, 8 and 13 TeV. The default fit model comprises all known Λ resonances as well as a nonresonant contribution with quantum numbers $J^P = \frac{3}{2}^-$. The presented amplitude model provides a detailed description of the $\Lambda_b^0 \rightarrow pK^- \gamma$ decay with possible applications ranging from searches for beyond the Standard Model physics in $\Lambda_b^0 \rightarrow pK^- \ell^+ \ell^-$ decays to QCD studies and a possible measurement of the photon polarisation in $\Lambda_b^0 \rightarrow pK^- \gamma$ decays using polarised Λ_b^0 baryons from Z decays at future e^+e^- colliders.

Table 3: Fit fractions (top) and interference fit fractions (bottom) determined using the amplitude model. The values are given in %. The uncertainties from internal and external sources, determined by the numerical convolution procedure are labelled $\sigma_{\text{syst}}^{\text{internal}}$ and $\sigma_{\text{syst}}^{\text{external}}$.

Observable	Value	σ_{stat}	$\sigma_{\text{syst}}^{\text{internal}}$	$\sigma_{\text{syst}}^{\text{external}}$	σ_{syst}
$\Lambda(1405)$	3.5	+0.3 -0.4	+0.9 -0.0	+1.3 -0.6	+1.9 -0.3
$\Lambda(1520)$	10.4	+0.4 -0.2	+0.7 -0.0	+1.7 -1.6	+2.2 -1.2
$\Lambda(1600)$	15.6	+0.6 -0.9	+0.8 -0.2	+3.9 -5.0	+4.3 -4.6
$\Lambda(1670)$	1.3	+0.2 -0.2	+0.3 -0.2	+1.2 -0.3	+1.3 -0.2
$\Lambda(1690)$	7.7	+0.4 -0.8	+1.8 -0.1	+5.1 -1.0	+6.2 -0.2
$\Lambda(1800)$	18.3	+1.3 -1.6	+1.4 -1.1	+3.2 -6.0	+3.2 -6.2
$\Lambda(1810)$	0.1	+0.9 -0.4	+1.7 -0.4	+4.0 -0.7	+4.8 -0.7
$\Lambda(1820)$	8.3	+0.4 -0.7	-0.2 -1.4	+1.9 -4.8	+1.0 -5.7
$\Lambda(1830)$	0.3	+0.4 -0.4	+0.6 -0.5	+1.5 -0.9	+1.6 -0.9
$\Lambda(1890)$	11.2	+0.7 -0.6	+0.5 -0.6	+4.3 -5.1	+4.6 -4.9
$\Lambda(2100)$	7.3	+0.5 -0.5	+1.1 -0.6	+1.1 -2.8	+1.4 -2.9
$\Lambda(2110)$	6.5	+0.6 -0.7	+1.7 -0.0	+5.4 -0.9	+6.3 -0.2
$\Lambda(2350)$	1.0	+0.2 -0.1	+0.8 -0.0	+0.0 -0.2	+0.8 -0.1
$\text{NR}(3/2^-)$	2.8	+0.5 -0.4	+0.2 -1.9	+3.0 +0.3	+2.4 -1.3
$\Lambda(1405), \Lambda(1670)$	-0.7	+0.1 -0.2	+0.2 -0.2	+0.5 -0.8	+0.5 -0.9
$\Lambda(1405), \Lambda(1800)$	7.6	+0.7 -0.8	+1.2 -2.0	+0.6 -3.5	+0.9 -4.6
$\Lambda(1520), \Lambda(1690)$	0.5	+0.5 -0.3	+0.3 -0.9	+0.6 -2.6	+0.5 -3.0
$\Lambda(1520), \text{NR}(3/2^-)$	-0.6	+0.4 -0.4	+1.0 -0.6	+1.6 -3.2	+2.1 -3.0
$\Lambda(1600), \Lambda(1810)$	-1.9	+1.5 -1.0	+1.3 -1.5	+4.1 -2.9	+3.9 -3.6
$\Lambda(1670), \Lambda(1800)$	-4.8	+0.5 -0.4	+0.4 -0.6	+1.5 -2.0	+1.5 -2.1
$\Lambda(1690), \text{NR}(3/2^-)$	3.9	+0.4 -0.4	+0.1 -3.0	+1.2 -2.7	+0.3 -4.7
$\Lambda(1820), \Lambda(2110)$	1.1	+0.7 -0.5	+0.2 -2.1	+2.5 -3.9	+1.9 -4.8

Acknowledgements

We express our gratitude to our colleagues in the CERN accelerator departments for the excellent performance of the LHC. We thank the technical and administrative staff at the LHCb institutes. We acknowledge support from CERN and from the national agencies: CAPES, CNPq, FAPERJ and FINEP (Brazil); MOST and NSFC (China); CNRS/IN2P3 (France); BMBF, DFG and MPG (Germany); INFN (Italy); NWO (Netherlands); MNiSW and NCN (Poland); MCID/IFA (Romania); MICINN (Spain); SNSF and SER (Switzerland); NASU (Ukraine); STFC (United Kingdom); DOE NP and NSF (USA). We acknowledge the computing resources that are provided by CERN, IN2P3 (France), KIT and DESY (Germany), INFN (Italy), SURF (Netherlands), PIC (Spain), GridPP (United Kingdom), CSCS (Switzerland), IFIN-HH (Romania), CBPF (Brazil), and Polish WLCG (Poland). We are indebted to the communities behind the multiple open-source software packages on which we depend. Individual groups or members have received support from ARC and ARDC (Australia); Key Research Program of Frontier Sciences of CAS, CAS PIFI, CAS CCEPP, Fundamental Research Funds for the Central Universities, and Sci. & Tech. Program of Guangzhou (China); Minciencias (Colombia); EPLANET, Marie Skłodowska-Curie Actions, ERC and NextGenerationEU (European Union); A*MIDEX, ANR, IPhU and Labex P2IO, and Région Auvergne-Rhône-Alpes (France); AvH Foundation (Germany); ICSC (Italy); GVA, XuntaGal, GENCAT, Inditex, InTalent and Prog. Atracción Talento, CM (Spain); SRC (Sweden); the Leverhulme Trust, the Royal Society and UKRI (United Kingdom). A portion of this work was awarded the Martin Schmeißer Medal.

Appendices

A Logarithmic scale plots of $m_{\Lambda_b^0}(pK^-)$

The plots in Fig. 7 are equivalent to the top plots in Fig. 4 with a logarithmic vertical axis in order to make all components visible. This means the plots contain the background corrected data distributions in the proton-kaon invariant mass. The plots also contain the full fit model and the individual components. Note that there are regions where the interference terms become negative but this cannot be displayed on a logarithmic scale.

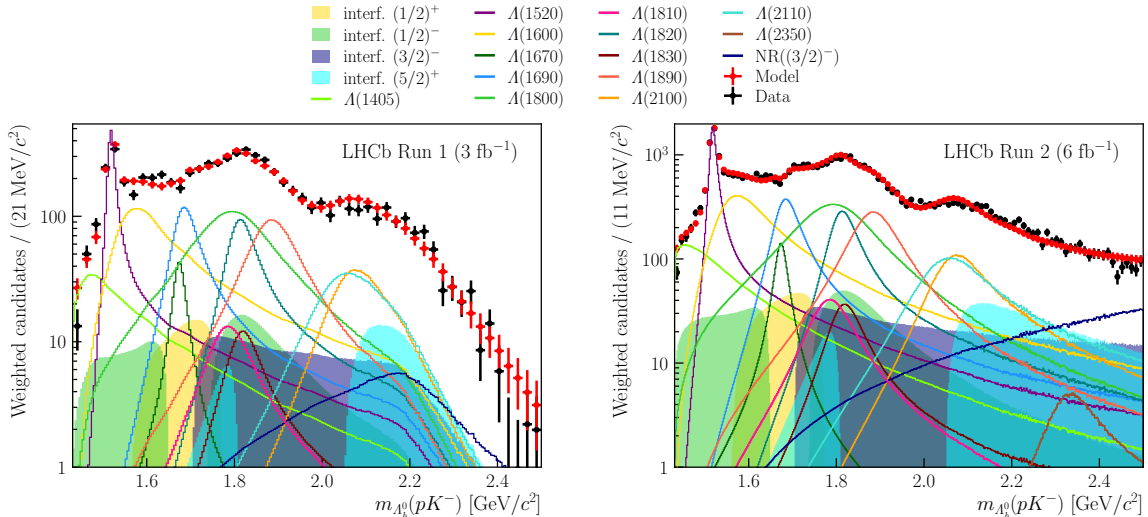


Figure 7: Background-subtracted distribution of the proton-kaon invariant-mass (black dots) for the (left) Run 1 and (right) Run 2 data samples on a logarithmic scale. Also shown is a sample generated according to the result of a simultaneous fit of the default model to the data (red dots) and its components (lines) as well as the contributions due to interference between states with the same quantum numbers J^P (shaded areas).

B Projections for the reduced and second best models

The *reduced model* consists of the Λ resonances in Table 1. The *best* and second best model are based on the *reduced model*. Contrary to the *best model*, the second best model has no nonresonant component but instead the mass and width of the $\Lambda(2100)$ and $\Lambda(2110)$ states are floated in the fit.

Figure 8 shows the fit projections on the proton-photon and kaon-photon invariant-mass, as well as the proton helicity angle for the *reduced model*. Figure 9 shows the fit projections on the two-body invariant masses and the proton helicity angle for this fit. Figures 10 and 11 show the projections on the proton-kaon invariant mass for the *reduced model* and the second best model using a logarithmic scale.

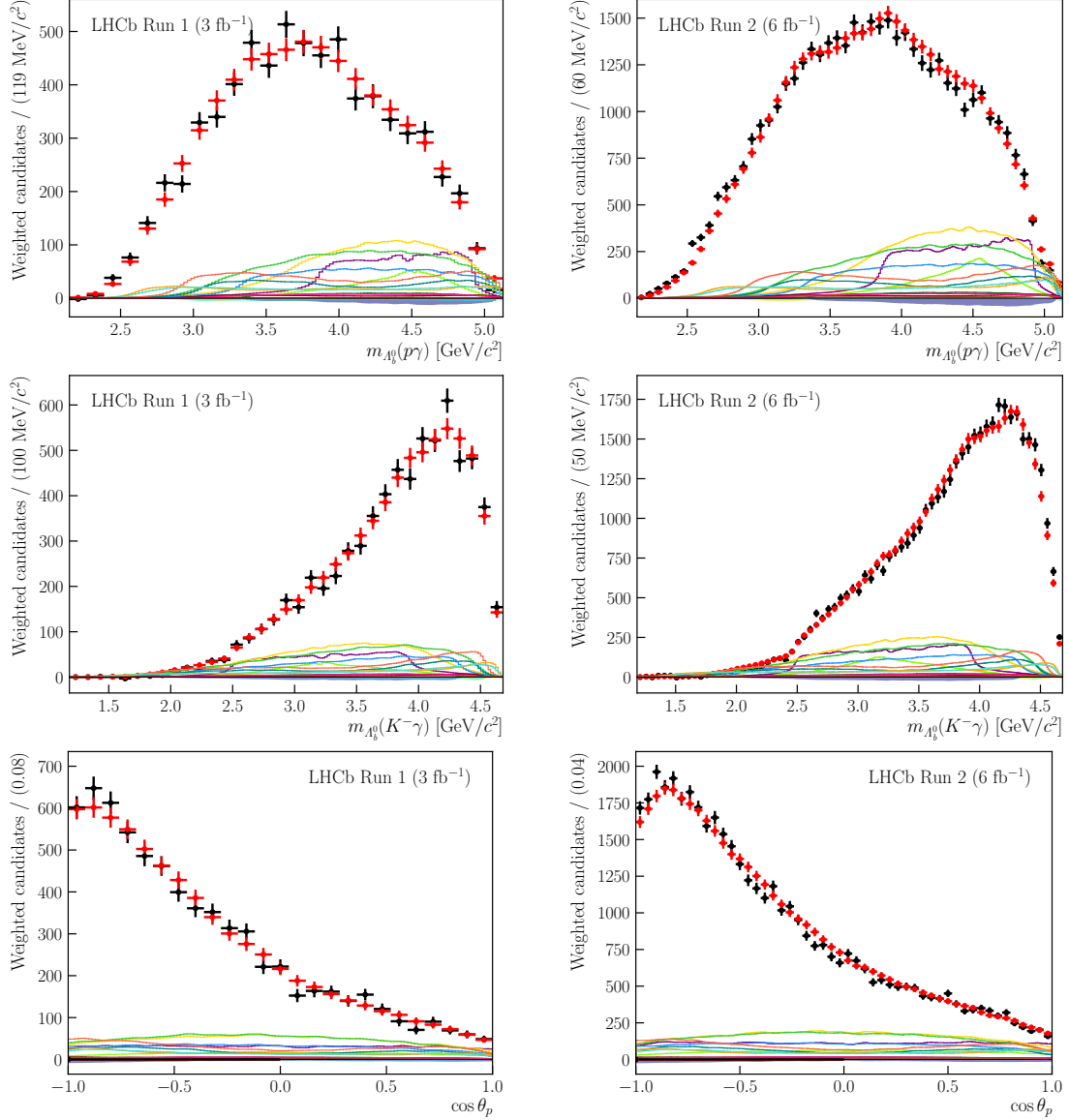


Figure 8: Background-subtracted distribution of (top) the proton-photon invariant-mass, (middle) the kaon-photon invariant-mass, and (bottom) the proton helicity angle (black dots) for the (left) Run 1 and (right) Run 2 data samples. Also shown is a sample generated according to the result of a simultaneous fit of the *reduced model* to the data (red dots) and its components (lines) as well as the contributions due to interference between states with the same quantum numbers J^P (shaded areas). See Fig. 3 for the legend.

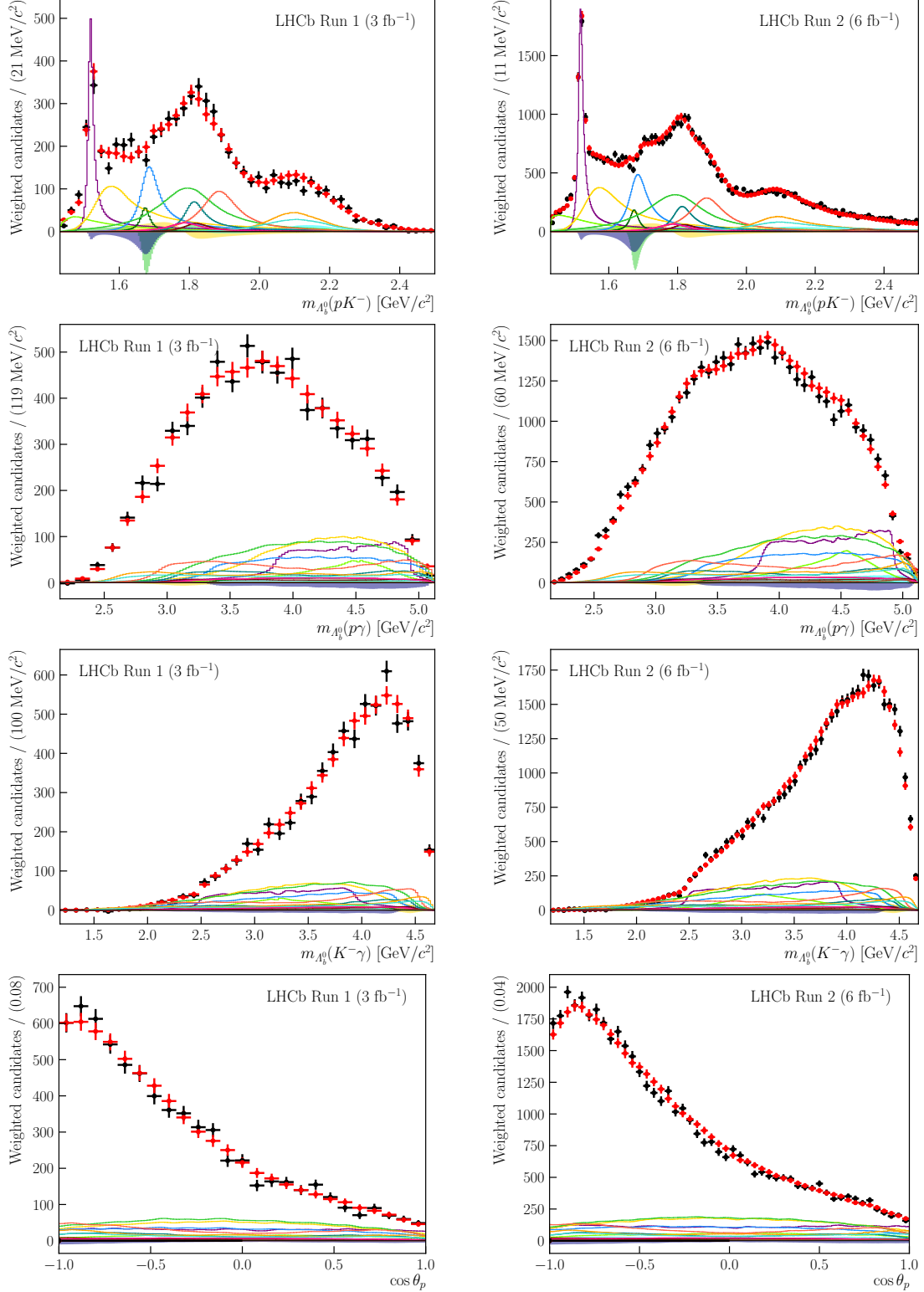


Figure 9: Background-subtracted distribution of (top three rows) the two-body invariant-masses and (bottom row) the proton helicity angle (black dots) for the (left) Run 1 and (right) Run 2 data samples. Also shown is a sample generated according to the result of a simultaneous fit of the second best model to the data (red dots) and its components (lines) as well as the contributions due to interference between states with the same quantum numbers J^P (shaded areas). See Fig. 3 for the legend.

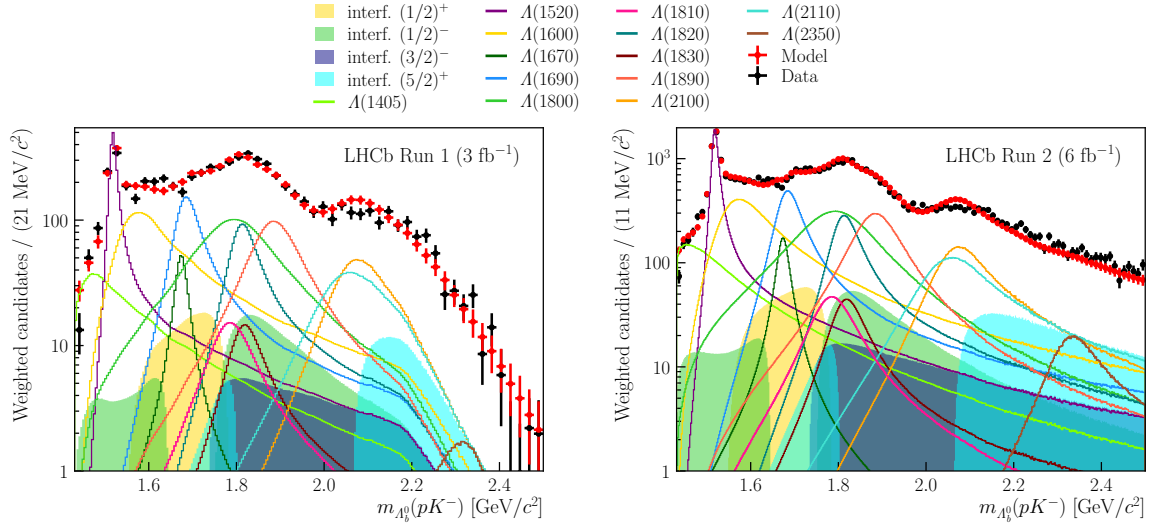


Figure 10: Background-subtracted distribution of the proton-kaon invariant-mass (black dots) for the (left) Run 1 and (right) Run 2 data samples on a logarithmic scale. Also shown is a sample generated according to the result of a simultaneous fit of the *reduced model* to the data (red dots) and its components (lines) as well as the contributions due to interference between states with the same quantum numbers J^P (shaded areas).

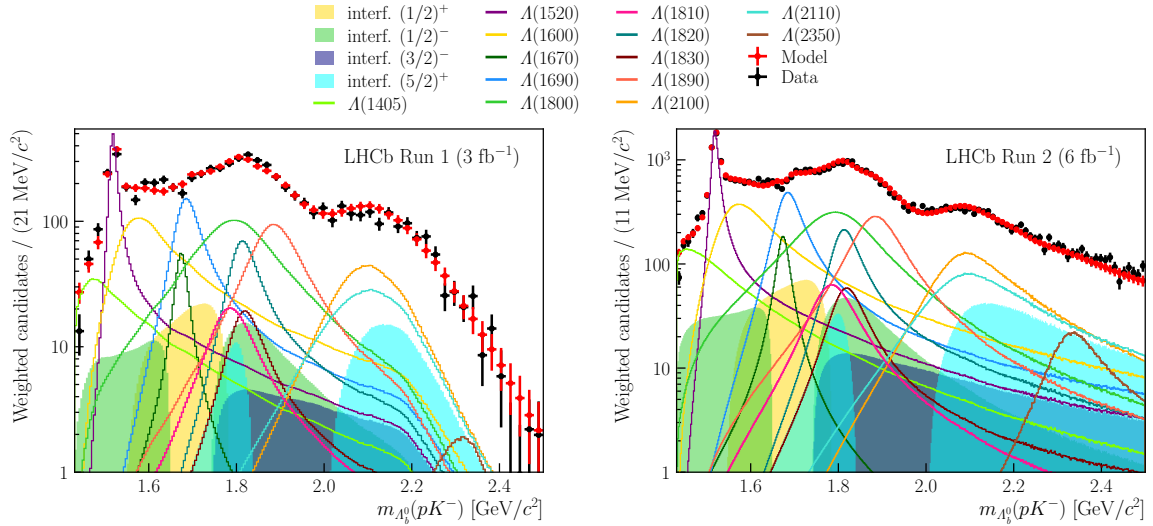


Figure 11: Background-subtracted distribution of the proton-kaon invariant-mass (black dots) for the (left) Run 1 and (right) Run 2 data samples on a logarithmic scale. Also shown is a sample generated according to the result of a simultaneous fit of the second best model to the data (red dots) and its components (lines) as well as the contributions due to interference between states with the same quantum numbers J^P (shaded areas).

C Couplings at the best fit point

Tables 4 and 5 give the value of the couplings, A_{LS} , obtained from the fit of the default model to data. These values serve primarily to construct the model and cannot be interpreted as measurements. Uncertainties for the couplings are not calculated as they generally are unstable such that minor changes (as are done when estimating systematic uncertainties) can result in very different couplings. The rightmost column indicates which couplings are dependent on the others via Eq. 12.

D Statistical correlations

Table 6 provides the statistical correlations between the observables.

Table 4: Magnitude, $|A_{LS}|$, and phase, $\arg(A_{LS})$, of the couplings at the best fit point of the default model for resonances $\Lambda(1405)$, $\Lambda(1520)$, $\Lambda(1600)$, $\Lambda(1670)$, $\Lambda(1690)$, $\Lambda(1800)$, $\Lambda(1810)$, and $\Lambda(1820)$.

Resonance	$2L$	$2S$	$ A_{LS} $	$\arg(A_{LS})$	additional comment
$\Lambda(1405)$	0	1	2.890	-0.672	
	2	1	2.137	-2.633	
	2	3	1.511	0.509	dependent via Eq. 12
	4	3	2.044	2.470	dependent via Eq. 12
$\Lambda(1520)$	0	1	0.400	-0.016	
	2	1	0.542	0.147	
	2	3	2.063	1.649	
	4	3	1.142	2.083	
	4	5	0.590	-0.607	dependent via Eq. 12
	6	5	0.773	-0.944	dependent via Eq. 12
$\Lambda(1600)$	0	1	7.000	0.970	
	2	1	4.127	3.057	
	2	3	2.918	-0.085	dependent via Eq. 12
	4	3	4.950	-2.171	dependent via Eq. 12
$\Lambda(1670)$	0	1	0.182	2.694	
	2	1	0.394	0.549	
	2	3	0.279	-2.592	dependent via Eq. 12
	4	3	0.129	-0.447	dependent via Eq. 12
$\Lambda(1690)$	0	1	0.371	-2.977	
	2	1	2.426	0.694	
	2	3	1.328	0.263	
	4	3	2.918	0.648	
	4	5	1.225	-2.599	dependent via Eq. 12
	6	5	1.418	0.824	dependent via Eq. 12
$\Lambda(1800)$	0	1	1.000	0.000	fixed in the fit
	2	1	4.418	-1.498	
	2	3	3.124	1.643	dependent via Eq. 12
	4	3	0.707	3.142	dependent via Eq. 12
$\Lambda(1810)$	0	1	1.453	-2.702	
	2	1	0.374	-1.129	
	2	3	0.264	2.012	dependent via Eq. 12
	4	3	1.027	0.440	dependent via Eq. 12
$\Lambda(1820)$	2	3	0.692	-2.965	
	4	3	3.166	-1.937	
	4	5	2.258	-1.733	
	6	5	3.023	-1.299	
	6	7	0.931	2.510	dependent via Eq. 12
	8	7	2.157	-1.984	dependent via Eq. 12

Table 5: Magnitude, $|A_{LS}|$, and phase, $\arg(A_{LS})$, of the couplings at the best fit point of the default model for resonances $\Lambda(1830)$, $\Lambda(1890)$, $\Lambda(2100)$, $\Lambda(2110)$, $\Lambda(2350)$, and the non-resonant component.

Resonance	$2L$	$2S$	$ A_{LS} $	$\arg(A_{LS})$	additional comment
$\Lambda(1830)$	2	3	0.646	2.337	
	4	3	0.881	-2.763	
	4	5	0.894	0.643	
	6	5	0.764	-2.560	
	6	7	0.536	2.018	dependent via Eq. 12
	8	7	0.931	-2.707	dependent via Eq. 12
$\Lambda(1890)$	0	1	2.070	-1.103	
	2	1	1.312	0.175	
	2	3	1.449	3.118	
	4	3	3.918	1.441	
	4	5	2.724	-1.376	dependent via Eq. 12
	6	5	1.455	0.109	dependent via Eq. 12
$\Lambda(2100)$	4	5	2.378	-0.537	
	6	5	5.087	1.139	
	6	7	3.192	1.384	
	8	7	6.932	1.924	
	8	9	3.088	-0.778	dependent via Eq. 12
	10	9	3.946	1.106	dependent via Eq. 12
$\Lambda(2110)$	2	3	2.093	2.382	
	4	3	6.217	-2.358	
	4	5	2.348	-1.664	
	6	5	6.899	-1.546	
	6	7	3.044	2.015	dependent via Eq. 12
	8	7	4.810	-2.427	dependent via Eq. 12
$\Lambda(2350)$	6	7	0.509	-1.829	
	8	7	0.670	-0.946	
	8	9	1.751	-1.344	
	10	9	0.848	-0.286	
	10	11	0.471	-2.076	dependent via Eq. 12
	12	11	0.396	-0.711	dependent via Eq. 12
NR($3/2^-$)	0	1	1.368	0.598	
	2	1	8.811	3.131	
	2	3	7.525	-0.006	
	4	3	5.694	-2.808	
	4	5	2.895	0.426	dependent via Eq. 12
	6	5	9.075	3.132	dependent via Eq. 12

Table 6: Statistical correlations between the observables in percent obtained from bootstrapping the data. In the interest of space, the J^P specification of the nonresonant component of the best model, $\text{NR}(\frac{3}{2}^-)$, is dropped and the resonances are only referred to by their mass. A single mass refers to the fit fraction of a state, two masses refer to the interference fit fraction of the given combination.

	1405	1520	1600	1670	1690	1800	1810	1820	1830	1890	2100	2110	2350	NR	1405, 1670	1520, 1690	1405, 1800	1670, 1800	1600, 1810	1820, 2110	1520, NR	1690, NR	
1405	100																						
1520	8	100																					
1600	11	-14	100																				
1670	-37	-9	-33	100																			
1690	-7	25	-33	30	100																		
1800	-24	-13	-8	34	14	100																	
1810	21	-3	13	-20	-31	-41	100																
1820	2	3	2	3	6	-11	3	100															
1830	16	20	-8	-20	-27	-36	33	-11	100														
1890	-3	4	11	-3	-25	-33	50	1	14	100													
2100	-21	-14	-16	21	-24	-0	8	9	28	3	100												
2110	-10	20	-5	-9	-2	27	15	-3	-9	23	-26	100											
2350	-10	-14	-15	14	4	36	14	-14	-12	-4	-3	19	100										
NR	5	7	-9	-6	-36	-2	7	-28	28	3	4	5	9	100									
1405, 1670	15	5	47	-52	-7	-19	-5	-6	-5	-8	-31	-20	-21	-23	100								
1520, 1690	-2	-11	34	-11	-53	-26	5	2	17	2	22	-28	-18	2	36	100							
1405, 1800	-40	-13	-45	18	10	-11	-15	-11	6	-9	26	-8	12	16	-34	2	100						
1670, 1800	45	14	26	-93	-27	-58	36	2	26	11	-19	2	-17	2	44	12	-20	100					
1600, 1810	-3	-3	-16	5	21	-0	-66	-18	-39	-35	-30	-22	-32	-13	20	-13	-9	-4	100				
1820, 2110	22	-18	2	-3	5	-37	-12	-5	11	-34	2	-73	-31	-16	19	20	1	12	31	100			
1520, NR	8	-6	-6	1	2	-39	45	-5	9	20	-21	-6	6	-22	-8	-7	-4	16	-12	19	100		
1690, NR	-17	-28	-12	17	9	-5	-31	2	-22	-33	2	-54	-3	-8	14	12	13	-14	40	35	-15	100	

References

- [1] LHCb collaboration, R. Aaij *et al.*, *Test of lepton universality using $\Lambda_b^0 \rightarrow pK^- \ell^+ \ell^-$ decays*, JHEP **05** (2020) 040, [arXiv:1912.08139](#).
- [2] LHCb collaboration, R. Aaij *et al.*, *Observation of the decay $\Lambda_b^0 \rightarrow pK^- \mu^+ \mu^-$ and search for CP violation*, JHEP **06** (2017) 108, [arXiv:1703.00256](#).
- [3] LHCb collaboration, R. Aaij *et al.*, *Measurement of the $\Lambda_b^0 \rightarrow \Lambda(1520)\mu^+\mu^-$ differential branching fraction*, Phys. Rev. Lett. **131** (2023) 151801, [arXiv:2302.08262](#).
- [4] V. J. Rives Molina, *Study of b-hadron decays into two hadrons and a photon at LHCb and first observation of b-baryon radiative decays*, PhD thesis, Barcelona U., 2016.
- [5] L. Mott and W. Roberts, *Rare dileptonic decays of Λ_b in a quark model*, Int. J. Mod. Phys. **A27** (2012) 1250016, [arXiv:1108.6129](#).
- [6] L. Mott and W. Roberts, *Lepton polarization asymmetries for FCNC decays of the Λ_b baryon*, Int. J. Mod. Phys. **A30** (2015) 1550172, [arXiv:1506.04106](#).
- [7] S. Meinel and G. Rendon, *$\Lambda_b \rightarrow \Lambda^*(1520)\ell^+\ell^-$ form factors from lattice QCD*, Phys. Rev. **D103** (2021) 074505, [arXiv:2009.09313](#).
- [8] S. Meinel and G. Rendon, *$\Lambda_c \rightarrow \Lambda^*(1520)$ form factors from lattice QCD and improved analysis of the $\Lambda_b \rightarrow \Lambda^*(1520)$ and $\Lambda_b \rightarrow \Lambda_c^*(2595, 2625)$ form factors*, Phys. Rev. **D105** (2022) 054511, [arXiv:2107.13140](#).
- [9] M. Bordone, *Heavy quark expansion of $\Lambda_b \rightarrow \Lambda^*(1520)$ form factors beyond leading order*, Symmetry **13** (2021) 531, [arXiv:2101.12028](#).
- [10] Y. Amhis, M. Bordone, and M. Reboud, *Dispersive analysis of $\Lambda_b \rightarrow \Lambda(1520)$ local form factors*, JHEP **02** (2023) 010, [arXiv:2208.08937](#).
- [11] A. V. Sarantsev *et al.*, *Hyperon II: Properties of excited hyperons*, Eur. Phys. J. A **55** (2019) 180, [arXiv:1907.13387](#).
- [12] M. Matveev *et al.*, *Hyperon I: Partial-wave amplitudes for $K^- p$ scattering*, Eur. Phys. J. **A55** (2019) 179, [arXiv:1907.03645](#).
- [13] LHCb collaboration, R. Aaij *et al.*, *Observation of $J/\psi p$ resonances consistent with pentaquark states in $\Lambda_b^0 \rightarrow J/\psi p K^-$ decays*, Phys. Rev. Lett. **115** (2015) 072001, [arXiv:1507.03414](#).
- [14] G. Hiller, M. Knecht, F. Legger, and T. Schietinger, *Photon polarization from helicity suppression in radiative decays of polarized Λ_b to spin-3/2 baryons*, Phys. Lett. **B649** (2007) 152, [arXiv:hep-ph/0702191](#).
- [15] M. F. M. Lutz *et al.*, *Resonances in QCD*, Nucl. Phys. **A948** (2016) 93, [arXiv:1511.09353](#).
- [16] T. Sjöstrand, S. Mrenna, and P. Skands, *A brief introduction to PYTHIA 8.1*, Comput. Phys. Commun. **178** (2008) 852, [arXiv:0710.3820](#).

- [17] I. Belyaev *et al.*, *Handling of the generation of primary events in Gauss, the LHCb simulation framework*, J. Phys. Conf. Ser. **331** (2011) 032047.
- [18] D. J. Lange, *The EvtGen particle decay simulation package*, Nucl. Instrum. Meth. **A462** (2001) 152.
- [19] N. Davidson, T. Przedzinski, and Z. Was, *PHOTOS interface in C++: Technical and physics documentation*, Comp. Phys. Comm. **199** (2016) 86, [arXiv:1011.0937](#).
- [20] Geant4 collaboration, S. Agostinelli *et al.*, *Geant4: A simulation toolkit*, Nucl. Instrum. Meth. **A506** (2003) 250.
- [21] Geant4 collaboration, J. Allison *et al.*, *Geant4 developments and applications*, IEEE Trans. Nucl. Sci. **53** (2006) 270.
- [22] R. Aaij *et al.*, *The LHCb trigger and its performance in 2011*, JINST **8** (2013) P04022, [arXiv:1211.3055](#).
- [23] R. Aaij *et al.*, *Design and performance of the LHCb trigger and full real-time reconstruction in Run 2 of the LHC*, JINST **14** (2019) P04013, [arXiv:1812.10790](#).
- [24] T. Likhomanenko *et al.*, *LHCb topological trigger reoptimization*, J. Phys. Conf. Ser. **664** (2015) 082025.
- [25] L. Breiman, J. H. Friedman, R. A. Olshen, and C. J. Stone, *Classification and regression trees*, Wadsworth international group, Belmont, California, USA, 1984.
- [26] M. Pivk and F. R. Le Diberder, *sPlot: A statistical tool to unfold data distributions*, Nucl. Instrum. Meth. **A555** (2005) 356, [arXiv:physics/0402083](#).
- [27] M. J. Oreglia, *A study of the reactions $\psi' \rightarrow \gamma\gamma\psi$* , PhD thesis, Stanford University, 1980.
- [28] M. Rosenblatt, *Remarks on some nonparametric estimates of a density function*, The Annals of Mathematical Statistics **27** (1956) 832 .
- [29] Particle Data Group, R. L. Workman *et al.*, *Review of particle physics*, Prog. Theor. Exp. Phys. **2022** (2022) 083C01.
- [30] W. D. Hulsbergen, *Decay chain fitting with a Kalman filter*, Nucl. Instrum. Meth. **A552** (2005) 566, [arXiv:physics/0503191](#).
- [31] J. Albrecht, Y. Amhis, A. Beck, and C. Marin Benito, *Towards an amplitude analysis of the decay $\Lambda_b^0 \rightarrow pK^-\gamma$* , JHEP **06** (2020) 116, [arXiv:2002.02692](#).
- [32] LHCb collaboration, R. Aaij *et al.*, *Measurement of the $\Lambda_b^0 \rightarrow J/\psi\Lambda$ angular distribution and the Λ polarisation in pp collisions*, JHEP **06** (2020) 110, [arXiv:2004.10563](#).
- [33] R. H. Dalitz, *On the analysis of τ -meson data and the nature of the τ -meson*, Phil. Mag. Ser. 7 **44** (1953) 1068.
- [34] BaBar collaboration, B. Aubert *et al.*, *An amplitude analysis of the decay $B^\pm \rightarrow \pi^\pm\pi^\pm\pi^\mp$* , Phys. Rev. **D72** (2005) 052002, [arXiv:hep-ex/0507025](#).

- [35] E. P. Wigner, *Group theory and its application to the quantum mechanics of atomic spectra*, Academic Press, New York, 1959.
- [36] LHCb collaboration, R. Aaij *et al.*, *Study of the $D^0 p$ amplitude in $\Lambda_b^0 \rightarrow D^0 p \pi^-$ decays*, JHEP **05** (2017) 030, arXiv:1701.07873.
- [37] J. M. Blatt and V. F. Weisskopf, *Theoretical nuclear physics*, Springer, New York, 1952.
- [38] G. Breit and E. Wigner, *Capture of slow neutrons*, Phys. Rev. **49** (1936) 519.
- [39] LHCb collaboration, R. Aaij *et al.*, *Amplitude analysis of the $\Lambda_c^+ \rightarrow p K^- \pi^+$ decay and Λ_c^+ baryon polarization measurement in semileptonic beauty hadron decays*, Phys. Rev. **D108** (2023) 012023, arXiv:2208.03262.
- [40] S. M. Flatté, *Coupled - channel analysis of the $\pi\eta$ and $\bar{K}K$ systems near $\bar{K}K$ threshold*, Phys. Lett. **B63** (1976) 224.
- [41] LHCb collaboration, R. Aaij *et al.*, *Isospin amplitudes in $\Lambda_b^0 \rightarrow J/\psi \Lambda(\Sigma^0)$ and $\Xi_b^0 \rightarrow J/\psi \Xi^0(\Lambda)$ decays*, Phys. Rev. Lett. **124** (2020) 111802, arXiv:1912.02110.
- [42] A. Dery, M. Ghosh, Y. Grossman, and S. Schacht, *$SU(3)_F$ analysis for beauty baryon decays*, JHEP **03** (2020) 165, arXiv:2001.05397.
- [43] Y. Xie, *sFit: a method for background subtraction in maximum likelihood fit*, arXiv:0905.0724.
- [44] C. Langenbruch, *Parameter uncertainties in weighted unbinned maximum likelihood fits*, Eur. Phys. J. **C82** (2022) 393, arXiv:1911.01303.
- [45] A. Morris, *Using TensorFlow for amplitude fits - the TensorFlowAnalysis package*, 2018. doi: 10.5281/zenodo.1415413.
- [46] ARGUS collaboration, H. Albrecht *et al.*, *Search for hadronic $b \rightarrow u$ decays*, Phys. Lett. **B241** (1990) 278.

LHCb collaboration

R. Aaij³⁵ , A.S.W. Abdelmotteleb⁵⁴ , C. Abellan Beteta⁴⁸, F. Abudinén⁵⁴ , T. Ackernley⁵⁸ , B. Adeva⁴⁴ , M. Adinolfi⁵² , P. Adlarson⁷⁸ , C. Agapopoulou⁴⁶ , C.A. Aidala⁷⁹ , Z. Ajaltouni¹¹, S. Akar⁶³ , K. Akiba³⁵ , P. Albicocco²⁵ , J. Albrecht¹⁷ , F. Alessio⁴⁶ , M. Alexander⁵⁷ , A. Alfonso Albero⁴³ , Z. Aliouche⁶⁰ , P. Alvarez Cartelle⁵³ , R. Amalric¹⁵ , S. Amato³ , J.L. Amey⁵² , Y. Amhis^{13,46} , L. An⁶ , L. Anderlini²⁴ , M. Andersson⁴⁸ , A. Andreianov⁴¹ , P. Andreola⁴⁸ , M. Andreotti²³ , D. Andreou⁶⁶ , A. Anelli^{28,o} , D. Ao⁷ , F. Archilli^{34,u} , M. Argenton²³ , S. Arguedas Cuendis⁹ , A. Artamonov⁴¹ , M. Artuso⁶⁶ , E. Aslanides¹² , M. Atzeni⁶² , B. Audurier¹⁴ , D. Bacher⁶¹ , I. Bachiller Perea¹⁰ , S. Bachmann¹⁹ , M. Bachmayer⁴⁷ , J.J. Back⁵⁴ , P. Baladron Rodriguez⁴⁴ , V. Balagura¹⁴ , W. Baldini²³ , J. Baptista de Souza Leite² , M. Barbetti^{24,l} , I. R. Barbosa⁶⁷ , R.J. Barlow⁶⁰ , S. Barsuk¹³ , W. Barter⁵⁶ , M. Bartolini⁵³ , J. Bartz⁶⁶ , F. Baryshnikov⁴¹ , J.M. Basels¹⁶ , G. Bassi^{32,r} , B. Batsukh⁵ , A. Battig¹⁷ , A. Bay⁴⁷ , A. Beck⁵⁴ , M. Becker¹⁷ , F. Bedeschi³² , I.B. Bediaga² ,

A. Beiter⁶⁶ , S. Belin⁴⁴ , V. Bellee⁴⁸ , K. Belous⁴¹ , I. Belov²⁶ , I. Belyaev⁴¹ ,
 G. Benane¹² , G. Bencivenni²⁵ , E. Ben-Haim¹⁵ , A. Berezhnoy⁴¹ , R. Bernet⁴⁸ ,
 S. Bernet Andres⁴² , H.C. Bernstein⁶⁶ , C. Bertella⁶⁰ , A. Bertolin³⁰ , C. Betancourt⁴⁸ ,
 F. Betti⁵⁶ , J. Bex⁵³ , Ia. Bezshyiko⁴⁸ , J. Bhom³⁸ , M.S. Bieker¹⁷ , N.V. Biesuz²³ ,
 P. Billoir¹⁵ , A. Biolchini³⁵ , M. Birch⁵⁹ , F.C.R. Bishop¹⁰ , A. Bitadze⁶⁰ , A. Bizzeti ,
 M.P. Blago⁵³ , T. Blake⁵⁴ , F. Blanc⁴⁷ , J.E. Blank¹⁷ , S. Blusk⁶⁶ , D. Bobulska⁵⁷ ,
 V. Bocharnikov⁴¹ , J.A. Boelhaue¹⁷ , O. Boente Garcia¹⁴ , T. Boettcher⁶³ , A.
 Bohare⁵⁶ , A. Boldyrev⁴¹ , C.S. Bolognani⁷⁶ , R. Bolzonella^{23,k} , N. Bondar⁴¹ ,
 F. Borgato^{30,46} , S. Borghi⁶⁰ , M. Borsato^{28,o} , J.T. Borsuk³⁸ , S.A. Bouchiba⁴⁷ ,
 T.J.V. Bowcock⁵⁸ , A. Boyer⁴⁶ , C. Bozzi²³ , M.J. Bradley⁵⁹ , S. Braun⁶⁴ ,
 A. Brea Rodriguez⁴⁴ , N. Breer¹⁷ , J. Brodzicka³⁸ , A. Brossa Gonzalo⁴⁴ , J. Brown⁵⁸ ,
 D. Brundu²⁹ , A. Buonaura⁴⁸ , L. Buonincontri³⁰ , A.T. Burke⁶⁰ , C. Burr⁴⁶ ,
 A. Bursche⁶⁹ , A. Butkevich⁴¹ , J.S. Butter⁵³ , J. Buytaert⁴⁶ , W. Byczynski⁴⁶ ,
 S. Cadeddu²⁹ , H. Cai⁷¹ , R. Calabrese^{23,k} , L. Calefice¹⁷ , S. Cali²⁵ , M. Calvi^{28,o} ,
 M. Calvo Gomez⁴² , J. Cambon Bouzas⁴⁴ , P. Campana²⁵ , D.H. Campora Perez⁷⁶ ,
 A.F. Campoverde Quezada⁷ , S. Capelli^{28,o} , L. Capriotti²³ , R. Caravaca-Mora⁹ ,
 A. Carbone^{22,i} , L. Carcedo Salgado⁴⁴ , R. Cardinale^{26,m} , A. Cardini²⁹ ,
 P. Carniti^{28,o} , L. Carus¹⁹ , A. Casais Vidal⁶² , R. Caspary¹⁹ , G. Casse⁵⁸ ,
 J. Castro Godinez⁹ , M. Cattaneo⁴⁶ , G. Cavallero²³ , V. Cavallini^{23,k} , S. Celani⁴⁷ ,
 J. Cerasoli¹² , D. Cervenkov⁶¹ , S. Cesare^{27,n} , A.J. Chadwick⁵⁸ , I. Chahrour⁷⁹ ,
 M. Charles¹⁵ , Ph. Charpentier⁴⁶ , C.A. Chavez Barajas⁵⁸ , M. Chefdeville¹⁰ ,
 C. Chen¹² , S. Chen⁵ , Z. Chen⁷ , A. Chernov³⁸ , S. Chernyshenko⁵⁰ ,
 V. Chobanova^{44,y} , S. Cholak⁴⁷ , M. Chrzaszcz³⁸ , A. Chubykin⁴¹ , V. Chulikov⁴¹ ,
 P. Ciambrone²⁵ , M.F. Cicala⁵⁴ , X. Cid Vidal⁴⁴ , G. Ciezarek⁴⁶ , P. Cifra⁴⁶ ,
 P.E.L. Clarke⁵⁶ , M. Clemencic⁴⁶ , H.V. Cliff⁵³ , J. Closier⁴⁶ , J.L. Cobbley⁶⁰ ,
 C. Cocha Toapaxi¹⁹ , V. Coco⁴⁶ , J. Cogan¹² , E. Cogneras¹¹ , L. Cojocariu⁴⁰ ,
 P. Collins⁴⁶ , T. Colombo⁴⁶ , A. Comerma-Montells⁴³ , L. Congedo²¹ , A. Contu²⁹ ,
 N. Cooke⁵⁷ , I. Corredoira⁴⁴ , A. Correia¹⁵ , G. Corti⁴⁶ , J.J. Cottee Meldrum⁵² ,
 B. Couturier⁴⁶ , D.C. Craik⁴⁸ , M. Cruz Torres^{2,g} , E. Curras Rivera⁴⁷ , R. Currie⁵⁶ ,
 C.L. Da Silva⁶⁵ , S. Dadabaev⁴¹ , L. Dai⁶⁸ , X. Dai⁶ , E. Dall'Occo¹⁷ , J. Dalseno⁴⁴ ,
 C. D'Ambrosio⁴⁶ , J. Daniel¹¹ , A. Danilina⁴¹ , P. d'Argent²¹ , A. Davidson⁵⁴ ,
 J.E. Davies⁶⁰ , A. Davis⁶⁰ , O. De Aguiar Francisco⁶⁰ , C. De Angelis^{29,j} ,
 J. de Boer³⁵ , K. De Bruyn⁷⁵ , S. De Capua⁶⁰ , M. De Cian^{19,46} ,
 U. De Freitas Carneiro Da Graca^{2,b} , E. De Lucia²⁵ , J.M. De Miranda² , L. De Paula³ ,
 M. De Serio^{21,h} , D. De Simone⁴⁸ , P. De Simone²⁵ , F. De Vellis¹⁷ , J.A. de Vries⁷⁶ ,
 F. Debernardis^{21,h} , D. Decamp¹⁰ , V. Dedu¹² , L. Del Buono¹⁵ , B. Delaney⁶² ,
 H.-P. Dembinski¹⁷ , J. Deng⁸ , V. Denysenko⁴⁸ , O. Deschamps¹¹ , F. Dettori^{29,j} ,
 B. Dey⁷⁴ , P. Di Nezza²⁵ , I. Diachkov⁴¹ , S. Didenko⁴¹ , S. Ding⁶⁶ , V. Dobishuk⁵⁰ ,
 A. D. Docheva⁵⁷ , A. Dolmatov⁴¹ , C. Dong⁴ , A.M. Donohoe²⁰ , F. Dordei²⁹ ,
 A.C. dos Reis² , L. Douglas⁵⁷ , A.G. Downes¹⁰ , W. Duan⁶⁹ , P. Duda⁷⁷ ,
 M.W. Dudek³⁸ , L. Dufour⁴⁶ , V. Duk³¹ , P. Durante⁴⁶ , M. M. Duras⁷⁷ ,
 J.M. Durham⁶⁵ , A. Dziurda³⁸ , A. Dzyuba⁴¹ , S. Easo^{55,46} , E. Eckstein⁷³ , U. Egede¹ ,
 A. Egorychev⁴¹ , V. Egorychev⁴¹ , C. Eirea Orro⁴⁴ , S. Eisenhardt⁵⁶ , E. Ejopu⁶⁰ ,
 S. Ek-In⁴⁷ , L. Eklund⁷⁸ , M. Elashri⁶³ , J. Ellbracht¹⁷ , S. Ely⁵⁹ , A. Ene⁴⁰ ,
 E. Eppele⁶³ , S. Escher¹⁶ , J. Eschle⁴⁸ , S. Esen⁴⁸ , T. Evans⁶⁰ , F. Fabiano^{29,j,46} ,
 L.N. Falcao² , Y. Fan⁷ , B. Fang^{71,13} , L. Fantini^{31,q} , M. Faria⁴⁷ , K. Farmer⁵⁶ ,
 D. Fazzini^{28,o} , L. Felkowski⁷⁷ , M. Feng^{5,7} , M. Feo⁴⁶ , M. Fernandez Gomez⁴⁴ ,
 A.D. Fernez⁶⁴ , F. Ferrari²² , F. Ferreira Rodrigues³ , S. Ferreres Sole³⁵ , M. Ferrillo⁴⁸ ,
 M. Ferro-Luzzi⁴⁶ , S. Filippov⁴¹ , R.A. Fini²¹ , M. Fiorini^{23,k} , M. Firlej³⁷ ,
 K.M. Fischer⁶¹ , D.S. Fitzgerald⁷⁹ , C. Fitzpatrick⁶⁰ , T. Fiutowski³⁷ , F. Fleuret¹⁴ ,

M. Fontana²² , F. Fontanelli^{26,m} , L. F. Foreman⁶⁰ , R. Forty⁴⁶ , D. Foulds-Holt⁵³ ,
M. Franco Sevilla⁶⁴ , M. Frank⁴⁶ , E. Franzoso^{23,k} , G. Frau¹⁹ , C. Frei⁴⁶ ,
D.A. Friday⁶⁰ , L. Frontini^{27,n} , J. Fu⁷ , Q. Fuehring¹⁷ , Y. Fujii¹ , T. Fulghesu¹⁵ ,
E. Gabriel³⁵ , G. Galati^{21,h} , M.D. Galati³⁵ , A. Gallas Torreira⁴⁴ , D. Galli^{22,i} ,
S. Gambetta⁵⁶ , M. Gandelman³ , P. Gandini²⁷ , H. Gao⁷ , R. Gao⁶¹ , Y. Gao⁸ ,
Y. Gao⁶ , Y. Gao⁸, M. Garau^{29,j} , L.M. Garcia Martin⁴⁷ , P. Garcia Moreno⁴³ ,
J. García Pardiñas⁴⁶ , B. Garcia Plana⁴⁴, K. G. Garg⁸ , L. Garrido⁴³ , C. Gaspar⁴⁶ ,
R.E. Geertsema³⁵ , L.L. Gerken¹⁷ , E. Gersabeck⁶⁰ , M. Gersabeck⁶⁰ , T. Gershon⁵⁴ ,
Z. Ghorbanimoghaddam⁵², L. Giambastiani³⁰ , F. I. Giasemis^{15,e} , V. Gibson⁵³ ,
H.K. Giemza³⁹ , A.L. Gilman⁶¹ , M. Giovannetti²⁵ , A. Gioventù⁴³ ,
P. Gironella Gironell⁴³ , C. Giugliano^{23,k} , M.A. Giza³⁸ , E.L. Gkougkousis⁵⁹ ,
F.C. Glaser^{13,19} , V.V. Gligorov¹⁵ , C. Göbel⁶⁷ , E. Golobardes⁴² , D. Golubkov⁴¹ ,
A. Golutvin^{59,41,46} , A. Gomes^{2,a,†} , S. Gomez Fernandez⁴³ , F. Goncalves Abrantes⁶¹ ,
M. Goncerz³⁸ , G. Gong⁴ , J. A. Gooding¹⁷ , I.V. Gorelov⁴¹ , C. Gotti²⁸ ,
J.P. Grabowski⁷³ , L.A. Granado Cardoso⁴⁶ , E. Graugés⁴³ , E. Graverini^{47,s} ,
L. Grazette⁵⁴ , G. Graziani , A. T. Grecu⁴⁰ , L.M. Greeven³⁵ , N.A. Grieser⁶³ ,
L. Grillo⁵⁷ , S. Gromov⁴¹ , C. Gu¹⁴ , M. Guarise²³ , M. Guittiere¹³ , V. Guliaeva⁴¹ ,
P. A. Günther¹⁹ , A.-K. Guseinov⁴¹ , E. Gushchin⁴¹ , Y. Guz^{6,41,46} , T. Gys⁴⁶ ,
T. Hadavizadeh¹ , C. Hadjivasiliou⁶⁴ , G. Haefeli⁴⁷ , C. Haen⁴⁶ , J. Haimberger⁴⁶ ,
M. Hajheidari⁴⁶, T. Halewood-leagas⁵⁸ , M.M. Halvorsen⁴⁶ , P.M. Hamilton⁶⁴ ,
J. Hammerich⁵⁸ , Q. Han⁸ , X. Han¹⁹ , S. Hansmann-Menzemer¹⁹ , L. Hao⁷ ,
N. Harnew⁶¹ , T. Harrison⁵⁸ , M. Hartmann¹³ , C. Hasse⁴⁶ , J. He^{7,c} , K. Heijhoff³⁵ ,
F. Hemmer⁴⁶ , C. Henderson⁶³ , R.D.L. Henderson^{1,54} , A.M. Hennequin⁴⁶ ,
K. Hennessy⁵⁸ , L. Henry⁴⁷ , J. Herd⁵⁹ , P. Herrero Gascon¹⁹ , J. Heuel¹⁶ ,
A. Hicheur³ , G. Hijano Mendizabal⁴⁸, D. Hill⁴⁷ , S.E. Hollitt¹⁷ , J. Horswill⁶⁰ ,
R. Hou⁸ , Y. Hou¹⁰ , N. Howarth⁵⁸, J. Hu¹⁹, J. Hu⁶⁹ , W. Hu⁶ , X. Hu⁴ ,
W. Huang⁷ , W. Hulsbergen³⁵ , R.J. Hunter⁵⁴ , M. Hushchyn⁴¹ , D. Hutchcroft⁵⁸ ,
M. Idzik³⁷ , D. Ilin⁴¹ , P. Ilten⁶³ , A. Inglessi⁴¹ , A. Iniukhin⁴¹ , A. Ishteev⁴¹ ,
K. Ivshin⁴¹ , R. Jacobsson⁴⁶ , H. Jage¹⁶ , S.J. Jaimes Elles^{45,72} , S. Jakobsen⁴⁶ ,
E. Jans³⁵ , B.K. Jashal⁴⁵ , A. Jawahery^{64,46} , V. Jevtic¹⁷ , E. Jiang⁶⁴ , X. Jiang^{5,7} ,
Y. Jiang⁷ , Y. J. Jiang⁶ , M. John⁶¹ , D. Johnson⁵¹ , C.R. Jones⁵³ , T.P. Jones⁵⁴ ,
S. Joshi³⁹ , B. Jost⁴⁶ , N. Jurik⁴⁶ , I. Juszczak³⁸ , D. Kaminaris⁴⁷ , S. Kandybei⁴⁹ ,
Y. Kang⁴ , M. Karacson⁴⁶ , D. Karpenkov⁴¹ , M. Karpov⁴¹ , A. M. Kauniskangas⁴⁷ ,
J.W. Kautz⁶³ , F. Keizer⁴⁶ , D.M. Keller⁶⁶ , M. Kenzie⁵³ , T. Ketel³⁵ , B. Khanji⁶⁶ ,
A. Kharisova⁴¹ , S. Kholodenko³² , G. Khreich¹³ , T. Kirn¹⁶ , V.S. Kirsebom⁴⁷ ,
O. Kitouni⁶² , S. Klaver³⁶ , N. Kleijne^{32,r} , K. Klimaszewski³⁹ , M.R. Kmiec³⁹ ,
S. Koliiev⁵⁰ , L. Kolk¹⁷ , A. Konoplyannikov⁴¹ , P. Kopciwicz^{37,46} , P. Koppenburg³⁵ ,
M. Korolev⁴¹ , I. Kostiuk³⁵ , O. Kot⁵⁰, S. Kotriakhova , A. Kozachuk⁴¹ ,
P. Kravchenko⁴¹ , L. Kravchuk⁴¹ , M. Kreps⁵⁴ , S. Kretzschmar¹⁶ , P. Krokovny⁴¹ ,
W. Krupa⁶⁶ , W. Krzemien³⁹ , J. Kubat¹⁹, S. Kubis⁷⁷ , W. Kucwicz³⁸ ,
M. Kucharczyk³⁸ , V. Kudryavtsev⁴¹ , E. Kulikova⁴¹ , A. Kupsc⁷⁸ , B. K. Kutsenko¹² ,
D. Lacarrere⁴⁶ , A. Lai²⁹ , A. Lampis²⁹ , D. Lancierini⁴⁸ , C. Landesa Gomez⁴⁴ ,
J.J. Lane¹ , R. Lane⁵² , C. Langenbruch¹⁹ , J. Langer¹⁷ , O. Lantwin⁴¹ ,
T. Latham⁵⁴ , F. Lazzari^{32,s} , C. Lazzeroni⁵¹ , R. Le Gac¹² , S.H. Lee⁷⁹ ,
R. Lefèvre¹¹ , A. Leflat⁴¹ , S. Legotin⁴¹ , M. Lehuraux⁵⁴ , O. Leroy¹² , T. Lesiak³⁸ ,
B. Leverington¹⁹ , A. Li⁴ , H. Li⁶⁹ , K. Li⁸ , L. Li⁶⁰ , P. Li⁴⁶ , P.-R. Li⁷⁰ , S. Li⁸ ,
T. Li^{5,d} , T. Li⁶⁹ , Y. Li⁸, Y. Li⁵ , Z. Li⁶⁶ , Z. Lian⁴ , X. Liang⁶⁶ , C. Lin⁷ ,
T. Lin⁵⁵ , R. Lindner⁴⁶ , V. Lisovsky⁴⁷ , R. Litvinov^{29,j} , F. L. Liu¹ , G. Liu⁶⁹ ,
H. Liu⁷ , K. Liu⁷⁰ , Q. Liu⁷ , S. Liu^{5,7} , Y. Liu⁵⁶ , Y. Liu⁷⁰, Y. L. Liu⁵⁹ ,
A. Lobo Salvia⁴³ , A. Loi²⁹ , J. Lomba Castro⁴⁴ , T. Long⁵³ , J.H. Lopes³ 

A. Lopez Huertas⁴³ , S. López Soliño⁴⁴ , G.H. Lovell⁵³ , C. Lucarelli^{24,l} ,
 D. Lucchesi^{30,p} , S. Luchuk⁴¹ , M. Lucio Martinez⁷⁶ , V. Lukashenko^{35,50} , Y. Luo⁶ ,
 A. Lupato³⁰ , E. Luppi^{23,k} , K. Lynch²⁰ , X.-R. Lyu⁷ , G. M. Ma⁴ , R. Ma⁷ ,
 S. Maccolini¹⁷ , F. Machefert¹³ , F. Maciuc⁴⁰ , B. M. Mack⁶⁶ , I. Mackay⁶¹ , L. M.
 Mackey⁶⁶ , L.R. Madhan Mohan⁵³ , M. M. Madurai⁵¹ , A. Maevskiy⁴¹ ,
 D. Magdalinski³⁵ , D. Maisuzenko⁴¹ , M.W. Majewski³⁷ , J.J. Malczewski³⁸ , S. Malde⁶¹ ,
 B. Malecki^{38,46} , L. Malentacca⁴⁶ , A. Malinin⁴¹ , T. Maltsev⁴¹ , G. Manca^{29,j} ,
 G. Mancinelli¹² , C. Mancuso^{27,13,n} , R. Manera Escalero⁴³ , D. Manuzzi²² ,
 D. Marangotto^{27,n} , J.F. Marchand¹⁰ , R. Marchevski⁴⁷ , U. Marconi²² , S. Mariani⁴⁶ ,
 C. Marin Benito⁴³ , J. Marks¹⁹ , A.M. Marshall⁵² , P.J. Marshall⁵⁸ , G. Martelli^{31,q} ,
 G. Martellotti³³ , L. Martinazzoli⁴⁶ , M. Martinelli^{28,o} , D. Martinez Santos⁴⁴ ,
 F. Martinez Vidal⁴⁵ , A. Massafferri² , M. Materok¹⁶ , R. Matev⁴⁶ , A. Mathad⁴⁸ ,
 V. Matiunin⁴¹ , C. Matteuzzi⁶⁶ , K.R. Mattioli¹⁴ , A. Mauri⁵⁹ , E. Maurice¹⁴ ,
 J. Mauricio⁴³ , P. Mayencourt⁴⁷ , M. Mazurek⁴⁶ , M. McCann⁵⁹ , L. Mcconnell²⁰ ,
 T.H. McGrath⁶⁰ , N.T. McHugh⁵⁷ , A. McNab⁶⁰ , R. McNulty²⁰ , B. Meadows⁶³ ,
 G. Meier¹⁷ , D. Melnychuk³⁹ , M. Merk^{35,76} , A. Merli^{27,n} , L. Meyer Garcia³ ,
 D. Miao^{5,7} , H. Miao⁷ , M. Mikhasenko^{73,f} , D.A. Milanés⁷² , A. Minotti^{28,o} ,
 E. Minucci⁶⁶ , T. Miralles¹¹ , S.E. Mitchell⁵⁶ , B. Mitreska¹⁷ , D.S. Mitzel¹⁷ ,
 A. Modak⁵⁵ , A. Mödden¹⁷ , R.A. Mohammed⁶¹ , R.D. Moise¹⁶ , S. Mokhnenko⁴¹ ,
 T. Mombächer⁴⁶ , M. Monk^{54,1} , I.A. Monroy⁷² , S. Monteil¹¹ , A. Morcillo Gomez⁴⁴ ,
 G. Morello²⁵ , M.J. Morello^{32,r} , M.P. Morgenthaler¹⁹ , J. Moron³⁷ , A.B. Morris⁴⁶ ,
 A.G. Morris¹² , R. Mountain⁶⁶ , H. Mu⁴ , Z. M. Mu⁶ , E. Muhammad⁵⁴ ,
 F. Muheim⁵⁶ , M. Mulder⁷⁵ , K. Müller⁴⁸ , F. Muñoz-Rojas⁹ , R. Murta⁵⁹ ,
 P. Naik⁵⁸ , T. Nakada⁴⁷ , R. Nandakumar⁵⁵ , T. Nanut⁴⁶ , I. Nasteva³ ,
 M. Needham⁵⁶ , N. Neri^{27,n} , S. Neubert⁷³ , N. Neufeld⁴⁶ , P. Neustroev⁴¹,
 R. Newcombe⁵⁹ , J. Nicolini^{17,13} , D. Nicotra⁷⁶ , E.M. Niel⁴⁷ , N. Nikitin⁴¹ , P. Nogga⁷³,
 N.S. Nolte⁶² , C. Normand^{10,29} , J. Novoa Fernandez⁴⁴ , G. Nowak⁶³ , C. Nunez⁷⁹ , H.
 N. Nur⁵⁷ , A. Oblakowska-Mucha³⁷ , V. Obraztsov⁴¹ , T. Oeser¹⁶ , S. Okamura^{23,k,46} ,
 R. Oldeman^{29,j} , F. Oliva⁵⁶ , M. Olocco¹⁷ , C.J.G. Onderwater⁷⁶ , R.H. O'Neil⁵⁶ ,
 J.M. Otalora Goicochea³ , T. Ovsianikova⁴¹ , P. Owen⁴⁸ , A. Oyanguren⁴⁵ ,
 O. Ozcelik⁵⁶ , K.O. Padeken⁷³ , B. Pagare⁵⁴ , P.R. Pais¹⁹ , T. Pajero⁶¹ ,
 A. Palano²¹ , M. Palutan²⁵ , G. Panshin⁴¹ , L. Paolucci⁵⁴ , A. Papanestis⁵⁵ ,
 M. Pappagallo^{21,h} , L.L. Pappalardo^{23,k} , C. Pappenheimer⁶³ , C. Parkes⁶⁰ ,
 B. Passalacqua^{23,k} , G. Passaleva²⁴ , D. Passaro^{32,r} , A. Pastore²¹ , M. Patel⁵⁹ ,
 J. Patoc⁶¹ , C. Patrignani^{22,i} , C.J. Pawley⁷⁶ , A. Pellegrino³⁵ , M. Pepe Altarelli²⁵ ,
 S. Perazzini²² , D. Pereima⁴¹ , A. Pereiro Castro⁴⁴ , P. Perret¹¹ , A. Perro⁴⁶ ,
 K. Petridis⁵² , A. Petrolini^{26,m} , S. Petrucci⁵⁶ , J. P. Pfaller⁶³ , H. Pham⁶⁶ ,
 L. Pica^{32,r} , M. Piccini³¹ , B. Pietrzyk¹⁰ , G. Pietrzyk¹³ , D. Pinci³³ , F. Pisani⁴⁶ ,
 M. Pizzichemi^{28,o} , V. Placinta⁴⁰ , M. Plo Casaus⁴⁴ , F. Polci^{15,46} , M. Poli Lener²⁵ ,
 A. Poluektov¹² , N. Polukhina⁴¹ , I. Polyakov⁴⁶ , E. Polycarpo³ , S. Ponce⁴⁶ ,
 D. Popov⁷ , S. Poslavskii⁴¹ , K. Prasanth³⁸ , C. Prouve⁴⁴ , V. Pugatch⁵⁰ ,
 G. Punzi^{32,s} , W. Qian⁷ , N. Qin⁴ , S. Qu⁴ , R. Quagliani⁴⁷ , R.I. Rabadan Trejo⁵⁴ ,
 B. Rachwal³⁷ , J.H. Rademacker⁵² , M. Rama³² , M. Ramírez García⁷⁹ ,
 M. Ramos Pernas⁵⁴ , M.S. Rangel³ , F. Ratnikov⁴¹ , G. Raven³⁶ ,
 M. Rebollo De Miguel⁴⁵ , F. Redi⁴⁶ , J. Reich⁵² , F. Reiss⁶⁰ , Z. Ren⁷ ,
 P.K. Resmi⁶¹ , R. Ribatti^{32,r} , G. R. Ricart^{14,80} , D. Riccardi^{32,r} , S. Ricciardi⁵⁵ ,
 K. Richardson⁶² , M. Richardson-Slipper⁵⁶ , K. Rinnert⁵⁸ , P. Robbe¹³ ,
 G. Robertson⁵⁷ , E. Rodrigues^{58,46} , E. Rodriguez Fernandez⁴⁴ ,
 J.A. Rodriguez Lopez⁷² , E. Rodriguez Rodriguez⁴⁴ , A. Rogovskiy⁵⁵ , D.L. Rolf⁴⁶ ,
 A. Rollings⁶¹ , P. Roloff⁴⁶ , V. Romanovskiy⁴¹ , M. Romero Lamas⁴⁴ ,

A. Romero Vidal⁴⁴ , G. Romolini²³ , F. Ronchetti⁴⁷ , M. Rotondo²⁵ , S. R. Roy¹⁹ ,
 M.S. Rudolph⁶⁶ , T. Ruf⁴⁶ , M. Ruiz Diaz¹⁹ , R.A. Ruiz Fernandez⁴⁴ ,
 J. Ruiz Vidal^{78,z} , A. Ryzhikov⁴¹ , J. Ryzka³⁷ , J.J. Saborido Silva⁴⁴ , R. Sadek¹⁴ ,
 N. Sagidova⁴¹ , N. Sahoo⁵¹ , B. Saitta^{29,j} , M. Salomoni^{28,o} , C. Sanchez Gras³⁵ ,
 I. Sanderswood⁴⁵ , R. Santacesaria³³ , C. Santamarina Rios⁴⁴ , M. Santimaria²⁵ ,
 L. Santoro² , E. Santovetti³⁴ , A. Saputi^{23,46} , D. Saranin⁴¹ , G. Sarpis⁵⁶ ,
 M. Sarpis⁷³ , A. Sarti³³ , C. Satriano^{33,t} , A. Satta³⁴ , M. Saur⁶ , D. Savrina⁴¹ ,
 H. Sazak¹¹ , L.G. Scantlebury Smead⁶¹ , A. Scarabotto¹⁵ , S. Schael¹⁶ , S. Scherl⁵⁸ , A.
 M. Schertz⁷⁴ , M. Schiller⁵⁷ , H. Schindler⁴⁶ , M. Schmelling¹⁸ , B. Schmidt⁴⁶ ,
 S. Schmitt¹⁶ , H. Schmitz⁷³ , O. Schneider⁴⁷ , A. Schopper⁴⁶ , N. Schulte¹⁷ ,
 S. Schulte⁴⁷ , M.H. Schune¹³ , R. Schwemmer⁴⁶ , G. Schwering¹⁶ , B. Sciascia²⁵ ,
 A. Sciuccati⁴⁶ , S. Sellam⁴⁴ , A. Semennikov⁴¹ , M. Senghi Soares³⁶ , A. Sergi^{26,m} ,
 N. Serra^{48,46} , L. Sestini³⁰ , A. Seuthe¹⁷ , Y. Shang⁶ , D.M. Shangase⁷⁹ ,
 M. Shapkin⁴¹ , R. S. Sharma⁶⁶ , I. Shchemerov⁴¹ , L. Shchutka⁴⁷ , T. Shears⁵⁸ ,
 L. Shekhtman⁴¹ , Z. Shen⁶ , S. Sheng^{5,7} , V. Shevchenko⁴¹ , B. Shi⁷ ,
 E.B. Shields^{28,o} , Y. Shimizu¹³ , E. Shmanin⁴¹ , R. Shorkin⁴¹ , J.D. Shupperd⁶⁶ ,
 R. Silva Coutinho⁶⁶ , G. Simi³⁰ , S. Simone^{21,h} , N. Skidmore⁶⁰ , R. Skuza¹⁹ ,
 T. Skwarnicki⁶⁶ , M.W. Slater⁵¹ , J.C. Smallwood⁶¹ , E. Smith⁶² , K. Smith⁶⁵ ,
 M. Smith⁵⁹ , A. Snoch³⁵ , L. Soares Lavra⁵⁶ , M.D. Sokoloff⁶³ , F.J.P. Soler⁵⁷ ,
 A. Solomin^{41,52} , A. Solovev⁴¹ , I. Solovyev⁴¹ , R. Song¹ , Y. Song⁴⁷ , Y. Song⁴ , Y. S.
 Song⁶ , F.L. Souza De Almeida⁶⁶ , B. Souza De Paula³ , E. Spadaro Norella^{27,n} ,
 E. Spedicato²² , J.G. Speer¹⁷ , E. Spiridenkov⁴¹ , P. Spradlin⁵⁷ , V. Sriskaran⁴⁶ ,
 F. Stagni⁴⁶ , M. Stahl⁴⁶ , S. Stahl⁴⁶ , S. Stanislaus⁶¹ , E.N. Stein⁴⁶ , O. Steinkamp⁴⁸ ,
 O. Stenyakin⁴¹ , H. Stevens¹⁷ , D. Strelakina⁴¹ , Y. Su⁷ , F. Suljik⁶¹ , J. Sun²⁹ ,
 L. Sun⁷¹ , Y. Sun⁶⁴ , P.N. Swallow⁵¹ , K. Swientek³⁷ , F. Swystun⁵⁴ , A. Szabelski³⁹ ,
 T. Szumlak³⁷ , M. Szymanski⁴⁶ , Y. Tan⁴ , S. Taneja⁶⁰ , M.D. Tat⁶¹ , A. Terentev⁴⁸ ,
 F. Terzuoli^{32,v} , F. Teubert⁴⁶ , E. Thomas⁴⁶ , D.J.D. Thompson⁵¹ , H. Tilquin⁵⁹ ,
 V. Tisserand¹¹ , S. T'Jampens¹⁰ , M. Tobin⁵ , L. Tomassetti^{23,k} , G. Tonani^{27,n,46} ,
 X. Tong⁶ , D. Torres Machado² , L. Toscano¹⁷ , D.Y. Tou⁴ , C. Trippel⁴² , G. Tuci¹⁹ ,
 N. Tuning³⁵ , L.H. Uecker¹⁹ , A. Ukleja³⁷ , D.J. Unverzagt¹⁹ , E. Ursov⁴¹ ,
 A. Usachov³⁶ , A. Ustyuzhanin⁴¹ , U. Uwer¹⁹ , V. Vagnoni²² , A. Valassi⁴⁶ ,
 G. Valenti²² , N. Valls Canudas⁴² , H. Van Hecke⁶⁵ , E. van Herwijnen⁵⁹ ,
 C.B. Van Hulse^{44,x} , R. Van Laak⁴⁷ , M. van Veghel³⁵ , R. Vazquez Gomez⁴³ ,
 P. Vazquez Regueiro⁴⁴ , C. Vázquez Sierra⁴⁴ , S. Vecchi²³ , J.J. Velthuis⁵² ,
 M. Veltri^{24,w} , A. Venkateswaran⁴⁷ , M. Vesterinen⁵⁴ , M. Vieites Diaz⁴⁶ ,
 X. Vilasis-Cardona⁴² , E. Vilella Figueras⁵⁸ , A. Villa²² , P. Vincent¹⁵ , F.C. Volle¹³ ,
 D. vom Bruch¹² , V. Vorobyev⁴¹ , N. Voropaev⁴¹ , K. Vos⁷⁶ , G. Vouters¹⁰ , C. Vrahas⁵⁶ ,
 J. Walsh³² , E.J. Walton¹ , G. Wan⁶ , C. Wang¹⁹ , G. Wang⁸ , J. Wang⁶ ,
 J. Wang⁵ , J. Wang⁴ , J. Wang⁷¹ , M. Wang²⁷ , N. W. Wang⁷ , R. Wang⁵² ,
 X. Wang⁶⁹ , X. W. Wang⁵⁹ , Y. Wang⁸ , Z. Wang¹³ , Z. Wang⁴ , Z. Wang⁷ ,
 J.A. Ward^{54,1} , M. Waterlaet⁴⁶ , N.K. Watson⁵¹ , D. Websdale⁵⁹ , Y. Wei⁶ ,
 B.D.C. Westhenry⁵² , D.J. White⁶⁰ , M. Whitehead⁵⁷ , A.R. Wiederhold⁵⁴ ,
 D. Wiedner¹⁷ , G. Wilkinson⁶¹ , M.K. Wilkinson⁶³ , M. Williams⁶² ,
 M.R.J. Williams⁵⁶ , R. Williams⁵³ , F.F. Wilson⁵⁵ , W. Wislicki³⁹ , M. Witek³⁸ ,
 L. Witola¹⁹ , C.P. Wong⁶⁵ , G. Wormser¹³ , S.A. Wotton⁵³ , H. Wu⁶⁶ , J. Wu⁸ ,
 Y. Wu⁶ , K. Wyllie⁴⁶ , S. Xian⁶⁹ , Z. Xiang⁵ , Y. Xie⁸ , A. Xu³² , J. Xu⁷ , L. Xu⁴ ,
 L. Xu⁴ , M. Xu⁵⁴ , Z. Xu¹¹ , Z. Xu⁷ , Z. Xu⁵ , D. Yang⁴ , S. Yang⁷ , X. Yang⁶ ,
 Y. Yang^{26,m} , Z. Yang⁶ , Z. Yang⁶⁴ , V. Yeroshenko¹³ , H. Yeung⁶⁰ , H. Yin⁸ , C. Y.
 Yu⁶ , J. Yu⁶⁸ , X. Yuan⁵ , E. Zaffaroni⁴⁷ , M. Zavertyaev¹⁸ , M. Zdybal³⁸ ,
 M. Zeng⁴ , C. Zhang⁶ , D. Zhang⁸ , J. Zhang⁷ , L. Zhang⁴ , S. Zhang⁶⁸ ,

S. Zhang⁶ , Y. Zhang⁶ , Y. Z. Zhang⁴ , Y. Zhao¹⁹ , A. Zharkova⁴¹ , A. Zhelezov¹⁹ , X. Z. Zheng⁴ , Y. Zheng⁷ , T. Zhou⁶ , X. Zhou⁸ , Y. Zhou⁷ , V. Zhovkovska⁵⁴ , L. Z. Zhu⁷ , X. Zhu⁴ , X. Zhu⁸ , Z. Zhu⁷ , V. Zhukov^{16,41} , J. Zhuo⁴⁵ , Q. Zou^{5,7} , D. Zuliani³⁰ , G. Zunica⁶⁰ .

¹*School of Physics and Astronomy, Monash University, Melbourne, Australia*

²*Centro Brasileiro de Pesquisas Físicas (CBPF), Rio de Janeiro, Brazil*

³*Universidade Federal do Rio de Janeiro (UFRJ), Rio de Janeiro, Brazil*

⁴*Center for High Energy Physics, Tsinghua University, Beijing, China*

⁵*Institute Of High Energy Physics (IHEP), Beijing, China*

⁶*School of Physics State Key Laboratory of Nuclear Physics and Technology, Peking University, Beijing, China*

⁷*University of Chinese Academy of Sciences, Beijing, China*

⁸*Institute of Particle Physics, Central China Normal University, Wuhan, Hubei, China*

⁹*Consejo Nacional de Rectores (CONARE), San Jose, Costa Rica*

¹⁰*Université Savoie Mont Blanc, CNRS, IN2P3-LAPP, Annecy, France*

¹¹*Université Clermont Auvergne, CNRS/IN2P3, LPC, Clermont-Ferrand, France*

¹²*Aix Marseille Univ, CNRS/IN2P3, CPPM, Marseille, France*

¹³*Université Paris-Saclay, CNRS/IN2P3, IJCLab, Orsay, France*

¹⁴*Laboratoire Leprince-Ringuet, CNRS/IN2P3, Ecole Polytechnique, Institut Polytechnique de Paris, Palaiseau, France*

¹⁵*LPNHE, Sorbonne Université, Paris Diderot Sorbonne Paris Cité, CNRS/IN2P3, Paris, France*

¹⁶*I. Physikalisches Institut, RWTH Aachen University, Aachen, Germany*

¹⁷*Fakultät Physik, Technische Universität Dortmund, Dortmund, Germany*

¹⁸*Max-Planck-Institut für Kernphysik (MPIK), Heidelberg, Germany*

¹⁹*Physikalisches Institut, Ruprecht-Karls-Universität Heidelberg, Heidelberg, Germany*

²⁰*School of Physics, University College Dublin, Dublin, Ireland*

²¹*INFN Sezione di Bari, Bari, Italy*

²²*INFN Sezione di Bologna, Bologna, Italy*

²³*INFN Sezione di Ferrara, Ferrara, Italy*

²⁴*INFN Sezione di Firenze, Firenze, Italy*

²⁵*INFN Laboratori Nazionali di Frascati, Frascati, Italy*

²⁶*INFN Sezione di Genova, Genova, Italy*

²⁷*INFN Sezione di Milano, Milano, Italy*

²⁸*INFN Sezione di Milano-Bicocca, Milano, Italy*

²⁹*INFN Sezione di Cagliari, Monserrato, Italy*

³⁰*Università degli Studi di Padova, Università e INFN, Padova, Padova, Italy*

³¹*INFN Sezione di Perugia, Perugia, Italy*

³²*INFN Sezione di Pisa, Pisa, Italy*

³³*INFN Sezione di Roma La Sapienza, Roma, Italy*

³⁴*INFN Sezione di Roma Tor Vergata, Roma, Italy*

³⁵*Nikhef National Institute for Subatomic Physics, Amsterdam, Netherlands*

³⁶*Nikhef National Institute for Subatomic Physics and VU University Amsterdam, Amsterdam, Netherlands*

³⁷*AGH - University of Science and Technology, Faculty of Physics and Applied Computer Science, Kraków, Poland*

³⁸*Henryk Niewodniczanski Institute of Nuclear Physics Polish Academy of Sciences, Kraków, Poland*

³⁹*National Center for Nuclear Research (NCBJ), Warsaw, Poland*

⁴⁰*Horia Hulubei National Institute of Physics and Nuclear Engineering, Bucharest-Magurele, Romania*

⁴¹*Affiliated with an institute covered by a cooperation agreement with CERN*

⁴²*DS4DS, La Salle, Universitat Ramon Llull, Barcelona, Spain*

⁴³*ICCUB, Universitat de Barcelona, Barcelona, Spain*

⁴⁴*Instituto Galego de Física de Altas Enerxías (IGFAE), Universidade de Santiago de Compostela, Santiago de Compostela, Spain*

⁴⁵*Instituto de Física Corpuscular, Centro Mixto Universidad de Valencia - CSIC, Valencia, Spain*

⁴⁶*European Organization for Nuclear Research (CERN), Geneva, Switzerland*

- ⁴⁷*Institute of Physics, Ecole Polytechnique Fédérale de Lausanne (EPFL), Lausanne, Switzerland*
- ⁴⁸*Physik-Institut, Universität Zürich, Zürich, Switzerland*
- ⁴⁹*NSC Kharkiv Institute of Physics and Technology (NSC KIPT), Kharkiv, Ukraine*
- ⁵⁰*Institute for Nuclear Research of the National Academy of Sciences (KINR), Kyiv, Ukraine*
- ⁵¹*University of Birmingham, Birmingham, United Kingdom*
- ⁵²*H.H. Wills Physics Laboratory, University of Bristol, Bristol, United Kingdom*
- ⁵³*Cavendish Laboratory, University of Cambridge, Cambridge, United Kingdom*
- ⁵⁴*Department of Physics, University of Warwick, Coventry, United Kingdom*
- ⁵⁵*STFC Rutherford Appleton Laboratory, Didcot, United Kingdom*
- ⁵⁶*School of Physics and Astronomy, University of Edinburgh, Edinburgh, United Kingdom*
- ⁵⁷*School of Physics and Astronomy, University of Glasgow, Glasgow, United Kingdom*
- ⁵⁸*Oliver Lodge Laboratory, University of Liverpool, Liverpool, United Kingdom*
- ⁵⁹*Imperial College London, London, United Kingdom*
- ⁶⁰*Department of Physics and Astronomy, University of Manchester, Manchester, United Kingdom*
- ⁶¹*Department of Physics, University of Oxford, Oxford, United Kingdom*
- ⁶²*Massachusetts Institute of Technology, Cambridge, MA, United States*
- ⁶³*University of Cincinnati, Cincinnati, OH, United States*
- ⁶⁴*University of Maryland, College Park, MD, United States*
- ⁶⁵*Los Alamos National Laboratory (LANL), Los Alamos, NM, United States*
- ⁶⁶*Syracuse University, Syracuse, NY, United States*
- ⁶⁷*Pontifícia Universidade Católica do Rio de Janeiro (PUC-Rio), Rio de Janeiro, Brazil, associated to ³*
- ⁶⁸*School of Physics and Electronics, Hunan University, Changsha City, China, associated to ⁸*
- ⁶⁹*Guangdong Provincial Key Laboratory of Nuclear Science, Guangdong-Hong Kong Joint Laboratory of Quantum Matter, Institute of Quantum Matter, South China Normal University, Guangzhou, China, associated to ⁴*
- ⁷⁰*Lanzhou University, Lanzhou, China, associated to ⁵*
- ⁷¹*School of Physics and Technology, Wuhan University, Wuhan, China, associated to ⁴*
- ⁷²*Departamento de Física , Universidad Nacional de Colombia, Bogota, Colombia, associated to ¹⁵*
- ⁷³*Universität Bonn - Helmholtz-Institut für Strahlen und Kernphysik, Bonn, Germany, associated to ¹⁹*
- ⁷⁴*Eotvos Lorand University, Budapest, Hungary, associated to ⁴⁶*
- ⁷⁵*Van Swinderen Institute, University of Groningen, Groningen, Netherlands, associated to ³⁵*
- ⁷⁶*Universiteit Maastricht, Maastricht, Netherlands, associated to ³⁵*
- ⁷⁷*Tadeusz Kosciuszko Cracow University of Technology, Cracow, Poland, associated to ³⁸*
- ⁷⁸*Department of Physics and Astronomy, Uppsala University, Uppsala, Sweden, associated to ⁵⁷*
- ⁷⁹*University of Michigan, Ann Arbor, MI, United States, associated to ⁶⁶*
- ⁸⁰*Departement de Physique Nucleaire (SPhN), Gif-Sur-Yvette, France*

^a*Universidade de Brasília, Brasília, Brazil*

^b*Centro Federal de Educação Tecnológica Celso Suckow da Fonseca, Rio De Janeiro, Brazil*

^c*Hangzhou Institute for Advanced Study, UCAS, Hangzhou, China*

^d*School of Physics and Electronics, Henan University , Kaifeng, China*

^e*LIP6, Sorbonne Université, Paris, France*

^f*Excellence Cluster ORIGINS, Munich, Germany*

^g*Universidad Nacional Autónoma de Honduras, Tegucigalpa, Honduras*

^h*Università di Bari, Bari, Italy*

ⁱ*Università di Bologna, Bologna, Italy*

^j*Università di Cagliari, Cagliari, Italy*

^k*Università di Ferrara, Ferrara, Italy*

^l*Università di Firenze, Firenze, Italy*

^m*Università di Genova, Genova, Italy*

ⁿ*Università degli Studi di Milano, Milano, Italy*

^o*Università di Milano Bicocca, Milano, Italy*

^p*Università di Padova, Padova, Italy*

^q*Università di Perugia, Perugia, Italy*

^r*Scuola Normale Superiore, Pisa, Italy*

^s*Università di Pisa, Pisa, Italy*

^t*Università della Basilicata, Potenza, Italy*

^u *Università di Roma Tor Vergata, Roma, Italy*

^v *Università di Siena, Siena, Italy*

^w *Università di Urbino, Urbino, Italy*

^x *Universidad de Alcalá, Alcalá de Henares, Spain*

^y *Universidade da Coruña, Coruña, Spain*

^z *Department of Physics/Division of Particle Physics, Lund, Sweden*

[†] *Deceased*



First observation of the $\Lambda_b^0 \rightarrow D^+ D^- \Lambda$ decay

LHCb collaboration[†]

Abstract

The $\Lambda_b^0 \rightarrow D^+ D^- \Lambda$ decay is observed for the first time using proton-proton collision data collected by the LHCb experiment at a center-of-mass energy of 13 TeV, corresponding to an integrated luminosity of 5.3 fb^{-1} . Using the $B^0 \rightarrow D^+ D^- K_S^0$ decay as a reference channel, the product of the relative production cross-section and decay branching fractions is measured to be

$$\mathcal{R} = \frac{\sigma_{\Lambda_b^0}}{\sigma_{B^0}} \times \frac{\mathcal{B}(\Lambda_b^0 \rightarrow D^+ D^- \Lambda)}{\mathcal{B}(B^0 \rightarrow D^+ D^- K_S^0)} = 0.179 \pm 0.022 \pm 0.014,$$

where the first uncertainty is statistical and the second is systematic. The known branching fraction of the reference channel, $\mathcal{B}(B^0 \rightarrow D^+ D^- K_S^0)$, and the cross-section ratio, $\sigma_{\Lambda_b^0}/\sigma_{B^0}$, previously measured by LHCb are used to derive the branching fraction of the $\Lambda_b^0 \rightarrow D^+ D^- \Lambda$ decay

$$\mathcal{B}(\Lambda_b^0 \rightarrow D^+ D^- \Lambda) = (1.24 \pm 0.15 \pm 0.10 \pm 0.28 \pm 0.11) \times 10^{-4},$$

where the third and fourth contributions are due to uncertainties of $\mathcal{B}(B^0 \rightarrow D^+ D^- K_S^0)$ and $\sigma_{\Lambda_b^0}/\sigma_{B^0}$, respectively. Inspection of the $D^+ \Lambda$ and $D^+ D^-$ invariant-mass distributions suggests a rich presence of intermediate resonances in the decay. The $\Lambda_b^0 \rightarrow D^{*+} D^- \Lambda$ decay is also observed for the first time as a partially reconstructed component in the $D^+ D^- \Lambda$ invariant mass spectrum.

Submitted to JHEP

© 2024 CERN for the benefit of the LHCb collaboration. CC BY 4.0 licence.

[†]Authors are listed at the end of this paper.

1 Introduction

Beauty baryons containing at least one b quark have rich phenomenology, but most of them have not been fully explored yet. The large sample of beauty baryons produced at the Large Hadron Collider (LHC) provides an unprecedented opportunity to enrich our knowledge of beauty baryons and better understand strong and weak interactions. The $b \rightarrow c$ transition underlies the main decay modes of beauty baryons. From the late 1990s to the early 2010s, beauty baryon decays involving charmed baryons in the final state were almost exclusively known and long considered dominant [1–3]. Since 2014, however, decays with a c quark hadronizing into a meson instead of a baryon have been commonly discovered by the LHCb experiment, with sizable branching fractions as well [4–6]. Among these, $b \rightarrow c\bar{c}s$ transitions provided the place to observe the first decays into systems made of a baryon and a charmonium resonance [7–10]. For such final states, a significant contribution due to intermediate pentaquark states has been established [11–14]. Another class of decays that originate from $b \rightarrow c\bar{c}s$ transitions is the decay of a Λ_b^0 baryon into a charmed baryon and an anti-charmed meson [15], which allows a precise measurement of the Λ_b^0 baryon mass to be performed due to the limited phase space of the reaction.

This paper presents the first observation of the $\Lambda_b^0 \rightarrow D^+D^-\Lambda$ decay,¹ referred to hereafter as the signal channel. This decay is of interest as it can proceed via two types of two-body intermediate states: one involving a charmed baryon and an anti-charm meson, and the other through charmonium(-like) states. As discussed in Ref. [16], a D^+D^- bound state can be produced near the D^+D^- mass threshold, and open-charmed pentaquark states with quark content $\bar{c}sudd$ might be present in the $D^-\Lambda$ final state. Figure 1 shows the example diagrams resulting in these intermediate states that might contribute to the $\Lambda_b^0 \rightarrow D^+D^-\Lambda$ decay, which originates from a $b \rightarrow c\bar{c}s$ transition. These include the Ξ_c^{*++} baryon decaying to $D^+\Lambda$, the $X(3700)$ state decaying to D^+D^- and pentaquark states $P_{\bar{c}s}$ decaying to $D^-\Lambda$.

This analysis is performed using proton-proton (pp) collision data collected by the LHCb experiment from 2016 to 2018 at a center-of-mass energy of 13 TeV, corresponding to an integrated luminosity of 5.3 fb^{-1} . The branching fraction \mathcal{B} of the $\Lambda_b^0 \rightarrow D^+D^-\Lambda$ decay is determined by taking the $B^0 \rightarrow D^+D^-K_S^0$ decay as a reference channel. The latter has a decay topology similar to that of the signal channel, allowing for the cancellation of some systematic uncertainties in the branching fraction measurement. The primary measured quantity is the product of the relative production cross-section between Λ_b^0 and B^0 hadrons and their decay branching fraction ratio, defined as

$$\mathcal{R} \equiv \frac{\sigma_{\Lambda_b^0}}{\sigma_{B^0}} \times \frac{\mathcal{B}(\Lambda_b^0 \rightarrow D^+D^-\Lambda)}{\mathcal{B}(B^0 \rightarrow D^+D^-K_S^0)}, \quad (1)$$

where $\sigma_{\Lambda_b^0}$ (σ_{B^0}) is the production cross-section of the Λ_b^0 (B^0) hadron, and \mathcal{B} denotes the branching fractions. The branching fraction of the $\Lambda_b^0 \rightarrow D^+D^-\Lambda$ decay is then derived using the value of the cross-section ratio, $\sigma_{\Lambda_b^0}/\sigma_{B^0}$, previously measured at the LHCb experiment [17] and the known branching fraction of the reference channel [18].

¹The inclusion of charge-conjugate modes is always implied.

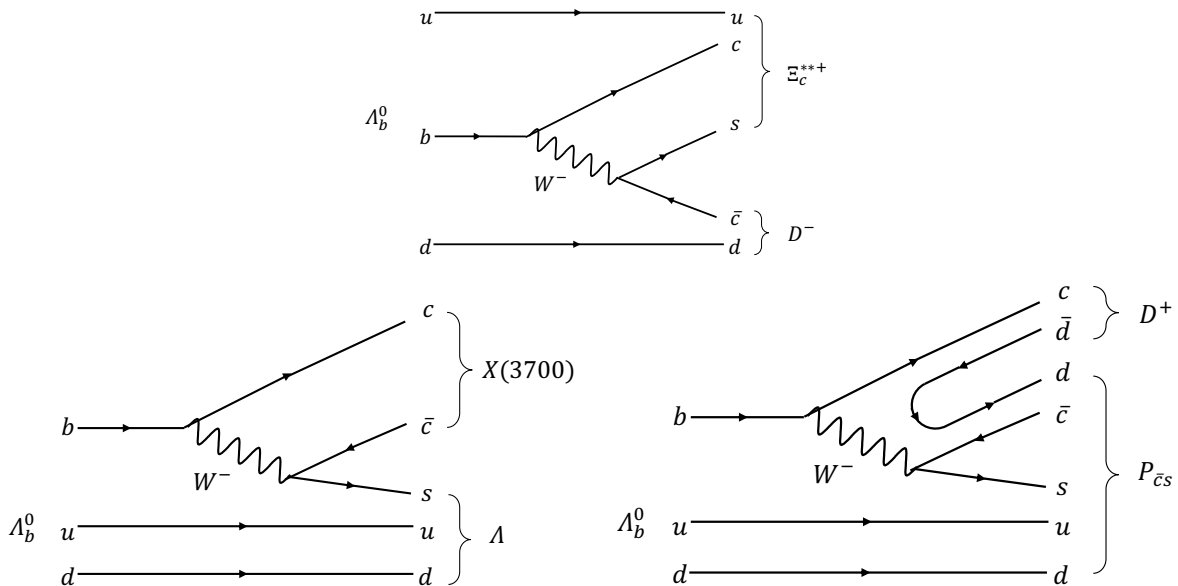


Figure 1: Example diagrams resulting in intermediate states that might contribute to the $\Lambda_b^0 \rightarrow D^+ D^- \Lambda$ decay.

2 Detector and data samples

The LHCb detector [19, 20] is a single-arm forward spectrometer covering the pseudorapidity range $2 < \eta < 5$, designed for the study of particles containing b or c quarks. The detector includes a high-precision tracking system consisting of a silicon-strip vertex detector surrounding the pp interaction region, a large-area silicon-strip detector located upstream of a dipole magnet with a bending power of about 4 Tm, and three stations of silicon-strip detectors and straw drift tubes placed downstream of the magnet. The tracking system provides a measurement of the momentum, p , of charged particles with a relative uncertainty that varies from 0.5% at low momentum to 1.0% at 200 GeV/ c . The minimum distance of a track to a primary pp collision vertex (PV), the impact parameter, is measured with a resolution of $(15 + 29/p_T) \mu\text{m}$, where p_T is the component of the momentum transverse to the beam, in GeV/ c . Different types of charged hadrons are distinguished using information from two ring-imaging Cherenkov detectors. Photons, electrons and hadrons are identified by a calorimeter system consisting of scintillating-pad and preshower detectors, an electromagnetic and a hadronic calorimeter.

The online event selection is performed by a trigger, which consists of a hardware stage, based on information from the calorimeter and muon systems, followed by a software stage, which applies a full event reconstruction. At the hardware trigger stage, events are required to have a hadron with a transverse energy above 3.5 GeV in the calorimeters. The software trigger requires a two-, three- or four-track secondary vertex with a significant displacement from any PV. At least one charged particle from the secondary vertex must have a $p_T > 1.6$ GeV/ c and be inconsistent with originating from any PV.

Simulation samples are required to model the effects of the detector acceptance and the imposed selection requirements, and to study the invariant mass distributions of

reconstructed $\Lambda_b^0 \rightarrow D^+D^-\Lambda$ and $B^0 \rightarrow D^+D^-K_S^0$ decays. The simulation samples are generated with Λ_b^0 or B^0 signal decays uniformly distributed in the $D^+D^-\Lambda$ or $D^+D^-K_S^0$ phase space. In the simulation, pp collisions are generated using PYTHIA [21] with a specific LHCb configuration [22]. Decays of unstable particles are described by EVTGEN [23], in which final-state radiation is generated using PHOTOS [24]. The interaction of the generated particles with the detector, and its response, are implemented using the GEANT4 toolkit [25] as described in Ref. [26].

3 Selection of candidates

In the offline reconstruction, charged tracks of kaons, pions and protons are combined to form $D^+ \rightarrow K^-\pi^+\pi^+$, $\Lambda \rightarrow p\pi^-$ and $K_S^0 \rightarrow \pi^+\pi^-$ decays, which are then used to build the $\Lambda_b^0 \rightarrow D^+D^-\Lambda$ and $B^0 \rightarrow D^+D^-K_S^0$ candidates. It is worth noting that the Λ and K_S^0 candidates (collectively referred to as the V^0 particles) are reconstructed according to two different categories. In the LL category, they decay closely enough to the PV such that the final-state particles are reconstructed using the full tracking system. In the DD category, the V^0 particles decay downstream of the vertex detector. Consequently, the V^0 candidates have better momentum, mass and vertex resolution in the LL category than in the DD one, while the V^0 candidates in the DD category have higher efficiency.

A series of selection criteria are applied to the formed beauty-hadron candidates to suppress the background. The selection starts with loose requirements on kinematics, particle identification (PID) and variables that exploit the relatively long lifetime of beauty hadrons. Firstly, all final-state particles are required to have good track-fit quality and be displaced from any PV. Furthermore, these particles must have $p_T > 0.1 \text{ GeV}/c$ and $p > 2 \text{ GeV}/c$, and be identified with a high significance as a pion, a kaon or a proton, using information from the tracking system and PID detectors. The scalar sum of p_T of the D^\pm candidates' decay products must be larger than $1.8 \text{ GeV}/c$, with at least one of these having $p_T > 0.5 \text{ GeV}/c$ and $p > 5 \text{ GeV}/c$. The D^+ and V^0 candidates are required to have a good-quality decay vertex that is significantly displaced from any PV. The invariant mass of D^+ candidates should lie within $25 \text{ MeV}/c^2$ of the known mass [18]. Moreover, V^0 candidates should have $p_T > 250 \text{ MeV}/c$ and an invariant mass within $6.6 (5.4) \text{ MeV}/c^2$ of the known masses [18] for the $DD (LL)$ category. The beauty hadron candidate formed by combining the D^\pm and V^0 hadrons must have a good decay vertex displaced from its associated PV, which is defined as the PV that is the most compatible with the flight direction of the beauty candidate. Additionally, its decay time is required to be greater than 0.2 ps , and its momentum must point back to the associated PV. The final-state tracks of the Λ_b^0 baryon must have a scalar p_T sum larger than $5 \text{ GeV}/c$, and at least one of the final-state particles must have p_T larger than $1.7 \text{ GeV}/c$ and p larger than $10 \text{ GeV}/c$, and at least two of them must have p_T larger than $0.5 \text{ GeV}/c$ and p larger than $5 \text{ GeV}/c$. A kinematic fit to the whole decay chain is performed with the D^+ and V^0 constrained to their known masses [18] and the beauty-candidate momentum constrained to point back to the associated PV [27], which helps to improve the beauty-candidate mass resolution.

To further suppress the combinatorial background, a Boosted Decision Tree (BDT) [28, 29] classifier implemented in the TMVA toolkit [30] is employed. Given the similar topology of the $\Lambda_b^0 \rightarrow D^+D^-\Lambda$ and $B^0 \rightarrow D^+D^-K_S^0$ decays, the BDT classifier is trained using $\Lambda_b^0 \rightarrow D^+D^-\Lambda$ samples and is applied to both decay modes, helping to

cancel certain systematic uncertainties associated with the efficiency determination in the branching fraction measurement. The BDT classifier training uses candidate Λ_b^0 decays in the high mass sideband ($5.80 < m(D^+D^-A) < 6.15 \text{ GeV}/c^2$) in data, which serves as a proxy for the background, and simulated $\Lambda_b^0 \rightarrow D^+D^-A$ signal decays. The training is performed separately for the LL and DD categories. The BDT classifier combines variables including the beauty-hadron decay topology, PID information of final-state particles and kinematic properties of the Λ_b^0 , D^\pm , A and final-state candidates, to discriminate between the signal and the background. The optimal requirement on the BDT response is determined by maximising the Punzi figure of merit $\epsilon/(\frac{5}{2} + \sqrt{B})$ [31], where ϵ is the signal efficiency and B is the background yield in the data signal region. The signal region is chosen as $\pm 25 \text{ MeV}/c^2$ around the known Λ_b^0 mass [18]. The signal efficiency ϵ is estimated from simulated samples, and the background yield B is estimated by a linear extrapolation of the yield in the high-mass data sideband to the signal region. The requirements on the BDT response are optimized separately for the signal and the reference channels but are found to be similar. The optimal requirement on the BDT response rejects about 99% of the combinatorial background while maintaining a signal efficiency of about 80%.

The background from the $K_S^0 \rightarrow \pi^+\pi^-$ decay, which may be reconstructed as the $A \rightarrow p\pi^-$ decay due to misidentification of a pion as a proton, is investigated. This cross-feed background is suppressed by imposing a tight PID requirement on the proton track if the $p\pi^-$ invariant mass under the $\pi^+\pi^-$ hypothesis is consistent with the K_S^0 meson mass. The remaining cross-feed background in the $B^0 \rightarrow D^+D^-K_S^0$ decay is found to be negligible. The background from $\Lambda_b^0 \rightarrow D^+K^+\pi^-\pi^-A$, $\Lambda_b^0 \rightarrow K^-\pi^+\pi^+D^-A$ and $\Lambda_b^0 \rightarrow K^-\pi^+\pi^+K^+\pi^-\pi^-A$ decays is referred to hereafter as the non-double-charm (NDC) background. This background involves the same set of final-state particles as the signal decays but there is only one or no intermediate D^\pm meson. The NDC background is largely suppressed by the imposed requirement on the D^\pm invariant mass. However, any residual NDC background can produce a peak in the D^+D^-A invariant mass distribution, and its yield is estimated using the same method as in Refs. [32, 33], based on the number of candidates in the D^\pm mass sidebands, positioned within a range of 35 to 90 MeV/c^2 from the known D^\pm mass. The fraction of the NDC background in the Λ_b^0 sample is estimated from a fit to the D^+D^-A invariant mass distribution in the D^\pm mass sidebands and is found to be $(6 \pm 7)\%$ and $(6 \pm 3)\%$ for the LL and DD categories, respectively. Similar results are measured for the $B^0 \rightarrow D^+D^-K_S^0$ decay channel. The obtained NDC yield is subtracted from the beauty-hadron yield.

4 Signal yield determination

The invariant mass distributions of the Λ_b^0 and B^0 candidates after applying all the aforementioned selection requirements are shown in Figs. 2 and 3, respectively. The distributions are characterized by three significant peaking structures, one for the signal decay and the other two for partially reconstructed beauty-hadron decays, and a wide smooth combinatorial background. These components are fit with an extended unbinned maximum-likelihood method to determine the Λ_b^0 and B^0 signal yields.

The signal peak is described by the sum of two Gaussian functions sharing the same mean value. The common mean and the average resolution of the two Gaussian functions are free parameters in the fit, while the relative fractions of the two components and the

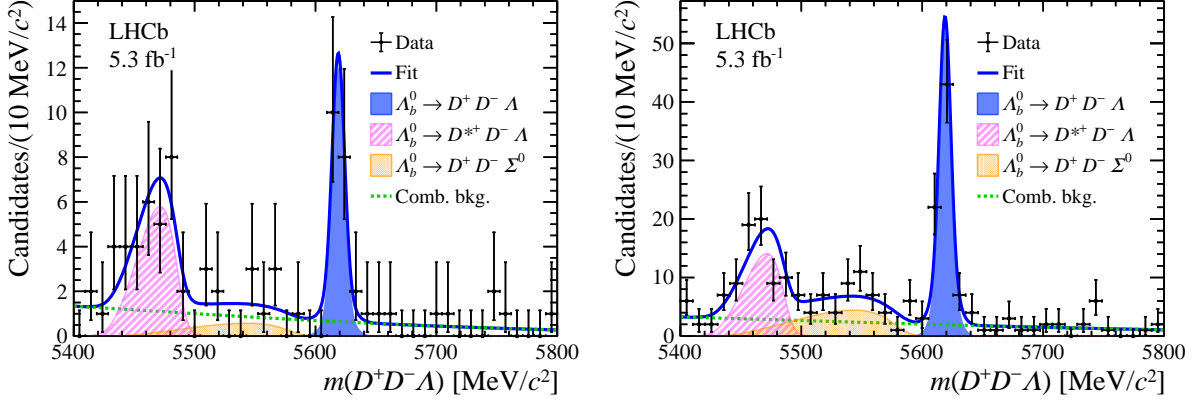


Figure 2: Invariant mass distribution of $\Lambda_b^0 \rightarrow D^+ D^- \Lambda$ candidates near the signal region with the fit results superimposed, for the (left) LL and (right) DD categories, respectively.

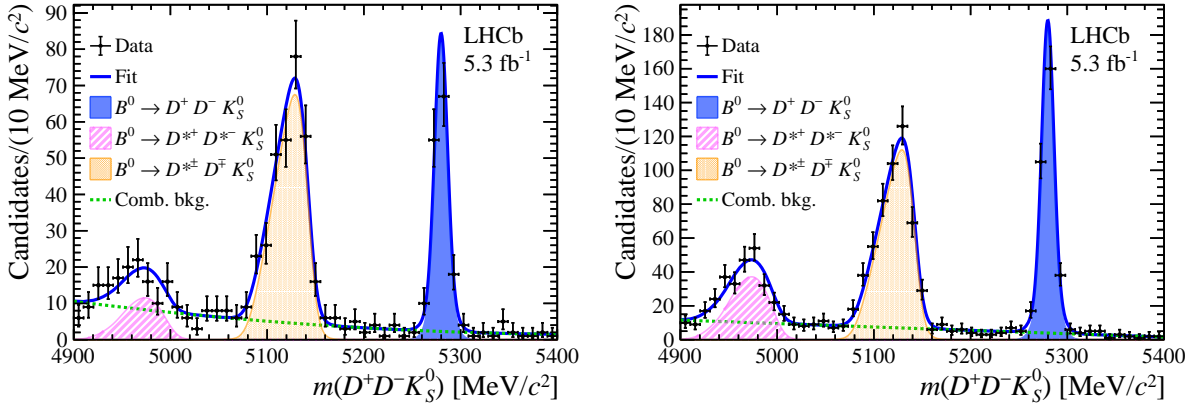


Figure 3: Invariant mass distribution of $B^0 \rightarrow D^+ D^- K_S^0$ candidates with the fit results superimposed, for the (left) LL and (right) DD categories, respectively.

ratio of their widths are fixed to the values obtained from the simulation. In Fig. 2, the peaking background closer to the signal peak originates from the $\Lambda_b^0 \rightarrow D^+ D^- \Lambda$ decay where the γ is not included. The left peaking background is consistent with $\Lambda_b^0 \rightarrow D^{*\pm}(\rightarrow D^\pm \pi^0) D^\mp \Lambda$ decays with the π^0 not included. In Fig. 3, the partially reconstructed backgrounds in the $B^0 \rightarrow D^+ D^- K_S^0$ mass spectrum are consistent with the $B^0 \rightarrow D^{*+} D^{*-} K_S^0$ and $B^0 \rightarrow D^{*+} D^- K_S^0$ decays, where the π^0 in the $D^{*\pm} \rightarrow D^\pm \pi^0$ decay is not included. The shapes of the partially reconstructed backgrounds are obtained from a fast simulation [34], and convolved with the experimental resolution. The combinatorial background is modelled empirically by slowly varying functions, namely the ARGUS function [35] for the $\Lambda_b^0 \rightarrow D^+ D^- \Lambda$ mode and a second-order polynomial for the $B^0 \rightarrow D^+ D^- K_S^0$ mode, with all parameters free in the fit. The fit of $m(D^+ D^- \Lambda)$ distribution is performed over a larger range than what is shown in Fig. 2 to better constrain the combinatorial background. The fit is performed simultaneously for the LL and DD samples, and the mean of the signal Gaussians is shared.

The fit results are shown in Fig. 2 for $\Lambda_b^0 \rightarrow D^+D^-\Lambda$ candidates and in Fig. 3 for the $B^0 \rightarrow D^+D^-K_S^0$ candidates. The signal yields for the $\Lambda_b^0 \rightarrow D^+D^-\Lambda$ and $B^0 \rightarrow D^+D^-K_S^0$ decays are determined to be 19 ± 5 and 143 ± 13 for the *LL* category, 73 ± 9 and 309 ± 18 for the *DD* category, respectively. The statistical significance of the $\Lambda_b^0 \rightarrow D^+D^-\Lambda$ decay evaluated using the likelihood-ratio test [36] is 16 standard deviations (σ). Thus, this represents the first observation of the $\Lambda_b^0 \rightarrow D^+D^-\Lambda$ decay mode. The left peaking structure in the $D^+D^-\Lambda$ invariant mass distributions exhibits a statistical significance of 9σ using the same method as above. This structure is consistent with the $\Lambda_b^0 \rightarrow D^{*+}D^-\Lambda$ decay, being thus observed for the first time in the $D^+D^-\Lambda$ invariant mass spectrum.

5 Branching fraction measurement

The branching fraction of the $\Lambda_b^0 \rightarrow D^+D^-\Lambda$ decay is measured with respect to that of the $B^0 \rightarrow D^+D^-K_S^0$ decay as

$$\mathcal{R} = \frac{N_{\Lambda_b^0}^{\text{corr}}}{N_{B^0}^{\text{corr}}} \times \frac{\mathcal{B}(K_S^0 \rightarrow \pi^+\pi^-)}{\mathcal{B}(\Lambda \rightarrow p\pi^-)}, \quad (2)$$

where $N_{X_b}^{\text{corr}}$ is the efficiency corrected yield of the $X_b = \Lambda_b^0$ or B^0 decay. The branching fractions $\mathcal{B}(\Lambda \rightarrow p\pi^-)$ and $\mathcal{B}(K_S^0 \rightarrow \pi^+\pi^-)$ are taken from Ref. [18]. The efficiency corrected yield is determined as

$$N_{X_b}^{\text{corr}} = \sum_i \frac{w_i}{\epsilon_i}, \quad (3)$$

where the sum runs over all the selected candidates in the signal or reference channel. The weight w_i assigned to each candidate is calculated using the invariant mass fit result following the *sPlot* technique [37], which is used to statistically subtract the background contribution in the data sample. The ϵ_i denotes the total experimental efficiency, which is calculated as a function of the final-state phase-space coordinates, represented by the two-dimensional plot of the two-body invariant mass distributions $m(D^+D^-)$ and $m(D^+V^0)$, and it is estimated for the *LL* and *DD* categories separately. The efficiency function is determined using simulated samples, which have been calibrated such that the distributions of several key variables match the data, including the PID response, Λ_b^0 kinematics and the total charged-track multiplicity. The relative variation of the total experimental efficiency across the phsp space is around 20% for both the signal and reference channels in the *LL* and *DD* categories.

After the subtraction of the aforementioned NDC background, \mathcal{R} is determined to be 0.172 ± 0.047 and 0.181 ± 0.025 for the *LL* and *DD* categories, respectively, where the uncertainties are statistical.

6 Systematic uncertainties

The systematic uncertainties on the branching fraction measurement, apart from external inputs, are generally related to either the signal yields or the efficiencies. Due to the similar topology of the signal and reference decays, many sources of systematic uncertainties are either cancelled or largely suppressed in the ratio of branching fractions. The remaining systematic uncertainties are outlined below and summarized in Table 1.

The determination of the signal yields in the Λ_b^0 and B^0 decay channels is affected by the choice of the fit models for the various components, which in turn influences the branching fraction measurement. To test the signal model, alternative fits are performed by either fixing all the shape parameters to those obtained from the simulation or by using a Hypatia function [38] with the parameters of mean and resolution floated in the fit. In order to study the systematic uncertainty associated with the combinatorial background modelling, the range of the beauty-hadron invariant mass used in the fit is modified. The relative deviation of the branching fraction obtained in these alternative fits from the baseline result is found to be 3.4% at most, which is taken to be the systematic uncertainty due to the invariant mass modelling.

The distributions of the discriminating variables used in the BDT classifier are found to be consistent between the simulation and background-subtracted data of the reference channel. Additionally, given the overlap of the distributions of discriminating variables between the signal and reference channels in simulation, no corresponding systematic uncertainties are quoted. To validate the effect of the possible overtraining of the BDT classifier on the beauty-hadron invariant mass distribution, a fit is performed excluding the candidates used in the BDT training. The relative difference of the new branching fraction with respect to the baseline result is found to be 2.5% and is taken as the corresponding uncertainty.

The estimated NDC background fractions in the signal and reference channels suffer from the limited size of the data samples. These uncertainties are propagated to the branching fraction measurement causing a relative uncertainty of 4.5%.

The efficiencies are estimated from simulated samples, so systematic contributions arise due to the limited size of the samples, and due to the imperfect simulation of the detector response and particle kinematics. The relative uncertainty due to the limited size of the simulation samples is 3.9%. Corrections of the simulation samples for their different PID response and beauty-hadron kinematic distributions than in data are subject to uncertainties. Specifically, the systematic uncertainty associated with the corrections of the PID response is evaluated using alternative correction templates [39] and measuring the relative change of efficiencies, which is found to be negligible. The uncertainties on the corrections of the Λ_b^0 distributions are propagated to the branching fraction measurement using pseudoexperiments. For every pseudoexperiment, the correction factor in each bin of the Λ_b^0 transverse momentum and rapidity is varied following a Gaussian distribution. The mean and width of the Gaussian function are taken as the baseline correction factor and its uncertainty. Also, the branching fraction is calculated for each pseudoexperiment, and then a set of branching fractions is obtained, whose standard deviation is taken as the systematic uncertainty, calculated to be 1.5%.

The hardware-trigger response is approximately modelled in the simulation, therefore, a data-driven calibration is performed to align the efficiency in the simulation with that in the data [40]. The uncertainties on the calibration factors are propagated to the branching fraction measurement, resulting in a relative uncertainty of 0.5%.

The experimental efficiency is measured in bins of the final-state phase space. The choice of the binning scheme introduces another source of systematic uncertainty. The efficiency, recalculated using coarser bins, results in a relative change in the branching fraction of 2.6%. This value is thus quoted as a systematic uncertainty.

Besides the contributions outlined above, there are also further uncertainties due to the external inputs. They come from the limited knowledge of the branching fractions

Table 1: Summary of relative systematic uncertainties on the branching fraction measurement.

Source	Relative uncertainty (%)
Modelling of the invariant mass distribution	3.4
BDT classifier training	2.5
Subtraction of NDC background	4.5
Size of simulation samples	3.9
Corrections to simulation samples	1.5
Trigger efficiency	0.5
Binning scheme of two-body invariant mass	2.6
Total systematic uncertainty	7.8

of the intermediate decays $\Lambda \rightarrow p\pi^-$, $K_S^0 \rightarrow \pi^+\pi^-$ and that of the reference channel $B^0 \rightarrow D^+D^-K^0$ [41]. Finally, another source is the uncertainty from the measurement of the beauty-hadron production cross-section ratio performed by LHCb, which is 9.1% [17]. The total uncertainty due to the external inputs is 24.7%, which is the dominant uncertainty compared with the statistical and systematic ones.

7 Results and summary

The product of the ratio of branching fractions and the corresponding beauty-hadron production cross-section is measured to be

$$\mathcal{R} = \frac{\sigma_{\Lambda_b^0}}{\sigma_{B^0}} \times \frac{\mathcal{B}(\Lambda_b^0 \rightarrow D^+D^-\Lambda)}{\mathcal{B}(B^0 \rightarrow D^+D^-K_S^0)} = 0.179 \pm 0.022 \pm 0.014, \quad (4)$$

where the first uncertainty is statistical and the second is systematic. This result represents a weighted average of the LL and DD samples, with weights calculated using the statistical uncertainties.

The relative production cross-section $\sigma_{\Lambda_b^0}/\sigma_{B^0}$ is equal to the ratio of hadronization fractions, $f_{\Lambda_b^0}/f_{B^0}$, which has been measured by LHCb as a function of the p_T of the Λ_b^0 baryon [17]. Averaging over the p_T distribution of the Λ_b^0 baryon in data gives $\sigma_{\Lambda_b^0}/\sigma_{B^0} = 0.541 \pm 0.048$. Using the known branching fraction of $\mathcal{B}(B^0 \rightarrow D^+D^-K^0)$ [41] and assuming equal probabilities for observing a K^0 meson as a K_S^0 or K_L^0 mass eigenstate, the $\Lambda_b^0 \rightarrow D^+D^-\Lambda$ absolute branching fraction is determined to be

$$\mathcal{B}(\Lambda_b^0 \rightarrow D^+D^-\Lambda) = (1.24 \pm 0.15 \pm 0.10 \pm 0.28 \pm 0.11) \times 10^{-4}, \quad (5)$$

where the first uncertainty is statistical, the second is systematic, and the third and fourth come from the uncertainties on the $B^0 \rightarrow D^+D^-K_S^0$ branching fraction and the beauty-hadron production cross-section ratio [17], respectively.

As emphasized in Figs. 4 and 5, where the invariant mass distributions $m(D^+D^-)$, $m(D^+V^0)$ and $m(D^-V^0)$ are shown, these decays are particularly noteworthy for their potential in probing possible resonant structures. These invariant mass distributions, in which the combinatorial background is subtracted using the *sPlot* technique, strongly depart from the phase space distributions obtained in simulation. Such deviations suggest the presence of a variety of resonant structures, which are likely to include excited Ξ_c^+

states, the $D\bar{D}$ bound state $X(3700)$, and possibly pentaquarks. These open the door to future discoveries in upcoming studies with larger datasets.

In summary, the $\Lambda_b^0 \rightarrow D^+D^-\Lambda$ decay is observed for the first time using proton-proton collision data collected by the LHCb experiment at a center-of-mass energy of 13 TeV, corresponding to an integrated luminosity of 5.3 fb^{-1} . The branching fraction of the $\Lambda_b^0 \rightarrow D^+D^-\Lambda$ decay is determined, which is a key step towards probing potential intermediate resonant states. The peaking structure in the $D^+D^-\Lambda$ invariant mass distribution, which is consistent with the $\Lambda_b^0 \rightarrow D^{*+}D^-\Lambda$ decay, is also reported. Future studies will be needed to measure the branching fraction of the $\Lambda_b^0 \rightarrow D^{*+}D^-\Lambda$ decay. The indications of various resonant structures in the $\Lambda_b^0 \rightarrow D^+D^-\Lambda$ decay also call for future exploration in similar decay channels, like the $\Lambda_b^0 \rightarrow D^0\bar{D}^0\Lambda$ decay.

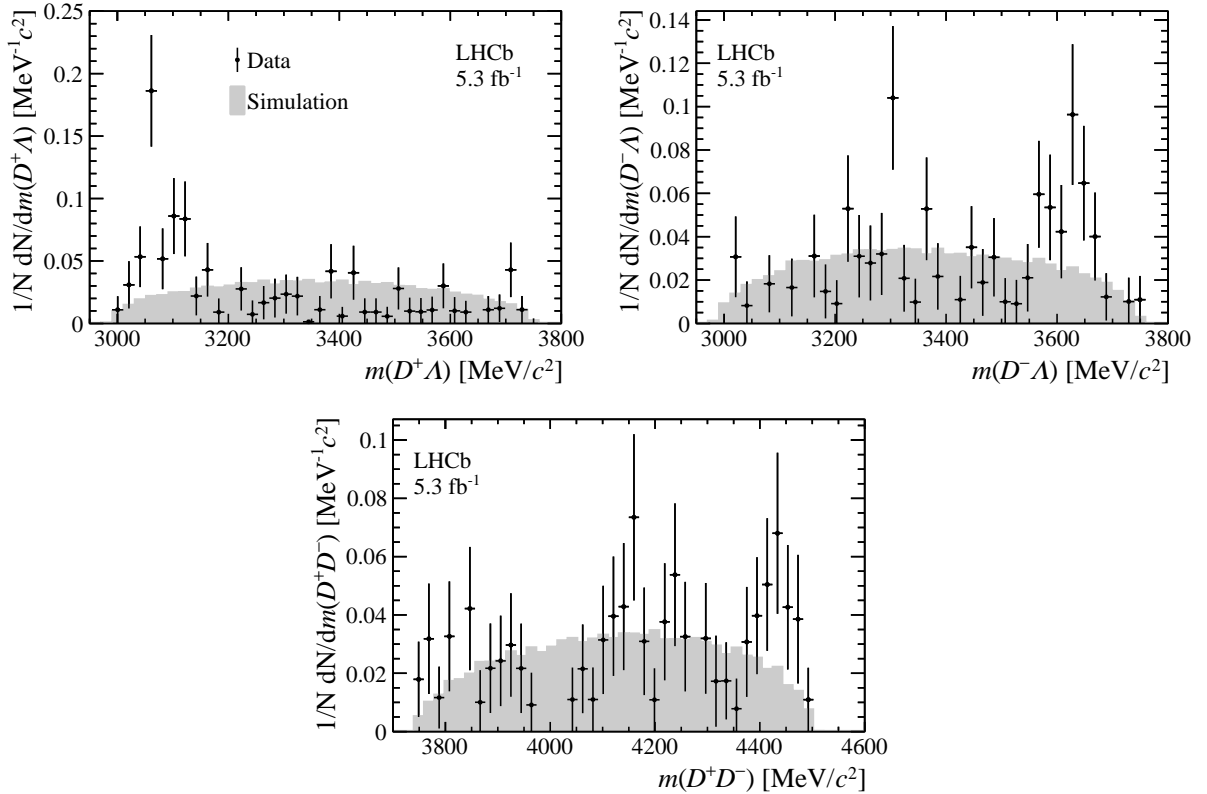


Figure 4: Normalized and background-subtracted invariant mass distributions of the (left) $D^+\Lambda$, (right) $D^-\Lambda$ and (bottom) D^+D^- systems in the $\Lambda_b^0 \rightarrow D^+D^-\Lambda$ decay, compared with the distributions in simulation samples.

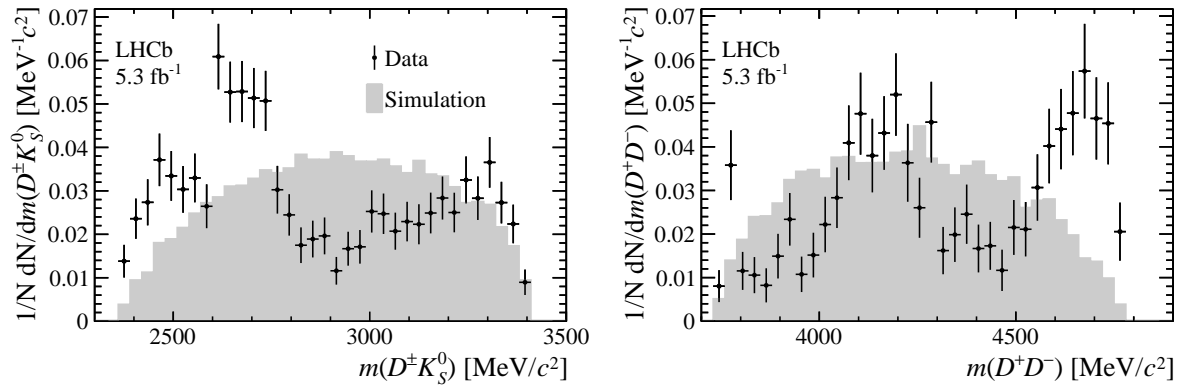


Figure 5: Normalized and background-subtracted invariant mass distributions of the (left) $D^\pm K_S^0$ and (right) $D^+ D^-$ systems in the $B^0 \rightarrow D^+ D^- K_S^0$ decay, compared with the distributions in the simulation sample.

Acknowledgements

We express our gratitude to our colleagues in the CERN accelerator departments for the excellent performance of the LHC. We thank the technical and administrative staff at the LHCb institutes. We acknowledge support from CERN and from the national agencies: CAPES, CNPq, FAPERJ and FINEP (Brazil); MOST and NSFC (China); CNRS/IN2P3 (France); BMBF, DFG and MPG (Germany); INFN (Italy); NWO (Netherlands); MNiSW and NCN (Poland); MCID/IFA (Romania); MICINN (Spain); SNSF and SER (Switzerland); NASU (Ukraine); STFC (United Kingdom); DOE NP and NSF (USA). We acknowledge the computing resources that are provided by CERN, IN2P3 (France), KIT and DESY (Germany), INFN (Italy), SURF (Netherlands), PIC (Spain), GridPP (United Kingdom), CSCS (Switzerland), IFIN-HH (Romania), CBPF (Brazil), and Polish WLCG (Poland). We are indebted to the communities behind the multiple open-source software packages on which we depend. Individual groups or members have received support from ARC and ARDC (Australia); Key Research Program of Frontier Sciences of CAS, CAS PIFI, CAS CCEPP, Fundamental Research Funds for the Central Universities, and Sci. & Tech. Program of Guangzhou (China); Minciencias (Colombia); EPLANET, Marie Skłodowska-Curie Actions, ERC and NextGenerationEU (European Union); A*MIDEX, ANR, IPhU and Labex P2IO, and Région Auvergne-Rhône-Alpes (France); AvH Foundation (Germany); ICSC (Italy); GVA, XuntaGal, GENCAT, Inditex, InTalent and Prog. Atracción Talento, CM (Spain); SRC (Sweden); the Leverhulme Trust, the Royal Society and UKRI (United Kingdom).

References

- [1] ALEPH collaboration, D. Buskulic *et al.*, *Measurement of the mass of the Λ_b^0 baryon*, Phys. Lett. **B380** (1996) 442.
- [2] CDF collaboration, A. Abulencia *et al.*, *Measurement of $\sigma(\Lambda_b^0)/\sigma(\bar{B}^0) \times \mathcal{B}(\Lambda_b^0 \rightarrow \Lambda_c^+ \pi^-)/\mathcal{B}(\bar{B}^0 \rightarrow D^+ \pi^-)$ in $p\bar{p}$ collisions at $\sqrt{s} = 1.96$ TeV*, Phys. Rev. Lett. **98** (2007) 122002, [arXiv:hep-ex/0601003](#).
- [3] LHCb collaboration, R. Aaij *et al.*, *Measurements of the branching fractions for $B_{(s)}^0 \rightarrow D_{(s)} \pi \pi \pi$ and $\Lambda_b^0 \rightarrow \Lambda_c^+ \pi \pi \pi$* , Phys. Rev. **D84** (2011) 092001, Erratum *ibid.* **D85** (2012) 039904, [arXiv:1109.6831](#).
- [4] LHCb collaboration, R. Aaij *et al.*, *Study of beauty baryon decays to $D^0 p h^-$ and $\Lambda_c^+ h^-$ final states*, Phys. Rev. **D89** (2014) 032001, [arXiv:1311.4823](#).
- [5] LHCb collaboration, R. Aaij *et al.*, *Observation of the $\Lambda_b^0 \rightarrow J/\psi p \pi^-$ decay*, JHEP **07** (2014) 103, [arXiv:1406.0755](#).
- [6] LHCb collaboration, R. Aaij *et al.*, *Observation of $\Lambda_b^0 \rightarrow D^+ p \pi^- \pi^-$ and $\Lambda_b^0 \rightarrow D^{*+} p \pi^- \pi^-$ decays*, JHEP **03** (2022) 109, [arXiv:2112.02013](#).
- [7] D0 collaboration, V. M. Abazov *et al.*, *Direct observation of the strange b baryon Ξ_b^-* , Phys. Rev. Lett. **99** (2007) 052001, [arXiv:0706.1690](#).

- [8] CDF collaboration, T. Aaltonen *et al.*, *Observation of the Ω_b^- and Measurement of the Properties of the Ξ_b^- and Ω_b^-* , Phys. Rev. **D80** (2009) 072003, arXiv:0905.3123.
- [9] LHCb collaboration, R. Aaij *et al.*, *Study of the productions of Λ_b^0 and \bar{B}^0 hadrons in pp collisions and first measurement of the $\Lambda_b^0 \rightarrow J/\psi p K^-$ branching fraction*, Chin. Phys. **C40** (2016) 011001, arXiv:1509.00292.
- [10] LHCb collaboration, R. Aaij *et al.*, *Measurement of the ratio of branching fractions of the decays $\Lambda_b^0 \rightarrow \psi(2S)\Lambda$ and $\Lambda_b^0 \rightarrow J/\psi\Lambda$* , JHEP **03** (2019) 126, arXiv:1902.02092.
- [11] LHCb collaboration, R. Aaij *et al.*, *Observation of a $J/\psi\Lambda$ resonance consistent with a strange pentaquark candidate in $B^- \rightarrow J/\psi\Lambda\bar{p}$ decays*, Phys. Rev. Lett. **131** (2023) 031901, arXiv:2210.10346.
- [12] LHCb collaboration, R. Aaij *et al.*, *Observation of a narrow pentaquark state, $P_c(4312)^+$, and of two-peak structure of the $P_c(4450)^+$* , Phys. Rev. Lett. **122** (2019) 222001, arXiv:1904.03947.
- [13] LHCb collaboration, R. Aaij *et al.*, *Search for weakly decaying b -flavored pentaquarks*, Phys. Rev. **D97** (2018) 032010, arXiv:1712.08086.
- [14] LHCb collaboration, R. Aaij *et al.*, *Observation of $J/\psi p$ resonances consistent with pentaquark states in $\Lambda_b^0 \rightarrow J/\psi p K^-$ decays*, Phys. Rev. Lett. **115** (2015) 072001, arXiv:1507.03414.
- [15] LHCb collaboration, R. Aaij *et al.*, *Study of beauty hadron decays into pairs of charm hadrons*, Phys. Rev. Lett. **112** (2014) 202001, arXiv:1403.3606.
- [16] L.-L. Wei *et al.*, *Search for a $D\bar{D}$ bound state in the $\Lambda_b^0 \rightarrow \Lambda D\bar{D}$ process*, Phys. Rev. **D103** (2021) 114013, arXiv:2102.03704.
- [17] LHCb collaboration, R. Aaij *et al.*, *Measurement of b -hadron fractions in 13 TeV pp collisions*, Phys. Rev. **D100** (2019) 031102(R), arXiv:1902.06794.
- [18] Particle Data Group, R. L. Workman *et al.*, *Review of particle physics*, Prog. Theor. Exp. Phys. **2022** (2022) 083C01.
- [19] LHCb collaboration, A. A. Alves Jr. *et al.*, *The LHCb detector at the LHC*, JINST **3** (2008) S08005.
- [20] LHCb collaboration, R. Aaij *et al.*, *LHCb detector performance*, Int. J. Mod. Phys. **A30** (2015) 1530022, arXiv:1412.6352.
- [21] T. Sjöstrand, S. Mrenna, and P. Skands, *A brief introduction to PYTHIA 8.1*, Comput. Phys. Commun. **178** (2008) 852, arXiv:0710.3820; T. Sjöstrand, S. Mrenna, and P. Skands, *PYTHIA 6.4 physics and manual*, JHEP **05** (2006) 026, arXiv:hep-ph/0603175.
- [22] I. Belyaev *et al.*, *Handling of the generation of primary events in Gauss, the LHCb simulation framework*, J. Phys. Conf. Ser. **331** (2011) 032047.

- [23] D. J. Lange, *The EvtGen particle decay simulation package*, Nucl. Instrum. Meth. **A462** (2001) 152.
- [24] N. Davidson, T. Przedzinski, and Z. Was, *PHOTOS interface in C++: Technical and physics documentation*, Comp. Phys. Comm. **199** (2016) 86, [arXiv:1011.0937](#).
- [25] Geant4 collaboration, J. Allison *et al.*, *Geant4 developments and applications*, IEEE Trans. Nucl. Sci. **53** (2006) 270; Geant4 collaboration, S. Agostinelli *et al.*, *Geant4: A simulation toolkit*, Nucl. Instrum. Meth. **A506** (2003) 250.
- [26] M. Clemencic *et al.*, *The LHCb simulation application, Gauss: Design, evolution and experience*, J. Phys. Conf. Ser. **331** (2011) 032023.
- [27] W. D. Hulsbergen, *Decay chain fitting with a Kalman filter*, Nucl. Instrum. Meth. **A552** (2005) 566, [arXiv:physics/0503191](#).
- [28] L. Breiman, J. H. Friedman, R. A. Olshen, and C. J. Stone, *Classification and regression trees*, Wadsworth international group, Belmont, California, USA, 1984.
- [29] Y. Freund and R. E. Schapire, *A decision-theoretic generalization of on-line learning and an application to boosting*, J. Comput. Syst. Sci. **55** (1997) 119.
- [30] H. Voss, A. Hoecker, J. Stelzer, and F. Tegenfeldt, *TMVA - Toolkit for Multivariate Data Analysis with ROOT*, PoS **ACAT** (2007) 040; A. Hoecker *et al.*, *TMVA 4 — Toolkit for Multivariate Data Analysis with ROOT. Users Guide.*, [arXiv:physics/0703039](#).
- [31] G. Punzi, *Sensitivity of searches for new signals and its optimization*, eConf **C030908** (2003) MODT002, [arXiv:physics/0308063](#).
- [32] LHCb collaboration, R. Aaij *et al.*, *Amplitude analysis of the $B^+ \rightarrow D^+ D^- K^+$ decay*, Phys. Rev. **D102** (2020) 112003, [arXiv:2009.00026](#).
- [33] LHCb collaboration, R. Aaij *et al.*, *First observation of the $B^+ \rightarrow D_s^+ D_s^- K^+$ decay*, Phys. Rev. **D108** (2023) 034012, [arXiv:2211.05034](#).
- [34] G. A. Cowan, D. C. Craik, and M. D. Needham, *RapidSim: an application for the fast simulation of heavy-quark hadron decays*, Comput. Phys. Commun. **214** (2017) 239, [arXiv:1612.07489](#).
- [35] ARGUS collaboration, H. Albrecht *et al.*, *Search for hadronic $b \rightarrow u$ decays*, Phys. Lett. **B241** (1990) 278.
- [36] S. S. Wilks, *The large-sample distribution of the likelihood ratio for testing composite hypotheses*, Ann. Math. Stat. **9** (1938) 60.
- [37] M. Pivk and F. R. Le Diberder, *sPlot: A statistical tool to unfold data distributions*, Nucl. Instrum. Meth. **A555** (2005) 356, [arXiv:physics/0402083](#).
- [38] D. Martínez Santos and F. Dupertuis, *Mass distributions marginalized over per-event errors*, Nucl. Instrum. Meth. **A764** (2014) 150, [arXiv:1312.5000](#).

- [39] R. Aaij *et al.*, *Selection and processing of calibration samples to measure the particle identification performance of the LHCb experiment in Run 2*, Eur. Phys. J. Tech. Instr. **6** (2019) 1, [arXiv:1803.00824](#).
- [40] A. Martin Sanchez, P. Robbe, and M.-H. Schune, *Performances of the LHCb L0 Calorimeter Trigger*, LHCb-PUB-2011-026, CERN-LHCb-PUB-2011-026, CERN, Geneva, 2012.
- [41] BaBar collaboration, P. del Amo Sanchez *et al.*, *Measurement of the $B \rightarrow \bar{D}^{(*)} D^{(*)} K$ branching fractions*, Phys. Rev. **D83** (2011) 032004, [arXiv:1011.3929](#).

LHCb collaboration

R. Aaij³⁵ , A.S.W. Abdelmotteleb⁵⁴ , C. Abellan Beteta⁴⁸ , F. Abudinén⁵⁴ ,
T. Ackernley⁵⁸ , J. A. Adams⁶⁶ , A. A. Adefisoye⁶⁶ , B. Adeva⁴⁴ , M. Adinolfi⁵² ,
P. Adlarson⁷⁹ , C. Agapopoulou⁴⁶ , C.A. Aidala⁸⁰ , Z. Ajaltouni¹¹ , S. Akar⁶³ ,
K. Akiba³⁵ , P. Albicocco²⁵ , J. Albrecht¹⁷ , F. Alessio⁴⁶ , M. Alexander⁵⁷ ,
Z. Aliouche⁶⁰ , P. Alvarez Cartelle⁵³ , R. Amalric¹⁵ , S. Amato³ , J.L. Amey⁵² ,
Y. Amhis^{13,46} , L. An⁶ , L. Anderlini²⁴ , M. Andersson⁴⁸ , A. Andreianov⁴¹ ,
P. Andreola⁴⁸ , M. Andreotti²³ , D. Andreou⁶⁶ , A. Anelli^{28,p} , D. Ao⁷ ,
F. Archilli^{34,v} , M. Argenton²³ , S. Arguedas Cuendis⁹ , A. Artamonov⁴¹ ,
M. Artuso⁶⁶ , E. Aslanides¹² , M. Atzeni⁶² , B. Audurier¹⁴ , D. Bacher⁶¹ ,
I. Bachiller Perea¹⁰ , S. Bachmann¹⁹ , M. Bachmayer⁴⁷ , J.J. Back⁵⁴ ,
P. Baladron Rodriguez⁴⁴ , V. Balagura¹⁴ , W. Baldini²³ , J. Baptista de Souza Leite⁵⁸ ,
M. Barbetti^{24,m} , I. R. Barbosa⁶⁷ , R.J. Barlow⁶⁰ , S. Barsuk¹³ , W. Barter⁵⁶ ,
M. Bartolini⁵³ , J. Bartz⁶⁶ , F. Baryshnikov⁴¹ , J.M. Basels¹⁶ , G. Bassi³² ,
B. Batsukh⁵ , A. Battig¹⁷ , A. Bay⁴⁷ , A. Beck⁵⁴ , M. Becker¹⁷ , F. Bedeschi³² ,
I.B. Bediaga² , A. Beiter⁶⁶ , S. Belin⁴⁴ , V. Bellee⁴⁸ , K. Belous⁴¹ , I. Belov²⁶ ,
I. Belyaev³³ , G. Benane¹² , G. Bencivenni²⁵ , E. Ben-Haim¹⁵ , A. Berezhnoy⁴¹ ,
R. Bernet⁴⁸ , S. Bernet Andres⁴² , C. Bertella⁶⁰ , A. Bertolin³⁰ , C. Betancourt⁴⁸ ,
F. Betti⁵⁶ , J. Bex⁵³ , Ia. Bezshyiko⁴⁸ , J. Bhom³⁸ , M.S. Bieker¹⁷ , N.V. Biesuz²³ ,
P. Billoir¹⁵ , A. Biolchini³⁵ , M. Birch⁵⁹ , F.C.R. Bishop¹⁰ , A. Bitadze⁶⁰ ,
A. Bizzeti , T. Blake⁵⁴ , F. Blanc⁴⁷ , J.E. Blank¹⁷ , S. Blusk⁶⁶ , V. Bocharnikov⁴¹ ,
J.A. Boelhauve¹⁷ , O. Boente Garcia¹⁴ , T. Boettcher⁶³ , A. Bohare⁵⁶ ,
A. Boldyrev⁴¹ , C.S. Bolognani⁷⁶ , R. Bolzonella^{23,l} , N. Bondar⁴¹ , F. Borgato^{30,46} ,
S. Borghi⁶⁰ , M. Borsato^{28,p} , J.T. Borsuk³⁸ , S.A. Bouchiba⁴⁷ , T.J.V. Bowcock⁵⁸ ,
A. Boyer⁴⁶ , C. Bozzi²³ , M.J. Bradley⁵⁹ , A. Brea Rodriguez⁴⁴ , N. Breer¹⁷ ,
J. Brodzicka³⁸ , A. Brossa Gonzalo⁴⁴ , J. Brown⁵⁸ , D. Brundu²⁹ , E. Buchanan⁵⁶ ,
A. Buonauro⁴⁸ , L. Buonincontri³⁰ , A.T. Burke⁶⁰ , C. Burr⁴⁶ , A. Bursche⁶⁹ ,
A. Butkevich⁴¹ , J.S. Butter⁵³ , J. Buytaert⁴⁶ , W. Byczynski⁴⁶ , S. Cadeddu²⁹ ,
H. Cai⁷¹ , R. Calabrese^{23,l} , L. Calefice⁴³ , S. Cali²⁵ , M. Calvi^{28,p} , M. Calvo Gomez⁴² ,
J. I. Cambon Bouzas⁴⁴ , P. Campana²⁵ , D.H. Campora Perez⁷⁶ ,
A.F. Campoverde Quezada⁷ , S. Capelli^{28,p} , L. Capriotti²³ , R. Caravaca-Mora⁹ ,
A. Carbone^{22,j} , L. Carcedo Salgado⁴⁴ , R. Cardinale^{26,n} , A. Cardini²⁹ ,
P. Carniti^{28,p} , L. Carus¹⁹ , A. Casais Vidal⁶² , R. Caspary¹⁹ , G. Casse⁵⁸ ,
J. Castro Godinez⁹ , M. Cattaneo⁴⁶ , G. Cavallero²³ , V. Cavallini^{23,l} , S. Celani¹⁹ ,
J. Cerasoli¹² , D. Cervenkov⁶¹ , S. Cesare^{27,o} , A.J. Chadwick⁵⁸ , I. Chahrour⁸⁰ ,
M. Charles¹⁵ , Ph. Charpentier⁴⁶ , C.A. Chavez Barajas⁵⁸ , M. Chefdeville¹⁰ ,
C. Chen¹² , S. Chen⁵ , Z. Chen⁷ , A. Chernov³⁸ , S. Chernyshenko⁵⁰ ,
V. Chobanova⁷⁸ , S. Cholak⁴⁷ , M. Chrzaszcz³⁸ , A. Chubykin⁴¹ , V. Chulikov⁴¹ ,
P. Ciambrone²⁵ , X. Cid Vidal⁴⁴ , G. Ciezarek⁴⁶ , P. Cifra⁴⁶ , P.E.L. Clarke⁵⁶ ,
M. Clemencic⁴⁶ , H.V. Cliff⁵³ , J. Closier⁴⁶ , C. Cocha Toapaxi¹⁹ , V. Coco⁴⁶ ,
J. Cogan¹² , E. Cogneras¹¹ , L. Cojocariu⁴⁰ , P. Collins⁴⁶ , T. Colombo⁴⁶ ,
A. Comerma-Montells⁴³ , L. Congedo²¹ , A. Contu²⁹ , N. Cooke⁵⁷ , I. Corredoira⁴⁴ ,
A. Correia¹⁵ , G. Corti⁴⁶ , J.J. Cottee Meldrum⁵² , B. Couturier⁴⁶ , D.C. Craik⁴⁸ ,
M. Cruz Torres^{2,g} , E. Curras Rivera⁴⁷ , R. Currie⁵⁶ , C.L. Da Silva⁶⁵ , S. Dadabaev⁴¹ ,
L. Dai⁶⁸ , X. Dai⁶ , E. Dall’Occo¹⁷ , J. Dalseno⁴⁴ , C. D’Ambrosio⁴⁶ , J. Daniel¹¹ ,
A. Danilina⁴¹ , P. d’Argent²¹ , A. Davidson⁵⁴ , J.E. Davies⁶⁰ , A. Davis⁶⁰ ,
O. De Aguiar Francisco⁶⁰ , C. De Angelis^{29,k} , F. De Benedetti⁴⁶ , J. de Boer³⁵ ,
K. De Bruyn⁷⁵ , S. De Capua⁶⁰ , M. De Cian^{19,46} , U. De Freitas Carneiro Da Graca^{2,b} ,
E. De Lucia²⁵ , J.M. De Miranda² , L. De Paula³ , M. De Serio^{21,h} , D. De Simone⁴⁸ 

P. De Simone²⁵ , F. De Vellis¹⁷ , J.A. de Vries⁷⁶ , F. Debernardis^{21,h} , D. Decamp¹⁰ ,
 V. Dedu¹² , L. Del Buono¹⁵ , B. Delaney⁶² , H.-P. Dembinski¹⁷ , J. Deng⁸ ,
 V. Denysenko⁴⁸ , O. Deschamps¹¹ , F. Dettori^{29,k} , B. Dey⁷⁴ , P. Di Nezza²⁵ ,
 I. Diachkov⁴¹ , S. Didenko⁴¹ , S. Ding⁶⁶ , L. Dittmann¹⁹ , V. Dobishuk⁵⁰ , A. D.
 Docheva⁵⁷ , A. Dolmatov⁴¹ , C. Dong⁴ , A.M. Donohoe²⁰ , F. Dordei²⁹ ,
 A.C. dos Reis² , A. D. Dowling⁶⁶ , A.G. Downes¹⁰ , W. Duan⁶⁹ , P. Duda⁷⁷ ,
 M.W. Dudek³⁸ , L. Dufour⁴⁶ , V. Duk³¹ , P. Durante⁴⁶ , M. M. Duras⁷⁷ ,
 J.M. Durham⁶⁵ , O. D. Durmus⁷⁴ , A. Dziurda³⁸ , A. Dzyuba⁴¹ , S. Easo⁵⁵ ,
 E. Eckstein⁷³ , U. Egede¹ , A. Egorychev⁴¹ , V. Egorychev⁴¹ , S. Eisenhardt⁵⁶ ,
 E. Ejopu⁶⁰ , S. Ek-In⁴⁷ , L. Eklund⁷⁹ , M. Elashri⁶³ , J. Ellbracht¹⁷ , S. Ely⁵⁹ ,
 A. Ene⁴⁰ , E. Epple⁶³ , S. Escher¹⁶ , J. Eschle⁴⁸ , S. Esen¹⁹ , T. Evans⁶⁰ ,
 F. Fabiano^{29,k,46} , L.N. Falcao² , Y. Fan⁷ , B. Fang^{71,13} , L. Fantini^{31,r} , M. Faria⁴⁷ ,
 K. Farmer⁵⁶ , D. Fazzini^{28,p} , L. Felkowski⁷⁷ , M. Feng^{5,7} , M. Feo⁴⁶ ,
 M. Fernandez Gomez⁴⁴ , A.D. Fernez⁶⁴ , F. Ferrari²² , F. Ferreira Rodrigues³ ,
 S. Ferreres Sole³⁵ , M. Ferrillo⁴⁸ , M. Ferro-Luzzi⁴⁶ , S. Filippov⁴¹ , R.A. Fini²¹ ,
 M. Fiorini^{23,l} , K.M. Fischer⁶¹ , D.S. Fitzgerald⁸⁰ , C. Fitzpatrick⁶⁰ , F. Fleuret¹⁴ ,
 M. Fontana²² , L. F. Foreman⁶⁰ , R. Forty⁴⁶ , D. Foulds-Holt⁵³ , M. Franco Sevilla⁶⁴ ,
 M. Frank⁴⁶ , E. Franzoso^{23,l} , G. Frau¹⁹ , C. Frei⁴⁶ , D.A. Friday⁶⁰ , J. Fu⁷ ,
 Q. Fuehring¹⁷ , Y. Fujii¹ , T. Fulghesu¹⁵ , E. Gabriel³⁵ , G. Galati^{21,h} ,
 M.D. Galati³⁵ , A. Gallas Torreira⁴⁴ , D. Galli^{22,j} , S. Gambetta⁵⁶ , M. Gandelman³ ,
 P. Gandini²⁷ , H. Gao⁷ , R. Gao⁶¹ , Y. Gao⁸ , Y. Gao⁶ , Y. Gao⁸ , M. Garau^{29,k} ,
 L.M. Garcia Martin⁴⁷ , P. Garcia Moreno⁴³ , J. García Pardiñas⁴⁶ , K. G. Garg⁸ ,
 L. Garrido⁴³ , C. Gaspar⁴⁶ , R.E. Geertsema³⁵ , L.L. Gerken¹⁷ , E. Gersabeck⁶⁰ ,
 M. Gersabeck⁶⁰ , T. Gershon⁵⁴ , Z. Ghorbanimoghaddam⁵² , L. Giambastiani³⁰ , F.
 I. Giasemis^{15,e} , V. Gibson⁵³ , H.K. Giemza³⁹ , A.L. Gilman⁶¹ , M. Giovannetti²⁵ ,
 A. Gioventù⁴³ , P. Gironella Gironell⁴³ , C. Giugliano^{23,l} , M.A. Giza³⁸ ,
 E.L. Gkoukousis⁵⁹ , F.C. Glaser^{13,19} , V.V. Gligorov¹⁵ , C. Göbel⁶⁷ , E. Golobardes⁴² ,
 D. Golubkov⁴¹ , A. Golutvin^{59,41,46} , A. Gomes^{2,a,†} , S. Gomez Fernandez⁴³ ,
 F. Goncalves Abrantes⁶¹ , M. Goncerz³⁸ , G. Gong⁴ , J. A. Gooding¹⁷ ,
 I.V. Gorelov⁴¹ , C. Gotti²⁸ , J.P. Grabowski⁷³ , L.A. Granado Cardoso⁴⁶ ,
 E. Graugés⁴³ , E. Graverini^{47,t} , L. Grazette⁵⁴ , G. Graziani , A. T. Grecu⁴⁰ ,
 L.M. Greeven³⁵ , N.A. Grieser⁶³ , L. Grillo⁵⁷ , S. Gromov⁴¹ , C. Gu¹⁴ ,
 M. Guarise²³ , M. Guittiere¹³ , V. Guliaeva⁴¹ , P. A. Günther¹⁹ , A.-K. Guseinov⁴⁷ ,
 E. Gushchin⁴¹ , Y. Guz^{6,41,46} , T. Gys⁴⁶ , K. Habermann⁷³ , T. Hadavizadeh¹ ,
 C. Hadjivasilou⁶⁴ , G. Haefeli⁴⁷ , C. Haen⁴⁶ , J. Haimberger⁴⁶ , M. Hajheidari⁴⁶ ,
 M.M. Halvorsen⁴⁶ , P.M. Hamilton⁶⁴ , J. Hammerich⁵⁸ , Q. Han⁸ , X. Han¹⁹ ,
 S. Hansmann-Menzemer¹⁹ , L. Hao⁷ , N. Harnew⁶¹ , T. Harrison⁵⁸ , M. Hartmann¹³ ,
 J. He^{7,c} , K. Heijhoff³⁵ , F. Hemmer⁴⁶ , C. Henderson⁶³ , R.D.L. Henderson^{1,54} ,
 A.M. Hennequin⁴⁶ , K. Hennessy⁵⁸ , L. Henry⁴⁷ , J. Herd⁵⁹ , P. Herrero Gascon¹⁹ ,
 J. Heuel¹⁶ , A. Hicheur³ , G. Hijano Mendizabal⁴⁸ , D. Hill⁴⁷ , S.E. Hollitt¹⁷ ,
 J. Horswill⁶⁰ , R. Hou⁸ , Y. Hou¹⁰ , N. Howarth⁵⁸ , J. Hu¹⁹ , J. Hu⁶⁹ , W. Hu⁶ ,
 X. Hu⁴ , W. Huang⁷ , W. Hulsbergen³⁵ , R.J. Hunter⁵⁴ , M. Hushchyn⁴¹ ,
 D. Hutchcroft⁵⁸ , D. Ilin⁴¹ , P. Ilten⁶³ , A. Inglessi⁴¹ , A. Iniukhin⁴¹ , A. Ishteev⁴¹ ,
 K. Ivshin⁴¹ , R. Jacobsson⁴⁶ , H. Jage¹⁶ , S.J. Jaimes Elles^{45,72} , S. Jakobsen⁴⁶ ,
 E. Jans³⁵ , B.K. Jashal⁴⁵ , A. Jawahery^{64,46} , V. Jevtic¹⁷ , E. Jiang⁶⁴ , X. Jiang^{5,7} ,
 Y. Jiang⁷ , Y. J. Jiang⁶ , M. John⁶¹ , D. Johnson⁵¹ , C.R. Jones⁵³ , T.P. Jones⁵⁴ ,
 S. Joshi³⁹ , B. Jost⁴⁶ , N. Jurik⁴⁶ , I. Juszczak³⁸ , D. Kaminaris⁴⁷ , S. Kandybei⁴⁹ ,
 Y. Kang⁴ , M. Karacson⁴⁶ , D. Karpenkov⁴¹ , A. Kauniskangas⁴⁷ , J.W. Kautz⁶³ ,
 F. Keizer⁴⁶ , M. Kenzie⁵³ , T. Ketel³⁵ , B. Khanji⁶⁶ , A. Kharisova⁴¹ ,
 S. Kholodenko³² , G. Khreich¹³ , T. Kirn¹⁶ , V.S. Kirsebom^{28,p} , O. Kitouni⁶² ,

S. Klaver³⁶ , N. Kleijne^{32,s} , K. Klimaszewski³⁹ , M.R. Kmiec³⁹ , S. Koliiev⁵⁰ ,
 L. Kolk¹⁷ , A. Konoplyannikov⁴¹ , P. Kopciewicz^{37,46} , P. Koppenburg³⁵ ,
 M. Korolev⁴¹ , I. Kostiuk³⁵ , O. Kot⁵⁰ , S. Kotriakhova , A. Kozachuk⁴¹ ,
 P. Kravchenko⁴¹ , L. Kravchuk⁴¹ , M. Kreps⁵⁴ , S. Kretzschmar¹⁶ , P. Krokovny⁴¹ ,
 W. Krupa⁶⁶ , W. Krzemien³⁹ , J. Kubat¹⁹ , S. Kubis⁷⁷ , W. Kucewicz³⁸ ,
 M. Kucharczyk³⁸ , V. Kudryavtsev⁴¹ , E. Kulikova⁴¹ , A. Kupsc⁷⁹ , B. K. Kutsenko¹² ,
 D. Lacarrere⁴⁶ , A. Lai²⁹ , A. Lampis²⁹ , D. Lancierini⁵³ , C. Landesa Gomez⁴⁴ ,
 J.J. Lane¹ , R. Lane⁵² , C. Langenbruch¹⁹ , J. Langer¹⁷ , O. Lantwin⁴¹ ,
 T. Latham⁵⁴ , F. Lazzari^{32,t} , C. Lazzeroni⁵¹ , R. Le Gac¹² , R. Lefèvre¹¹ ,
 A. Leflat⁴¹ , S. Legotin⁴¹ , M. Lehuraux⁵⁴ , E. Lemos Cid⁴⁶ , O. Leroy¹² ,
 T. Lesiak³⁸ , B. Leverington¹⁹ , A. Li⁴ , H. Li⁶⁹ , K. Li⁸ , L. Li⁶⁰ , P. Li⁴⁶ ,
 P.-R. Li⁷⁰ , S. Li⁸ , T. Li^{5,d} , T. Li⁶⁹ , Y. Li⁸ , Y. Li⁵ , Z. Li⁶⁶ , Z. Lian⁴ ,
 X. Liang⁶⁶ , S. Libralon⁴⁵ , C. Lin⁷ , T. Lin⁵⁵ , R. Lindner⁴⁶ , V. Lisovskiy⁴⁷ ,
 R. Litvinov^{29,k} , F. L. Liu¹ , G. Liu⁶⁹ , K. Liu⁷⁰ , Q. Liu⁷ , S. Liu^{5,7} , Y. Liu⁵⁶ ,
 Y. Liu⁷⁰ , Y. L. Liu⁵⁹ , A. Lobo Salvia⁴³ , A. Loi²⁹ , J. Lomba Castro⁴⁴ , T. Long⁵³ ,
 J.H. Lopes³ , A. Lopez Huertas⁴³ , S. López Soliño⁴⁴ , G.H. Lovell⁵³ , C. Lucarelli^{24,m} ,
 D. Lucchesi^{30,q} , S. Luchuk⁴¹ , M. Lucio Martinez⁷⁶ , V. Lukashenko^{35,50} , Y. Luo⁶ ,
 A. Lupato³⁰ , E. Luppi^{23,l} , K. Lynch²⁰ , X.-R. Lyu⁷ , G. M. Ma⁴ , R. Ma⁷ ,
 S. Maccolini¹⁷ , F. Machefert¹³ , F. Maciuc⁴⁰ , B. M. Mack⁶⁶ , I. Mackay⁶¹ , L. M.
 Mackey⁶⁶ , L.R. Madhan Mohan⁵³ , M. M. Madurai⁵¹ , A. Maevskiy⁴¹ ,
 D. Magdalinski³⁵ , D. Maisuzenko⁴¹ , M.W. Majewski³⁷ , J.J. Malczewski³⁸ , S. Malde⁶¹ ,
 B. Malecki^{38,46} , L. Malentacca⁴⁶ , A. Malinin⁴¹ , T. Maltsev⁴¹ , G. Manca^{29,k} ,
 G. Mancinelli¹² , C. Mancuso^{27,13,o} , R. Manera Escalero⁴³ , D. Manuzzi²² ,
 D. Marangotto^{27,o} , J.F. Marchand¹⁰ , R. Marchevski⁴⁷ , U. Marconi²² , S. Mariani⁴⁶ ,
 C. Marin Benito⁴³ , J. Marks¹⁹ , A.M. Marshall⁵² , P.J. Marshall⁵⁸ , G. Martelli^{31,r} ,
 G. Martellotti³³ , L. Martinazzoli⁴⁶ , M. Martinelli^{28,p} , D. Martinez Santos⁴⁴ ,
 F. Martinez Vidal⁴⁵ , A. Massafferi² , M. Materok¹⁶ , R. Matev⁴⁶ , A. Mathad⁴⁶ ,
 V. Matiunin⁴¹ , C. Matteuzzi⁶⁶ , K.R. Mattioli¹⁴ , A. Mauri⁵⁹ , E. Maurice¹⁴ ,
 J. Mauricio⁴³ , P. Mayencourt⁴⁷ , M. Mazurek³⁹ , M. McCann⁵⁹ , L. McConnell²⁰ ,
 T.H. McGrath⁶⁰ , N.T. McHugh⁵⁷ , A. McNab⁶⁰ , R. McNulty²⁰ , B. Meadows⁶³ ,
 G. Meier¹⁷ , D. Melnychuk³⁹ , M. Merk^{35,76} , A. Merli^{27,o} , L. Meyer Garcia³ ,
 D. Miao^{5,7} , H. Miao⁷ , M. Mikhasenko^{73,f} , D.A. Milanese⁷² , A. Minotti^{28,p} ,
 E. Minucci⁶⁶ , T. Miralles¹¹ , B. Mitreska¹⁷ , D.S. Mitzel¹⁷ , A. Modak⁵⁵ ,
 A. Mödden¹⁷ , R.A. Mohammed⁶¹ , R.D. Moise¹⁶ , S. Mokhnenko⁴¹ ,
 T. Mombächer⁴⁶ , M. Monk^{54,1} , S. Monteil¹¹ , A. Morcillo Gomez⁴⁴ , G. Morello²⁵ ,
 M.J. Morello^{32,s} , M.P. Morgenthaler¹⁹ , A.B. Morris⁴⁶ , A.G. Morris¹² ,
 R. Mountain⁶⁶ , H. Mu⁴ , Z. M. Mu⁶ , E. Muhammad⁵⁴ , F. Muheim⁵⁶ ,
 M. Mulder⁷⁵ , K. Müller⁴⁸ , F. Muñoz-Rojas⁹ , R. Murta⁵⁹ , P. Naik⁵⁸ ,
 T. Nakada⁴⁷ , R. Nandakumar⁵⁵ , T. Nanut⁴⁶ , I. Nasteva³ , M. Needham⁵⁶ ,
 N. Neri^{27,o} , S. Neubert⁷³ , N. Neufeld⁴⁶ , P. Neustroev⁴¹ , J. Nicolini^{17,13} ,
 D. Nicotra⁷⁶ , E.M. Niel⁴⁷ , N. Nikitin⁴¹ , P. Nogga⁷³ , N.S. Nolte⁶² , C. Normand⁵² ,
 J. Novoa Fernandez⁴⁴ , G. Nowak⁶³ , C. Nunez⁸⁰ , H. N. Nur⁵⁷ ,
 A. Oblakowska-Mucha³⁷ , V. Obraztsov⁴¹ , T. Oeser¹⁶ , S. Okamura^{23,l,46} ,
 A. Okhotnikov⁴¹ , R. Oldeman^{29,k} , F. Oliva⁵⁶ , M. Olocco¹⁷ , C.J.G. Onderwater⁷⁶ ,
 R.H. O'Neil⁵⁶ , J.M. Otalora Goicochea³ , P. Owen⁴⁸ , A. Oyanguren⁴⁵ , O. Ozcelik⁵⁶ ,
 K.O. Padeken⁷³ , B. Pagare⁵⁴ , P.R. Pais¹⁹ , T. Pajero⁶¹ , A. Palano²¹ ,
 M. Palutan²⁵ , G. Panshin⁴¹ , L. Paolucci⁵⁴ , A. Papanestis⁵⁵ , M. Pappagallo^{21,h} ,
 L.L. Pappalardo^{23,l} , C. Pappenheimer⁶³ , C. Parkes⁶⁰ , B. Passalacqua²³ ,
 G. Passaleva²⁴ , D. Passaro^{32,s} , A. Pastore²¹ , M. Patel⁵⁹ , J. Patoc⁶¹ ,
 C. Patrignani^{22,j} , C.J. Pawley⁷⁶ , A. Pellegrino³⁵ , M. Pepe Altarelli²⁵ ,

S. Perazzini²² , D. Pereima⁴¹ , A. Pereiro Castro⁴⁴ , P. Perret¹¹ , A. Perro⁴⁶ ,
 K. Petridis⁵² , A. Petrolini^{26,n} , S. Petrucci⁵⁶ , J. P. Pfaller⁶³ , H. Pham⁶⁶ ,
 L. Pica^{32,s} , M. Piccini³¹ , B. Pietrzyk¹⁰ , G. Pietrzyk¹³ , D. Pinci³³ , F. Pisani⁴⁶ ,
 M. Pizzichemi^{28,p} , V. Placinta⁴⁰ , M. Plo Casasus⁴⁴ , F. Polci^{15,46} , M. Poli Lener²⁵ ,
 A. Poluektov¹² , N. Polukhina⁴¹ , I. Polyakov⁴⁶ , E. Polycarpo³ , S. Ponce⁴⁶ ,
 D. Popov⁷ , S. Poslavskii⁴¹ , K. Prasanth³⁸ , C. Prouve⁴⁴ , V. Pugatch⁵⁰ ,
 G. Punzi^{32,t} , W. Qian⁷ , N. Qin⁴ , S. Qu⁴ , R. Quagliani⁴⁷ , R.I. Rabadan Trejo⁵⁴ ,
 J.H. Rademacker⁵² , M. Rama³² , M. Ramírez García⁸⁰ , M. Ramos Pernas⁵⁴ ,
 M.S. Rangel³ , F. Ratnikov⁴¹ , G. Raven³⁶ , M. Rebollo De Miguel⁴⁵ , F. Redi^{27,i} ,
 J. Reich⁵² , F. Reiss⁶⁰ , Z. Ren⁷ , P.K. Resmi⁶¹ , R. Ribatti^{32,s} , G. R. Ricart^{14,81} ,
 D. Riccardi^{32,s} , S. Ricciardi⁵⁵ , K. Richardson⁶² , M. Richardson-Slipper⁵⁶ ,
 K. Rinnert⁵⁸ , P. Robbe¹³ , G. Robertson⁵⁷ , E. Rodrigues⁵⁸ ,
 E. Rodriguez Fernandez⁴⁴ , J.A. Rodriguez Lopez⁷² , E. Rodriguez Rodriguez⁴⁴ ,
 A. Rogovskiy⁵⁵ , D.L. Rolf⁴⁶ , P. Roloff⁴⁶ , V. Romanovskiy⁴¹ , M. Romero Lamas⁴⁴ ,
 A. Romero Vidal⁴⁴ , G. Romolini²³ , F. Ronchetti⁴⁷ , M. Rotondo²⁵ , S. R. Roy¹⁹ ,
 M.S. Rudolph⁶⁶ , T. Ruf⁴⁶ , M. Ruiz Diaz¹⁹ , R.A. Ruiz Fernandez⁴⁴ ,
 J. Ruiz Vidal^{79,z} , A. Ryzhikov⁴¹ , J. Ryzka³⁷ , J. J. Saavedra-Arias⁹ ,
 J.J. Saborido Silva⁴⁴ , R. Sadek¹⁴ , N. Sagidova⁴¹ , D. Sahoo⁷⁴ , N. Sahoo⁵¹ ,
 B. Saitta^{29,k} , M. Salomoni^{28,p} , C. Sanchez Gras³⁵ , I. Sanderswood⁴⁵ ,
 R. Santacesaria³³ , C. Santamarina Rios⁴⁴ , M. Santimaria²⁵ , L. Santoro² ,
 E. Santovetti³⁴ , A. Saputi^{23,46} , D. Saranin⁴¹ , G. Sarpis⁵⁶ , M. Sarpis⁷³ ,
 A. Sarti³³ , C. Satriano^{33,u} , A. Satta³⁴ , M. Saur⁶ , D. Savrina⁴¹ , H. Sazak¹⁶ ,
 L.G. Scantlebury Smead⁶¹ , A. Scarabotto¹⁷ , S. Schael¹⁶ , S. Scherl⁵⁸ , A. M.
 Schertz⁷⁴ , M. Schiller⁵⁷ , H. Schindler⁴⁶ , M. Schmelling¹⁸ , B. Schmidt⁴⁶ ,
 S. Schmitt¹⁶ , H. Schmitz⁷³ , O. Schneider⁴⁷ , A. Schopper⁴⁶ , N. Schulte¹⁷ ,
 S. Schulte⁴⁷ , M.H. Schune¹³ , R. Schwemmer⁴⁶ , G. Schwering¹⁶ , B. Sciascia²⁵ ,
 A. Sciuccati⁴⁶ , S. Sellam⁴⁴ , A. Semennikov⁴¹ , T. Senger⁴⁸ , M. Senghi Soares³⁶ ,
 A. Sergi²⁶ , N. Serra⁴⁸ , L. Sestini³⁰ , A. Seuthe¹⁷ , Y. Shang⁶ , D.M. Shangase⁸⁰ ,
 M. Shapkin⁴¹ , R. S. Sharma⁶⁶ , I. Shchemerov⁴¹ , L. Shchutska⁴⁷ , T. Shears⁵⁸ ,
 L. Shekhtman⁴¹ , Z. Shen⁶ , S. Sheng^{5,7} , V. Shevchenko⁴¹ , B. Shi⁷ ,
 E.B. Shields^{28,p} , Y. Shimizu¹³ , E. Shmanin⁴¹ , R. Shorkin⁴¹ , J.D. Shupperd⁶⁶ ,
 R. Silva Coutinho⁶⁶ , G. Simi³⁰ , S. Simone^{21,h} , N. Skidmore⁵⁴ , T. Skwarnicki⁶⁶ ,
 M.W. Slater⁵¹ , J.C. Smallwood⁶¹ , E. Smith⁶² , K. Smith⁶⁵ , M. Smith⁵⁹ ,
 A. Snoch³⁵ , L. Soares Lavra⁵⁶ , M.D. Sokoloff⁶³ , F.J.P. Soler⁵⁷ , A. Solomin^{41,52} ,
 A. Solovov⁴¹ , I. Solovyev⁴¹ , R. Song¹ , Y. Song⁴⁷ , Y. Song⁴ , Y. S. Song⁶ ,
 F.L. Souza De Almeida⁶⁶ , B. Souza De Paula³ , E. Spadaro Norella^{27,o} ,
 E. Spedicato²² , J.G. Speer¹⁷ , E. Spiridenkov⁴¹ , P. Spradlin⁵⁷ , V. Sriskaran⁴⁶ ,
 F. Stagni⁴⁶ , M. Stahl⁴⁶ , S. Stahl⁴⁶ , S. Stanislaus⁶¹ , E.N. Stein⁴⁶ , O. Steinkamp⁴⁸ ,
 O. Stenyakin⁴¹ , H. Stevens¹⁷ , D. Strekalina⁴¹ , Y. Su⁷ , F. Suljik⁶¹ , J. Sun²⁹ ,
 L. Sun⁷¹ , Y. Sun⁶⁴ , W. Sutcliffe⁴⁸ , P.N. Swallow⁵¹ , F. Swystun⁵³ , A. Szabelski³⁹ ,
 T. Szumlak³⁷ , Y. Tan⁴ , S. Taneja⁶⁰ , M.D. Tat⁶¹ , A. Terentev⁴⁸ , F. Terzuoli^{32,w} ,
 F. Teubert⁴⁶ , E. Thomas⁴⁶ , D.J.D. Thompson⁵¹ , H. Tilquin⁵⁹ , V. Tisserand¹¹ ,
 S. T'Jampens¹⁰ , M. Tobin⁵ , L. Tomassetti^{23,l} , G. Tonani^{27,o,46} , X. Tong⁶ ,
 D. Torres Machado² , L. Toscano¹⁷ , D.Y. Tou⁴ , C. Trippel⁴² , G. Tuci¹⁹ ,
 N. Tuning³⁵ , L.H. Uecker¹⁹ , A. Ukleja³⁷ , D.J. Unverzagt¹⁹ , E. Ursov⁴¹ ,
 A. Usachov³⁶ , A. Ustyuzhanin⁴¹ , U. Uwer¹⁹ , V. Vagnoni²² , A. Valassi⁴⁶ ,
 G. Valenti²² , N. Valls Canudas⁴² , H. Van Hecke⁶⁵ , E. van Herwijnen⁵⁹ ,
 C.B. Van Hulse^{44,y} , R. Van Laak⁴⁷ , M. van Veghel³⁵ , R. Vazquez Gomez⁴³ ,
 P. Vazquez Regueiro⁴⁴ , C. Vázquez Sierra⁴⁴ , S. Vecchi²³ , J.J. Velthuis⁵² ,
 M. Veltri^{24,x} , A. Venkateswaran⁴⁷ , M. Vesterinen⁵⁴ , M. Vieites Diaz⁴⁶ ,

X. Vilasis-Cardona⁴² , E. Vilella Figueras⁵⁸ , A. Villa²² , P. Vincent¹⁵ , F.C. Volle¹³ ,
D. vom Bruch¹² , V. Vorobyev⁴¹ , N. Voropaev⁴¹ , K. Vos⁷⁶ , G. Vouters¹⁰ , C. Vrahas⁵⁶ ,
J. Wagner¹⁷ , J. Walsh³² , E.J. Walton^{1,54} , G. Wan⁶ , C. Wang¹⁹ , G. Wang⁸ ,
J. Wang⁶ , J. Wang⁵ , J. Wang⁴ , J. Wang⁷¹ , M. Wang²⁷ , N. W. Wang⁷ ,
R. Wang⁵² , X. Wang⁶⁹ , X. W. Wang⁵⁹ , Y. Wang⁸ , Z. Wang¹³ , Z. Wang⁴ ,
Z. Wang²⁷ , J.A. Ward^{54,1} , M. Waterlaet⁴⁶ , N.K. Watson⁵¹ , D. Websdale⁵⁹ ,
Y. Wei⁶ , B.D.C. Westhenry⁵² , D.J. White⁶⁰ , M. Whitehead⁵⁷ , A.R. Wiederhold⁵⁴ ,
D. Wiedner¹⁷ , G. Wilkinson⁶¹ , M.K. Wilkinson⁶³ , M. Williams⁶² ,
M.R.J. Williams⁵⁶ , R. Williams⁵³ , F.F. Wilson⁵⁵ , W. Wislicki³⁹ , M. Witek³⁸ ,
L. Witola¹⁹ , C.P. Wong⁶⁵ , G. Wormser¹³ , S.A. Wotton⁵³ , H. Wu⁶⁶ , J. Wu⁸ ,
Y. Wu⁶ , K. Wyllie⁴⁶ , S. Xian⁶⁹ , Z. Xiang⁵ , Y. Xie⁸ , A. Xu³² , J. Xu⁷ , L. Xu⁴ ,
L. Xu⁴ , M. Xu⁵⁴ , Z. Xu¹¹ , Z. Xu⁷ , Z. Xu⁵ , D. Yang⁴ , S. Yang⁷ , X. Yang⁶ ,
Y. Yang^{26,n} , Z. Yang⁶ , Z. Yang⁶⁴ , V. Yeroshenko¹³ , H. Yeung⁶⁰ , H. Yin⁸ , C. Y.
Yu⁶ , J. Yu⁶⁸ , X. Yuan⁵ , E. Zaffaroni⁴⁷ , M. Zavertyaev¹⁸ , M. Zdybal³⁸ ,
M. Zeng⁴ , C. Zhang⁶ , D. Zhang⁸ , J. Zhang⁷ , L. Zhang⁴ , S. Zhang⁶⁸ ,
S. Zhang⁶ , Y. Zhang⁶ , Y. Z. Zhang⁴ , Y. Zhao¹⁹ , A. Zharkova⁴¹ , A. Zhelezov¹⁹ ,
X. Z. Zheng⁴ , Y. Zheng⁷ , T. Zhou⁶ , X. Zhou⁸ , Y. Zhou⁷ , V. Zhovkovska⁵⁴ , L. Z.
Zhu⁷ , X. Zhu⁴ , X. Zhu⁸ , V. Zhukov¹⁶ , J. Zhuo⁴⁵ , Q. Zou^{5,7} , D. Zuliani³⁰ ,
G. Zunica⁴⁷ .

¹*School of Physics and Astronomy, Monash University, Melbourne, Australia*

²*Centro Brasileiro de Pesquisas Físicas (CBPF), Rio de Janeiro, Brazil*

³*Universidade Federal do Rio de Janeiro (UFRJ), Rio de Janeiro, Brazil*

⁴*Center for High Energy Physics, Tsinghua University, Beijing, China*

⁵*Institute Of High Energy Physics (IHEP), Beijing, China*

⁶*School of Physics State Key Laboratory of Nuclear Physics and Technology, Peking University, Beijing, China*

⁷*University of Chinese Academy of Sciences, Beijing, China*

⁸*Institute of Particle Physics, Central China Normal University, Wuhan, Hubei, China*

⁹*Consejo Nacional de Rectores (CONARE), San Jose, Costa Rica*

¹⁰*Université Savoie Mont Blanc, CNRS, IN2P3-LAPP, Annecy, France*

¹¹*Université Clermont Auvergne, CNRS/IN2P3, LPC, Clermont-Ferrand, France*

¹²*Aix Marseille Univ, CNRS/IN2P3, CPPM, Marseille, France*

¹³*Université Paris-Saclay, CNRS/IN2P3, IJCLab, Orsay, France*

¹⁴*Laboratoire Leprince-Ringuet, CNRS/IN2P3, Ecole Polytechnique, Institut Polytechnique de Paris, Palaiseau, France*

¹⁵*LPNHE, Sorbonne Université, Paris Diderot Sorbonne Paris Cité, CNRS/IN2P3, Paris, France*

¹⁶*I. Physikalisches Institut, RWTH Aachen University, Aachen, Germany*

¹⁷*Fakultät Physik, Technische Universität Dortmund, Dortmund, Germany*

¹⁸*Max-Planck-Institut für Kernphysik (MPIK), Heidelberg, Germany*

¹⁹*Physikalisches Institut, Ruprecht-Karls-Universität Heidelberg, Heidelberg, Germany*

²⁰*School of Physics, University College Dublin, Dublin, Ireland*

²¹*INFN Sezione di Bari, Bari, Italy*

²²*INFN Sezione di Bologna, Bologna, Italy*

²³*INFN Sezione di Ferrara, Ferrara, Italy*

²⁴*INFN Sezione di Firenze, Firenze, Italy*

²⁵*INFN Laboratori Nazionali di Frascati, Frascati, Italy*

²⁶*INFN Sezione di Genova, Genova, Italy*

²⁷*INFN Sezione di Milano, Milano, Italy*

²⁸*INFN Sezione di Milano-Bicocca, Milano, Italy*

²⁹*INFN Sezione di Cagliari, Monserrato, Italy*

³⁰*Università degli Studi di Padova, Università e INFN, Padova, Padova, Italy*

³¹*INFN Sezione di Perugia, Perugia, Italy*

³²*INFN Sezione di Pisa, Pisa, Italy*

- ³³ INFN Sezione di Roma La Sapienza, Roma, Italy
- ³⁴ INFN Sezione di Roma Tor Vergata, Roma, Italy
- ³⁵ Nikhef National Institute for Subatomic Physics, Amsterdam, Netherlands
- ³⁶ Nikhef National Institute for Subatomic Physics and VU University Amsterdam, Amsterdam, Netherlands
- ³⁷ AGH - University of Krakow, Faculty of Physics and Applied Computer Science, Kraków, Poland
- ³⁸ Henryk Niewodniczanski Institute of Nuclear Physics Polish Academy of Sciences, Kraków, Poland
- ³⁹ National Center for Nuclear Research (NCBJ), Warsaw, Poland
- ⁴⁰ Horia Hulubei National Institute of Physics and Nuclear Engineering, Bucharest-Magurele, Romania
- ⁴¹ Affiliated with an institute covered by a cooperation agreement with CERN
- ⁴² DS4DS, La Salle, Universitat Ramon Llull, Barcelona, Spain
- ⁴³ ICCUB, Universitat de Barcelona, Barcelona, Spain
- ⁴⁴ Instituto Galego de Física de Altas Enerxías (IGFAE), Universidade de Santiago de Compostela, Santiago de Compostela, Spain
- ⁴⁵ Instituto de Física Corpuscular, Centro Mixto Universidad de Valencia - CSIC, Valencia, Spain
- ⁴⁶ European Organization for Nuclear Research (CERN), Geneva, Switzerland
- ⁴⁷ Institute of Physics, Ecole Polytechnique Fédérale de Lausanne (EPFL), Lausanne, Switzerland
- ⁴⁸ Physik-Institut, Universität Zürich, Zürich, Switzerland
- ⁴⁹ NSC Kharkiv Institute of Physics and Technology (NSC KIPT), Kharkiv, Ukraine
- ⁵⁰ Institute for Nuclear Research of the National Academy of Sciences (KINR), Kyiv, Ukraine
- ⁵¹ University of Birmingham, Birmingham, United Kingdom
- ⁵² H.H. Wills Physics Laboratory, University of Bristol, Bristol, United Kingdom
- ⁵³ Cavendish Laboratory, University of Cambridge, Cambridge, United Kingdom
- ⁵⁴ Department of Physics, University of Warwick, Coventry, United Kingdom
- ⁵⁵ STFC Rutherford Appleton Laboratory, Didcot, United Kingdom
- ⁵⁶ School of Physics and Astronomy, University of Edinburgh, Edinburgh, United Kingdom
- ⁵⁷ School of Physics and Astronomy, University of Glasgow, Glasgow, United Kingdom
- ⁵⁸ Oliver Lodge Laboratory, University of Liverpool, Liverpool, United Kingdom
- ⁵⁹ Imperial College London, London, United Kingdom
- ⁶⁰ Department of Physics and Astronomy, University of Manchester, Manchester, United Kingdom
- ⁶¹ Department of Physics, University of Oxford, Oxford, United Kingdom
- ⁶² Massachusetts Institute of Technology, Cambridge, MA, United States
- ⁶³ University of Cincinnati, Cincinnati, OH, United States
- ⁶⁴ University of Maryland, College Park, MD, United States
- ⁶⁵ Los Alamos National Laboratory (LANL), Los Alamos, NM, United States
- ⁶⁶ Syracuse University, Syracuse, NY, United States
- ⁶⁷ Pontifícia Universidade Católica do Rio de Janeiro (PUC-Rio), Rio de Janeiro, Brazil, associated to ³
- ⁶⁸ School of Physics and Electronics, Hunan University, Changsha City, China, associated to ⁸
- ⁶⁹ Guangdong Provincial Key Laboratory of Nuclear Science, Guangdong-Hong Kong Joint Laboratory of Quantum Matter, Institute of Quantum Matter, South China Normal University, Guangzhou, China, associated to ⁴
- ⁷⁰ Lanzhou University, Lanzhou, China, associated to ⁵
- ⁷¹ School of Physics and Technology, Wuhan University, Wuhan, China, associated to ⁴
- ⁷² Departamento de Física, Universidad Nacional de Colombia, Bogota, Colombia, associated to ¹⁵
- ⁷³ Universität Bonn - Helmholtz-Institut für Strahlen und Kernphysik, Bonn, Germany, associated to ¹⁹
- ⁷⁴ Eotvos Lorand University, Budapest, Hungary, associated to ⁴⁶
- ⁷⁵ Van Swinderen Institute, University of Groningen, Groningen, Netherlands, associated to ³⁵
- ⁷⁶ Universiteit Maastricht, Maastricht, Netherlands, associated to ³⁵
- ⁷⁷ Tadeusz Kosciuszko Cracow University of Technology, Cracow, Poland, associated to ³⁸
- ⁷⁸ Universidade da Coruña, A Coruna, Spain, associated to ⁴²
- ⁷⁹ Department of Physics and Astronomy, Uppsala University, Uppsala, Sweden, associated to ⁵⁷
- ⁸⁰ University of Michigan, Ann Arbor, MI, United States, associated to ⁶⁶
- ⁸¹ Departement de Physique Nucleaire (SPhN), Gif-Sur-Yvette, France

^a Universidade de Brasília, Brasília, Brazil

^b Centro Federal de Educação Tecnológica Celso Suckow da Fonseca, Rio De Janeiro, Brazil

^c Hangzhou Institute for Advanced Study, UCAS, Hangzhou, China

^d*School of Physics and Electronics, Henan University , Kaifeng, China*

^e*LIP6, Sorbonne Universite, Paris, France*

^f*Excellence Cluster ORIGINS, Munich, Germany*

^g*Universidad Nacional Autónoma de Honduras, Tegucigalpa, Honduras*

^h*Università di Bari, Bari, Italy*

ⁱ*Università degli studi di Bergamo, Bergamo, Italy*

^j*Università di Bologna, Bologna, Italy*

^k*Università di Cagliari, Cagliari, Italy*

^l*Università di Ferrara, Ferrara, Italy*

^m*Università di Firenze, Firenze, Italy*

ⁿ*Università di Genova, Genova, Italy*

^o*Università degli Studi di Milano, Milano, Italy*

^p*Università di Milano Bicocca, Milano, Italy*

^q*Università di Padova, Padova, Italy*

^r*Università di Perugia, Perugia, Italy*

^s*Scuola Normale Superiore, Pisa, Italy*

^t*Università di Pisa, Pisa, Italy*

^u*Università della Basilicata, Potenza, Italy*

^v*Università di Roma Tor Vergata, Roma, Italy*

^w*Università di Siena, Siena, Italy*

^x*Università di Urbino, Urbino, Italy*

^y*Universidad de Alcalá, Alcalá de Henares , Spain*

^z*Department of Physics/Division of Particle Physics, Lund, Sweden*

[†]*Deceased*

Observation of the decay $h_c \rightarrow 3(\pi^+\pi^-)\pi^0$

M. Ablikim¹, M. N. Achasov^{4,c}, P. Adlarson⁷⁵, O. Afedulidis³, X. C. Ai⁸⁰, R. Aliberti³⁵, A. Amoroso^{74A,74C}, Q. An^{71,58,a}, Y. Bai⁵⁷, O. Bakina³⁶, I. Balossino^{29A}, Y. Ban^{46,h}, H.-R. Bao⁶³, V. Batzskaya^{1,44}, K. Begzsuren³², N. Berger³⁵, M. Berlowski⁴⁴, M. Bertani^{28A}, D. Bettoni^{29A}, F. Bianchi^{74A,74C}, E. Bianco^{74A,74C}, A. Bortone^{74A,74C}, I. Boyko³⁶, R. A. Briere⁵, A. Brueggemann⁶⁸, H. Cai⁷⁶, X. Cai^{1,58}, A. Calcaterra^{28A}, G. F. Cao^{1,63}, N. Cao^{1,63}, S. A. Cetin^{62A}, J. F. Chang^{1,58}, G. R. Che⁴³, G. Chelkov^{36,b}, C. Chen⁴³, C. H. Chen⁹, Chao Chen⁵⁵, G. Chen¹, H. S. Chen^{1,63}, H. Y. Chen²⁰, M. L. Chen^{1,58,63}, S. J. Chen⁴², S. L. Chen⁴⁵, S. M. Chen⁶¹, T. Chen^{1,63}, X. R. Chen^{31,63}, X. T. Chen^{1,63}, Y. B. Chen^{1,58}, Y. Q. Chen³⁴, Z. J. Chen^{25,i}, Z. Y. Chen^{1,63}, S. K. Choi^{10A}, G. Cibinetto^{29A}, F. Cossio^{74C}, J. J. Cui⁵⁰, H. L. Dai^{1,58}, J. P. Dai⁷⁸, A. Dbeysi¹⁸, R. E. de Boer³, D. Dedovich³⁶, C. Q. Deng⁷², Z. Y. Deng¹, A. Denig³⁵, I. Denysenko³⁶, M. Destefanis^{74A,74C}, F. De Mori^{74A,74C}, B. Ding^{66,1}, X. X. Ding^{46,h}, Y. Ding⁴⁰, Y. Ding³⁴, J. Dong^{1,58}, L. Y. Dong^{1,63}, M. Y. Dong^{1,58,63}, X. Dong⁷⁶, M. C. Du¹, S. X. Du⁸⁰, Y. Y. Duan⁵⁵, Z. H. Duan⁴², P. Egorov^{36,b}, Y. H. Fan⁴⁵, J. Fang⁵⁹, J. Fang^{1,58}, S. S. Fang^{1,63}, W. X. Fang¹, Y. Fang¹, Y. Q. Fang^{1,58}, R. Farinelli^{29A}, L. Fava^{74B,74C}, F. Feldbauer³, G. Felici^{28A}, C. Q. Feng^{71,58}, J. H. Feng⁵⁹, Y. T. Feng^{71,58}, M. Fritsch³, C. D. Fu¹, J. L. Fu⁶³, Y. W. Fu^{1,63}, H. Gao⁶³, X. B. Gao⁴¹, Y. N. Gao^{46,h}, Yang Gao^{71,58}, S. Garbolino^{74C}, I. Garzia^{29A,29B}, L. Ge⁸⁰, P. T. Ge⁷⁶, Z. W. Ge⁴², C. Geng⁵⁹, E. M. Gersabeck⁶⁷, A. Gilman⁶⁹, K. Goetzen¹³, L. Gong⁴⁰, W. X. Gong^{1,58}, W. Gradl³⁵, S. Gramigna^{29A,29B}, M. Greco^{74A,74C}, M. H. Gu^{1,58}, Y. T. Gu¹⁵, C. Y. Guan^{1,63}, Z. L. Guan²², A. Q. Guo^{31,63}, L. B. Guo⁴¹, M. J. Guo⁵⁰, R. P. Guo⁴⁹, Y. P. Guo^{12,g}, A. Guskov^{36,b}, J. Gutierrez⁷², K. L. Han⁶³, T. T. Han¹, F. Hanisch³, X. Q. Hao¹⁹, F. A. Harris⁶⁵, K. K. He⁵⁵, K. L. He^{1,63}, F. H. Heinsius³, C. H. Heinz³⁵, X. G. Heng^{1,58,63}, C. Herold⁶⁰, T. Holtmann³, P. C. Hong³⁴, G. Y. Hou^{1,63}, X. T. Hou^{1,63}, Y. R. Hou⁶³, Z. L. Hou¹, B. Y. Hu⁵⁹, H. M. Hu^{1,63}, J. F. Hu^{56,j}, S. L. Hu^{12,g}, T. Hu^{1,58,63}, Y. Hu¹, G. S. Huang^{71,58}, K. X. Huang⁵⁹, L. Q. Huang^{31,63}, X. T. Huang⁵⁰, Y. P. Huang¹, T. Hussain⁷³, F. Hölzken³, N. Hüskens³⁵, N. Hüskens^{27,35}, N. in der Wiesche⁶⁸, J. Jackson²⁷, S. Janchiv³², J. H. Jeong^{10A}, Q. Ji¹, Q. P. Ji¹⁹, W. Ji^{1,63}, X. B. Ji^{1,63}, X. L. Ji^{1,58}, Y. Y. Ji⁵⁰, X. Q. Jia⁵⁰, Z. K. Jia^{71,58}, D. Jiang^{1,63}, H. B. Jiang⁷⁶, P. C. Jiang^{46,h}, S. S. Jiang³⁹, T. J. Jiang¹⁶, X. S. Jiang^{1,58,63}, Y. Jiang⁶³, J. B. Jiao⁵⁰, J. K. Jiao³⁴, Z. Jiao²³, S. Jin⁴², Y. Jin⁶⁶, M. Q. Jing^{1,63}, X. M. Jing⁶³, T. Johansson⁷⁵, S. Kabana³³, N. Kalantar-Nayestanaki⁶⁴, X. L. Kang⁹, X. S. Kang⁴⁰, M. Kavatsyuk⁶⁴, B. C. Ke⁸⁰, V. Khachatryan²⁷, A. Khoukaz⁶⁸, R. Kiuchi¹, O. B. Kolcu^{62A}, B. Kopf³, M. Kuessner³, X. Ku^{1,63}, N. Kumar²⁶, A. Kupsc^{44,75}, W. Kühn³⁷, J. J. Lane⁶⁷, P. Larin¹⁸, L. Lavezzi^{74A,74C}, T. T. Lei^{71,58}, Z. H. Lei^{71,58}, M. Lellmann³⁵, T. Lenz³⁵, C. Li⁴⁷, C. Li⁴³, C. H. Li³⁹, Cheng Li^{71,58}, D. M. Li⁸⁰, F. Li^{1,58}, G. Li¹, H. B. Li^{1,63}, H. J. Li¹⁹, H. N. Li^{56,j}, Hui Li⁴³, J. R. Li⁶¹, J. S. Li⁵⁹, Ke Li¹, L. J. Li^{1,63}, L. K. Li¹, Lei Li⁴⁸, M. H. Li⁴³, P. R. Li^{38,l}, Q. M. Li^{1,63}, Q. X. Li⁵⁰, R. Li^{17,31}, S. X. Li¹², T. Li⁵⁰, W. D. Li^{1,63}, W. G. Li^{1,a}, X. Li^{1,63}, X. H. Li^{71,58}, X. L. Li⁵⁰, X. Z. Li⁵⁹, Xiaoyu Li^{1,63}, Y. G. Li^{46,h}, Z. J. Li⁵⁹, Z. X. Li¹⁵, Z. Y. Li⁷⁸, C. Liang⁴², H. Liang^{1,63}, H. Liang^{71,58}, Y. F. Liang⁵⁴, Y. T. Liang^{31,63}, G. R. Liao¹⁴, L. Z. Liao⁵⁰, J. Libby²⁶, A. Limphirat⁶⁰, C. C. Lin⁵⁵, D. X. Lin^{31,63}, T. Lin¹, B. J. Liu¹, B. X. Liu⁷⁶, C. Liu³⁴, C. X. Liu¹, F. H. Liu⁵³, Fang Liu¹, Feng Liu⁶, G. M. Liu^{56,j}, H. Liu^{38,k,l}, H. B. Liu¹⁵, H. M. Liu^{1,63}, Huanhuan Liu¹, Huihui Liu²¹, J. B. Liu^{71,58}, J. Y. Liu^{1,63}, K. Liu^{38,k,l}, K. Y. Liu⁴⁰, Ke Liu²², L. Liu^{71,58}, L. C. Liu⁴³, Lu Liu⁴³, M. H. Liu^{12,g}, P. L. Liu¹, Q. A. Liu⁶³, S. B. Liu^{71,58}, T. Liu^{12,g}, W. K. Liu⁴³, W. M. Liu^{71,58}, X. Liu^{38,k,l}, X. Liu³⁹, Y. Liu^{38,k,l}, Y. Liu⁸⁰, Y. B. Liu⁴³, Z. A. Liu^{1,58,63}, Z. D. Liu⁹, Z. Q. Liu⁵⁰, X. C. Lou^{1,58,63}, F. X. Lu⁵⁹, H. J. Lu²³, J. G. Lu^{1,58}, X. L. Lu¹, Y. Lu⁷, Y. P. Lu^{1,58}, Z. H. Lu^{1,63}, C. L. Luo⁴¹, J. R. Luo⁵⁹, M. X. Luo⁷⁹, T. Luo^{12,g}, X. L. Luo^{1,58}, X. R. Lyu⁶³, Y. F. Lyu⁴³, F. C. Ma⁴⁰, H. Ma⁷⁸, H. L. Ma¹, J. L. Ma^{1,63}, L. L. Ma⁵⁰, M. M. Ma^{1,63}, Q. M. Ma¹, R. Q. Ma^{1,63}, T. Ma^{71,58}, X. T. Ma^{1,63}, X. Y. Ma^{1,58}, Y. Ma^{46,h}, Y. M. Ma³¹, F. E. Maas¹⁸, M. Maggiora^{74A,74C}, S. Malde⁶⁹, Y. J. Mao^{46,h}, Z. P. Mao¹, S. Marcello^{74A,74C}, Z. X. Meng⁶⁶, J. G. Messchendorp^{13,64}, G. Mezzadri^{29A}, H. Miao^{1,63}, T. J. Min⁴², R. E. Mitchell²⁷, X. H. Mo^{1,58,63}, B. Moses²⁷, N. Yu. Muchnoi^{4,c}, J. Muskalla³⁵, Y. Nefedov³⁶, F. Nerling^{18,e}, L. S. Nie²⁰, I. B. Nikolaev^{4,c}, Z. Ning^{1,58}, S. Nisar^{11,m}, Q. L. Niu^{38,k,l}, W. D. Niu⁵⁵, Y. Niu⁵⁰, S. L. Olsen⁶³, Q. Ouyang^{1,58,63}, S. Pacetti^{28B,28C}, X. Pan⁵⁵, Y. Pan⁵⁷, A. Pathak³⁴, P. Patteri^{28A}, Y. P. Pei^{71,58}, M. Pelizaeus³, H. P. Peng^{71,58}, Y. Y. Peng^{38,k,l}, K. Peters^{13,e}, J. L. Ping⁴¹, R. G. Ping^{1,63}, S. Plura³⁵, V. Prasad³³, F. Z. Qi¹, H. Qi^{71,58}, H. R. Qi⁶¹, M. Qi⁴², T. Y. Qi^{12,g}, S. Qian^{1,58}, W. B. Qian⁶³, C. F. Qiao⁶³, X. K. Qiao⁸⁰, J. J. Qin⁷², L. Q. Qin¹⁴, L. Y. Qin^{71,58}, X. S. Qin⁵⁰, Z. H. Qin^{1,58}, J. F. Qiu¹, Z. H. Qu⁷², C. F. Redmer³⁵, K. J. Ren³⁹, A. Rivetti^{74C}, M. Rolo^{74C}, G. Rong^{1,63}, Ch. Rosner¹⁸, S. N. Ruan⁴³, N. Salone⁴⁴, A. Sarantsev^{36,d}, Y. Schelhaas³⁵, K. Schoenning⁷⁵, M. Scodreggio^{29A}, K. Y. Shan^{12,g}, W. Shan²⁴, X. Y. Shan^{71,58}, Z. J. Shang^{38,k,l}, J. F. Shangguan⁵⁵, L. G. Shao^{1,63}, M. Shao^{71,58}, C. P. Shen^{12,g}, H. F. Shen^{1,8}, W. H. Shen⁶³, X. Y. Shen^{1,63}, B. A. Shi⁶³, H. Shi^{71,58}, H. C. Shi^{71,58}, J. L. Shi^{12,g}, J. Y. Shi¹, Q. Q. Shi⁵⁵, S. Y. Shi⁷², X. Shi^{1,58}, J. J. Song¹⁹, T. Z. Song⁵⁹, W. M. Song^{34,1}, Y. J. Song^{12,g}, Y. X. Song^{46,h,n}, S. Sosio^{74A,74C}, S. Spataro^{74A,74C}, F. Stieler³⁵, Y. J. Su⁶³, G. B. Sun⁷⁶, G. X. Sun¹, H. Sun⁶³, H. K. Sun¹, J. F. Sun¹⁹, K. Sun⁶¹, L. Sun⁷⁶, S. S. Sun^{1,63}, T. Sun^{51,f}, W. Y. Sun³⁴, Y. Sun⁹, Y. J. Sun^{71,58}, Y. Z. Sun¹, Z. Q. Sun^{1,63}, Z. T. Sun⁵⁰, C. J. Tang⁵⁴, G. Y. Tang¹, J. Tang⁵⁹, M. Tang^{71,58}, Y. A. Tang⁷⁶, L. Y. Tao⁷², Q. T. Tao^{25,i}, M. Tat⁶⁹, J. X. Teng^{71,58}, V. Thoren⁷⁵, W. H. Tian⁵⁹, Y. Tian^{31,63}, Z. F. Tian⁷⁶, I. Uman^{62B}, Y. Wan⁵⁵, S. J. Wang⁵⁰, B. Wang¹, B. L. Wang⁶³, Bo Wang^{71,58}, D. Y. Wang^{46,h}, F. Wang⁷², H. J. Wang^{38,k,l}, J. J. Wang⁷⁶, J. P. Wang⁵⁰, K. Wang^{1,58}, L. L. Wang¹, M. Wang⁵⁰, Meng Wang^{1,63}, N. Y. Wang⁶³, S. Wang^{12,g}, S. Wang^{38,k,l}, T. Wang^{12,g}, T. J. Wang⁴³, W. Wang⁵⁹, W. Wang⁷², W. P. Wang^{35,71,o}, X. Wang^{46,h}, X. F. Wang^{38,k,l}, X. J. Wang³⁹, X. L. Wang^{12,g}, X. N. Wang¹, Y. Wang⁶¹, Y. D. Wang⁴⁵, Y. F. Wang^{1,58,63}, Y. L. Wang¹⁹, Y. N. Wang⁴⁵, Y. Q. Wang¹, Yaqian Wang¹⁷, Yi Wang⁶¹, Z. Wang^{1,58}, Z. L. Wang⁷², Z. Y. Wang^{1,63}, Ziyi Wang⁶³, D. H. Wei¹⁴, F. Weidner⁶⁸, S. P. Wen¹, Y. R. Wen³⁹, U. Wiedner³, G. Wilkinson⁶⁹, M. Wolke⁷⁵, L. Wollenberg³, C. Wu³⁹, J. F. Wu^{1,8}, L. H. Wu¹, L. J. Wu^{1,63}, X. Wu^{12,g}, X. H. Wu³⁴, Y. Wu^{71,58}, Y. H. Wu⁵⁵, Y. J. Wu³¹, Z. Wu^{1,58}, L. Xia^{71,58}, X. M. Xian³⁹, B. H. Xiang^{1,63}, T. Xiang^{46,h}, D. Xiao^{38,k,l}, G. Y. Xiao⁴², S. Y. Xiao¹, Y. L. Xiao^{12,g}, Z. J. Xiao⁴¹, C. Xie⁴², X. H. Xie^{46,h}, Y. Xie⁵⁰, Y. G. Xie^{1,58}, Y. H. Xie⁶, Z. P. Xie^{71,58}, T. Y. Xing^{1,63}, C. F. Xu^{1,63}, C. J. Xu⁵⁹, G. F. Xu¹, H. Y. Xu⁶⁶, M. Xu^{71,58}, Q. J. Xu¹⁶, Q. N. Xu³⁰, W. Xu¹, W. L. Xu⁶⁶, X. P. Xu⁵⁵, Y. C. Xu⁷⁷, Z. P. Xu⁴², Z. S. Xu⁶³, F. Yan^{12,g},

L. Yan^{12,g}, W. B. Yan^{71,58}, W. C. Yan⁸⁰, X. Q. Yan¹, H. J. Yang^{51,f}, H. L. Yang³⁴, H. X. Yang¹, Tao Yang¹, Y. Yang^{12,g}, Y. F. Yang⁴³, Y. X. Yang^{1,63}, Yifan Yang^{1,63}, Z. W. Yang^{38,k,l}, Z. P. Yao⁵⁰, M. Ye^{1,58}, M. H. Ye⁸, J. H. Yin¹, Z. Y. You⁵⁹, B. X. Yu^{1,58,63}, C. X. Yu⁴³, G. Yu^{1,63}, J. S. Yu^{25,i}, T. Yu⁷², X. D. Yu^{46,h}, Y. C. Yu⁸⁰, C. Z. Yuan^{1,63}, J. Yuan³⁴, L. Yuan², S. C. Yuan¹, Y. Yuan^{1,63}, Y. J. Yuan⁴⁵, Z. Y. Yuan⁵⁹, C. X. Yue³⁹, A. A. Zafar⁷³, F. R. Zeng⁵⁰, S. H. Zeng⁷², X. Zeng^{12,g}, Y. Zeng^{25,i}, Y. J. Zeng⁵⁹, X. Y. Zhai³⁴, Y. C. Zhai⁵⁰, Y. H. Zhan⁵⁹, A. Q. Zhang^{1,63}, B. L. Zhang^{1,63}, B. X. Zhang¹, D. H. Zhang⁴³, G. Y. Zhang¹⁹, H. Zhang^{71,58}, H. Zhang⁸⁰, H. C. Zhang^{1,58,63}, H. H. Zhang⁵⁹, H. H. Zhang³⁴, H. Q. Zhang^{1,58,63}, H. R. Zhang^{71,58}, H. Y. Zhang^{1,58}, J. Zhang⁵⁹, J. Zhang⁸⁰, J. J. Zhang⁵², J. L. Zhang²⁰, J. Q. Zhang⁴¹, J. S. Zhang^{12,g}, J. W. Zhang^{1,58,63}, J. X. Zhang^{38,k,l}, J. Y. Zhang¹, J. Z. Zhang^{1,63}, Jianyu Zhang⁶³, L. M. Zhang⁶¹, Lei Zhang⁴², P. Zhang^{1,63}, Q. Y. Zhang³⁴, R. Y. Zhang^{38,k,l}, Shuihan Zhang^{1,63}, Shulei Zhang^{25,i}, X. D. Zhang⁴⁵, X. M. Zhang¹, X. Y. Zhang⁵⁰, Y. Zhang⁷², Y. T. Zhang⁸⁰, Y. H. Zhang^{1,58}, Y. M. Zhang³⁹, Yan Zhang^{71,58}, Yao Zhang¹, Z. D. Zhang¹, Z. H. Zhang¹, Z. L. Zhang³⁴, Z. Y. Zhang⁴³, Z. Y. Zhang⁷⁶, Z. Z. Zhang⁴⁵, G. Zhao¹, J. Y. Zhao^{1,63}, J. Z. Zhao^{1,58}, Lei Zhao^{71,58}, Ling Zhao¹, M. G. Zhao⁴³, N. Zhao⁷⁸, R. P. Zhao⁶³, S. J. Zhao⁸⁰, Y. B. Zhao^{1,58}, Y. X. Zhao^{31,63}, Z. G. Zhao^{71,58}, A. Zhemchugov^{36,b}, B. Zheng⁷², B. M. Zheng³⁴, J. P. Zheng^{1,58}, W. J. Zheng^{1,63}, Y. H. Zheng⁶³, B. Zhong⁴¹, X. Zhong⁵⁹, H. Zhou⁵⁰, J. Y. Zhou³⁴, L. P. Zhou^{1,63}, S. Zhou⁶, X. Zhou⁷⁶, X. K. Zhou⁶, X. R. Zhou^{71,58}, X. Y. Zhou³⁹, Y. Z. Zhou^{12,g}, J. Zhu⁴³, K. Zhu¹, K. J. Zhu^{1,58,63}, K. S. Zhu^{12,g}, L. Zhu³⁴, L. X. Zhu⁶³, S. H. Zhu⁷⁰, S. Q. Zhu⁴², T. J. Zhu^{12,g}, W. D. Zhu⁴¹, Y. C. Zhu^{71,58}, Z. A. Zhu^{1,63}, J. H. Zou¹, J. Zu^{71,58}

(BESIII Collaboration)

¹ *Institute of High Energy Physics, Beijing 100049, People's Republic of China*

² *Beihang University, Beijing 100191, People's Republic of China*

³ *Bochum Ruhr-University, D-44780 Bochum, Germany*

⁴ *Budker Institute of Nuclear Physics SB RAS (BINP), Novosibirsk 630090, Russia*

⁵ *Carnegie Mellon University, Pittsburgh, Pennsylvania 15213, USA*

⁶ *Central China Normal University, Wuhan 430079, People's Republic of China*

⁷ *Central South University, Changsha 410083, People's Republic of China*

⁸ *China Center of Advanced Science and Technology, Beijing 100190, People's Republic of China*

⁹ *China University of Geosciences, Wuhan 430074, People's Republic of China*

¹⁰ *Chung-Ang University, Seoul, 06974, Republic of Korea*

¹¹ *COMSATS University Islamabad, Lahore Campus, Defence Road, Off Raiwind Road, 54000 Lahore, Pakistan*

¹² *Fudan University, Shanghai 200433, People's Republic of China*

¹³ *GSI Helmholtzcentre for Heavy Ion Research GmbH, D-64291 Darmstadt, Germany*

¹⁴ *Guangxi Normal University, Guilin 541004, People's Republic of China*

¹⁵ *Guangxi University, Nanning 530004, People's Republic of China*

¹⁶ *Hangzhou Normal University, Hangzhou 310036, People's Republic of China*

¹⁷ *Hebei University, Baoding 071002, People's Republic of China*

¹⁸ *Helmholtz Institute Mainz, Staudinger Weg 18, D-55099 Mainz, Germany*

¹⁹ *Henan Normal University, Xinxiang 453007, People's Republic of China*

²⁰ *Henan University, Kaifeng 475004, People's Republic of China*

²¹ *Henan University of Science and Technology, Luoyang 471003, People's Republic of China*

²² *Henan University of Technology, Zhengzhou 450001, People's Republic of China*

²³ *Huangshan College, Huangshan 245000, People's Republic of China*

²⁴ *Hunan Normal University, Changsha 410081, People's Republic of China*

²⁵ *Hunan University, Changsha 410082, People's Republic of China*

²⁶ *Indian Institute of Technology Madras, Chennai 600036, India*

²⁷ *Indiana University, Bloomington, Indiana 47405, USA*

²⁸ *INFN Laboratori Nazionali di Frascati, (A)INFN Laboratori Nazionali di Frascati, I-00044, Frascati, Italy; (B)INFN*

Sezione di Perugia, I-06100, Perugia, Italy; (C)University of Perugia, I-06100, Perugia, Italy

²⁹ *INFN Sezione di Ferrara, (A)INFN Sezione di Ferrara, I-44122, Ferrara, Italy; (B)University of Ferrara, I-44122, Ferrara, Italy*

³⁰ *Inner Mongolia University, Hohhot 010021, People's Republic of China*

³¹ *Institute of Modern Physics, Lanzhou 730000, People's Republic of China*

³² *Institute of Physics and Technology, Peace Avenue 54B, Ulaanbaatar 13330, Mongolia*

³³ *Instituto de Alta Investigación, Universidad de Tarapacá, Casilla 7D, Arica 1000000, Chile*

³⁴ *Jilin University, Changchun 130012, People's Republic of China*

³⁵ *Johannes Gutenberg University of Mainz, Johann-Joachim-Becher-Weg 45, D-55099 Mainz, Germany*

³⁶ *Joint Institute for Nuclear Research, 141980 Dubna, Moscow region, Russia*

³⁷ *Justus-Liebig-Universität Giessen, II. Physikalisches Institut, Heinrich-Buff-Ring 16, D-35392 Giessen, Germany*

³⁸ *Lanzhou University, Lanzhou 730000, People's Republic of China*

³⁹ *Liaoning Normal University, Dalian 116029, People's Republic of China*

⁴⁰ *Liaoning University, Shenyang 110036, People's Republic of China*

⁴¹ *Nanjing Normal University, Nanjing 210023, People's Republic of China*

⁴² *Nanjing University, Nanjing 210093, People's Republic of China*

⁴³ *Nankai University, Tianjin 300071, People's Republic of China*

- ⁴⁴ National Centre for Nuclear Research, Warsaw 02-093, Poland
- ⁴⁵ North China Electric Power University, Beijing 102206, People's Republic of China
- ⁴⁶ Peking University, Beijing 100871, People's Republic of China
- ⁴⁷ Qufu Normal University, Qufu 273165, People's Republic of China
- ⁴⁸ Renmin University of China, Beijing 100872, People's Republic of China
- ⁴⁹ Shandong Normal University, Jinan 250014, People's Republic of China
- ⁵⁰ Shandong University, Jinan 250100, People's Republic of China
- ⁵¹ Shanghai Jiao Tong University, Shanghai 200240, People's Republic of China
- ⁵² Shanxi Normal University, Linfen 041004, People's Republic of China
- ⁵³ Shanxi University, Taiyuan 030006, People's Republic of China
- ⁵⁴ Sichuan University, Chengdu 610064, People's Republic of China
- ⁵⁵ Soochow University, Suzhou 215006, People's Republic of China
- ⁵⁶ South China Normal University, Guangzhou 510006, People's Republic of China
- ⁵⁷ Southeast University, Nanjing 211100, People's Republic of China
- ⁵⁸ State Key Laboratory of Particle Detection and Electronics, Beijing 100049, Hefei 230026, People's Republic of China
- ⁵⁹ Sun Yat-Sen University, Guangzhou 510275, People's Republic of China
- ⁶⁰ Suranaree University of Technology, University Avenue 111, Nakhon Ratchasima 30000, Thailand
- ⁶¹ Tsinghua University, Beijing 100084, People's Republic of China
- ⁶² Turkish Accelerator Center Particle Factory Group, (A)Istinye University, 34010, Istanbul, Turkey; (B)Near East University, Nicosia, North Cyprus, 99138, Mersin 10, Turkey
- ⁶³ University of Chinese Academy of Sciences, Beijing 100049, People's Republic of China
- ⁶⁴ University of Groningen, NL-9747 AA Groningen, The Netherlands
- ⁶⁵ University of Hawaii, Honolulu, Hawaii 96822, USA
- ⁶⁶ University of Jinan, Jinan 250022, People's Republic of China
- ⁶⁷ University of Manchester, Oxford Road, Manchester, M13 9PL, United Kingdom
- ⁶⁸ University of Muenster, Wilhelm-Klemm-Strasse 9, 48149 Muenster, Germany
- ⁶⁹ University of Oxford, Keble Road, Oxford OX13RH, United Kingdom
- ⁷⁰ University of Science and Technology Liaoning, Anshan 114051, People's Republic of China
- ⁷¹ University of Science and Technology of China, Hefei 230026, People's Republic of China
- ⁷² University of South China, Hengyang 421001, People's Republic of China
- ⁷³ University of the Punjab, Lahore-54590, Pakistan
- ⁷⁴ University of Turin and INFN, (A)University of Turin, I-10125, Turin, Italy; (B)University of Eastern Piedmont, I-15121, Alessandria, Italy; (C)INFN, I-10125, Turin, Italy
- ⁷⁵ Uppsala University, Box 516, SE-75120 Uppsala, Sweden
- ⁷⁶ Wuhan University, Wuhan 430072, People's Republic of China
- ⁷⁷ Yantai University, Yantai 264005, People's Republic of China
- ⁷⁸ Yunnan University, Kunming 650500, People's Republic of China
- ⁷⁹ Zhejiang University, Hangzhou 310027, People's Republic of China
- ⁸⁰ Zhengzhou University, Zhengzhou 450001, People's Republic of China
- ^a Deceased
- ^b Also at the Moscow Institute of Physics and Technology, Moscow 141700, Russia
- ^c Also at the Novosibirsk State University, Novosibirsk, 630090, Russia
- ^d Also at the NRC "Kurchatov Institute", PNPI, 188300, Gatchina, Russia
- ^e Also at Goethe University Frankfurt, 60323 Frankfurt am Main, Germany
- ^f Also at Key Laboratory for Particle Physics, Astrophysics and Cosmology, Ministry of Education; Shanghai Key Laboratory for Particle Physics and Cosmology; Institute of Nuclear and Particle Physics, Shanghai 200240, People's Republic of China
- ^g Also at Key Laboratory of Nuclear Physics and Ion-beam Application (MOE) and Institute of Modern Physics, Fudan University, Shanghai 200443, People's Republic of China
- ^h Also at State Key Laboratory of Nuclear Physics and Technology, Peking University, Beijing 100871, People's Republic of China
- ⁱ Also at School of Physics and Electronics, Hunan University, Changsha 410082, China
- ^j Also at Guangdong Provincial Key Laboratory of Nuclear Science, Institute of Quantum Matter, South China Normal University, Guangzhou 510006, China
- ^k Also at MOE Frontiers Science Center for Rare Isotopes, Lanzhou University, Lanzhou 730000, People's Republic of China
- ^l Also at Lanzhou Center for Theoretical Physics, Lanzhou University, Lanzhou 730000, People's Republic of China
- ^m Also at the Department of Mathematical Sciences, IBA, Karachi 75270, Pakistan
- ⁿ Also at Ecole Polytechnique Federale de Lausanne (EPFL), CH-1015 Lausanne, Switzerland
- ^o Also at Helmholtz Institute Mainz, Staudinger Weg 18, D-55099 Mainz, Germany

(Dated: March 7, 2024)

Based on $(2712.4 \pm 14.1) \times 10^6$ $\psi(3686)$ events collected with the BESIII detector, we study the decays $h_c \rightarrow 3(\pi^+\pi^-)\pi^0$, $h_c \rightarrow 2(\pi^+\pi^-)\omega$, $h_c \rightarrow 2(\pi^+\pi^-)\pi^0\eta$, $h_c \rightarrow 2(\pi^+\pi^-)\eta$, and $h_c \rightarrow p\bar{p}$ via $\psi(3686) \rightarrow \pi^0 h_c$. The decay channel $h_c \rightarrow 3(\pi^+\pi^-)\pi^0$ is observed for the first time, and its

branching fraction is determined to be $(9.28 \pm 1.14 \pm 0.77) \times 10^{-3}$, where the first uncertainty is statistical and the second is systematic. In addition, first evidence is found for the modes $h_c \rightarrow 2(\pi^+\pi^-)\pi^0\eta$ and $h_c \rightarrow 2(\pi^+\pi^-)\omega$ with significances of 4.8σ and 4.7σ , and their branching fractions are determined to be $(7.55 \pm 1.51 \pm 0.77) \times 10^{-3}$ and $(4.00 \pm 0.86 \pm 0.35) \times 10^{-3}$, respectively. No significant signals of $h_c \rightarrow 2(\pi^+\pi^-)\eta$ and $h_c \rightarrow p\bar{p}$ are observed, and the upper limits of the branching fractions of these decays are determined to be $< 6.19 \times 10^{-4}$ and $< 4.40 \times 10^{-5}$ at the 90% confidence level, respectively.

I. INTRODUCTION

Studies of charmonium decays play an important role in understanding the structure of quantum chromodynamics (QCD). Despite the success of QCD in describing many aspects of the strong interaction, some applications in charmonium decay mechanism remain challenging and inconsistencies between experimental results and theoretical predictions have been reported [1].

Since the discovery of the spin-singlet charmonium state $h_c(^1P_1)$ in 2005 [2, 3], many theoretical and experimental efforts have been made to understand its properties. Kuang predicted the branching fraction (BF) $\mathcal{B}(h_c \rightarrow \text{light hadrons})$ to be $(8.8 \pm 0.8)\%$ and $(48 \pm 7)\%$ with the perturbative QCD(PQCD) and non-relativistic QCD (NRQCD) models [4], respectively. Godfrey made a prediction of $\mathcal{B}(h_c \rightarrow ggg) = 57\%$ based on QCD calculations [5]. The significant differences between the results of these calculations arise from the use of different computational methods based on various theoretical models and the consideration of different effects. Recently BESIII reported the BF of the electric dipole (E1) transition to be $\mathcal{B}(h_c \rightarrow \gamma\eta_c) = (57.66_{-3.50}^{+3.62} \pm 0.58)\%$ [6], which is reasonably close to some theoretical predictions [4, 5]. This implies that nearly half of h_c decays are non-E1 modes. However, the sum of the BFs of the known h_c non-E1 decays is only about 4% [7, 8], indicating that the search for new h_c decay modes is well motivated.

In massless QCD models, the $h_c(^1P_1)$ decay into $p\bar{p}$ is forbidden due to the helicity selection rule [9]. However, the observation of the decays $\eta_c/\chi_{c0} \rightarrow p\bar{p}$ [7] and the observation of h_c formation in the $p\bar{p}$ annihilation [10] indicate substantial contributions from the effects of finite masses. These observations have stimulated theoretical calculations for the decay $h_c \rightarrow p\bar{p}$, arising from which a large BF of the order of 10^{-3} is suggested [11, 12]. However, searches until now have not observed a significant signal [13]. Further experimental study of this decay is highly desirable to understand better the underlying dynamical mechanism in $h_c \rightarrow p\bar{p}$ decay.

In this paper, we report searches for the undiscovered decay channels of $h_c \rightarrow 3(\pi^+\pi^-)\pi^0$, $h_c \rightarrow 2(\pi^+\pi^-)\omega$, $h_c \rightarrow 2(\pi^+\pi^-)\pi^0\eta$, $h_c \rightarrow 2(\pi^+\pi^-)\eta$, and $h_c \rightarrow p\bar{p}$ via $\psi(3686) \rightarrow \pi^0 h_c$, performed through the analysis of $(2712.4 \pm 14.1) \times 10^6$ $\psi(3686)$ events [14] collected with the BESIII detector in 2009, 2012 and 2021.

II. BESIII DETECTOR AND MONTE CARLO SIMULATION

The BESIII detector [15] records e^+e^- collisions provided by the BEPCII storage ring [16] in the center-of-mass energy range from 2.0 to 4.95 GeV, with a peak luminosity of $1 \times 10^{33} \text{ cm}^{-2}\text{s}^{-1}$ achieved at $\sqrt{s} = 3.77$ GeV. BESIII has collected large data samples in this energy region [17–19]. The cylindrical core of the BESIII detector covers 93% of the full solid angle and consists of a helium-based multilayer drift chamber (MDC), a plastic scintillator time-of-flight system (TOF), and a CsI(Tl) electromagnetic calorimeter (EMC), which are all enclosed in a superconducting solenoidal magnet providing a 1.0 T magnetic field (0.9 T in 2012). The magnet is supported by an octagonal flux-return yoke with modules of resistive plate muon counters (MUC) interleaved with steel. The charged-particle momentum resolution at 1 GeV/c is 0.5%, and the dE/dx resolution is 6% for the electrons from Bhabha scattering. The EMC measures photon energy with a resolution of 2.5% (5%) at 1 GeV in the barrel (end-cap) region. The time resolution of the TOF barrel part is 68 ps, while that of the end-cap part is 110 ps. The end-cap TOF system was upgraded in 2015 using multi-gap resistive plate chamber technology, providing a time resolution of 60 ps, which benefits $\sim 83\%$ of the data used in this analysis [20–22].

Monte Carlo (MC) simulated data samples produced with a GEANT4-based [23] software package, which includes the geometric description [24] of the BESIII detector and the detector response, are used to optimize the event selection criteria, to estimate the signal efficiency and the level of background. The simulation models the beam-energy spread and initial-state radiation in the e^+e^- annihilation using the generator KKMC [25, 26]. The inclusive MC sample includes the production of the $\psi(3686)$ resonance, the initial-state radiation production of the J/ψ meson, and the continuum processes incorporated in KKMC. Particle decays are generated by EVTGEN [27, 28] for the known decay modes with BFs taken from the Particle Data Group (PDG) [7] and LUNDCHARM [29, 30] for the unknown ones. Final-state radiation from charged final-state particles is included using the PHOTOS package [31].

For the exclusive MC simulation samples, the five channels of interest are generated using a phase-space (PHSP) model for each signal mode.

III. EVENT SELECTION

Charged tracks reconstructed in the MDC are required to originate from a region within 10 cm from the nominal interaction point (IP) along the symmetry axis of the MDC (z axis), and within 1 cm in the perpendicular plane. The track polar angle θ measured with respect to the z axis must be within the fiducial volume of the MDC, $|\cos\theta| < 0.93$. The tracks are assumed to be protons for $h_c \rightarrow p\bar{p}$ decay and pions for other decay modes. Finally, a vertex fit constraining all charged particles to originate from a common vertex is performed.

Photon candidates are reconstructed from isolated electromagnetic showers produced in the crystals of the EMC. The deposited energy of each shower must be greater than 25 MeV in the barrel region ($|\cos\theta| < 0.80$) or greater than 50 MeV in the end-cap region ($0.86 < |\cos\theta| < 0.92$). To suppress electronic noise and energy depositions not associated with the event, the EMC cluster timing is required to be within 700 ns of the start time of the reconstructed event. To form a π^0 candidate, the invariant mass of the selected $\gamma\gamma$ pair is constrained to the known π^0 mass [7] by a one-constraint (1C) kinematic fit, and the χ^2_{1C} is required to be less than 20. To form an η candidate, the invariant mass of the selected $\gamma\gamma$ pair is constrained to the known η mass [7], and the χ^2_{1C} is required to be less than 200.

To further suppress background, a (4+N)C kinematic fit is performed, which constrains the 4-momentum of the final state to that of the initial system, while the masses of all π^0 and η candidates (denoted by N) are constrained to their nominal masses. The kinematics of the final state tracks are updated through the above kinematic fit. A requirement is placed on the $\chi^2_{(4+N)C}$ value of the (4+N)C fit depending on the final state (see Table 1). The value of the requirement is determined by maximizing the figure of merit (FOM), defined as $S/\sqrt{S+B}$. Here, S and B are the expected numbers of signal and background events, respectively, obtained from the MC simulation. If there is any excess of photon candidates in an event, then all combinations are considered and the one with the smallest $\chi^2_{(4+N)C}$ is kept.

To suppress contamination from decays with unexpected numbers of photons, such as $\psi(3686) \rightarrow \gamma\chi_{c2}$ with χ_{c2} decaying to the same final states as the h_c , we require $\chi^2_{4C,n\gamma} < \chi^2_{4C,(n-1)\gamma}$ for $h_c \rightarrow 3(\pi^+\pi^-)\pi^0$, $h_c \rightarrow 2(\pi^+\pi^-)\omega$, and $h_c \rightarrow 2(\pi^+\pi^-)\pi^0\eta$. Here $\chi_{4C,n\gamma}$ is obtained from a 4C kinematic fit including n photons expected for the signal candidate, while $\chi^2_{4C,(n-1)\gamma}$ is determined from an additional 4C fit with one missing photon compared to the signal decay, respectively. Similarly, in the $h_c \rightarrow 2(\pi^+\pi^-)\pi^0\eta$ mode, the background of $\psi(3686) \rightarrow 2(\pi^+\pi^-)3\pi^0$ is suppressed by requiring $\chi^2_{7C}(2\pi^0\eta 2(\pi^+\pi^-)) < \chi^2_{7C}(3\pi^0 2(\pi^+\pi^-))$.

The J/ψ -related background is vetoed by the requirements on the $\pi^0\pi^0$, $\pi^+\pi^-$, and η recoil-mass windows. The mass windows are listed in Table 1, where

RM denotes the recoiling mass, defined as $RM(X) = \sqrt{(p_{\psi(3686)} - p_X)^2}$, where $p_{\psi(3686)}$ and p_X are the four momenta of $\psi(3686)$ and X , respectively. For the $h_c \rightarrow p\bar{p}$ reconstruction the background from lepton pairs originating from J/ψ decays is suppressed by requiring $|\cos\theta_{p(\bar{p})}| < 0.8$, where $\theta_{p(\bar{p})}$ is the polar angle of the proton (antiproton) candidate. The energy of the π^0 from the h_c decay is typically larger than the energy of the bachelor π^0 from $\psi(3686) \rightarrow \pi^0 h_c$. In events with two neutral pions, that one with smaller energy is denoted π^0_L while the other is denoted π^0_H . The bachelor π^0_L should not form any resonance in combination with other final-state particles. Therefore, additional vetoes, summarized in Table 1, are applied to suppress background from $\eta, \omega \rightarrow \pi^+\pi^-\pi^0_L$.

In the case of candidate $h_c \rightarrow 3(\pi^+\pi^-)\pi^0$ decays, we examine the invariant-mass spectrum of $\pi^+\pi^-\pi^0_H$ to check for the presence of an ω intermediate state. The ω signal region for $h_c \rightarrow 2(\pi^+\pi^-)\omega$ is set to be $|M(\pi^+\pi^-\pi^0_H) - m_\omega| < 20$ MeV/ c^2 and the ω sideband region is set to be $60 < |M(\pi^+\pi^-\pi^0_H) - m_\omega| < 100$ MeV/ c^2 , where m_ω is the known ω mass [7], as shown in Fig. 1. All mass windows are determined to account for the respective mass resolutions.

Table 1. Requirements on $\chi^2_{(4+N)C}$, mass windows and the polar angle of the proton or antiproton ($\cos\theta_{p(\bar{p})}$) for different signal decays. M and m denote the measured invariant mass and the known mass [7] of the indicated particle, respectively.

Mode	$\chi^2_{(4+N)C}$	Veto (MeV/ c^2)
$3(\pi^+\pi^-)\pi^0$	< 35	$ RM(\pi^+\pi^-) - m_{J/\psi} > 12$
		$ RM(\pi^0\pi^0) - m_{J/\psi} > 30$
		$M(\pi^+\pi^-\pi^0_L) - m_\eta > 17$
$2(\pi^+\pi^-)\pi^0\eta$	< 20	$ RM(\pi^+\pi^-) - m_{J/\psi} > 8$
		$ RM(\pi^0\pi^0) - m_{J/\psi} > 18$
		$ RM(\eta) - m_{J/\psi} > 7$
		$M(\pi^+\pi^-\pi^0_L) - m_\eta > 12$
$2(\pi^+\pi^-)\eta$	< 25	$M(\pi^+\pi^-\pi^0_L) - m_\omega > 26$
		$ RM(\pi^+\pi^-) - m_{J/\psi} > 15$
		$ RM(\eta) - m_{J/\psi} > 10$
		$M(\pi^+\pi^-\pi^0_L) - m_\eta > 15$
$p\bar{p}$	< 15	$M(\pi^+\pi^-\pi^0_L) - m_\omega > 26$
		$ \cos\theta_{p(\bar{p})} < 0.8$

The invariant-mass distributions for the four h_c decay modes and the intermediate process $h_c \rightarrow 2(\pi^+\pi^-)\omega$, after all selection criteria, are shown in Fig. 2. The potential backgrounds are investigated with the inclusive $\psi(3686)$ MC events, using the event-type analysis tool TopoAna [32]. It is found that for the $h_c \rightarrow 2(\pi^+\pi^-)\pi^0\eta$ selection there are peaking background contributions from $\psi(3686) \rightarrow \pi^0 h_c$, $h_c \rightarrow \gamma\eta_c$, $\eta_c \rightarrow 2(\pi^+\pi^-)\eta$ or $\eta_c \rightarrow 2(\pi^+\pi^-\pi^0)$, and for the $h_c \rightarrow 2(\pi^+\pi^-)\eta$ selection there are peaking background contributions from $h_c \rightarrow \gamma\eta_c$, $\eta_c \rightarrow \pi^+\pi^-\eta'$, $\eta' \rightarrow \pi^+\pi^-\gamma$ or $\eta_c \rightarrow 2(\pi^+\pi^-)\pi^0$.

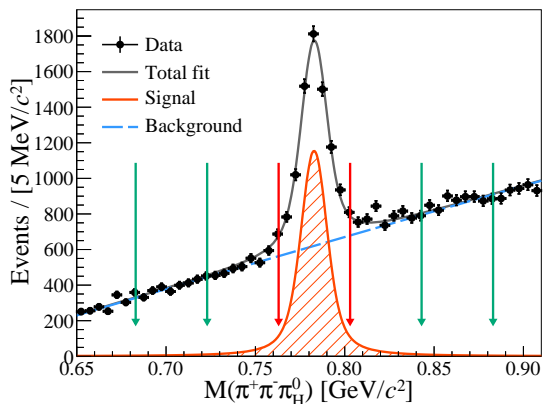


Fig. 1. The $M_{\pi^+\pi^-\pi_H^0}$ distribution of the accepted candidates in data. The dotted error bars represent the distribution of different $\pi^+\pi^-\pi_H^0$ combinations overlaid. The pair of red arrows shown the ω signal region, and the pair of green arrows show the ω sideband region.

Misidentification of photons as π^0/η in these background processes can contaminate the signal region. The size of these background contributions is estimated through MC studies and included in the fit. The BF of the decay $\eta_c \rightarrow 2(\pi^+\pi^-)\pi^0$ is currently unknown, which is reflected in the assignment of the systematic uncertainties. Additionally, the BFs for the other PDG [7].

To investigate contamination from continuum background, the same selection criteria are applied to the data samples collected at the center-of-mass energy of 3.65 GeV, corresponding to an integrated luminosity of 454 pb⁻¹. No h_c candidates are found. Therefore, continuum background is considered to be at a negligible level.

IV. SIGNAL YIELDS

The number of h_c signal events $N_{h_c}^{\text{obs}}$ for each signal decay mode is determined from maximum likelihood fits to the corresponding mass spectra, as shown in Fig. 2. For the channels where a signal is observed, the signal shape is described by a convolution of the MC-simulated shape and a Gaussian function accounting for the difference in mass resolution between data and MC simulation, where the width of the Gaussian function is a free parameter in the fit. For the channels with no significant signals observed ($h_c \rightarrow 2(\pi^+\pi^-)\eta$ and $h_c \rightarrow p\bar{p}$) only the MC-simulated shapes are used. In the fit to the $h_c \rightarrow 2(\pi^+\pi^-)\pi^0\eta$ decay, two additional normalized peaking background components from $h_c \rightarrow \gamma\eta_c, \eta_c \rightarrow 2(\pi^+\pi^-)\eta$ and $h_c \rightarrow \gamma\eta_c, \eta_c \rightarrow 2(\pi^+\pi^-\pi^0)$ are included with fixed background contributions of 3.9 and 35.4 events, respectively. Additionally, for the $h_c \rightarrow 2(\pi^+\pi^-)\eta$ mode, a contribution of 20 events is included

from $h_c \rightarrow \gamma\eta_c, \eta_c \rightarrow \pi^+\pi^-\eta'$ background. The remaining non-peaking background shape is described by an ARGUS function [33], with endpoint fixed at the kinematic threshold of 3.551 GeV/c². The statistical significance of the $h_c \rightarrow 3(\pi^+\pi^-)\pi^0$ decay is greater than 5σ , and that of the intermediate process $h_c \rightarrow 2(\pi^+\pi^-)\omega$ in the $3(\pi^+\pi^-)\pi^0$ final state is 4.7σ . The significance for the $h_c \rightarrow 2(\pi^+\pi^-)\pi^0\eta$ mode is determined to be 4.8σ . For each signal decay mode, the significance is estimated from the likelihood difference with and without signal component included in the fit, taking into account the change in the number of degrees of freedom. The systematic uncertainties are considered in determining the final signal significance. The signal yield for $h_c \rightarrow 2(\pi^+\pi^-)\omega$ is evaluated by performing a simultaneous fit to the $M(3(\pi^+\pi^-)\pi^0)$ spectra for the events in both ω signal and sideband regions using the signal and background shapes described above. The width of the Gaussian function used for smearing is fixed to the value obtained from the fit for the $h_c \rightarrow 3(\pi^+\pi^-)\pi^0$ decay. The h_c yield in the ω sideband region is scaled by a factor $f_\omega = 0.50$, which takes into account the relative difference in the number of events between ω signal and sideband regions, as shown in Fig. 1. Specifically, in the fitting of the $\pi^+\pi^-\pi^0$ invariant mass spectrum, the signal component is modeled with a double Gaussian function. The remaining combinatorial background shape is described by a first-order polynomial function.

Since no significant signals of $h_c \rightarrow 2(\pi^+\pi^-)\eta$ and $h_c \rightarrow p\bar{p}$ are observed, the upper limits of the signal yields for these decays are determined to be 33.7 and 12.4, respectively. The upper limit has already incorporated the systematic uncertainty, and the corresponding method is discussed in Section V.

The BFs of the h_c decay channels are calculated with

$$\mathcal{B}(h_c \rightarrow X) = \frac{N_{h_c}^{\text{obs}}}{N_{\psi(3686)} \cdot \mathcal{B}(\psi(3686) \rightarrow \pi^0 h_c) \cdot \prod_i \mathcal{B}_i \cdot \varepsilon}. \quad (1)$$

Here, $N_{h_c}^{\text{obs}}$ is the number of observed h_c signal events, $N_{\psi(3686)}$ is the total number of $\psi(3686)$ events, X denotes a given final state, \mathcal{B}_i is the BF of the i -th intermediate state taken from the PDG [7], and ε is the detection efficiency. The results and related numerical information are given in Table 2.

V. SYSTEMATIC UNCERTAINTIES

The sources of systematic uncertainties in the BF measurements are associated with the tracking efficiency, photon-detection efficiency, π^0 or η reconstruction efficiency, kinematic fit, signal-yield extraction, choice of theoretical model, etc. The evaluated contributions to the systematic uncertainties are listed in Table 3 and discussed below.

- (i) **Tracking efficiency:** The tracking efficiency of charged pions is estimated by studying the control

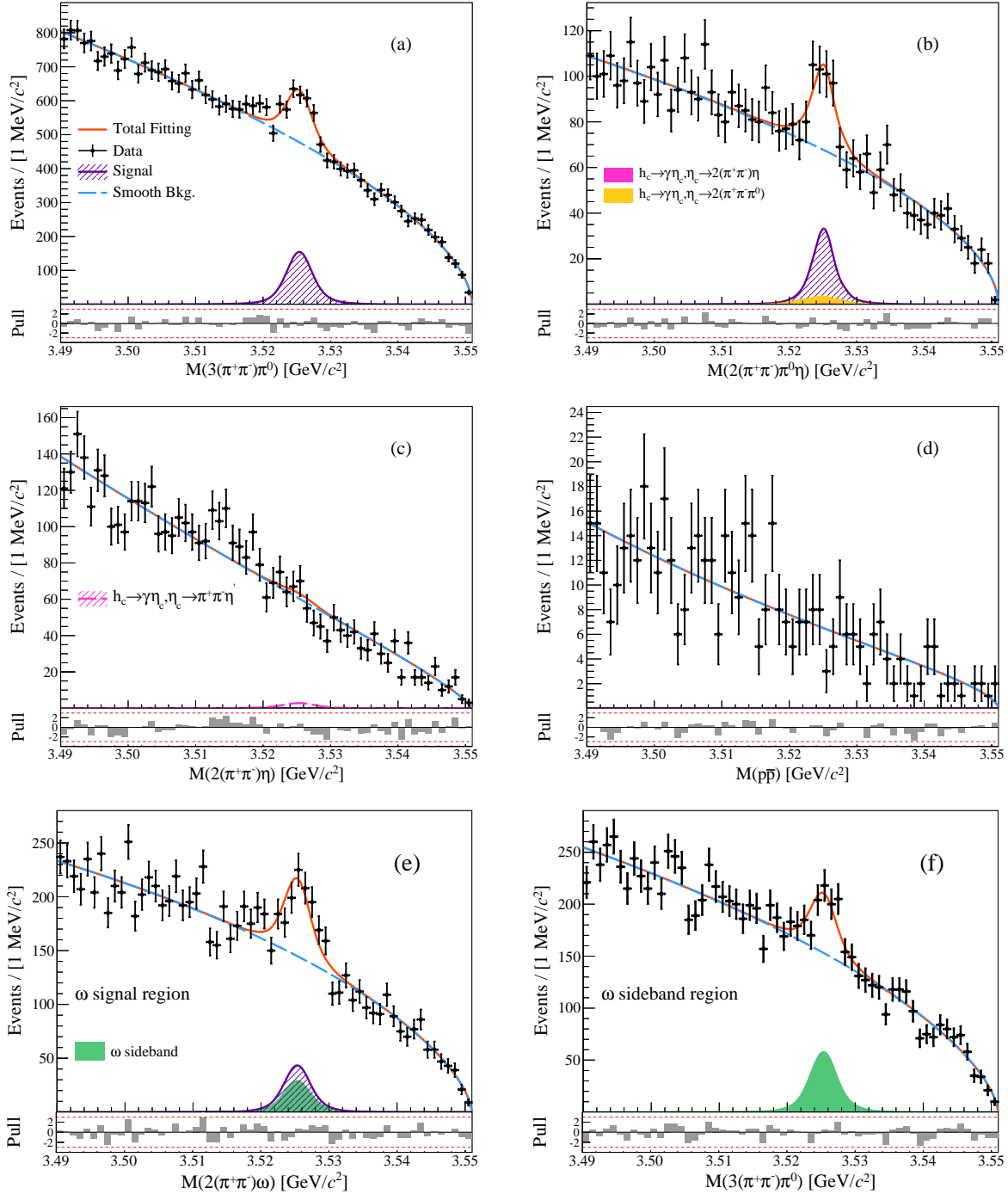


Fig. 2. Fits to the invariant-mass distributions of (a) $h_c \rightarrow 3(\pi^+\pi^-)\pi^0$, (b) $h_c \rightarrow 2(\pi^+\pi^-)\pi^0\eta$, (c) $h_c \rightarrow 2(\pi^+\pi^-)\eta$, (d) $h_c \rightarrow p\bar{p}$, (e) $h_c \rightarrow 2(\pi^+\pi^-)\omega$ in the ω signal region and (f) $h_c \rightarrow 3(\pi^+\pi^-)\pi^0$ in the ω sideband region. The green histogram shows the scaled h_c peak obtained from the fit to the events inside the ω sideband region. The lower panels of each plot show the fit residuals expressed in number of standard deviations.

sample of $J/\psi \rightarrow \pi^+\pi^-\pi^0$ decays. The MC simulation is re-weighted in two-dimensional $(\cos\theta, p_t)$ intervals according to the efficiencies obtained from the control sample, where θ is the polar angle and p_t is the transverse momentum of the charged pion.

The observed change in the selection efficiency is assigned as the systematic uncertainty. The systematic uncertainties associated with the tracking efficiencies of protons (antiprotons) are estimated with the control samples $J/\psi \rightarrow p\bar{p}\pi^+\pi^-$ decays [35].

Table 2. The number of observed signal events $N_{h_c}^{obs}$, the detection efficiency, the product BF $\mathcal{B}(\psi(3686) \rightarrow \pi^0 h_c) \times \mathcal{B}(h_c \rightarrow X)$, and the absolute BF $\mathcal{B}(h_c \rightarrow X)$. The first and second uncertainties are statistical and systematic, respectively.

Final state (X)	$N_{h_c}^{obs}$	$\epsilon(\%)$	$\mathcal{B}(\psi(3686) \rightarrow \pi^0 h_c) \times \mathcal{B}(h_c \rightarrow X)$		$\mathcal{B}(h_c \rightarrow X)$
			This study	Previous BESIII result	
$3(\pi^+\pi^-\pi^0)$	834.7 ± 102.3	4.64 ± 0.01	$(6.79 \pm 0.83 \pm 0.56) \times 10^{-6}$	$< 7.56 \times 10^{-6}$ [7]	$(9.28 \pm 1.14 \pm 0.77) \times 10^{-3}$
$2(\pi^+\pi^-\pi^0)\eta$	154.4 ± 30.8	2.68 ± 0.01	$(5.33 \pm 1.10 \pm 0.56) \times 10^{-6}$	–	$(7.55 \pm 1.51 \pm 0.77) \times 10^{-3}$
$2(\pi^+\pi^-\eta)$	< 33.7	7.05 ± 0.01	$< 4.53 \times 10^{-7}$	–	$< 6.19 \times 10^{-4}$
$p\bar{p}$	12.4	14.35 ± 0.02	$< 3.22 \times 10^{-8}$	$< 1.3 \times 10^{-7}$ [13]	$< 4.40 \times 10^{-5}$
$2(\pi^+\pi^-\omega)$	236.9 ± 50.9	3.42 ± 0.01	$(2.93 \pm 0.63 \pm 0.26) \times 10^{-6}$	–	$(4.00 \pm 0.86 \pm 0.35) \times 10^{-3}$

An uncertainty of 1.0% per track is assigned.

- (ii) **Photon-detection efficiency:** The photon-detection efficiency is studied using a control sample of $e^+e^- \rightarrow \gamma\mu^+\mu^-$ events. The difference in the photon detection efficiencies between data and MC simulation, 0.5%, is assigned as the systematic uncertainty for each photon.
- (iii) **π^0 and η reconstruction efficiency:** Based on a control sample of $e^+e^- \rightarrow \omega\pi^0$ events at $\sqrt{s} = 3.773$ GeV, the difference of the π^0 reconstruction efficiencies between data and MC simulation is studied and found to have the following dependence on momentum: $(0.06 - 2.41 \cdot p [\text{GeV}/c])\%$. The systematic uncertainty associated with this difference is calculated by averaging this function over the π^0 momentum distribution in each signal decay mode. The uncertainty due to the choice of η mass window is determined to be 1.0% per η , from studies of a high purity control sample of $J/\psi \rightarrow p\bar{p}\eta$ decays [36].
- (iv) **Kinematic fit:** The systematic uncertainty associated with the kinematic fit is estimated by comparing the efficiencies with and without a helix parameter correction applied to the signal MC events [37]. The assigned systematic uncertainties are (2.1-3.2)% for the different signal decay modes.
- (v) **Signal-yield extraction:**
 - **Mass window:** To evaluate the systematic uncertainty associated with the choice of mass window, we perform a Barlow test [38] to examine the deviation in significance (ζ) between the baseline fit and that performed for the systematic test. The deviation in significance is defined as

$$\zeta = \frac{|V_{\text{nominal}} - V_{\text{test}}|}{\sqrt{|\sigma_V^2_{\text{nominal}} - \sigma_V^2_{\text{test}}|}}, \quad (2)$$

where V represents the BF; σ_V is the statistical uncertainty on V . For each signal decay, the mass window is varied by up to one times the corresponding mass resolution, with a step of 0.25 times the mass resolution. If the ζ value is not

greater than 2, its effect is assumed to be negligible. For the decays where no significant signal is observed, the corresponding systematic uncertainty is assigned as the maximum difference within the various test ranges mentioned earlier (unless otherwise specified, similar situations are estimated using the same method). Additionally, the systematic uncertainty associated with the choice of ω mass window is estimated from a control sample of $\psi(3686) \rightarrow K^+K^-\omega$ decays. The differences in the acceptance efficiencies between data and MC simulation are taken as the corresponding systematic uncertainties.

- **Fit range:** The systematic uncertainty arising from the choice of fit range is similarly investigated using the Barlow test. To determine the corresponding ζ distribution, we systematically adjust the fit range by shrinking the interval (3480, 3551) MeV/ c^2 to (3500, 3551) MeV/ c^2 , with a step size of 2 MeV/ c^2 .
- **Signal shape:** To estimate the systematic uncertainty associated with the choice of signal shape, we use an alternative MC-simulated shape convolved with a double Gaussian function. The difference relative to the nominal fit is taken as the systematic uncertainty.
- **Background shape:** The uncertainties due to the choice of background shape is estimated by replacing the ARGUS function with a second-order Chebychev polynomial function. The change in the fitted signal yield is taken as the systematic uncertainty.
- **η_c peaking background:** The uncertainty associated with the knowledge of the η_c peaking background is estimated according to the uncertainty of the corresponding BF measurements [7, 39] or by including this contribution in the fit, assuming $\mathcal{B}(\eta_c \rightarrow 2(\pi^+\pi^-\pi^0))$ is equal to $\mathcal{B}(\eta_c \rightarrow 2(\pi^+\pi^-\eta))$, and assigning the largest differences between these and the baseline results as the systematic uncertainty.
- **Wrong-combination background:** The uncertainty due to the wrong-combination background

(WCB) in the π^0 reconstruction is investigated by studying the matching angle between generated and reconstructed momenta. Events containing candidates with matching angles greater than 10° are classified as the WCB background. The possible bias due to WCB is estimated by comparing the signal yields with and without including the WCB contribution in the fits. The difference in the fitted signal yield is taken as the systematic uncertainty.

- **Normalization factor:** The systematic uncertainty related to the normalization factor in calculating the non- ω contribution in extracting the number of the $h_c \rightarrow 2(\pi^+\pi^-)\omega$ signal events is estimated by producing multi-dimensional Gaussian random numbers with the covariance matrix from the fit as input. A group of normalization factors is obtained from this procedure and the standard deviation of the corresponding distribution is taken as the systematic uncertainty.
- **ω sideband:** The systematic uncertainty due to the choice of ω sideband region is determined by widening and narrowing the range by one standard deviation of the ω mass resolution. The largest change relative to the fitted signal yield for $h_c \rightarrow 2(\pi^+\pi^-)\omega$ is taken as the corresponding systematic uncertainty.
- (vi) **Theoretical model:** There is a potential systematic bias associated with the choice of theoretical model for the primary decay of $\psi(3686) \rightarrow \pi^0 h_c$ and the sequential decay $h_c \rightarrow \text{hadrons}$, since these decays are not understood well at present. The difference in reconstruction efficiencies between simulated events generated with the PHSP model and the model proposed in Refs. [27, 28] is assigned as the systematic uncertainty for $\psi(3686) \rightarrow \pi^0 h_c$. The difference in efficiencies between events generated with the PHSP model and the mixed model including additional intermediate states is taken as the systematic uncertainty for $h_c \rightarrow \text{hadrons}$.
- (vii) **MC sample size:** The statistical uncertainty in the reconstruction efficiency associated with the finite MC sample size can be calculated as $\Delta_\epsilon = \sqrt{\epsilon(1-\epsilon)/N}$, where ϵ is the reconstruction efficiency and N is the total number of generated events. The relative uncertainty from this source is Δ_ϵ/ϵ .
- (viii) **Input BFs:** The uncertainties in the knowledge of the BFs of $\mathcal{B}(\psi(3686) \rightarrow \pi^0 h_c)$, $\mathcal{B}(\eta \rightarrow \gamma\gamma)$, and $\mathcal{B}(\omega \rightarrow \pi^+\pi^-\pi^0)$, which are 5.6% [39], 0.5% [7], and 0.8% [7], respectively, are assigned as individual systematic uncertainties.
- (ix) **$N_{\psi(3686)}$:** The total number of $\psi(3686)$ events in the sample is determined from inclusive hadronic $\psi(3686)$ decays with an uncertainty of 0.5% [14].

The systematic uncertainties are summarized in Table 3. For each signal decay mode the total systematic uncertainty is obtained by adding all contributions in quadrature under the assumption that they are independent.

The systematic uncertainty from the upper limit of signal events $N_{h_c}^{\text{obs}}$ at 90% confidence level includes additive sources and multiplicative sources. To account for the additive systematic uncertainties related to the fits, several alternative fits are performed. These alternative fits involve signal shape, background shape, η_c peaking-background shape as well as different fit ranges and the one resulting the most conservative upper limit is chosen. Then, the multiplicative systematic uncertainty is incorporated in the calculation of the upper limit via [40, 41]

$$L'(N) = \int_0^1 L\left(\frac{S}{\hat{S}}N\right) \exp\left[-\frac{(S-\hat{S})}{2\sigma_S^2}\right] dS, \quad (3)$$

where, $L(N)$ is the likelihood distribution as a function of signal events, N ; S is the expected efficiency and \hat{S} is the nominal efficiency; σ_S is its multiplicative systematic uncertainty coming from Table 3. Following these steps, the corresponding likelihood distribution can be obtained as shown in Fig. 3. The assumed yields for processes $h_c \rightarrow 2(\pi^+\pi^-)\eta$ and $h_c \rightarrow p\bar{p}$ at 90% confidence level are set as upper limits, and the corresponding BF calculated using Equation 1 is the upper limit BF, as shown in Table 2.

VI. SUMMARY

By analyzing $(2712.4 \pm 14.1) \times 10^6$ $\psi(3686)$ events collected in the BESIII experiment, we report the observation of $h_c \rightarrow 3(\pi^+\pi^-)\pi^0$, as well as evidence for the decays $h_c \rightarrow 2(\pi^+\pi^-)\pi^0\eta$ and $h_c \rightarrow 2(\pi^+\pi^-)\omega$. We have also searched for $h_c \rightarrow 2(\pi^+\pi^-)\eta$ and $h_c \rightarrow p\bar{p}$, but no significant signal is observed for either decay. The measured BFs or upper limits at the 90% confidence level are listed in Table 2. The upper limit on $\mathcal{B}(h_c \rightarrow p\bar{p})$ is a factor of three lower than that set in previous studies [13]. Furthermore, the limit is a factor of 100 lower than the predictions found in Refs. [11, 12], which indicates the need for improved theoretical calculations as well as more sensitive measurements.

ACKNOWLEDGMENTS

The BESIII Collaboration thanks the staff of BEPCII and the IHEP computing center for their strong support. This work is supported in part by National Key R&D Program of China under Contracts Nos. 2020YFA0406300, 2020YFA0406400; National Natural Science Foundation of China (NSFC) under Contracts Nos. 11635010, 11735014, 11835012, 11935015, 11935016, 11935018, 11961141012, 12022510, 12025502,

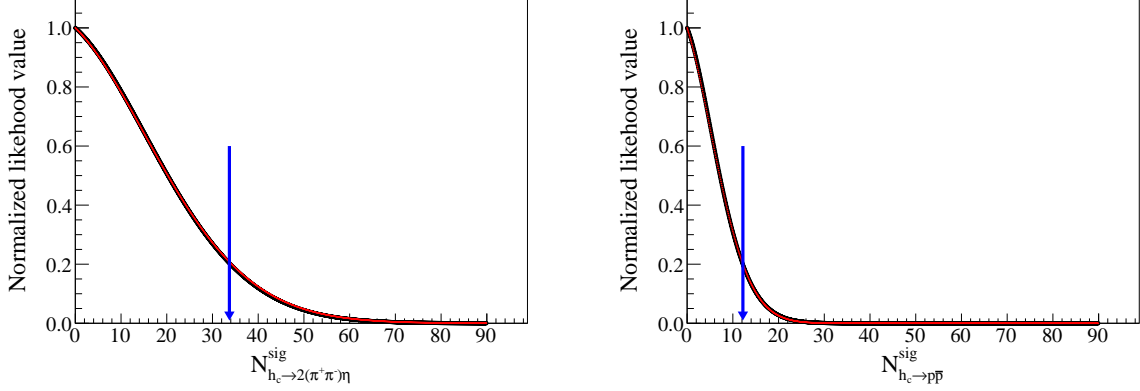


Fig. 3. The normalized likelihood distribution for (up panel) $h_c \rightarrow 2(\pi^+\pi^-)\eta$ and (down panel) $h_c \rightarrow p\bar{p}$ mode. The results obtained with and without incorporating the systematic uncertainties are shown in blue dots and black dots, respectively. The arrow is the position of the upper limit on the signal yields at 90% confidence level.

Table 3. Relative systematic uncertainties (in percent) for each h_c decay channel. The dash indicates that the systematic uncertainty is not applicable. Asterisk denotes that the additive systematic uncertainty values are invalid.

Source	$3(\pi^+\pi^-)\pi^0$	$2(\pi^+\pi^-)\pi^0\eta$	$2(\pi^+\pi^-)\eta$	$p\bar{p}$	$2(\pi^+\pi^-)\omega$
Tracking	2.3	1.6	1.4	2.0	2.3
Photon efficiency	2.0	3.0	2.0	1.0	2.0
π^0 reconstruction	2.1	2.2	0.5	0.5	1.6
η reconstruction	–	1.0	1.0	–	–
Kinematic fit	2.1	2.3	2.5	3.2	2.3
Mass window	negligible	1.2	6.8	–	1.1
Signal shape	0.8	0.3	*	*	2.1
Background shape	2.6	4.1	*	*	2.5
η_c peaking-background shape	–	1.8	*	–	–
WCB	1.3	1.9	–	–	negligible
Fit range	negligible	negligible	–	–	negligible
Normalization factor	–	–	–	–	0.5
ω sideband	–	–	–	–	3.8
Theoretical model	3.1	5.0	0.1	negligible	0.6
MC sample size	0.2	0.1	0.1	0.3	0.4
Input BF's	5.6	5.6	5.6	5.6	5.7
$N_{\psi(3686)}$	0.5	0.5	0.5	0.5	0.5
Sum	8.3	10.2	9.6	6.9	8.8

12035009, 12035013, 12061131003, 12192260, 12192261, 12192262, 12192263, 12192264, 12192265, 12221005, 12225509, 12235017, 12150004; Program of Science and Technology Development Plan of Jilin Province of China under Contract No. 20210508047RQ and 20230101021JC; the Chinese Academy of Sciences (CAS) Large-Scale Scientific Facility Program; the CAS Center for Excellence in Particle Physics (CCEPP); Joint Large-Scale Scientific Facility Funds of the NSFC and CAS under Contract No. U1832207; CAS Key Research Program of Frontier Sciences under Contracts Nos. QYZDJ-SSW-SLH003, QYZDJ-SSW-SLH040; 100 Talents Program of CAS; The Institute of Nuclear and Particle Physics (INPAC) and Shanghai Key Laboratory for Particle Physics and Cosmology; European Union's

Horizon 2020 research and innovation programme under Marie Skłodowska-Curie grant agreement under Contract No. 894790; German Research Foundation DFG under Contracts Nos. 455635585, Collaborative Research Center CRC 1044, FOR5327, GRK 2149; Istituto Nazionale di Fisica Nucleare, Italy; Ministry of Development of Turkey under Contract No. DPT2006K-120470; National Research Foundation of Korea under Contract No. NRF-2022R1A2C1092335; National Science and Technology fund of Mongolia; National Science Research and Innovation Fund (NSRF) via the Program Management Unit for Human Resources & Institutional Development, Research and Innovation of Thailand under Contract No. B16F640076; Polish National Science Centre under Contract No. 2019/35/O/ST2/02907; The Swedish Research

-
- [1] E. Eichten, S. Godfrey, H. Mahlke, and J. L. Rosner, *Rev. Mod. Phys.* **80**, 1161 (2008).
- [2] P. Rubin *et al.* [CLEO Collaboration], *Phys. Rev. D* **72**, 092004 (2005).
- [3] J. L. Rosner *et al.* [CLEO Collaboration], *Phys. Rev. Lett.* **95**, 102003 (2005).
- [4] Yu-Ping Kuang, *Phys. Rev. D* **65**, 094024 (2002).
- [5] Stephen Godfrey and Jonathan L. Rosner, *Phys. Rev. D* **66**, 014012 (2002).
- [6] M. Ablikim *et al.* [BESIII Collaboration], *Phys. Rev. D* **106**, 072007 (2022).
- [7] P. L. Workman *et al.* [Particle Data Group], *Prog. Theor. Exp. Phys.* **2022**, 083C01 (2022).
- [8] M. Ablikim *et al.* [BESIII Collaboration], *High Energ. Phys.* **2022**, 108 (2022).
- [9] Stanley J. Brodsky and G. Peter Lepage, *Phys. Rev. D* **24**, 2848 (1981).
- [10] M. Andreotti *et al.* [Fermilab E835 Collaboration], *Phys. Rev. D* **72**, 032001 (2005).
- [11] X.H. Liu and Q. Zhao, *J. Phys. G* **38**, 035007 (2011).
- [12] S. Barsuk, J. He, E. Kou, and B. Viaud, *Phys. Rev. D* **86**, 034011 (2012).
- [13] M. Ablikim *et al.* [BESIII Collaboration], *Phys. Rev. D* **88**, 112001 (2013).
- [14] M. Ablikim *et al.* [BESIII Collaboration], *Chin. Phys. C* **42**, 023001 (2018).
- [15] M. Ablikim *et al.* [BESIII Collaboration], *Nucl. Instrum. Meth. A* **614**, 345 (2010).
- [16] C. H. Yu *et al.*, Proceedings of IPAC2016, Busan, Korea (JACoW, Busan, 2016), <https://accelconf.web.cern.ch/ipac2016/>.
- [17] M. Ablikim *et al.* [BESIII Collaboration], *Chin. Phys. C* **44**, 040001 (2020).
- [18] J. Lu, Y. Xiao, X. Ji, *Radiat. Detect. Technol. Methods* **4**, 337 C344 (2020).
- [19] J. W. Zhang, L. H. Wu, S. S. Sun *et al.*, *Radiat. Detect. Technol. Methods* **6**, 289 C293 (2022).
- [20] X. Li *et al.*, *Radiat. Detect. Technol. Meth.* **1** 13 (2017).
- [21] Y. X. Guo *et al.*, *Radiat. Detect. Technol. Meth.* **1** 15 (2017).
- [22] P. Cao *et al.*, *Nucl. Instrum. Meth. A* **953**, 163053 (2020).
- [23] S. Agostinelli *et al.* [GEANT4 Collaboration], *Nucl. Instrum. Meth. A* **506**, 250 (2003).
- [24] K. X. Huang, *et al.*, *Nucl. Sci. Tech.* **33**, 142 (2022).
- [25] S. Jadach, B. F. L. Ward, and Z. Was, *Comput. Phys. Commun.* **130**, 260 (2000).
- [26] S. Jadach, B. F. L. Ward, and Z. Was, *Phys. Rev. D* **63**, 113009 (2001).
- [27] R. G. Ping, *Chin. Phys. C* **32**, 599 (2008).
- [28] D. J. Lange, *Nucl. Instrum. Meth. A* **462**, 152 (2001).
- [29] J. C. Chen, G. S. Huang, X. R. Qi, D. H. Zhang, and Y. S. Zhu, *Phys. Rev. D* **62**, 034003 (2000).
- [30] R. L. Yang, R. G. Ping, and H. Chen, *Chin. Phys. Lett.* **31**, 061301 (2014).
- [31] E. Richter-Was, *Phys. Lett. B* **303**, 163 (1993).
- [32] X. Y. Zhou, S. X. Du, G. Li and C. P. Shen, *Comput. Phys. Commun.* **258**, 107540 (2021).
- [33] H. Albrecht *et al.* *Phys. Lett. B* **340**, 217 (1994).
- [34] Gary J. Feldman and Robert D. Cousins, *Phys. Rev. D* **57**, 3873 (1998).
- [35] W. L. Yuan, X.-C. Ai, X.-B. Ji, S.-J. Chen, Y. Zhang, L.-H. Wu, L.-L. Wang, and Y. Yuan, *Chin. Phys. C* **40**, 026201 (2016).
- [36] M. Ablikim *et al.* [BESIII Collaboration], *Phys. Rev. D* **81**, 052005 (2010).
- [37] M. Ablikim *et al.* [BESIII Collaboration], *Phys. Rev. D* **87**, 012002 (2013).
- [38] O. Behnke, K. Kroninger, G. Schott, and T. H. Schorner-Sadenius, *Wiley-VCH, Berlin, Germany*, 2013.
- [39] M. Ablikim *et al.* [BESIII Collaboration], *Phys. Rev. D* **106**, 072007 (2022).
- [40] K. Stenson, [arXiv:physics/0605236](https://arxiv.org/abs/physics/0605236).
- [41] X.X. Liu, X.R. Lyu, and Y.S. Zhu, *Chin. Phys. C* **39**, 113001 (2015).

Strengthening nuclear symmetry energy constraints using multiple resonant shattering flares of neutron stars with realistic mass uncertainties

Duncan Neill^{1*}, David Tsang¹, William G. Newton²

¹*Department of Physics, University of Bath, Claverton Down, Bath, BA1 1AL*

²*Department of Physics and Astronomy, Texas A&M University-Commerce, Commerce, TX, 75429-3011*

Accepted XXX. Received YYY; in original form ZZZ

ABSTRACT

With current and planned gravitational-wave (GW) observing runs, coincident multimessenger timing of Resonant Shattering Flares (RSFs) and GWs may soon allow for neutron star (NS) asteroseismology to be used to constrain the nuclear symmetry energy, an important property of fundamental nuclear physics that influences the composition and equation of state of NSs. In this work we examine the effects of combining multiple RSF detections on these symmetry energy constraints, and consider how realistic uncertainties in the masses of the progenitor NSs may weaken them. We show that the detection of subsequent multimessenger events has the potential to substantially improve constraints beyond those obtained from the first, and that this improvement is insensitive to the mass of the NSs which produce the RSFs and its uncertainty. This sets these asteroseismic constraints apart from bulk NS properties such as radius, for which the NS mass is highly important, meaning that any multimessenger RSF and GW events can equally improve our knowledge of fundamental physics.

Key words: dense matter – stars: neutron – stars: oscillations – neutron star mergers – gravitational waves – equation of state

1 INTRODUCTION

Neutron stars (NSs) provide a unique environment in which to study fundamental physics, as they consist of matter that is both extremely dense and neutron-rich without having the high temperatures required to produce these conditions in terrestrial experiments. There is a well established link between the composition and structure of NSs and the zero temperature equation of state (EOS) of bulk nuclear matter (Lattimer & Prakash 2001; Li et al. 2019), which describes the binding energy of nuclear matter as a function of density and asymmetry (proton-to-neutron ratio). In particular, the neutron-rich matter found in NSs is sensitive to the asymmetry dependence of the nuclear EOS, which is encapsulated by the nuclear symmetry energy: the difference in binding energy between symmetric ($N=Z$) and pure neutron ($N=A$) matter. The symmetry energy is also important for various properties of nuclei, such as the thickness of neutron skins (the neutron-rich layer that surrounds the more symmetric core of a neutron-rich nucleus) (Chen et al. 2010; Piekarewicz et al. 2012) and certain giant resonances (which excite collective oscillations of nucleons within nuclei, some of which produce relative displacements between the protons and neutrons) (Trippa et al. 2008; Roca-Maza et al. 2013). Of particular interest are recent precision measurements of the neutral weak form factors of ^{48}Ca and ^{208}Pb (Adhikari et al. 2021, 2022), from which the neutron skin can be extracted, which have been shown to in tension with each other for the majority of nuclear energy-density functionals (Reed et al. 2022; Zhang & Chen 2022; Reinhard & Nazarewicz 2022; Yüksel & Paar 2023). Furthering our understanding of the symmetry energy using probes independent from current nuclear experimental techniques is important

to resolve these tensions and learn more about fundamental physics and improve our ability to model dense matter.

Various methods exist to infer structural or compositional properties of NSs from astronomical observations (Lattimer & Prakash 2007; Raithe 2019), which can subsequently be used to impose constraints on the nuclear symmetry energy through NS modelling. Of particular interest are the transient gravitational waves (GWs) detected from Neutron Star-Neutron Star (NSNS) (Abbott et al. 2017, 2020b) and Black Hole-Neutron Star (BHNS) (Abbott et al. 2021b) binary mergers, which have opened the way to a new era of multimessenger NS astronomy involving GWs and electromagnetic counterparts (e.g. Smartt et al. 2017; Margalit & Metzger 2017; Radice et al. 2018; Troja et al. 2018; Abbott et al. 2018). While at this time only a small number of such transients have been detected, the O4 LIGO GW observing run has already detected multiple BHNS merger candidates, and with the increased sensitivity of LIGO and Virgo in this and future runs we can expect to observe many more mergers involving NSs in the near future.

Other methods to measure NS properties include pulse-profile modelling of X-ray emission (Riley et al. 2019; Miller et al. 2019; Riley et al. 2021; Miller et al. 2021), measuring the relativistic Shapiro delay of radiation from pulsars in binary systems (Fonseca et al. 2021), and modelling outbursts from low-mass X-ray binaries (Galloway et al. 2008; Özel et al. 2016; Nättilä et al. 2017). However, a common theme of these methods is that they constrain NS properties which are sensitive to the nature of matter within the NS core (Essick et al. 2021), where most of the star’s mass is located. Matter within the ultra-dense NS core may transition to an exotic phase, but the type of matter it becomes and the density at which the transition occurs are highly uncertain, meaning that while constraints on core-dependent properties are useful for testing various exotic models they can not

* E-mail: dn431@bath.ac.uk

reliably be used to constrain properties of nucleonic matter, such as the symmetry energy. Instead, we must look for ways to probe the lower density – but still very dense and neutron-rich – NS crust, where matter can more confidently be assumed to be nucleonic.

Perhaps the most compelling methods to probe specific properties of matter within NSs are those that involve asteroseismic normal modes. Different families of modes are sensitive to different NS properties (McDermott et al. 1988), some of which are dominated by the composition and structure of the NS crust. Various NS phenomena that may contain signatures of modes have been identified (Lai 1994; Kokkotas & Schafer 1995; Andersson 1998; Duncan 1998; Israel et al. 2005; Strohmayer & Watts 2005; Levin 2007; Tsang et al. 2012; Sotani 2024), which could allow for features of these modes and the NS properties on which they depend to be constrained.

Tsang et al. (2012) proposed the existence of resonant shattering flares, and that coincident detection of such a flare alongside gravitational waves could allow a measurement of the frequency at which the crust-core interface mode oscillates. Resonant shattering flares (RSFs) are brief flares of gamma-rays produced when a NS normal mode is resonantly excited by the tidal field of its inspiralling binary partner and reaches an amplitude sufficient to deform the NS crust beyond its breaking strain (Tsang et al. 2012). This causes the crust to repeatedly fracture while the mode is near resonance, resulting in a build-up of seismic energy that eventually causes the crust to shatter upon reaching its elastic limit, scattering the seismic waves to higher frequencies. A strongly magnetised NS can then have its magnetic field couple to these high frequency waves, resulting in the emission of a fireball. During a mode’s resonance multiple such fireballs can be emitted (Neill et al. 2022), and collisions between them will produce internal shocks capable of scattering electrons to high energies, resulting in non-thermal synchrotron emission detectable as a brief flare of gamma-rays: a RSF. Multimessenger detection of GWs and a RSF from an inspiralling binary would allow us to measure the frequency of the resonant mode, as the GW frequency directly informs us of the orbital frequency, which at the time of the RSF will be around half the frequency of the (quadrupolar) resonantly excited mode.

As a mode must be strongly excited in order to shatter the NS crust, resonant shattering flares can only be triggered by modes that become resonant shortly before a NSNS or BHNS merger, when the tidal forces between a NS and its binary partner are strong. Additionally, the mode must primarily displace matter within the NS crust in order to reach its breaking strain efficiently. In previous works the crust-core interface mode (*i*-mode) was identified to satisfy these requirements (Tsang et al. 2012) and its frequency was found to be sensitive to the shear speed at the base of the NS crust (Neill et al. 2021). The shear speed is sensitive to the proton fraction of the crust and thus in turn depends on the nuclear symmetry energy. A measurement of the *i*-mode’s frequency obtained from multimessenger GW and RSF timing could therefore be used to constrain the symmetry energy at around half nuclear saturation density.

Neill et al. (2023) examined these symmetry energy constraints by performing Bayesian inference of the parameters of a NS meta-model using injected *i*-mode frequency data, and found that a single multimessenger event would provide constraints similar in strength to those from terrestrial nuclear experiments. However, that work fixed the mass of the NS from which the *i*-mode frequency was measured, ignoring any consequences of mass uncertainty. Given that other prominent NS observables – such as radius or tidal deformability – can have strong dependences on the NS’s mass, we wish to examine the mass-dependence of the *i*-mode frequency, to determine its effect on the nuclear constraints obtainable from RSFs.

It was also suggested in Neill et al. (2022) that RSFs might not be uncommon, in which case we may be able to obtain multiple measurements of the *i*-mode frequency in the near future. The first aim of this work is therefore to investigate whether accounting for realistic uncertainty in the mass of a NS (inferred from the GW signal of its binary merger) significantly affects the symmetry energy constraints obtained from a measurement of its *i*-mode frequency. The second is to determine whether those symmetry energy constraints could be improved by combining data from multiple multimessenger GW and RSF detections, as subsequent events will reduce the effect of statistical uncertainties in the data and allow us to probe the mass-frequency relationship.

We will begin in Section 2 by briefly describing the NS meta-model we use to generate NS models from a set of nuclear physics parameters, and then will examine the relationship between NS mass and *i*-mode frequency. After that, in Section 3 we will construct an artificial set of merging NSNS and BHNS binaries and use standard GW analysis methods to obtain realistic uncertainties for the masses of the objects in these binaries. These masses and their uncertainties will then be used in Section 4 along with injected *i*-mode frequency measurements – which include estimates of the uncertainty resulting from coincident RSF and GW timing – to investigate how combining multiple multimessenger RSF and GW events could affect symmetry energy constraints. In Section 5 we will discuss the results and what they mean for how *i*-mode frequency measurements could be used in the future, as well as some of the limitations of this work. Finally in Section 6 we will give our conclusions.

2 MODELLING NEUTRON STARS

2.1 Neutron star meta-model and choice of injected model

Our method for generating NS models from a set of nuclear physics parameters has been described in several previous works (Newton et al. 2013; Balliet et al. 2021; Neill et al. 2021), so here we shall only give a brief overview. The binding energy of bulk nuclear matter can be expanded in isospin asymmetry ($\delta = 1 - 2x_p$, with x_p being the proton fraction) to give

$$E(n, \delta) = E_0(n) + \delta^2 E_{\text{sym}} + \dots, \quad (1)$$

with the symmetry energy E_{sym} being the energy required to deviate from an equal concentration of neutrons and protons. The symmetry energy can further be expanded in density around nuclear saturation ($n_{\text{sat}} \sim 0.16 \text{ fm}^{-3}$) with expansion parameters ($J, L, K_{\text{sym}}, Q_{\text{sym}}, \dots$). We model the strong force between nucleons in bulk matter using a Skyrme type phenomenological effective potential with an extended density dependence (Skyrme 1958; Davesne et al. 2016; Zhang & Chen 2016; Lim & Holt 2017). The phenomenological parameters of this model can be related to the symmetry energy parameters, with the extended density dependence allowing three symmetry energy parameters (J, L and K_{sym}) to be chosen independently, rather than just two which is the case in most Skyrme models (Dutra et al. 2012). In the NS inner crust this model’s energy density functional is used with the compressible liquid droplet model (CLDM) to obtain the equilibrium structure of spherical nuclear clusters and pure neutron fluid (Newton et al. 2013; Balliet et al. 2021; Newton et al. 2022), while in the core it is used to obtain the composition of uniform matter. The transition between these regions is located where the energy density of uniform matter matches the energy density obtained from the CLDM. This meta-model produces NS crusts and cores that are connected in a consistent way, allowing for simultaneous

systematic exploration of how core and crust-dependent neutron star observables inform us of nucleonic matter properties.

As the Skyrme model describes nucleonic matter, it might not be valid at the very high densities found within the cores of massive NSs, where exotic phases of matter may appear. To avoid assumptions about the nature of matter in NS cores we therefore switch to a polytropic NS EOS model at $1.5n_{\text{sat}}$, with a piecewise transition at $2.7n_{\text{sat}}$ to allow more freedom in the core model (Read et al. 2009; Steiner et al. 2010). This gives us two additional parameters: the polytropic indices γ_1 and γ_2 . These polytropes gives us sufficient model freedom explore a wide range of NS cores, and the restrictions they place on the core model and the lack of information they provide about its composition should not be important in this work, as the i -mode is insensitive to the core. While they do not have the freedom to explore in detail the range of possible cores introduced when allowing for exotic matter, they do reproduce the consequence of exotic matter that is most significant for this work, which is that properties of matter within the NS core will not be directly dependent on the symmetry energy parameters.

The parameters of this meta-model are therefore J , L , K_{sym} , γ_1 and γ_2 . For any set of values for these parameters we can construct a unique NS EOS including relevant compositional properties of the crust, such as the shear modulus. Such an EOS can then be used in the TOV equations (Oppenheimer & Volkoff 1939; Tolman 1939) to obtain equilibrium NS structures, which can in turn be used with Yoshida & Lee (2002)'s linearised relativistic pulsation equations to calculate (in the Cowling approximation) the frequency of the quadrupolar i -mode (f_{2i}). The TOV equations can also be augmented to calculate NS tidal deformability (Hinderer et al. 2010) (the degree to which a NS is deformed by an external tidal field), which is relevant for GWs.

For the purpose of this work we choose a set of parameter values to inject, which we will attempt to recover using i -mode frequency measurements. For the symmetry energy parameters we choose values that are generally consistent with experimental constraints: $J = 31$ MeV, $L = 50$ MeV and $K_{\text{sym}} = -100$ MeV. For the core polytrope parameters meanwhile we choose $\gamma_1 = \gamma_2 = 3.0$, as for our chosen symmetry energy parameter values they result in a mass-radius relationship (shown in Figure 1) which broadly agrees with astrophysical constraints (Özel et al. 2016; Abbott et al. 2018; Riley et al. 2019; Miller et al. 2019; Riley et al. 2021; Fonseca et al. 2021), with $R_{1.4} = 12.2$ km and $M_{\text{max}} = 2.17 M_{\odot}$.

2.2 Relationship between NS mass and i -mode frequency

In Figure 1 we plot the relationship between i -mode frequency and NS mass for our injected NS model, and the relationships obtained by individually changing each of the injected parameters by a small amount. To provide some context for how varying the meta-model parameters affects the resulting NS model, we also plot the relationships between NS mass and radius and between NS mass and tidal deformability, to show how changing the parameter values affects these more commonly considered NS properties. We can see that the mass-frequency relationship is near-linear and has a shape that only changes slightly for different sets of parameters.

The changes are small when compared to the sensitivity of the mass-radius relationship to those parameters, and from the wider range of relationships shown in grey it is clear that there is much more freedom in the shape of the mass-radius relationship than the mass-frequency relationship. For a given EOS, the mass-frequency relationship is nearly linear with the difference in i -mode frequency across the full range of NS masses being similar to changes caused

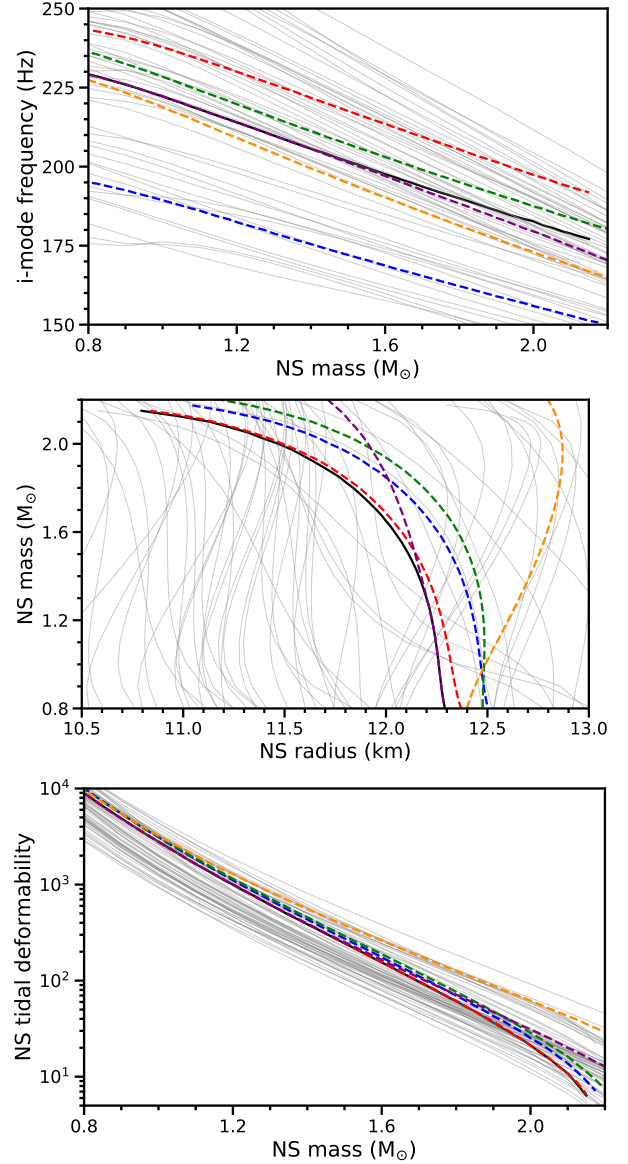


Figure 1. The i -mode frequency, radius, and tidal deformability as functions of NS mass for various NS models, showing the dependences of these properties and their relationships with NS mass on the choice of model. The i -mode frequency's mass dependence appears to be similar for all of the models, in contrast to the radius's more complex dependence. Six models are highlighted, with the solid black lines being for the model generated with our injected meta-model parameter values ($J = 31$ MeV, $L = 50$ MeV, $K_{\text{sym}} = -100$ MeV, $\gamma_1 = 3.0$, $\gamma_2 = 3.0$). The dashed lines give some indication of how significant the model parameters are for these NS properties by changing one of the parameters by a small amount while keeping the others at our injected values: blue has $J = 32$ MeV, red has $L = 60$ MeV, green has $K_{\text{sym}} = -50$ MeV, orange has $\gamma_1 = 4.0$, and purple has $\gamma_2 = 4.0$.

by small variations of the meta-model parameters and less than the frequency uncertainty we may expect from coincident timing (Tsang et al. 2012). It is therefore unclear whether uncertainty in NS mass will have a significant effect on any parameter constraints inferred from measurements of the i -mode frequency, and whether combining multiple measurements to probe the mass-frequency relationship would be useful, and motivates our work in this study.

3 MASSES OF NSS AND BHS IN MERGING BINARIES

3.1 Artificial set of binary mergers

To investigate whether combining *i*-mode frequency measurements from several multimessenger RSF and GW events could allow us to constrain neutron star structure and the nuclear symmetry energy better than with a single measurement, we must first construct an artificial set of binary systems to serve as the progenitors of injected events. The rate at which we may observe multimessenger RSF and GW events is unclear. The upper limit estimated by Neill et al. (2022) was ~ 3 events per year (combining those from BHNS and NSNS binaries). This suggests that while they may not be rare, we should not expect a very large number of these mergers, in agreement with the current absence of any such multimessenger detections. We therefore choose to have 5 binaries in our set of artificial systems: a small number that is not too unreasonable a hope for observations in the next decade or so.

Assuming that there is a single NS EOS and that all NSs have time to spin down and cool to negligible temperatures prior to binary merger, any differences between the *i*-modes of NSs will be related to their masses, and so we shall focus on the masses of the NSs in our binary systems. To have our injected events be consistent with currently known mergers, we draw these masses from the extragalactic NS mass distribution inferred by Landry & Read (2021) from observed GW signals produced by compact binary mergers involving NSs (specifically, their “FLAT” model). While the small number of such events means that this distribution is unlikely to accurately predict future detections, it will be sufficient for this work. Using a NS population inferred from GW observations will bias our NS masses towards larger values since they produce louder GW signals, but that is appropriate for this work as we are only interested in binary mergers that could be detected in GWs. We do not know of any correlation between RSF detectability and NS mass, as their emission mechanism has not been studied in detail.

The mass of the binary companion to a NS RSF progenitor will strongly affect their GW signal and thus influence the uncertainty in the NS’s mass, so we must also select masses for the companions in each binary we use. We will consider both BHNS and NSNS binaries, as – unlike SGRBs or Kilonovae – RSFs can be produced by NSs in BHNS binaries as easily as those in NSNS binaries (Neill et al. 2022). The binary population synthesis of BPASS (Eldridge et al. 2017; Stanway & Eldridge 2018) finds that there is approximately one BHNS for every four NSNS systems, and while GW signals from more massive binary mergers are detectable at greater distances, the luminosities of RSFs may not have such a strong dependence on mass. As the distances at which RSFs may be visible (Neill et al. 2022) are similar to the current GW detection range for NSNS mergers (Abbott et al. 2020a), we therefore assume that RSFs produced by BHNS mergers beyond the NSNS range will not be detected. This means that approximately 20% of multimessenger events will originate from BHNS binaries, and so we will have one of our five random binaries be a BHNS system. While we draw NS masses from Landry & Read (2021)’s extragalactic NS mass distribution, for the BH’s mass we randomly select a value from the range 3–30 M_{\odot} . We ignore any correlations that may exist between the masses of the two objects in a binary.

Aside from combining *i*-mode frequency measurements for NSs that have a realistic distribution of masses, we shall also examine the extreme case where multimessenger RSF and GW events are detected for NSs with very high and low masses. Combining frequency measurements from these extremes will provide the strongest discriminating power for small differences between the slopes of the

(near-linear, see Figure 1) mass-frequency relationships of different NS models. This case will therefore maximise the benefit of a obtaining second measurement for probing the mass-frequency relationship. The NS with the lowest known mass is the binary partner of the pulsar J0453+1559, which has a mass of $1.174^{+0.004}_{-0.004} M_{\odot}$ (Martinez et al. 2015). Lower mass NSs would be physically stable (Haensel et al. 2002), but it is doubtful that a much lower mass NS could be produced, as most formation channels will favour producing white dwarfs for masses well below the Chandrasekhar limit. The maximum NS mass is a topic of much interest as it is important for the NS population and is closely related to the high density behaviour of NS EOS. The most massive NS with a well-determined mass is the pulsar J0740+6620 with mass $2.08^{+0.07}_{-0.07} M_{\odot}$ (Fonseca et al. 2021), and other astrophysical constraints typically place the limit between 2.0 and 2.3 M_{\odot} (see, e.g. Margalit & Metzger 2017; Rezzolla et al. 2018). For our extreme NS masses we choose to use binaries with $m_2 = 1.0 M_{\odot}$ and $m_2 = 2.0 M_{\odot}$ NSs, where m_2 is the mass of the lighter object in the binary. We shall not investigate how the masses of their companions affect the results and simply set them to $m_1 = m_2 + 0.1 M_{\odot}$.

It may be possible for both of the NSs in a NSNS binary to produce a RSF, resulting in two RSFs separated by a duration determined by how the difference in their masses affects their *i*-mode frequencies. However, mechanisms by which a bright flare could be produced when the NS crust resonantly shatters typically require the NS to have a strong *surface* magnetic field (Tsang et al. 2012; Neill et al. 2022). Most NSNS systems will have been born and evolved as a binary, and for a binary to merge within the Hubble time it must be fairly tight, meaning that the first star to collapse and become a NS will likely accrete a significant amount of matter during the evolution of its binary partner. NSs that accrete a significant amount of matter will have their magnetic fields buried (Alpar et al. 1982; Bhattacharya & van den Heuvel 1991; Cumming et al. 2001), making it unlikely that they will be capable of producing RSFs. In the majority of NSNS binaries the NS that formed first will be the more massive one, and so we shall assume that the less massive NSs in our binaries are always the ones to produce the RSFs, while the more massive ones do not. Two RSFs could be produced by a binary that formed dynamically in a dense stellar environment (Ye et al. 2020), or from a binary that initially had a large separation such that no accretion took place but was later ‘kicked’ (Ghodla et al. 2022) into a closer orbit, but these scenarios will be rare and so we shall not consider them here.

3.2 NS mass uncertainty from GW inference

For a real multimessenger event the masses of the objects in the binary will not be well known, as while GWs allow for a precise measurement of the binary’s chirp mass,

$$\mathcal{M} = \frac{m_1^{3/5} m_2^{3/5}}{m_1^{1/5} + m_2^{1/5}}, \quad (2)$$

they do not strongly constrain the masses of the individual objects. However, the dependence of *i*-mode frequency on NS mass shown in Figure 1 is strong enough that the frequency range corresponding to a large mass uncertainty could be comparable to the uncertainty in *i*-mode frequency values measured using coincident GW and RSF timing (Tsang et al. 2012). When inferring the parameters of our NS meta-model using such frequency measurements we should therefore account for the uncertainty in the mass of the NS which produced the RSF.

We could try to estimate reasonable mass uncertainties by examin-

ing the results of real GW analyses, but currently only a small number of binary mergers involving NSs have been detected (Abbott et al. 2019, 2020b, 2021b) and so such estimates might not be representative of all mergers. Instead, to get estimates of the uncertainties in the masses of objects involved in binary mergers, we use `Billby` (Ashton et al. 2019) to obtain realistic posterior probability distributions for the analysis of those binary’s GW signals. `Billby` is a Python module for performing Bayesian inference, with its main focus being GW binary parameter inference. It also contains functionality to generate synthetic GW signals from a provided set of binary parameters, allowing us to inject our artificial binaries and then investigate the precision to which their masses can be recovered.

We assume that preliminary analysis of a GW signal will allow for a strong prior on its chirp mass and consequently determine whether it originates from a NSNS binary with reasonable confidence. To generate the synthetic GW signal for a binary and perform parameter recovery we must inject a set of extrinsic and intrinsic parameters (i.e. parameters that are and are not dependent on the observer’s position relative to the binary system). The full parameter space of this is very large, and so rather than recovering every parameter we reduce computation times by fixing some parameters that we do not expect to have significant degeneracy with NS mass to their injected values. The parameter which we do not fix are listed in Table 1, alongside the priors we use for their recovery. As is typical for GWs, rather than directly inferring the separate masses of the objects in the binary we infer the mass ratio and chirp mass, as they more directly affect GW signals. When generating synthetic GW signals, we assume detections involving the LIGO (Livingston and Hanford) and Virgo interferometers, and use estimates of their O4 sensitivities (Abbott et al. 2020a)¹. Note that, in light of current detector status, these sensitivities might only be achieved in the second half of O4 or during O5.

Aside from the mass ratio and chirp mass, the other intrinsic parameters we recover are spin and tidal deformability. The spin of the more massive object in the binary is included in our inferences with the same low-spin prior as Abbott et al. (2017), which is based on not having observations of NS in close binaries with high spins. We do not include the spin of the less massive object, because in order to produce a bright RSF it must have a strong magnetic field (Neill et al. 2022) and such a field will cause its spin to decay to near-zero long before merger. It is worth noting that in GWs there can be significant degeneracy between mass and spin, and so broader spin priors could increase mass uncertainty (e.g. Abbott et al. 2017), but we do not concern ourselves with that here. For simplicity we also assume that the spin and orbit axes are perfectly aligned.

Tidal deformability is the property of NS matter that has the lowest-order effect on GW emission. For each of our NSs we use our injected EOS to calculate its injected value, which scales with NS mass as m^{-5} . This strong mass-dependence means that the reasonable range for tidal deformability values varies by up to an order of magnitude for different NS masses, and so using the same prior at all masses would result in it being either too tightly constrained at low mass or a too broad at high mass, making the posteriors sensitive to the choice of prior. We therefore choose to use a mass-dependent tidal deformability prior. Using a large selection of samples from our NS meta-model over wide parameter ranges, we find that the range of mass-tidal deformability relationships is contained within the bounds

$$500m^{-4-m} \leq \Lambda(m) \leq 10000m^{-4-m} \quad (3)$$

where m is the NS mass in units of solar masses. The distribution of mass-tidal deformability relationships from these samples is non-uniform and might be better fit by a truncated normal distribution, but for simplicity we shall just use a uniform prior between these bounds. We use equation (3) for both Λ_1 and Λ_2 , ignoring that their values should be correlated for two NSs that share the same EOS. Λ_1 is of course fixed to zero for BHs.

The injected tidal deformability values are obtained from our injected EOS, but for the other parameters listed in Table 1 we randomly draw values to inject from their priors. Aside from the parameters we sample, other properties such as the binary inclination, sky location and luminosity distance need injected values, which we draw from uninformed probability distributions: the isotropic $p(i) = \sin(i)$ for binary inclination, uniform-in-sky for sky location, uniform-in-volume for luminosity distance, and so on. However, the extrinsic parameters – in particular luminosity distance and binary inclination – strongly affect the GW signal-to-noise ratio (SNR). Therefore, as we are only interested in mergers that are detected in GWs and not those that are too weak to be clearly detected, for each injected event we repeatedly sample sets of extrinsic parameters until we find a set for which the SNR is $\gtrsim 8$ in all three LIGO and Virgo interferometers, comfortably above the threshold for a GW trigger (Abbott et al. 2021a). We also restrict the luminosity distance to below 200 Mpc, as beyond this distance NSNS mergers will rarely have high SNRs.

We use the `IMRPhenomPv2_NRTidal` and `IMRPhenomNSBH` waveform models to inject and recover NSNS and BHNS mergers, respectively. For computational expediency we use `Billby`’s implementation of the relative binning method (Krishna et al. 2023) with the precision parameter $\epsilon = 0.001$ radians, which allows for the inferences to be completed in hours instead of days or weeks. Posteriors for one of our artificial binaries, which consists of NSs with masses 1.167 and 1.342 M_\odot , are shown in Figure 2. Comparing these to the posteriors of an inference for the same GW signal without relative binning, the difference is small, so this precision seems reasonable. As expected, the chirp mass of the binary is well constrained while the mass ratio (and thus the separate masses of the NSs) is more uncertain. Some uncertainty is introduced to the chirp mass through its correlation with the poorly recovered spin χ_1 , but it is still very accurately determined. However, if a prior were used which allowed higher spins – which would be more reasonable in the case of, for example, a dynamically formed NSNS binary – then this correlation could be more impactful. Our other injected binaries result in posteriors that are qualitatively similar to those shown in Figure 2.

We convert the mass ratio and chirp mass posterior samples used in Figure 2 into the masses of the individual NSs, which are shown in Figure 3. These are reasonably well constrained, having uncertainties of $\sim 0.1 M_\odot$, and the inferences for our other injected binaries give similar uncertainties. From Figure 1 we can see that over a range of a few times $0.1 M_\odot$ the change in i -mode frequency is not large relative to changes from small variations of our meta-model’s parameters, which could indicate that mass uncertainty will not affect the results of parameter inference using i -mode frequency measurements. In the next section we shall perform such inferences to see if this is the case.

4 PARAMETER INFERENCE USING MASS-DEPENDENT i -MODE FREQUENCY MEASUREMENTS

4.1 Prior parameter distribution and current constraints

We begin constructing our prior by selecting broad parameter ranges: $25 < J < 43$ MeV, $5 < L < 158$ MeV, $-520 < K_{\text{sym}} < 200$ MeV,

¹ <https://dcc.ligo.org/LIGO-T2000012/public>

Intrinsic parameter	Symbol	Prior distribution
Mass ratio	q	Uniform from 0.125 to 1.0
Chirp mass	\mathcal{M}	Uniform in component masses from $\mathcal{M}_{\text{in}} - 0.2 M_{\odot}$ to $\mathcal{M}_{\text{in}} + 0.2 M_{\odot}$
Tidal deformability of 1st object	Λ_1	Uniform from $500m_1^{-4-m_1}$ to $10000m_1^{-4-m_1}$
Tidal deformability of 2nd object	Λ_2	Uniform from $500m_2^{-4-m_2}$ to $10000m_2^{-4-m_2}$
Higher mass object's aligned spin	χ_1	Uniform from 0 to 0.05
Extrinsic parameter	Symbol	Prior distribution
Polarisation angle	ψ	Uniform from 0 to π
Orbital phase at coalescence	ϕ	Uniform from 0 to 2π
Time of coalescence	t_c	Uniform from $t_{c,\text{in}} - 0.1$ to $t_{c,\text{in}} + 0.1$

Table 1. The parameters included in our Bayesian analyses of NSNS merger GW signals with `Billby`, and their prior probability distributions. The subscript “in” indicates the injected value of the parameter. The prior for Λ_1 is only for NSNS binaries, as its value is fixed to zero for BHNS binaries. In addition to these parameters, the prior is shaped by separate constraints on the masses of each object in the binary (see text).

$1.001 < \gamma_1 < 20 \text{ MeV}$ and $1.001 < \gamma_2 < 20 \text{ MeV}$. We reject any section of this parameter space which produces an unstable nuclear matter equation of state. To this we add the constraint that the NS maximum mass must satisfy $2.1 < M_{\text{max}} < 2.5 M_{\odot}$. The lower bound of $2.1 M_{\odot}$ is above the mass ranges we obtain from GW inference for all of our artificial binaries, meaning that our prior already contains all of the maximum NS mass information these GW analyses would provide. Our inferences using *i*-mode frequency data in this Section will therefore not be contaminated by also containing new information about the NS maximum mass, isolating the benefit of probing the *i*-mode frequency. The upper bound sits comfortably above the values suggested by current observations (Fonseca et al. 2021; Romani et al. 2022) and helps to limit the parameter space of our meta-model that produces more improbable models. These maximum mass constraints mainly affect the ranges of our meta-model’s core polytrope parameters, as the maximum mass is sensitive to the high-density equation of state.

The polytropes that we use in the core result in the speed of sound (c_s) continually increasing with density, and have no physical content to prevent it from becoming greater than the speed of light. To ensure that this most basic of physical requirements is satisfied, if the parameter values of a sample from the prior would result in the speed of sound becoming greater than the speed of light at a density that can be found in NSs – i.e. anywhere below the central density of the maximum mass NS – then we simply set its prior probability to zero. This approximately translates to rejecting samples with $\gamma_1 \gtrsim 5$, and with high γ_2 when γ_1 is not very low.

The prior we have constructed is very wide, and our knowledge of the symmetry energy is better than that as multimessenger RSF and GW events are of course not the only way to constrain the symmetry energy parameters. We shall therefore also consider various experimental constraints on NSs and nuclear matter, to which we can then add information from RSFs. We list the nuclear physics constraints we consider in Table 2. These constraints are from combining the results of various experimental in quadrature (Newton & Cromcombe 2021), and so the errors given in the Table’s caption are optimistic lower bounds. We use each of the listed values as the mean of a normal distribution, with its error as its standard deviation. Our nuclear physics likelihood for a sample from the prior is then the product of all of the normal distributions at the values produced by that sample.

The main effect of this nuclear physics data is to constrain the lower order symmetry energy parameters, and in particular J . This can be seen from the results plotted in grey in Figure 5, where the J range is substantially smaller than the 25 to 43 MeV range chosen for our

Nucleus	E_B (MeV)	r_{ch} (fm)	r_{np} (fm)	α_D (fm ³)
¹⁶ O	127.62	2.699		
⁴⁰ Ca	342.05	3.478		
⁴⁸ Ca	415.99	3.477	0.195	2.07
⁵⁶ Ni	483.99	3.477		
¹³² Sn	1102.85	4.709		
²⁰⁸ Pb	1636.43	5.501	0.178	19.6

Table 2. Nuclear data we include in our inferences to incorporate our current understanding of the symmetry energy parameters. From left to right: binding energies, charge radii, neutron skin thicknesses, and dipole polarisabilities. We take the errors on the binding energies and charge radii to be 3 MeV for all binding energies, 0.02fm for all charge radii. We 0.013 and 0.011 fm (0.22 and 0.6 fm³) for the neutron skins (dipole polarisabilities) of ⁴⁸Ca and ²⁰⁸Pb, with the neutron skin errors from a number of measurements compiled in Newton & Cromcombe (2021), and references therein.

prior. We can also see that correlations appear between the J and L parameters, and between the L and K_{sym} parameters. Nuclear masses give their most stringent constraints a little above half saturation density. If J is higher, then in order to reach the same value of the sub-saturation symmetry energy, the slope of the symmetry energy must be steeper - i.e. L must be larger. Likewise, for a given value of J , if we increase L , then the slope must change more rapidly to maintain the same value of the sub-saturation symmetry energy. This results in the positive correlations seen in Figure 5 (Lattimer & Lim 2013).

4.2 Injected *i*-mode frequency measurements

Now that we have results for current constraints, we can add measurements of NS properties from multimessenger GW and RSF events to examine how they might improve our understanding of NSs and nuclear matter. Multimessenger RSF and GW events allow for measurements of the *i*-mode frequency within their progenitor NSs, which can be used to infer the structure and composition of the NS crust (Neill et al. 2023). A RSF occurs when a NS’s (quadrupolar) *i*-mode is resonant with the binary orbit, and the frequency of (quadrupolar) GWs is twice the orbital frequency, meaning that the GW frequency at the time at which a RSF occurs (f_{RSF}) will be approximately equal to the frequency of that NS’s *i*-mode (f_{2i}). However, the finite duration of a RSF means that a measurement of the *i*-mode frequency from coinci-

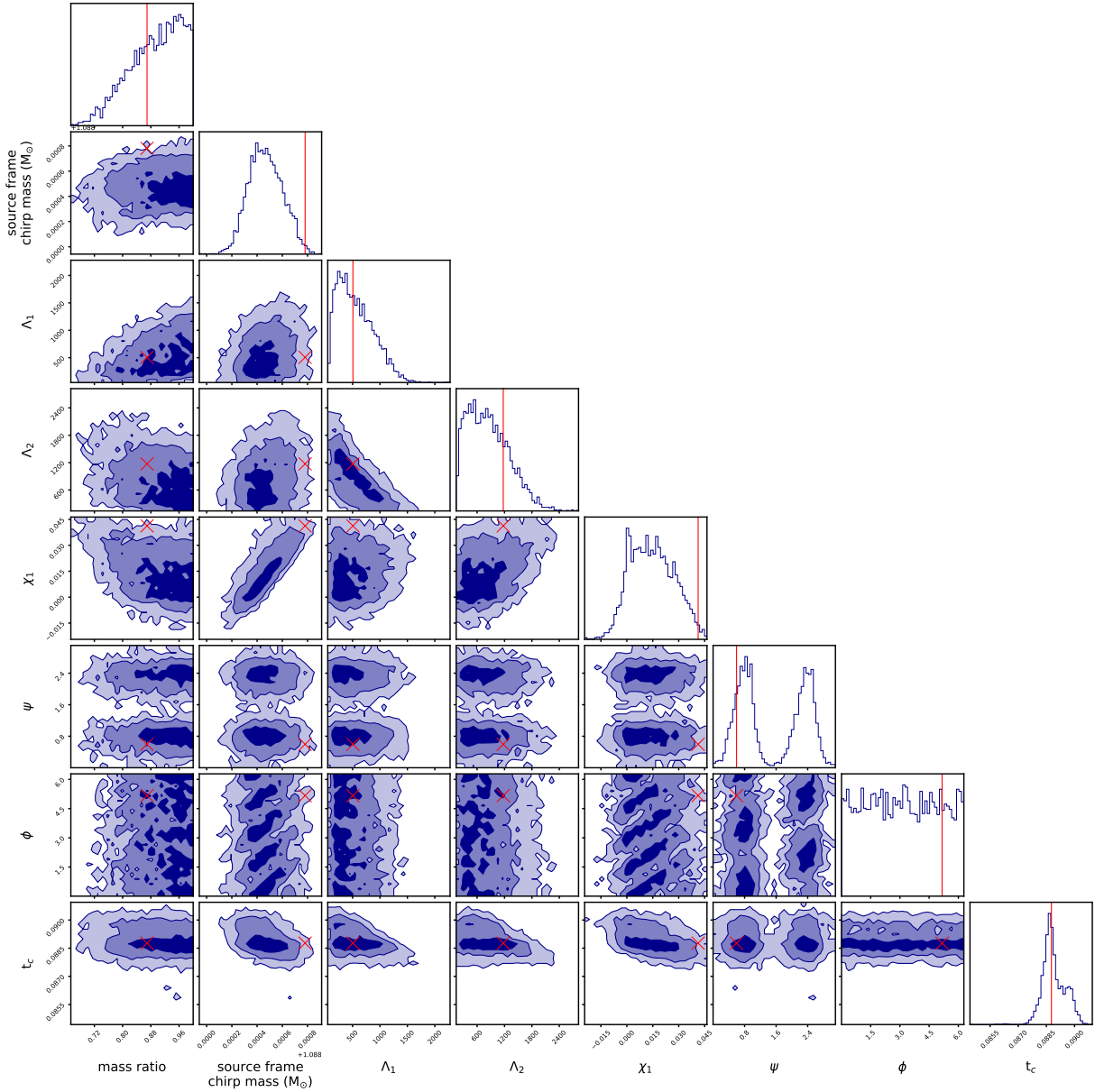


Figure 2. Example posteriors for a NSNS binary’s parameters recovered using Bayesian inference of an injected GW signal with Bilby, showing the scale of the uncertainties we can expect from such a signal. The first four parameters describe the masses and tidal deformabilities of both objects in the binary, and the fifth is the spin of the more massive one. The remaining three are extrinsic (observer-dependent) parameters. Other parameters could be relevant to GW inference, but for computational expediency they have been fixed to their injected values during this inference. The injected values of the inferred parameters are shown as red lines or markers on each plot. The priors used are given in Table 1.

dent GW and RSF timing will include some uncertainty, on the order of the change in GW frequency over the duration of the flare. For each injected binary system we therefore estimate this uncertainty to construct a probability distribution for the i -mode frequency.

We choose to use a normal distribution for each frequency measurement, centred on the value calculated using our injected NS model for a NS with mass m_2 (i.e., that NS’s “true” i -mode frequency). We calculate i -mode frequency values by combining the outputs of the TOV equations with Yoshida & Lee (2002)’s relativistic pulsation equations. For the i -mode frequency distribution’s standard deviation, we use the change in GW frequency during the

i -mode’s resonance (Tsang et al. 2012):

$$\delta f \sim t_{\text{res}} \left. \frac{\partial f_{\text{GW}}}{\partial t} \right|_{f_{\text{RSF}}} \sim 11.19 \text{ Hz} \left(\frac{M}{1.2 M_{\odot}} \right)^{\frac{5}{6}} \left(\frac{f_{\text{RSF}}}{200 \text{ Hz}} \right)^{\frac{11}{6}}. \quad (4)$$

The likelihood that a NS with mass m_{NS} following the EOS corresponding to the parameter values $\theta \equiv \{J, L, K_{\text{sym}}, \gamma_1, \gamma_2\}$ produced an injected RSF is therefore

$$L(f_{\text{RSF}}|\theta, m_{\text{NS}}) = \exp\left(-\frac{1}{2} \frac{(f_{2i}(\theta, m_{\text{NS}}) - f_{\text{RSF}})^2}{\delta f^2}\right) \quad (5)$$

where for our injections $f_{\text{RSF}} = f_{2i}(\Phi, m_2)$, with Φ being the injected parameter values.

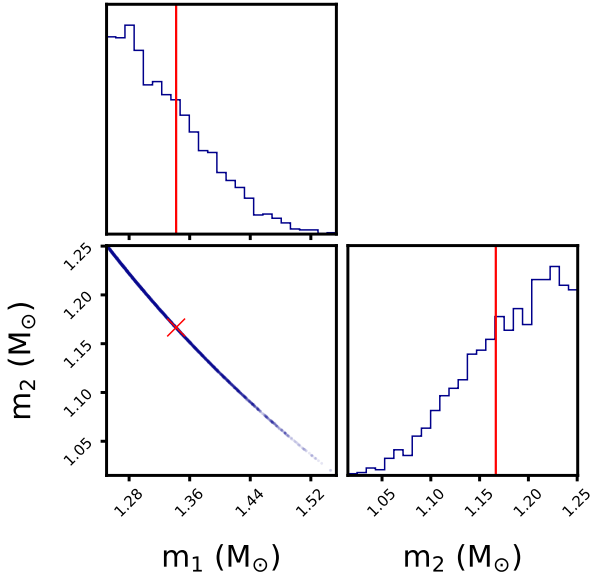


Figure 3. The NS mass posteriors corresponding to the chirp mass and mass ratio posteriors from Figure 2. This m_2 posterior is the mass uncertainty we use for this NS in our meta-model parameter inferences in Section 4.

In Figure 4 we combine the uncertainty in i -mode frequency from coincident timing with the uncertainty in m_2 from GW analysis to show how our 5 injected mergers with random masses inform us of the injected mass-frequency relationship. We can see that the BHNS binary (orange) gives qualitatively different mass and frequency information to the NSNS binaries (red, green, blue, cyan). The BHNS has a larger frequency uncertainty because its higher chirp mass causes a higher rate of change of orbital frequency during resonance, while the NSNS binaries’ mass distributions have sharp cutoffs at half their total masses. This is because total mass is well constrained by GW analysis, meaning that there is a strong upper limit on the mass of the less massive object in a binary. The NSNS binaries are all close enough to being equal mass that this affects their posteriors, while the BHNS binary is clearly not near equal mass. However, the changes in the mass-frequency relationship across the mass uncertainty ranges are small for all of these binaries. Given that this relationship is similar for all of the NS models shown in Figure 1, we therefore expect that the relative likelihoods of different NS models will be similar to the relative likelihoods obtained when fixing the masses to their injected values.

Each i -mode frequency measurement included in an inference that is taken from a different RSF introduces additional parameters: the parameters of the binary that can affect the NS i -mode frequency. In this work we assume that the NS’s mass is the only one of these parameters that could significantly affect the i -mode, as while properties such as the NS’s spin and temperature can affect the i -mode we expect that they will be negligible (approximately zero in the cases of spin and temperature) for any NS that produces a RSF. However, adding even one extra parameter per i -mode frequency measurement means that the computation time required to sample the parameter space will increase significantly as more measurements are considered. To keep our computation times reasonable for this work, we avoid increasing the parameter space by not fully including the NS masses as parameters to be inferred. Instead, for each measurement we marginalise over the mass parameter in Bayes equation to find the

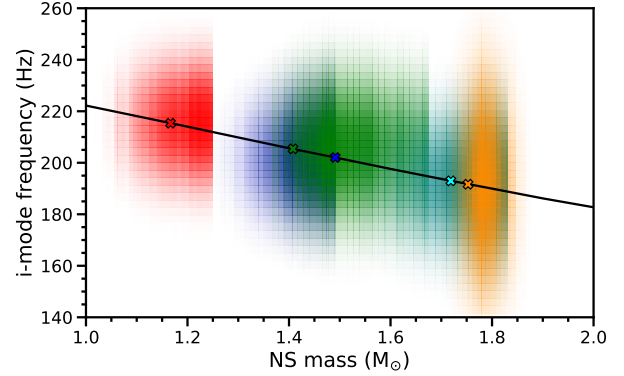


Figure 4. The injected data we use for the masses and i -mode frequencies of five NSs, showing the sort of information we can expect to obtain from multimessenger RSF and GW events. The evidence from each merger is shown in a different colour, with darker shades indicating greater evidence. The injected i -mode frequency and mass values are shown as markers (with the same colours as their evidences), which lie along the injected NS model’s mass-frequency relationship.

likelihood function:

$$L(f_{\text{RSF},i}|\theta) = \int L(f_{\text{RSF},i}|\theta, m_{2,i}) \pi(\theta, m_{2,i}) dm_{2,i}, \quad (6)$$

where the integral is over the range of Bilby’s posterior for m_2 in this binary ($p_{\text{GW}}(m_2)$), and π is the probability distribution given by

$$\pi(\theta, m_{2,i}) = \begin{cases} p_{\text{GW}}(m_2) & \text{if } m_2 \leq m_{\text{max}}(\theta) \\ 0 & \text{if } m_2 > m_{\text{max}}(\theta). \end{cases} \quad (7)$$

This marginalisation over mass means that the posteriors from our inferences will not show any correlations that might exist between the masses and the other parameters, but the weakness of the mass-frequency relationship means that such correlations are unlikely to be significant.

When combining measurements of the i -mode frequency from several multimessenger RSF and GW events, the total likelihood function for our Bayesian inference is simply the product of likelihood functions for each event,

$$L(f_{\text{RSF},1}, \dots, f_{\text{RSF},N}|\theta) = \prod_{i=1}^N L(f_{\text{RSF},i}|\theta), \quad (8)$$

since we can safely assume that binary mergers are isolated from each other. This total likelihood can then be used alongside the prior probability distribution

$$\pi(\theta) = \frac{1}{A_{\gamma_1 \gamma_2}(J, L, K_{\text{sym}})} \quad (9)$$

which we introduced in Section 4.1 to obtain the posterior distribution. To do this, we use the Markov chain Monte Carlo (MCMC) method via the emcee python module (Foreman-Mackey et al. 2013).

4.3 Recovering the injected NS meta-model parameter values

We first examine whether the mass uncertainty from GW analysis can affect the results of meta-model parameter inferences that use i -mode frequency measurements. The posteriors of an inference using no frequency measurements (i.e., only including the experimental nuclear data) and of inferences using the measurement shown in green in Figure 4 with and without its mass uncertainty are shown in

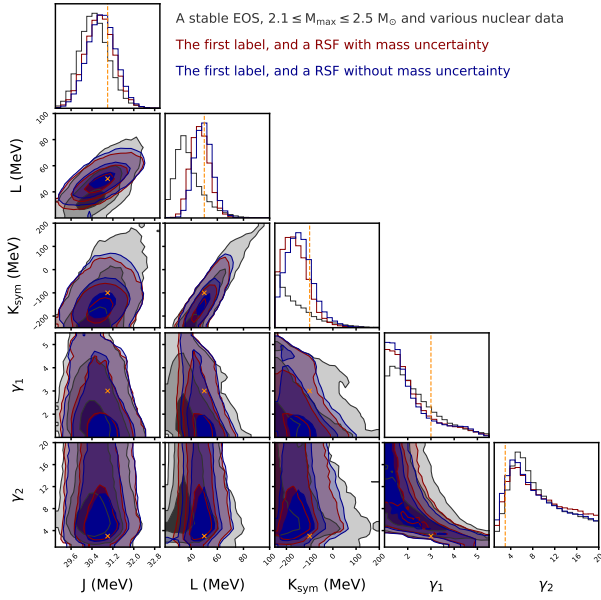


Figure 5. Posteriors probability distributions from Bayesian inferences of our NS meta-model’s parameters using different data, showing that *i*-mode frequency measurements from multimessenger RSF and GW events can improve on symmetry energy constraints from nuclear physics, and that including realistic uncertainty in NS mass has only a small impact on the results. The grey posteriors are for an inference using data from nuclear experiment and a constraint on the maximum NS mass, while the red and blue posteriors are for inferences that also included a single *i*-mode frequency measurement (the green one in Figure 4) with and without mass uncertainty (respectively). The injected values are indicated by the orange markers and dashed lines.

Figure 5. From this we can see that mass uncertainty has little effect of the posteriors, even in the relatively extreme case of this particular data where the injected mass value is far from the center of the mass range inferred with Bi1by. This Figure confirms that marginalising over mass in our likelihood function does not lose much information, as two different mass distributions giving almost identical posteriors indicates that correlations between the model parameters and the NS mass are insignificant.

As found by (Neill et al. 2023), Figure 5 shows that a single *i*-mode frequency measurement can improve symmetry energy constraints obtained from nuclear experiment. We next examine how combining measurements from several multimessenger events could further strengthen these constraints: posteriors for inferences using 1 and 5 injected frequency measurements (with mass uncertainty) are shown in Figure 6. From this we see that little information is gained about the core as the polytrope parameters change little with additional *i*-mode frequency data, but the symmetry energy is better constrained with additional measurements. While the posteriors for J are similar as it is already well constrained by nuclear experiment, the L and K_{sym} posteriors are substantially improved.

Figure 6 includes data from four NSNS binaries and one BHNS binary, but in Figure 4 we saw that these different types of binary can give qualitatively different *i*-mode frequency measurements. Therefore, to investigate whether symmetry energy constraints obtained from a RSF depend the type of binary which produced it, we compare the results of inferences using *i*-mode frequency measurements from a single NSNS binary and from a single BHNS binary. To eliminate other variables we inject two new binaries with identical extrinsic parameters and the same NS mass of $m_2 = 1.4M_{\odot}$, but that have different masses for the binary partner: $m_1 = 1.6M_{\odot}$ or

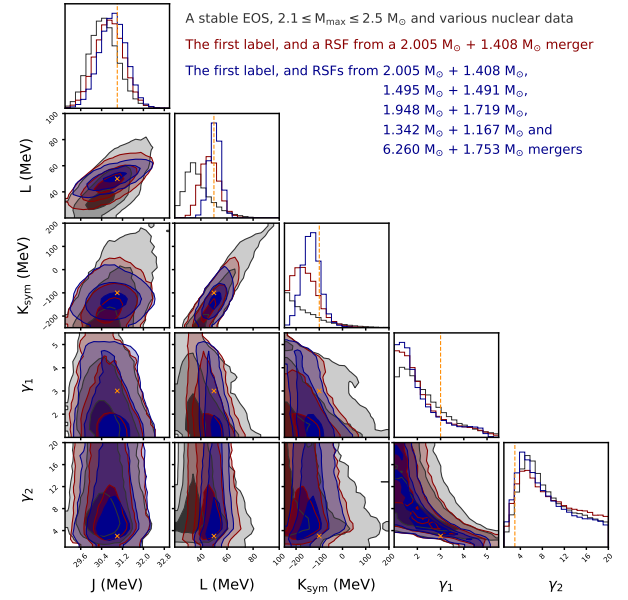


Figure 6. Similar to Figure 5, but for the posteriors of inferences using 1 (red) and 5 (blue) of the *i*-mode frequency measurements from Figure 4, showing that measurements after the first continue to improve the symmetry energy constraints. Both inferences included NS mass uncertainty. The labels give the injected masses of the compact binary mergers for which the measurements were constructed.

$m_1 = 7.0M_{\odot}$. The posteriors of their meta-model parameter inferences are shown in Figure 7. Both noticeably improve over the prior for L and K_{sym} , but the NSNS binary gives better constraints.

Much of the benefit of measuring the masses and radii of multiple NSs comes from the increased knowledge of the mass-radius relationship, the shape of which can vary significantly for different EOSs. Compared to posteriors for a single measurement, the posteriors for five frequency measurements shown in Figure 6 may similarly benefit from having information about the mass-frequency relationship, but this systematic benefit is combined with statistical improvements from having more data. To separate these effects, we compare posteriors of an inference using two frequency measurements from NSs with very different masses – which maximises the influence of the (near-linear) mass-frequency relationship – to posteriors of inferences using two identical measurements. From this Figure however we can see that there is little benefit to probing the mass-frequency relationship, as two frequency measurements from identical NSs can be just as good for constraining the symmetry energy parameters as two measurements from NSs with very different masses. Any multimessenger RSFs and GW events detected after the first will therefore be useful for constraining the symmetry energy, not just those that probe a new section of the mass-frequency relationship.

5 DISCUSSION

From Figures 5, 6, 7 and 8 we can see that there is some benefit to having measurements of the *i*-mode frequency from multiple different multimessenger events, and that the mass of the NS which produced a RSF has little impact on the symmetry energy constraints that can be obtained from it. This does not mean that NS mass is irrelevant for RSFs, as it may still have an effect on the RSF emission mechanism that could make it easier to detect RSFs from higher or

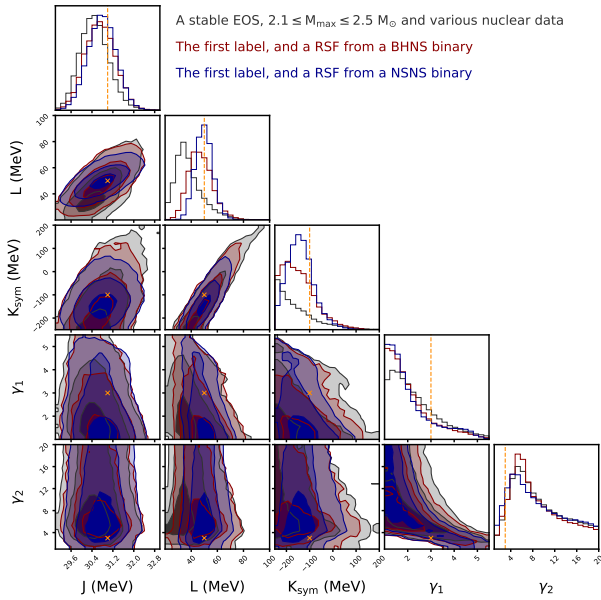


Figure 7. Similar to Figure 5, but comparing posteriors of inferences using i -mode frequency and NS mass measurements from a single BHNS merger (red) and from a single NSNS merger (blue). The NSNS merger appears to give better constraints, indicating that frequency uncertainty from coincident RSF and GW timing is more significant than how the i -mode frequency may change over realistic mass uncertainties. All properties of the injected binaries are identical except for the primary mass.

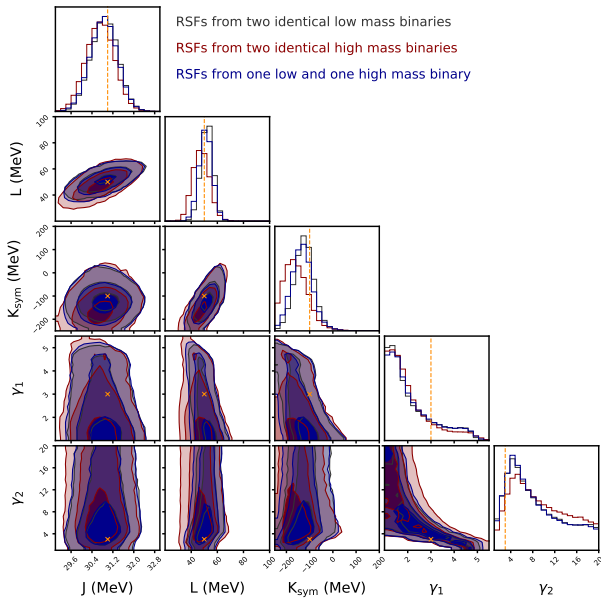


Figure 8. Similar to Figure 6, but isolating the benefit of probing the mass-frequency relationship, which is shown to be negligible as the blue posteriors do not recover the injected parameters significantly better than the other posteriors. Each inference uses i -mode frequency measurements from two RSFs, with grey (red) using two identical low mass (high mass) NS progenitors, while blue uses one low mass and one high mass progenitor. All three require a stable EOS and reasonable maximum mass, and include various nuclear data.

lower mass NSs, but once a RSF is detected alongside GWs it is as useful as any other.

Figure 6 also shows that there is little change in the inferred values of the core polytrope parameters when using additional i -mode frequency measurements, which is due to the i -mode frequency having little dependence on the NS core (as found in Neill et al. 2023). This sets it apart from bulk properties such as NS radius and tidal deformability, and means that it can be used to probe the composition of the NS crust and outer core without concern for the type of matter present deeper within the core, which is currently uncertain.

Higher-order terms in the symmetry energy expansion control the EOS further away from saturation density. In our model the expansion coefficients of the symmetry energy at higher order than K_{sym} are correlated with the lower order parameters, but it has been shown that the size of the effects of the fourth-order term Q_{sym} may not be negligible down to $0.5n_{\text{sat}}$ and up to $1.5n_{\text{sat}}$, with the crust composition showing some sensitivity to that parameter (Carreau et al. 2019). It is therefore important to extend the model to include freedom in that parameter in future studies, as degeneracies between it and the J , L and K_{sym} parameters considered in this work may affect their posteriors.

The symmetry energy expansion is around nuclear saturation, but the i -mode frequency is sensitive to neutron star properties at the crust core transition around half that density. Model dependencies arise in our posteriors for the parameters of the expansion from how the symmetry energy may evolve between these densities in our model. Therefore, while the symmetry energy parameters at saturation are more commonly considered in the literature, it may be more useful to examine posteriors on the symmetry energy itself. Figure 9 shows posteriors for the nuclear symmetry energy that, for our meta-model, correspond to the posteriors for its first three parameters shown in Figure 6, incorporating effects of the higher-order parameters that are not free within our model. Figure 9 therefore shows what the symmetry energy parameter posteriors actually mean in the context of our meta-model, and we see that i -mode frequency measurements mainly inform us of the symmetry energy around half saturation density (highlighted in the inset). Freedom in how the symmetry energy varies with density for any particular sample is also limited by model-dependencies, but that is not shown in here.

One should interpret the symmetry energy constraints above nuclear saturation density in Figure 9 with care. Although they appear improved with i -mode measurements, the lack of freedom for the terms at higher order than K_{sym} in our model reduces the freedom to explore density dependencies at higher densities and leading to an over-optimistic constraint there. The density to which the constraints from our model are robust should be explored further. However, the constraints up to saturation density are on a firmer footing, as that is where the i -mode is sensitive to.

The NSNS binary used for Figure 7 had higher mass uncertainty and lower frequency uncertainty than the BHNS binary, so its better parameter recovery indicates that the frequency uncertainty has a more significant effect on these posteriors. The frequency uncertainty from equation (4) is lower for the NSNS binary because of its lower chirp mass, so applying this result more broadly would suggest that binaries with lower masses are slightly better for RSF and GW coincident timing. The difference between the posteriors for two high and two low mass NSNS binaries in Figure 8 appears to support this. However, as equation (4) is only a rough approximation, binary mass might not actually be a primary contributor to RSF duration, and variables unrelated to the binary – such as the configurations of instruments involved in a detection – could be more important for the uncertainty in the duration of real multimessenger events.

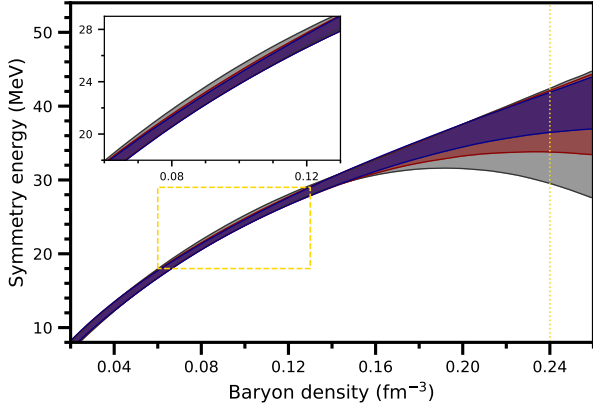


Figure 9. Nuclear symmetry energy posteriors corresponding to the posteriors for its parameters shown in Figure 6, showing how they are related within our model-dependent setup. At any given density the shaded regions contain the central 90% of symmetry energy values for samples in the posteriors, and the same colours are used as in Figure 6. The inset highlights the density range that *i*-mode frequency measurements inform us of (indicated by the yellow box), which is around the crust-core transition density. The vertical line indicates the density beyond which the symmetry energy has no effect on our models since we switch to a polytropic model for the NS EOS. As we have seen in Figures 5–8, the nuclear data constrains the magnitude of the symmetry energy at a density of around 0.1 fm^{-3} . Resonant shattering flares meanwhile constrain the slope and curvature of the symmetry energy at that density: differences that show up at higher densities where the improvement from the astrophysical data is more apparent.

The mass-frequency relationships shown in Figure 1 are all very similar and near-linear, meaning that when we measure mass and frequency we are effectively just constraining the intercept of a linear relationship. Measurements from different NSs therefore all effectively inform us of the same one property. This is supported by Figure 8, which shows that constraining the mass-frequency relationship does not provide much advantage over measuring a single point along it. The changes we see in Figure 6 when adding more multimessenger measurements are therefore primarily due to the statistical improvements of measuring the same property multiple times. It is possible that the similarity of the mass-frequency relationships shown in Figure 1 is particular to our meta-model and that methods of generating NS models that have more freedom could allow for more variety, in which case it would be more beneficial to detect RSFs from NSs with a variety of different masses.

While in this work we have not carried forward any information about tidal deformability from GW analysis to the meta-model parameter inference, combining tidal deformability inferences with *i*-mode frequency measurements could be extremely interesting, as the former is sensitive to the properties of whichever type of matter exists in the NS core while the latter depends on the nucleonic crust. An *i*-mode frequency measurement from a multimessenger RSF and GW event could be used to confidently constrain the properties of nucleonic matter in NSs at a low density, which could then be expanded up to higher densities to compare to the properties inferred from tidal deformability. Inconsistency between the properties of nucleonic matter inferred at high and low densities would indicate that matter is not nucleonic in the core or that current nucleonic models are insufficient to explain both high and low density matter, giving some insight into the mysterious nature of extremely dense nuclear matter.

All of the posteriors we have shown are for inferences which in-

cluded the experimental nuclear data listed in Table 2. Without this data to reduce the size of the symmetry energy parameter space subsequent frequency measurements are much less useful, as degeneracies between the different parameters would be much more significant. It is therefore important to not just analyse this astrophysical data in a vacuum, but rather combine it with terrestrial nuclear physics.

5.1 Model dependence and caveats

The Skyrme model is one model for the nuclear interaction and has different density dependencies than, for example, relativistic mean-field models. However, extended Skyrme models increase the freedom in the density dependence and offset this problem. Nevertheless, the possibility remains that systematically different predictions of the EOS and crust composition may be made by different nuclear models, and should be explored in the future.

Our inferences using Bilby in Section 3.2 contain several simplifications to make them quicker. For example, while the tidal deformability prior we used in Section 3.2 was roughly based on our meta-model it did not exactly follow it, and in particular we did not account for how the tidal deformabilities of two NSs with the same EOS and different masses should be correlated. Inferring the meta-model parameters and then calculating the tidal deformability would be a more complete way to account for our choice of model, or alternatively a different tidal deformability prior could be used that considers a wider variety of NS models than just those produced by our meta-model. We also fixed several extrinsic and intrinsic properties, such as the sky position and luminosity distance of the binary, and for real data these would be included, making these inferences significantly longer and possibly increasing NS mass uncertainty through correlations with these extra parameters. However, even if mass uncertainty were significantly higher, from Figure 5 it does not seem likely that it would strongly affect the symmetry energy parameter inferences.

It is worth noting that for a real multimessenger event it would be better to perform a single parameter inference incorporating both the GW signal and coincident timing, rather than separating them into two as we have done in this work. It would allow for complementary information from these data to be combined in a statistically consistent way, and help to avoid losing relevant information, such as how we did not carry forward the tidal deformability posteriors from Bilby to our meta-model parameter inferences. In this work it has not been a significant problem and separating it into two steps made it our inferences simpler to perform, but when working with real data we should be more cautious.

We chose to construct our prior for the meta-model parameters to be uniform in the viable $J - L - K_{\text{sym}} - \gamma_1 - \gamma_2$ parameter space. However, as we have constructed the core with polytropes that cause the sound speed to monotonically increase with density, fixed the density of the transition to the polytropic model (to $1.5n_{\text{sat}}$), and required that viable EOSs remain causal at least until the central density of their most massive NSs, this prior will be somewhat biased towards combinations of J , L and K_{sym} that result in lower sound speeds at the polytropic transition density, since lower sound speeds allow wider viable spaces for γ_1 and γ_2 . This is not necessarily physical, as other models – such as those that include exotic matter in the NS core – can have sound speed vary more freely throughout the core and so do not need to have low values at low densities in order to remain causal.

Figure 10 is similar to Figure 9 but attempts to remove the bias towards low sound speeds at the polytropic transition density by using a prior that is uniform in the 3D J - L - K_{sym} space obtained when

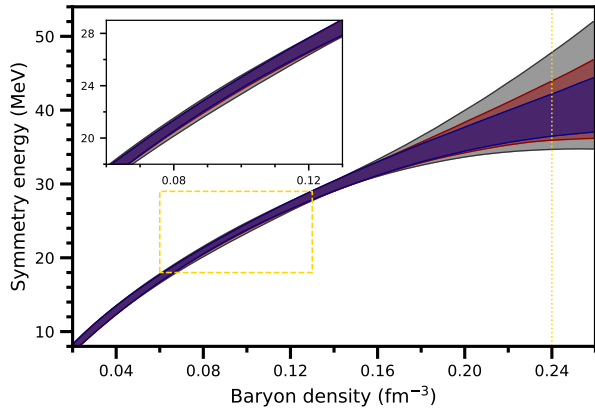


Figure 10. Similar to Figure 9, but for posteriors obtained when using a prior designed to reduce the impact of how we chose to construct models for the NS core. The posteriors informed by several *i*-mode frequency measurements are similar to those in Figure 9, indicating that while the choice of prior has some influence it is not very important when considering a reasonable amount of data.

marginalising over the core polytrope parameters. This is done by giving any 5D sample a prior probability that is inversely proportional to the area of the viable $\gamma_1 - \gamma_2$ space at its $J-L-K_{\text{sym}}$ values. This causes the prior to artificially favour NS EOSs that are soft above $1.5n_{\text{sat}}$, rather than soft below $1.5n_{\text{sat}}$ as the prior used in the rest of this work does. However, by comparing Figures 10 and 9 we can see that the posteriors informed by *i*-mode frequency data are similar regardless of the choice of prior, indicating that it is not of great importance. This means that, so long as a reasonable prior is used, the quantitatively meaningful results for real data should not be too sensitive to the choice of prior.

The frequency uncertainty obtained from coincident RSF and GW timing is significant. By comparing Figures 1 and 4 we can see that the uncertainty we assumed with equation (4) is not small when compared to the effects of changing the meta-model parameters, so reducing it could help to further constrain the parameters. Equation (4) uses a rough approximation for the duration of the resonance and does not involve any consideration of the uncertain strength of the neutron star crust, and so the actual range of GW frequencies during which the *i*-mode is sufficiently excited to shatter the NS crust may be significantly longer or shorter. However, coincident RSF and GW timing might not be the only way to infer the *i*-mode frequency from a detected RSF. Other methods involving analysis of the RSF lightcurve – its duration, luminosity, variability timescale, etc. – could provide additional insight into the *i*-mode and the NS crust, which could be used to improve a frequency measurement or obtain one where no GWs are detected.

6 CONCLUSION

The mass of a neutron star is important for its bulk properties such as radius and tidal deformability. In particular, the relationships between these properties and mass are sensitive to the equation of state of the neutron star core, so probing them by obtaining measurements from several neutrons stars with known different masses provides new insights into the physics of dense matter. In this work, we have investigated whether having multiple measurements of the crust-core interface mode’s frequency – as could be obtained from coincident timing of resonant shattering flares and gravitational waves – would

provide a similar improvement for our understanding of matter within neutron stars. Using realistic uncertainties in neutron star masses inferred with gravitational wave analysis and conservative uncertainties in *i*-mode frequency measurements obtained from coincident timing, we found that combining frequency measurements from NSs with different masses noticeably improves the nuclear symmetry energy constraints obtained from them. We found that this is not so much due to the mass-dependence of the *i*-mode frequency – as it is only a weak dependence and is similar across the range of neutron star models we considered – but rather is the general statistical improvements from having multiple measurements of the same property. This means that any additional frequency measurements could be useful, not just those from NSs with masses that are well-determined or that have not been seen previously.

While obtaining multiple *i*-mode frequency measurements from coincident RSF and GW timing could strengthen constraints on the NS model and the nuclear symmetry energy parameters, it is just as important to combine these constraints with those from other sources to break degeneracies between the symmetry energy parameters. Bulk NS properties – which are more commonly inferred from NS observations – might not be reliable for this as the nature of the NS core is unknown, but other NS asteroseismic observables and data from nuclear experiment can fill this role, as NS meta-models such as the one used in this work allow us to consistently connect neutron star structure to the fundamental properties of nucleonic matter. In light of the results of the recent PREX-II (Adhikari et al. 2021) and CREX (Adhikari et al. 2022) experiments, combining data from new methods of probing nuclear matter is particularly interesting as it opens new ways to explore the tension between them.

Efforts to probe NSs with astrophysical observables are progressing at a steady pace, with constraints on masses, radii and tidal deformabilities (e.g. Abbott et al. 2017, 2019; Riley et al. 2019, 2021; Fonseca et al. 2021) giving us an increasing amount of insight into their structure. While a multimessenger RSF and GW event has yet to be observed, the findings of Neill et al. (2023) – that coincident timing of these events allows us to probe a different region of the NS to most observables – and of this work – that even with realistic uncertainties we only require a single such detection to obtain strong constraints – makes them highly interesting. However, this work has also shown that observing several multimessenger events is beneficial for our understanding of nuclear matter, particularly when combined with data from experimental nuclear physics.

Multimessenger detections of binary mergers are of great interest to the astrophysical community, and we remain optimistic about the possibility of observing multimessenger RSF and GW events in the remainder of the O4 LIGO/Virgo observing run, or early in O5. We have shown such observations with the sensitivity of those runs would allow us to obtain strong astrophysical constraints on NS crust composition and the nuclear symmetry energy, meaning that they are interesting for nuclear physics as well.

ACKNOWLEDGEMENTS

This work used the Isambard 2 UK National Tier-2 HPC Service (<http://gw4.ac.uk/isambard/>) operated by GW4 and the UK Met Office, and funded by EPSRC (EP/T022078/1). The authors gratefully acknowledge the University of Bath’s Research Computing Group (doi.org/10.15125/b6cd-s854) for their support in this work. DN and DT were supported by the UK Science and Technology Facilities Council (ST/X001067/1) and the Royal Society (RGS/R1/231499). WGN was supported by NASA (80NSSC18K1019). We also thank

Natalie Williams and Hannah Middleton for useful discussion about the usage of Bilby.

DATA AVAILABILITY

The posterior samples generated for this work are available upon request. This work made use of `emcee` (Foreman-Mackey et al. 2013) version 3.1 and `Bilby` (Ashton et al. 2019) version 2.1.

REFERENCES

- Abbott B. P., et al., 2017, *Phys. Rev. Lett.*, **119**, 161101
- Abbott B. P., et al., 2018, *Phys. Rev. Lett.*, **121**, 161101
- Abbott B. P., et al., 2019, *Physical Review X*, **9**, 011001
- Abbott B. P., et al., 2020a, *Living Reviews in Relativity*, **23**, 3
- Abbott B. P., et al., 2020b, *ApJ*, **892**, L3
- Abbott R., et al., 2021a, *arXiv e-prints*, p. arXiv:2111.03606
- Abbott R., et al., 2021b, *ApJ*, **915**, L5
- Adhikari D., et al., 2021, *Phys. Rev. Lett.*, **126**, 172502
- Adhikari D., et al., 2022, *Phys. Rev. Lett.*, **129**, 042501
- Alpar M. A., Cheng A. F., Ruderman M. A., Shaham J., 1982, *Nature*, **300**, 728
- Andersson N., 1998, *ApJ*, **502**, 708
- Ashton G., et al., 2019, *ApJS*, **241**, 27
- Balliet L. E., Newton W. G., Cantu S., Budimir S., 2021, *ApJ*, **918**, 79
- Bhattacharya D., van den Heuvel E. P. J., 1991, *Physics Reports*, **203**, 1
- Carreau T., Gulminelli F., Margueron J., 2019, *European Physical Journal A*, **55**, 188
- Chen L.-W., Ko C. M., Li B.-A., Xu J., 2010, *Phys. Rev. C*, **82**, 024321
- Cumming A., Zweibel E., Bildsten L., 2001, *ApJ*, **557**, 958
- Davesne D., Pastore A., Navarro J., 2016, *A&A*, **585**, A83
- Duncan R. C., 1998, *ApJ*, **498**, L45
- Dutra M., Lourenço O., Sá Martins J. S., Delfino A., Stone J. R., Stevenson P. D., 2012, *Phys. Rev. C*, **85**, 035201
- Eldridge J. J., Stanway E. R., Xiao L., McClelland L. A. S., Taylor G., Ng M., Greis S. M. L., Bray J. C., 2017, *Publ. Astron. Soc. Australia*, **34**, e058
- Essick R., Landry P., Schwenk A., Tews I., 2021, *Phys. Rev. C*, **104**, 065804
- Fonseca E., et al., 2021, *ApJ*, **915**, L12
- Foreman-Mackey D., Hogg D. W., Lang D., Goodman J., 2013, *PASP*, **125**, 306
- Galloway D. K., Muno M. P., Hartman J. M., Psaltis D., Chakrabarty D., 2008, *ApJS*, **179**, 360
- Ghodla S., van Zeist W. G. J., Eldridge J. J., Stevance H. F., Stanway E. R., 2022, *MNRAS*, **511**, 1201
- Haensel P., Zdunik J. L., Douchin F., 2002, *A&A*, **385**, 301
- Hinderer T., Lackey B. D., Lang R. N., Read J. S., 2010, *Phys. Rev. D*, **81**, 123016
- Israel G. L., et al., 2005, *ApJ*, **628**, L53
- Kokkotas K. D., Schafer G., 1995, *MNRAS*, **275**, 301
- Krishna K., Vijaykumar A., Ganguly A., Talbot C., Biscoveanu S., George R. N., Williams N., Zimmerman A., 2023, *arXiv e-prints*, p. arXiv:2312.06009
- Lai D., 1994, *MNRAS*, **270**, 611
- Landry P., Read J. S., 2021, *ApJ*, **921**, L25
- Lattimer J. M., Lim Y., 2013, *ApJ*, **771**, 51
- Lattimer J. M., Prakash M., 2001, *The Astrophysical Journal*, **550**, 426
- Lattimer J. M., Prakash M., 2007, *Phys. Rep.*, **442**, 109
- Levin Y., 2007, *MNRAS*, **377**, L59
- Li B.-A., Krastev P. G., Wen D.-H., Zhang N.-B., 2019, *European Physical Journal A*, **55**, 117
- Lim Y., Holt J. W., 2017, *Phys. Rev. C*, **95**, 065805
- Margalit B., Metzger B. D., 2017, *ApJ*, **850**, L19
- Martinez J. G., et al., 2015, *ApJ*, **812**, 143
- McDermott P. N., van Horn H. M., Hansen C. J., 1988, *ApJ*, **325**, 725
- Miller M. C., et al., 2019, *ApJ*, **887**, L24
- Miller M. C., et al., 2021, *ApJ*, **918**, L28
- Nättilä J., Miller M. C., Steiner A. W., Kajava J. J. E., Suleimanov V. F., Poutanen J., 2017, *A&A*, **608**, A31
- Neill D., Newton W. G., Tsang D., 2021, *MNRAS*, **504**, 1129
- Neill D., Tsang D., van Eerten H., Ryan G., Newton W. G., 2022, *MNRAS*, **514**, 5385
- Neill D., Preston R., Newton W. G., Tsang D., 2023, *Phys. Rev. Lett.*, **130**, 112701
- Newton W. G., Crocombe G., 2021, *Phys. Rev. C*, **103**, 064323
- Newton W. G., Gearheart M., Li B.-A., 2013, *ApJS*, **204**, 9
- Newton W. G., Preston R., Balliet L., Ross M., 2022, *Physics Letters B*, **834**, 137481
- Oppenheimer J. R., Volkoff G. M., 1939, *Physical Review*, **55**, 374
- Özel F., Psaltis D., Güver T., Baym G., Heinke C., Guillot S., 2016, *ApJ*, **820**, 28
- Piekarewicz J., Agrawal B. K., Colò G., Nazarewicz W., Paar N., Reinhard P. G., Roca-Maza X., Vretenar D., 2012, *Phys. Rev. C*, **85**, 041302
- Radice D., Perego A., Zappa F., Bernuzzi S., 2018, *ApJ*, **852**, L29
- Raithel C. A., 2019, *European Physical Journal A*, **55**, 80
- Read J. S., Lackey B. D., Owen B. J., Friedman J. L., 2009, *Phys. Rev. D*, **79**, 124032
- Reed B., Horowitz C., PREX/CREX Collaboration Team 2022, in APS April Meeting Abstracts. p. H12.007
- Reinhard P.-G., Nazarewicz W., 2022, *Phys. Rev. C*, **105**, L021301
- Rezzolla L., Most E. R., Weih L. R., 2018, *ApJ*, **852**, L25
- Riley T. E., et al., 2019, *ApJ*, **887**, L21
- Riley T. E., Watts A. L., et al., 2021, *ApJ*, **918**, L27
- Roca-Maza X., Brenna M., Agrawal B. K., Bortignon P. F., Colò G., Cao L.-G., Paar N., Vretenar D., 2013, *Phys. Rev. C*, **87**, 034301
- Romani R. W., Kandel D., Filippenko A. V., Brink T. G., Zheng W., 2022, *ApJ*, **934**, L17
- Skyrme T. H. R., 1958, *Nuclear Physics*, **9**, 615
- Smartt S. J., et al., 2017, *Nature*, **551**, 75
- Sotani H., 2024, *Phys. Rev. D*, **109**, 023030
- Stanway E. R., Eldridge J. J., 2018, *MNRAS*, **479**, 75
- Steiner A. W., Lattimer J. M., Brown E. F., 2010, *ApJ*, **722**, 33
- Strohmayer T. E., Watts A. L., 2005, *ApJ*, **632**, L111
- Tolman R. C., 1939, *Physical Review*, **55**, 364
- Trippa L., Colò G., Vigezzi E., 2008, *Phys. Rev. C*, **77**, 061304
- Troja E., et al., 2018, *MNRAS*, **478**, L18
- Tsang D., Read J. S., Hinderer T., Piro A. L., Bondarescu R., 2012, *Phys. Rev. Lett.*, **108**, 011102
- Ye C. S., Fong W.-f., Kremer K., Rodriguez C. L., Chatterjee S., Fragione G., Rasio F. A., 2020, *ApJ*, **888**, L10
- Yoshida S., Lee U., 2002, *A&A*, **395**, 201
- Yüksel E., Paar N., 2023, *Physics Letters B*, **836**, 137622
- Zhang Z., Chen L.-W., 2016, *Phys. Rev. C*, **94**, 064326
- Zhang Z., Chen L.-W., 2022, *arXiv e-prints*, p. arXiv:2207.03328

This paper has been typeset from a $\text{\TeX}/\text{\LaTeX}$ file prepared by the author.

Microscopic description of hexadecapole collectivity in even-even rare-earth nuclei around $N = 90$

L. Lotina^{1,*} and K. Nomura^{2,3,†}

¹*Department of Physics, Faculty of Science, University of Zagreb, HR-10000 Zagreb, Croatia*

²*Department of Physics, Hokkaido University, Sapporo 060-0810, Japan*

³*Nuclear Reaction Data Center, Hokkaido University, Sapporo 060-0810, Japan*

(Dated: March 7, 2024)

We present an extensive study of hexadecapole correlations in the rare-earth region around $N = 90$ and the effects these correlations have on various nuclear properties, such as the low-energy spectra, as well as quadrupole, hexadecapole and monopole transition strengths. In order to examine hexadecapole correlations, we employ a mapped *sdg* interacting boson model, with parameters derived from a self-consistent mean-field calculations with a relativistic energy density functional. We apply this model to even-even isotopes of Nd, Sm, Gd, Dy and Er ($Z = 60 - 68$) with the neutron number $N = 84 - 96$. The obtained results show a good agreement with the experiment. By comparing the results with the ones obtained from a simpler mapped *sd* interacting boson model, we show that the inclusion of hexadecapole, *g* boson is necessary to improve the results of the $J^\pi \geq 6^+$ yrast energies in the nuclei with $N = 84$ and 86 , being near the neutron shell closure. The *sdg* interacting boson model increases the quadrupole transition strengths between yrast states in the $N = 90$ and 92 well deformed nuclei, which is in good agreement with the experiment for most of those isotopes. The presence of *g* bosons does have an important effect on hexadecapole transition strengths, although experimental data for such transitions are limited. The obtained monopole transition strengths do not differ significantly from the ones obtained from the simpler *sd* model.

I. INTRODUCTION

Nuclear deformations play an important role in describing various nuclear properties [1, 2], e.g. excitation energies and decays. The dominant deformations in nuclei, the quadrupole ones, have been extensively studied. More and more attention is recently being paid to higher-order deformations, such as the octupole and hexadecapole ones. The effects of hexadecapole correlations are often overshadowed by large quadrupole effects. Nevertheless, they have been found to exist in a wide spectrum of nuclei, ranging from light nuclei [3] to heavy nuclei [4]. The main effect of hexadecapole correlations on the low-lying energy spectrum of the nucleus is the appearance of the low-lying $K = 4^+$ band with an enhanced $B(E4; 4^+ \rightarrow 0^+)$ transition strength. Another effect can be observed in even-even rare-earth nuclei near $N = 82$ shell closure, where the ratio of the ground-state band energies $R_{4/2} = E_x(4^+)/E_x(2^+)$ becomes less than 2. Besides that, hexadecapole deformations were shown to play a significant role in heavy ion collisions [4], fission [5], and are predicted to have an influence on the neutrinoless double beta decay matrix elements in open shell nuclei [6]. All of this provides us with a good reason to study hexadecapole correlations in nuclei and their effects on the low-lying excitation spectra and transitions.

A useful framework for studying the effects of nuclear deformations is the interacting boson model (IBM) [7]. In the simplest version of the IBM, the nucleus can be

viewed as a system composed of a doubly-magic core nucleus, and valence nucleons grouped into *s* ($L^\pi = 0^+$) and *d* ($L^\pi = 2^+$) bosons. The main assumption of the model is that the main contribution to the low-lying excitation energy spectra comes from the pairing correlations between aforementioned bosons. In the version of the model called IBM-1, it is assumed that the neutron and proton bosons are identical [7]. This model has been successfully used to study the effects of deformations in nuclei [8]. Since the IBM is a phenomenological model, in recent times, a method was developed that derives the parameters of the IBM Hamiltonian from a self-consistent mean-field (SCMF) model with energy density functionals (EDFs) [9]. This method has been successfully applied in studying quadrupole [9–12] and octupole correlations [13, 14] in nuclei. The inclusion of the hexadecapole degree of freedom in the IBM is done by the inclusion of *g* boson with $L^\pi = 4^+$, whose importance in the IBM has been extensively studied [8, 15–21]. While the *sdg*-IBM has been extensively studied as a phenomenological model, it is useful to study the model through a more microscopic picture, e.g. the aforementioned mapping method, since that could lead us to a better understanding of the microscopic origin of the hexadecapole collectivity in nuclei.

In the preceding article [22], we have explored the hexadecapole collectivity in $^{148-160}\text{Gd}$ isotopes by using the *sdg*-IBM-1 with the Hamiltonian parameters being derived by the mapping method of Ref. [9], and have showed the validity and usefulness of such approach. The aim of the present article is to extend the study to a wider range of even-even rare-earth isotopes, $^{144-156}\text{Nd}$, $^{146-158}\text{Sm}$, $^{148-160}\text{Gd}$, $^{150-162}\text{Dy}$ and $^{152-164}\text{Er}$. We choose the rare-

* llotina.phy@pmf.hr

† nomura@sci.hokudai.ac.jp

earth isotopes for our study due to the fact that hexadecapole correlations were observed in that region [1, 23–27], as well as due to the fact that triaxiality does not play a significant role in these isotopes, as evident from the SCMF calculations with the Skyrme force [10] and Gogny force [28]. By comparing our model with a simpler mapped *sd*-IBM-1, we explore the effects of hexadecapole correlations on the low-lying excitation energy spectra of these isotopes, and also on the monopole, quadrupole and hexadecapole transition strengths.

The paper is organized as follows. In Sec. II we describe our model. Section III gives the quadrupole-hexadecapole potential energy surfaces for the studied nuclei. Results of the spectroscopic properties, including the excitation spectra of low-lying states, electric quadrupole, hexadecapole, and monopole transition properties, are discussed in Sec. IV. Summary of the main results and some perspectives for future work are given in Sec. V.

II. MODEL DESCRIPTION

We begin our analysis with the SCMF calculations. The model employed for SCMF calculations is the multi-dimensionally constrained relativistic mean-field (MDC-RMF) model [29–31], which allows one to set constraints on various deformation parameters. For our analysis, we carried out the SCMF calculations for axially symmetric shapes in the (β_2, β_4) plane, by setting the constraints on the mass quadrupole Q_{20} and hexadecapole Q_{40} moments. The dimensionless quadrupole β_2 and hexadecapole β_4 deformation parameters are related to the mass moments through the relation:

$$\beta_\lambda = \frac{4\pi}{3AR^\lambda} \langle \hat{Q}_{\lambda 0} \rangle \quad (1)$$

with $R = 1.2A^{1/3}$ fm. The quadrupole-hexadecapole constrained potential energy surfaces (PESs) are calculated within the relativistic Hartree-Bogoliubov (RHB) framework [32, 33], with the chosen energy density functional being the density-dependent point-coupling (DD-PC1) interaction [33, 34], combined with the separable pairing interaction of finite range developed in Ref. [35]. A detailed description of the MDC-RMF model can be found in Refs. [30, 31].

Due to the fact that SCMF calculations necessarily break several symmetries, these calculations alone cannot be used to study excited states and transitions in the nucleus. To study those properties of the nucleus, we use the *sdg*-IBM-1 model. A simple version of the *sdg*-IBM-1 Hamiltonian is given by the following relation, similar to the one from [20]:

$$\hat{H}_{sdg} = \epsilon_d \hat{n}_d + \epsilon_g \hat{n}_g + \kappa_2 \hat{Q}^{(2)} \cdot \hat{Q}^{(2)} + \kappa_4 \hat{Q}^{(4)} \cdot \hat{Q}^{(4)}. \quad (2)$$

The first two terms represent the *d* and *g* boson number operators, $\hat{n}_d = d^\dagger \cdot \tilde{d}$ and $\hat{n}_g = g^\dagger \cdot \tilde{g}$. The second

term represents the quadrupole-quadrupole interaction with the quadrupole operator defined as

$$\hat{Q}^{(2)} = (s^\dagger \tilde{d} + d^\dagger s) + \chi_{dd}^{(2)} (d^\dagger \times \tilde{d})^{(2)} + \chi_{dg}^{(2)} (d^\dagger \times \tilde{g} + g^\dagger \times \tilde{d})^{(2)} + \chi_{gg}^{(2)} (g^\dagger \times \tilde{g})^{(2)}, \quad (3)$$

while the last term represents the hexadecapole-hexadecapole interaction, with the hexadecapole operator defined as:

$$\hat{Q}^{(4)} = (s^\dagger \tilde{g} + g^\dagger s) + \chi_{dd}^{(4)} (d^\dagger \times \tilde{d})^{(4)} + \chi_{dg}^{(4)} (d^\dagger \times \tilde{g} + g^\dagger \times \tilde{d})^{(4)} + \chi_{gg}^{(4)} (g^\dagger \times \tilde{g})^{(4)}. \quad (4)$$

Since this Hamiltonian is too complex, due to the number of parameters it contains, a simplification can be made by assuming three symmetry limits, $U(5) \otimes U(9)$, $SU(3)$ and $SO(15)$, which leads to a Hamiltonian [21]:

$$\hat{H}_{sdg} = \epsilon_d \hat{n}_d + \epsilon_g \hat{n}_g + \kappa \hat{Q}^{(2)} \cdot \hat{Q}^{(2)} + \kappa (1 - \chi^2) \hat{Q}^{(4)} \cdot \hat{Q}^{(4)}, \quad (5)$$

with

$$\hat{Q}^{(2)} = (s^\dagger \tilde{d} + d^\dagger s) + \chi \left[\frac{11\sqrt{10}}{28} (d^\dagger \times \tilde{d})^{(2)} - \frac{9}{7} (d^\dagger \times \tilde{g} + g^\dagger \times \tilde{d})^{(2)} + \frac{3\sqrt{55}}{14} (g^\dagger \times \tilde{g})^{(2)} \right] \quad (6)$$

and

$$\hat{Q}^{(4)} = s^\dagger \tilde{g} + g^\dagger s \quad (7)$$

being the quadrupole and hexadecapole operators, respectively.

The parameters ϵ_d , ϵ_g , κ and χ are determined by the mapping procedure [9]. The first step is connecting the IBM to the geometric model by calculating the expectation value of the Hamiltonian in a coherent state $|\phi\rangle \propto (1 + \tilde{\beta}_2 d_0^\dagger + \tilde{\beta}_4 g_0^\dagger)^{N_B} |0\rangle$, with N_B representing the number of bosons, i.e., the number of pairs of valence nucleon, and $|0\rangle$ representing the boson vacuum [21]. For Nd, Sm, Gd and Dy isotopes, the boson vacuum corresponds to the double shell closures $(N, Z) = (82, 50)$, i.e., the doubly magic nucleus ^{132}Sn , while for the Er isotopes, since the valence neutrons are considered hole-like, the corresponding boson vacuum is taken to be $(N, Z) = (82, 82)$. The expectation value, $\langle \phi | \hat{H} | \phi \rangle / \langle \phi | \phi \rangle$, gives us the PES of the IBM, and is denoted $E_{\text{IBM}}(\tilde{\beta}_2, \tilde{\beta}_4)$, with $\tilde{\beta}_2$ and $\tilde{\beta}_4$ being boson analogues of the quadrupole β_2 and β_4 deformations, respectively. The parameters of the Hamiltonian are fitted so that the energy surface of the IBM approximates the PES obtained from the SCMF calculations, $E_{\text{SCMF}}(\beta_2, \beta_4)$, in the vicinity of the minimum:

$$E_{\text{SCMF}}(\beta_2, \beta_4) \approx E_{\text{IBM}}(\tilde{\beta}_2, \tilde{\beta}_4). \quad (8)$$

Following the method of Refs. [9, 14], the relation between bosonic and fermionic deformation parameters is

assumed to be linear, $\tilde{\beta}_2 = C_2\beta_2$, $\tilde{\beta}_4 = C_4\beta_4$. This leaves us with 6 parameters in total to be determined. In the case of lighter rare-earth isotopes, Nd and Sm, the Hamiltonian from Eq. (6) is shown to be inadequate to reproduce the SCMF PES, due to the obtained ratios $\beta_4^{\min}/\beta_2^{\min}$ being larger than in heavier rare-earth isotopes. To solve this problem, an independent parameter σ was introduced in the quadrupole operator of Eq. (6) as:

$$\hat{Q}^{(2)} = (s^\dagger \tilde{d} + d^\dagger s) + \chi \left[\frac{11\sqrt{10}}{28} (d^\dagger \times \tilde{d})^{(2)} - \frac{9}{7} \sigma (d^\dagger \times \tilde{g} + g^\dagger \times \tilde{g})^{(2)} + \frac{3\sqrt{55}}{14} (g^\dagger \times \tilde{g})^{(2)} \right], \quad (9)$$

with constraint $-1 \leq \chi\sigma \leq +1$. If $\chi = \sigma = +1$, the quadrupole operator corresponds to the generator of the SU(3) algebra [36]. It should be noted that, while the hexadecapole terms and the $(g^\dagger \times \tilde{g})^{(2)}$ are included in the Hamiltonian, their contribution to the IBM PES, as well as to the excitation energies, is minimal, and they could, in principle, be omitted from the Hamiltonian.

In order to study the effects of hexadecapole correlations in nuclei, the *sdg* IBM has to be compared with a simpler *sd* IBM, with a Hamiltonian given by the relation [7]:

$$\hat{H}_{sd} = \epsilon_d \hat{n}_d + \kappa \hat{Q}^{(2)} \cdot \hat{Q}^{(2)}, \quad (10)$$

with

$$\hat{Q}^{(2)} = s^\dagger \tilde{d} + d^\dagger s + \chi (d^\dagger \times \tilde{d})^{(2)} \quad (11)$$

being the quadrupole operator. The mapping is performed so that the energy of the *sd* IBM approximates the SCMF PES along the $\beta_4 = 0$ line in the vicinity of the minimum [22]:

$$E_{\text{SCMF}}(\beta_2, \beta_4 = 0) \approx E_{\text{IBM}}(\tilde{\beta}_2), \quad (12)$$

while the relation between the bosonic and fermionic quadrupole deformation parameters is again assumed to be linear, $\tilde{\beta}_2 = C_2^{sd}\beta_2$.

The transition strengths are defined as [14]:

$$B(E\lambda; J \rightarrow J') = \frac{1}{2J+1} |\langle J' | |\hat{T}^{(E\lambda)}| |J\rangle|^2, \quad (13)$$

with $|J\rangle$ and $\langle J'|$ being the wave functions of the initial and final states, respectively. The operators considered are the quadrupole operator

$$\hat{T}^{(E2)} = e_2^{sdg, sd} \hat{Q}^{(2)}, \quad (14)$$

with $\hat{Q}^{(2)}$ corresponding to the quadrupole operator of the *sdg*- or *sd*-IBM [Eqs. (2), (6), and (10)], the hexadecapole operator, defined as

$$\hat{T}^{(E4)} = e_4^{sdg} \left[s^\dagger \tilde{g} + g^\dagger s + (d^\dagger \times \tilde{d})^{(4)} \right] \quad (15)$$

for the *sdg*-IBM, and

$$\hat{T}^{(E4)} = e_4^{sd} (d^\dagger \times \tilde{d})^{(4)} \quad (16)$$

for the *sd*-IBM, and the monopole operator, defined as [37]

$$\hat{T}^{(E0)} = (e_n N + e_p Z) \left(\eta \frac{\hat{n}_d}{N_B} + \gamma \frac{\hat{n}_g}{N_B} \right) \quad (17)$$

for the *sdg*-IBM, and

$$\hat{T}^{(E0)} = (e_n N + e_p Z) \eta \frac{\hat{n}_d}{N_B} \quad (18)$$

for the *sd*-IBM. The $e_2^{sdg, sd}$ coefficients are fitted for each isotope so that the experimentally measured transition strength $B(E2; 2_1^+ \rightarrow 0_1^+)$ from the first 2^+ state to the ground state should be reproduced. Similarly, the $e_4^{sdg, sd}$ coefficients are fitted to the $B(E4; 4_1^+ \rightarrow 0_1^+)$ transition strength. In the case of monopole transitions, following Ref. [37], monopole strengths are defined as

$$\rho(E0) = \frac{\langle J' | \hat{T}^{(E0)} | J \rangle}{eR^2}, \quad (19)$$

with $R = 1.2A^{1/3}\text{fm}$ being the nuclear radius. The parameters $e_{p,n}$ are chosen to be $e_n = 0.50e$, $e_p = e$, following Ref. [37]. However, a different choice from the one in Ref. [37] is made for these parameters, $\eta = \gamma = 0.75 \text{ fm}^2$. This is due to the fact that the Hamiltonians used in this paper are different from ones used in the aforementioned paper. Most of the experimental data are taken from the National Nuclear Data Center (NNDC) database [38].

III. MAPPING THE SCMF RESULTS ONTO THE IBM SPACE

Figures 1-5 show the PESs of the even-even Nd, Sm, Gd, Dy and Er isotopes with the neutron number within the range $N = 84 - 94$, up to 2.7 MeV in energy. The PESs for the $N = 96$ nuclei are not shown due to their similarity to those of the $N = 94$ ones. In addition, the PESs for the Gd isotopes, have already been presented in Ref. [22], but are depicted in Fig. 3 for completeness. From the figures, one can notice that both the quadrupole and hexadecapole deformation parameters increase with the neutron number. The saddle point in the oblate ($\beta_2 < 0$) area is lower in energy for the $N \leq 90$ nuclei and can be seen in the PES. For heavier isotopes, the saddle point becomes higher in energy and cannot be seen in the figures. Quadrupole deformations have a similar structural evolution in all isotopes, starting from $\beta_2^{\min} = 0.1$ at $N = 84$, except for the oblate deformed ^{148}Gd ($\beta_2^{\min} = -0.05$), with the maximum $\beta_2^{\min} = 0.35$ calculated for those nuclei with $N = 94$ and 96. It should be noted that, while ^{148}Gd is predicted to be oblate deformed in the ground state, the PES of this nucleus shows

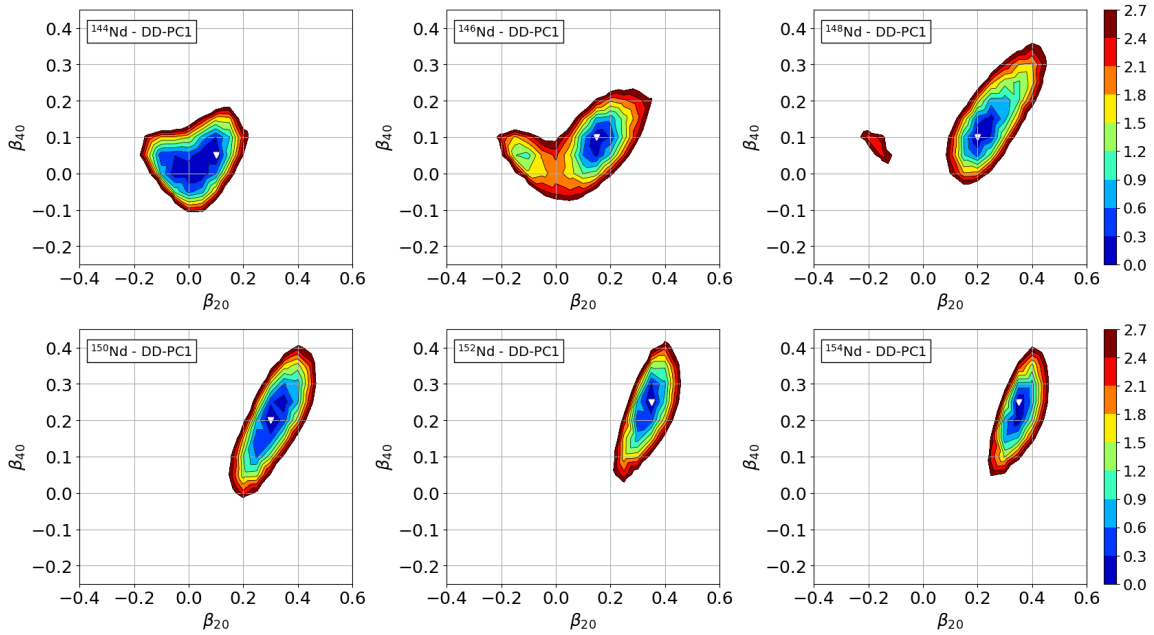


FIG. 1. Axially-symmetric quadrupole (β_{20}) and hexadecapole (β_{40}) constrained energy surfaces for the $^{144-154}\text{Nd}$ isotopes calculated within the relativistic Hartree-Bogoliubov method using the DD-PC1 energy density functional and the pairing force of finite range. Energy difference between neighboring contours is 0.1 MeV, and the absolute minimum is indicated by an open triangle.

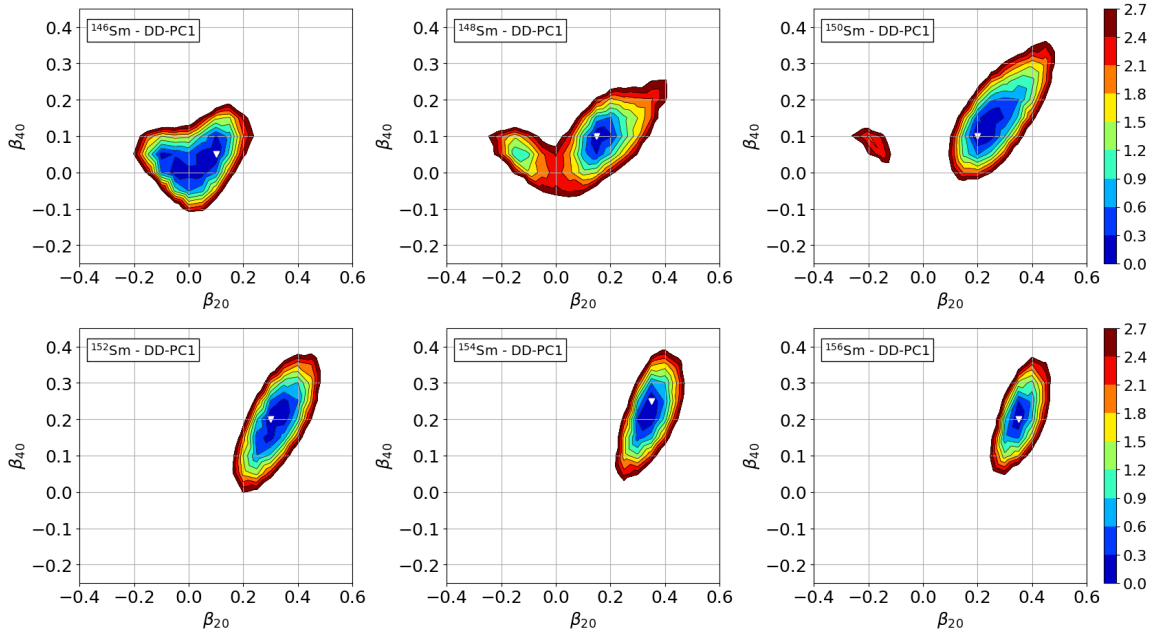


FIG. 2. Same as the caption for Fig. 1, but for $^{146-156}\text{Sm}$

a significant softness with respect to both quadrupole and hexadecapole deformation. The structural evolution of hexadecapole deformations is also similar in all isotopes. Larger hexadecapole deformations in the minimum are obtained for lighter nuclei, Nd and Sm, the largest being

$\beta_4^{\min} = 0.25$ ($^{152,154}\text{Nd}, ^{154}\text{Sm}$). In Gd, Dy and Er isotopes, the largest hexadecapole deformation in the minimum is $\beta_4^{\min} = 0.15$, present in the $N \geq 90$ region. In Dy and Er isotopes, it can be seen that the energy minima for the nuclei in the deformed region (with $N \geq 90$)

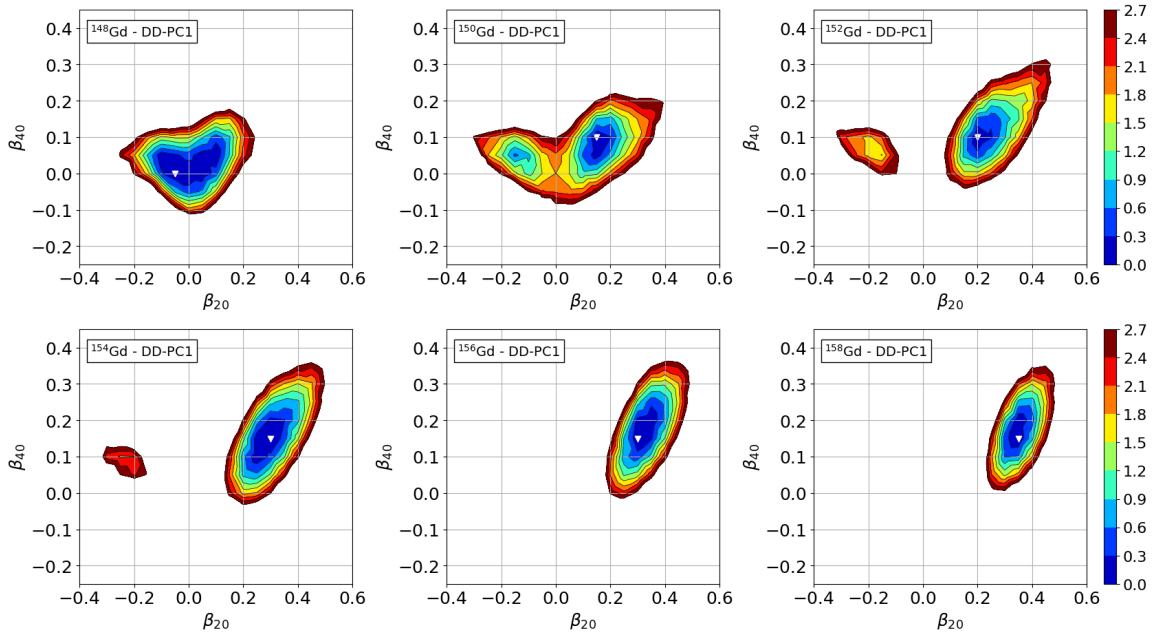


FIG. 3. Same as the caption for Fig. 1, but for $^{148-158}\text{Gd}$.

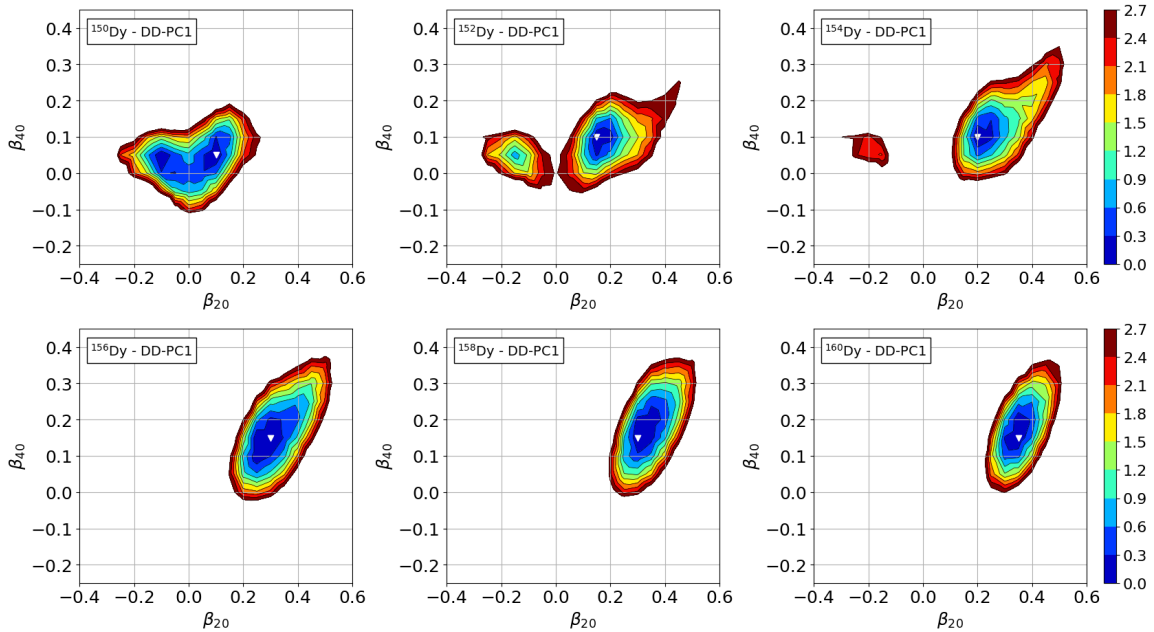


FIG. 4. Same as the caption for Fig. 1, but for $^{150-160}\text{Dy}$.

become softer in the β_4 direction compared to those for the $N = 86$ and 88 nuclei.

The corresponding *sdg*-IBM PESs are shown in Figs. 6-10. One can see that the mapping procedure reproduces some of the basic properties of the SCMF PES, such as the position of the absolute minimum and the saddle point in the $N = 84 - 90$ nuclei. The IBM surface is significantly larger from the SCMF surface, which is a

general feature of the IBM due to the restricted boson space of the model. This was already discussed in the case of quadrupole - octupole mapping [14]. The “tail - like” structure that can be seen in the SCMF PES at $N = 88$ in each isotopic chain, is also not reproduced by the IBM due to the complexities of the SCMF model, which cannot be reproduced by a simple Hamiltonian. While three-body terms would provide an improvement

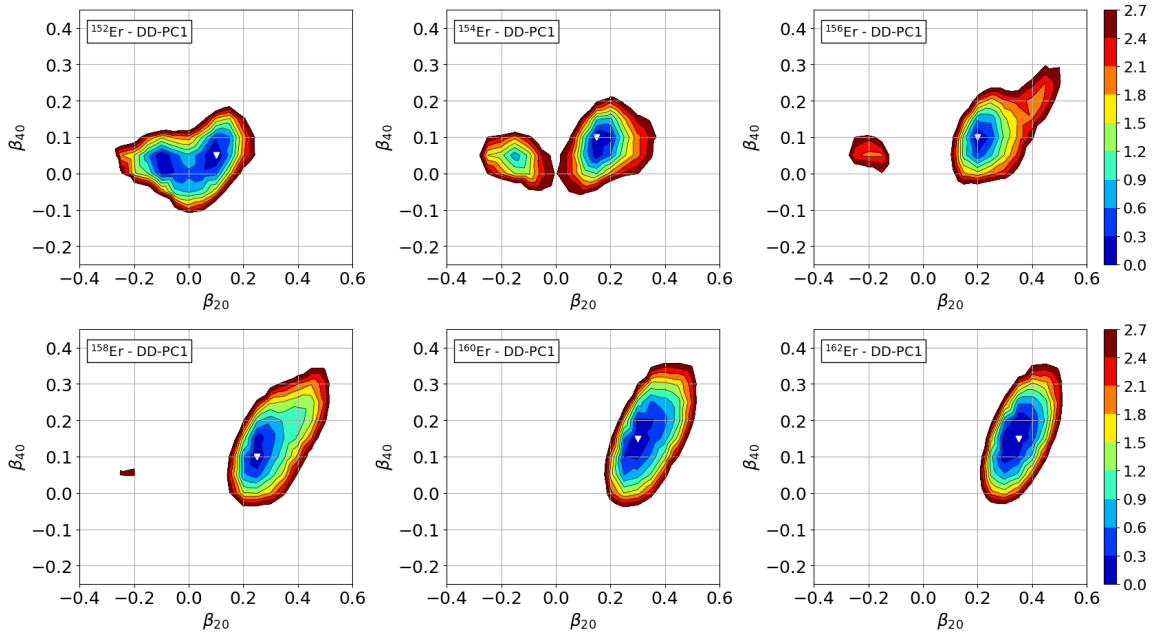


FIG. 5. Same as the caption for Fig. 1, but for $^{152-162}\text{Er}$

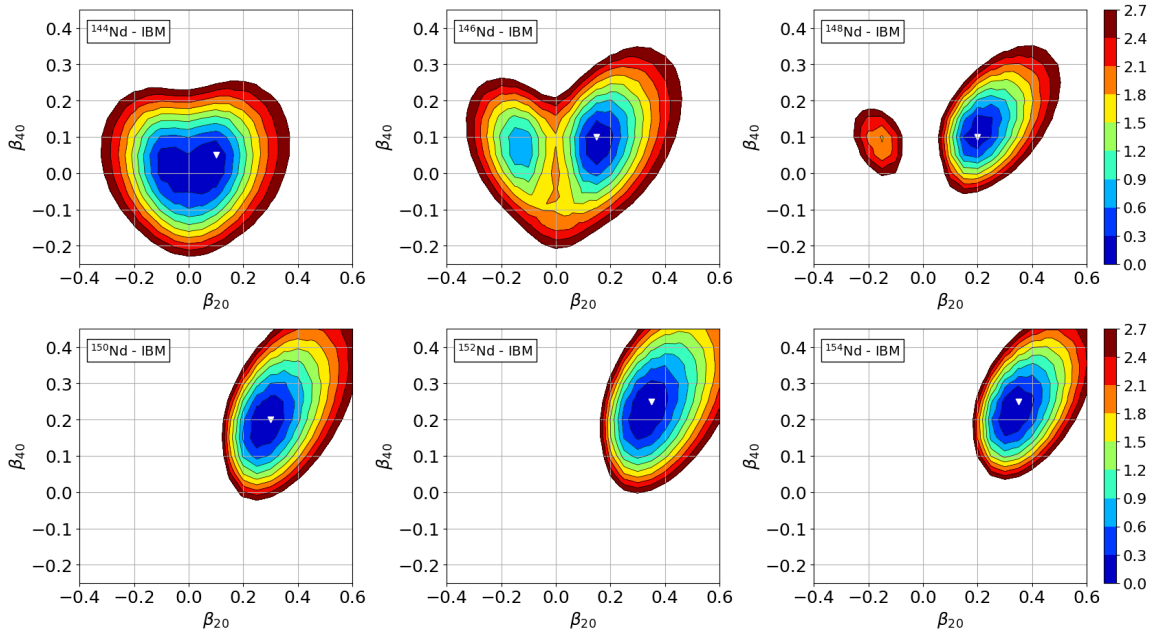


FIG. 6. Same as the caption for Fig. 1, but for the mapped *sdq*-IBM energy surfaces of $^{144-154}\text{Nd}$

to the IBM PES, such terms are rarely included in the Hamiltonian and are beyond the scope of this study. In the case of the *sd*-IBM mapping, the goal was to approximately reproduce the energy as a function of the β_2 parameter, with the focus on reproducing the position of the energy minimum, the energy at $\beta_2 = 0$, and the saddle point in the oblate region.

The parameters of the *sdq*- and *sd*-IBM are shown in

Figs.11 and 12. The value of parameter σ from Eq. (9), not shown in Fig. 11, is set to $\sigma = 3.5$ for $^{144,146}\text{Nd}$ and $^{146,148}\text{Sm}$, and $\sigma = 2.8$ for other Nd and Sm isotopes, while for Gd, Dy and Er isotopes, it is set to $\sigma = 1.0$ [see the quadrupole operator in Eq. (6)]. In both the *sdq*- and *sd*-IBM, the parameter ϵ_d has a maximum value in the near shell-closure region, and its value decreases as we move towards the deformed region. The same hap-

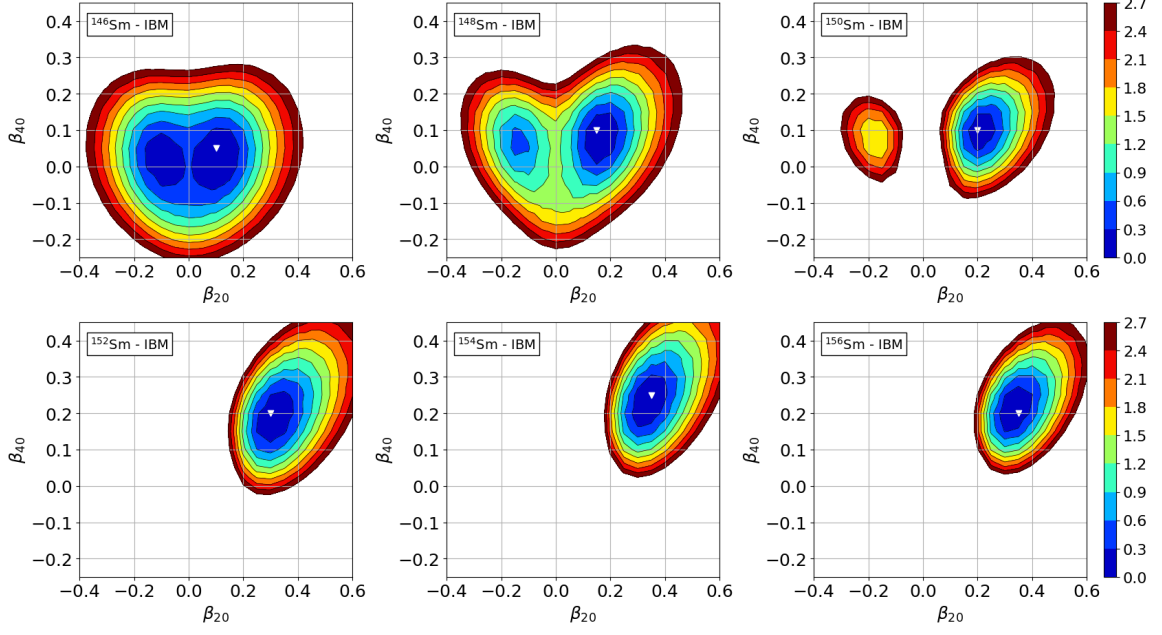


FIG. 7. Same as the caption for Fig. 1, but for the mapped *sdg*-IBM energy surfaces of $^{146-156}\text{Sm}$

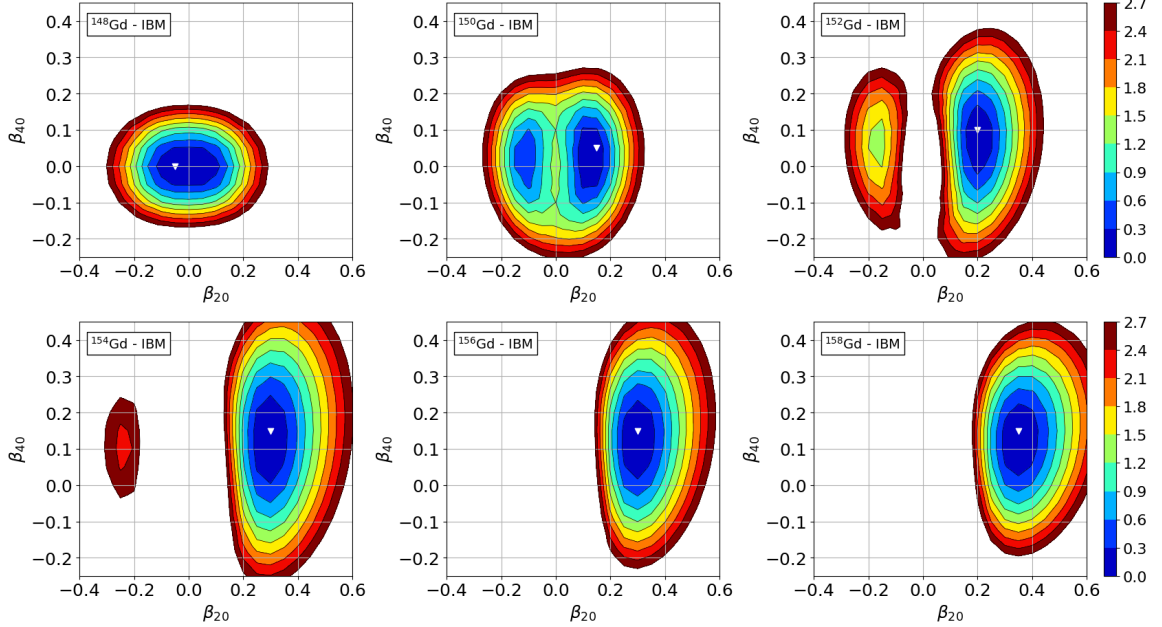


FIG. 8. Same as the caption for Fig. 1, but for the mapped *sdg*-IBM energy surfaces of $^{148-158}\text{Gd}$

pens with the parameter χ . In the *sd*-IBM, on the other hand, the parameter starts from a positive value in the near shell-closure region and decreases more sharply as we move into the deformed region, achieving significantly lower values from the χ parameter in the *sdg*-IBM. The C_2 parameter also shows similar evolution in both models. The κ parameter in the *sdg*-IBM tends to decrease when moving to the deformed region and increase at the

end of the deformed region. This is also the case in the *sd*-IBM, except in the case of Gd and Dy isotopes, for which κ increases when moving into the deformed region. As for the parameters only present in the *sdg*-IBM, g boson energy ϵ_g values fluctuate between $\epsilon_g = 1.0$ and $\epsilon_g = 1.3$ MeV, while the C_4 parameter behaves similarly to the C_2 parameter, the difference being that the C_4 parameter values tend to be smaller than the C_2 values for

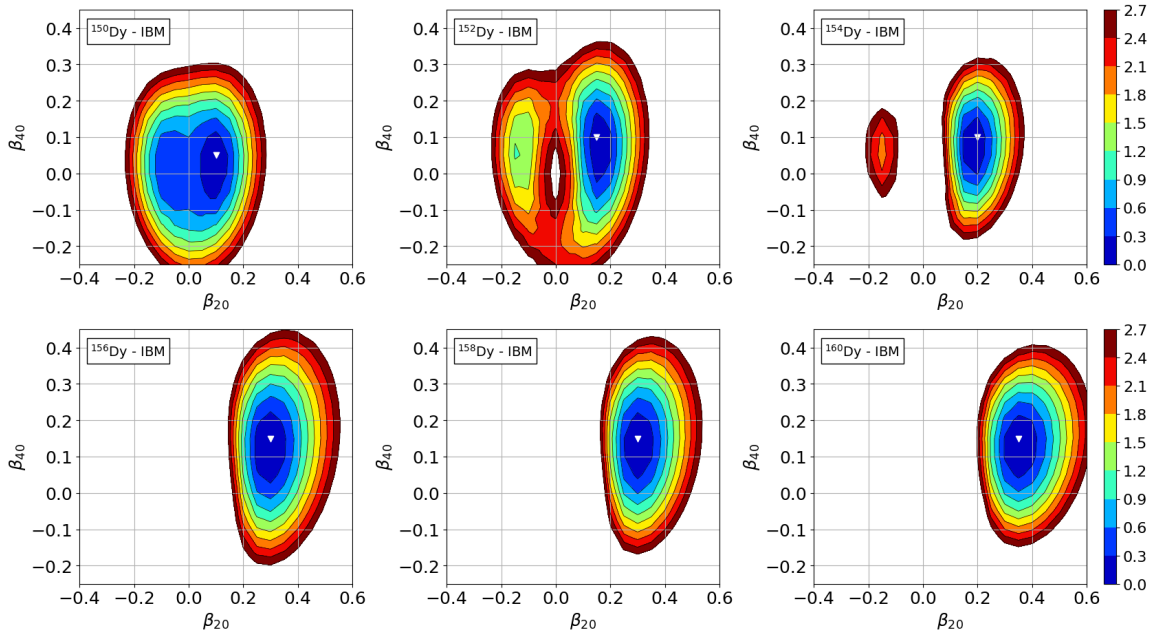


FIG. 9. Same as the caption for Fig. 1, but for the mapped *sdg*-IBM energy surfaces of $^{150-160}\text{Dy}$

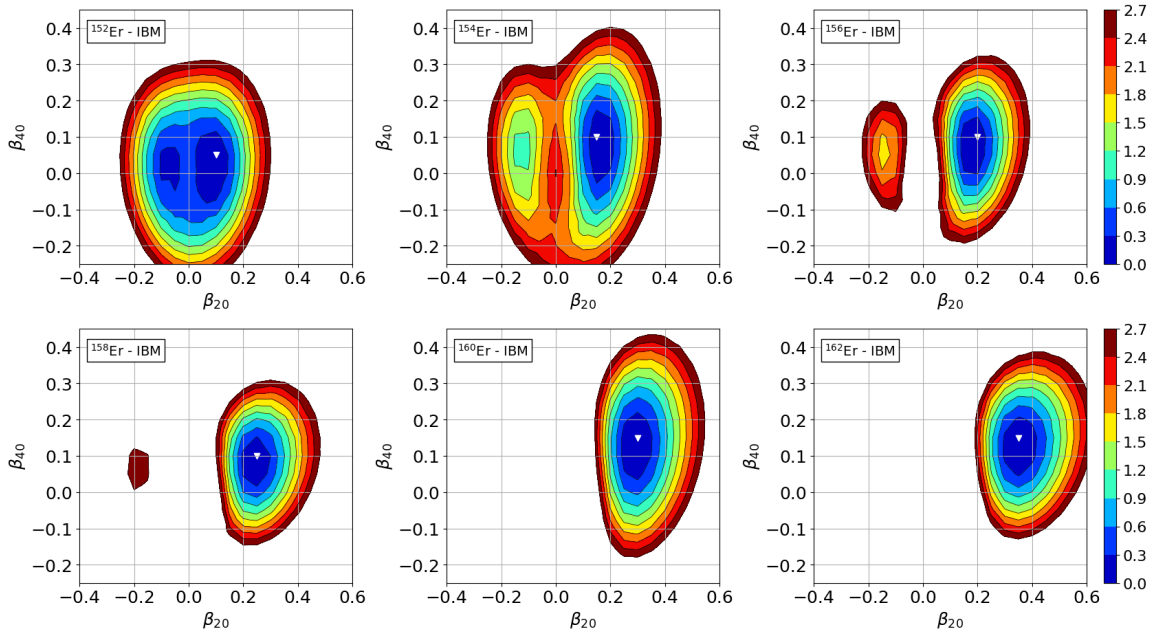


FIG. 10. Same as the caption for Fig. 1, but for the mapped *sdg*-IBM energy surfaces of $^{152-162}\text{Er}$

the same boson number N_B . Previous phenomenological *sdg*-IBM calculations on $^{152,154}\text{Sm}$ have set the *g* boson energy to be $\epsilon_g = 1.4$ MeV and 1.5 MeV, respectively [39]. We note, however, that with those values we are not able to reproduce the desired β_4^{min} obtained through the SCMF calculations.

IV. RESULTS OF THE SPECTROSCOPIC CALCULATIONS

In this section, we show the excitation energies and transition strengths. The computer program ARB-MODEL [40] is employed to obtain these quantities. The results of the *sdg*-IBM are compared with the results of

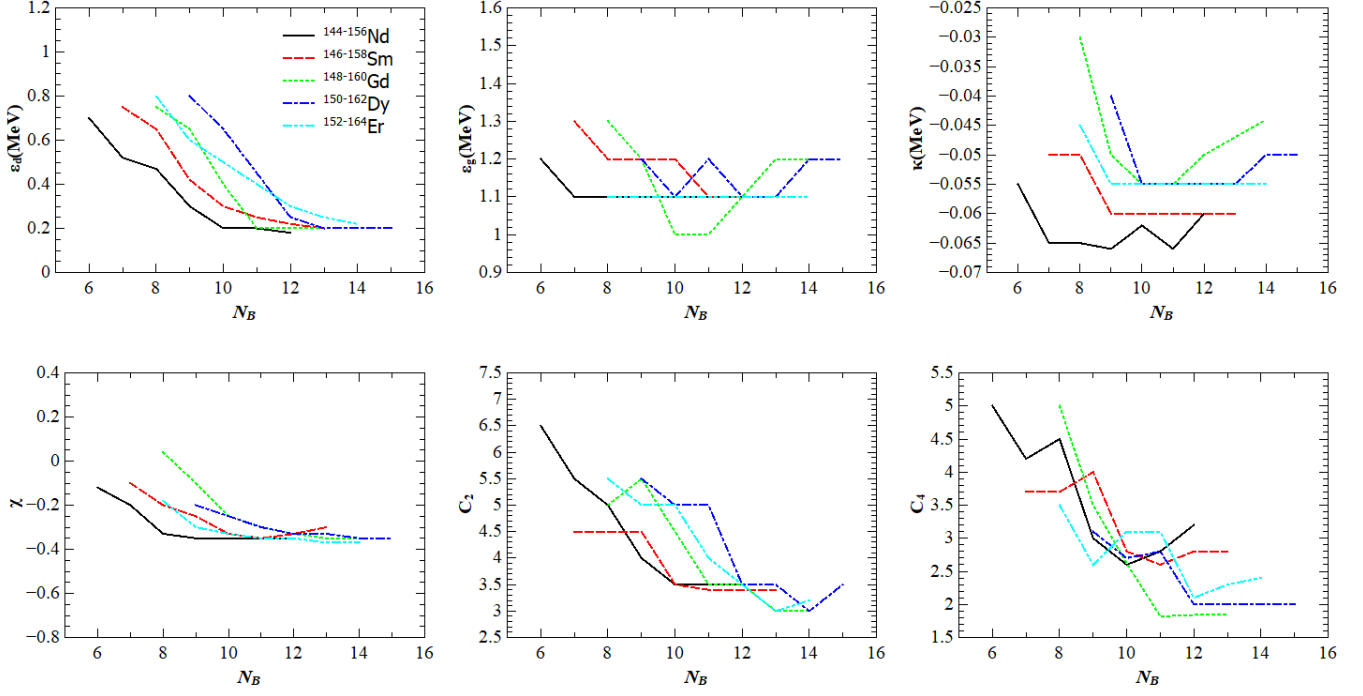


FIG. 11. Parameters of the *sdg* - IBM Hamiltonian (5) as functions of the boson number N_B .

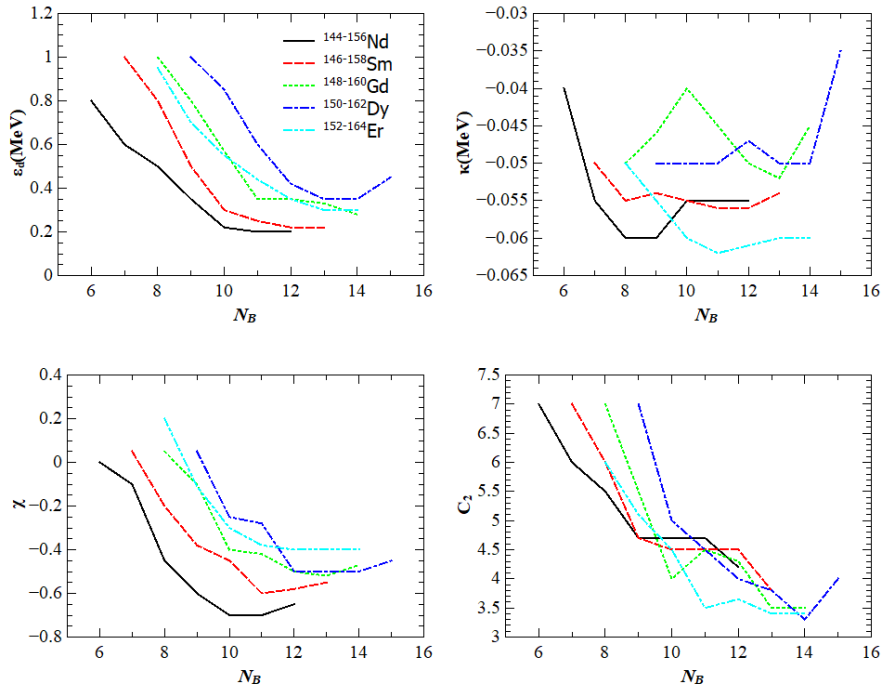


FIG. 12. Parameters of the *sd* - IBM Hamiltonian (10) as functions of the boson number N_B .

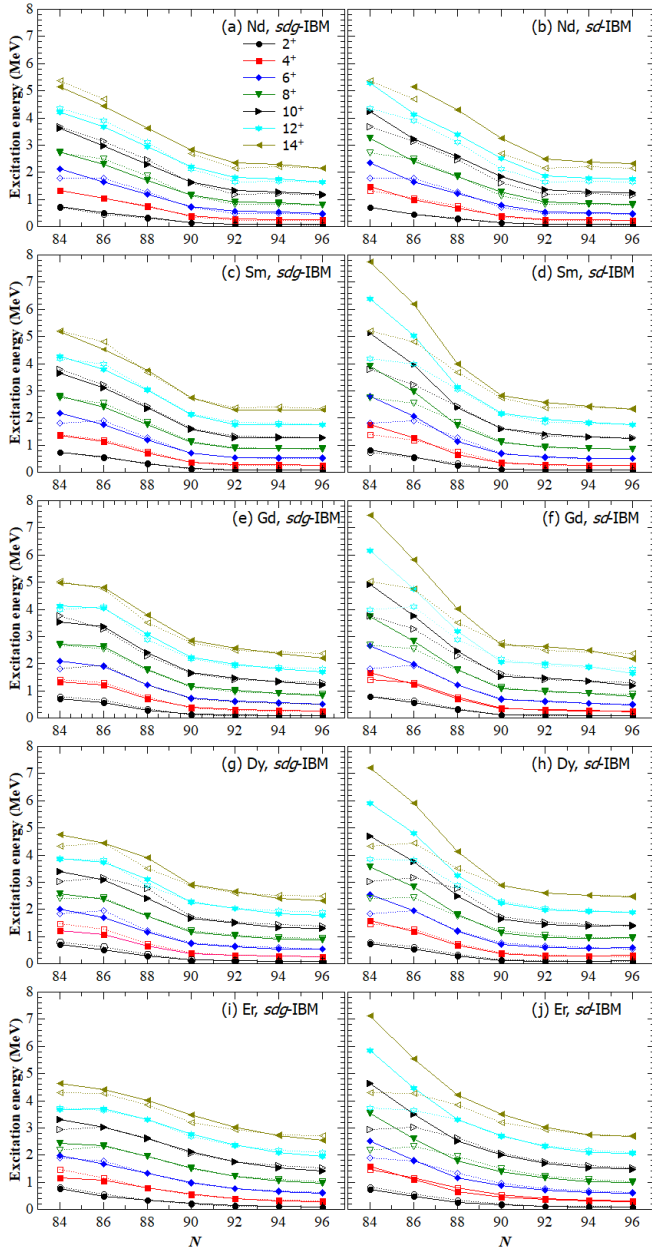


FIG. 13. Calculated excitation energies of the yrast band states up to spin $J^\pi = 14^+$ as functions of the neutron number N within the mapped sdg -IBM (left column) and sd -IBM (right column), represented by solid symbols connected by solid lines. Experimental data are taken from Ref. [38], and are depicted as open symbols connected by dotted lines.

the sd -IBM to show the effects of g bosons. The results obtained from both models are also compared with the experimental data available at the NNDC database [38].

A. Excitation energies

Figure 13 shows the calculated excitation energies of the yrast band states with spin $J^\pi = 2^+ - 14^+$. As

can be seen from the figure, the sdg -IBM significantly improves the description of the $J^\pi \geq 6^+$ states in the $N \leq 88$ nuclei. This can be explained by looking at the expectation value of the g boson number operator, which is for those states calculated to be $\langle \hat{n}_g \rangle \geq 1$. The energies of the yrast band states in the near shell-closure region are lowered due to the presence of g boson.

TABLE I. Energy ratios $R_{4/2} = E_x(4_1^+)/E_x(2_1^+)$ for the nearly spherical nuclei with $N=84$ and 86 , calculated with the mapped sd - and sdg -IBM, as compared to the experimental values [38].

Nucleus	sd -IBM	sdg -IBM	Experiment
^{144}Nd	2.11	1.78	1.89
^{146}Nd	2.25	2.05	2.02
^{146}Sm	2.12	1.83	1.85
^{148}Sm	2.20	1.98	2.14
^{148}Gd	2.13	1.86	1.81
^{150}Gd	2.18	2.15	2.02
^{150}Dy	2.15	1.71	1.81
^{152}Dy	2.21	2.16	2.05
^{152}Er	2.14	1.54	1.83
^{152}Er	2.24	2.17	2.07

We also summarize the energy ratios $R_{4/2}$ for the $N = 84$ and 86 nuclei in Table I. In the $N = 84$ nuclei, the sdg -IBM predicts the ratios to be $R_{4/2} < 2$, which is in agreement with the experiment. This is also an effect of the g boson presence, since this cannot be obtained with sd -IBM calculations. A significantly low ratio, $R_{4/2} = 1.54$, is obtained for ^{152}Er , compared to the experimental value of $R_{4/2} = 1.83$. This is due to the fact that the sdg -IBM predicts the 4_1^+ state somewhat lower in energy from the experimental value. This could be improved by considering the values of the parameter σ to be $\sigma > 1.0$ for this nucleus. The calculated $R_{4/2}$ ratio that is lower than 2 nevertheless agrees with experiment qualitatively, which however cannot be realized in the sd -IBM, giving $R_{4/2} = 2.14 > 2$. In the $N = 86$ nuclei, there is no significant difference between ratios obtained with the sdg - and sd -IBM. The two exceptions are ^{146}Nd , where the sdg -IBM predicts a lower ratio, which is closer to the experimental value, and ^{148}Sm , where the sdg -IBM predicts a $R_{4/2} < 2$ value, which does not agree with the experiment.

Figure 14 compares the calculated and experimental excitation energies of the 0_2^+ , 2_3^+ and 4_3^+ states, which may be associated with the $K^\pi = 0^+$ band usually present in the deformed region. Note that for ^{160}Dy , the observed 0^+ level at 1280 keV, which is suggested to the bandhead of the first excited $K = 0^+$ band, is shown in the plot [Figs. 14(g) and 14(h)], while there are additional two excited 0^+ levels at 681 keV and 703 keV, but with spin and parity not firmly established. As one sees in Fig. 14, the sdg -IBM does not provide an improved description of the 0_2^+ states compared to the sd -IBM, since the expectation value of the g boson number operator for

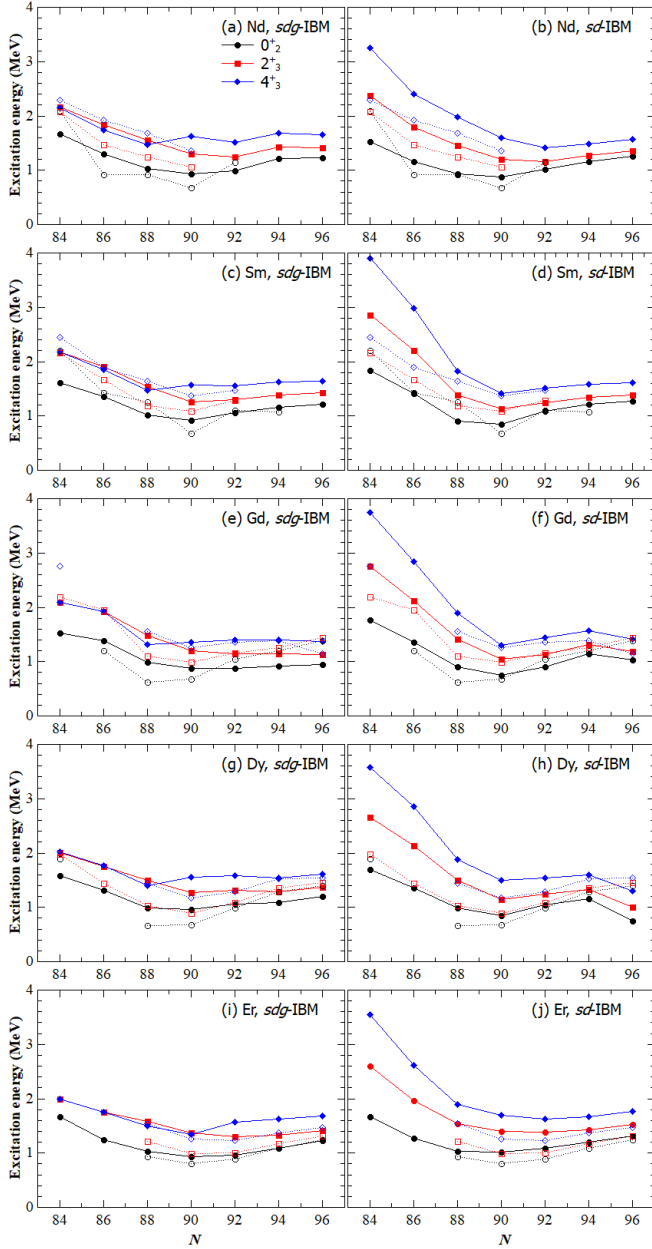


FIG. 14. Same as Fig. 13, but for the 0_2^+ , 2_3^+ , and 4_3^+ states.

the 0_2^+ state is calculated to be $\langle \hat{n}_g \rangle \approx 0$. On the other hand, the *sdg*-IBM predicts a significantly lower 2_3^+ and 4_3^+ states for $N \leq 88$, which is in agreement with the experiment. However, in the nuclei with $N = 84$ and 86 , the two states are almost equal in energy, and in the $N = 88$ nuclei, the 4_3^+ state becomes lower in energy from the 2_3^+ state, which contradicts the experiment. In the $N \geq 90$ deformed region, both *sdg*- and *sd*-IBM yield similar results. Overall, the 2_3^+ and 4_3^+ states, calculated by the *sdg*-IBM, are closer in energies to the corresponding experimental values in the near shell-closure region. The *sdg*-IBM, however, predicts the 4_3^+ energy level to be so low as to be close to or even below the 2_3^+ one, which

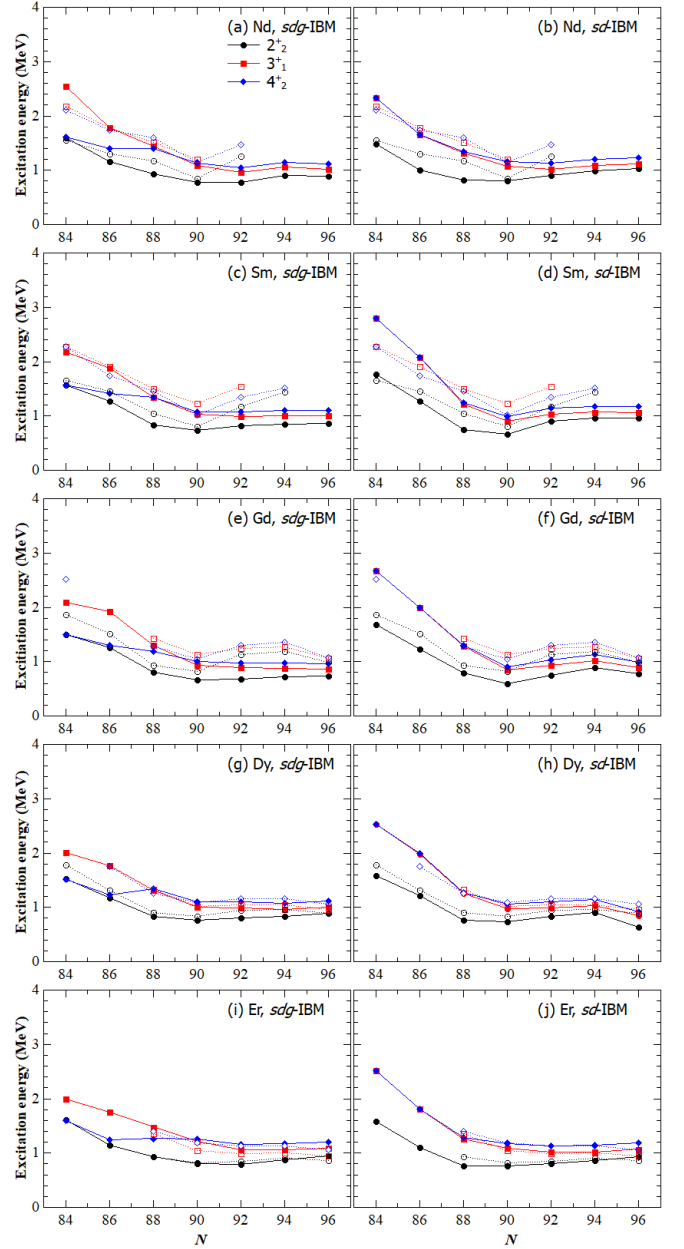


FIG. 15. Same as Fig. 13, but for the 2_2^+ , 3_1^+ , and 4_2^+ states.

does not agree with the experiment. The description of 0_2^+ states is not improved in the *sdg*-IBM.

Figure 15 shows the excitation energies of the 2_2^+ , 3_1^+ , and 4_2^+ states, associated with the γ vibrational band. The effect of including g bosons on the states 2_2^+ and 3_1^+ is minor, with only some small improvements in the $N \leq 88$ Nd and Sm. The 4_2^+ energy level is, however, significantly low compared to the one obtained with the *sd*-IBM and to the observed level. In the $N = 84$ nuclei, the 4_2^+ state is predicted to be almost equal in energy to the 2_2^+ state, contrary to the experiment. In the $N \geq 90$ deformed region, there are no significant differences between the *sdg*- and *sd*-IBM. The fact that the *sdg*-IBM

predicts a significantly lower 4_2^+ state compared to the experiment, points to the fact that the chosen Hamiltonian may not be suitable for the description of such states in the region near shell closures. A Hamiltonian with more independent parameters could potentially solve this problem. However, the inclusion of more independent parameters would make the mapping procedure more involved. We also note that the choice of the EDF, as well as the choice of the pairing interaction, affects the calculated spectrum. We leave those two problems for a separate study.

B. Transition strengths

1. Quadrupole transitions

Figure 16 shows the $B(E2; J \rightarrow J - 2)$ transition strengths in the ground state bands of the well deformed $N = 90$ and 92 isotopes. We consider these isotopes due to the fact that most of the data on $E2$ transitions is available in these isotopes, which makes them the ideal cases to examine when comparing the $E2$ transition strengths between the sdg - and sd -IBM. The effective charges $e_2^{sdg, sd}$ are fitted to reproduce the experimental data on the first $B(E2; 2^+ \rightarrow 0^+)$ transition [38]. One can notice a significant difference between the behavior of the ground state band $E2$ transitions in Nd and Sm isotopes, compared to heavier ones. In Nd and Sm, the predicted transition strengths for states $J^\pi \geq 6^+$ are significantly larger than the sd -IBM calculated transitions, which is not the case in other isotopes. This can be explained by the fact that in those isotopes, the $(d^\dagger \times \tilde{g} + g^\dagger \times \tilde{d})^{(2)}$ term of the quadrupole operator $\hat{Q}^{(2)}$ contributes more to the calculated transitions due to the larger values of the parameter $\sigma > 1.0$. The calculated transition strengths, especially in the $^{152,154}\text{Sm}$ seem to correspond to the axial rotor calculations [20, 39]. It can be seen that the sdg -IBM in the shown Nd and Sm isotopes improves the results of the $B(E2; J \rightarrow J - 2)$ strengths for $J = 6^+, 8^+, 10^+$. In Gd, Dy and Er isotopes, the sdg -IBM only slightly increases the $E2$ transition strengths from $J^\pi \geq 6^+$ states compared to the sd -IBM, which can be attributed to the fact that the value of the parameter $\sigma = 1.0$ is chosen. At $N = 90$, both models underestimate the measured transition strengths, while at $N = 92$, both models reproduce the measured strengths well. Due to the fact that the margins of error are quite large in $N = 92$ Dy and Er isotopes, it cannot be concluded whether the sdg -IBM improves the description of higher $E2$ transition strengths in those isotopes.

2. Hexadecapole transitions

Figure 17 shows the $B(E4; 4_n^+ \rightarrow 0_1^+)$ ($n = 1, 2, 3, 4$) transition strengths. The $e_4^{sdg, sd}$ effective charges are fitted to experimental data on the $B(E4; 4_1^+ \rightarrow 0_1^+)$ from

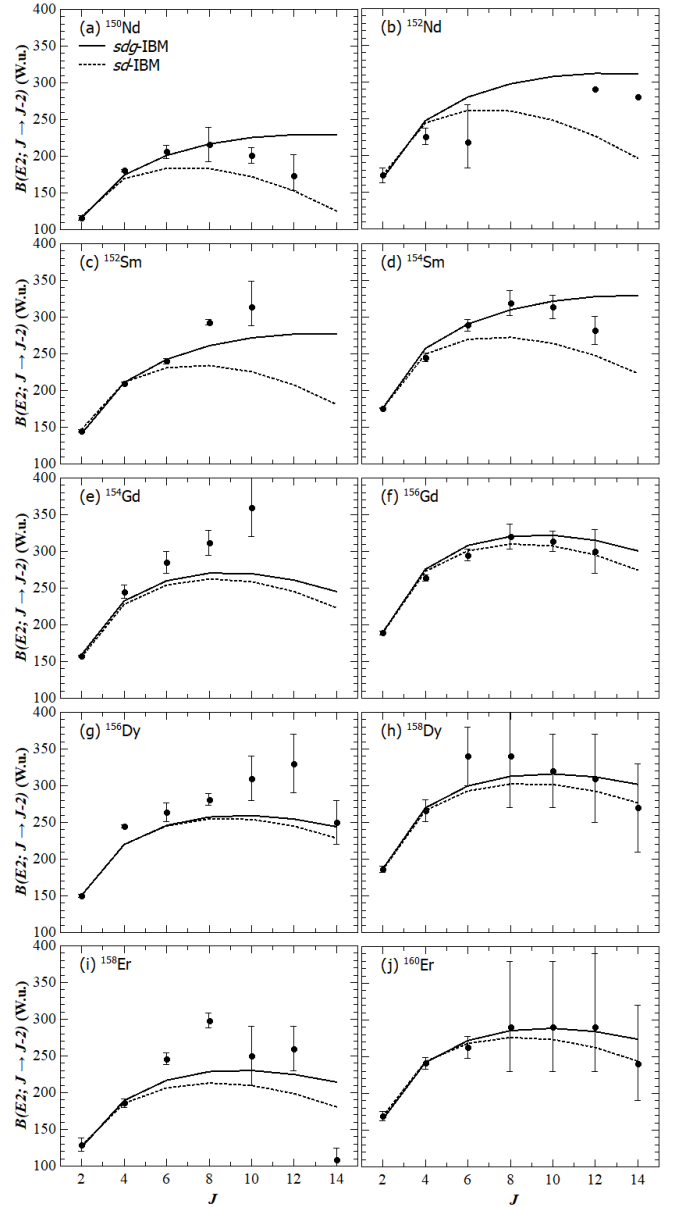


FIG. 16. $B(E2)$ transition strengths in the ground state band of the well-deformed $N = 90$ (left) and $N = 92$ (right) nuclei as functions of spin J , calculated with the mapped sdg -IBM (solid curves) and sd -IBM (dotted curves). The experimental data, represented by solid circles, are adopted from Ref. [38].

the first 4^+ state to the ground state [25–27, 38]. For isotopes with no available experimental data, effective charge values are chosen so that they start from lower values, peak around $N = 92$ and then decrease again. These transition strengths are shown in Figs. 17(a) and 17(b). In Figs. 17(c)-(h), $E4$ transition strengths from higher 4^+ states are shown. The sdg -IBM predicts several large $E4$ transition strengths from these states in certain isotopes, which is expected in the case of hexadecapole deformed nuclei with a $K = 4^+$ band. The sd -IBM predicts all of these transition strengths to vanish, which points to the

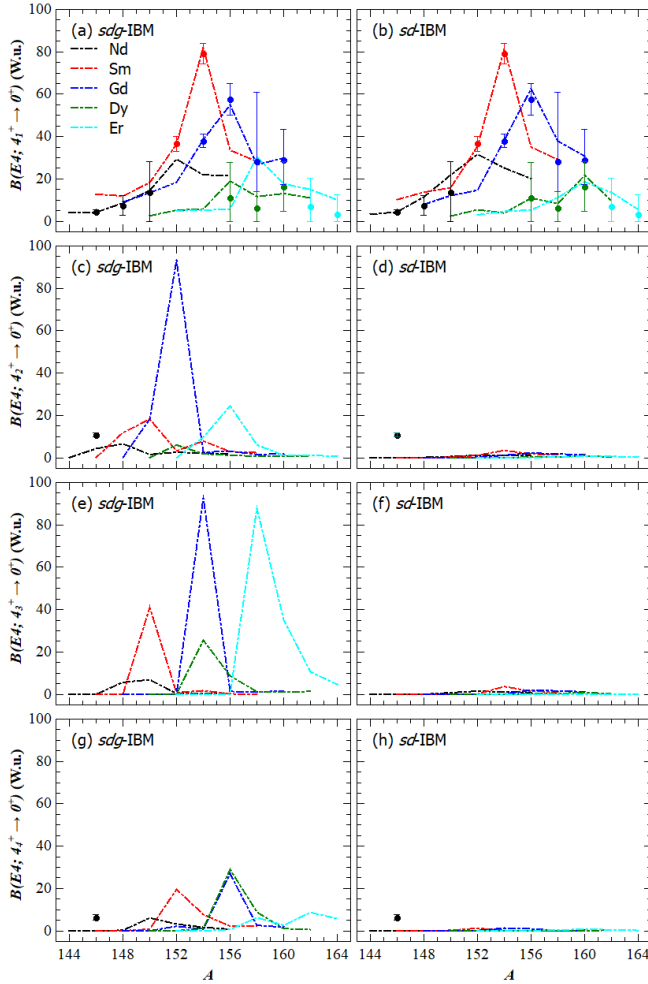


FIG. 17. $B(E4)$ strengths in W.u. for the transitions of the first [panels (a) and (b)], second [panels (c) and (d)], third [panels (e) and (f)], and fourth [panels (g) and (h)] 4^+ state to the 0_1^+ ground state as functions of the mass number A , calculated with the mapped sdg -IBM (left column) and sd -IBM (right column). Experimental data are taken from Refs. [25–27, 38], and are indicated by solid circles in the plots.

necessity of considering the g boson in the description of $E4$ transitions from higher 4^+ states. Unfortunately, due to the lack of experimental data on these $E4$ transitions, it is not possible to see how well the mapped sdg -IBM predicts the values of these transition strengths.

3. Monopole transitions

Figure 18 shows the monopole strengths $\rho^2(E0; 0_i^+ \rightarrow 0_j^+)$, with $i = 2, 3$ and $j = 1, 2$, for isotopes of Sm and Gd. We choose to show these isotopes, since the experimental data on monopole strengths is only available for these isotopes [38, 41]. The choice of $\eta = \gamma = 0.75 \text{ fm}^2$ is made to reproduce most of the available experimental data. The sdg -IBM does not significantly improve the calcu-

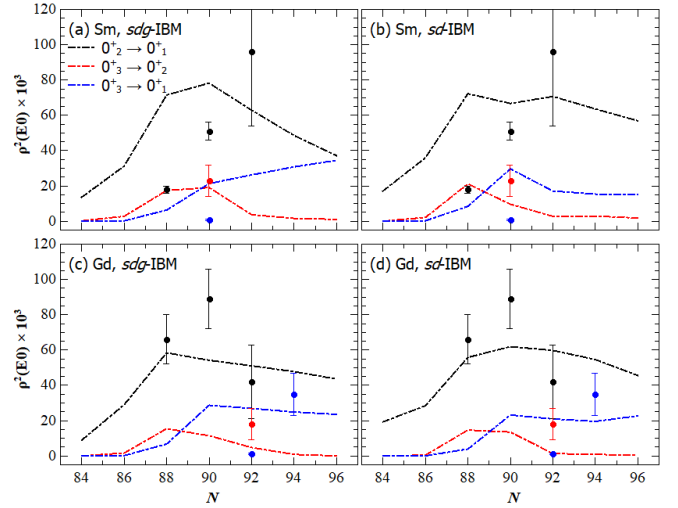


FIG. 18. $\rho^2(E0; 0_i^+ \rightarrow 0_j^+)$ values as functions of the neutron number N for Sm and Gd isotopes, calculated with the mapped sdg -IBM (left column) and sd -IBM (right column). Experimental values are adopted from Refs. [38, 41], and are plotted as solid circles.

lated monopole strengths compared to the sd -IBM. Both models overestimate the strengths of $0_2^+ \rightarrow 0_1^+$ transitions in $^{150,152}\text{Sm}$ and underestimate the same strength in ^{154}Gd . The calculated strengths of ^{154}Sm and $^{152,156}\text{Gd}$ are within the margins of error of the measured strengths. The sdg -IBM does slightly improve the description of the $0_3^+ \rightarrow 0_2^+$ transition in ^{154}Sm and the $0_3^+ \rightarrow 0_1^+$ transition in the ^{158}Gd . Overall, the sdg -IBM does not differ significantly from the sd -IBM in the description of the monopole strengths, which is expected, since the sdg -IBM calculations do not predict a presence of g boson in 0^+ states up to 0_3^+ . For example, in ^{154}Sm , the lowest 0^+ state that contains one g boson, with the expectation value $\langle \hat{n}_g \rangle \approx 1$, is the 0_5^+ state. In principle, it is possible to fit η and γ separately for each isotope. However, since our goal was to see the effect of g boson in monopole transitions, we follow the method of [37] and set fixed values of η and γ parameters.

V. SUMMARY

We have shown an extended analysis of the impact of hexadecapole deformations on the excitation energy spectra and transition strengths in even-even rare-earth nuclei, ranging from the near spherical to the well deformed ones. The quadrupole-hexadecapole constrained SCMF PES has been mapped onto the corresponding PES of the IBM, and this procedure completely determines the parameters of the sdg -IBM Hamiltonian, based on the microscopic calculations. The inclusion of g boson has a significant effect on $J^\pi \geq 6^+$ yrast states in the $N \leq 88$ nuclei near neutron magic number $N = 82$. The mapped sdg -IBM lowers the energies of aforementioned states to

agree with the observed spectra. In the case of nonyrast states and corresponding bands, the *sd*-IBM seems to be sufficient in the description of such states, with the *sdg*-IBM making only a minor contribution, e.g. 2_3^+ and 4_3^+ states of the $K^\pi = 0^+$ band in the $N = 84$ and 86 nuclei. As for the transitions, in the well deformed nuclei with $N = 90$ and 92 , the *sdg*-IBM calculation yields higher $B(E2; J \rightarrow J - 2)$ values for $J^\pi \geq 6^+$ yrast states, which does seem to be an improvement of the results, especially in the case of $^{150,152}\text{Nd}$ and $^{152,154}\text{Sm}$. In the case of monopole transitions between 0^+ states, the effect of the g boson seems to be minor. In the well deformed region, the *sdg*-IBM predicts the existence of the $K^\pi = 4^+$ band with an enhanced $B(E4; 4^+ \rightarrow 0^+)$ hexadecapole transition to the ground states. The fact that the *sd*-IBM cannot predict larger hexadecapole transition strengths from higher 4^+ states, points to a necessity of including the g boson in the description of the hexadecapole transitions. Unfortunately, due to the lack of experimental

data on such transitions, it is not possible to see how well the *sdg*-IBM reproduces such transitions. Now that we have shown the usefulness of the mapped *sdg*-IBM, we can expand our study to the even-odd and odd-odd rare-earth nuclei, as well as extend our model to the more complex *sdg*-IBM-2 to study properties such as scissors modes in rare-earth nuclei. It could also be interesting to systematically study how sensitive the parameters are to the choice of the EDF in the SCMF calculations.

ACKNOWLEDGMENTS

The work of L.L. is financed within the Tenure Track Pilot Programme of the Croatian Science Foundation and the École Polytechnique Fédérale de Lausanne, and the project TTP-2018-07-3554 Exotic Nuclear Structure and Dynamics, with funds from the Croatian-Swiss Research Programme.

-
- [1] A. Bohr and B. R. Mottelson, *Nuclear Structure*, Vol. II (Benjamin, New York, USA, 1975).
- [2] P. Ring and P. Schuck, *The Nuclear Many-Body Problem* (Springer-Verlag, Berlin, 1980).
- [3] Y. Gupta, B. Nayak, U. Garg, K. Hagino, K. Howard, N. Sensharma, M. Şenyiğit, W. Tan, P. O'Malley, M. Smith, R. Gandhi, T. Anderson, R. deBoer, B. Frentz, A. Gyurjinyan, O. Hall, M. Hall, J. Hu, E. Lamere, Q. Liu, A. Long, W. Lu, S. Lyons, K. Ostdiek, C. Seymour, M. Skulski, and B. Vande Kolk, *Phys. Lett. B* **806**, 135473 (2020).
- [4] W. Ryssens, G. Giacalone, B. Schenke, and C. Shen, *Phys. Rev. Lett.* **130**, 212302 (2023).
- [5] J. Chi, Y. Qiang, C. Gao, and J. Pei, *Nuclear Physics A* **1032**, 122626 (2023).
- [6] J. Engel and J. Menéndez, *Rep. Prog. Phys.* **80**, 046301 (2017).
- [7] F. Iachello and A. Arima, *The interacting boson model* (Cambridge University Press, Cambridge, 1987).
- [8] R. F. Casten and D. D. Warner, *Rev. Mod. Phys.* **60**, 389 (1988).
- [9] K. Nomura, N. Shimizu, and T. Otsuka, *Phys. Rev. Lett.* **101**, 142501 (2008).
- [10] K. Nomura, N. Shimizu, and T. Otsuka, *Phys. Rev. C* **81**, 044307 (2010).
- [11] K. Nomura, T. Otsuka, R. Rodríguez-Guzmán, L. M. Robledo, and P. Sarriguren, *Phys. Rev. C* **83**, 014309 (2011).
- [12] K. Nomura, N. Shimizu, D. Vretenar, T. Nikšić, and T. Otsuka, *Phys. Rev. Lett.* **108**, 132501 (2012).
- [13] K. Nomura, D. Vretenar, and B.-N. Lu, *Phys. Rev. C* **88**, 021303 (2013).
- [14] K. Nomura, D. Vretenar, T. Nikšić, and B.-N. Lu, *Phys. Rev. C* **89**, 024312 (2014).
- [15] T. Otsuka, *Nucl. Phys. A* **368**, 244 (1981).
- [16] T. Otsuka, A. Arima, and N. Yoshinaga, *Phys. Rev. Lett.* **48**, 387 (1982).
- [17] T. Otsuka and J. N. Ginocchio, *Phys. Rev. Lett.* **55**, 276 (1985).
- [18] T. Otsuka and M. Sugita, *Phys. Lett. B* **209**, 140 (1988).
- [19] Y. D. Devi and V. K. B. Kota, *Z. Phys. A* **337**, 15 (1990).
- [20] S. Kuyucak, *Nucl. Phys. A* **570**, 187 (1994).
- [21] P. Van Isacker, A. Bouldjedri, and S. Zerguine, *Nucl. Phys. A* **836**, 225 (2010).
- [22] L. Lotina and K. Nomura, *Phys. Rev. C* **109**, 034304 (2024).
- [23] D. Hendrie, N. Glendenning, B. Harvey, O. Jarvis, H. Duhm, J. Saudinos, and J. Mahoney, *Phys. Lett. B* **26**, 127 (1968).
- [24] K. A. Erb, J. E. Holden, I. Y. Lee, J. X. Saladin, and T. K. Saylor, *Phys. Rev. Lett.* **29**, 1010 (1972).
- [25] H. Wollersheim and T. W. Elze, *Nucl. Phys. A* **278**, 87 (1977).
- [26] R. M. Ronningen, J. H. Hamilton, L. Varnell, J. Lange, A. V. Ramayya, G. Garcia-Bermudez, W. Lourens, L. L. Riedinger, F. K. McGowan, P. H. Stelson, R. L. Robinson, and J. L. C. Ford, *Phys. Rev. C* **16**, 2208 (1977).
- [27] R. M. Ronningen, R. B. Piercey, J. H. Hamilton, C. F. Maguire, A. V. Ramayya, H. Kawakami, B. van Nooijen, R. S. Grantham, W. K. Dagenhart, and L. L. Riedinger, *Phys. Rev. C* **16**, 2218 (1977).
- [28] S. Hilaire and M. Girod, *Eur. Phys. J. A* **33**, 237 (2007).
- [29] S.-G. Zhou, *Physica Scripta* **91**, 063008 (2016).
- [30] B.-N. Lu, J. Zhao, E.-G. Zhao, and S.-G. Zhou, *Phys. Rev. C* **89**, 014323 (2014).
- [31] J. Zhao, B.-N. Lu, E.-G. Zhao, and S.-G. Zhou, *Phys. Rev. C* **95**, 014320 (2017).
- [32] D. Vretenar, A. V. Afanasjev, G. A. Lalazissis, and P. Ring, *Phys. Rep.* **409**, 101 (2005).
- [33] T. Nikšić, D. Vretenar, and P. Ring, *Prog. Part. Nucl. Phys.* **66**, 519 (2011).
- [34] T. Nikšić, D. Vretenar, and P. Ring, *Phys. Rev. C* **78**, 034318 (2008).
- [35] Y. Tian, Z. Y. Ma, and P. Ring, *Phys. Lett. B* **676**, 44 (2009).
- [36] V. K. B. Kota, J. V. der Jeugt, H. E. D. Meyer, and G. V. Berghé, *Journal of Mathematical Physics* **28**, 1644 (1987).

- [37] S. Zerguine, P. Van Isacker, and A. Bouldjedri, *Phys. Rev. C* **85**, 034331 (2012).
- [38] Brookhaven National Nuclear Data Center, <http://www.nndc.bnl.gov>.
- [39] S. Kuyucak and V.-S. Lac, *Phys. Rev. C* **47**, 1815 (1993).
- [40] S. Heinze, computer program ARBMODEL, University of Cologne (2008).
- [41] T. Kibédi and R. Spear, *At. Data and Nucl. Data Tables* **89**, 77 (2005).

Quark Counting, Drell-Yan West, and the Pion Wave Function

Mary Alberg^{1,2} and Gerald A. Miller²

¹*Department of Physics, Seattle University, Seattle, Washington 98122, USA*

²*Department of Physics, University of Washington, Seattle, WA 98195-1560, USA*

(Dated: March 7, 2024 - 2:9)

The relation between the pion's quark distribution function, $q(x)$, its light-front wave function, and the elastic charge form factor, $F(\Delta^2)$ is explored. The square of the leading-twist pion wave function at a special probe scale, ζ_H , is determined using models and Poincare covariance from realistic results for $q(x)$. This wave function is then used to compute form factors with the result that the Drell-Yan-West and quark counting relationships are not satisfied. A new relationship between $q(x)$ and $F(\Delta^2)$ is proposed.

INTRODUCTION

The structure of the pion continues to be of interest to many physicists. There are plans to measure the pion electromagnetic form factor at JLab and at the planned EIC [1]. There are also plans to re-measure the quark distribution of the pion, $q(x)$ via a new Drell-Yan measurement [2]. Much recent and old theoretical attention has been devoted to determining and understanding the behavior of the valence pion quark distribution function, $q_v(x)$, at high values of Bjorken x , see *e.g.* the review [3].

Much of the recent interest stems from efforts to understand the behavior at high x . While many use the parameterization $q_v(x) \sim x^\alpha(1-x)^\beta$ there is a controversy over the value of β and its dependence on the variables x and the resolution scale, Q^2 . See, for example, the differing approaches of [4],[5] and [6, 7]. Ref. [4] finds that $\beta = 1$ at low resolution scales, rising to 1.5 at $Q^2 = 27$ GeV², while [7] finds that $\beta = 2 + \gamma(Q^2)$ with γ positive and increasing at Q^2 rises. Both sets of authors claim agreement with the available data set. The small values of β result from perturbative QCD and the larger values from non-perturbative techniques. Indeed, [5] finds that the value of β can lie between 1 and 2.5 depending on the technique used to resum the contributions of large logarithms in computing the relationship between $q(x)$ and the measured Drell-Yan cross section data. It would be beneficial to find the relation (if any) between the behavior at large values of x and the underlying dynamics.

The wide interest in the form factor and distribution function originates in the early hypotheses of the connection between the two observable quantities. Drell & Yan [8] and West [9] suggested a relation between $q(x)$ for large values of x and the elastic proton's Dirac form factor $F_1(\Delta^2)$, where Δ^2 is the negative of the square of the four-momentum transfer to the target hadron, at large values of Δ^2 . Different aspects of the wave function are used to compute distribution functions and form factors, so the following relation is very surprising, namely

$$\lim_{x \rightarrow 1} q(x) = (1-x)^{n_H} \quad (1)$$

leads to the result

$$\lim_{\Delta^2 \rightarrow \infty} F_1(\Delta^2) \propto \frac{1}{(\Delta^2)^{(n_H+1)/2}}, \quad (2)$$

with n_H the number of partons in the hadron. The F_1 form factor is the matrix element of the plus-component of the electromagnetic current operator between proton states of the same spin. So the proof would provide the same relations for the pion. The original papers are heavily quoted now despite the ancient nature of these relations.

Another relationship between structure functions and form factors is obtained from the use of perturbative QCD and leads to quark counting rules for the proton and pion obtained in [10–13] and reviewed in [14]. These are

$$\lim_{x \rightarrow 1} q(x, Q^2) \propto (1-x)^{2n_H-3+2|\Delta_s|+\Delta\gamma}, \quad (3)$$

$$\lim_{\Delta^2 \rightarrow \infty} F_H(\Delta^2) \propto \frac{1}{(\Delta^2)^{n_H-1}}, \quad (4)$$

with $\Delta\gamma$ a correction accounting for evolution that vanishes at a starting scale ζ_H^2 , n_H is the minimum number of elementary constituents of the hadron, and we have taken the number of spectators to be $n_H - 1$. The quantity Δ_s is the difference between the z -components of the quark and hadron spin. Thus for a proton the dominant term at high x has $|\Delta S_z| = 0$ and for a pion $|\Delta S_z| = 1/2$. The two sets of relations (Eq. (1), Eq. (2)) and (Eq. (3), Eq. (4)) are approximately the same for the proton at ζ_H^2 : namely, $q(x) \sim (1-x)^3$ and $F_1 \sim 1/\Delta^4$ with $n_H = 3$. There are two sets of predictions for the pion $q(x) \sim (1-x)^2$, $F(\Delta^2) \sim 1/\Delta^3$ for Drell-Yan West, and $q(x) = (1-x)^2$, $F(\Delta^2) \sim 1/\Delta^2$ for the quark counting rules. We now focus on the pion.

The current literature tells us that the relation between the high- x behavior of $q(x)$ and the pion form factor is interesting. In other words, what can the value of β be used for? We aim to study the connection between $q(x)$ and the square of the pion valence light-front wave function.

LIGHT-FRONT ANALYSIS

Hadronic wave functions depend on a factorization scale, ζ at which the hadron is probed. It has been widely argued that [7, 15, 16] there is a scale at which the hadron consists of only valence quarks linked to quarks of the quark-parton model as an object dressed by quark-gluon QCD interactions as obtained from the quark gap equation. Gluon emission from valence quarks begins at ζ_H [17]. Thus, at ζ_H the dressed valence u and \bar{d} quarks carry all of the momentum of the π^+ and each constituent (of equal mass) carries 1/2 of the pion momentum. The result of every calculation of pionic properties that respects Poincare covariance, and the Ward-Green-Takahashi identities along with the consequences of dynamical symmetry breaking inherent in the quark gap-equation has these features. See *e.g.* Ref. [18].

The relation between the light-front wave function, evaluated at the hadron scale ζ_H^2 , is given by

$$q(x) = \frac{1}{\pi} \int \frac{d^2 k_\perp}{x(1-x)} |\Phi(x, k_\perp)|^2 \quad (5)$$

where $\Phi(x, k_\perp)$ is the wave function of the $q\bar{q}$ component. The function Φ represents the leading-twist component of the pion wave function, in which the quark and antiquark spins combine to 0. This component dominates computations of the high-momentum transfer form factor and the high x behavior of $q(x)$. The normalization is $\int_0^1 dx q(x) = 1$. We drop the explicit dependence on ζ_H^2 to simplify the equations.

There is a special feature of the wave function at ζ_H . Rotational invariance requires that $\Phi(x, k_\perp)$ is a function of a single variable, $\Phi(M_0^2)$, with $M_0^2 \equiv \frac{k_\perp^2 + M^2}{x(1-x)}$, and M is the constituent quark mass [19, 20]. The key point is that in the two-body sector one may construct a self-consistent representation of the Poincare generators. Both k_\perp^2 and M^2 are dimensionless variables measured in terms of an appropriate intrinsic momentum scale, Λ^2 . Then changing variables to $z = M_0^2$ leads to the exact

$$F(\Delta^2) = \frac{1}{\pi} \int_0^1 dx \int \frac{d^2 k_\perp}{x(1-x)} \Phi\left(\frac{k_\perp^2 + M^2}{x(1-x)}\right) \Phi\left(\frac{(\mathbf{k}_\perp + (1-x)\mathbf{\Delta})^2 + M^2}{x(1-x)}\right), \quad (10)$$

where the plus-component of the space-like momentum transfer to the proton is taken as zero, so that the momentum transfer, $(\mathbf{\Delta})$ is in a transverse (\perp) direction.

To see if there is a connection between $F(\Delta^2)$ and $q(x)$ we use model wave functions to compute both quantities.

result,

$$q(x) = \int_{\frac{M^2}{x(1-x)}}^{\infty} dz |\Phi(z)|^2. \quad (6)$$

A curious feature is that if $M = 0$, $q(x) = 1$ in disagreement with realistic extractions of $q(x)$ at the hadronic scale [7]. Moreover, the idea that there is a scale ζ_H goes along with the feature that spontaneous symmetry breaking causes M to be significantly larger than its current quark value. Thus we do not expect that $q(x)$ is constant when evaluated at ζ_H .

The next step is to take x to be near unity so that

$$q_{x \rightarrow 1}(x) \approx \int_{\frac{M^2}{1-x}}^{\infty} dz |\Phi(z)|^2. \quad (7)$$

The lower limit is large $M^2/(1-x) \gg 1$. This shows immediately the connection between the large x behavior and the high-momentum part of the light front wave function. An interesting relation can be obtained by differentiating Eq. (7) with respect to x :

$$q'_{x \rightarrow 1}(x) = -\frac{M^2}{(1-x)^2} |\Phi(\frac{M^2}{1-x})|^2. \quad (8)$$

Given a model wave function one can obtain the high x behavior of $q'(x)$ and thus also that of $q(x)$ at ζ_H^2 . Then DGLAP evolution can be used to obtain the structure functions at larger values of probe scales.

Moreover, the finite nature of $q'(x)$ at $x \rightarrow 1$ immediately gives information about the high momentum behavior of the pion wave function. Namely,

$$\lim_{x \rightarrow 1} |\Phi(\frac{M^2}{1-x})|^2 = c(1-x)^2 f(1-x), \quad (9)$$

where c is a finite number and $f(1-x)$ is finite as $x \rightarrow 1$. Thus the high x behavior of $q(x)$ tells us about specific features of the pion wave function. Can one say more?

Form factors are matrix elements of a conserved current and so are independent of the factorization scale [21] so that one may evaluate the form factor using the constraint at ζ_H . Then the form factor is given by the expression

The connection between wave functions and $q(x)$ is given by Eq. (6).

It is convenient to use a flexible power law (PL) form:

$$|\Phi^{\text{PL}}(z)|^2 \rightarrow \frac{K}{(z)^{n+1}}, q^{\text{PL}} \sim (1-x)^n \quad (11)$$

with $n \geq 1$. This form does not build in the asymptotic behavior predicted by using perturbative QCD. However, the applicability of perturbative QCD to exclusive processes at non-asymptotic, experimentally realizable values of the momentum transfer has been questioned [22–26] for a variety of reasons including lack of knowledge of the non-perturbative part of the wave function, convergence issues, higher twist effects and those of Sudakov suppression. Radyushkin [23] wrote, “for accessible energies and momentum transfers the soft (nonperturbative) contributions dominate over those due to the hard quark rescattering subprocesses”. Much of the problems are related to the importance of the high- x region in computing the form factors that Feynman argued [27] was dominant. Despite progress in understanding non-perturbative aspects using lattice QCD (see *e.g.* [28], and Dyson-Schwinger techniques (see *e.g.* [7, 29], we believe that it is worthwhile to examine models of non-perturbative wave functions.

With $n = 1$, $F(\Delta^2) \sim 1/\Delta^3$ with Drell-Yan-West and $F \sim 1/\Delta^2$ with quark counting. These predictions can be checked by doing the exact model calculation. We thus expect the asymptotic form factor to behave as $\sim 1/\Delta^2$, Eq. (4), if quark counting is correct. We now check to see if the quark counting relations are respected if Eq. (11) describes the wave function.

Note that in the non-relativistic limit that the integral appearing in Eq. (10) is dominated by values of x near $1/2$, and if $\Delta^2 \gg (M^2)$ then $F_{\text{NR}}(\Delta^2) \sim \Phi(1/2\Delta^2) \sim (1/\Delta^2)^{(n+1)/2}$ in accord with Eq. (2). This result is similar to the non-relativistic arguments presented by Brodsky & Lepage [30]. However, the region of x near unity is very important because the effects of a large value of Δ are mitigated.

To understand this, let’s compute the form factor using Eq. (11) in Eq. (10) with $m \equiv (n + 1)/2$. Combining denominators using the Feynman parametrization and integrating over the transverse momentum variable leads to the result

$$F_m(\Delta^2) = CK_m \int_0^1 dx \int_0^1 du \frac{(x(1-x))^{2m-1} (u(1-u))^{m-1}}{(1+\Delta^2(1-x)^2 u(1-u))^{2m-1}}, \quad (12)$$

with Δ^2 expressed in units of M^2 , and $CK_m = \frac{\Gamma(4m)\Gamma(m+1)}{\Gamma(m)^2\Gamma(2m)}$. A brief look at the integrand of Eq. (12) shows why it is difficult to determine the asymptotic behavior of $F(\Delta^2)$. The value of Δ^2 can be taken to be large, but the multiplying factor, $(1-x)^2 u(1-u)$ can be very small. One must do the integral first and then take Δ^2 to be large. Closed form expressions for F_m can be obtained for values of m between 1 and 3, and the asymptotic forms of F_m for $n = 1, 2, 3$ are shown in Table I.

n	$\lim_{\Delta^2 \rightarrow \infty} F_m(\Delta^2)$
1	$6 \left(\frac{\log^2(\Delta^2) - 4 \log(\Delta^2) + 8}{2\Delta^2} - \frac{2(\log(\Delta^2) + 2)}{\Delta^4} \right)$
2	$180\sqrt{\pi} \left(\frac{(\Delta^2 - 6) \log(\sqrt{\Delta^2} + \sqrt{\frac{\Delta^2}{4} + 1})}{(\Delta^2)^{5/2}} + \frac{16 - 5\sqrt{\Delta^2 + 4}}{2\Delta^4} \right)$
3	$840 \left(\frac{3(\log^2(\Delta^2) - 3 \log(\Delta^2) + 7)}{\Delta^6} + \frac{3 \log(\Delta^2) - 14}{6\Delta^4} \right)$

TABLE I. Asymptotic behavior of F_m . The two leading terms are kept, and $n = 2m - 1$.

The results in Table I and Eq. (11) show that the Drell-Yan-West relations Eq. (1) and Eq. (2) are violated by the logarithms, which are not related to those of perturbative QCD that involve the strong coupling constant α_S . If one uses the quark counting relations Eq. (3), Eq. (4) with $\Delta\gamma = 0$ from using the hadronic scale, and $n = 2n_s, n_H = n_s + 1 = n/2 + 1$ the powers of Δ^2 do not match. In particular, if $n = 2$ quark counting rules would say $F \sim 1/\Delta^2$ instead we observe that $F \sim \log \Delta/\Delta^3$. Moreover, the appearance of logarithms in Table 1 shows that the approach to asymptotic limit is extremely slow. Power law wave functions are not consistent with quark counting rules, but nevertheless are relevant. This is because terms like $\Delta^2(1-x)^2 u(1-u)$ appear in the integrals resulting from the evaluation of Feynman diagrams and the values of x and u approach unity when evaluating integrals.

REALISTIC FORM FACTORS

The next step is to see if the power law form has any phenomenological relevance. To this end, we note that $q(x)$ at ζ_H^2 is described as a parameter-free prediction of the pion valence-quark distribution function in Ref. [7, 29]:

$$q(x) = 375.32x^2(1-x)^2 [1 - 2.5088\sqrt{x(1-x)} + 2.0250x(1-x)]^2, \\ \equiv \sum_{N=4}^8 C_N (x(1-x))^{N/2}. \quad (13)$$

This distribution is defined as Model 1. The corresponding pion wave function can then be written in a more general form than Eq. (11) as

$$\Phi(z) = \frac{1}{\sqrt{\pi}} \sum_{n=3}^5 \frac{A_n}{z^{n/2}}. \quad (14)$$

Then, using Eq. (5)

$$q(x) = \sum_{n=3}^5 \sum_{N=4}^8 \frac{2}{N} A_n A_{N+2-n} (x(1-x))^{N/2}. \quad (15)$$

Then A_n is determined by equating Eq. (15) with Eq. (13). The result is

$$q(x) = \sum_{n=3}^5 \sum_{N=4}^8 \tilde{C}(n, N+2-n) (x(1-x))^{N/2}, \quad (16)$$

with $\tilde{C}(3,3) = C_4$, $\tilde{C}(3,4) = C_5$, $\tilde{C}(3,5) = 3C_6 - (7/4)^2 C_7^2/C_8$, $\tilde{C}(4,4) = (7/4)^2 C_7^2/C_8$, $\tilde{C}(4,5) = 7/4 C_7$, $\tilde{C}(5,5) = 4C_8$, and $\tilde{C}(n,m) = \tilde{C}(m,n)$.

The form factor is obtained from Eq. (10) and is given by

$$F(\Delta^2) = \sum_{m,n=3}^5 \tilde{C}(n,m) I_{nm}(\Delta^2)$$

$$I_{nm} \equiv \frac{\delta_{n+m,N+2}}{B(n/2,m/2)} \int_0^1 dx (x(1-x))^{N/2-1} \int_0^1 du \frac{u^{n/2-1}(1-u)^{m/2-1}}{(1-\Delta^2(1-x)^2u(1-u))} \quad (17)$$

with B the beta function. The results are shown in Fig. 1. The units of Δ^2 are converted to GeV^2 by introducing a mass scale. We use $M = 134 \text{ MeV}$ to reproduce measured data.

An alternative model, Model 2 is presented in Ref. [18]:

$$\tilde{q}(x) = 213.32(x(1-x))^2 \times (1 - 2.9342\sqrt{x(1-x)} + 2.2911x(1-x)). \quad (19)$$

This quark distribution can be rewritten in a form consistent with $\Phi^2(M^2/x(1-x))$:

$$\tilde{q}(x) = \frac{C}{(\Lambda^2 + \frac{M^2}{x(1-x)})^\alpha}. \quad (20)$$

The constants are given by $\frac{M^2}{\Lambda^2} = 0.0550309$ and $\alpha = 3.26654703$. and C is for normalization. Note that the end-point behavior of the two expressions Eq. (19) and Eq. (20) are very different with latter $\sim (1-x)^{3.27}$ instead of an exponent of 2. Nevertheless, the first 11 moments are reproduced to better than 1%. The next 5 to better than 2%. The two distributions are experimentally indistinguishable, showing the elusive behavior of the end-point behavior of $q(x)$.

Using Eq. (6) yields the square of the wave function to be

$$\Phi^2(z) = \frac{\alpha C}{\Lambda^{2\alpha}(1+z)^{1+\alpha}}. \quad (21)$$

Then using Eq. (10) the form factor is found to be

$$\tilde{F}(\Delta^2) = K \int_0^1 dx \int_0^1 du \frac{(x(1-x))^\alpha (u(1-u))^{\frac{1}{2}(\alpha-1)}}{[x(1-x) + M^2 + \Delta^2(1-x)^2u(1-u)]^\alpha} \quad (22)$$

Integration over u leads to the generalized parton distribution $H(x, \Delta^2)$:

$$H(x, \Delta^2) \propto \frac{((1-x)x)^{2\beta-1} {}_2F_1\left(\frac{1}{2}, 2\beta-1; \beta+\frac{1}{2}; \frac{(1-x)^2\Delta^2}{(1-x)^2\Delta^2+4(M^2+(1-x)x)}\right)}{(4(M^2+(1-x)x)+\Delta^2(1-x)^2)^{1-2\beta}} \quad (23)$$

where $\beta = (1+\alpha)/2$ and ${}_2F_1$ is the hypergeometric function and $H(x,0) = \tilde{q}(x)$. Both M^2 and Δ^2 are given in units of Λ^2 . We choose $\Lambda^2 = 0.36 \text{ GeV}^2$ to reproduce data. The corresponds to $M = 140 \text{ MeV}$.

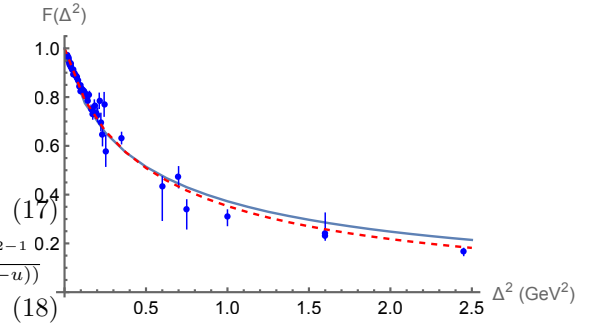


FIG. 1. $F(\Delta^2)$ Solid - Model 1, $F(\Delta^2)$ of Eq. (10). Dashed - Model 2, $\tilde{F}(\Delta^2)$ of Eq. (22). The data for $\Delta^2 \leq 0.253 \text{ GeV}^2$ are from CERN Ref. [31]. The data for higher values are from JLab [32].

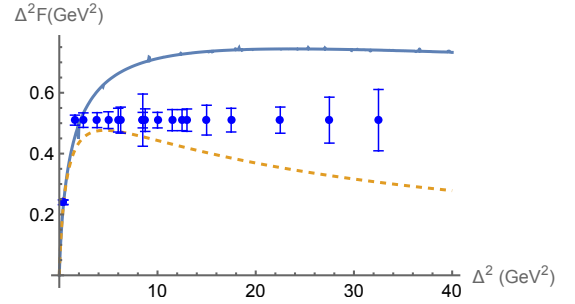


FIG. 2. $\Delta^2 F(\Delta^2)$ in units of GeV^2 . Solid - Model 1, $F(\Delta^2)$ of Eq. (10). Dashed - Model 2, $\tilde{F}(\Delta^2)$ of Eq. (22). The projected error bars for the data points between $\Delta^2 = 0.375$ and 6 GeV^2 are from [33] and G. M. Huber (private communication). The projected error bars for the data points between $\Delta^2 = 8.50$ and 15 GeV^2 are from [34] and show what might be possible at a 22 GeV facility at JLab. The projected error bars for higher values of Δ^2 are from G. M. Huber (private communication) and [35]. In each case the values of $F(\Delta^2)$ are arbitrary.

The result for both form factors are shown in Fig. 2. There are significant differences in the region that is not yet experimentally explored.

CONCLUSIONS

If the non-perturbative pion wave function can be modeled as a power-law form, or if the high- x behavior is important for computing the form factor, both the Drell-Yan & West relations and quark counting rules for the pion are not correct. Based on our calculations we propose that the Drell-Yan-West relations should be modified to

$$\lim_{x \rightarrow 1} q(x) = (1-x)^{n_H} \rightarrow F_1(\Delta^2) \sim \frac{\log(\Delta^2)}{(\Delta^2)^{(n_H+1)/2}}, \quad (24)$$

with $q(x)$ evaluated at the hadron scale ζ_H^2 , and with the log not accompanied by a factor involving the strong coupling constant, α_S .

ACKNOWLEDGEMENTS

The work of M.A. is partially supported by the Research in Undergraduate Institutions Program of the US National Science Foundation under Grant No. 2012982. The work of G.A.M. is partially supported by the DOE Office of Science, Office of Nuclear Physics under Grant DE-FG02-97ER-41014. We thank Garth Huber for providing the data in Figs. 1 & 2. We thank Craig Roberts for many useful discussions. This work is inspired by the QGT Topical Collaboration.

-
- [1] Arlene C. Aguilar *et al.*, “Pion and Kaon Structure at the Electron-Ion Collider,” *Eur. Phys. J. A* **55**, 190 (2019), [arXiv:1907.08218 \[nucl-ex\]](#).
- [2] B. Adams *et al.*, “Letter of Intent: A New QCD facility at the M2 beam line of the CERN SPS (COMPASS++/AMBER),” (2018), [arXiv:1808.00848 \[hep-ex\]](#).
- [3] Roy J. Holt and Craig D. Roberts, “Distribution Functions of the Nucleon and Pion in the Valence Region,” *Rev. Mod. Phys.* **82**, 2991–3044 (2010), [arXiv:1002.4666 \[nucl-th\]](#).
- [4] Guy F. de Teramond, Tianbo Liu, Raza Sabbir Sufian, Hans Günter Dosch, Stanley J. Brodsky, and Alexandre Deur (HLFHS), “Universality of Generalized Parton Distributions in Light-Front Holographic QCD,” *Phys. Rev. Lett.* **120**, 182001 (2018), [arXiv:1801.09154 \[hep-ph\]](#).
- [5] P. C. Barry, Chueng-Ryong Ji, N. Sato, and W. Melnitchouk (Jefferson Lab Angular Momentum (JAM)), “Global QCD Analysis of Pion Parton Distributions with Threshold Resummation,” *Phys. Rev. Lett.* **127**, 232001 (2021), [arXiv:2108.05822 \[hep-ph\]](#).
- [6] Z. F. Cui, Minghui Ding, J. M. Morgado, K. Raya, D. Binosi, L. Chang, F. De Soto, C. D. Roberts, J. Rodríguez-Quintero, and S. M. Schmidt, “Emergence of pion parton distributions,” *Phys. Rev. D* **105**, L091502 (2022), [arXiv:2201.00884 \[hep-ph\]](#).
- [7] Z. F. Cui, Minghui Ding, J. M. Morgado, K. Raya, D. Binosi, L. Chang, J. Papavassiliou, C. D. Roberts, J. Rodríguez-Quintero, and S. M. Schmidt, “Concerning pion parton distributions,” *Eur. Phys. J. A* **58**, 10 (2022), [arXiv:2112.09210 \[hep-ph\]](#).
- [8] S. D. Drell and Tung-Mow Yan, “Connection of Elastic Electromagnetic Nucleon Form-Factors at Large Q^{*2} and Deep Inelastic Structure Functions Near Threshold,” *Phys. Rev. Lett.* **24**, 181–185 (1970).
- [9] Geoffrey B. West, “Phenomenological model for the electromagnetic structure of the proton,” *Phys. Rev. Lett.* **24**, 1206–1209 (1970).
- [10] Stanley J. Brodsky and Glennys R. Farrar, “Scaling Laws at Large Transverse Momentum,” *Phys. Rev. Lett.* **31**, 1153–1156 (1973).
- [11] Stanley J. Brodsky and Glennys R. Farrar, “Scaling Laws for Large Momentum Transfer Processes,” *Phys. Rev. D* **11**, 1309 (1975).
- [12] Glennys R. Farrar and Darrell R. Jackson, “Pion and Nucleon Structure Functions Near $x=1$,” *Phys. Rev. Lett.* **35**, 1416 (1975).
- [13] Glennys R. Farrar and Darrell R. Jackson, “The Pion Form-Factor,” *Phys. Rev. Lett.* **43**, 246 (1979).
- [14] Dennis W. Sivers, “WHAT CAN WE COUNT ON?” *Ann. Rev. Nucl. Part. Sci.* **32**, 149–175 (1982).
- [15] R. L. Jaffe and Graham G. Ross, “Normalizing the Renormalization Group Analysis of Deep Inelastic Leptonproduction,” *Phys. Lett. B* **93**, 313–317 (1980).
- [16] A. De Rújula and François Martin, “Structure of hadron structure functions,” *Phys. Rev. D* **22**, 1787–1808 (1980).
- [17] Stanley J. Brodsky and G. Peter Lepage, “Perturbative Quantum Chromodynamics,” *Prog. Math. Phys.* **4**, 255–422 (1979).
- [18] Minghui Ding, Khépani Raya, Daniele Binosi, Lei Chang, Craig D Roberts, and Sebastian M. Schmidt, “Symmetry, symmetry breaking, and pion parton distributions,” *Phys. Rev. D* **101**, 054014 (2020), [arXiv:1905.05208 \[nucl-th\]](#).
- [19] M V Terent’ev, “On the structure of the wave functions of mesons considered as bound states of relativistic quarks,” *Sov. J. Nucl. Phys. (Engl. Transl.; (United States))* **24**, 1 (1976).
- [20] L. L. Frankfurt and M. I. Strikman, “High-Energy Phenomena, Short Range Nuclear Structure and QCD,” *Phys. Rept.* **76**, 215–347 (1981).
- [21] M. Diehl, “Generalized parton distributions,” *Phys. Rept.* **388**, 41–277 (2003), [arXiv:hep-ph/0307382](#).
- [22] Nathan Isgur and C. H. Llewellyn Smith, “The Applicability of Perturbative QCD to Exclusive Processes,” *Nucl. Phys. B* **317**, 526–572 (1989).
- [23] A.V. Radyushkin, “Hadronic form factors: Perturbative qcd vs qcd sum rules,” *Nuclear Physics A* **532**, 141–154 (1991).
- [24] Adam Szczepaniak, Anatoly Radyushkin, and Chueng-Ryong Ji, “Consistent analysis of $O(\alpha_s)$ corrections to pion elastic form-factor,” *Phys. Rev. D* **57**, 2813–2822 (1998), [arXiv:hep-ph/9708237](#).
- [25] G. A. Miller and J. Pasupathy, “Higher twist and higher order contributions to the pion electromagnetic form-factor,” *Z. Phys. A* **348**, 123–127 (1994).
- [26] Hsiang-nan Li and George F. Sterman, “The Perturbative pion form-factor with Sudakov suppression,” *Nucl. Phys. B* **381**, 129–140 (1992).
- [27] Richard P. Feynman, *Photon-Hadron Interactions* (W. A. Benjamin, Inc., Reading, 1972).
- [28] A. Abdel-Rehim *et al.*, “Nucleon and pion structure with lattice QCD simulations at physical value of the pion mass,” *Phys. Rev. D* **92**, 114513 (2015), [Erratum: *Phys.Rev.D* 93, 039904 (2016)], [arXiv:1507.04936 \[hep-lat\]](#).
- [29] Zhu-Fang Cui, Minghui Ding, Fei Gao, Khépani Raya, Daniele Binosi, Lei Chang, Craig D Roberts, Jose Rodríguez-Quintero, and Sebastian M Schmidt, “Kaon and pion parton distributions,” *Eur. Phys. J. C* **80**, 1064 (2020).
- [30] Stanley J. Brodsky and G. Peter Lepage, “Exclusive Processes in Quantum Chromodynamics,” *Adv. Ser. Direct. High Energy Phys.* **5**, 93–240 (1989).
- [31] S. R. Amendolia *et al.* (NA7), “A Measurement of the Space - Like Pion Electromagnetic Form-Factor,” *Nucl. Phys. B* **277**, 168 (1986).
- [32] G. M. Huber *et al.* (Jefferson Lab), “Charged pion form-factor between $Q^{*2} = 0.60\text{-GeV}^{*2}$ and 2.45-GeV^{*2} . II. Determination of, and results for, the pion form-factor,” *Phys. Rev. C* **78**, 045203 (2008), [arXiv:0809.3052](#)

- [33] [nucl-ex]. “Measurement of the Charged Pion Form Factor to High Q^2 ,” https://www.jlab.org/exp_prog/proposals/06/PR12-06-101.pdf.
- [34] A. Accardi *et al.*, “Strong Interaction Physics at the Luminosity Frontier with 22 GeV Electrons at Jefferson Lab,” (2023), [arXiv:2306.09360](https://arxiv.org/abs/2306.09360) [nucl-ex].
- [35] A. Bylinkin *et al.*, “Detector requirements and simulation results for the EIC exclusive, diffractive and tagging physics program using the ECCE detector concept,” *Nucl. Instrum. Meth. A* **1052**, 168238 (2023), [arXiv:2208.14575](https://arxiv.org/abs/2208.14575) [physics.ins-det].

Neutron radius determination of ^{133}Cs and constraint on the weak mixing angle

Y. Huang,^{1,2} S. Y. Xia,^{3,4} Y. F. Li,^{3,4} X. L. Tu,^{1,*} J. T. Zhang,¹ C. J. Shao,¹
K. Yue,¹ P. Ma,¹ Y. F. Niu,⁵ Z. P. Li,⁶ Y. Kuang,⁶ X. Q. Liu,² J. F. Han,² P.
Egelhof,⁷ Yu. A. Litvinov,⁷ M. Wang,¹ Y. H. Zhang,¹ X. H. Zhou,¹ and Z. Y. Sun¹

¹*Institute of Modern Physics, Chinese Academy of Sciences, Lanzhou 730000, China*

²*Key Laboratory of Radiation Physics and Technology of the Ministry of Education,
Institute of Nuclear Science and Technology, Sichuan University, Chengdu 610064, China*

³*Institute of High Energy Physics, Chinese Academy of Sciences, Beijing 100049, China*

⁴*School of Physical Sciences, University of Chinese Academy of Sciences, Beijing 100049, China*

⁵*School of Nuclear Science and Technology, Lanzhou University, Lanzhou 730000, China*

⁶*School of Physical Science and Technology, Southwest University, Chongqing 400715, China*

⁷*GSI Helmholtzzentrum für Schwerionenforschung GmbH, D-64291 Darmstadt, Germany*

(Dated: March 7, 2024)

Proton- ^{133}Cs elastic scattering at low momentum transfer is performed using an in-ring reaction technique at the Cooler Storage Ring at the Heavy Ion Research Facility in Lanzhou. Recoil protons from the elastic collisions between the internal H_2 -gas target and the circulating ^{133}Cs ions at 199.4 MeV/u are detected by a silicon-strip detector. The matter radius of ^{133}Cs is deduced by describing the measured differential cross sections using the Glauber model. Employing the adopted proton distribution radius, a point-neutron radius of 4.86(21) fm for ^{133}Cs is obtained. With the newly determined neutron radius, the weak mixing angle $\sin^2\theta_W$ is independently extracted to be 0.227(28) by fitting the coherent elastic neutrino-nucleus scattering data. This work limits the $\sin^2\theta_W$ value in a range smaller than the ones proposed by the previous independent approaches.

The weak mixing angle, $\sin^2\theta_W$, is a fundamental parameter in the $SU(2)_L \times U(1)_Y$ electroweak theory of the Standard Model (SM) [1]. Any deviation from the expected $\sin^2\theta_W$ value in SM may serve as an indicative signature of new physics. Historically, the masses of top quark and Higgs boson were successfully predicted by the higher order diagram calculations with the measured $\sin^2\theta_W$ [1].

To precisely constrain the $\sin^2\theta_W$ value, various methods are developed to measure the dependence of $\sin^2\theta_W$ on the transferred momentum [2, 3]. At very low momentum transfer, for instance, one uses the atomic parity nonconservation (PNC) measurements of ^{133}Cs [4, 5]. However, as pointed out in Ref. [6], the $\sin^2\theta_W$ determination via the PNC depends on many theoretical corrections. There is an obvious difference for the PNC amplitude correction associated with neutron skin effects [7]. The effects of the unknown neutron distribution radius of ^{133}Cs on the PNC were addressed about 25 years ago [8].

Recently the coherent elastic neutrino-nucleus scattering (CE ν NS) was observed using a CsI[Na] detector at the Oak Ridge National Laboratory [9]. The CE ν NS measurement provides a clear method to constrain $\sin^2\theta_W$ at low momentum transfer [10] and consequently allows one to investigate neutrino nonstandard interactions [11], dark matter [12], and light vector Z' mediator [13] (see Refs. [6, 14] for details). Although majority of observables were experimentally measured, there was still a lack of precision neutron radii of ^{133}Cs and ^{127}I [11, 13, 15] in interpreting the CE ν NS-CsI data. As underscored by the COHERENT collaboration [11], the uncertainty in the CE ν NS-CsI cross section calculations

is dominated by the neutron distributions of ^{133}Cs and ^{127}I . The influence of the neutron radii on the CE ν NS-CsI data interpretation was also addressed by other independent investigations [15]. In a word, inaccurate or biased treatment of the neutron radii of ^{133}Cs and ^{127}I would lead to the misidentification of possible signals of new physics [15]. Usually, $\sin^2\theta_W$ can be deduced through a fit to the CE ν NS-CsI data by fixing neutron radii from theoretical predictions of various models [11, 16–18]. Alternatively, the neutron radii can be deduced by assuming a fixed $\sin^2\theta_W$ value [19]. Up to date, the reported (average) neutron radii of ^{133}Cs spread from 4.6 fm through 6.6 fm [10, 16, 17, 19–26].

The accurate determination of the neutron radius for ^{133}Cs has garnered significant attention across the atomic, nuclear, and particle physics communities owing to its significance in fundamental researches. However, it is challenging to experimentally measure the neutron radius of ^{133}Cs in normal kinematics, due to the low melting point of 28°C and spontaneous ignition in air. In this Letter, we introduce an innovative approach to determine the neutron radius of ^{133}Cs by measuring the proton elastic scattering at low momentum transfer using an in-ring reaction technique and inverse kinematics. We elucidate the impact of this determination on the $\sin^2\theta_W$ extraction from the recent CE ν NS-CsI data.

The novel in-ring reaction experiment was carried out at the experimental Cooler Storage Ring (CSRe) of the Heavy Ion Research Facility in Lanzhou (HIRFL) [27]. Such kinds of experiments are especially suited for the small-angle differential cross section measurements at low momentum transfer [28, 29]. CSRe, which is equipped

with the electron cooler [30] and the internal H₂-gas-jet target [31], was operated for an in-ring reaction experiment at a magnetic rigidity of about 5.205 Tm. The ¹³³Cs²⁷⁺ beam with an energy of 204 MeV/u from the main storage ring (CSRm) was stripped off all bound electrons utilizing an aluminum foil with a thickness of 0.21 mm at the radioactive ion beam line (RIBLL2). Then the ¹³³Cs⁵⁵⁺ ions with an energy of about 199.4 MeV/u were transported through RIBLL2, and injected into CSRe. The stored ¹³³Cs⁵⁵⁺ ions in CSRe interacted repeatedly with the H₂-gas target of about 10¹² atoms/cm² thickness [31]. The electron cooling at CSRe was operated to compensate for the energy loss of the ions caused by the collisions with the gas target and residual gas. The recoil protons from the *p*-¹³³Cs elastic scattering within angular range from about 85° to 90° in the laboratory system were measured by a double-sided silicon-strip detector (DSSD) with a typical energy resolution of better than 1%. The employed 1000 μm thick DSSD had an active area of 64 × 64 mm² and was segmented into 32 × 32 strips. The proton energy and detection efficiency were calibrated by radioactive sources [29]. Figure 1 illustrates the scatter plot of the recoil proton energy versus the strip number of DSSD. Further experimental details were described in our previous works [29, 32, 33].

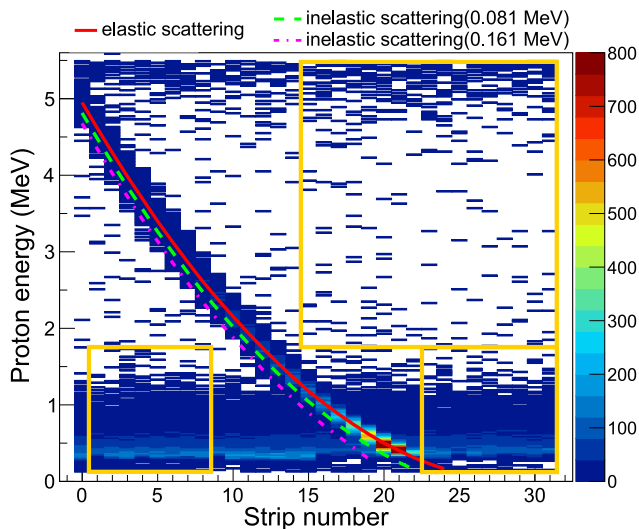


FIG. 1. Scatter plot of the recoil proton energy versus the strip number of DSSD. The solid (red), dashed (green), and dash-dotted (pink) lines denote the calculated proton energies for elastic and two inelastic scattering channels, respectively. For more details see text.

Given the fact that the flight paths and energies of recoil protons are hardly altered by secondary collisions with the thin gas target, the relative small-angle differential cross sections $\frac{d\sigma}{d\Omega}(\theta)$ of *p*-¹³³Cs elastic scattering are

determined via [29]

$$\frac{d\sigma}{d\Omega}(\theta) = \frac{1}{\sin\theta} \left(\frac{\Delta N_{\text{all}}}{\Delta\theta} - \frac{\Delta N_{\text{bg}}}{\Delta\theta} \right), \quad (1)$$

where ΔN_{all} is the number of all measured events in the scattering angle interval $\Delta\theta$ in the center-of-mass (c.m.) frame, and ΔN_{bg} is the corresponding background estimated by the measured events in the rectangles enclosed by the yellow solid lines, see Fig. 1. The scattering angles θ were determined by the proton kinematic energies K_{lab} via the relation of $2m_p K_{\text{lab}} = 2p^2(1 - \cos\theta)$, with m_p and p being the proton rest mass and the c.m. momentum, respectively. The uncertainties of θ are smaller than the used $\Delta\theta$ value of 0.1°. To reduce the effects of solid angle and detection efficiency [29], only single coincidence events between *X* and *Y* strips within the energy range of about 0.6 MeV through 3.6 MeV were considered. As shown in Fig. 1, the events of elastic scattering are mixed, to some extent, with those of inelastic scattering associated with the low-lying 0.08- and 0.16-MeV excited states [34]. Nevertheless, according to the FRESKO calculations [35] with the phenomenological optical model [36], the inelastic scattering cross sections are several orders of magnitude smaller than those of the elastic scattering in the measured small angular range and, especially, the trend of obtained $\frac{d\sigma}{d\Omega}(\theta)$ values agrees well with the FRESKO calculations, see the insert of Fig. 2. Therefore, the contribution of the inelastic scattering can be safely ignored. The measured small-angle $\frac{d\sigma}{d\Omega}(\theta)$ values are shown in Fig. 2.

It is well known that the small-angle elastic $\frac{d\sigma}{d\Omega}(\theta)$ distributions are sensitive to matter distribution radius [28, 29, 37–40]. Especially, the reaction mechanism is relatively simple at small angles and thus correction terms of reaction models are negligible compared to the cases of large angle scattering [41, 42]. In addition, the model-dependent errors related to the hadronic probes [43] can also be effectively reduced through calibrating the input parameters of reaction models using the well-known nuclear radii [29, 44–46]. Therefore, many experimental setups at various facilities are developed to determine the matter radii by measuring the small-angle $\frac{d\sigma}{d\Omega}(\theta)$ of *p*-nucleus elastic scattering [28, 29, 32, 37–39]. In the present work, a well established procedure [41, 46, 47] based on the Glauber multiple-scattering theory [48] is employed to extract the matter radius of ¹³³Cs through describing the measured $\frac{d\sigma}{d\Omega}(\theta)$. The $\frac{d\sigma}{d\Omega}(\theta)$ values are expressed in the Glauber model as a function of the matter density distribution $\rho(r)$ and the proton-nucleon scattering amplitude $f_{pi}(q)$ with $i = n$ or p , see Ref. [47] for details. To reduce the model-dependent errors of matter radius, the scattering amplitude parameters were calibrated at 200 MeV [45] to be $\sigma_{pp} = 1.788(20)$ fm², $\sigma_{pn} = 3.099(27)$ fm², $\alpha_{pp} = 0.893(17)$, $\alpha_{pn} = 0.325(23)$, and $\beta_{pp} = \beta_{pn} = 0.528(41)$ fm², which are adopted here to calculate the $f_{pi}(q)$. Note that these

values can reproduce the well-known matter radius of ^{16}O [45].

In the radius fitting procedure, the $\rho(r)$ is described by the two-parameter Fermi model as

$$\rho(r) = \frac{\rho(0)}{1 + \exp[(r - R)/a]}, \quad (2)$$

with $\rho(0)$, R , and a being the density normalization factor, half-density radius, and diffuseness parameter, respectively. Although the R and a values cannot be simultaneously constrained by $\frac{d\sigma}{d\Omega}(\theta)$ in small angular range [29], the matter radius is almost independent of a for the medium-heavy nuclei [47]. Thus, following the methods in [29, 47, 49, 50], we set $a = 0.53(3)$ fm, which was deduced from the neighbouring $^{116,124}\text{Sn}$ and ^{208}Pb nuclei [47]. Additionally, a free cross section normalization factor L_0 is introduced as in Refs. [29, 40, 47] to reduce the radius uncertainty from the absolute $\frac{d\sigma}{d\Omega}(\theta)$ normalization. Subsequently, R and L_0 are freely adjusted to fit the experimental $\frac{d\sigma}{d\Omega}(\theta)$ with the Glauber model.

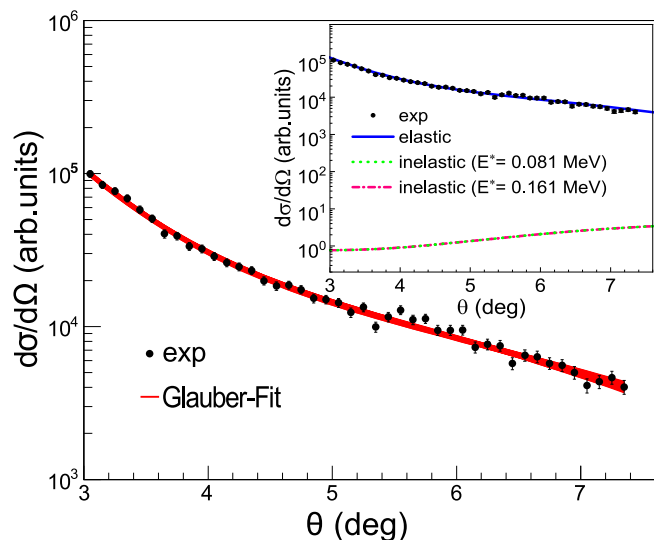


FIG. 2. The measured $\frac{d\sigma}{d\Omega}(\theta)$ for p - ^{133}Cs elastic scattering and the 2σ distribution of fit curves (red). The insert shows the calculated elastic and inelastic differential cross sections using FRESKO [35]. Conveniently $\frac{d\sigma}{d\Omega}(\theta)$ are normalized to the FRESKO calculations.

As shown in Fig. 2, the measured $\frac{d\sigma}{d\Omega}(\theta)$ are well described with the Glauber model by adjusting R and L_0 . With the obtained R and fixed a , a root-mean-square (rms) point-matter radius R_{pm} for ^{133}Cs is determined to be

$$R_{\text{pm}} = \left(\frac{\int \rho(r)r^4 dr}{\int \rho(r)r^2 dr} \right)^{\frac{1}{2}} = 4.811 \pm 0.127 \text{ fm}, \quad (3)$$

where uncertainties from statistics, input parameters, and Glauber model are about 0.12 fm, 0.03 fm, and

0.03 fm, respectively. The radius uncertainties caused by statistics and input parameters are estimated by using the randomly sampled experimental $\frac{d\sigma}{d\Omega}(\theta)$ and input parameters within 2σ band [47], respectively. The model-dependent error at 200 MeV is estimated by comparing the well-known proton radii with the matter radii of the $N = Z$ nuclei [45], where similar proton and matter radii are expected. To check the effects of background, only recoil protons with energies > 1 MeV were analyzed, and a consistent radius of 4.825 fm is obtained. Details and reliability considerations about radius determinations can be found in Refs. [29, 47].

With the obtained R_{pm} , a point-neutron distribution radius R_{pn} of ^{133}Cs is determined to be

$$R_{\text{pn}} = \sqrt{\frac{A}{N}R_{\text{pm}}^2 - \frac{Z}{N}R_{\text{pp}}^2} = 4.86 \pm 0.21 \text{ fm}, \quad (4)$$

where N , Z , and A are the neutron, proton, and mass number, respectively. The adopted point-proton radius R_{pp} of 4.740(5) fm for ^{133}Cs is deduced from charge radius [29, 51].

We extract the neutron skin of ^{133}Cs to be $R_{\text{pn}} - R_{\text{pp}} = 0.12(21)$ fm. Meanwhile, using the linear relationships, established by various effective interactions [52], we also derive the neutron skin to be 0.14 fm from the Parity-violating electron scattering data of ^{48}Ca and ^{208}Pb [53, 54]. The two values are consistent with each other, and agree to the value of 0.13 fm calculated by the empirical linear relationship from the antiprotonic atom experiment [55]. The latter was adopted to estimate the PNC amplitude correction associated with the neutron skin effects [56].

Now we discuss the impact of the neutron radius on the $\sin^2\theta_W$ determination employing the CE ν NS-CsI data [11]. For the description of the CE ν NS-CsI data in SM, $\sin^2\theta_W$ and the neutron distribution form factor $F_n(q^2)$ are involved, see Ref. [26] for details. The folded-neutron radii $R_{\text{fn}}(\text{Cs})$ and $R_{\text{fn}}(\text{I})$ for ^{133}Cs and ^{127}I are indispensable to determine the corresponding $F_n(q^2)$. Previous analyses indicated that different parameterizations of nuclear form factors would not lead to different $\sin^2\theta_W$ [10, 13, 26]. In this work, the Helm form factor is adopted to calculate the expected CE ν NS-CsI signal event number, which is related to R_{fn} through the diffraction radius R_0 defined as [26]

$$R_0(\text{K}) = \sqrt{5/3[R_{\text{fn}}(\text{K})^2 - 3s^2]}, \quad (5)$$

where $s = 0.9$ fm is the surface thickness and $\text{K} = \text{I}$ or Cs . The R_{fn} can be directly determined from the point-neutron radius via $[R_{\text{pn}}^2 + (0.864 \text{ fm})^2]^{1/2}$ [18].

Figure 3 depicts the CE ν NS-CsI signal event number as a function of the photoelectron number expected with different $R_{\text{fn}}(\text{Cs})$. In this work, the radius $R_{\text{fn}}(\text{I})$ is determined using the $R_{\text{fn}}(\text{Cs})$ value via $R_{\text{fn}}(\text{Cs}) - R_{\text{fp}}(\text{Cs}) + R_{\text{fp}}(\text{I})$ considering that ^{133}Cs and ^{127}I

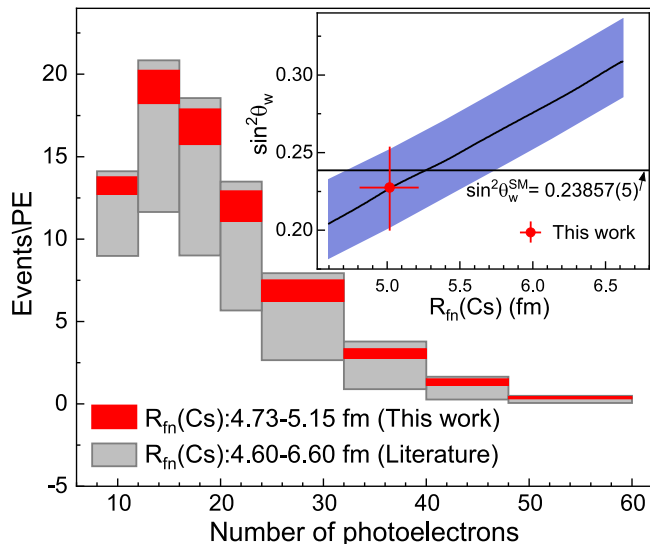


FIG. 3. The expected $\text{CE}\nu\text{NS-CsI}$ signal event number as a function of the photoelectron number calculated by using different neutron radii of ^{133}Cs . The gray area is obtained by using the reported (average) neutron radii of ^{133}Cs ranging from 4.6 fm [17] to 6.6 fm [26], see Fig. 4(b). The red values are calculated with the presently deduced radius. The inset shows a correlation between $R_{\text{fn}}(\text{Cs})$ and $\sin^2\theta_W$, where the blue area is the uncertainty caused by the $\text{CE}\nu\text{NS-CsI}$ data [11].

have almost the same neutron skin thicknesses [55], where the folded-proton radius $R_{\text{fp}}(\text{K})$ is determined by the well-known charge radius [18, 51]. It is evident that the shape of the expected event spectrum is significantly affected by the adopted neutron radius of ^{133}Cs , which is similar as addressed in Ref. [15]. As indicated in the inset of Fig. 3, there exists a strong correlation between the values of $R_{\text{fn}}(\text{Cs})$ and $\sin^2\theta_W$ in the $\text{CE}\nu\text{NS-CsI}$ data analysis. An incorrect neutron radius can thus introduce significant shift in the estimation of $\sin^2\theta_W$.

Previously, a method was used combining the $\text{CE}\nu\text{NS}$ and PNC data to precisely constrain $\sin^2\theta_W$ [26]. However, possible new physics in either the $\text{CE}\nu\text{NS}$ or PNC process may be ignored in such analysis due to the assumption that the two processes give the same $\sin^2\theta_W$ value. In addition, the PNC amplitude corrections depend on theory [6], which may result in different values of $\sin^2\theta_W$ [26].

To avoid any improper input of neutron radius and $\sin^2\theta_W$, we performed an independent two-dimensional (2D) fit as Refs. [10, 26] using both R_{fn} and $\sin^2\theta_W$ as free adjustable parameters. The $\sin^2\theta_W$ value from the best fit is shown in Fig. 4 as the blue symbol. The blue curves represent the distributions of the $\sin^2\theta_W$ values obtained from fitting procedures under different confidence levels (CL). Because of the strong correlation of the two free parameters, the independent 2D fit can not yield a well-constrained $\sin^2\theta_W$ value, nor the realistic

neutron radius, as shown in Fig. 4. Therefore accurate neutron radius is essential to deduce the $\sin^2\theta_W$ value and then to search for new physics beyond SM.

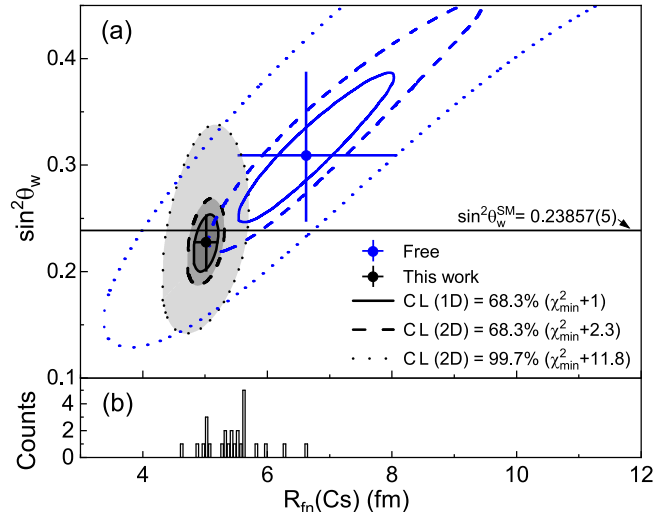


FIG. 4. (a) The χ_{all}^2 contours in the plane of R_{fn} versus $\sin^2\theta_W$. The blue curves and point represent results when both R_{fn} and $\sin^2\theta_W$ are free variables in the $\text{CE}\nu\text{NS-CsI}$ data fitting. The black curves and point add the constraint imposed by the presently deduced radius. (b) The distribution of reported neutron radii of ^{133}Cs [10, 16, 17, 19–26] deduced from the $\text{CE}\nu\text{NS-CsI}$ data [9, 11].

To show the impact of our newly determined neutron radius on the $\sin^2\theta_W$ value, the expected $\text{CE}\nu\text{NS}$ events are fitted to the experimental events by adjusting $\sin^2\theta_W$ and $R_{\text{fn}}^{\text{fit}}(\text{Cs})$ via the chi-square function defined here as

$$\chi_{\text{all}}^2 = \chi_{\text{CsI}}^2(R_{\text{fn}}^{\text{fit}}(\text{Cs}), \sin^2\theta_W) + \left(\frac{R_{\text{fn}}^{\text{fit}}(\text{Cs}) - R_{\text{fn}}^{\text{exp}}(\text{Cs})}{\sigma^{\text{exp}}} \right)^2, \quad (6)$$

where σ^{exp} is the uncertainty of $R_{\text{fn}}^{\text{exp}}(\text{Cs})$. The χ_{CsI}^2 was constructed (see Ref. [26] for details) and used for the free two-dimensional fit as mentioned above. The used $R_{\text{fn}}^{\text{exp}}(\text{Cs})$ of 4.936(210) fm is obtained by the presently deduced point-neutron radius. Now, for the first time we fix the range of neutron radii in the second term of Eq. (6). As a consequence, $\sin^2\theta_W$ of 0.227(28) is independently extracted from the best fit to the $\text{CE}\nu\text{NS-CsI}$ data [11] as shown with the black symbol in Fig. 4, the uncertainty of which is mainly caused by the $\text{CE}\nu\text{NS-CsI}$ data [11] (see the red symbol and blue area in the inset of Fig. 3). The black curves represent the distributions of the $\sin^2\theta_W$ values obtained from fitting procedures for different CL. Compared to the $\sin^2\theta_W$ value of $0.309_{-0.063}^{+0.078}$ determined by the free independent 2D fit, our analysis well constrains the $\sin^2\theta_W$ value and improves its precision by a factor of about 2.5.

Our determined value $\sin^2\theta_W = 0.227(28)$ agrees within error bars with the SM prediction of 0.23857(5) at

low momentum transfer [57]. We note that our central value is marginally lower than the SM prediction. This is consistent with the trend observed in the PNC $\sin^2\theta_W$ estimation by Particle Data Group at 0.2367(18) [57]. In order to study the significance of the possible deviation from the SM prediction, it deserves to further improve the precision of $\sin^2\theta_W$.

In conclusion, the proton elastic scattering off ^{133}Cs at 199.4 MeV/u was investigated in inverse kinematics at HIRFL-CSR. Combined with the proton distribution radius, a point-neutron radius of 4.86(21) fm for ^{133}Cs was extracted. For the first time we fix the range of neutron radii of ^{133}Cs in the $\text{CE}\nu\text{NS-CsI}$ data analysis, and consequently the weak mixing angle was extracted independently with high accuracy. Our work constitutes a new approach for the interpretation of high precision $\text{CE}\nu\text{NS-CsI}$ data in the near future.

We thank the staffs in the accelerator division for providing a stable beam. This work is supported in part by the National Key R&D Program of China (Grant No. 2023YFA1606401), by the NSFC (Grants No. 12022504, No. 12121005, No. 12375115, No. 12075255, and No. 12275186), and by the CAS Open Research Project of large research infrastructures.

* tuxiaolin@impcas.ac.cn

- [1] F. Suekane, *Quantum Oscillations, Lecture Notes in Physics* **985**, Springer Nature Switzerland AG 2021.
- [2] K. S. Kumar, S. Mantry, W. J. Marciano, and P. A. Souder, *Annu. Rev. Nucl. Part. Sci.* **63**, 237 (2013).
- [3] The ALEPH Collaboration, The DELPHI Collaboration, The L3 Collaboration, The OPAL Collaboration, The SLD Collaboration, The LEP Electroweak Working Group, The SLD Electroweak, and Heavy Flavour Groups, *Phys. Rep.* **427**, 257 (2006).
- [4] V. A. Dzuba, J. C. Berengut, V. V. Flambaum, and B. Roberts, *Phys. Rev. Lett.* **109**, 203003 (2012).
- [5] C. S. Wood, S. C. Bennett, D. Cho, B. P. Masterson, J. L. Roberts, C. E. Tanner, and C. E. Wieman, *Science* **275**, 1759 (1997).
- [6] M. Cadeddu, F. Dordei, and C. Giunti, *Europhys. Lett.* **143**, 34001 (2023).
- [7] B. K. Sahoo, B. P. Das, and H. Spiesberger, *Phys. Rev. D* **103**, L111303 (2021).
- [8] S. J. Pollock and M. C. Welliver, *Phys. Lett. B* **464**, 177 (1999).
- [9] D. Akimov, J. B. Albert, P. An, C. Awe, P. S. Barbeau, B. Becker, V. Belov, A. Brown, A. Bolozdynya, B. Cabrera-Palmer *et al.*, *Science* **357**, 1123 (2017).
- [10] X. -R. Huang and L. -W. Chen, *Phys. Rev. D* **100**, 071301(R) (2019).
- [11] D. Akimov, P. An, C. Awe, P. S. Barbeau, B. Becker, V. Belov, I. Bernardi, M. A. Blackston, C. Bock, A. Bolozdynya *et al.*, *Phys. Rev. Lett.* **129**, 081801 (2022).
- [12] D. Akimov, P. An, C. Awe, P. S. Barbeau, B. Becker, V. Belov, I. Bernardi, M. A. Blackston, C. Bock, A. Bolozdynya *et al.*, *Phys. Rev. Lett.* **130**, 051803 (2023).
- [13] M. Cadeddu, N. Cargioli, F. Dordei, C. Giunti, Y. F. Li, E. Picciau, and Y. Y. Zhang, *J. High Energy Phys.* **01**, 116 (2021).
- [14] P. S. Barbeau, Yu. Efremenko, and K. Scholberg, *Annu. Rev. Nucl. Part. Sci.* **73**, 41 (2023).
- [15] D. Aristizabal Sierra, J. Liao, and D. Marfatia, *J. High Energy Phys.* **06**, 141 (2019).
- [16] D. K. Papoulias, *Phys. Rev. D* **102**, 113004 (2020).
- [17] A. N. Khan and W. Rodejohann, *Phys. Rev. D* **100**, 113003 (2019).
- [18] M. Cadeddu, F. Dordei, C. Giunti, Y. F. Li, E. Picciau, and Y. Y. Zhang, *Phys. Rev. D* **102**, 015030 (2020).
- [19] M. Cadeddu, C. Giunti, Y. F. Li, and Y. Y. Zhang, *Phys. Rev. Lett.* **120**, 072501 (2018).
- [20] M. Cadeddu, F. Dordei, C. Giunti, Y. F. Li, and Y. Y. Zhang, *Phys. Rev. D* **101**, 033004 (2020).
- [21] M. Cadeddu, N. Cargioli, F. Dordei, C. Giunti, Y. F. Li, E. Picciau, C. A. Ternes, and Y. Y. Zhang, *Phys. Rev. C* **104**, 065502 (2021).
- [22] P. Coloma, I. Esteban, M. C. Gonzalez-Garcia, and J. Menéndez, *J. High Energy Phys.* **08**, 030 (2020).
- [23] M. Cadeddu and F. Dordei, *Phys. Rev. D* **99**, 033010 (2019).
- [24] V. De Romeri, O. G. Miranda, D. K. Papoulias, G. Sanchez Garcia, M. Tórtola, and J. W. F. Valle, *J. High Energy Phys.* **04**, 035 (2023).
- [25] D. K. Papoulias, T. S. Kosmas, R. Sahu, V. K. B. Kota, and M. Hota, *Phys. Lett. B* **800**, 135133 (2020).
- [26] M. Atzori Corona, M. Cadeddu, N. Cargioli, F. Dordei, C. Giunti, and G. Masia, *Eur. Phys. J. C* **83**, 683 (2023).
- [27] J. W. Xia, W. L. Zhan, B. W. Wei, Y. J. Yuan, M. T. Song, W. Z. Zhang, X. D. Yang, P. Yuan, D. Q. Gao, H. W. Zhao *et al.*, *Nucl. Instrum. Methods Phys. Res. A* **488**, 11 (2002).
- [28] X. Liu, P. Egelhof, O. Kiselev, and M. Mütterer, *Phys. Lett. B* **809**, 135776 (2020).
- [29] J. T. Zhang, P. Ma, Y. Huang, X. L. Tu, P. Sarriguren, Z. P. Li, Y. Kuang, W. Horiuchi, T. Inakura, L. Xayavong *et al.*, *Phys. Rev. C* **108**, 014614 (2023).
- [30] L. J. Mao, H. Zhao, X. D. Yang, J. Li, J. C. Yang, Y. J. Yuan, V. V. Parkhomchuk, V. B. Reva, X. M. Ma, T. L. Yan *et al.*, *Nucl. Instrum. Methods Phys. Res. A* **808**, 29 (2016).
- [31] C. J. Shao, R. C. Lu, X. H. Cai, D. Y. Yu, F. F. Ruan, Y. L. Xue, J. M. Zhang, D. K. Torpokov, and D. Nikolenko, *Nucl. Instrum. Methods Phys. Res. B* **317**, 617 (2013).
- [32] K. Yue, J. T. Zhang, X. L. Tu, C. J. Shao, H. X. Li, P. Ma, B. Mei, X. C. Chen, Y. Y. Yang, X. Q. Liu *et al.*, *Phys. Rev. C* **100**, 054609 (2019).
- [33] J. T. Zhang, K. Yue, H. X. Li, X. L. Tu, C. J. Shao, P. Ma, B. Mei, X. C. Chen, Y. Y. Yang, X. Q. Liu *et al.*, *Nucl. Instrum. Methods Phys. Res. A* **948**, 162848 (2019).
- [34] Yu. Khazov, A. Rodionov, and F. G. Kondev, *Nucl. Data Sheets* **112**, 855 (2011).
- [35] I. J. Thompson, *Comput. Phys. Rep.* **7**, 167 (1988); <http://www.fresco.org.uk/>.
- [36] A. J. Koning and J. P. Delaroche, *Nucl. Phys. A* **713**, 231 (2003).
- [37] G. D. Alkhazov, M. N. Andronenko, A. V. Dobrovolsky, P. Egelhof, G. E. Gavrilov, H. Geissel, H. Irnich, A. V. Khanzadeev, G. A. Korolev, A. A. Lobodenko *et al.*, *Phys. Rev. Lett.* **78**, 2313 (1997).
- [38] G. A. Korolev, A. V. Dobrovolsky, A. G. Inglessi, G. D.

- Alkhazov, P. Egelhof, A. Estradé, I. Dillmann, F. Farinon, H. Geissel, S. Ilieva *et al.*, *Phys. Lett. B* **780**, 200 (2018).
- [39] M. von Schmid, T. Aumann, S. Bagchi, S. Bönig, M. Csatlós, I. Dillmann, C. Dimopoulou, P. Egelhof, V. Eremin, T. Furuno *et al.*, *Eur. Phys. J. A* **59**, 83 (2023).
- [40] Y. Huang, L. Xayavong, X. L. Tu, J. Geng, Z. P. Li, J. T. Zhang, and Z. H. Li, *Phys. Lett. B* **847**, 138293 (2023).
- [41] G. D. Alkhazov, S. L. Belostotsky, and A. A. Vorobyov, *Phys. Rep.* **42**, 89 (1978).
- [42] I. N. Kudryavtsev and A. P. Soznik, *J. Phys. G: Nucl. Part. Phys.* **15**, 1377 (1989).
- [43] M. Thiel, C. Sfienti, J. Piekarewicz, C. J. Horowitz, and M. Vanderhaeghen, *J. Phys. G: Nucl. Part. Phys.* **46**, 093003 (2019).
- [44] S. Terashima, H. Sakaguchi, H. Takeda, T. Ishikawa, M. Itoh, T. Kawabata, T. Murakami, M. Uchida, Y. Yasuda, M. Yosoi *et al.*, *Phys. Rev. C* **77**, 024317 (2008).
- [45] Y. Huang, J. T. Zhang, Y. Kuang, J. Geng, X. L. Tu, K. Yue, W. H. Long, and Z. P. Li, *Eur. Phys. J. A* **59**, 4 (2023).
- [46] G. D. Alkhazov, A. V. Dobrovolsky, P. Egelhof, H. Geissel, H. Irnich, A. V. Khanzadeev, G. A. Korolev, A. A. Lobodenko, G. Münzenberg, M. Mutterer *et al.*, *Nucl. Phys. A* **712**, 269 (2002).
- [47] Y. Huang, X. Y. Wu, X. L. Tu, Z. P. Li, Y. Kuang, J. T. Zhang, and Z. H. Li, *Phys. Rev. C* **108**, 054610 (2023).
- [48] R. J. Glauber, in *Lectures in Theoretical Physics*, edited by W. E. Brittin and L. G. Dunham (Interscience, New York, 1959), Vol. 1, p. 315.
- [49] M. Tanaka, M. Takechi, A. Homma, M. Fukuda, D. Nishimura, T. Suzuki, Y. Tanaka, T. Moriguchi, D. S. Ahn, A. Aimaganbetov *et al.*, *Phys. Rev. Lett.* **124**, 102501 (2020).
- [50] T. Suzuki, H. Geissel, O. Bochkarev, L. Chulkov, M. Golovkov, D. Hirata, H. Irnich, Z. Janas, H. Keller, T. Kobayashi *et al.*, *Phys. Rev. Lett.* **75**, 3241 (1995).
- [51] I. Angeli and K. P. Marinova, *At. Data Nucl. Data Tables* **99**, 69 (2013).
- [52] M. Cadeddu, N. Cargioli, F. Dordei, C. Giunti, and E. Picciau, *Phys. Rev. D* **104**, L011701 (2021).
- [53] D. Adhikari, H. Albataineh, D. Androic, K. Aniol, D. S. Armstrong, T. Averett, C. Ayerbe Gayoso, S. Barcus, V. Bellini, R. S. Beminiwattha *et al.*, *Phys. Rev. Lett.* **126**, 172502 (2021).
- [54] D. Adhikari, H. Albataineh, D. Androic, K. A. Aniol, D. S. Armstrong, T. Averett, C. Ayerbe Gayoso, S. K. Barcus, V. Bellini, R. S. Beminiwattha *et al.*, *Phys. Rev. Lett.* **129**, 042501 (2022).
- [55] A. Trzcińska, J. Jastrzębski, P. Lubiński, F. J. Hartmann, R. Schmidt, T. von Egidy, and B. Klos, *Phys. Rev. Lett.* **87**, 082501 (2001).
- [56] A. Derevianko, *Phys. Rev. A* **65**, 012106 (2001).
- [57] P. A. Zyla, R. M. Barnett, J. Beringer, O. Dahl, D. A. Dwyer, D. E. Groom, C. J. Lin, K. S. Lugovsky, E. Pianori, D. J. Robinson *et al.* (Particle Data Group), *Prog. Theor. Exp. Phys.* **2020**, 083C01 (2020).